Department of Chemical Engineering

Imperial College London

SW7 2AZ, United Kingdom

# Thermophysical Properties of Hydrocarbons with Dissolved Carbon Dioxide

Weparn Julian Tay

March 2017

A thesis submitted in part fulfilment of the requirements for the degree of
Doctor of Philosophy in Chemical Engineering of Imperial College London
and the Diploma of Imperial College London

Originality and Copyright Declaration

*This is an original work by the author, and all else is appropriately referenced. The copyright of this thesis rests with the author and is made available under a Creative Commons Attribution Non-Commercial No Derivatives licence. Researchers are free to copy, distribute or transmit the thesis on the condition that they attribute it, that they do not use it for commercial purposes and that they do not alter, transform or build upon it. For any reuse or redistribution, researchers must make clear to others the licence terms of this work.*

Dedicated to my family

Keng, Serina and Eelyn

# Acknowledgements

The chapter of my life at Imperial is finally coming to an end. During these years, I have met so many wonderful people who have made my time at Imperial College an enjoyable and unforgettable experience. This work would not have been possible without the direct and indirect contribution of many people. Firstly, I would like to my express my sincerest gratitude to my supervisor, Professor J. P. Martin Trusler for his invaluable support, patience and guidance throughout this research. It has been a great honour to be working with Martin, and his expertise in thermophysical properties has a major contribution towards the success of this work. Secondly, I would like to thank the first person I met at Imperial who is also my academic mentor, Professor Geoffrey C. Maitland who offered me the opportunity to be part of the Imperial family. His commitment and passion for energy research has always motivated and inspired me to continue to work as an engineer/scientist. I am grateful for his countless encouragement and advice in many aspects throughout my time in Imperial. I would like to acknowledge and thank Professor Jean-Pierre E. Grolier for providing me with an excellent opportunity for an external research placement in France. I am grateful for the financial support of the Engineering and Physical Sciences Research Council (EPSRC) which provided the full funding for this work.

I would like to thank the people from the mechanical and electrical workshops, in particular: Mr. Gavin Barnes, Mr. Richard Wallington and Mr. Chin Lang for their help and co-operation throughout this work. I would like to give special thanks to everyone in the Thermophysical Group, both present and the past. It has been a privilege to work alongside a group of friendly, knowledgeable and passionate scientists. I am grateful for having the best colleagues in Imperial and thank you for making my PhD journey a memorable time of my life.

Lastly, I would like to dedicate this thesis to my family, Keng, Serina and Eelyn. Words can't express how lucky I am to have such loving parents and sister. I would like to thank my beloved parents who provide me with an opportunity to shine in an educational environment. Without their continuous support and encouragement, this PhD would not be possible, and I wouldn't have grown into the person I am today.

Weparn Julian Tay

2017

# Abstract

Although the thermophysical properties of hydrocarbons have been studied extensively, there remain important gaps in the literature for high-temperature and high-pressure (HTHP) conditions and for mixtures of hydrocarbons with $CO_2$ and other inorganic gases. In this work, thermophysical properties of hydrocarbons with the addition of carbon dioxide ($CO_2$) were studied under conditions of elevated temperatures and pressures that are representative of $CO_2$ injection into hydrocarbon fields for purposes of carbon storage, enhanced oil recovery (EOR) or both. The main focus of this research is to investigate the thermophysical properties experimentally mainly density and sound-speed, in relation to (hydrocarbon + $CO_2$) systems. The representative hydrocarbons chosen were: *n*-pentane, *n*-heptane, *n*-nonane and methylbenzene.

Speed-of-sound measurements for (*n*-pentane, *n*-heptane, *n*-nonane, methylbenzene, $CO_2$ + *n*-nonane and $CO_2$ + methylbenzene) were performed using the double path pulse-echo technique in a state-of-the-art apparatus. It is based on an ultrasonic cell with a single 5 MHz ultrasound transducer placed between two unequally spaced parallel reflectors. The speed-of-sound measurements were carried out at temperatures ranging from (263.15 to 473.15) K and at pressures up to 390 MPa. The path-length of the ultrasonic cell was pre-calibrated with deionised water at $T$ = 298.15 K and $p$ = 1 MPa against the speed-of-sound given by the 1995 equation-of-state formulation of the International Association for the Properties of Water and Steam (IAPWS-95) which for that state point, has an uncertainty of 0.005%. The expanded uncertainty of the sound-speed measurements presented in this work, in general, is less than 0.1 %. The experiment sound-speed data collected were fitted with an empirical polynomial correlation with average absolute relative deviations ($\Delta_{AARD}$) of approximately 0.06 % which is consistent with the specified uncertainty of the measurements. The addition of $CO_2$ decreases the overall speed-of-sound in the $CO_2$ + hydrocarbons mixtures. Density measurements were carried out for (*n*-heptane, *n*-nonane, methylbenzene, $CO_2$, $CO_2$ + *n*-heptane, $CO_2$ + *n*-nonane and $CO_2$ + methylbenzene) with a vibrating-tube densimeter (VTD) at a temperature range of (283.15 to 473.15) K and pressures up to 68 MPa. The measurements were associated with an absolute uncertainty of less than 1 $kg \cdot m^{-3}$. Different calibration methods of the VTD were reviewed and a new calibration method based on the physical parameters of the densimeter was proposed. The VTD used in the present work was calibrated under vacuum, helium and water over the full temperature and pressure range of interest. The experimental densities show a typical density trend for liquids: increase with pressure but decrease with temperature. The experimental density for pure components was fitted by the modified Tait equation, permitted the interpolation/extrapolation of the data as a function of temperature and pressure to compare with the available literature. The average absolute relative deviations between the experimental data and the predictions were approximately 0.04 % across the pressure and temperature

range investigated. For the density of the binary mixtures, a density crossover was observed with the addition of $CO_2$. A non-linear empirical correlation was developed which fitted the experimental data with an $\Delta_{AARD}$ of approximately 0.1 %. The excess molar volumes were calculated from the binary mixtures densities, showing a highly non-ideal mixing behaviour of the binary systems studied. The results were correlated with the Redlich-Kister polynomial equation. Bubble pressures for ($CO_2$ + *n*-heptane and $CO_2$ + methylbenzene) were obtained by combining the binary mixtures densities with the saturated-phase densities. In the cases where the speed-of-sound and density for pure hydrocarbons were measured (*n*-heptane, *n*-nonane and methylbenzene), the experimental data were combined with knowledge of isobaric heat capacity to derive a complete spectrum of thermodynamic properties over the range of temperatures and pressures covered by the sound-speed measurements by means of thermodynamic integration. In addition, a study on the thermophysical properties of two types of hydrocarbon oils has been carried out. Viscosity and isobaric heat capacity measurements have been included on top of the properties mentioned above; empirical correlations were developed for the measured properties.

Lastly, the experimental data for the hydrocarbon systems have been compared with predictions calculated from various types of equations of state (EoSs): PPR78, SAFT-γ Mie, and the multi-parameter Helmholtz energy explicit equations of state. It can be concluded that the agreement between the experimental data and predictions from these models is satisfactory. However, there is scope for further improvement in the performance of the equations of state in relation to the binary mixtures considered in this work. The present work greatly extends the available literature by providing an accurate set of both experimental density and speed-of-sound data over a large temperature range of (283.15 to 473.15) K with pressures up to 390 MPa. The results obtained in this study will permit equations of state and other thermodynamic models to be tested in a more rigorous manner. Further experimental studies and research areas were identified at the end of the thesis.

# Table of Contents

Abstract ..... 5
List of Publications ..... 11
List of Figures ..... 12
List of Tables ..... 19
Chapter 1: Introduction ..... 24
1.1 Energy and Climate Change ..... 24
1.2 Carbon Capture and Storage (CCS) Process ..... 25
1.2.1 Carbon Capture ..... 26
1.2.2 Carbon Transportation ..... 27
1.2.3 Carbon Storage ..... 27
1.2.4 Enhanced Oil Recovery ..... 28
1.2.5 CCS Challenges ..... 30
1.3 Project Motivations and Scientific Significance ..... 30
1.4 Scopes and Objectives ..... 33
1.5 Thesis Outline ..... 35
Chapter 2: Speed-of-Sound and Density: Measurement Techniques and Literature Review ..... 36
2.1 Overview ..... 36
2.2 Speed-of-Sound ..... 37
2.2.1 Speed-of-Sound Measurement Techniques ..... 38
2.2.2 Review of the Available Experimental Data ..... 45
2.3 Density ..... 51
2.3.1 Density Measuring Techniques ..... 52
2.3.2 Review of the Available Experimental Data ..... 60
2.4 Summary ..... 68
Chapter 3: Equations of State ..... 69
3.1 Overview ..... 69
3.2 Introduction ..... 70
3.3 Cubic Equations of State ..... 70
3.3.1 Van der Waals (vdW) Equation of State ..... 71
3.3.2 Soave-Redlich-Kwong (SRK) Equation of State ..... 71
3.3.3 Peng-Robinson (PR) Equation of State ..... 73
3.3.4 Patel and Teja (PT) Equation of State ..... 74
3.3.5 Volume Translation ..... 74
3.3.6 Mixing Rules and Binary Interactions ..... 76
3.3.7 Predictive Cubic Equation of State ..... 77
3.4 The Statistical Associating Fluid Theory (SAFT) ..... 78
3.4.1 SAFT-γ Mie ..... 80

3.4.2 Un-like Binary Interaction Parameters ..... 81
3.5 Helmholtz Energy Explicit Models for Pure Components ..... 83
3.6 Helmholtz Energy Explicit Models for Mixtures ..... 84
3.6.1 GERG-2004 and GERG-2008 ..... 87
3.6.2 Multi-Fluid Helmholtz Energy Approximation (Optimisation) ..... 88
3.7 Integration of Thermodynamic Properties ..... 89
3.8 Excess Molar Volume ..... 91
3.9 Modelling Approaches ..... 92
3.10 Summary ..... 94
Chapter 4: Apparatus Design and Experimental Methodology ..... 95
4.1 Overview ..... 95
4.2 Speed-of-Sound Apparatus ..... 96
4.2.1 Ultrasonic Cell ..... 96
4.2.2 Pressure Vessel ..... 97
4.2.3 Temperature and Pressure Control ..... 98
4.2.4 Magnetic Circulating Pump ..... 98
4.2.5 Fluid Handling System ..... 99
4.2.6 Measurement Methodology ..... 100
4.2.7 Assembly of the Ultrasonic Cell ..... 101
4.2.8 Calibration ..... 103
4.2.9 Uncertainty Analysis ..... 105
4.3 Density Measurement Set-up ..... 106
4.3.1 Measurement Methodology ..... 107
4.3.2 Calibration ..... 108
4.3.3 Uncertainty Analysis ..... 116
4.4 Variable Volume Cell ..... 117
4.4.1 Liquid Mixture Preparation ..... 118
4.4.2 Uncertainty Analysis ..... 119
4.5 Materials ..... 119
4.6 Sample Preparation (Degassing & Drying) ..... 120
4.7 Summary ..... 120
Chapter 5: Measurements on Pure Hydrocarbons and Pure $CO_2$ ..... 121
5.1 Overview ..... 121
5.2 Introduction ..... 122
5.3 Experimental Uncertainty ..... 122
5.4 *n*-Pentane ..... 123
5.4.1 Literature Review ..... 123
5.4.2 Experimental Speed-of-Sound Results and Discussion ..... 123

5.4.4 Modelling ..... 128
5.5 *n*-Heptane ..... 130
5.5.1 Literature Review ..... 130
5.5.2 Experimental Density Results and Discussion ..... 131
5.5.3 Experimental Speed-of-Sound Results and Discussion ..... 134
5.5.5 Modelling ..... 138
5.5.6 Derived Thermophysical Properties ..... 139
5.6 *n*-Nonane ..... 143
5.6.1 Literature Review ..... 143
5.6.2 Experimental Density Results and Discussion ..... 144
5.6.3 Experimental Speed-of-Sound Results and Discussion ..... 148
5.6.5 Modelling ..... 152
5.6.6 Derived Thermodynamic Properties ..... 153
5.7 Methylbenzene ..... 159
5.7.1 Literature Review ..... 159
5.7.2 Experimental Density Results and Discussion ..... 160
5.7.3 Experimental Speed-of-Sound Results and Discussion ..... 164
5.7.5 Modelling ..... 168
5.7.6 Derived Thermophysical Properties ..... 170
5.8 Carbon Dioxide ..... 176
5.8.1 Literature Review ..... 176
5.8.2 Experimental Density Results and Discussion ..... 176
5.8.4 Modelling ..... 178
5.9 Summary ..... 180
Chapter 6: Measurements on Binary Mixtures of Hydrocarbons and $CO_2$ ..... 181
6.1 Overview ..... 181
6.2 Introduction ..... 182
6.3 Experimental Uncertainty ..... 182
6.4 $CO_2$ + *n*-Heptane ..... 183
6.4.1 Literature Review ..... 183
6.4.2 Experimental Results and Discussion ..... 183
6.4.3 Bubble Pressure Determination ..... 189
6.4.4 Modelling ..... 192
6.4.5 Optimisation of SAFT-γ Mie ..... 199
6.5 $CO_2$ + *n*-Nonane ..... 202
6.5.1 Literature Review ..... 202
6.5.2 Experimental Density Results and Discussion ..... 203
6.5.3 Experimental Speed-of-Sound Results and Discussion ..... 204

6.5.4 Modelling ..... 211
6.6 $CO_2$ + Methylbenzene ..... 220
6.6.1 Literature Review ..... 220
6.6.2 Experimental Density Results and Discussion ..... 220
6.6.3 Bubble Pressure Determination ..... 225
6.6.4 Experimental Speed-of-Sound Results and Discussion ..... 229
6.6.5 Modelling ..... 233
6.7 Summary ..... 242
Chapter 7: Measurements of Calibration Fluids ..... 244
7.1 Overview ..... 244
7.2 Introduction ..... 245
7.3 Experimental Apparatus and Procedures ..... 245
7.3.1 Speed-of-Sound Apparatus ..... 245
7.3.2 Density Apparatus – Vibrating-Tube Densimeter ..... 245
7.3.3 Isobaric Heat Capacity Apparatus– Flow Calorimeter ..... 245
7.3.4 Viscosity Apparatus – Vibrating-Wire Viscometer ..... 247
7.4 Results and Discussions ..... 249
7.4.1 Sound-speed Measurement ..... 249
7.4.2 Density Measurement ..... 254
7.4.3 Isobaric Heat Capacity Measurement ..... 256
7.4.4 Thermodynamic Integration ..... 256
7.4.5 Viscosity Measurement ..... 257
7.5 Summary and Conclusions ..... 263
Chapter 8: Conclusions and Recommendations for Future Work ..... 265
8.1 Summary and Conclusions ..... 265
8.2 Contribution of This Work ..... 269
8.3 Recommendation for Future Work ..... 270
8.3.1 Further Experimental Investigation ..... 270
8.3.2 Further Modelling Investigation ..... 271
List of References ..... 273
Appendix A: ..... 294
Appendix B: ..... 304
Appendix C: ..... 320

# List of Publications

1. May, E. F.; Tay, W. J.; Nania, M.; Aleji, A.; Al-Ghafri, S.; Trusler, J. P. M. Physical Apparatus Parameters and Model for Vibrating Tube Densimeters at Pressures to 140 MPa and Temperatures to 473 K. *Review of Scientific Instruments* **2014**, *85*
2. Tay, W. J.; Trusler, J. P. M. Density, Sound Speed and Derived Thermophysical Properties of *n*-Nonane at Temperatures Between (283.15 and 473.15) K and at Pressures up to 390 MPa. Journal of Chemical & Engineering Data (In preparation)
3. Tay, W. J.; Trusler, J. P. M. Density, Sound Speed and Derived Thermophysical Properties of Methylbenzene at Temperatures Between (283.15 and 473.15) K and at Pressures up to 390 MPa. Journal of Chemical & Engineering Data (In preparation)
4. Tay, W. J.; Trusler, J. P. M. Speed of sound in the Binary Systems ($CO_2$ + *n*-Nonane) and ($CO_2$ + Methylbenzene) at Temperatures Between (283.15 and 473.15) K and at Pressures up to 390 MPa. Journal of Chemical & Engineering Data (In preparation)
5. Sanchez-Vicente, Y.; Tay, W. J.; Al Ghafri S. Z. Thermodynamics of ($CO_2$ + n-Heptane) System (Applied Energy) (In preparation)
6. Tay, W. J.; Sanchez-Vicente, Y.; Al Ghafri S. Z. Thermodynamics of ($CO_2$ + Methylbenzene) System (Energy) (In preparation)

# List of Figures

**Figure 1.1** Different pathways to reduce GHG emissions to achieve the 2 °C scenario proposed by IEA…….....24

**Figure 1.2** Key CCS projects developments……...……..26

**Figure 1.3** Schematic of the enhanced oil recovery process…….29

**Figure 2.1** Cross-section view of a high-pressure speed-of-sound apparatus with a spherical resonator……...……..39

**Figure 2.2** Schematic of an acoustic interferometer…….……..…...41

**Figure 2.3** Principle of the phase comparison pulse-echo method with two reflectors…….…...42

**Figure 2.4** The sound-speed correction due to diffraction for (4 and 5) MHz operation for the pulse-echo measurements…….……...44

**Figure 2.5** (*left*) Schematic of a double-sinker densimeter (*right*) The working principle of the single-sinker densimeter…..……...……...…55

**Figure 2.6** Schematic of a vibrating-wire densimeter……...57

**Figure 2.7** Top view and side view schematic of the vibrating-tube densimeter……..58

**Figure 3.1** Schematic illustration of the SAFT framework……..….79

**Figure 4.1** Schematic of the 5 MHz ultrasonic cell of the speed-of-sound apparatus……..…97

**Figure 4.2** Schematic of 4 kbar pressure vessel and plug of the speed-of-sound apparatus…….....97

**Figure 4.3** Exploded view of the magnetic circulating pump……...99

**Figure 4.4** P&ID for the liquid sound-speed apparatus……...101

**Figure 4.5** Schematic of the assembly of the ultrasonic cell…….....101

**Figure 4.6** Visualisation of the ultrasonic cell……102

**Figure 4.7** P&ID for high-pressure density apparatus……..…….....107

**Figure 4.8** Polynomial model: Comparison between the experimental data calculated from the calibration curve and the predictions from the equations of state across six isotherms……..114

**Figure 4.9** Physical model: Comparison between the experimental data calculated from the calibration curve and the predictions from the equations of state across six isotherms……..115

**Figure 4.10** Schematic of the variable volume cell…….……....118

**Figure 5.1** (*top*) Experimental sound-speed $c$ in *n*-pentane as a function of pressure across 11 isotherms. (*bottom*) Deviations of the experimental speed-of-sound in *n*-pentane from the values $c_{\mathrm{fit}}$ calculated from the empirical correlation as a function of pressure and temperature……124

**Figure 5.2** Deviations between the experimental sound-speed $c_{\mathrm{exp}}$ in *n-p*entane and predictions calculated from two reference equations of state $c_{\mathrm{EoS}}$. (*top*) Original EoS developed by Span and Wagner. (*bottom*) New EoS..…..……..…125

**Figure 5.3** Comparison between experimental sound-speed from literature $c_{\mathrm{exp}}$ in *n*-pentane and values calculated from the empirical correlation $c_{\mathrm{fit}}$ at six isotherms…….….127

**Figure 5.4** (*top*) Comparison between experimental speed-of-sound in *n*-pentane and values calculated with SAFT-γ Mie. (*bottom*) Deviations between the experimental speed-of-sound $c_{exp}$ and the predictions from SAFT-γ Mie EoS $c_{EoS}$ across ten isotherms……..……..129
**Figure 5.5** (*top*) Experimental density $\rho$ of *n*-heptane as a function of pressure across nine isotherms. (*bottom*) Deviations between the experimental densities $\rho_{exp}$ and the values calculated using the Tait equation $\rho_{fit}$…….……132
**Figure 5.6** Deviations between the experimental densities $\rho_{exp}$ from the calculated densities using the *n*-heptane equation of state $\rho_{EoS}$ across nine isotherms…….....132
**Figure 5.7** Deviation plots between the experimental density from the literature $\rho_{exp}$ and values calculated using the modified Tait equation $\rho_{fit}$ for $CO_2$ + *n*-heptane……...……...133
**Figure 5.8** (*top*) Experimental sound-speeds *c* in *n*-heptane as a function of pressure across nine isotherms. (*bottom*) Deviations of the experimental speed-of-sound in *n*-heptane from the values $c_{fit}$ calculated from the empirical correlation as a function of pressure and temperature…….…...136
**Figure 5.9** Comparison between the experimental literature data $c_{exp}$ and sound-speed calculated from the empirical correlation $c_{fit}$ for *n*-heptane……...……137
**Figure 5.10** (*top*) Deviations of the experimental density $\rho_{exp}$ in *n*-heptane from the values calculated from SAFT-γ Mie EoS $\rho_{EoS}$ across nine isotherms. (*bottom*) Deviations of the experimental speed-of-sound $c_{exp}$ in *n*-heptane from the values calculated from SAFT-γ Mie EoS $c_{EoS}$ across nine isotherms……..……138
**Figure 5.11** (*top*) Experimental isobaric heat capacity data $c_{p,exp}$ for *n*-heptane taken from the literature. (*bottom*) Deviations between the experimental isobaric heat capacity data $c_{p,exp}$ for *n*-heptane and values calculated from the polynomial correlation $c_{p,fit}$…….……..140
**Figure 5.12** Deviations between the derived density $\rho_{exp}$, isobaric heat capacity $c_{p,exp}$, isothermal compressibility $\beta_{exp}$ and isobaric expansivity $\alpha_{exp}$ and values calculated from the EoS across eight isotherms. ……....141
**Figure 5.13** (*top*) Experimental density $\rho$ of *n*-nonane as a function of pressure across nine isotherms. (*bottom*) Deviations between experimental densities $\rho_{exp}$ and the values calculated using the modified Tait equation $\rho_{fit}$……..…….145
**Figure 5.14** Deviations between the experimental densities $\rho_{exp}$ of *n*-nonane and the values calculated using the EoS developed by Lemmon and Span across nine isotherms……..……146
**Figure 5.15** Deviation plots between the experimental densities obtained from the literature $\rho_{exp}$ and the values calculated using the modified Tait equation at six temperatures…….....147
**Figure 5.16** (*top*) Experimental sound-speed *c* in *n*-nonane along nine isotherms. (*bottom*) Deviations of the experimental speed-of-sound in *n*-nonane $c_{exp}$ from the values calculated from the empirical correlation $c_{fit}$ as a function of pressure and temperature…….…...149
**Figure 5.17** Deviations of the experimental speed-of-sound $c_{exp}$ in *n*-nonane from the values calculated from the reference EoS $c_{EoS}$……150

**Figure 5.18** Comparison between the literature data $c_{exp}$ and sound-speed calculated from the empirical correlation $c_{fit}$……..……..151
**Figure 5.19** (*top*) Deviations between the experimental density $\rho_{exp}$ in *n*-nonane from the values calculated from SAFT-γ Mie EoS $\rho_{EoS}$ across nine isotherms. (*bottom*) Deviations of the experimental speed-of-sound $c_{exp}$ in *n*-nonane from the values calculated from SAFT-γ Mie $c_{EoS}$ across nine isotherms……..……152
**Figure 5.20** Experimental isobaric heat capacity data $c_p$ for *n*-nonane taken from the literature...…154
**Figure 5.21** Deviations between the isobaric heat capacity data $c_{p,exp}$ and the values calculated using the polynomial correlation $c_{p,fit}$ at saturated pressure from temperatures between (283 and 473) K..154
**Figure 5.22** Deviations between derived density $\rho$, isobaric heat capacity $c_p$, isothermal compressibility $\beta$ and isobaric expansivity $\alpha$ and values calculated from the reference EoS up to 390 MPa across eight isotherms……..…156
**Figure 5.23** Change in density and isobaric heat capacity, arising from sound-speed cosinusodal perturbation with amplitude of 0.1 %.....157
**Figure 5.24** Change in isobaric expansivity and isothermal compressibility, arising from sound-speed cosinusodal perturbation with amplitude of 0.1 %.....158
**Figure 5.25** (*top*) Experimental density of methylbenzene as a function of pressure across nine isotherms. (*bottom*) Deviations of experimental densities $\rho_{exp}$ from the calculated densities using the modified Tait equation $\rho_{fit}$. ……...……...161
**Figure 5.26** Deviations of experimental densities $\rho_{exp}$ of methylbenzene from the values calculated from the EoS $\rho_{EoS}$ across nine isotherms……..162
**Figure 5.27** Deviation plots of the literature data $\rho_{exp}$ and the values calculated using modified Tait equation $\rho_{fit}$……...163
**Figure 5.28** (*top*) Experimental sound-speed data in methylbenzene along nine isotherms. (*bottom*) Deviations of the experimental speed-of-sound in methylbenzene $c_{exp}$ from the values $c_{fit}$ calculated from the empirical correlation with parameters fitted to the experimental data a function of pressures and temperatures……...……...165
**Figure 5.29** Deviations of experimental speed-of-sound $c_{exp}$ of methylbenzene from the values calculated from the refernce EoS $c_{EoS}$ across nine isotherms……..…..…....166
**Figure 5.30** Comparison between the literature data $c_{exp}$ and sound-speeds calculated from the empirical correlation $c_{fit}$……..…….167
**Figure 5.31** (*top*) Deviations of the experimental density $\rho_{exp}$ in methylbenzene from the values calculated from SAFT-γ Mie $\rho_{EoS}$. (*bottom*) Deviations of the experimental speed-of-sound in methylbenzene, $c_{exp}$ from the values $c_{EoS}$ calculated from SAFT-γ Mie across nine isotherms…..…169
**Figure 5.32** Experimental isobaric heat capacities $c_p$ of methylbenzene in the literature from (283.15 to 473.15) K……..……171

**Figure 5.33** Deviations of the experimental isobaric heat capacity of methylbenzene in literature $c_{p,exp}$ from the values calculated from the polynomial correlation $c_{p,fit}$……...….171

**Figure 5.34** Deviations between derived density $\rho$, isobaric heat capacity $c_p$, isothermal compressibility $\beta$ and isobaric expansivity $\alpha$ and values calculated from the EoS up to 390 MPa across eight isotherms……..……...……172

**Figure 5.35** Change in density and isobaric heat capacity, arising from sound speed cosinusodal perturbation with amplitude of 0.1 %.....174

**Figure 5.36** Change in isobaric expansivity and isothermal compressibility, arising from sound speed cosinusodal perturbation with amplitude of 0.1 %.....175

**Figure 5.37** (*top*) Pressure as a function of experimental density $\rho$ of carbon dioxide across nine isotherms. (*bottom*) Deviations between the experimental densities $\rho_{exp}$ and the calculated densities using the empirical correlation $\rho_{fit}$……..…….177

**Figure 5.38** (*top*) Deviations of the experimental density $\rho_{exp}$ in $CO_2$ from the values calculated from SAFT-γ Mie $\rho_{EoS}$. (*bottom*) Deviations of the experimental speed-of-sound in $CO_2$, $c_{exp}$ from the values $c_{EoS}$ calculated from SAFT-γ Mie across nine isotherms……..…...179

**Figure 6.1** Compressed-liquid densities $\rho$ against pressure for $CO_2$ + *n*-heptane system at four mole fractions of $CO_2$ and at six temperatures…….….185

**Figure 6.2** Comparison of compressed-liquid densities $\rho$ of $CO_2$ + *n*-heptane at (*left*) 323 K and (*right*) 348 K between our work and literature data…….....186

**Figure 6.3** Deviations of the experimental pressure $p_{exp}$ from values calculated with the empirical correlation $p_{fit}$ at six temperatures…..……...187

**Figure 6.4** Excess molar volume $V_m^E$ of $CO_2$ + *n*-heptane system versus the mole fraction of $CO_2$ at six temperatures and at nine isobars……....188

**Figure 6.5** Compressed-liquid densities and saturated-phase densities versus pressure for $CO_2$ + *n*-heptane system at four mole fractions of $CO_2$ at six temperatures…….....190

**Figure 6.6** Bubble pressures $p_b$ for $CO_2$ + *n*-heptane as a function of $CO_2$ mole fraction at four temperatures…….....192

**Figure 6.7** Comparisons between the experimental compressed-liquid density of $CO_2$ + *n*-heptane and the predictions from SAFT-γ Mie and PPR78 EoS at nine temperatures and at four mole fractions of $CO_2$……...…196

**Figure 6.8** Deviation plots between the experimental compressed-liquid density $\rho_{exp}$ and the predictions from SAFT-γ Mie and PPR78 EoS $\rho_{EoS}$ for $CO_2$ + *n*-heptane at nine isotherms and at four mole fractions of $CO_2$……..197

**Figure 6.9** Comparisons between the experimental compressed-liquid density of $CO_2$ + *n*-heptane and the predictions from GERG-2008 EoS at nine temperatures and at four mole fractions of $CO_2$……...198

**Figure 6.10** Comparison of the compressed-liquid density predictions with the optimised and un-optimised parameters $\varepsilon_{kl}$ and $\lambda_{kl}^{r}$ of SAFT-γ Mie for $CO_2$ + *n*-heptane at two mole fractions of $CO_2$ at three scenarios……..201

**Figure 6.11** Compressed-liquid densities $\rho$ against pressure for $CO_2$ + *n*-nonane system at four mole fractions of $CO_2$ and at six temperatures……..205

**Figure 6.12** Deviations between the experimental pressure $p_{exp}$ and values calculated from the empirical correlation $p_{fit}$, $\Delta p = p_{exp} - p_{fit}$ for $CO_2$ + *n*-nonane at six temperatures…….....206

**Figure 6.13** Excess molar volume $V_m^E$ of $CO_2$ + *n*-nonane system versus the mole fraction of $CO_2$ at six temperatures and at ten isotherms…….....207

**Figure 6.14** Experimental sound-speed *c* in $CO_2$ + *n*-nonane across nine isotherms as a function of pressure at four compositions…….....209

**Figure 6.15** Deviations of the experimental speed-of-sound $c_{exp}$ in $CO_2$ + *n*-nonane from the values calculated with the empirical correlation $c_{fit}$ as a function of pressure and temperature…….210

**Figure 6.16** Comparisons between the experimental compressed-liquid density of $CO_2$ + *n*-nonane and the predictions from SAFT-γ Mie and PPR78 EoS at nine temperatures and at four mole fractions of $CO_2$…….....214

**Figure 6.17** Deviation plots between the experimental compressed-liquid density $\rho_{exp}$ for $CO_2$ + *n*-nonane and the predictions from SAFT-γ Mie and PPR78 EoS $\rho_{EoS}$ at nine isotherms……...215

**Figure 6.18** Comparisons between the experimental compressed-liquid density of $CO_2$ + *n*-nonane and the predictions from GERG-2008 EoS at nine temperatures and four mole fractions of $CO_2$….216

**Figure 6.19** Comparison between experimental sound-speed in $CO_2$ + *n*-nonane and predictions from SAFT-γ Mie and GERG-2008 across nine isotherms as a function of pressure……...…...217

**Figure 6.20** Deviations between experimental sound-speed $c_{exp}$ of $CO_2$ + *n*-nonane and predictions from SAFT-γ Mie $c_{EoS}$ across nine isotherms as a function of pressure……...……...218

**Figure 6.21** Deviations between experimental sound-speed $c_{exp}$ of $CO_2$ + *n*-nonane and predictions from GERG-2008 $c_{EoS}$ across nine isotherms as a function of pressure.....219

**Figure 6.22** Compressed-liquid densities $\rho$ against pressure for $CO_2$ + methylbenzene system at four mole fractions of $CO_2$ and at nine temperatures……...222

**Figure 6.23** Comparison of the compressed-liquid densities of $CO_2$ + methylbenzene measured in this work and by Pohler and Kiran across five isotherms……..……223

**Figure 6.24** Deviations between the experimental pressure $p_{exp}$ for $CO_2$ + methylbenzene and the values calculated with the empirical correlation $p_{fit}$, $\Delta p = p_{exp} - p_{fit}$ at six temperatures…….....224

**Figure 6.25** Excess molar volume $V_m^E$ of $CO_2$ + methylbenzene system versus the mole fraction of $CO_2$ at six temperatures and at ten isobars.....226

**Figure 6.26** Compressed-liquid densities and saturated-phase densities versus pressure for $CO_2$ + methylbenzene system at four mole fractions of $CO_2$ and at six temperatures……...….227

**Figure 6.27** Bubble pressures $p_b$ for $CO_2$ + methylbenzene as a function of the $CO_2$ mole fraction at four temperatures……...228
**Figure 6.28** Experimental sound-speed $c$ in $CO_2$ + methylbenzene across nine isotherms as a function of pressure at four compositions…….….231
**Figure 6.29** Deviations of the experimental speed-of-sound $c_{exp}$ in $CO_2$ + methylbenzene from the values calculated from the empirical correlation $c_{fit}$ as a function of pressure and temperature…….232
**Figure 6.30** Comparisons between the experimental compressed-liquid density $\rho_{exp}$ of $CO_2$ + methylbenzene and the predictions from SAFT-γ Mie and PPR78 EoS at nine temperatures and at four mole fractions of $CO_2$……..236
**Figure 6.31** Deviation plots between the experimental compressed-liquid density $\rho_{exp}$ for $CO_2$ + methylbenzene and the predictions from SAFT-γ Mie and PPR78 EoS $\rho_{EoS}$ at nine isotherms……..237
**Figure 6.32** Comparisons between the experimental compressed-liquid density $\rho$ of $CO_2$ + methylbenzene and the predictions from multi-fluid Helmholtz energy approximation at nine temperatures and at four mole fractions of $CO_2$……..238
**Figure 6.33** Comparison between experimental sound-speed in $CO_2$ + methylbenzene and predictions from SAFT-γ Mie and multi-fluid Helmholtz energy approximation model developed by Bell and Lemmon across nine isotherms as a function of pressure…….…...239
**Figure 6.34** Deviations between the experimental sound-speed $c_{exp}$ of $CO_2$ + methylbenzene and the predictions from SAFT-γ Mie $c_{EoS}$ across nine isotherms as a function of pressure……..….240
**Figure 6.35** Deviations between the experimental sound-speed $c_{exp}$ of $CO_2$ + methylbenzene and the predictions from the multi-fluid Helmholtz energy approximation model $c_{EoS}$ across nine isotherms as a function of pressure……..……..…241
**Figure 7.1** Schematic of the calorimeter cell……..246
**Figure 7.2** (*left*) Vibrating-wire sensor, (*centre*) soft-iron magnet yoke, (*right*) electrical circuit….248
**Figure 7.3** (*left*) gold-plated piezo-transducer before and after the experiment, (*centre*) residue from lead wire corrosion, (*right*) seal extrusion on pressure vessel cap……...250
**Figure 7.4** (*top*) Experimental sound-speeds in Fluid A across ten isotherms at pressures up to 300 MPa. (*bottom*) Deviations between the experimental sound-speeds and values calculated from the correlation……251
**Figure 7.5** (*top*) Experimental sound-speeds in Fluid B across ten isotherms at pressures up to 300 MPa. (*bottom*) Deviations between the experimental sound-speeds and values calculated from the correlation……252
**Figure 7.6** Comparison between the sound-speeds measured for Fluid A and Fluid B and predictions from EoSs of methylbenzene and dodecane at (*top*) 298.15 K and (*bottom*) 373.15 K……..253
**Figure 7.7** Experimental density in (*top*) Fluid A and (*bottom*) Fluid B across ten isotherms……...255

**Figure 7.8** Comparison between the densities extrapolated for Fluid A and Fluid B and predictions from EoSs of methylbenzene and dodecane at 0.1 MPa……..……255
**Figure 7.9** Gold-plated iron yoke for viscometer (*left*) before and (*right*) after the experiment……257
**Figure 7.10** Isobaric heat capacity measurements in Fluid A and Fluid B at temperatures up to 393.15 K at saturation pressure……..……..……258
**Figure 7.11** Comparison of the isobaric heat capacities measured for Fluid A and Fluid B and predictions from EoSs of methylbenzene and dodecane…….258
**Figure 7.12** Comparison between the densities derived from the sound-speed data up to 300 MPa for Fluid A and Fluid B and predictions from EoS of methylbenzene and dodecane at (*top*) 373.15 K and (*bottom*) 473.15 K……259
**Figure 7.13** Dynamic viscosity of (*top*) Fluid A and (*bottom*) Fluid B across ten isotherms at pressures up to 300 MPa……..261
**Figure 7.14** Comparison between the viscosities measured for Fluid A and Fluid B and predictions from EoSs of methylbenzene, dodecane and hexadecane at (*top*) 373.15 K and (*bottom*) 473.15 K..262
**Figure A.1** Detailed drawings of the 4 kbar pressure vessel and a list of serviceable parts from SITEC.....294
**Figure A.2** Detailed drawings of the high-pressure syringe pump and a list of serviceable parts from SITEC……..……...295
**Figure A.3a** Detailed drawings with the dimensions of the variable volume cell…….....296
**Firgure A.3b** Detailed drawings with the dimensions of the variable volume cell……297

# List of Tables

**Table 2.1** Experimental speed-of-sound studies for liquid alkanes ($C_5$ to $C_{16}$) conducted at elevated temperatures and pressures…….…...47

**Table 2.2** Experimental speed-of-sound studies for benzene and methylbenzene conducted at elevated temperatures and pressures……....50

**Table 2.3** Experimental speed-of-sound studies for carbon dioxide conducted at elevated temperatures and pressures…….....51

**Table 2.4** Experimental density studies for linear alkanes from ($C_5$ to $C_{16}$) conducted at elevated temperatures and pressures in the past 20 years……61

**Table 2.5** Experimental density studies for benzene and methylbenzene conducted at elevated temperatures and pressures in the past 20 years……64

**Table 2.6** Experimental density studies for carbon dioxide conducted at elevated temperatures and pressures…….……....65

**Table 2.7** Experimental density studies for binary mixtures of $CO_2$ + alkanes ($C_5$ to $C_{16}$) conducted at elevated temperatures and pressures……..66

**Table 2.8** Experimental density studies for $CO_2$ + benzene and $CO_2$ + methylbenzene conducted at elevated temperatures and pressures…….....67

**Table 3.1** Values of the Rackett compressibility factor $Z_{RA}$ for volume translation for the first ten *n*-alkanes published by the American Petroleum Institute (API)……..75

**Table 3.2** Parameters for the multi-fluid Helmholtz energy approximation model given by Bell and Lemmon…….....88

**Table 4.1** PRT calibration parameters for ITS-90 equation……103

**Table 4.2** Uncertainty budget for speed-of-sound in $CO_2$ + *n*-nonane at the median state point in terms of standard uncertainty $u$(x) of the dimensionless parameter (x) and arising contribution $u_r(c)$ to the overall standard relative uncertainty of speed-of-sound……..106

**Table 4.3** Summary of the seven VTD apparatus parameters used in the calibration model reported by May *et al.* and their determination methods……110

**Table 4.4** Period of oscillation readings, $\tau_0$ of the vibrating-tube densimeter under vacuum at temperatures from (283.15 to 473.15) K……..112

**Table 4.5** Coefficients of the polynomial calibration model for the vibrating-tube densimeter, DMA HP. The calibration was carried out under vacuum, helium and water at *T*: (283.15 to 473.15) K and *p*: (0.1 to 65) MPa……113

**Table 4.6** Coefficients of the physical calibration model for the vibrating-tube densimeter, DMA HP. The calibration was carried out under vacuum, helium and water at *T*: (283.15 to 473.15) K and *p*: (0.1 to 65) MPa…….……...113

**Table 4.7** Uncertainty budget for density for $CO_2$ + methylbenzene at the median state point in terms of standard uncertainty $u$(x) of the dimensionless parameter (x) and arising contribution $u_r(\rho)$ to the overall standard relative uncertainty of density…….....116
**Table 4.8** Specifications of the o-rings in the variable volume cell…….....116
**Table 4.9** Description of chemical samples, where $x$ denotes mole fraction and $\rho_e$ denotes electrical resistivity……..…119
**Table 5.1** Fitting parameters of the empirical correlation for the speed-of-sound measurements in *n*-pentane together with the statistical parameters, average absolute deviation $\Delta_{AARD}$ and maximum absolute deviation $\Delta_{MARD}$…….128
**Table 5.2** SAFT-γ Mie like parameters for functional groups $CH_3$ and $CH_2$, $v_k^*$ the number of segments, $S_k$ the shape factor, $\varepsilon_{kk}$ the interaction energy, $\sigma_{kk}$ the segment diameter, and $\lambda_{kk}^r$ and $\lambda_{kk}^a$ the repulsive and attractive exponents, respectively……....128
**Table 5.3** Fitting parameters of the modified Tait equation for the compressed-liquid density measurements of *n*-heptane together with the statistical parameters, $\Delta_{AARD}$ and $\Delta_{MARD}$…….134
**Table 5.4** Fitting parameters of the empirical correlation for the speed-of-sound measurements in *n*-heptane together with the statistical parameters, average absolute deviation, $\Delta_{AARD}$ and maximum absolute deviation $\Delta_{MARD}$…….135
**Table 5.5** Parameters of the isobaric heat capacity correlation for *n*-heptane……....139
**Table 5.6** Isobaric heat capacities $c_p$ studies of *n*-heptane; $T$ and $p$ refer to the temperature and pressure ranges examined, respectively……...……142
**Table 5.7** Fitting parameters of the modified Tait equation for the compressed-liquid density measurements of *n*-nonane together with the statistical parameters, $\Delta_{AARD}$ and $\Delta_{MARD}$…….....145
**Table 5.8** Fitting parameters of the empirical correlation for the speed-of-sound measurements in *n*-nonane together with the statistical parameters, average absolute deviation, $\Delta_{AARD}$ and maximum absolute deviation $\Delta_{MARD}$……...…..149
**Table 5.9** Isobaric heat capacities $c_p$ studies of *n*-nonane; $T$ and $p$ refer to the temperature and pressure ranges examined, respectively……...…153
**Table 5.10** Parameters of the isobaric heat capacity correlation for *n*-nonane……..……..…154
**Table 5.11** Fitting parameters of the modified Tait equation for the compressed-liquid density measurements of methylbenzene together with the statistical parameters, $\Delta_{AARD}$ and $\Delta_{MARD}$…….160
**Table 5.12** Fitting parameters of the empirical correlation for the speed-of-sound measurements in methylbenzene together with the statistical parameters, average absolute deviation, $\Delta_{AARD}$ and maximum absolute deviation $\Delta_{MARD}$……164
**Table 5.13** SAFT-γ Mie like parameters for functional groups aCH and $aCCH_3$, $v_k^*$ the number of segments, $S_k$ the shape factor, $\varepsilon_{kk}$ the interaction energy, $\sigma_{kk}$ the segment diameter, and $\lambda_{kk}^r$ and $\lambda_{kk}^a$ the repulsive and attractive exponents, respectively…….…...168

**Table 5.14** Isobaric heat capacities $c_p$ studies of methylbenzene; $T$ and $p$ refer to the temperature and pressure ranges examined, respectively……..……..170

**Table 5.15** Parameters of the isobaric heat capacity correlation for methylbenzene……...…...170

**Table 5.16** SAFT-γ Mie like parameters for functional group $CO_2$, $v_k^*$ the number of segments, $S_k$ the shape factor, $\varepsilon_{kk}$ the interaction energy, $\sigma_{kk}$ the segment diameter, and $\lambda_{kk}^{r}$ and $\lambda_{kk}^{a}$ the repulsive and attractive exponents, respectively……..……..178

**Table 6.1** Bubble pressures $p_b$ for $CO_2$ + *n*-heptane system at temperatures and $CO_2$ mole fractions $x$ determined from the intersection between the compressed-liquid densities and the saturated-phase densities[a]……..……191

**Table 6.2** Experimental parameters for three equations of state for the compressed-liquid density predictions of $CO_2$ + *n*-heptane……..……...194

**Table 6.3:** Average absolute relative deviations $\Delta_{AARD}$ between the experimental compressed-liquid density and the predictions from PPR78, SAFT-γ Mie and GERG-2008 EoSs for $CO_2$ + *n*-heptane at four compositions, and the overall average absolute relative deviations $\Delta_{AARD,overall}$. VT represents volume translation……..……...195

**Table 6.4** Optimisation of SAFT-γ Mie cross-interaction parameters: the values for the group dispersion energies, $\varepsilon_{kl}$ and the repulsive component, $\lambda_{kl}$, the experimental dataset and the weight factor used for each optimisation……..……200

**Table 6.5** Experimental parameters for two equations of state……...211

**Table 6.6** Average absolute relative deviations $\Delta_{AARD}$ between the experimental compressed-liquid density, speed-of-sound and the predictions from PPR78, SAFT-γ Mie and GERG-2008 EoSs for $CO_2$ + *n*-nonane at four compositions, and the overall average absolute relative deviations $\Delta_{AARD,overall}$...212

**Table 6.7:** Average absolute relative deviations $\Delta_{AARD}$ between the experimental compressed-liquid density, speed-of-sound and the predictions from PPR78, SAFT-γ Mie and GERG-2008 EoSs for $CO_2$ + *n*-nonane at four compositions, and the overall average absolute relative deviations $\Delta_{AARD,overall}$...213

**Table 6.8** Bubble pressures $p_b$ for $CO_2$ + methylbenzene system at temperatures and $CO_2$ mole fractions $x$ determined from the intersection between the compressed-liquid densities and the saturated-phase densities[a]……..……...…… 228

**Table 6.9** Experimental parameters for three equations of state…….233

**Table 6.10** Average absolute relative deviations $\Delta_{AARD}$ between the experimental compressed-liquid density, speed-of-sound and the predictions from PPR78, SAFT-γ Mie and Multi-fluid approximation EoSs for $CO_2$ + methylbenzene at four compositions, and the overall average absolute relative deviations $\Delta_{AARD,overall}$……..…..234

**Table A.4** Calibration density $\rho$ for the vibrating-tube densimeter (DMA-HP) measured with water, helium and vacuum at temperature $T$, pressure $p$ and period of oscillation $\tau$……..298

**Table B.1** Experimental speed-of-sound $c$ in *n*-pentane as a function of temperature and pressure, $T$: (263.21 to 473.15) K and $p$: (1 to 390) MPa……304

**Table B.2** Experimental compressed-liquid density $\rho$ for *n*-heptane as a function of temperature and pressure, *T*: (283.15 to 473.15) K and *p*: (1 to 68) MPa……..305

**Table B.3** Experimental speed-of-sound *c* in *n*-heptane as a function of temperature and pressure, *T*: (283.14 to 473.15) K and *p*: (1 to 180) MPa……307

**Table B.4** Derived thermophysical properties for *n*-heptane at *T*: (298.15 to 473.15) K and pressures up to 180 MPa: density $\rho$, isobaric heat capacity $c_p$, isothermal compressibility $\beta$ and isobaric expansivity $\alpha$……308

**Table B.5** Experimental compressed-liquid density $\rho$ for *n*-nonane as a function of temperature and pressure, *T*: (283.15 to 473.15) K and *p*: (1 to 65) MPa……..309

Table B.6 Experimental speed-of-sound *c* in *n*-nonane as a function of temperature and pressure, *T*: (283.15 to 473.15) K and *p*: (1 to 390) MPa……310

**Table B.7** Derived thermophysical properties for *n*-nonane at *T*: (298.15 to 473.15) K and pressures up to 390 MPa: density $\rho$, isobaric heat capacity $c_p$, isothermal compressibility $\beta$ and isobaric expansivity $\alpha$……312

**Table B.8** Experimental compressed-liquid density $\rho$ for methylbenzene as a function of temperature and pressure, *T*: (283.15 to 473.15) K and *p*: (1 to 65) MPa……...313

**Table B.9** Experimental speed-of-sound *c* in methylbenzene as a function of temperature and pressure, *T*: (283.15 to 473.15) K and *p*: (1 to 390) MPa……315

**Table B.10** Derived thermophysical properties for methylbenzene at *T*: (298.15 to 473.15) K and pressures up to 390 MPa: density $\rho$, isobaric heat capacity $c_p$, isothermal compressibility $\beta$ and isobaric expansivity $\alpha$……..316

**Table B.11** Experimental compressed-liquid density $\rho$ for carbon dioxide as a function of temperature and pressure, *T*: (283.15 to 473.15) K and *p*: (10 to 65) MPa…….317

**Table B.12** Parameters *A*, *B* and $\rho_r$ in the empirical correlation for compressed-liquid densities and the values of the average absolute deviation, $\Delta_{AAD,}$ and average absolute relative deviation, $\Delta_{AARD}$ for $CO_2$.....319

**Table C.1** Experimental compressed-liquid density $\rho$ for $CO_2$ + *n*-heptane at four compositions as a function of temperature and pressure, *T*: (283.15 to 473.15) K and *p*: (10 to 68) MPa……...320

**Table C.2** Parameters *A*, *B* and $\rho_r$ in the empirical correlation for compressed-liquid densities and the values of the average absolute deviation, $\Delta_{AAD,}$ and average absolute relative deviation, $\Delta_{AARD}$ for ($CO_2$ + *n*-heptane) system……325

**Table C.3** Parameters of the Redlich-Kister correlation for the excess molar volume of $CO_2$ + *n*-heptane and the average absolute deviation $\Delta_{AAD}$……327

**Table C.4** Experimental compressed-liquid density $\rho$ for $CO_2$ + *n*-nonane at four compositions as a function of temperature and pressure, *T*: (283.15 to 473.15) K and *p*: (10 to 68) MPa……...329

**Table C.5** Parameters *A*, *B* and $\rho_r$ in the empirical correlation for compressed-liquid densities and the values of the average absolute deviation, $\Delta_{AAD,}$ and average absolute relative deviation, $\Delta_{AARD}$ for ($CO_2$ + *n*-nonane) system…….334

**Table C.6** Parameters of the Redlich-Kister correlation for the excess molar volume of $CO_2$ + *n*-nonane and the average absolute deviation $\Delta_{AAD}$…….336

**Table C.7** Experimental speed-of-sound $c$ in $CO_2$ + $n$-nonane at four compositions as a function of temperature and pressure, $T$: (283.15 to 473.15) K and $p$: (10 to 390) MPa……...338

**Table C.8** Fitting parameters for the speed-of-sound correlation for $CO_2$ + $n$-nonane at four compositions……342

**Table C.9** Experimental compressed-liquid density $\rho$ for $CO_2$ + methylbenzene at four compositions as a function of temperature and pressure, $T$: (283.15 to 473.15) K and $p$: (10 to 65) MPa……...343

**Table C.10** Parameters $A$, $B$ and $\rho_r$ in the empirical correlation for compressed-liquid densities and the values of the average absolute deviation, $\Delta_{AAD,}$ and average absolute relative deviation, $\Delta_{AARD}$ for $CO_2$ + methylbenzene system…….……348

**Table C .11** Parameters of the Redlich-Kister correlation for the excess molar volume of $CO_2$ + methylbenzene…….349

**Table C.12** Experimental speed-of-sound $c$ in $CO_2$ +methylbenzene at four compositions as a function of temperature and pressure, $T$: (283.15 to 473.15) K and $p$: (10 to 390) MPa…….351

**Table C.13** Fitting parameters for the speed-of-sound correlation for $CO_2$ + methylbenzene at four compositions.……...356

# Chapter 1: Introduction

## 1.1 Energy and Climate Change

The demand for energy has been increasing for the past decades due to an expansion in population and an increase in energy consumption. According to The International Energy Agency (IEA), the world's energy consumption has doubled since the 1970s. The IEA predicts that the energy demand will continue to grow by nearly one-third between 2013 and 2040 with most net growth coming from the non-OECD[1] countries [1]. Energy production and use account for around two-thirds of global greenhouse-gas (GHG) emission [2]. According to the Emission Database for Global Atmospheric Research (EDGAR), global emission of $CO_2$ was 33.4 billion tonnes in 2011, which is 48% more than that of two decades ago. Over the past century, the atmospheric $CO_2$ level has increased more than 39%, from 280 ppm during the pre-industrial time to the record high level of 400 ppm in 2013 [3]. Global warming and climate change are perhaps the most serious problems faced by the global society in the 21st century. To limit the damages brought by climate change, representatives from 195 countries gathered in Paris in December 2015 at the 21st Conference of the Parties (COP 21) to discuss the means to combat climate change. It has been agreed to limit global warming to an average of no more than 2.0 °C and to pursue efforts to limit warming to 1.5 °C by 2100 [4]. A substantial and sustained reduction in $CO_2$ emissions is required to tackle the problem such that the concentration of $CO_2$ in the atmosphere is limited to about 450 ppm. The pathway to reduce greenhouse gas emission will involve a mix of technologies including: deploying renewable energy, nuclear power, improving energy efficiency and carbon capture and storage.

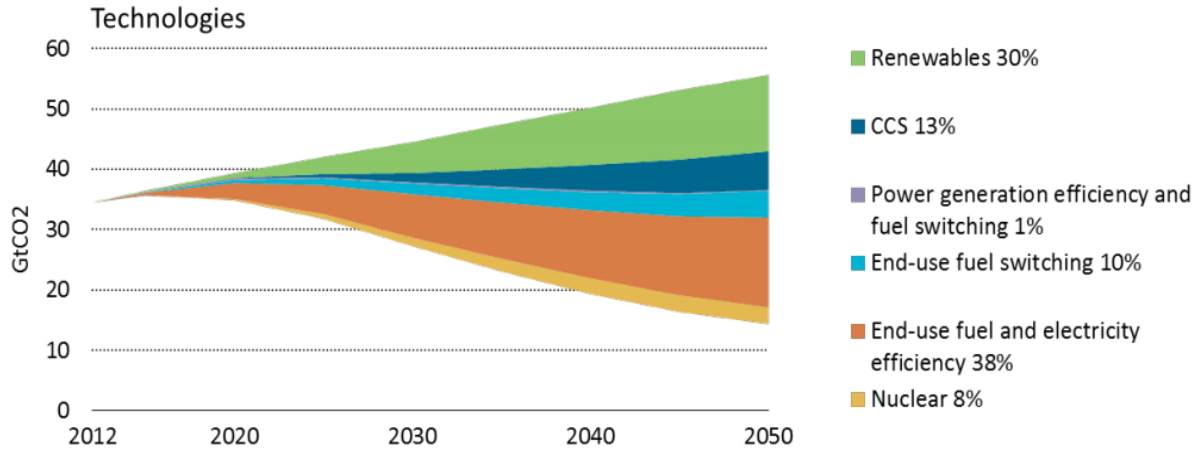



**Figure 1.1** Different pathways to reduce GHG emissions to achieve the 2 °C scenario proposed by IEA. Reproduced from Energy Technology Perspectives 2015 [1].

[1] Organisation for Economic Co-operation and Development

Approximately 80 % of the world's current energy comes from fossil fuels [5], and the IEA estimated that fossil fuels will still provide 60 % of the world's primary energy by 2040 despite the objective of keeping the temperature increase below to 2.0 °C [6]. Energy derived from fossil fuels contributes to the vast majority of $CO_2$ emissions, so reductions in this sector are essential. To continue exploitation of fossil fuels, Carbon Capture and Storage (CCS) is the only technology at this moment that can reduce emissions on a significant scale from fossil fuel power plants and other industrial processes [2]. According to the Intergovernmental Panel on Climate Change's (IPCC) Fifth Assessment Synthesis Report, the deployment of CCS will significantly reduce the risk of not meeting climate goals and is also the most important technology in minimising the cost of achieving the required emission reduction before 2100 [7]. Therefore CCS is a key part of the energy mix in order to achieve the global GHG emission target by 2100.

## 1.2 Carbon Capture and Storage (CCS) Process

Carbon capture and storage is a technology that could allow the continued use of fossil fuels in a medium term. The IEA states that "*CCS is the only technology available today that has the potential to protect the climate while preserving the value of fossil fuel reserves and existing infrastructure*" [8]. Other sources such as the IPCC also said CCS is the quickest and most cost-effective abatement option, they predicted that the global GHG mitigation costs will increase 138 % without CCS [9]. According to the predictions, CCS will contribute to reducing the global $CO_2$ emissions by about four billion tonnes in 2040 and six billion tonnes in 2050 in order to meet the 2 °C scenario [6]. This technology consists of three main processes: carbon capture, carbon transport and carbon storage. In carbon capture, anthropogenic $CO_2$ is being separated from other industrial and energy-related sources. $CO_2$ is then compressed to a liquid-phase state, and transport to an appropriate storage location via pipelines. Lastly, $CO_2$ is injected into geological reservoirs under careful monitoring, and the $CO_2$ should be trapped permanently. In 2016, two significant projects have just launched – the Emirates Steel Industries CCS Project [10] in Abu Dhabi and the Tomakomai CCS Demonstration Project [11] in Japan. The Abu Dhabi project [12] is the world's first large-scale operation of CCS to iron and steel production which captures approximately 0.8 Mtpa of $CO_2$ and the captured $CO_2$ is used for EOR. The Japanese CCS project captures $CO_2$ at a hydrogen production facility at a rate of least 0.1 Mtpa and the $CO_2$ is injected into near-shore geological storage.




**Figure 1.2** Key CCS projects developments: Sleipner $CO_2$ storage project (Norway), Petrobras Santos basin pre-salt oil field CCS project (Brazil), Boundary Dam CCS project, Quest project (Canada), Abu Dhabi CCS project (UAE), Gorgon $CO_2$ inject project (Australia) and Jilin oil field EOR demonstration project (China). Reproduced from the Global Status of CCS Summary Report [2].

### 1.2.1 Carbon Capture

Major $CO_2$ emission sources mainly come from the combustion of fossil fuels used in power generation and industrial processes such as coal-fired power plants, steel and cement manufacture plants, etc [2]. There are three primary methods of $CO_2$ capture: pre-combustion, post-combustion and oxy-fuel combustion. All of these methods have demonstrated the potential to achieve (80 to 90) % $CO_2$ capture efficiency. The capture process typically accounts for 70 % of the overall cost of the CCS chain; hence new technologies development and processes optimisation currently have been the key focus in the capture research to reduce cost [13]. Separation of $CO_2$ during the pre- or post-combustion methods is usually achieved by solvent absorption such as amine absorption. CCS technologies can be retrofitted onto some of the existing fossil-fuelled based power plants. However, this will cause energy penalty to the existing plants as it reduces the net plant efficiency and the power plants effectively require more fuel to generate each kilowatt–hour of electricity. The Quest project [14] run by Shell was launched in Alberta, Canada in November 2015, is the world's first commercial-scale CCS project. Quest is designed to capture and safely store more than one million tonnes of $CO_2$ each year which is equivalent to the emissions from about 250,000 cars. As of September 2016, it has captured and stored more than 1 Mt of $CO_2$. Another significant project known as the SasksPower's Boundary Dam Integrated Carbon Capture and Storage Project [15] is the largest commercial-scale CCS project to be installed in a coal-fired power plant (Canada). The $CO_2$ capture technology was retrofitted onto an existing coal-fired facility it had captured 1 Mt of $CO_2$ from the power generation facility since the operation started.

### 1.2.2 Carbon Transportation

Carbon Transport is an essential part of the CCS chain as $CO_2$ capture sources are usually separated from the storage locations, hence requiring transportation of $CO_2$ from the capture sites to the storage areas. The $CO_2$ quality required for transport may influence the choice and the operation requirements of capture technology, i.e. the potential impurities in the $CO_2$ stream: $H_2O$, $N_2$, $H_2$, $O_2$ and $H_2S$ may affect the integrity of the pipelines [16, 17]. Carbon transportation is typically achieved via pipelines, but ships, trucks and trains have been used for early demonstration of $CO_2$ transport. However, road and rail tankers are uneconomical compared to pipelines and ships, except on a small scale, and are unlikely for large-scale CCS deployment. During this process, $CO_2$ is typically compressed above 8 MPa and transferred as a liquid or a supercritical fluid to avoid two-phase flow regimes and to increase the density of $CO_2$ [17]; this reduces the energy consumption and the cost of using compressors. However, small changes in temperature, pressure or impurity concentration can have a large impact on the density of the fluid. This greatly affects the amount of $CO_2$ that can be transferred (flowrate) and greatly influence the pipeline designs. Current research is focused on reducing cost and further improving safety by developing new predictive models for $CO_2$ pipeline design. The challenge for the future transport technology is to develop long-term strategies to cluster $CO_2$ sources and develop $CO_2$ pipeline networks that will optimise the CCS process [8].

### 1.2.3 Carbon Storage

Carbon storage refers to the geological storage of anthropogenic carbon dioxide to achieve long-term isolation from the atmosphere, in which $CO_2$ is injected into suitable geologic formations that are typically located between one and three kilometres underground. There are several suitable sites for carbon storage: deep saline aquifers, depleted oil and gas fields, oil fields with the potential for enhanced oil recovery (EOR) and un-minable coal seams. Out of these storage options, it is expected the saline aquifers will provide the greatest quantities of $CO_2$ storage, followed by oil and gas reservoirs [18, 19]. Oil and gas reservoirs are a favourable option for sequestration of $CO_2$ due to their known geological seal. Once $CO_2$ is underground, $CO_2$ can be efficiently stored through a variety of trapping mechanisms. There are four main trapping mechanisms: (1) structural trapping ($CO_2$ is stored and sealed below impermeable cap rocks), (2) capillary trapping ($CO_2$ trapped by capillary forces in the porous reservoir rocks) (3) solubility trapping (dissolution of $CO_2$ into the native reservoir fluid) and lastly (4) mineral trapping (mineralisation of $CO_2$ and turned into new chemical components) [20]. The identification of suitable $CO_2$ storage reservoirs is critical to CCS deployment. There have been potential storage sites identified in countries such as Australia, China, Canada, United States and the European Union [20]. The choice of storage sites depends mainly on three technical requirements: (1) containment (ability to store $CO_2$ securely with low and manageable risks), (2) capacity (ability to store a required amount of $CO_2$ permanently) and (3) injectivity (ability to accept $CO_2$ at an

appropriate rate in relation to the capture process). Site characterisation and selection are crucial for successful geological storage and techniques used for the exploration of oil and gas reservoirs have been implemented for characterising geological sites for $CO_2$; for example the usage of seismic data to evaluate storage formations and seals. Computer simulation of storage reservoir dynamics and monitoring methods from existing applications are also being developed further for design and operation of geological storage. In addition, monitoring of storage sites and detection of leakage are paramount to an overall risk management strategy for geological storage projects [21, 22]. A variety of proven technologies has been deployed at pilot and commercial-scale projects, demonstrating the successful measurement, monitoring and verification of injected $CO_2$ in the subsurface. Based on observation and analysis of current $CO_2$ storage sites, engineering systems and models, the fraction of $CO_2$ retained in reservoirs is likely to exceed 99% over 100 years, and is likely to exceed 99% over 1000 years. The risk of leakage is expected to decrease over time as another trapping mechanism such as mineralisation will provide additional trapping. There are three on-going $CO_2$ storage projects; the Sleipner project [23] by Statoil in the North Sea (Norway), the Weyburn project (Canada) [24] and the In Salah project (Algeria) [25]. Since the beginning of operation in 1996, the Sleipner project has injected over 16 Mt of $CO_2$ underground.

### 1.2.4 Enhanced Oil Recovery

Enhanced oil recovery (EOR) helps to extract hydrocarbons when the oil left in reservoirs after traditional recovery methods have reached their economic limits (increase sweep efficiency). The principle behind EOR is to alter the oil flow properties and oil-rock interactions in the reservoir, enabling more production. The percentage of original oil in place (OOIP) remaining after primary and secondary recovery varies from field to field, but a study on 10 US producing regions found that about two-thirds of the original oil in place remains after traditional recovery methods [26]. There are several ways to enhance oil recovery; water-flooding with polymers or chemicals or low salinity, hydrocarbon gases injection and $CO_2$ injection. Water-flooding is often used for its availability and low-cost; surfactants are sometimes added to the flooding water to lower the interfacial tension between the water-rich phase and the hydrocarbon-rich phase, which promotes recovery of oil trapped by capillary forces. Light hydrocarbon gases are also used as they are miscible with the crude oil in the reservoir. Recently, the use of carbon dioxide in EOR has gained much popularity due to its high availability, low-cost, non-toxic and non-flammable characteristics [27]. Currently, the largest single use of anthropogenic $CO_2$ is for EOR processes which consume more than 60 Mt $CO_2$ per year. At sufficiently high pressure, $CO_2$ is usually miscible with crude oil and this avoids a formation of an interface between the crude oil and $CO_2$ (less potential for trapping due to capillary forces). The same study suggested that about 23 % of the remaining oil could be produced using $CO_2$ flood technologies [26]. However, it is worth noting that $CO_2$ may cause fouling inside the reservoir due to asphaltenes

precipitation. Therefore $CO_2$ is not always favourable for EOR in all reservoirs and the choice of EOR solvent is highly dependent on the physical properties of crude oil.

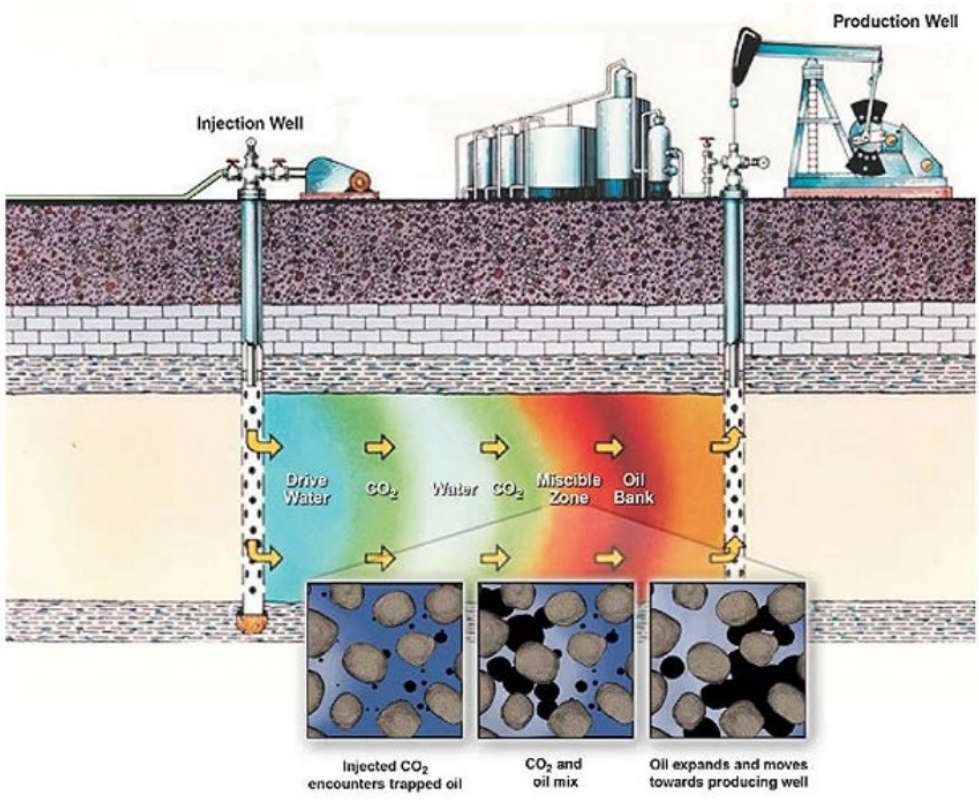



**Figure 1.3** Enhanced oil recovery process

During $CO_2$-EOR, the injection of $CO_2$ changes certain thermophysical properties of the crude oil; these include interfacial tension, wettability, viscosity, density and phase behaviour. The injected $CO_2$ can be either immiscible or miscible with the crude oil depending on the reservoir pressure. This defining reservoir pressure is known as the minimum miscibility pressure (MMP) which is often determined by laboratory–scale experiments with oil + $CO_2$ mixtures such as the slim-tube experiment [28]. At a typical reservoir temperature and pressure condition, complete miscibility of $CO_2$ is rarely achieved; however, it can extract hydrocarbons from the oil if the pressure is high enough. Essentially, two phases are formed during $CO_2$ injection: one phase is rich in $CO_2$ and light hydrocarbons, and the other is rich in heavier hydrocarbons. The $CO_2$-rich phase is a low-viscosity that travels quickly away from the injection well, contacting fresh oil from which it extracts further hydrocarbons. In this miscible or partially-miscible $CO_2$ displacement, a fraction of the oil is dissolved in the $CO_2$ and transported to the production wells. In addition, the carbon dioxide dissolved in the heavier hydrocarbon-rich phase can decrease the oil density and viscosity of the oil which aids the extraction process [27]. This expanded oil can also flow through the reservoir towards the production wells. Once the production is complete, part of the injected $CO_2$ can be potentially stored

permanently in the reservoir for the purpose of climate change mitigation. The fraction of $CO_2$ that can be retained underground depends on physical and geological properties on the storage site. At the moment, EOR processes are implemented worldwide to improve the recovery of the remaining oil in place. The first $CO_2$-EOR project was commenced at the Weyburn field in Saskatchewan, Canada in 2000. Another significant $CO_2$-EOR project is the Uthmaniyah demonstration project [29]. It started in July 2015 and is located in the eastern province of the Kingdom of Saudi Arabia; it primarily focuses on research and development of CCS.

### 1.2.5 CCS Challenges

CCS is technologically feasible and could be significant in meeting the global reduction of $CO_2$ emission target; however, there are still barriers in deploying CCS at full scale. The implementation of large-scale CCS plants requires extensive funding which in the present energy market, cannot be justified. Currently, implementing CCS lacks significant and long-term financial rewards, and without financial backing from private entities or governments, the task of implementing CCS at a large scale is more challenging and arduous. For example, two CCS demonstration projects in the UK, the Peterhead CCS project and the White Rose CCS project [30, 31] have been cancelled after the government's decision to cut the funding for CCS demonstration. Instead, the UK government have decided to invest in other low-carbon technologies namely the renewables which generally have wider acceptance from the public. With the competitions from renewable energies and the lack of public confidence and understanding, these have made implementing CCS even harder. To date, there have been 38 large-scale CCS projects around the world, either in operation, under construction or in various stages of development planning [32]. Most of the CCS projects have utilised $CO_2$ for EOR purposes as the overall CCS cost can be compensated by the EOR revenues. While the technology of $CO_2$-EOR has become more mature, there is still relatively little experience with the combination of $CO_2$ capture, transport and storage in a fully integrated CCS system. IPCC suggested that the integration of capture, transport and storage in full-scale projects is needed to gain the knowledge and experience required to accelerate the CCS deployment [33]. Both knowledge and experience not only will reduce the uncertainty about $CO_2$ capture, transport and storage, but also reduce the overall cost which is important to enable its large-scale deployment. As can be seen, CCS remains a huge challenge ahead, and more research and development of different stages of the process is necessary.

## 1.3 Project Motivations and Scientific Significance

Thermophysical properties are among the most fundamental scientific consideration with regards to a wide range of industrial processes including the crude oil extraction and the CCS processes. The fluid properties of interest include vapour-liquid equilibrium (VLE) data, density, heat capacities, speed-of-

sound and viscosity, often have great significance and are key to process design optimisation with respect to economy, operability and safety. For instance, thermophysical properties of hydrocarbon systems are of particular importance to the oil and gas industry as they are required throughout their entire value chain. In the upstream operation, thermophysical properties data are used when designing the injection and production strategies; in the downstream business, the design of production and separation facilities is dependent on the $p\rho T$ properties. Carbon dioxide is naturally present in the reservoir fluid, but it is also injected into hydrocarbon fields for enhanced oil recovery (EOR) purposes to increase the sweep efficiency. During EOR, $CO_2$ is injected into the reservoir and causes a change in the physical properties of the crude oil. To understand how $CO_2$ mixes with hydrocarbons, there has been an increase in interest in the fluid property behaviour of carbon dioxide and hydrocarbon mixtures [34-36]. Knowledge of thermophysical properties for mixtures of $CO_2$ and hydrocarbons is essential for the optimisation of the carbon capture and storage process. Conducting experiments on the thermophysical properties of $CO_2$ and $CO_2$-rich binary mixtures of hydrocarbons should be able to provide a fundamental basis for understanding the CCS process.

Studying thermophysical properties experimentally is considered the most accurate way as experimental data can be obtained through high-accuracy measurements with small uncertainty. However, direct measurements of thermophysical properties under high-temperature and high-pressure (HTHP) conditions are not straightforward regarding equipment design and procedures; providing these data is challenging and time-consuming from an experimental perspective. Therefore predictive models remain necessary for predicting properties accurately at conditions that are not experimentally measured. Processes in the industry normally involve multicomponent systems over an extensive range of operational conditions from atmospheric to supercritical states. At the moment, the industry relies on predictive thermodynamic models and reservoir/process simulations to simulate the thermophysical properties of hydrocarbons at reservoir conditions. To ensure robust and safe operations, the thermodynamic models used for these simulations are required to be optimised and validated with a wide range of accurate experimental data [37]. These models performance can only be as accurate as the quality of the experimental results and therefore it is of great importance to have reliable measurements of the thermophysical properties to develop high-accuracy models.

Although thermophysical properties of hydrocarbons have been studied extensively, to our understanding, there remain gaps in the literature at elevated conditions. The available experimental data measured under HTHP conditions are scarce. The lack of experimental data hinders the validation and development of the models, and this scarcity of data issue has been highlighted in several works [38-40]. Therefore there is a need to provide high-accuracy experimental data at the

widest temperature and pressure range possible of representative system to address the scarcity issue and to facilitate the development of models.

Among all thermophysical properties, sound-speed in particular, has gained popularity in recent years as it contains numerous applications. Petroleum geologists measures the speed-of-sound in rocks, known as the reflection seismology, for the detection of crude oil and hydrocarbon exploration. Seismic reflection technique works on the principle of the time taken for the reflected sound waves to travel through a matter of varying densities and the speed at which sound travels through rock depends on mineral composition, porosity and fluid saturation [41]. In academia, the speed-of-sound as a function of temperature and pressure can provide valuable information for the characterisation of real fluids such as the calculation of the virial coefficients for gases [42, 43], the determination of phase equlibria and the critical point [44, 45]. Sound-speed also has an important role in the development and verification of equations of state due to its experimental accuracy [46].

As mentioned, direct measurements of thermophysical properties such as density and heat capacities at high-temperature, high-pressure (HTHP) conditions are challenging and less reliable regarding equipment design and experimental accuracy. Speed-of-sound measurement in fluids through ultrasound can still maintain the high-accuracy under extreme conditions which offers an indirect way of obtaining the thermophysical properties. Due to the simplicity and rapidity of ultrasonic measurements, this has led to a large amount of studies on the thermophysical properties with this method. With the close linkage of ultrasonic sound-speed, volumetric properties and enthalpic properties of fluids, it is possible to extract important thermodynamic properties using thermodynamic relations, given in the following form:

$$c^2 = \left[ \left( \frac{\partial \rho}{\partial p} \right)_T - \left( \frac{T}{\rho^2 c_p} \right) \left( \frac{\partial \rho}{\partial T} \right)_p^2 \right]^{-1} . \tag{1.1}$$

From the expression, it is then possible to calculate all observable thermodynamic properties once the sound-speed $c$, density $\rho$, and isobaric heat capacity $c_p$ are known for all temperatures and pressures of interest. The method of deriving thermophysical properties from sound velocity data has been tested and used by several authors in the past [47-51].

## 1.4 Scopes and Objectives

The aim of this research was to study the fundamental physical chemistry of systems that are crucial to many industrial processes as well as the $CO_2$-driven enhanced oil recovery process. The main objective of the present work was to perform experimental measurements of thermophysical properties in wide ranges of temperature and pressure to understand the behaviour of pure hydrocarbons and $CO_2$ + hydrocarbons systems under reservoir conditions. Studying simplified mixtures can provide valuable information about their behaviour under operating conditions both from a fundamental and model development point of view. The collected experimental data were implemented to test the predictive abilities of several available thermodynamic models. These data also aim to address the scarcity issue of thermophysical data for hydrocarbons in the literature under extreme conditions.

Accurate density and speed-of-sound measurements of representative pure hydrocarbons and binary mixtures of hydrocarbons and $CO_2$ were carried out. Before the measurement campaign, a comprehensive literature review was conducted to evaluate both the quantity and quality of the existing data and to identify the knowledge gaps in the literature. The experiments were conducted in the single-liquid-phase at sub-critical and supercritical conditions. To accomplish these measurements, a built-in-house ultrasonic cell was used to measure the speed-of-sound from temperatures between (263.15 and 473.15) K and pressures up to 400 MPa, and the density measurements were carried out with a vibrating-tube densimeter at temperatures from (283.15 to 473.15) K at pressures up to 70 MPa. The measuring apparatus was calibrated and validated before measurements to ensure the correctness and the accuracy of the data. The experimental data were represented by empirical correlations which permitted interpolations within the range of pressures and temperatures studied. In the cases with available literature data, comparisons were made with the experimental results.

For pure hydrocarbon systems measured, the collected speed-of-sound and density data were combined with isobaric heat capacity data and a full spectrum of thermophysical properties as a function of temperature and pressure were derived via the thermodynamic integration. The derived properties were compared with the predictions calculated from their reference equations of state. In the cases of binary mixtures of $CO_2$ + hydrocarbons, experiments were performed in a wide range of compositions to study the effects of the addition of $CO_2$ on hydrocarbons' density and speed-of-sound. These data would help to understand the behaviour of $CO_2$-rich mixtures and could be used to test the modelling aspects of different thermodynamic models.

Furthermore, one of the objectives was to test several different thermodynamic models against the collected experimental data. Comparing experimental data with the predictions of various equations of state will allow the understanding of the capabilities and limitations of the available predictive models. The predictive capability of the Predictive Peng-Robinson (PPR78) equation of state, SAFT-γ Mie equation of state and several multi-parameter Helmholtz energy explicit equations of state was evaluated. These models have been successfully applied to the study of the thermophysical properties of hydrocarbon systems in the past; they have been rarely tested with second derivative properties such as the speed-of-sound in binary $CO_2$ + hydrocarbon systems, as measured data were scarce in the literature. Typically, pure component and binary mixture thermodynamic data are used in the calibration and optimisation of the predictive models. Once the thermodynamic models are optimised with reliable data, they can be employed for predicting other thermophysical properties such as phase behaviour and density of relevant systems at a much wider range of conditions. The new experimental data would allow testing of the models and provide a basis for improving the performance of the EoSs through parameter optimisations.

Finally, in line with the overall research objectives, an addition study on the speed-of-sound, density, isobaric heat capacity and viscosity of two calibration fluids (mixtures of hydrocarbons) were performed at temperatures between (263.15 and 473.15) K and at pressures up to 300 MPa. The viscosity and the isobaric heat capacity measurements were carried out by means of the vibrating-wire and the flow calorimetry techniques, respectively. The experimental results were fitted with empirical models and the modelling capability of the correlations was evaluated. The performance of the vibrating-wire viscometer and the flow calorimeter at high-temperatures was also tested.

Overall, the outcome of this research should provide more understanding about the thermophysical properties of hydrocarbons and hydrocarbons with dissolved $CO_2$ at high-temperature, high-pressure conditions. Although the measurements were carried out at pressures much higher than the typical pressure limits of industrial processes or reservoir conditions, it is helpful in the development of equations of state to have data over the widest possible range of thermodynamic states. The measured speed-of-sound and density data together with the derived thermophysical properties data of the present work can evaluate the capabilities and accuracies of several widely used thermodynamic models. These will benefit both the oil and gas industry and academia where precise thermophysical properties of hydrocarbons are required.

## 1.5 Thesis Outline

The rest of this thesis commences in Chapter 2 with a discussion of the theoretical background and literature of speed-of-sound and density, measurement equipment and techniques together with the research developments in the field. This is followed in Chapter 3 by a review of the modelling approaches relevant to the present work. Complete descriptions of the measuring equipment used in the work and calibration methods are outlined in Chapter 4. A large part of this PhD research is presented, analysed and discussed in detail in Chapters 5 and 6. Chapter 5 focuses on the measurements of pure hydrocarbon systems, while measurements of hydrocarbons with the addition of $CO_2$ are discussed in Chapter 6. These two chapters include the collection of experimental speed-of-sound and density data, detailed analyses, comparison with available literature data and comparison with several thermodynamic models including the predictive cubic equation of state, SAFT-γ Mie equation of state and Helmholtz free energy based equations of state. Chapter 7 summarises the work carried out on two industrial fluids which includes experimental isobaric heat capacity and viscosity measurement as well as the sound-speed and density measurement. The thesis finishes with the main conclusions and recommendations for future work which are summarised in Chapter 8.

# Chapter 2: Speed-of-Sound and Density: Measurement Techniques and Literature Review

## 2.1 Overview

This chapter gives the summary of the major techniques available for measuring speed-of-sound and density, focusing predominantly on high-pressure applications. The steady-state and the transient methods for speed-of-sound measurement were described; examples of the apparatus which implements these techniques are presented. For density measurements, the direct and indirect techniques are introduced. In addition, a comprehensive literature review of the available speed-of-sound and density data for pure hydrocarbons and binary systems of $CO_2$ + hydrocarbons are also given in this chapter.

## 2.2 Speed-of-Sound

Sound waves are longitudinal waves which propagate via a series of compressions and rarefactions in a medium which can be either gas, liquid or solid. In longitudinal waves, the particle motion is in the same direction as the movement of the wave, these are also know as the primary waves (p-waves). The speed-of-sound in a fluid is a thermodynamic property that changes with temperature $T$ and pressure $p$. Derived from the first law of thermodynamics, the speed-of-sound $c$ is defined as the isentropic pressure variation with respect to density for a single-phase flow, described fundamentally in the following expression:

$$c^2 = \left(\frac{\partial p}{\partial \rho}\right)_S , \tag{2.1}$$

where $p$, $\rho$ and $S$ denote pressure, density and entropy, respectively. Speed-of-sound data are able to give direct and precise information on the adiabatic properties of a fluid since sound propagation is assumed to be an irreversible adiabatic process. For convenience, the isentropic partial derivative in Equation (2.1) can be changed into isothermal and either isobaric or isochoric partial derivatives depending on which pair of independent variables are preferred, by using standard thermodynamic relations. The speed-of-sound can be expressed in the following form:

$$\begin{aligned} c^2 &= \left[\left(\frac{\partial \rho}{\partial p}\right)_T - \left(\frac{T}{\rho^2 c_p}\right)\left(\frac{\partial \rho}{\partial T}\right)_p^2\right]^{-1} \\ c^2 &= \left[\left(\frac{\partial p}{\partial \rho}\right)_T + \left(\frac{T}{\rho^2 c_v}\right)\left(\frac{\partial p}{\partial T}\right)_\rho^2\right] \end{aligned} , \tag{2.2}$$

where $c_p$ and $c_v$ are the specific isobaric and isochoric heat capacities, respectively. This expression relates the speed-of-sound to density and isobaric heat capacity and it can be seen that a full spectrum of thermophysical properties can be derived with the knowledge of these properties [47, 50, 52]. A detailed description of the mathematical analysis required to obtain the appropriate data is presented in Chapter 3. The thermophysical properties that can be determined via this method include density, isobaric and isochoric heat capacities, isentropic and isothermal compressibilities and isobaric expansivity. As a result, speed-of-sound data would be of great help in providing thermophysical properties. In addition speed-of-sound data are always important to academic research as well as industrial operations. For example, knowledge of single-phase liquid sound velocities as a function of temperature and pressure is of great importance for fundamental theories of liquids which are used for the validation of thermodynamic models and they are implemented in many fields of technology, such as the extraction of oil and gas mixtures from reservoirs at elevated temperatures and pressures. One of the most common techniques to measure the speed-of-sound in fluids is by ultrasonic methods. These techniques have been used increasingly for determining equations of state and thermodynamic

properties of liquids at elevated pressures due to their simplicity and rapidity of the experimental procedure and they will be discussed in details in the following section.

## 2.2.1 Speed-of-Sound Measurement Techniques

There are many different experimental techniques for speed-of-sound measurement in fluids over a wide temperature and pressure range. The most common techniques to measure speed-of-sound can be categorised as variable-frequency fixed cavity resonators, variable path-length fixed frequency interferometer, and time-of-flight methods. The section gives a summary of the two most commonly used methods to measure sound-speed: (1) the steady-state methods and (2) the transient methods.

*2.2.1.1 Steady-State Techniques*

The steady state technique involves the use of a constant wave source in which standing waves are formed inside an acoustic cavity. The steady state methods are typically used for measuring sound-speed in gas up to pressures of the order of 10 MPa. However, this technique is only effective when the walls of the acoustic cavity reflect sound efficiently, so this technique is ideal for gases as the characteristic acoustic impedance is too small for liquids [53]. Different operation modes are available when using the steady state method: (1) variable volume acoustic cavity, (2) fixed volume acoustic cavity, operating at either (3) low frequency or (4) high frequency. Variable volume cavity which involves greater design complexity is usually used for liquid studies and fixed volume for gas studies. Variable volume cavity instruments, also known as interferometers normally contain a hollow tube closed at one end with a transducer and a movable piston which allows the change of acoustic cavity. The transducer operates at a fixed frequency which produces standing waves within the cavity. The speed-of-sound is obtained by adjusting the acoustic cavity with the piston until resonance occurs at the corresponding operating frequency. Resonance occurs when the length of the cavity is adjusted to an integer multiple of $\lambda/2$, where $\lambda$ is the wavelength of the sound at a specific pressure and temperature. [53]. The interferometers can be operated in a single- or a double-transducer arrangement. In the single-transducer arrangement, resonance can be detected by measuring either the mechanical or the electrical impedance of the loaded transducer as the piston is displaced. In the double-transducer arrangement, a second transducer is fitted on the piston and the acoustic pressure is monitored as a function of displacement. Fixed volume cavity instruments, also known as acoustic resonator has a fixed acoustic cavity and normally with two transducers. One transducer acts as the emitter and the other as the detector. The method of determining speed-of-sound is to drive the transducer with a range of frequencies. The frequency of the sound wave is altered to which resonance occurs inside the acoustic cavity containing the experimental fluid. The methods used to determine the resonance frequencies in a fixed cavity resonator have been documented elsewhere [54, 55]. Acoustic resonators can be cylindrical or spherical in shape [42, 56]. It has to be noted that the resonance frequency for a specific experimental fluid is not only a function of temperature and pressure, but also

a function of the geometry. Spherical geometry is preferred to cylindrical as it has a favourable volume-to-surface ratio which produces sharper resonances [57]. However, spherical resonators are harder to fabricate. The typical relative uncertainty obtained with a spherical resonator at pressures below 1 MPa is in the order of $10^{-5}$ [58]. There has been several designs of the spherical resonators [56, 59-61] and Figure 2.1 below shows a schematic of a spherical resonator designed by Ewing and Goodwin.

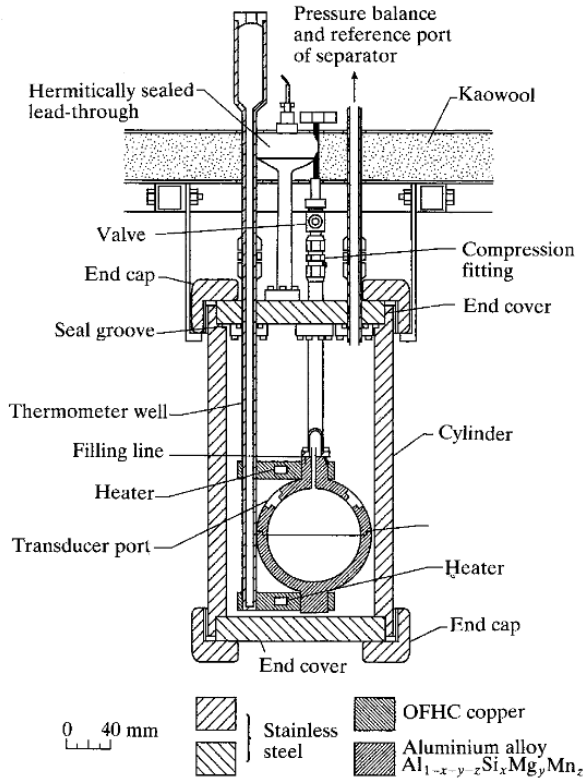



**Figure 2.1** Cross-section view of a high-pressure speed-of-sound apparatus with a spherical resonator. Reproduced from Ewing and Goodwin [60].

Measuring the speed-of-sound in either high or low-frequency offer both advantages and disadvantages. In low-frequency operation, the sound wavelength is the same order of magnitude as the dimension of the cavity, this usually gives a good resolution but boundary-layer effects may be large. Whereas in high-frequency operation, it avoids the large boundary-layer effects but resulting at a lower resolution. Therefore, the high-frequency operation is more suitable for the study of liquids and low-frequency operation is more appropriate for gases. A more detailed analysis of boundary-layer effects and associated theory are given by Trusler [53].

*2.2.1.2 Transient Techniques*

The sound-speed in fluids can be determined, often with very high precision, with the transient method. This method determines the speed-of-sound from a measurement of the time taken for a pulse to travel a known distance in the liquid under investigation. The transient methods can be divided into

two categories: pulse methods and reverberation techniques. The pulse technique is regarded as a non-destructive measuring technique which is widely used in the field of material testing. Most sound-speed measurements for liquids are carried out with the pulse method. The pulse method is also known as the sharp pulse method. Pulse methods are typically used with carrier frequencies from about 1 MHz upwards, but lower frequency operation can also be used for fluids with large absorption coefficient [53]. The adsorption effect of fluids will be discussed in the following section. The pulse method is the simplest way of determining speed-of-sound; the method consists of a fixed path-length cell with two transducers placed at the opposite ends of a known distance apart in a fluid. A single pulse is fired from one transducer and propagates to another transducer through the fluid. The time-of-flight is measured by an interval timer or an oscilloscope. In general, the speed-of-sound $c$ can be determined using a simple relation with a distance $L$ and time of flight $t$:

$$c = \frac{L}{t}. \tag{2.3}$$

This method was used in the 1980s by Takagi and Teranishi [62-65] who studied the speed-of-sound in various organic liquids and mixtures at pressures up to 210 MPa and temperatures between (278.15 and 343.15) K. Their ultrasonic cell contained a pair of 1 MHz transducer separated by a fixed path-length and the time-of-flight was measured using an electric time interval counter. However, this method does not measure the time-of-flight to a high accuracy since it is affected by diffraction of signals and electronic time delays in the transducer during signal transfer. Hence this method is associated with a high uncertainty, and the experimental data are considered accurate to 0.3%. In recent years, two significant improvements to the pulse technique that are able to reduce/eliminate electronic time delay error and diffraction error arise during measurement have been reported: (1) the pulse-echo-overlap method and (2) the pulse-echo phase comparison method. In the pulse-echo-overlap method, the excitation signal is delayed by a delay circuit and is made to overlap onto the signal travelling in the sample; the speed-of-sound is determined from the retardation time from the delay circuit and the path-length of the measuring cell. Sound-speed measured with this technique was considered accurate to 0.1 %. This method was used by Daridon and co-workers [66-69] who studied the speed-of-sound in petroleum fluids at temperatures between (283.15 and 423.15) K at pressure up to 90 MPa. The same technique has also been used by Lainez and co-workers [70-72] who made measurements between (180 and 455) K at pressures up to 210 MPa for refrigerants and chlorinated compounds. The pulse-echo phase comparison technique (primarily used for measuring the speed-of-sound in liquid) was introduced by Kortbeek *et al.* [73] in 1985. It involved a single transducer held between two parallel reflectors. The sound-speed is measured from the difference between the round-trip transit times in two un-equal path-lengths. The transit time measured was corrected for the time delay by comparing the travelling times obtained for the first and second echo. The accuracy was estimated to 0.1 %. This technique normally involved a fixed path-length cell with a quartz transducer and reflector placed at both ends. In 1985, Sun, Kortbeek and co-workers [74] measured the effect of

pressure on the speed-of-sound and density of methylbenzene and heptane at pressures up to 260 MPa and temperatures between (185 and 320) K with this technique.

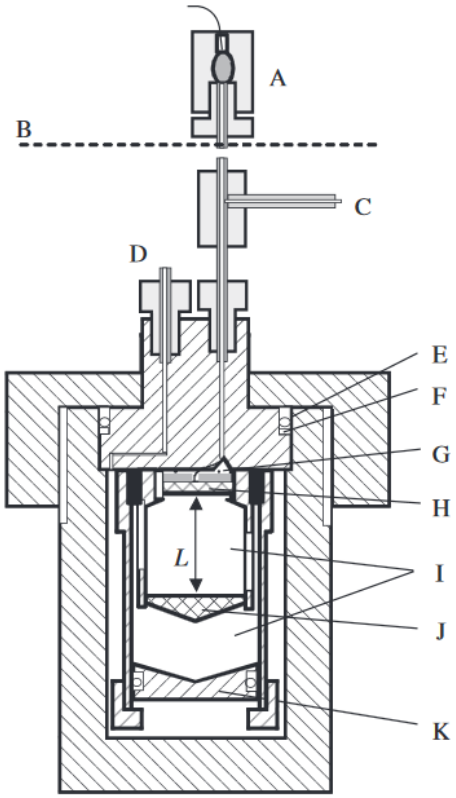



**Figure 2.2** Acoustic interferometer employing a free piston, reproduced from Takagi [75]. A, electrode; B, water level; C, tube leading to sample injection, pressure transducer; D, tube leading to the pressure generator line; E, O-ring; F, backup ring; G, spring; H, piezoelectric transducer; I, sample chamber; J, reflector; K, moveable piston; L, distance between transducer and reflector

Double pulse method is also used to measure the speed-of-sound in fluids. The principle is based on the phase comparison pulse-echo method proposed by Sun *et al.* [51, 74, 76, 77] who measured speed-of-sound in liquids at pressures up to 300 MPa. Their cell contained an X-cut quartz crystal of 2 MHz which served as both the transmitter and the receiver, was clamped in a hollow copper cylinder. Two copper reflectors placed at un-equal path-lengths of (4 and 6) cm from a transducer. At the start of the cycle, a pulse is fired from the transducer; the pulse travels to the left and the right of the transducer and reflects by both reflectors. After an appropriate time, a second pulse is introduced into the medium such that the echo of the first pulse travelling the longer path and the echo of the second pulse travelling the shorter path arrive at the quartz transducer simultaneously. With the amplitudes of the pulse adjusted, the two pulses can overlap with each other completely at certain frequencies. The transit time and sound velocity, therefore, can be determined by measuring the frequencies. Figure 2.3 below shows the principle of the method implemented by Sun *et al.*

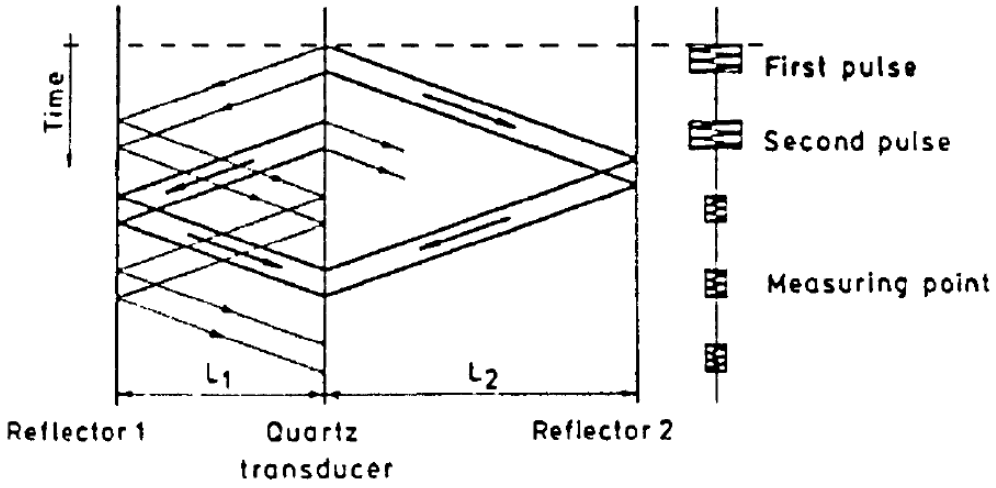



**Figure 2.3** Principle of the phase comparison pulse-echo method with two reflectors. Reproduced from Sun *et al.* [77]

The reverberation technique offers an advantage over the pulse technique for low-frequency operations. At low frequencies, the measurements of attenuation by the pulse methods are subject to large losses from beam spreading and become inaccurate. The reverberation method measures the half-width of a resonance under steady-state conditions and usually the fluid under study is contained within a fixed volume resonator. The reverberation time is the period required for the sound to decay and the speed-of-sound is derived together with the acoustic pressure. This type of operation is more generally focused on sound absorption measurements rather than sound-speed. A more detailed description of the reverberation technique and associated theory are given by Trusler [53].

*2.2.1.3 Source of Uncertainty*

Transient techniques are generally only suitable for homogenous liquids measurements; it is unsuitable for two-phase fluid measurements (i.e. liquid and gas) as the gas bubbles can cause excess sound attenuation due to scattering of the sound waves by the bubbles and bubble resonances. Apart from uncertainties arise from temperature and pressure, other main sources of uncertainty of an ultrasonic measurement can be determined based on two factors: the signal attenuation and signal-to-noise ratio. There are two causes of attenuation through a medium: (1) diffraction and (2) sound absorption. Diffraction error and absorption coefficient of the fluid determines the choice of the operating frequency of the transducer. In general, diffraction losses are relatively small compared to the sound absorption of the fluid at high frequencies (1 MHz or above). A high absorption coefficient fluid (mainly gases) will result in poor or no signal detection when a high frequency is applied. At low frequencies, pulses are subject to large loss from beam spreading and the measurement becomes inaccurate. The effect of diffraction and absorption will be discussed further in the following section.

**Diffraction Corrections [78]:** Due to the finite size of a piezo-transducer, the acoustic beam spreads out into a diffraction field which introduces errors in both attenuation and velocity measurement. The diffraction error is related to the ratio of source dimension to acoustic wavelength and therefore the diffraction error is significant for low frequencies and small transducers. The signal diffraction is an error coming from the measured transit times due to the phase advance of the ultrasonic pulses relative to a plane wave travelling through the same distance. The diffraction correction for the measured transit time is given as:

$$\delta t = \frac{[\phi(L_2) - \phi(L_1)]}{2\pi f}, \tag{2.4}$$

where $f$ is the operation frequency and $\varphi(L)$ is the phase advance as a function of the path length, $L$. A detailed analysis was undertaken by Williams [79], who assumed that a source vibrates harmonically like a piston. The receiver, which is equal in size and parallel to the source, responds to a mean acoustic pressure over its entire surface and not just at a point. This analysis is also valid, as in this case, where a reflector is used in place of the second transducer assuming that the reflector diameter is equal or greater than that of the source. The free field diffraction effect for a source of radius $b$ can be estimated by [53, 79]:

$$A\exp(i\phi) = 1 - \frac{4}{\pi}\int_0^{\frac{\pi}{2}} \exp\left[-\left(\frac{4b^2\pi i}{L\lambda}\right)\cos^2\theta\right]\sin^2\theta d\theta\,. \tag{2.5}$$

This equation describes the free-field diffraction effects in a single transducer, multiple reflectors system, provided that the diameter of the reflector is equal or greater than that of the transducer. From Equation (2.5), it can be seen that the required diffraction correction is a function of the path length difference, therefore, in theory, the dimension of the ultrasonic cell can be optimised to minimise the overall correction required for the time of flight. The use of the overlapping technique can also provide an advantage in which the majority of the diffraction effect cancels out. The sound field of a transducer is divided into two zones: the near-field and far-field. The near-field region refers to the area directly in front of the transducer where the echo amplitude goes through a series of maxima and minima. The last maximum is known as the near-field distance. The region beyond the near field region is known as the far-field where the sound field pressure gradually drops to zero. Giuliano Albo *et al*. [80] identified that the ultrasonic signals are perturbed in the near-field zone during ultrasonic measurement, and this phenomenon affects the reliability of the ultrasonic measurement. The near-field distance is a function of the transducer frequency, transducer diameter and the sound velocity profile of the medium. The expression for the near-field limit, $d_0$ can be estimated with the following expression:

$$d_0 = \frac{4r^2 - \lambda^2}{4\lambda}, \tag{2.6}$$

where $r$ is the radius of the source and $\lambda$ is the wavelength. As suggested, this phenomenon can be overcome by reducing the operating frequency and the design of the apparatus.

To see the effect of diffraction on sound-speed measurements, an estimation of the diffraction correction for (4 and 5) MHz operations was provided. From Figure 2.4, it can be seen that the diffraction correction ranges from (0.001 to 0.015) % between values of speed-of-sound between (300 and 1500) $m \cdot s^{-1}$ and up to 0.03 % at sound speed up to 2000 $m \cdot s^{-1}$. The diffraction corrections were calculated by using the expressions described in Equation (2.5) with $b$ = 4 mm (inner radius of the clamping rings) and it was found that this correction amounted to less than 0.02 % of the measured transit time difference. The results showed that the diffraction effect is smaller compared to the experimental uncertainty and therefore diffraction corrections were not considered in the present work.

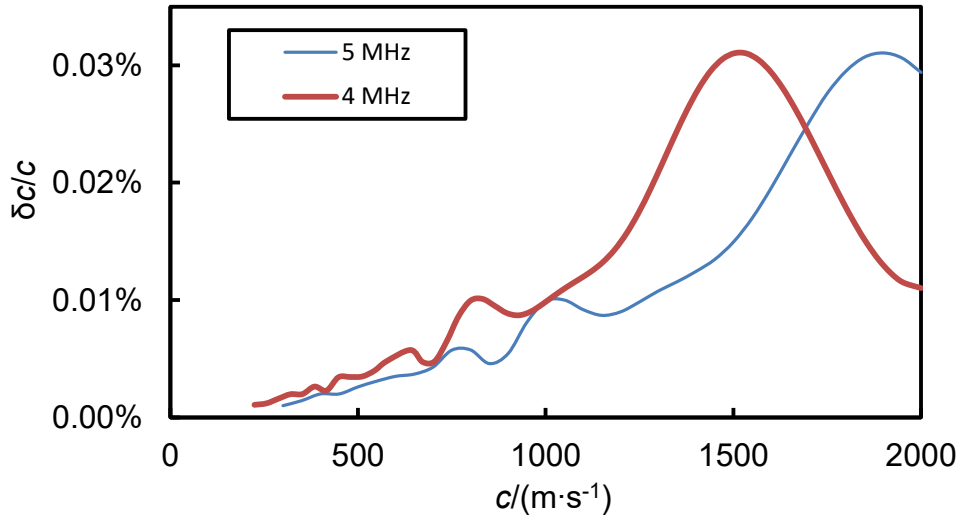



**Figure 2.4** The sound-speed correction due to diffraction for (4 and 5) MHz operation for the pulse-echo measurements.

**Sound Absorption and Thermal Relaxation:** Thermal relaxation is a potential source of systematic error in sound-speed measurements which can lead to dispersion and attenuation of sound [53]. In the case of high adsorption fluids, the thermal relaxation time which is inversely proportional to density can cause poor signal or no signal. Sound absorption occurs when the measuring frequency is higher than the inverse of relaxation time, in other words, sound adsorption has a strong influence when the wavelength of the sound wave is shorter that the thermal relaxation time. The thermal relaxation time is dominated by the time required for the transfer of energy from translational to vibrational modes of molecular motion. The sound absorption is associated with vibrational relaxation of molecules. The sound absorption coefficient, $\alpha$ at a frequency, $f$ can be estimated through the following expression [81]:

$$\frac{\alpha}{f^2} = \left[\frac{\pi(\gamma-1)\Delta}{f_0 c_0}\right]\frac{1}{1+(f/f_0)^2}, \tag{2.7}$$

where $\gamma$ is the heat capacity ratio, $\gamma = c_p/c_v$, $c_p$ and $c_v$ are the molar heat capacity at constant pressure and volume, respectively. $\Delta = c_{\text{vib}}/c_p$, $c_{\text{vib}}$ is the vibrational contribution to the molar heat capacity, $c_0$ is the speed-of-sound at zero frequency, $f_0 = [2\pi(1-\Delta)\tau_{11}]^{-1}$ is the appropriate relaxation frequency, and $\tau_{11}$ the isothermal vibrational relaxation time. For a pure substance, the inverse of the isothermal vibrational relaxation time is given by,

$$\tau_{11}^{-1} = (\bar{\upsilon}/\lambda)P_{11}^*,$$

where $P_{11}^*$ is the probability that a collision will give rise to vibration-translation energy exchange, $\bar{\upsilon}$ is the mean molecular speed, $\bar{\upsilon} = (8RT/\pi M)^{1/2}$, λ is the mean-free path, $\lambda = \left(\sqrt{2}\pi\sigma^2 n\right)^{-1}$. The speed-of-sound, $c$ at finite frequency is related to the speed-of-sound at zero frequency, $c_0$:

$$\left(\frac{c_0}{c}\right)^2 = 1 - \left[\frac{(\gamma-1)\Delta}{(1-\Delta)}\right]\frac{(f/f_0)^2}{1+(f/f_0)^2}. \tag{2.8}$$

From the above expressions, the dispersion and absorption effect arising from the vibration relaxation on the speed-of-sound measurement can be calculated. Sound absorption can also be affected by the viscosity of the fluid. The sound absorption increases with viscosity and the travel distance in the medium. Previously in our group, Lin and Trusler [81] have used the pulse-echo technique to study the speed-of-sound in $CO_2$. With $CO_2$ having a high absorption coefficient, they proposed a method to overcome the sound absorption problem during measurement. They introduced a doping agent (hydrocarbon) in the sample fluid in a small quantity. This changes the overall vibrational relaxation time of the sample enabling signals to be detected and in turn also improves the signal-to-noise ratio. In their work, propane was chosen as the doping agent, being nontoxic, noncorrosive, readily available in high chemical purity and miscible with $CO_2$.They measured the speed-of-sound in [$x$$CO_2$ + (1−$x$)$C_3H_8$] at four mole fractions between 0.938 and 0.998. Once the speed-of-sound in the mixtures was measured, the speeds-of-sound in pure $CO_2$ were obtained by extrapolating to limit $x$ = 1. Recently, Rivas *et al.* [82] also used a similar method to determine the speed-of-sound in pure $CO_2$ using the ultrasonic pulse technique. They used methanol as the doping agent to obtain the speed-of-sound in pure $CO_2$ at 5 MHz.

## 2.2.2 Review of the Available Experimental Data

Research in the speed-of-sound in liquid hydrocarbons at high pressure began with the work of Swanson [83] in 1934. He measured the speed-of-sound in several hydrocarbons at ambient temperature and pressure up to 30 MPa using an acoustic interferometer. In the relatively small pressure range of his experiments, a linear relationship between pressure and sound-speed was observed. Then in the 1950s, with the development of the pulse method [84, 85] of sound-speed

determination, experiments became easier and less time-consuming. This advancement led to a large amount of speed-of-sound data for organic liquids at elevated pressure was published. One of the studies of the speed-of-sound in hydrocarbons with the pulse method was carried out around 1967 by Boelhouwer [86]. He studied sound-speeds in liquid hexane, heptane, octane, nonane, dodecane and hexadecane at temperatures ranging from (253 to 473) K and at pressures up to 140 MPa using a 2 MHz pulse-echo technique. The sound-speed results were used to derive adiabatic compressibility. Van Itterbeek *et al.* [87] studied the speed-of-sound in liquid methane between (91 and 191) K with pressures up to 20 MPa (one of the earlier studies in the supercooled region). It was discovered that the change of sound-speed with pressure became very large and had a high degree of pressure dependence near the critical point for the hydrocarbon. Then in the 1970s, co-workers from Japan studied the speed-of-sound in methyl, ethyl, n-propyl and n-butyl acetate at pressures up to 30 MPa and temperatures between (278 and 308) K [88, 89]. They found out that the sound-speed in the esters increased parabolically with pressure. Bobik, Niepmann and co-workers [90-92] at Institut fur Thermo- und Fluiddynamik at Ruhr-Universitat Bochum extended both pressure and temperature range of the pulse technique. Sound-speed results were published for benzene at temperatures between (283 and 463) K and at pressures up to 62 MPa. A polynomial was proposed by them for the whole range of sound-speed as a function of temperature and pressure, given in the following form [90]:

$$c = \sum_{i=0}^{4}\sum_{j=0}^{4} a_{ij} p^i T^j \tag{2.9}$$

In the late 1980s, Van't Klooster, Muringer and Trappeneiers from the Van der Waals Laboratory used experimental results on the speed-of-sound to test the validity of equations of state [93]. They measured the effect of pressure on the speed-of-sound and density of methylbenzene and *n*-heptane at pressures up to 260 MPa, at temperatures ranging between (185 and 320) K. A spectrum of thermophysical properties were derived for both liquids from the measured sound-speed, following a thermodynamic integration method derived earlier by Davis and Gordon [48]. In their new adapted version of the mathematical model, a new correlation for sound-speed has been proposed and was given in the following form:

$$p - p_0 = \sum_{i=1}^{m}\sum_{j=0}^{n} a_{ij} \left(c - c_0\right)^i T^j \tag{2.10}$$

where $p_0$ = 0.1 MPa, $c_0$ is the sound velocity at 0.1 MPa and $a_{ij}$ are the coefficients. In the 1990s, Estrada-Alexanders *et al.* [49, 94] also described the methods by which all of the observable thermodynamic properties of a compressed gas can be determined from sound-speed data by numerical integration of a pair of partial differential equations. Other workers in this field include Daridon and co-workers [66, 67, 95, 96], who measured the speed-of-sound in various organic liquids as well as petroleum fluids. In recent years, global warming and the need to find new refrigerants to

replace the chlorine-based fluorocarbons (CFC), many research groups have put their attention to measuring the thermodynamic properties of various hydrofluorocarbons (HFC) at high pressure. More speed-of-sound data of refrigerants are published in the literature and examples can be found in these works [65, 75, 97-103].

An extensive literature survey on experimental sound-speed data in the twelve pure liquid-alkanes ($C_5$ to $C_{16}$), pure aromatics (benzene and methylbenzene) and pure $CO_2$ has been carried out. There remain significant gaps in the literature, especially in the HTHP conditions. Most experimental data was reported for atmospheric conditions and high-quality experimental data at elevated conditions for some of the liquid hydrocarbons limited. In general, the speed-of-sound in odd-numbered alkanes was less well studied compared to the even numbered alkanes. Hereby, we present the existing literature data for high-pressure speed-of-sound measurements only for each hydrocarbon and are listed in the Tables below. The information provided in the table includes the source of data, the temperature and pressure range studied and the number of measured points.

**Table 2.1** Experimental speed-of-sound studies for liquid alkanes ($C_5$ to $C_{16}$) conducted at elevated temperatures and pressures; *T*, *p* and No. of pts. refer to the temperature and pressure ranges, and the number of points examined, respectively.

| **Liquid Alkanes ($C_5$ to $C_{16}$)** | | | |
|---|---|---|---|
| | **Temperature and Pressure Ranges** | | |
| **Reference** | ***T*/K** | ***p*/MPa** | **No. Pts.** |
| | ***n*-pentane** | | |
| Swanson (1934) [83] | 297.05 | 0.1 – 11.2 | 6 |
| Richardson and Tait (1957) [84] | 288.15 – 317.15 | 0.1 – 55.2 | 47 |
| Richardson (1958) [104] | 288.55 | 3.4 – 55.2 | 11 |
| Kiryakov and Otpushchennikov (1971) [105] | 303.15 – 333.15 | 9.8 – 196.1 | 57 |
| Belinskii and Ikramov (1973) [106] | 293.15 – 313.15 | 0.1 – 784.5 | 48 |
| Otpushchennikov *et al.* (1974) [107] | 303.15 – 393.15 | 0.1 – 196.2 | 110 |
| Ismagilov and Ermakov (1982) [108] | 387.04 – 436.79 | 0.1 – 2.6 | 29 |
| Lainez *et al.* (1990) [72] | 263.14 – 433.25 | 0.2 – 212.8 | 220 |
| Zotov *et al.* (1995) [109] | 303.15 – 433.15 | 10.0 – 500.0 | 144 |
| Ding *et al.* (1997) [110] | 293.15 – 373.15 | 5.0 – 100.0 | 200 |
| Tahani (2011) [111] | 298.35 – 333.15 | 3.4 – 34.5 | 50 |
| | ***n*-hexane** | | |
| Rolling and Vogt (1960) [112] | 288.70 – 394.26 | 0.1 – 34.6 | 28 |
| Eden and Richardson (1960) [113] | 293.15 | 0.1 – 98.1 | 6 |
| Boelhouwer (1967) [86] | 253.15 – 333.15 | 0.1 – 140.1 | 40 |
| Allegra *et al.* (1970) [114] | 303.15 | 0.1 – 980.7 | 8 |
| Hawley *et al.* (1970) [115] | 303.00 | 0.1 – 392.3 | 5 |

| | | | |
|---|---|---|---|
| Badalyan *et al.* (1971) [116] | 303.15 – 333.15 | 9.8 – 117.7 | 48 |
| Kiryakov *et al.* (1971) [105] | 303.15 – 313.15 | 9.8 – 196.1 | 40 |
| Ermakov and Ismagilov (1976) [117] | 377.95 – 437.85 | 0.3 – 2.1 | 24 |
| Kagramanyan and Badalyan (1978) [118] | 333.15 – 373.15 | 10.1 – 202.6 | 34 |
| Ismagilov and Ermakov (1982) [108] | 383.97 – 459.95 | 0.1 – 2.6 | 48 |
| Takagi and Teranishi (1985) [64] | 298.15 | 0.1 – 100.0 | 3 |
| Bohidar (1988) [119] | 293.15 | 0.1 – 93.6 | 9 |
| Melikhov *et al.* (1991) | 293.15 | 10.0 – 600.0 | 17 |
| Zotov *et al.* (1995) [72] | 303.15 – 413.15 | 10.0 – 600.0 | 140 |
| Daridon *et al.* (1998) [68] | 293.15 – 373.15 | 0.1 – 150.0 | 275 |
| Khasanshin and Shchemelev (2001) [120] | 298.15 – 433.15 | 0.1 – 49.1 | 20 |
| Ball and Trusler (2001) [52] | 348.15 – 373.15 | 5.0 – 101.0 | 40 |
| Khasanshin *et al.* (2008) [121] | 298.15 – 433.15 | 0.1 – 100.1 | 48 |
| Tahani (2011) [111] | 298.35 – 333.15 | 3.4 – 34.5 | 50 |
| ***n*-heptane** | | | |
| Boelhouwer (1967) [86] | 253.15 – 453.15 | 0.1 – 140.1 | 60 |
| Kiryakov and Otpushchennikov (1971) [105] | 303.15 – 393.15 | 9.8 – 196.1 | 119 |
| Badalyan *et al.* (1971) [116] | 303.15 – 363.15 | 9.8 – 117.7 | 84 |
| Golik *et al.* (1982) [122] | 313.15 – 453.15 | 0.1 – 196.0 | 68 |
| Ismagilov and Ermakov (1982) [108] | 391.35 – 466.31 | 0.1 – 2.6 | 48 |
| Muringer *et al.* (1985) [93] | 185.70 – 310.70 | 0.1 – 263.4 | 113 |
| Nakamura *et al.* (1995) [123] | 299.15 | 0.1 – 1146.6 | 4 |
| Zotov *et al.* (1995) [109] | 303.15 – 433.15 | 10.0 – 600.0 | 160 |
| Daridon *et al.* (1999) [69] | 293.15 – 373.15 | 0.1 – 150.0 | 279 |
| Dzida and Ernst (2003) [124] | 293.10 – 318.18 | 0.1 – 121.6 | 59 |
| Dzida *et al.* (2005) [125] | 293.18 – 318.21 | 15.1 – 92.1 | 84 |
| Dzida and Cempa (2008) [126] | 292.88 – 318.28 | 15.2 – 101.3 | 42 |
| Dzida and Waleczek (2010) [127] | 292.86 – 318.25 | 15.2 – 101.3 | 42 |
| Hasanov (2012) [128] | 298.15 – 523.15 | 0.1 – 58.9 | 73 |
| ***n*-octane** | | | |
| Rolling and Vogt (1960) [112] | 288.70 – 394.26 | 0.1 – 34.6 | 30 |
| Boelhouwer (1967) [86] | 253.15 – 393.15 | 0.1 – 140.1 | 64 |
| Badalyan *et al.* (1970) [129] | 303.15 – 393.15 | 9.8 – 117.7 | 72 |
| Takagi and Teranishi (1985) [64] | 298.15 | 0.1 – 100.0 | 3 |
| Zotov *et al.* (1995) [109] | 303.15 – 393.15 | 10.0 – 300.0 | 80 |
| Ding *et al.* (1997) [110] | 293.15 – 363.15 | 5.0 – 90.0 | 142 |
| Khasanshin and Shchemelev (2001) [120] | 303.15 – 433.15 | 0.1 – 49.1 | 46 |
| Khasanshin, *et al.* (2008) [121] | 298.15 – 433.15 | 0.1 – 100.1 | 49 |
| Hasanov (2012) [128] | 298.15 – 523.15 | 0.1 – 58.9 | 74 |
| ***n*-nonane** | | | |
| Boelhouwer (1967) [86] | 253.15 – 413.15 | 0.1 – 140.1 | 89 |
| Badalyan *et al.* (1971) [116] | 303.15 – 393.15 | 9.8 – 117.7 | 120 |
| Zotov *et al.* (1995) [109] | 303.15 – 433.15 | 10.0 – 600.0 | 160 |

| | | | |
|---|---|---|---|
| Lago *et al.* (2006) [130] | 293.15 – 393.15 | 0.1 – 100.0 | 66 |
| | ***n*-decane** | | |
| Rolling and Vogt (1960) [112] | 288.70 – 394.26 | 0.1 – 34.6 | 30 |
| Badalyan *et al.* (1970) [129] | 303.15 – 413.15 | 9.8 – 117.7 | 84 |
| Kiryakov and Otpushchennikov (1971) | 303.15 – 393.15 | 9.8 – 196.1 | 100 |
| Takagi and Teranishi (1985) [64] | 298.15 | 0.1 – 100.0 | 3 |
| Ye *et al.* (1990) [131] | 303.15 – 413.15 | 0.1 – 60.0 | 121 |
| Zotov *et al.* (1995) [109] | 303.15 – 393.15 | 10.0 – 300.0 | 84 |
| Khasanshin and Shchemelev (2001) [120] | 298.15 – 433.15 | 0.1 – 49.1 | 40 |
| Khasanshin, *et al.* (2008) [121] | 298.15 – 433.15 | 0.1 – 100.1 | 48 |
| Nascimento *et al.* (2015) [132] | 313.15 – 333.15 | 5.0 – 25.0 | 15 |
| | ***n*-undecane** | | |
| Rolling and Vogt (1960) [112] | 288.70 – 394.26 | 0.1 – 34.6 | 30 |
| Otpushchennikov and Badalyan (1971) [105] | 303.15 – 413.15 | 9.8 – 117.7 | 84 |
| Zotov *et al.* (1995) [109] | 303.15 – 393.15 | 10.0 – 300.0 | 84 |
| Bessieres and Plantier (2007) [133] | 303.15 – 373.15 | 0.1 – 60.0 | 56 |
| Giuliano Albo *et al.* (2013) [80] | 278.00 – 318.00 | 1.0 – 100.0 | 30 |
| | ***n*-dodecane** | | |
| Badalyan *et al.* (1971) [129] | 253.15 – 393.15 | 0.1 – 140.1 | 85 |
| Takagi and Teranishi (1985) [64] | 303.15 – 393.15 | 9.8 – 117.7 | 3 |
| Zotov *et al.* (1995) [109] | 303.15 – 393.15 | 10.0 – 600.0 | 122 |
| Khasanshin and Shchemelev (2001) [120] | 298.15 – 433.15 | 0.1 – 49.1 | 30 |
| Dzida and Cempa (2008) [126] | 292.88 – 318.28 | 15.2 – 101.3 | 41 |
| | ***n*-tridecane** | | |
| Rolling and Vogt (1960) [112] | 288.70 – 394.26 | 0.1 – 34.6 | 30 |
| Golik *et al.* (1982) [122] | 313.15 – 453.15 | 0.1 – 196.0 | 64 |
| Daridon and Lagourette (2000) [134] | 293.15 – 373.15 | 0.1 – 149.6 | 276 |
| Khasanshin and Shchemelev (2001) [120] | 303.15 – 433.15 | 0.1 – 49.1 | 48 |
| | ***n*-tetradecane** | | |
| Takagi and Teranishi (1985) [64] | 298.15 | 0.1 – 50.0 | 2 |
| Daridon and Lagourette (2000) [134] | 293.15 – 373.15 | 0.1 – 149.6 | 251 |
| Khasanshin and Shchemelev (2001) [120] | 298.15 – 433.15 | 0.1 – 49.1 | 48 |
| Khasanshin, *et al.* (2004) [135] | 303.15 – 433.15 | 0.1 – 100.1 | 48 |
| | ***n*-pentadecane** | | |
| Khasanshin and Shchemelev (2001) [120] | 298.15 – 433.15 | 0.1 – 49.1 | 54 |
| Dovnar *et al.* (2001) [136] | 303.15 – 433.15 | 0.1 – 140.0 | 59 |
| Daridon *et al.* (2002) [137] | 293.15 – 383.15 | 0.1 – 149.6 | 170 |
| | ***n*-hexadecane** | | |
| Rolling and Vogt (1960) [112] | 310.93 – 394.26 | 0.1 – 34.6 | 23 |

| | | | |
|---|---|---|---|
| Boelhouwer (1967) [86] | 293.15 – 473.15 | 0.1 – 140.1 | 74 |
| Ye *et al.* (1990) [131] | 303.15 – 393.15 | 0.1 – 70.0 | 78 |
| Zotov *et al.* (1995) [109] | 303.15 – 433.15 | 10.0 – 140.0 | 97 |
| Khasanshin and Shchemelev (2001) [120] | 303.15 – 433.15 | 0.1 – 49.1 | 29 |
| Ball and Trusler (2001) [52] | 298.30 – 373.15 | 0.1 – 100.9 | 65 |
| Khasanshin *et al.* (2008) [121] | 298.15 – 433.15 | 0.1 – 100.1 | 43 |
| Nascimento *et al.* (2015) [132] | 313.15 – 333.15 | 5.0 – 25.0 | 15 |

**Table 2.2** Experimental speed-of-sound studies for benzene and methylbenzene conducted at elevated temperatures and pressures; $T$, $p$ and No. of pts. refer to the temperature and pressure ranges, and the number of points examined, respectively.

| **Benzene and Methylbenzene** | | | |
|---|---|---|---|
| | **Temperature and Pressure Ranges** | | |
| **Reference** | ***T*/K** | ***p*/MPa** | **No. Pts.** |
| | **benzene** | | |
| Swanson (1934) [83] | 298.65 | 0.1 – 34.3 | 12 |
| Richardson and Tait (1957) [138] | 292.15 – 313.15 | 0.1 – 67.4 | 62 |
| Takagi (1980) [139] | 313.15 – 673.15 | 0.1 – 100.0 | 100 |
| Mustafaev (1980) [140] | 303.15 | 0.1 – 90.0 | 15 |
| Takagi and Teranishi (1982) [141] | 293.15 – 313.15 | 0.1 – 90.0 | 27 |
| Ismagilov and Ermakov (1982) [108] | 393.99 – 467.36 | 0.1 – 2.6 | 48 |
| Takagi and Teranishi (1986) [65] | 293.15 – 313.15 | 0.1 – 101.3 | 18 |
| Takagi and Teranishi (1987) [62] | 293.15 – 323.15 | 0.1 – 170.0 | 69 |
| Sun *et al.* (1987) [77] | 283.13 – 323.15 | 0.1 – 170.0 | 90 |
| Bohidar (1988) [119] | 293.15 | 0.1 – 72.0 | 8 |
| Zotov *et al.* (1995) [109] | 303.15 – 413.15 | 10.0 – 500.0 | 136 |
| Takagi *et al.* (2004) [142] | 283.15 – 333.15 | 0.1 – 28.4 | 71 |
| Wegge *et al.* (2015) [143] | 283.20 – 353.21 | 0.1 – 30.1 | 35 |
| | **methylbenzene** | | |
| Swanson (1934) [83] | 298.15 | 0.1 – 30.4 | 11 |
| Hawley *et al.* (1970) [115] | 303.15 | 0.1 – 980.7 | 8 |
| Allegra *et al.* (1970) [114] | 303.00 – 348.00 | 0.1 – 522.5 | 13 |
| Mustafaev (1980) | 313.15 – 673.15 | 0.1 – 100.0 | 100 |
| Kreutzenbeck *et al.* (1983) [144] | 298.00 – 303.00 | 0.1 – 100.0 | 4 |
| Muringer *et al.* (1985) [93] | 173.20 – 320.30 | 0.1 – 263.4 | 88 |
| Takagi and Teranishi (1985) | 303.15 | 0.1 – 160.0 | 17 |
| Okhotin *et al.* (1987) [145] | 230.00 – 440.00 | 0.1 – 60.0 | 173 |
| Bohidar (1988) [119] | 293.15 | 0.1 – 93.6 | 9 |
| Okhotin *et al.* (1988) [146] | 183.16 – 523.15 | 0.1 – 58.9 | 248 |
| Zotov *et al.* (1995) [109] | 313.15 – 433.15 | 10.0 – 350.0 | 105 |
| Meier and Kabelac (2013) [147] | 240.00 – 420.00 | 0.1 – 100.2 | 273 |

**Table 2.3** Experimental speed-of-sound studies for carbon dioxide conducted at elevated temperatures and pressures; *T*, *p* and No. of pts. refer to the temperature and pressure ranges, and the number of points examined, respectively.

| **$CO_2$ (Gas and Liquid)** | | | |
|---|---|---|---|
| | **Temperature and Pressure Ranges** | | |
| **Reference** | ***T*/K** | ***p*/MPa** | **No. Pts.** |
| Herget (1940) [148] | 301.15 – 311.15 | 0.6 – 10.1 | 196 |
| Bass and Lamb (1958) [149] | 273.15 – 303.15 | 3.8 – 9.8 | 5 |
| Gruzdev and Slabnyak (1969) [150] | 293.00 – 413.00 | 0.1 – 3.9 | 32 |
| Vargaftik (1972) [151] | 300.00 – 1800.00 | 0.1 – 60.0 | 500 |
| Pitaevskaya and Bilevich (1973) [152] | 323.15 – 473.15 | 50.0 – 450.0 | 154 |
| Estrada-Alexanders and Trusler (1998) [153] | 220.00 – 450.00 | 0.3 – 14.2 | 61 |
| Tahani (2011) [111] | 283.12 – 303.73 | 17.2 | 7 |
| Liu *et al.* (2014) [154] | 260.00 – 332.75 | 0.2 – 1.0 | 52 |

A literature review on sound-speed data for binary mixtures of $CO_2$ + hydrocarbon has also been carried out. Unfortunately, no speed-of-sound data for such binary mixtures has been published.

## 2.3 Density

Fluid density in the basic definition is mass per unit volume. Experimental density data can be used to calculate other properties such as the excess molar volume, isothermal compressibility and isobaric expansivity, dynamic viscosity, interfacial tension with respect to composition, temperature and pressure [155, 156]. Single phase density can provide extremely useful information for the development of equations of state; together with vapour pressure, speed-of-sound and heat capacity data in the homogeneous fluid region, these form the basis of fundamental EoS that can calculate the entire range of fluid states. There are many applications that require accurate density in both the academia and the industry; for example, saturated-phase and single-phase densities are necessary for the fundamental development of equations of state and density as a function of temperature and pressure are crucial for the design of industrial plants, pipelines and pumps [17, 37]. The density measurement techniques are generally categorised into two ways: the direct and the indirect methods. In the direct methods, either mass or volume is measured directly to determine density. While in an indirect method, the density is usually derived from measuring other properties, such as buoyancy force and the frequency of a vibrating body. In the following section, the major techniques for both the direct and the indirect methods will be discussed.

## 2.3.1 Density Measuring Techniques

There are many established techniques to determine the density of a fluid accurately such as the weighing technique and the vibrating-body technique. Density determination by weighing is one of the original methods of measuring the density of the fluid. It uses the fundamental relationship between mass and volume to determine fluid density. Although different methods of density determination have been well-established in the literature and research, only the most accurate high-pressure density determination techniques will be discussed in detail in the following section. There are two main techniques for measuring density at high pressures: the buoyancy technique and the vibrating-body technique. For the two techniques, the main types of densimeter for high-pressure measurements are the suspended sinker densimeters and vibrating-body densimeters.

*2.3.1.1 Buoyancy Densimeters*

One of the most basic methods for density measurements of fluids is the buoyancy or hydrostatic method which is based on Archimedes' principles. The principle indicates that the upward buoyant force exerted on a body immersed in a fluid, either fully or partially submerged, is exactly equal to the weight of the displaced fluid. In a typical buoyancy densimeter, a suspended sinker with a known mass and volume is attached to a fine wire and is immersed in the sample liquid. The weight of a sinker is measured before and after the sinker is completely surrounded by fluid whose density is to be determined. The difference in weight of the sinker is equal to the weight of the displaced fluid. The density of a sample fluid in a buoyancy densimeter was determined by the simple relation:

$$\rho = \frac{W_s - W_s^*}{gV_s} = \frac{m_s - m_s^*}{V_s}, \tag{2.11}$$

where $m_s = W_s / g$ is the true mass of the sinker in the experimental set-up, $m^*_s$ is the apparent mass of the sinker surrounded by the sample fluid, $g$ is the gravity and $V_s$ is the true the temperature and pressure dependent sinker volume. The true mass of the sinker was accurately determined by weighting in the measuring cell under vacuum condition, the volume of the sinker is calibrated with a fluid with well-known density, typically water. It should be noted that the sinker and wire assembly should be immersed to the same depth as the calibration measurements to validate the experiment. There are three main types of densimeters that are designed based on the buoyancy principle for density measurements of fluids over wide ranges of temperature and pressure: (1) Hydrostatic balance densimeters; (2) Magnetic float and magnetic suspension densimeters and (3) Hydrostatic balance densimeters with magnetic suspension couplings.

**Hydrostatic Balance Densimeters:** The design of a hydrostatic balance densimeter is based on the Archimedes principle. Typically it contains a sinker (cylindrical or spherical) made of glass or metal that is suspended by a thin platinum wire on the weighing hook of a commercial analytical balance. This type of densimeters is usually used for density measurement of liquids at ambient pressure in

moderate temperature ranges. Further details and descriptions of other types of hydrostatic balance densimeters can be found in the work of Wagner et al. [157]

*2.3.1.2 Magnetic Float and Magnetic Suspension Densimeters*

Magnetic float densimeters consist of a float that is made of a hollow glass body that contains a magnet or a soft-iron core and the density of the float is usually less than the density of the liquid to be measured. During measurement, the magnetic float can be immersed in the sample liquid and is held in position by means of a solenoid placed under the sample cell. A controlled current through the solenoid generates a magnetic force which holds the float in a fixed position. The density of the liquid can be determined from the known mass and volume of the float and the magnetic force required to hold the flat in a fixed position. The current through the solenoid and the magnetic force on the float is calibrated with liquids with known density before measurement. Details and references on the magnetic float and magnetic suspension densimeters are also given in [157].

*2.3.1.3 Hydrostatic Balance Densimeters with Magnetic Suspension Couplings*

One of the most basic methods for density measurements of fluids is the buoyancy or hydrostatic method which is based on Archimedes' principles. The principle indicates that the upward buoyant force exerted on a body immersed in a fluid, either fully or partially submerged, is exactly equal to the weight of the displaced fluid. For this principle, the most advanced type of densimeter used is the hydrostatic balance densimeter in combination with magnetic suspension couplings. This type of densimeter can be used for accurate measurement of saturated liquid and saturated vapour densities of pure fluids. Beam first described a magnetic suspension balance in 1955 [158]. The main types of densimeters are the double-sinker densimeters and the single-sinker densimeters.

**Double Sinker and Single Sinker Densimeters:** The Two-Sinker densimeter was developed by Kleinrahm and Wagner [159] in the early 1980s to measurement saturated-liquid and saturated-vapour densities of pure fluids. This technique allows densities in the homogeneous gas and liquid region to be measured over wide ranges of temperature, pressure and density. Instead of one usual sinker, two specially matched sinkers are used: one is a gold plated quartz-glass sphere, and the other is a disk of solid gold. Both sinkers contain the same mass, same surface area and the same surface material, but different in volume. During measurements, the sinkers are put alternately on a sinker support which is connected to a commercial analytical balance by a thin wire via a magnetic suspension coupling. The apparent mass difference of the sinkers surrounded by the sample fluid is measured, and the density of the sample fluid in the measuring cell is determined by the simple equation:

$$\rho = \frac{\Delta m^* - \Delta m_{\mathrm{vac}}}{V_{\mathrm{S}} - V_{\mathrm{D}}}, \tag{2.12}$$

where $\rho$ is the fluid density, $\Delta m_{\mathrm{vac}} = (m_{\mathrm{S}} - m_{\mathrm{D}})$ corresponds to the mass difference of two sinkers measured under vacuum and $\Delta m^* = \left(m_{\mathrm{S}}^* - m_{\mathrm{D}}^*\right)$ is the mass difference of the sinkers surrounded by the

sample fluid. The volumes of the sinkers can be calibrated with water at reference condition. With this configuration, errors that reduce the density measurement accuracy can be eliminated, such as buoyant forces on the sinker suspension, the surface tension between the sample liquid and the suspension wire and the weighing uncertainty from the balance. The major advancement from the hydrostatic balance densimeter is the magnetic suspension system. The magnetic suspension coupling consists of an electromagnet attached to the underfloor weighing hook of an analytical balance, a permanent magnet connected to a thin wire to the sinker support, a position transducer and a control system. By means of this coupling the suspension force is transmitted without direct contact with the pressurised measuring cell to the balance at ambient atmosphere. Inside the coupling housing there is a permanent magnet to which the sinker to be weighed is linked by means of a load coupling and decoupling device. When the coupling is switched on, the permanent magnet is gently attracted to the electromagnet by means of a position sensor and a control system. The distance between the two magnets is controlled in such a way that the current through the electromagnet (with soft-iron core) is zero on average and the suspension force is then completely transmitted by the permanent magnet. A simplify version of the double-sinker densimeter was developed by Brachthauser *et al.* [160], and the design was improved by Klimeck *et al.* [161] in the following years. This version of the densimeter is known as the single-sinker densimeter. The principle of single-sinker densimeters is also based on the Archimedes principles and mainly consists of a pressure vessel, a commercial analytical balance and a sinker. The cylindrical sinker can be made of quartz glass and is contained inside a pressure-proof measuring cell. Apart from only one sinker, the magnetic suspension coupling is a new type compared to the double-sinker densimeter's. The densimeter contains two compensation masses that are placed directly on the balance pan; these masses ensure that the total loading on the balance is approximately the same for both the measuring-position and the zero-position. A diagram of the double-sinker and the single-sinker densimeter is shown in Figure 2.5 below. The density of a sample fluid in the measuring cell can be determined by the simple relation:

$$\rho = \frac{m_{\mathrm{S}} - \left[\left(W_{\mathrm{MP}} - m_{\mathrm{c1}}\right) - \left(W_{\mathrm{ZP}} - m_{\mathrm{c2}}\right)\right] - \rho_{\mathrm{air}}\left(V_{\mathrm{c1}} - V_{\mathrm{c2}}\right)}{V_{\mathrm{S}}}, \tag{2.13}$$

where $m$ is mass, $W$ is a balance reading, $V$ is volume and the subscripts S, c1, c2 MP, ZP refer to the sinker, compensation masses, measuring-position and zero-position, respectively. Typically the compensation masses are made of different materials, so that $V_{\mathrm{c1}}$ is approximately the same as $V_{\mathrm{c2}}$.

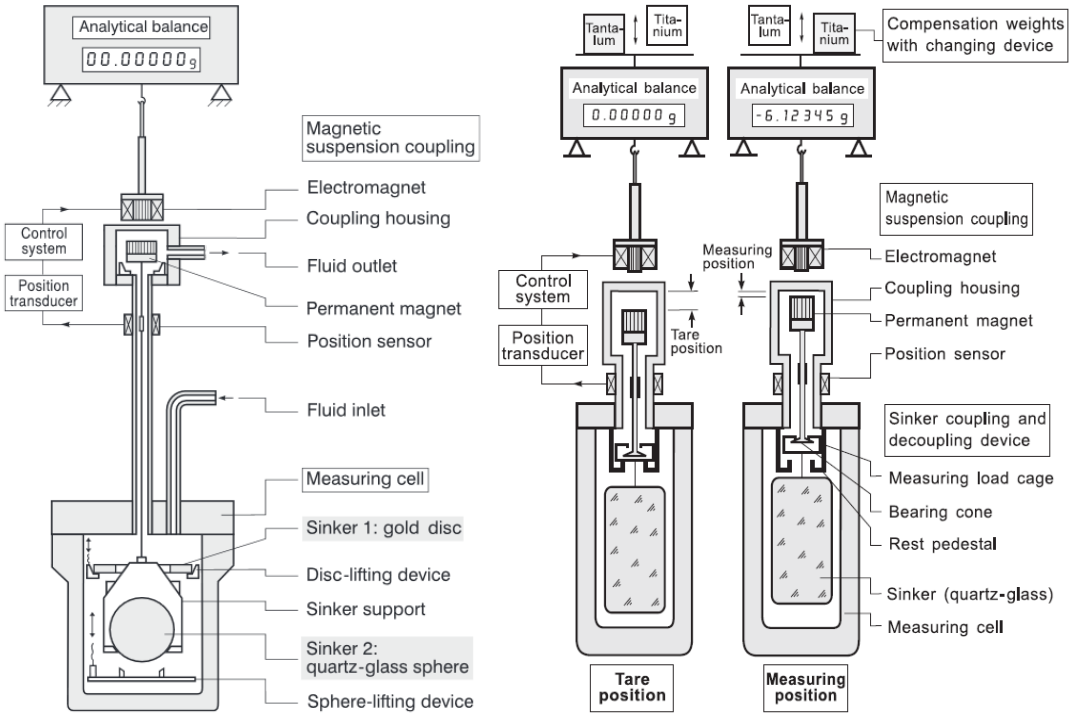



**Figure 2.5** (*left*) Schematic of a double-sinker densimeter. (*right*) The working principle of the single-sinker densimeter. Reproduced from Wagner and Kleinrahm [162].

*2.3.1.4 Vibrating-Body Densimeters*

Vibrating-body densimeters are known as the secondary densimeters in which density is determined indirectly from other properties. The frequency of the resonance of a solid surround by a fluid will depend upon the density of the fluid. The most important applications of vibrating-bodies to the measurement of the density of fluids are mainly categorised into two types: vibrating-wire densimeters and vibrating-tube densimeters. Apart from the two main vibrating-bodies densimeters, there are also the **v**ibrating-hollow cylinders and forks which are usually used for density measurements of gases, particularly to measure the density of natural gases in pipelines. The vibrating-wire densimeter is hydrostatic weighing densimeter in which a vibrating-wire force sensor is used to detect the weight of a sinker immersed in the sample fluid. The mass of the sinker is constant, but the fluid affects the apparent weight through the buoyancy of the sample fluid and changes the tension of the wire, hence changing the resonant frequency. The vibrating-tube technique, the density is deduced from the resonant frequency of a U-tube containing the sample fluid. The fluid sample affects the mass of the vibrating system and changes the resonant frequency. These techniques will be discussed further below.

**Vibrating-Wire Densimeters:** The use of the vibrating-wire technique was developed for measurements at medium temperatures and high pressures (over 100 MPa). Vibrating-wire sensors have been primarily used for viscosity measurements, but the principle can also be applied for density determination. It offers an advantage over the vibrating-tube densimeter as it has the ability to

measure viscosity simultaneously. It does not require a prediction of the volume of the containing cell at different conditions of temperature and pressure, so this made the vibrating-wire densimeter suitable for high-pressure density measurements. However, the method is restricted to liquids, since the measuring effect in gases is too small. The first vibrating-wire sensor was designed and built by Assael and Wakeham at Imperial College London around 1990 [163-165]. The working principle of vibrating-wire densimeter uses the Archimedes' principle to measure the density of a fluid. The vibrating-wire is tensioned by attaching a sinker to one end to enable both viscosity and density of the fluid. The buoyancy force acting on a sinker immersed in the test sample is equal to the mass of the displaced liquid which then alters the resonant frequency of a thin wire from which the mass is suspended. The resonant frequency of the wire carrying the mass is related to the fluid density by means of working equations which are based on a complete analysis of the fluid motion around the fluid [166, 167]. The expression for the resonance frequency of the wire is given as:

$$f_0 = \frac{1}{2L}\sqrt{\frac{(m-\rho V)g}{\rho_s \pi R^2}}\,, \tag{2.14}$$

where $f_0$ is the resonance frequency, $g$ is the acceleration of gravity, $m$ is the sinker mass (determined under vacuum), $\rho$ is the density of the fluid and sinker, $L$, $\rho_s$ and $R$ are the length, density and radius of the wire, respectively. The estimated uncertainty of this method for determining density is about 0.2% for high-pressure measurements up to 1 GPa. Figure 2.6 shows the vibrating-wire densimeter set-up by Padua *et al*. [167] The advantage of the vibrating-wire densimeter is that it is composed of solid bodies which are suitable for high-pressure measurements over a wider range of temperature. In addition, it does not require extensive calibration once the physical parameters of the sensor are determined. The vibrating-wire densimeter consists of a thin metal wire which the upper end is fixed, and the other is attached to a solid cylindrical weight. The solid weight is suspended by the wire where a variable frequency alternating current is supplied. The wire is mounted in between a uniform magnetic field so that it is forced to undergo steady-state transverse vibration in a fluid when the electrical circuit is complete. The frequency of the driving current is varied to locate the resonant frequency. The presence of the experimental fluid around the vibrating-wire changes the buoyancy effect on the solid weight and the resonant frequency of the transverse vibrations of the wire.

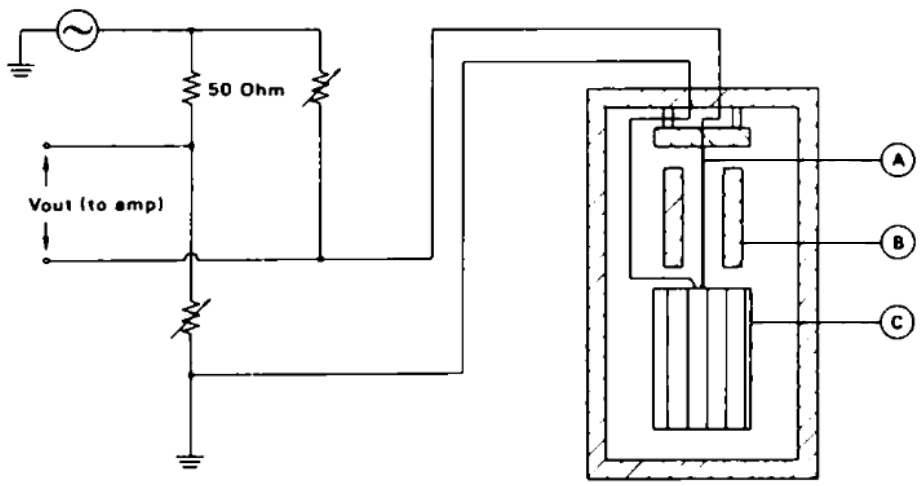



**Figure 2.6** Schematic of a vibrating-wire densimeter, reproduced from Padua *et al.* [167] (A) a vibrating wire, (B) a permanent magnet (C) a sinker. The set-up is enclosed by a high-pressure vessel. The driving signal and the signal detection are provided by a function generator and a lock-in amplifier, respectively.

**Vibrating-Tube Densimeters:** Among the different methods for the experimental determination of density at high temperatures and pressures, the vibrating-tube densimeter is widely regarded as being a precise, reliable and relatively rapid equipment and technique [168]. They are extensively used for precise measurements of fluid densities over a wide-range of temperature and pressures up to 100 MPa. Vibrating-tube technique can operate at high temperatures (above 473 K), but limited to lower pressures (below 100 MPa) because of tube deformation. They first type of vibrating-tube densimeter was developed by Kratky *et al.* [169], they proposed a density determination method based on the relationship between the resonating vibration period of a tube filled with the sample and its density. The method involves obtaining the natural vibration frequency of a tube that contains the fluid investigated. Since then a lot of developments have been made, and now the vibrating-tube densimeters are commercially produced by Anton Paar, Austria. The principle of the density determination by a vibrating-tube densimeter is that the period of oscillation of a U-shaped tube is related to the fluid sample density. The vibrating-tubes are usually made of stainless-steel or Hastelloy to resist corrosion for high-pressure densimeters, typically with a precision of about 0.1 $kg \cdot m^{-3}$. The precision can be increased if the tube is made of glass, but this configuration is restricted to only low-pressure density measurements. The values of the inner radius and out radius depend on the stiffness requirement of the equipment. The tube is normally anchored at both ends to a large counter mass to allow a harmonic vibration of the tube without interferences from other parts of the equipment. In some other configurations, the tube is sometimes suspended from approximate springs. The whole measuring cell is normally filled with a gas to reduce the friction between the tube and the

environment. The harmonic vibration of the tube and measurement of the vibration is normally achieved by a pair of drive element and pick-up element. As shown in Figure 2.7, the driving/detection unit contains a pair of magnets with each surrounded by one coil that is fixed to the end part of the tube. In the drive coil, an applied AC voltage to produce stationary oscillations in the tube and the periodic movement induces an alternating current in the pick-up coil which frequency is detected using a frequency counter.

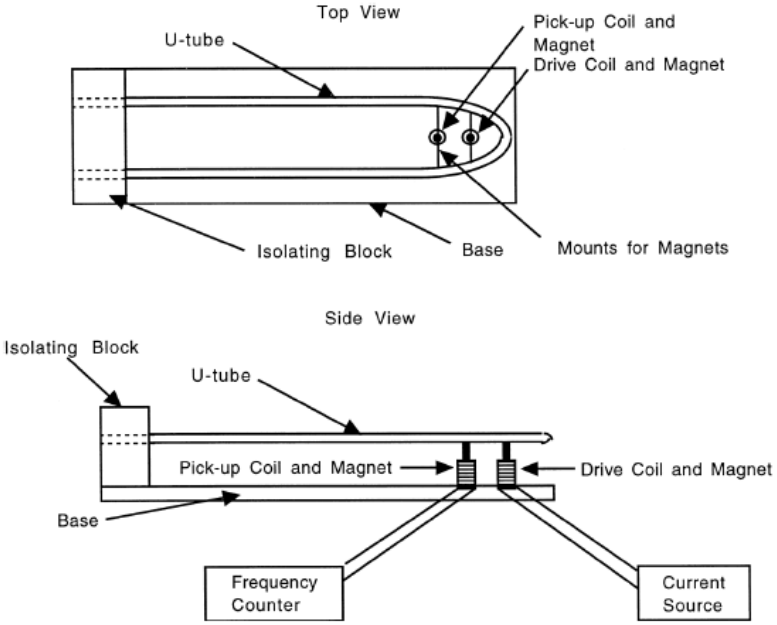



**Figure 2.7** Top view and side view schematic of the vibrating-tube densimeter which consists of a vibrating U-tube, a frequency counter, a pair of magnets and driving coils. Reproduced from the review by Holcomb and Outcalt [168].

The main components in a VTD include a U-shaped hollow tube with a fixed mass, $M_u$, for a given temperature and pressure, an internal volume, $V_u$, two magnets, a frequency counter and springs with an elastic constant $C$. The natural frequency of the vibrating tube can be defined by:

$$f = \frac{1}{2\pi}\sqrt{\frac{C}{M}} = \frac{1}{2\pi}\sqrt{\frac{C}{M_u + \rho V_u}}, \tag{2.15}$$

where $M$ is the total mass of the vibrating tube filled with fluid sample and $\rho$ is the unknown fluid density. Hence the period of oscillation $\tau$ can be described by:

$$\tau = 2\pi\sqrt{\frac{M_u + \rho V_u}{C}}. \tag{2.16}$$

From the expressions above, the density can be calculated by the following equation:

$$\rho = \frac{K}{4\pi^2 V}\tau^2 - \frac{m_0}{V} = A\tau^2 - B, \tag{2.17}$$

where $A$ and $B$ are so-called the working coefficients of the VTD. Once the working coefficients were obtained, the period of oscillation of the vibrating U-tube of the experimental fluid was then applied to the Equation (2.17) to determine the corresponding density. Vibrating-tube densimeter is known for its capability to measure densities at wide temperature and pressure range except for low gas densities. One of the examples of densimeter which have been developed using this technique is the Anton Paar 5000M. It allows density measurements to be carried out at atmospheric pressure and temperatures ranging from (283.15 to 363.15) K with a specified precision of 0.001 %. This equipment contains a vibrating glass U-tube with a temperature controlled to an accuracy of 0.1 K.

*2.3.1.5 Source of Uncertainty in a VTD*

Stabinger and co-workers [170] found that errors resulting from (1) non-linearity; (2) viscosity effect and (3) thermal effects which will be discussed briefly. Non-linearity refers to the mass distribution along the vibrating tube. In a well-constructed tube, it can be considered that the mass distribution is uniform, whether the tube is filled with a liquid or a gas. However, magnet fastened along the tube results in a non-uniform mass distribution of the system. This induces different deviation behaviour with respect to the working equation. To eliminate this effect, the VTD nowadays is designed such that the excitation of the vibrating tube is at the nodal points (points where no vibration occurs). The viscosity of a sample may affect the density obtained through VTD. For high-viscosity samples, the VTD may detect a higher mass which associated to the inertia momentum of the sample during vibration, in turn giving a high-density reading. The viscosity correction factor depends on the sample viscosity and the specific design of the mechanical oscillator. To address the problem, Anton Paar provided the viscosity correction for the densimeter (DMA-HPM) in the given form:

$$\frac{\rho - \rho_{\mathrm{corr}}}{\rho} = \left(0.4482\sqrt{\left(\eta / \mathrm{mPa \cdot s}\right)} - 0.1627\right) \cdot 10^{-4}, \tag{2.18}$$

where $\rho$ is initial density measured by the VTD, $\rho_{\mathrm{corr}}$ the corrected density due to the viscosity effect and $\eta$ the dynamic viscosity of the sample. The expression is valid for $\eta \leq 289$ mPa·s; for $\eta > 289$ mPa·s, a constant factor of $\Delta\rho/\rho = 7.5 \times 10^{-4}$ is applied [171]. However, the viscosity correction for density measurements was not considered in the present work due to the magnitude of the correction was very small compared to the experimental uncertainty and the samples measured contain similar viscosity as water. Lastly, the thermal effects refer to the ageing and thermal relaxation effects of the tube material. As it can be seen in Equation (2.16) above, both $A$ and $B$ depend on the inner volume of the vibrating-tube and the spring constant which is related to the Young's modulus of the material. Both quantities can experience physical change by ageing and thermal relaxation effects of the tube. Therefore, the parameters $A$ and $B$, obtained under the same thermodynamic conditions, can have different values depends on the time they are measured. To check the validity of the calibration, it has been recommended that the measurement of the period of oscillation under a test fluid (normally vacuum) should be tested to see if the values of $A$ and $B$ still hold.

*2.3.1.6 Choice of Calibration Fluids*

The classical calibration of the vibrating-tube densimeters typically involves measuring two fluids with known densities covering the temperature, pressure and density range required for the measurements. The period of oscillation readings are compared to known density and the measurements are adjusted accordingly. The choice of calibration fluids depends on several factors: (1) the density of the fluid must be known accurately; (2) stability over the $T$ and $p$ range of interest and (3) density is not a strong function of $T$ and $p$ with a similar viscosity to test fluids of interest. Water is the most commonly used calibration fluid as its density has been accurately determined over very wide ranges of temperature and pressure. The reference equation of state for water – the International Association for the Properties of Water and Steam (IAPWS-95) [172] has an uncertainty of 0.0001 % at atmospheric conditions and 0.001% at temperatures up to 423 K and pressures up to 10 MPa, for density. The density of water is not a strong function of temperature and pressure; hence small errors in the measured conditions have a small effect on the density. For the second calibration fluid, gases are considered. The best characterised gases include helium, nitrogen [173] and carbon dioxide [174]. For example, the EoS for helium developed by Ortiz-Vega [175] contains an uncertainty of 0.03 % up to 20 MPa for density. It has to be noted that when calibrating with a gas, the temperature and pressure measurements are more important than with a liquid calibration.

## 2.3.2 Review of the Available Experimental Data

Density measurements of hydrocarbons have been carried out over the past decades; most of these data have been used to calculate various thermodynamic properties and to construct equations of state. In 1987, Dymond and Malhotra [176] reviewed the available density data of several liquid alkanes ($C_6$ to $C_{16}$) in the literature. In their work, the applicability of the Tait equation for correlating the density of *n*-alkanes has also been examined. The original Tait equation was published more than 100 years ago by mathematician and physicist Peter Guthrie Tait [177]. He used this equation to fit his results on the compressibility of fresh water and seawater at different pressures. The modified Tait equation is given in the following form:

$$\rho = \rho_0 \left[ 1 - C \log_{10} \left( \frac{p + B}{p_0 + B} \right) \right]^{-1} . \tag{2.19}$$

Here $\rho$ and $\rho_0$ are the liquid density at $p$ and $p_0$, at most cases $p_0$ = 0.1 MPa; $C$ is a temperature-independent constant and $B$ is a temperature-dependent parameter. Dymond and Malhotra [176] showed that the parameter $C$ could be taken as constant, equal to 0.2 for various *n*-alkanes. Parameter $B$ is generally represented by a function of temperature, either linearly or quadratically; a generalised equation for $B$ that applies to all *n*-alkanes up to *n*-hexadecane except methane and *n*-pentane has also been proposed in the work of Dymond and Malhotra. The generalised equation for $B$ was given as:

$$B = 341.539 - 734.292T_{\mathrm{r}} + 411.189T_{\mathrm{r}}^2 - \left(\mathrm{C}_n - 6\right), \tag{2.20}$$

where $T_{\mathrm{r}}$ is the reduced temperature ($T/T_{\mathrm{c}}$) and $\mathrm{C}_n$ is the number of carbon atoms in the *n*-alkane molecule. In 1993, Assael *et al.* [178] gave an improved representation for the liquid densities of *n*-alkanes ($\mathrm{C}_1$ to $\mathrm{C}_{16}$) which covers an extended temperature and pressure range. The new correlation was able to correlate the liquid density of *n*-alkanes with an $\Delta_{\mathrm{AARD}}$ of 0.1 % from the experimental measurements. A literature review of the experimental density data for ($\mathrm{C}_1$ to $\mathrm{C}_{16}$) was also included in their work. Later, an updated overview of the density at elevated pressures of twelve liquid alkanes ($\mathrm{C}_5$ to $\mathrm{C}_{16}$) was carried out by Cibulka and Hnedkovsky [179]. The experimental data were fitted with the Tait equation and new parameters for the alkanes were provided. In general, the density of liquid alkanes ($\mathrm{C}_5$ to $\mathrm{C}_{16}$) is very well studied and the amount of density data for liquid alkanes in the literature is abundant. Since the last review, more experimental density data for the liquid alkanes have been published and the new experimental densities for liquid alkanes ($\mathrm{C}_5$ to $\mathrm{C}_{16}$), aromatics and pure $\mathrm{CO}_2$ in the past 20 years have been listed in the Tables below. Here, we only highlight the studies carried out at high pressures.

**Table 2.9** Experimental density studies for linear alkanes from ($\mathrm{C}_5$ to $\mathrm{C}_{16}$) conducted at elevated temperatures and pressures in the past 20 years; *T*, *p* and No. of pts. refer to the temperature and pressure ranges, and the number of points examined, respectively.

| **Alkanes ($\mathrm{C}_5$ to $\mathrm{C}_{16}$)** | | | |
|---|---|---|---|
| | **Temperature and Pressure Ranges** | | |
| **Reference** | ***T*/K** | ***p*/MPa** | **No. Pts.** |
| | ***n*-pentane** | | |
| Liu *et al.* (2010) [180] | 325.85 – 423.05 | 1.8 – 276.6 | 25 |
| NguyenHuynh *et al.* (2009) [181] | 373.15 – 423.15 | 0.6 – 1.6 | 2 |
| Peca and Dolecek (2003) [182] | 298.15 – 348.15 | 0.1 – 40.0 | 15 |
| Gozalpour *et al.* (2001) [183] | 323.00 | 7.0 – 139.7 | 9 |
| Tohidi *et al.* (2001) [184] | 323.00 – 423.00 | 6.9 – 138.1 | 27 |
| Byun *et al.* (2001) [185] | 323.15 – 423.15 | 7.1 – 241.5 | 84 |
| Pohler and Kiran (1997) [186] | 323.00 – 423.00 | 8.1 – 69.8 | 65 |
| Kiran *et al.* (1996) [187] | 348.00 – 423.00 | 8.1 – 64.8 | 52 |
| | ***n*-hexane** | | |
| Ivanis *et al.* (2015) [188] | 288.15 – 413.15 | 0.1 – 60.0 | 218 |
| Lampreia and Nieto de Castro (2011) [189] | 283.15 – 323.15 | 0.1 – 60.0 | 116 |
| Zhou *et al.* (2010) [190] | 293.15 – 313.15 | 0.1 – 40.0 | 30 |
| Valencia *et al.* (2009) [191] | 283.15 – 323.15 | 0.1 – 60.0 | 72 |
| Sanmamed *et al.* (2009) [192] | 283.15 – 323.15 | 0.1 – 60.0 | 117 |
| NguyenHuynh *et al.* (2009) [181] | 393.15 – 453.15 | 0.4 – 1.3 | 4 |
| Lasarte *et al.* (2008) [193] | 278.15 – 308.15 | 0.1 – 20.0 | 40 |

| | | | |
|---|---|---|---|
| Goldon *et al.* (2008) [194] | 283.15 – 333.15 | 0.1 – 35.0 | 63 |
| Camacho-Camacho and Galicia-Luna (2007) [195] | 312.12 – 362.40 | 1.0 – 25.0 | 150 |
| Kumagai *et al.* (2006) [196] | 273.15 – 333.15 | 0.1 – 30.0 | 16 |
| Verdier and Andersen (2005) [197] | 303.15 | 0.1 – 30.0 | 15 |
| Troncoso *et al.* (2003) [198] | 278.15 – 313.15 | 0.1 – 40.0 | 72 |
| Pecar and Dolecek (2003) [182] | 298.15 – 348.15 | 0.1 – 40.0 | 15 |
| **_n_-heptane** | | | |
| Pimentel-Rodas *et al.* (2016) [199] | 293.25 – 352.40 | 2.0 – 29.8 | 38 |
| Haghbakhsh *et al.* (2016) [200] | 313.15 – 393.15 | 0.3 – 44.5 | 165 |
| Iglesias-Silva *et al.* (2015) [201] | 283.15 – 363.16 | 0.1 – 66.2 | 629 |
| Alaoui *et al.* (2013) [202] | 298.15 – 393.15 | 0.1 – 140.0 | 136 |
| Zolghadr *et al.* (2013) [203] | 313.15 – 393.15 | 0.3 – 37.6 | 140 |
| Sagdeev *et al.* (2013) [204] | 298.15 – 470.61 | 0.1 – 245.2 | 52 |
| Schedemann *et al.* (2013) [205] | 298.07 – 447.11 | 0.8 – 129.9 | 432 |
| Quevedo-Nolasco *et al.* (2012) [206] | 313.18 – 353.06 | 1.0 – 25.0 | 75 |
| Lampreia and Nieto de Castro (2011) [189] | 283.15 – 323.15 | 0.1 – 60.0 | 117 |
| Sanmamed *et al.* (2009) [192] | 283.15 – 323.15 | 0.1 – 60.0 | 117 |
| Abdulagatov and Azizov (2007) [207] | 306.90 – 516.55 | 0.1 – 12.5 | 9 |
| Watson *et al.* (2006) [208] | 293.15 – 333.15 | 0.1 – 65.0 | 70 |
| Schilling *et al.* (2006) [209] | 233.15 – 393.15 | 0.1 – 30.0 | 151 |
| Abdulagatov and Azizov (2006) [207] | 307.61 – 500.47 | 4.4 – 12.5 | 8 |
| Verdier and Andersen (2005) [197] | 303.15 | 0.1 – 30.0 | 15 |
| Fandino *et al.* (2005) [210] | 278.15 – 353.15 | 0.1 – 45.0 | 99 |
| Pecar and Dolecek (2003) [182] | 298.15 – 348.15 | 0.1 – 40.0 | 15 |
| Acevedo *et al.* (2003) [211] | 278.15 – 353.15 | 0.1 – 25.0 | 81 |
| Moravkova and Linek (2002) [212] | 298.15 – 328.15 | 0.1 – 38.6 | 21 |
| Comunas *et al.* (2000) [213] | 283.15 – 323.15 | 0.5 – 12.2 | 65 |
| Ihmels (1998) [214] | 298.19 – 522.66 | 0.6 – 10.0 | 275 |
| Ulbig *et al.* (1997) [215] | 298.15 | 0.1 – 60.0 | 3 |
| Baylaucq *et al.* (1997) [216] | 303.15 – 343.15 | 0.1 – 100.0 | 18 |
| **_n_-octane** | | | |
| Schedemann *et al.* (2013) [205] | 288.15 – 308.15 | 0.1 – 40.0 | 18 |
| Gayol *et al.* (2013) [217] | 278.24 – 436.66 | 0.4 – 130.0 | 459 |
| Lampreia and Nieto de Castro (2011) [189] | 283.15 – 323.15 | 0.1 – 60.0 | 117 |
| Sato *et al.* (2010) [218] | 323.20 | 0.2 – 10.4 | 4 |
| Liu *et al.* (2010) [180] | 321.85 – 521.55 | 14.3 – 276.9 | 29 |
| Sanmamed *et al.* (2009) [192] | 283.15 – 323.15 | 0.1 – 60.0 | 117 |
| Moravkova *et al.* (2008) [219] | 298.15 – 328.15 | 0.1 – 39.6 | 92 |
| Goodwin *et al.* (2006) [220] | 323.15 – 423.09 | 0.1 – 68.4 | 44 |
| Kumagai *et al.* (2006) [196] | 273.15 – 333.15 | 0.1 – 30.0 | 16 |
| Abdulagatov and Azizov (2006) [207] | 311.89 – 516.64 | 4.7 – 11.5 | 8 |
| Moravkova and Linek (2003) [221] | 298.15 – 328.15 | 0.1 – 38.6 | 21 |

| | | | |
|---|---|---|---|
| Goodwin *et al.* (1996) [222] | 298.03 – 303.15 | 0.7 – 32.6 | 14 |
| | ***n*-nonane** | | |
| Valencia *et al.* (2009) [191] | 283.15 – 323.15 | 0.1 – 60.0 | 90 |
| Schilling *et al.* (2008) [209] | 233.15 – 373.15 | 0.1 – 30.0 | 136 |
| Moravkova *et al.* (2007) [223] | 298.15 – 328.15 | 0.1 – 39.6 | 92 |
| | ***n*-decane** | | |
| Kariznovi *et al.* (2013) [224] | 373.20 | 0.1 – 10.0 | 11 |
| Quevedo-Nolasco *et al.* (2012) [206] | 313.07 – 362.73 | 1.0 – 25.0 | 138 |
| Lampreia and Nieto de Castro (2011) [189] | 283.15 – 323.15 | 0.1 – 60.0 | 117 |
| Fandino *et al.* (2011) [225] | 283.15 – 398.15 | 0.1 – 130.0 | 89 |
| Liu *et al.* (2010) [180] | 324.45 – 520.15 | 14.6 – 278.8 | 28 |
| Sato *et al.* (2010) [218] | 323.10 – 333.10 | 0.1 – 10.2 | 7 |
| Valencia *et al.* (2009) [191] | 283.15 – 398.15 | 0.1 – 70.0 | 49 |
| Sanmamed *et al.* (2009) [192] | 283.15 – 323.15 | 0.1 – 60.0 | 90 |
| Caudwell *et al.* (2009) [226] | 298.15 – 373.15 | 0.1 – 191.7 | 32 |
| Segovia *et al.* (2009) [227] | 283.15 – 318.15 | 0.1 – 60.0 | 104 |
| Zuniga-Moreno *et al.* (2005) [228] | 313.09 – 362.63 | 1.0 – 25.1 | 148 |
| Verdier and Andersen (2005) [197] | 303.15 | 0.1 – 30.0 | 15 |
| Audonnet and Padua (2004) [229] | 303.15 – 393.15 | 0.1 – 76.2 | 40 |
| Troncoso *et al.* (2004) [230] | 283.15 – 328.15 | 0.1 – 40.0 | 90 |
| Bessieres *et al.* (2001) [231] | 308.15 – 368.15 | 20.0 – 40.0 | 21 |
| Tohidi *et al.* (2001) [184] | 323.00 | 4.7 – 139.8 | 9 |
| | ***n*-undecane** | | |
| Giuliano Albo *et al.* (2013) [80] | 278.00 – 318.00 | 1.0 – 60.0 | 20 |
| Elizalde-Solis *et al.* (2013) [232] | 313.15 – 362.91 | 1.0 – 25.0 | 150 |
| Valencia *et al.* (2009) [191] | 283.15 – 323.15 | 0.1 – 60.0 | 63 |
| | ***n*-dodecane** | | |
| Regueira *et al.* (2015) [233] | 278.15 – 463.15 | 0.1 – 60.0 | 59 |
| Zhang *et al.* (2014) [234] | 313.48 – 353.59 | 8.0 – 18.0 | 38 |
| Elizalde-Solis *et al.* (2007) [235] | 313.09 – 362.29 | 1.0 – 24.8 | 150 |
| Caudwell *et al.* (2004) [236] | 298.15 – 473.15 | 0.1 – 191.7 | 64 |
| | ***n*-tridecane** | | |
| Valencia *et al.* (2009) [191] | 283.15 – 323.15 | 0.1 – 60.0 | 63 |
| Elizalde-Solis *et al.* (2007) [235] | 313.09 – 362.25 | 1.0 – 25.0 | 150 |
| Dauge *et al.* (2001) [237] | 293.15 – 353.15 | 0.1 – 60.0 | 28 |
| | ***n*-tetradecane** | | |
| Kariznovi *et al.* (2013) [224] | 296.60 – 333.30 | 0.1 – 10.0 | 55 |
| Nourozieh *et al.* (2013) [238] | 373.20 | 0.1 – 10.0 | 11 |
| Kariznovi *et al.* (2011) [239] | 323.20 – 422.70 | 1.0 – 8.0 | 21 |

| | | | |
|---|---|---|---|
| Valencia *et al.* (2009) [191] | 283.15 – 323.15 | 0.1 – 60.0 | 56 |
| Tarassov *et al.* (1997) [240] | 324.50 – 433.20 | 25.0 – 200.0 | 32 |
| | ***n*-pentadecane** | | |
| no new data | | | |
| | ***n*-hexadecane** | | |
| Regueira *et al.* (2015) [233] | 298.15 – 463.15 | 0.1 – 60.0 | 51 |
| Haghbakhsh *et al.* (2015) [200] | 313.15 – 393.15 | 0.3 – 44.5 | 165 |
| Nascimento *et al.* (2015) [132] | 313.15 – 333.15 | 5.0 – 25.0 | 15 |
| Baled *et al.* (2014) [241] | 303.90 – 533.70 | 3.3 – 226.6 | 42 |
| Zolghadr *et al.* (2013) [203] | 313.15 – 393.15 | 0.3 – 44.5 | 165 |
| Wu *et al.* (2011) [242] | 323.65 – 522.55 | 14.1 – 262.3 | 31 |
| Outcalt *et al.* (2010) [243] | 310.00 – 470.00 | 1.0 – 50.7 | 92 |
| Rajagopal *et al.* (2009) [244] | 318.15 – 413.15 | 6.9 – 62.0 | 54 |
| Khasanshin *et al.* (2008) | 298.15 – 433.15 | 0.1 – 100.1 | 43 |
| Amorim *et al.* (2007) [245] | 318.15 – 413.15 | 6.9 – 62.1 | 54 |
| Khasanshin and Shchemelev (2001) [120] | 303.15 – 433.15 | 0.1 – 49.1 | 29 |
| Ball and Trusler (2001) [52] | 298.30 – 373.15 | 0.1 – 100.9 | 65 |
| Chang *et al.* (1998) [246] | 333.15 – 413.15 | 0.1 – 30.0 | 21 |

**Table 2.10** Experimental density studies for benzene and methylbenzene conducted at elevated temperatures and pressures in the past 20 years; $T$, $p$ and No. of pts. refer to the temperature and pressure ranges, and the number of points examined, respectively.

| **Benzene and Methylbenzene** | | | |
|---|---|---|---|
| | **Temperature and Pressure Ranges** | | |
| **Reference** | ***T*/K** | ***p*/MPa** | **No. Pts.** |
| | **benzene** | | |
| Moravkova *et al.* (2003) [247] | 298.15 – 328.15 | 1 – 396 | 92 |
| Fornefeld-Schwarz *et al.* (1997) [248] | 293.15 | 1 – 100 | 6 |
| | **Methylbenzene** | | |
| Ivanis *et al.* (2015) [188] | 288.15 – 413.15 | 0.1 – 60.0 | 222 |
| Guan *et al.* (2013) [249] | 296.40 – 333.20 | 0.1 – 10.0 | 55 |
| Sommer *et al.* (2011) [250] | 233.15 – 473.15 | 0.1 – 30.1 | 247 |
| Fandino *et al.* (2010) [171] | 298.15 – 398.15 | 0.1 – 60.0 | 53 |
| Chorazewski *et al.* (2010) [251] | 322.85 – 525.05 | 28.6 – 274.9 | 26 |
| Liu *et al.* (2010) [180] | 323.20 – 333.10 | 2.1 – 10.2 | 6 |
| Glen and Johns (2009) [252] | 293.14 – 373.37 | 0.6 – 30.1 | 74 |
| Segovia *et al.* (2009) [227] | 283.15 – 398.15 | 0.1 – 70.0 | 48 |
| Valencia *et al.* (2009) [191] | 283.15 – 323.15 | 0.1 – 60.0 | 72 |
| McLinden and Splett (2008) [253] | 213.15 – 473.16 | 0.1 – 35.6 | 1191 |

| | | | |
|---|---|---|---|
| Kiselev *et al.* (2008) [254] | 293.15 | 0.1 – 100.0 | 21 |
| Goodwin *et al.* (2006) [220] | 323.15 – 373.11 | 0.1 – 68.2 | 11 |
| Watson *et al.* (2006) [255] | 293.15 – 353.15 | 0.1 – 65.0 | 98 |
| Moravkova *et al.* (2005) [223] | 298.15 – 328.15 | 0.1 – 39.6 | 92 |
| Zeberg-Mikkelsen *et al.* (2005) [256] | 283.15 – 353.15 | 0.1 – 45.0 | 80 |
| Avelino *et al.* (2003) [257] | 222.51 – 348.13 | 0.1 – 80.6 | 80 |
| Gu and Brennecke (2002) [258] | 323.20 | 0.1 – 201.4 | 7 |
| Masui (2002) [259] | 298.18 – 423.05 | 0.1 – 30.2 | 65 |
| Ihmels and Gmehling (2001) [260] | 273.39 – 588.19 | 0.5 – 30.0 | 455 |
| Belonenko *et al.* (2000) [261] | 298.15 – 323.18 | 0.1 – 478.4 | 32 |
| Comunas *et al.* (2000) [213] | 283.15 – 323.15 | 0.5 – 12.2 | 65 |
| Franck *et al.* (1998) [262] | 303.15 – 583.15 | 3.4 – 297.4 | 175 |
| Fornefeld-Schwarz *et al.* (1997) [248] | 293.15 | 0.1 – 10.0 | 6 |
| Magee and Bruno (1996) [263] | 180.00 – 400.00 | 0.5 – 35.1 | 311 |
| Pohler and Kiran (1996) [264] | 323.00 – 423.00 | 3.4 – 64.8 | 69 |

**Table 2.6** Experimental density studies for carbon dioxide conducted at elevated temperatures and pressures; *T*, *p* and No. of pts. refer to the temperature and pressure ranges, and the number of points examined, respectively.

| **$CO_2$** | | | |
|---|---|---|---|
| | **Temperature and Pressure Ranges** | | |
| **Reference** | ***T*/K** | ***p*/MPa** | **No. Pts.** |
| | **$CO_2$** | | |
| Padua *et al.* (1994) [265] | 260.04 – 300.00 | 6.0 – 100.0 | 65 |
| Duarte-Garza *et al.* (1995) [266] | 240.00 – 300.00 | 1.6 – 34.5 | 33 |
| Harris and Yung (1995) [267] | 221.00 – 303.00 | 0.6 – 7.1 | 18 |
| Gokmenoglu *et al.* (1996) [268] | 297.00 – 304.00 | 6.1 – 31.1 | 18 |
| Teng *et al.* (1997) [269] | 288.00 | 6.0 – 30.0 | 2 |
| Lau *et al.* (1997) [270] | 240.00 – 300.00 | 1.6 – 34.5 | 33 |
| van der Gulik (1997) [271] | 220.00 – 303.05 | 0.6 – 453.2 | 223 |
| Ihmels and Gmehling (2001) [260] | 283.37 – 303.32 | 10.0 – 30.0 | 25 |
| Klimeck *et al.* (2001) [272] | 240.00 – 430.00 | 8.0 – 30.6 | 68 |
| Saleh and Wendland (2005) [273] | 233.07 – 293.09 | 1.0 – 5.7 | 14 |
| Liu *et al.* (2006) [274] | 318.00 | 10.1 – 36.2 | 5 |
| Pensado *et al.* (2008) [275] | 303.15 | 10.0 – 60.0 | 11 |
| Tallon and Fenton (2010) [276] | 291.30 – 292.10 | 6.1 – 30.1 | 9 |
| Gil *et al.* (2010) [277] | 293.15 | 5.7 – 8.5 | 7 |
| Mazzoccoli *et al.* (2012) [278] | 273.15 – 293.15 | 3.5 – 20.0 | 50 |
| Knez Hrncic *et al.* (2014) [279] | 293.00 | 8.0 – 44.7 | 16 |

A critical literature survey on experimental density data in binary mixtures of liquid alkanes ($C_5$ to $C_{16}$), aromatics (benzene and methylbenzene) and pure $CO_2$ has also been performed in this work. Hereby, we present the high-pressure density data only for each binary mixture and the available

density data for binary mixtures of $CO_2$ + hydrocarbons in the literature are listed in tables below. The listed experimental density data include both saturated-phase density and compressed-liquid density. The information provided includes the temperature and pressure range and the number of measured points.

**Table 2.11** Experimental density studies for binary mixtures of $CO_2$ + alkanes ($C_5$ to $C_{16}$) conducted at elevated temperatures and pressures; *T*, *p* and No. of pts. refer to the temperature and pressure ranges, and the number of points examined, respectively.

| **$CO_2$ + Alkanes ($C_5$ to $C_{15}$)** | | | |
|---|---|---|---|
| | **Temperature and Pressure Ranges** | | |
| **Reference** | ***T*/K** | ***p*/MPa** | **No. Pts.** |
| | **$CO_2$ + *n*-pentane** | | |
| Kiran *et al.* (1996) [187] | 323.00 – 398.00 | 8.6 – 65.0 | 153 |
| Chen *et al.* (2003) [280] | 318.15 – 323.15 | 2.2 – 15.2 | 146 |
| | **$CO_2$ + *n*-hexane** | | |
| Tolley *et al.* (1991) [281] | 313.15 | 6.3 – 12.5 | 98 |
| Zhu *et al.* (2006) [282] | 313.15 – 373.15 | 2.2 – 13.1 | 28 |
| | **$CO_2$ + *n*-heptane** | | |
| Rabe (1981) [283] | 220.00 – 300.00 | 1.0 – 6.6 | 69 |
| Khristoforov and Dautov (1987) [284] | 283.00 – 343.00 | | 7 |
| Fenghour *et al.* (2001) [285] | 316.28 – 459.37 | 4.5 – 55.5 | 24 |
| Medina-Bermudez *et al.* (2013) [286] | 313.00 – 363.00 | 5.0 – 25.0 | 501 |
| | **$CO_2$ + *n*-octane** | | |
| Yu *et al.* (2006) [287] | 313.20 – 393.20 | 1.1 – 14.4 | 47 |
| | **$CO_2$ + *n*-nonane** | | |
| | No data | | |
| | **$CO_2$ + *n*-decane** | | |
| Cullick and Mathis (1984) [36] | 310.92 – 403.08 | 6.7 – 34.7 | 83 |
| Nagarajan and Robinson (1986) [288] | 344.30 – 377.60 | 6.4 – 16.5 | 44 |
| Barrufet *et al.* (1996) [289] | 310.93 – 403.15 | 7.0 – 11.8 | 12 |
| Bessieres *et al.* (2001) [290] | 308.15 – 368.15 | 20.0 – 40.0 | 126 |
| Shaver *et al.* (2001) [291] | 344.30 | 1.4 – 12.7 | 30 |
| Tsuji *et al.* (2004) [292] | 344.30 | 3.6 – 11.6 | 6 |
| Zuniga-Moreno *et al.* (2005) [228] | 313.10 – 362.66 | 2.0 – 25.1 | 538 |
| Nourozieh *et al.* (2013) [293] | 323.20 | 1.0 – 6.0 | 6 |
| Mejia *et al.* (2014) [294] | 344.15 | 0.1 – 10.3 | 12 |
| | **$CO_2$ + *n*-undecane** | | |

| | | | |
|---|---|---|---|
| | No data | | |
| | **$CO_2$ + *n*-dodecane** | | |
| | No data | | |
| | **$CO_2$ + *n*-tridecane** | | |
| Enick *et al.* (1985) [295] | 310.80 – 313.00 | 8.2 – 8.5 | 3 |
| | **$CO_2$ + *n*-tetradecane** | | |
| Gasem *et al.* (1989) [296] | 344.30 | 11.0 – 16.3 | 18 |
| Kariznovi *et al.* (2013) [224] | 323.20 | 1.0 – 6.0 | 6 |
| | **$CO_2$ + *n*-pentadecane** | | |
| Tanaka *et al.* (1993) [297] | 313.15 | 1.7 – 6.4 | 8 |
| | **$CO_2$ + *n*-hexadecane** | | |
| King *et al.* (1984) [298] | 333.15 K | 0.2 – 16.4 | 14 |
| Tanaka *et al.* (1993) [297] | 313.15 K | 1.7 – 6.5 | 8 |

**Table 2.12** Experimental density studies for $CO_2$ + benzene and $CO_2$ + methylbenzene conducted at elevated temperatures and pressures; *T*, *p* and No. of pts. refer to the temperature and pressure ranges, and the number of points examined, respectively.

| **$CO_2$ + Benzene and $CO_2$ + Methylbenzene** | | | |
|---|---|---|---|
| | **Temperature and Pressure Ranges** | | |
| **Reference** | ***T*/K** | ***p*/MPa** | **No. Pts.** |
| | **$CO_2$ + benzene** | | |
| Nagarajan and Robinson (1987) [299] | 344.26 | 6.9 – 11.0 | 17 |
| | **$CO_2$ + methylbenzene** | | |
| Chang *et al.* (1995) [300] | 300.90 – 310.10 | 1.2 – 7.4 | 31 |
| Pohler and Kiran (1996) [264] | 323.00 – 398.00 | 7.9 – 64.8 | 108 |
| Park *et al.* (1990) [301] | 333.20 – 393.20 | 4.0 – 15.4 | 15 |

## 2.4 Summary

The review presented in this chapter aims to provide an overview of two main points which are considered relevant to this work: (1) the experimental techniques for speed-of-sound and density measurements and (2) a review of the available sound-speed and density data for hydrocarbons and $CO_2$ + hydrocarbons mixtures in the literature. The characteristics of the existing techniques for both properties measurements have been reported. A comprehensive literature review concerning the available experimental data for speed-of-sound and density has been carried out. The results showed that most of the speed-of-sound data for *n*-alkanes were measured at atmospheric conditions and only a few studies were conducted at high pressures for each compound. Unfortunately, no speed-of-sound data for binary mixtures of $CO_2$ + alkanes/aromatics can be found in the literature. On the other hand, there is an abundant amount of density data for liquid alkanes measured at high-pressure conditions in the literature. This literature review presented in this chapter aims to provide a basis for selection of systems to be measured in this research.

# Chapter 3: Equations of State

## 3.1 Overview

The focus of this chapter is to present several thermodynamic models that allow the predictions of thermophysical properties of ($CO_2$ + hydrocarbon) systems to be accurately calculated. A brief description of the widely used equation of state (EoS) models such as the cubic equations of state, the Statistical Associating Fluid Theory (SAFT) equations of state and the multi-parameter Helmholtz energy explicit equations of state are presented. These models are commonly used in both academia and industry due to their simplicity and accuracy. Different versions of the cubic EoS and SAFT EoS are first described, and a group contribution approach to both types of equations of state is introduced. Then, the Helmholtz energy explicit equations of state for pure and multi-components are discussed. Lastly, the thermodynamic integration technique which enables the derivation of thermophysical properties from the speed-of-sound data is reported.

## 3.2 Introduction

Direct measurement of experimental thermophysical properties are of vital importance, but it can be arduous and expensive. In this context, it is important to have accurate tools that are able to predict thermophysical properties for the design and selection of operation conditions, helping to reduce the amount of experimental work. Equations of state are widely used in the prediction of thermodynamic properties and phase equilibria of pure fluids and fluid mixtures. The term equation of state (EoS) is used to describe an empirical function that provides a relation between pressure, density, temperature and composition (for a mixture); this provides a prescription for the calculation of all of the configurationally and residual thermodynamic properties of the system.

$$f(p,\rho,T)=0 \tag{3.1}$$

An equation of state can provide good predictions for a wide range of thermophysical properties of both gaseous and liquid phases. Among different types of equations of state, cubic equations of state (cEoS) are the most commonly used in the oil and gas industry for the calculation of various thermophysical properties over wide ranges of temperature and pressure due to their (1) simplicity (simplicity in terms of mathematical formulation) and (2) reliability (reasonable uncertainty for the correlation and prediction of thermodynamic properties for both pure components and mixtures). Over the years there has been a lot of advancement in the cubic equations of state through the introduction of more defined attractive and repulsive terms, more sophisticated mixing and combining rules and new approaches to the binary interaction parameters calculation. Apart from the cubic equations of state, other forms of EoSs are also widely used in various applications for different components/mixtures. Molecular-based equations of state which have a foundation in statistical mechanics are commonly used for modelling mixtures with hydrocarbons and gases. Among them, the Statistical Associating Fluid Theory (SAFT) EoS has gained popularity due to its predictive capability of predicting thermodynamic properties of polar solvents and hydrogen-bonding fluids. In addition, multi-parameter Helmholtz energy explicit EoSs have also been widely used for accurate representation of different thermodynamic properties of fluids. Using the relationships between the thermodynamic properties, all thermodynamic properties can be calculated from combinations of the derivatives. These various types of equations of state will be discussed in detail in this chapter.

## 3.3 Cubic Equations of State

Cubic equations of state work well for fluids that contain simple molecules (non-associating), therefore they are suitable for thermodynamic calculations for most hydrocarbons. The cEoS are currently the most widely used models for a variety of practical applications, including reservoir simulations and chemical processes.

### 3.3.1 Van der Waals (vdW) Equation of State

The cubic equation of state was first introduced by J. D. van der Waals in 1873 in which the expression is capable of describing the volumetric behaviour, vapour-liquid equilibrium (VLE) and thermal properties of both pure substances and mixtures [302, 303]. The form of a cubic equation of state is generally relating pressure to the volume and temperature. van der Waals corrected the pressure and volume terms of the ideal gas equation, taking into account that the molecules are treated as rigid spheres that occupy space and they exert an attractive force within molecules. Therefore, he proposed that the volume term in the ideal gas equation should be replaced by some quantity that is smaller than $V$, in this case, $V - b$. Secondly, the attraction between the molecules must give rise to a reduction in pressure, then the a term in the equation. The original form of his expression is given as follows:

$$p = \frac{RT}{V_{\mathrm{m}} - b} - \frac{a}{V_{\mathrm{m}}^2} \tag{3.2}$$

The equation is cubic in molar volume, $V_m$, and contains two constants $a$ and $b$ which are known as the van der Waals coefficients. Parameter $b$ accounts for the volume occupied by the molecules and the term ($a/V^2$) accounts for the attractive intermolecular force between molecules. They are characteristic of each individual fluid but independent of temperature. For engineering applications with real fluids, both parameters, $a$ and $b$, are typically adjusted to reproduce the critical temperature and pressure of pure fluids. It is possible to obtain the values of these parameters with respect to the experimental critical temperature and critical pressure as follows:

$$a = \frac{27\left(RT_{\mathrm{c}}\right)^2}{64\,p_{\mathrm{c}}} \text{ and } b = \frac{RT_{\mathrm{c}}}{8p_{\mathrm{c}}} \tag{3.3}$$

The equation has its simplicity, but it fails to predict accurately due to the fact that it predicts a fixed value for the critical compression factor, $Z_c = p_cV_c / RT_c = 0.375$, which is always larger than experimental values (usually less than 0.3) for many common fluids. However, due to its simplicity, reliability and speed of computation, the equation is still one of the most frequently used equations of states for practical applications. Since then, there have been various development/modification on the original cEoS [304]. Hereby, the Soave-Redlich-Kwong [305], Peng-Robinson [306] and Patel and Teja EoSs are focused because of their popularity in the industry and academia. They are widely used for the calculations of the properties of pure components, binary and multi-component mixtures including VLE and single phase thermodynamic properties.

### 3.3.2 Soave-Redlich-Kwong (SRK) Equation of State

In 1949, Redlich and Kwong [307] modified the original equation of state by incorporating the conventional combining rules and considering temperature-dependant binary interaction parameters in the attractive term, but the vdW repulsive term was unchanged. With this modification, the equation

was proven to be very successful for the calculation of the properties of gas mixtures and it provides better fluid phase behaviour at low and high densities compared to the original vdW equation. However, it is still not capable of predicting liquid volumes with acceptable accuracy. The parameters of the equation are based entirely on the two critical properties, $T_c$ and $p_c$ and the acentric factor was not considered.

$$p = \frac{RT}{V_m - b} - \frac{a}{V_m(V_m + b)\sqrt{T}} \tag{3.4}$$

The parameters of the Redlich-Kwong equation can be estimated by the following expressions:

$$\begin{aligned} a &= \sum_{i=1}^{n}\sum_{j=1}^{n} x_i x_j (1 - k_{ij})\sqrt{(a_i)(a_j)} \\ b &= \sum_{i=1}^{n} x_i b_i \\ a_i &= 0.42748\frac{R^2 (T_{c,i})^{2.5}}{p_{c,i}} \\ b_i &= 0.08664\frac{RT_{c,i}}{p_{c,i}} \end{aligned} \tag{3.5}$$

It was mentioned that the agreement between the experimental data and model calculations can be improved when *a* and *b* are component and temperature dependent. The Redlich-Kwong equation proved to be very successful for the calculation of the properties of gas mixtures However, a major limitation of this equation of state is its ability to predict liquid-phase thermodynamic properties and VLE accurately. In 1972, Soave modified the Redlich-Kwong equation [305] by replacing the $a/\sqrt{T}$ term with a more general function of the temperature-dependent term, $a\alpha(T)$ which incorporates the acentric factor, $\omega$, in the attractive term. The acentric factor is a conceptual number introduced by Kenneth Pitzer, is a measure of the non-sphericity of molecules, which can be estimated through the critical *pVT* properties of the substances. This modification allowed accurate representations of vapour pressures of hydrocarbons. The modified equation became:

$$p = \frac{RT}{V_m - b} - \frac{a\alpha(T)}{V_m(V_m + b)} \tag{3.6}$$

The parameters of the Soave-Redlich-Kwong equation can be estimated by the following expressions:

$$\begin{aligned} a\alpha &= \sum_{i=1}^{n}\sum_{j=1}^{n} x_i x_j (1 - k_{ij})\sqrt{(a_i\alpha_i)(a_j\alpha_j)} \\ b &= \sum_{i=1}^{n} x_i b_i \\ \alpha_i &= \left[1 + (0.48508 + 1.55171\omega_i - 0.15613\omega_i^2)\left(1 - \sqrt{\frac{T}{T_{c,i}}}\right)\right]^2 \end{aligned} \tag{3.7}$$

Here, $\alpha(T)$ denotes the acentric factor which takes into account the molecular size and the shape effects. Soave showed that the modification significantly improved the Redlich-Kwong for pure hydrocarbons and hydrocarbons mixtures VLE predictions. The also lowered the constant compressibility to $Z_c = 0.333$. This cubic equation of state is known as the Soave-Redlich-Kwong Equation of State [305]. The SRK EoS is accepted to be capable of the VLE calculations, but it does not provide reliable liquid density.

### 3.3.3 Peng-Robinson (PR) Equation of State

With the success of the Soave-Redlich-Kwong EoS, it generated more interest in the academic community to improve the cubic equation of state further. In 1976, Peng and Robinson published their work on the modification of the cEoS [306]. They modified the equation with a different expression for the denominator of the attractive term and added in a more complicated function of temperature, $a\alpha(T)$, incorporating the acentric factor. The Peng-Robinson EoS is given by:

$$p = \frac{RT}{V_m - b} - \frac{a\alpha(T)}{V_m(V_m + b) + b(V_m - b)} \tag{3.8}$$

In 1978, Peng and Robinson published an improved version of their equation of state, which introduces the acentric factor into the equation and this gives more accurate vapour pressure predictions for the heavy hydrocarbons than those obtained by using PR76. The parameters can be calculated for individual components by the following expressions:

$$a\alpha = \sum_{i=1}^{n}\sum_{j=1}^{n} x_i x_j (1 - k_{ij})\sqrt{(a_i\alpha_i)(a_j\alpha_j)}$$

$$b = \sum_{i=1}^{n} x_i b_i$$

$$a_i = 0.45724\frac{(RT_{c,i})^2}{p_{c,i}}$$

$$b_i = 0.07780\frac{(RT_{c,i})}{p_{c,i}} \tag{3.9}$$

$$\alpha_i = \left[1 + n_i\left(1 - \sqrt{\frac{T}{T_{c,i}}}\right)\right]^2$$

$$\text{if } \omega_i \le 0.491\ldots n_i = 0.37464 + 1.54226\omega_i - 0.26992\omega_i^2$$

$$\text{if } \omega_i > 0.491\ldots n_i = 0.379642 + 1.48503\omega_i - 0.164423\omega_i^2 + 0.016666\omega_i^3$$

Here $p$ is the pressure, $T$ the temperature, $R$ the ideal gas constant, $a$ and $b$ are van der Waals coefficients, $T_c$ the critical temperature, $p_c$ the critical pressure and $\omega$, the acentric factor. Currently, the SRK EoS and PR EoS are the two most widely used EoSs in the oil and gas industry. However,

one of the drawbacks of these two equations is that the critical compressibility is always constant regardless of the component.

## 3.3.4 Patel and Teja (PT) Equation of State

In the above mentioned EoS, all contain two parameters in the models. Each one of them predicts a constant compressibility factor at the critical point $Z_c = p_c V_c / RT_c$ irrespective of the nature of the compound. For example vdW, $Z_c$ = 0.375; SRK, $Z_c$ = 0.333 and PR, $Z_c$ = 0.307 [308]. For some hydrocarbons, $Z_c$ is below 0.3 and this over-estimation of critical compressibility leads to an inaccurate prediction of volume in the liquid-phase. To correct this problem, Petal and Teja [309] proposed using four adjustable parameters to the cubic equation of state and is defined as:

$$p = \frac{RT}{V_m - b} - \frac{a\alpha(T)}{V_m(V_m + b) + c(V_m - b)}, \tag{3.10}$$

where parameters $a$, $\alpha$, $b$ and $c$ are functions of $T_c$ and $p_c$. Patel and Teja treated the apparent compressibility factor as an adjustable parameter which is a temperature dependant term. The term $\alpha$ appeared in SRK, PR and PT EoSs is so-called the Soave alpha function which determines the temperature dependency of the parameter $a$ and it was optimised to obtain a good representation of vapour pressure curves of pure, non-polar components. Alternative alpha functions have been proposed to improve the modelling capacities of cubic EoSs for polar components such as the Mathias-Coperman function, and the Boston-Mathias function for mixtures containing supercritical components [310-312].

## 3.3.5 Volume Translation

As mentioned, equations of state are used in commercial simulation software for predicting phase behaviour and thermodynamic properties. In general, EoSs require a few parameters that are usually obtained from critical properties. The cubic equations of state give relatively accurate results for predicting vapour-liquid equilibria, especially for non-polar systems. However, the accuracy for liquid density prediction is not as good as the VLE predictions. The common cEoS such as Soave-Redlich-Kwong (SRK) and Peng-Robinson (PR), which are two-parameter EoSs, as mentioned above have a constant critical compressibility which leads to under-prediction of liquid volume. Both EoSs predict the liquid density with an average deviation error of about 8 % [313]. In order to overcome this deficiency, a volume translated method has been developed by Peneloux *et al.* [314] In 1982, they developed a method of improving the volumetric predictions by introducing an extra parameter into the cubic equations of state which minimised the deviation between the predicted liquid molar volume and the experimental data. They found that having a certain translation along the volume axis may improve the prediction of liquid density while the predicted equilibrium conditions ($T$,$p$,$x$) remain unchanged. The feature of this method for a pure fluid is that the molar volume in the cubic equation

of state is replaced by a translated molar volume to enhance the liquid density predictions accuracy in the sub-critical region. The volume translation expression proposed by Peneloux *et al.* is given as follows:

$$v^{\mathrm{L}} = v^{\mathrm{EoS}} + \frac{c}{MW} \text{ and } \rho^{\mathrm{L}} = \frac{1}{v^{\mathrm{L}}} \tag{3.11}$$

The term $v^{\mathrm{L}}$ is the corrected liquid specific volume, $v^{\mathrm{EoS}}$ is the liquid specific volume calculated with SRK or PR EoS, $MW$ is the molecular weight, $\rho^{\mathrm{L}}$ is the liquid density. $c$ is the volume shift factor which is determined from the regression of experimental liquid density data. The term $c$ is a correction which depends only upon the fluid and the temperature. For a multi-component mixture, the parameter $c$ is obtained using a linear mixing rule, and in the absence of experimental regressed value, the volume shift factor can be estimated as follows:

$$\begin{aligned} c &= \sum_{i=1}^{n} x_i c_i \\ c &= \frac{0.40768 R T_{\mathrm{c}}}{p_{\mathrm{c}}} \left(0.29441 - Z_{\mathrm{RA}}\right) \end{aligned} \tag{3.12}$$

Here $R$ is the universal gas constant, $T_{\mathrm{c}}$ and $p_{\mathrm{c}}$ are the critical temperature and pressure, respectively. $Z_{\mathrm{RA}}$ is the Rackett compressibility factor [314] which was established by the American Petroleum Institute (API) (1973,1974). An approximate value for $Z_{\mathrm{RA}}$ can be obtained from the acentric number, defined as: $Z_{\mathrm{RA},i} = 0.2906 - 0.0878\omega_i$. The API published the values of $Z_{\mathrm{RA}}$ for the first ten *n*-alkanes, and the values are tabulated in Table 3.1. This modification allows the improvement on the predictions of the saturated liquid densities while having the same accuracy on the vapour pressure predictions.

**Table 3.1** Values of the Rackett compressibility factor $Z_{\mathrm{RA}}$ for volume translation for the first ten *n*-alkanes published by the American Petroleum Institute (API).

| **Alkane** | $Z_{\mathrm{RA}}$ | **Alkane** | $Z_{\mathrm{RA}}$ |
|---|---|---|---|
| Methane | 0.2894 | *n*-Hexane | 0.2636 |
| Ethane | 0.2813 | *n*-Heptane | 0.2607 |
| Propane | 0.2766 | *n*-Octane | 0.2568 |
| *n*-Butane | 0.2733 | *n*-Nonane | 0.2546 |
| *n*-Pentane | 0.2685 | *n*-Decane | 0.2507 |

In 1990, Magoulas and Tassios [315] also proposed a volume-translated version for the Peng-Robinson EoS in which the shift factor is represented by a universal function of reduced temperature $T_{\mathrm{r}} = T / T_{\mathrm{c}}$ and $\omega$, given as:

$$
\begin{aligned}
c_{\mathrm{c}} &= \frac{RT_{\mathrm{c}}}{p_{\mathrm{c}}}\left(0.3074 - Z_{\mathrm{c}}\right) \\
c_0 &= \frac{RT_{\mathrm{c}}}{p_{\mathrm{c}}}\left(-0.0145 + 0.0675\omega - 0.0849\omega^2 + 0.0673\omega^3 - 0.0174\omega^4\right), \\
c_1 &= -10.2447 - 28.6312\omega \\
c &= c_0 + \left(c_0 - c_{\mathrm{c}}\right)\exp\left(c_1\left|1 - T_{\mathrm{r}}\right|\right)
\end{aligned}
\tag{3.13}
$$

where $c_0$, $c_{\mathrm{c}}$ and $c_1$ are component-dependent parameters that are fitted to the molar volumes of several saturated liquid alkanes.

## 3.3.6 Mixing Rules and Binary Interactions

Mixing rules are used to obtain estimations for the parameters in an equation of state for a specified mixture from the parameters of the pure components. For the description of mixture parameters for the interactions between un-like components, combining rules are used. As mentioned previously, the cEoSs only require the values of critical temperature and pressure and the acentric factor for pure components calculations. To apply the equations of state to mixtures, a mixing rule can be used for the calculation of the values of the parameters $a$ and $b$ of the mixtures. The most commonly used classical mixing rule is the van der Waals one-fluid mixing rule in which the mixture is treated as a hypothetical pure comprising molecules whose $a$ and $b$ parameters are obtained as a weighted average of the parameters of the pure components. However, it has to be noted that this assumption is not true for properties near the critical point. This mixing rule has been found accurate enough to represent mixtures containing light hydrocarbons and $CO_2$. For n-component mixture, the mixing rule is given in the following form:

$$
\begin{aligned}
a_{\mathrm{mix}} &= \sum_{i=1}^{n}\sum_{j=1}^{n} x_i x_j a_{ij} \\
b_{\mathrm{mix}} &= \sum_{i=1}^{n}\sum_{j=1}^{n} x_i x_j b_{ij}
\end{aligned}
\tag{3.14}
$$

The terms $a_{ij}$ and $b_{ij}$ are the un-like interactions parameters, and the so-called combining rules can be used are commonly given as:

$$
\begin{aligned}
a_{ij} &= \sqrt{a_{ii}a_{jj}} \\
b_{ij} &= \frac{1}{2}\left(b_{ii} + b_{jj}\right)
\end{aligned}
\tag{3.15}
$$

It has been recognised that the use of a binary interaction parameter, $k_{ij}$ is required for the combining rule of $a_{ij}$ for SRK and PR EoSs, the combining rule becomes:

$$
a_{ij} = \left(1 - k_{ij}\right)\sqrt{\left(a_i\right)\left(a_j\right)} \tag{3.16}
$$

Moreover, the classical mixing rules become:

$$a = \sum_{i=1}^{n}\sum_{j=1}^{n} x_i x_j \left(1 - k_{ij}\right)\sqrt{\left(a_i\right)\left(a_j\right)}$$
$$b = \sum_{i=1}^{n} x_i b_i \tag{3.17}$$

The binary interaction parameter, $k_{ij}$ is an empirical factor to increase the accuracy of equations of state through a better representation of un-like pair interaction. With these expressions, they result in improvement in the VLE calculations for binary mixtures. The binary interaction parameter is often obtained by regression to experimental VLE data for the mixture of interest. However, these correlations are only applicable to specific mixtures in specific EoSs. The binary interaction parameters are sometimes difficult to be determined for multi-component systems and hence a group contribution approach to predict these values was proposed.

## 3.3.7 Predictive Cubic Equation of State

The binary interaction parameter $k_{ij}$ of a pair of components is usually a function of temperature and varies with different EoSs. The way usually to determine this binary interaction parameter is to fit against experimental VLE data at the temperature range of interest. However, binary VLE data are not always readily available for all components in the literature; therefore there has been lots of interest in predictive models from which the $k_{ij}$ parameters may by estimated without the need to fit any experimental data. Recently, the Predictive Peng-Robinson EoS (PPR78) was developed by Jaubert and co-workers [316-318] which used a group contribution method in estimating the temperature dependent binary interaction parameters, $k_{ij}(T)$ for the original Peng-Robinson EoS. The group contribution approach (GC) is developed based on the assumption that the properties of a given compound/mixture can be determined as functions of the chemically distinct functional groups that the compound/mixture comprises. The contribution of the functional group to the molecular properties is assumed to be independent of the molecular structure. Jaubert and co-workers assumed the binary interaction parameter between two component is a function of temperature and of the pure components critical temperatures, $T_{c,i}$ and $T_{c,j}$, critical pressures, $p_{c,I}$ and $p_{c,j}$ and the acentric factors $\omega_i$ and $\omega_j$. Combining different equations from the work of Peng and Robinson, Peneloux, the binary interaction parameter $k_{ij}(T)$ can be calculated based on a group contribution method:

$$k_{ij}\left(T\right) = \frac{-\frac{1}{2}\sum_{k=1}^{N_g}\sum_{l=1}^{N_g}\left(\alpha_{ik} - \alpha_{jk}\right)\left(\alpha_{il} - \alpha_{jl}\right)A_{kl}.\left(\frac{T_0}{T}\right)^{\left(\frac{B_{kl}}{A_{kl}}-1\right)} - \left(\frac{\sqrt{a_i(T)}}{b_i} - \frac{\sqrt{a_j(T)}}{bj}\right)^2}{2\frac{\sqrt{a_i(T).a_j(T)}}{b_i.b_j}}, \tag{3.18}$$

where $T$ is the temperature, $N_g$ the number of different functional groups present in the molecule defined by the contribution method. $\alpha_{ik}$ is the occurrence of group $k$ in component $i$ divided by the total number of groups present in that component. $A_{kl}$ and $B_{kl}$ are group parameters. $A_{kl} = A_{lk}$ and $B_{kl} =$

$B_{lk}$ (where $k$ and $l$ are two different groups) are constant parameters determined. Jaubert and co-workers first published the PPR78 with 6 functional groups and then expanded to 21 functional groups in the next few years including functional groups such as $CO_2$ and aromatic compounds [318]. They determined $A_{kl}$ and $B_{kl}$ by fitting a large database of experimental VLE data using the PR78 EoS with the Soave alpha function. With this approach, the properties of complex mixtures that contain components that can be presented in terms of the 21 functional groups may be computed with the knowledge of the critical temperature, critical pressure and acentric factor of each component. PPR78 model is considered one of the most accurate predictive cubic EoSs and is often used within the oil and gas industry for phase behaviour in particular. The predicted capability of these EoSs was demonstrated in the description of the fluid phase behaviour and densities of multicomponent mixtures of $CO_2$ and hydrocarbons in study by Vitu *et al.* [319]

The binary interaction parameter, $k_{ij}$ obtained using Equation (3.18) cannot be applied directly onto another EoS such as the SRK EoS directly. In order to calculate $k_{ij}$ for the predictive model of the SRK EoS, Jaubert and co-worker [320] proposed a method to transform the binary interaction parameters calculated from the PPR78 model for the use of SRK EoS. The result of this approach is the Predictive Soave-Redlich-Kwong ($PR_2SRK$) and the relationship between the two EoSs is detailed as follows:

$$
\begin{aligned}
&E_{ij}(T) = 2k_{ij}\delta_i\delta_j + (\delta_i - \delta_j)^2 \\
&E_{ij}^{\mathrm{SRK}}(T) = \xi \cdot E_{ij}^{\mathrm{PR}}(T) \\
&k_{ij}(T) = \frac{E_{ij}(T) - (\delta_i - \delta_j)^2}{2\delta_i\delta_j} \\
&\delta_i = \frac{\sqrt{a_i}}{b_i} \\
&k_{ij}^{\mathrm{SRK}}(T) = \frac{2\xi k_{ij}^{\mathrm{PR}}\delta_i^{\mathrm{PR}}\delta_j^{\mathrm{PR}} + \xi(\delta_i^{\mathrm{PR}} - \delta_j^{\mathrm{PR}})^2 - (\delta_i^{\mathrm{PR}} - \delta_j^{\mathrm{PR}})^2}{2\delta_i^{\mathrm{SRK}}\delta_j^{\mathrm{SRK}}}
\end{aligned}
\tag{3.19}
$$

In these equations, $\xi$ is the parameter linking the two equations of state. The parameter value linking the $k_{ij}$ from PPR78 EoS with the $k_{ij}$ from $PR_2SRK$ EoS is $\zeta = 0.80734$ which is reported by Jaubert *et al.* Their study also showed that similar accuracies were achieved when both PPR78 EoS and $PR_2SRK$ EoS were tested against the VLE data of binary systems with hydrocarbons [320].

## 3.4 The Statistical Associating Fluid Theory (SAFT)

The Statistical Associating Fluid Theory (SAFT) EoS is a state-of-the-art molecular-based method for modelling thermodynamic properties and phase behaviour of complex fluids. The statistical mechanical approach allows the thermodynamic properties of a fluid to be determined from the knowledge of its intermolecular potential function; it provides a detailed molecular description of a

fluid, in particular for polar solvents, electrolytes, hydrogen-bonding fluids and polymers. SAFT is a method that combines Wertheim's thermodynamic perturbation theory (TPT) for associating fluids. The original Wertheim's theory is a statistical mechanical approach to account for the thermodynamic properties of hard spherical associating fluids [321-325]. Proposed by Chapman *et al.* in 1990, SAFT combines in general a chain reference contribution with an associating perturbation term (system with specific interactions) which allows describing complex-chain and associating fluids [326, 327]. In the approach, molecules are modelled as associating chains formed of bonded identical spherical segments (normally referred as monomers) and the segment-segment interactions are described by intermolecular potentials (square-well, Lennard-Jones or Mie potential) (Vijande *et al.* and Tobaly *et al.*). This method is known as the homonuclear approach.

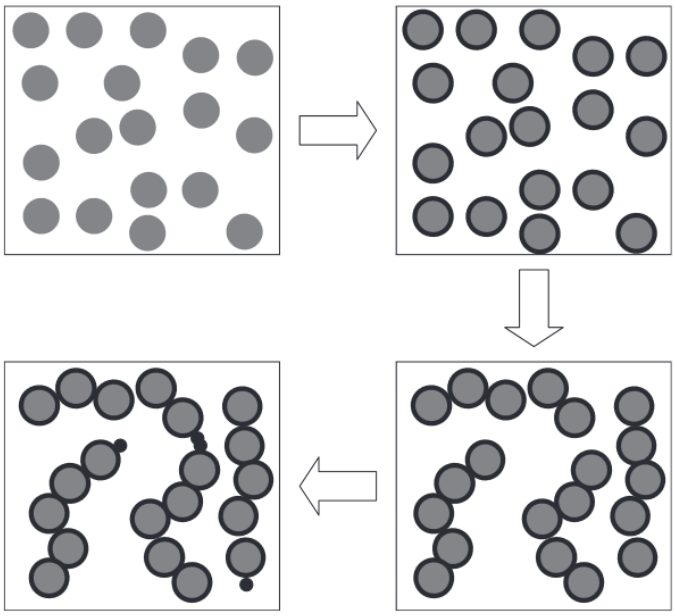


**Figure 3.1** Schematic illustration of the SAFT framework. The scheme begins with an initial monomer fluid that is used as a reference to form linear chains. Association sites are added to the molecules to mediate for hydrogen-bonding interactions. Reproduced from the review by McCabe and Galindo [328].

The generic SAFT equation is expressed as a sum of contributions to the Helmholtz free energy $A$ of the fluid, and takes the following form:

$$\frac{A}{Nk_BT} = \frac{A^{\text{ideal}}}{Nk_BT} + \frac{A^{\text{mono.}}}{Nk_BT} + \frac{A^{\text{chain}}}{Nk_BT} + \frac{A^{\text{assoc.}}}{Nk_BT}, \tag{3.20}$$

where $A^{\text{ideal}}$ is the free energy of an ideal gas mixture, $A^{\text{mono.}}$ accounts for segment-segment interaction (attractive and repulsive) of the reference monomeric system, $A^{\text{chain}}$ accounts for the change in the free energy due to the formation of molecules from segments, $A^{\text{assoc.}}$ is the term accounting for short-range

association interactions, $N$ is the total number of molecules, $k_B$ is the Boltzmann constant, and $T$ is the absolute temperature. The detailed derivation and analysis of each individual term can be found in the original publication. In Figure 3.1 the perturbation scheme used to construct an associating chain fluid with these contributions is represented. Since the first development of SAFT, there have been different versions and extensions of the SAFT EoS in the literature. The simplest SAFT approach is the SAFT-HS which models associating chains of hard sphere segments with the long-range attractive interactions [329, 330]. The SAFT-HS approach proves successful for modelling strongly hydrogen-bonded associating systems. Another version is the Soft-SAFT proposed by Johnson *et al.* This modification of SAFT has been applied to their study in alkanes and their binary mixtures. The approach uses different expressions that were fitted to simulation data to describe the Lennard-Jones chain [331-335]. The SAFT-VR [336, 337] describes the fluid as associating chains of molecules formed from hard-core monomers with attractive potentials of variable range, for example, the square well, LJ and Mie potential. A version that has become very popular for chain fluids is the perturbed-chain SAFT (PC-SAFT) in which a hard-chain, instead of a hard-sphere is considered as the reference system for the application of standards high-temperature perturbation theory to obtain the dispersion contribution [338-340]. Lafitte *et al.* [341, 342] found out that PC-SAFT can provide a more accurate description of both the phase behaviour and derivative properties, such as the isothermal compressibility and speed-of-sound of alkanes and their mixtures. Subsequently, PC-SAFT has been successfully applied to the study of a wide range of simple binary hydrocarbon mixtures. More recently, versions of the SAFT equation which coupled with group contribution formalism have been developed. In group contribution methods the properties of a pure component or a mixture are described in terms of functional groups that make up the molecules. The functional groups are characterised by sets of inter- and intra-molecular group parameters, and the assumption is that combinations of these functional group lead to the thermodynamic properties of the molecules of interest. This kind of GC approach can be a very useful predictive tool, as the thermophysical properties of a large number of pure components and mixtures can be assessed from the description of a few functional groups, without additional fitting to experimental data. The group contribution method has been applied within the SAFT framework where a more detailed heteronuclear molecular model with different types of monomeric segments is used to describe the different chemical functional groups that form a given molecule [343-345]. The model is called SAFT-γ, it has the advantage of permitting predictions of thermodynamic properties of mixtures based on pure component experimental data alone. A comprehensive review on the SAFT formalism is described in detail in the works of Muller and Gubbins [346], Economou [347] and McCabe and Galindo [328].

### 3.4.1 SAFT-γ Mie

SAFT-γ Mie is a group contribution method where the properties of the system of interest are described in terms of functional groups making up the molecules. This approach has been recognized

to have an improved description of different properties compared to other versions of the SAFT framework [348]. In the SAFT-γ Mie approach, the molecules are represented as a distinct functional group (segment) using fused heteronuclear model and the segment-segment interactions represented by a Mie potential (generalised Lennard-Jonesium). The assumption of the model is that combinations of the functional groups can lead to the thermodynamic properties of the molecules or mixtures of interest. The Mie intermolecular potential is a generalised Lennard-Jonesium potential, where the repulsive and attractive exponents that characterise the hardness/softness and the range of interaction are allowed to vary freely. The study by Lafitte and co-workers [342] showed that SAFT combined with Mie potential is better for the description of derivative properties when compared to the other versions of SAFT and the cubic EoSs. In the Mie potential approach, the potential interaction energy, $\Phi_{kl}^{\mathrm{Mie}}$, between non-associating segments *k* and *l* present in two different molecules is given as [349]:

$$\Phi_{kl}^{\mathrm{Mie}}\left(r_{kl}\right)=\varepsilon_{kl}C_{kl}\left[\left(\frac{\sigma_{kl}}{r_{kl}}\right)^{\lambda_{kl}^{\mathrm{r}}}-\left(\frac{\sigma_{kl}}{r_{kl}}\right)^{\lambda_{kl}^{\mathrm{a}}}\right] \tag{3.21}$$

where $r_{kl}$ is the centre-centre distance between segments, $\sigma_{kl}$ is the diameter of the segments, $\varepsilon_{kl}$ is the depth of the potential, $\lambda_{kl}^{\mathrm{r}}$ and $\lambda_{kl}^{\mathrm{a}}$ are the repulsive and attractive exponents of the un-like intersegment interactions and $C_{kl}$ is a constant given in the following form:

$$C_{kl}=\frac{\lambda_{kl}^{\mathrm{r}}}{\lambda_{kl}^{\mathrm{r}}-\lambda_{kl}^{\mathrm{a}}}\left(\frac{\lambda_{kl}^{\mathrm{r}}}{\lambda_{kl}^{\mathrm{a}}}\right)^{\frac{\lambda_{kl}^{\mathrm{r}}}{\lambda_{kl}^{\mathrm{r}}-\lambda_{kl}^{\mathrm{a}}}} \tag{3.22}$$

For the expression of each term and a full description of the SAFT-γ Mie model, they can be found in the original publications [350-352]. In summary, the like interaction parameters that characterise identical functional groups are as follows: $\varepsilon_{kk}$, $\sigma_{kk}$, $\lambda_{kk}^{\mathrm{r}}$, $\lambda_{kk}^{\mathrm{a}}$ and the number $v_k$ of segments that comprise the group. An additional parameter, the shape factor $S_k$, is used to characterise the extent to which the group contributes to the molecular properties of the system. These functional groups and interaction parameters are typically determined from experimental data across wide temperature and pressure ranges. However, in the case of components for which limited or no experimental data is available, the un-like interaction binary interaction parameters may also be estimated from combining rules.

## 3.4.2 Un-like Binary Interaction Parameters

For calculations of mixture properties in binary or multi-components mixtures, mixture-specific parameters have to be calculated based on pure component and binary interaction parameters with the use of mixing and combining rules. Mixing rules and combining rules for the like and un-like intermolecular parameters are employed to facilitate the study of binary and multi-component systems when the available experimental data are limited. There are many types of combining rules, for

example, the dispersion energy $\varepsilon_{kl}$ can be obtained using the segment diameter and like dispersion energy, the expression becomes:

$$\varepsilon_{kl} = \left(1 - k_{kl}\right)\sqrt{\varepsilon_{kk}\varepsilon_{ll}} \quad \text{or} \quad \varepsilon_{kl} = \frac{\sqrt{\sigma_{kk}^3 \sigma_{ll}^3}}{\sigma_{kl}^3}\sqrt{\varepsilon_{kk}\varepsilon_{ll}} \,. \tag{3.23}$$

Here $k_{kl}$ is an adjustable parameter which is mixture-specific and typically determined by fitting to relevant experimental data for the mixture of interest to improve the agreement with the experimental data. The un-like segment diameter can be obtained from a simple arithmetic mean (Lorentz rule) given as:

$$\sigma_{kl} = \frac{\sigma_{kk} + \sigma_{ll}}{2} \tag{3.24}$$

For the attractive $\lambda_{kl}^{\mathrm{a}}$ and repulsive $\lambda_{kl}^{\mathrm{r}}$ exponents of the un-like interaction, the combining rule is as follows:

$$\lambda_{kl} = 3 + \sqrt{\left(\lambda_{kk} - 3\right)\left(\lambda_{ll} - 3\right)} \tag{3.25}$$

The parameters that describe the contribution of the functional groups of the molecules are usually estimated from appropriate experimental data. As mentioned, in SAFT-γ Mie approach, the compounds are modelled as heteronuclear molecules formed from function groups. Each functional group is characterised by the following sets of parameters: the number of segments $v_k$, the shape factor $S_k$, the segment diameter $\sigma_{kl}$, the dispersion energy $\varepsilon_{kl}$ and the attractive $\lambda_{kl}^{\mathrm{a}}$ and repulsive $\lambda_{kl}^{\mathrm{r}}$ exponents of the potential. The un-like dispersion energy is typically treated as an adjustable parameter and is obtained by regression to experimental data. Sometimes this can also be estimated through pure components and used the combining rule discussed above. Using pure components data to predict properties of mixtures is considered as a unique characteristic of heteronuclear models. The parameters that describe each functional group are obtained by regression to pure components VLE data (i.e. vapour pressure), saturated liquid densities and single-phase densities at given temperatures and pressures. The temperature range of the VLE data is restricted to between the triple point and 90% of the critical temperature, data closer than 90 % of the critical temperature are generally not considered [350]. This is because including data close to the critical point would bias the parameters towards a more accurate representation of the critical point and results in a loss in their physical significance. Experimental data used for single-phase density are typically measured at high temperatures and pressure in the liquid and supercritical region. The objective function used in the parameter estimation procedure is given as:

$$\min f_{\mathrm{obj}} = w_1 \sum_{u=1}^{N_{p\mathrm{vap}}} \left[ \frac{p_{\mathrm{vap}}^{\mathrm{exp}}\left(T_u\right) - p_{\mathrm{vap}}^{\mathrm{cal}}\left(T_u\right)}{p_{\mathrm{vap}}^{\mathrm{exp}}\left(T_u\right)} \right]^2 + w_2 \sum_{v=1}^{N_{\rho\mathrm{sat}}} \left[ \frac{\rho_{\mathrm{sat}}^{\mathrm{exp}}\left(T_v\right) - \rho_{\mathrm{sat}}^{\mathrm{cal}}\left(T_v\right)}{\rho_{\mathrm{sat}}^{\mathrm{exp}}\left(T_v\right)} \right]^2 + w_3 \sum_{y=1}^{N_{\rho\mathrm{liq}}} \left[ \frac{\rho_{\mathrm{liq}}^{\mathrm{exp}}\left(T_y, p_y\right) - \rho_{\mathrm{liq}}^{\mathrm{cal}}\left(T_y, p_y\right)}{\rho_{\mathrm{liq}}^{\mathrm{exp}}\left(T_y, p_y\right)} \right]^2, \tag{3.26}$$

where $p_{vap}$, $\rho_{sat}$ and $\rho_{liq}$ denote vapour pressure, saturated-phase density and single-phase density, respectively. The parameter $w$ is a weight factor and normally equal weight factors are used. The estimations were performed with the commercially available gPROMS software package.

# 3.5 Helmholtz Energy Explicit Models for Pure Components

The equation of state expressed in a fundamental form explicit in the Helmholtz energy has become the most widely used method for calculating thermodynamic properties with high accuracy for many fluids [353]. The most fundamental form of the equation is expressed in terms of the Helmholtz energy with two independent variables: density and temperature, given as:

$$a(\rho,T) = a^0(\rho,T) + a^r(\rho,T). \tag{3.27}$$

The Helmholtz free energy is generally used in the dimensionless form, and Equation (3.27) becomes:

$$\frac{a(T,\rho)}{RT} = \alpha(\tau,\delta) = \alpha^0(\tau,\delta) + \alpha^r(\tau,\delta) \text{ with } \delta = \rho/\rho_r \text{ and } \tau = T_r/T \tag{3.28}$$

Here $a$ is the molar Helmholtz energy, $R$ the gas constant, $T$ the temperature and $\rho$ the density. Usually, the critical temperature $T_c$ and density $\rho_c$ are used for $T_r$ and $\rho_r$ to reduce the inverse temperature and the density. A Helmholtz Energy explicit equation of state is usually split into two parts. One part $\alpha^0$ describes the behaviour of the ideal gas at given values of temperature and density (contribution from an ideal gas where molecules do not interact with each other) and a second part $\alpha^r$ describes the residual behaviour of the real fluid (accounts for all kinds of interactions between molecules). The behaviour of fluids in the ideal-gas state can usually predicted by statistical thermodynamics with high accuracy, but no physically founded equation is known which can describe the real thermodynamic behaviour of fluids over the whole fluid region accurately [38]. Therefore, the residual part of the Helmholtz free energy $\alpha^r$, must be determined in an empirical way. The functional form of the equation for the residual part $\alpha^r$ can be presented in either polynomial terms or polynomial terms in combination with exponential functions, given as

$$\alpha_i^r = n_i \delta^{d_i} \tau^{t_i} \tag{3.29}$$

$$\alpha_i^r = n_i \delta^{d_i} \tau^{t_i} \exp\left(-\delta^{c_i}\right) \tag{3.30}$$

In Equation (3.29), the density exponent $d_i$ usually ranges from 1 to 5 and $t_i$ should be between $0 < t_i \leq 1$; for further details see Span and Wagner [354]. Nowadays, the standard functional forms of wide range pure substance equations of state contain an exponent up to $c_i = 6$ in Equation (3.30). These coefficients are normally determined from a large body of reliable experimental data over a wide range of thermodynamic states. All thermodynamic properties can be calculated from their relations to the reduced Helmholtz energy; if the model is able to represent all reliable experimental data for different properties within their respective uncertainty, it is considered a “reference equation of state”

[353]. Equations for calculating the selected thermodynamic properties from the mixture model are shown as below:

$$\text{Pressure}: p(\delta,\tau,x) = \rho RT\left(1+\delta\frac{\partial\alpha^{\mathrm{r}}}{\partial\delta}\right)$$

$$\text{Compressibility factor}: Z(\delta,\tau,x) = \left(1+\delta\frac{\partial\alpha^{\mathrm{r}}}{\partial\delta}\right)$$

$$\text{Isochoric heat capacity}: \frac{c_v(\delta,\tau,x)}{R} = -\tau^2\left[\left(\frac{\partial^2\alpha^0}{\partial\tau^2}\right)+\left(\frac{\partial^2\alpha^{\mathrm{r}}}{\partial\tau^2}\right)\right] \tag{3.31}$$

$$\text{Isobaric heat capacity}: \frac{c_p(\delta,\tau,x)}{R} = \frac{c_v}{R}+\frac{\left[1+\delta(\partial\alpha^{\mathrm{r}}/\partial\delta)-\delta\tau(\partial^2\alpha^{\mathrm{r}}/\partial\delta\partial\tau)\right]^2}{\left[1+2\delta(\partial\alpha^{\mathrm{r}}/\partial\delta)+\delta^2(\partial^2\alpha^{\mathrm{r}}/\partial\delta^2)\right]}$$

$$\text{Speed-of-sound}: \frac{c^2(\delta,\tau,x)M}{RT} = \frac{c_p}{c_v}\left[1+2\delta\left(\frac{\partial\alpha^{\mathrm{r}}}{\partial\delta}\right)+\delta^2\left(\frac{\partial^2\alpha^{\mathrm{r}}}{\partial\delta^2}\right)\right]$$

An example of a reference equation of state was developed by Lemmon and Span for 20 industrial fluids [40]. The 12 coefficients equation of state is capable of describing several hydrocarbons thermophysical properties with the same structure of Helmholtz energy explicit function with different parameters. The parameters of the reference equation of state were optimised simultaneously with pure components data sets. Typical uncertainties associated with the calculated properties are 0.2 % in density, 1 % to 2 % in heat capacity and liquid-phase speed-of-sound, and 0.2 % in vapour pressure for this EoS. Another example is the $CO_2$ equation of state which is also explicit in the Helmholtz free energy, developed by Span and Wagner [174]. It can calculate the thermophysical properties of $CO_2$ from the triple point temperature to 1100 K at pressures up to 800 MPa. In their work, the residual part of the equation was fitted to several thermophysical properties data which include $p\rho T$, saturated-phase density, speed-of-sound, specific heat capacities, specific enthalpy, specific internal energy and Joule-Thomson coefficient. A comprehensive review regarding the multi-parameter equations of state is covered extensively by a book written by Span [353].

# 3.6 Helmholtz Energy Explicit Models for Mixtures

A mixture equation of state should provide an accurate representation of the thermodynamic properties of the mixture over a wide range of compositions. Equations of state based on Helmholtz free energy is one of the most widely used methods to calculate accurate thermodynamic properties of mixtures over a wide range of compositions. The models use equations of state in the form of fundamental equations for each mixture component along with further correlation equations to take into account the residual mixture behaviour. Similarly, the equation of state for mixture of fluids is also split into the ideal part $a^0$ at a given $\rho$, $T$, and $x$, and the residual part $a^{\mathrm{r}}$. The function is given as:

$$a(\rho,T,x) = a^0(\rho,T,x)+a^{\mathrm{r}}(\rho,T,x). \tag{3.32}$$

Using the Helmholtz free energy in its dimensionless form $\alpha=a/(RT)$, Equation (3.32) becomes:

$$\alpha(\delta,\tau,x)=\alpha^0(\rho,T,x)+\alpha^{\mathrm{r}}(\delta,\tau,x), \tag{3.33}$$

where $\alpha$ is the Helmholtz energy, $\alpha^0$ and $a^{\mathrm{r}}$ are the ideal gas contribution to the Helmholtz energy and the residue Helmholtz energy respectively. It has to be noted that $a^0$ does not depend on $\delta$ and $\tau$ of the mixture, but on $\rho$ and $T$. The term $x$ is the composition, $\delta = \rho / \rho_{\mathrm{r}}$ is the reduced mixture density and $\tau = T_{\mathrm{r}} / T$ is the inverse reduced mixture temperature. Both $\rho_{\mathrm{r}}$ and $T_{\mathrm{r}}$ are dependent on the composition of the mixture:

$$\rho_{\mathrm{r}}=\rho_{\mathrm{r}}(x) \qquad \text{and} \qquad T_{\mathrm{r}}=T_{\mathrm{r}}(x) \tag{3.34}$$

The dimensionless form of the Helmholtz free energy for the ideal gas mixture $\alpha^0$ is given by:

$$\alpha^0(\rho,T,x)=\sum_{i=1}^{N}x_i\left[\alpha_i^0(p,T)+\ln x_i\right], \tag{3.35}$$

where $N$ is the number of components in the mixture, $\alpha_i^0$ is the dimensionless form of the Helmholtz free energy in the ideal-gas state of component $i$ and $x_i$ is the mole fraction of the component. The second sum in the equation $x_i \ln x_i$ is related to the entropy of mixing for the ideal gas. The composition-dependent reducing functions for density and temperature, $\rho_{\mathrm{r}}$ and $T_{\mathrm{r}}$, are based on the quadratic mixing rules proposed by Klimeck [39] and Kunz:

$$\begin{aligned}\frac{1}{\rho_{\mathrm{r}}(x)}&=\sum_{i=1}^{N}x_i^2\frac{1}{\rho_{\mathrm{c},i}}+\sum_{i=1}^{N-1}\sum_{j=i+1}^{N}\frac{2x_ix_j}{\rho_{\mathrm{c},ij}}\\ T_{\mathrm{r}}(x)&=\sum_{i=1}^{N}x_i^2T_{\mathrm{c},i}+\sum_{i=1}^{N-1}\sum_{j=i+1}^{N}2x_ix_jT_{\mathrm{c},ij}\end{aligned}, \tag{3.36}$$

where $\rho_{c,i}$ and $T_{c,i}$ are the critical density and critical temperature of pure component $i$, respectively,

$$\begin{aligned}\frac{1}{\rho_{c,ij}}&=\beta_{v,ij}\gamma_{v,ij}\frac{x_i+x_j}{\beta_{v,ij}^2x_i+x_j}\cdot\frac{1}{8}\left(\frac{1}{\rho_{c,i}^{1/3}}+\frac{1}{\rho_{c,j}^{1/3}}\right)^3\\ T_{c,ij}&=\beta_{T,ij}\gamma_{T,ij}\frac{x_i+x_j}{\beta_{T,ij}^2x_i+x_j}\cdot\left(T_{c,i}T_{c,j}\right)^{1/2}\end{aligned}. \tag{3.37}$$

The parameters $\beta$ and $\gamma$ are used to define the shapes of the reducing temperature lines and reducing density lines. There are four adjustable parameters in the composition-dependent Helmholtz reducing functions - $\beta_{T,ij}$, $\gamma_{T,ij}$, $\beta_{V,ij}$ and $\gamma_{V,ij}$, which are known as the reducing parameters which are not the same as the critical parameters of the mixtures. They are adjusted simultaneously in the non-linear fit of accurate experimental data. It has to be noted that the $\gamma$ parameters are symmetrical ($\gamma_{T,ij} = \gamma_{T,ji}$), but the $\beta$ parameters are not symmetrical ($\beta_{T,ij} = 1/\beta_{T,ji}$), thus the order of the fluids in the binary pair is important. For binary mixtures with limited or poor experimental data, these four binary interaction parameters are set to unity, and Equation (3.37) becomes:

$$\frac{1}{\rho_{c,ij}} = \frac{1}{8}\left(\frac{1}{\rho_{c,i}^{1/3}} + \frac{1}{\rho_{c,j}^{1/3}}\right)^3 \qquad (3.38)$$
$$T_{c,ij} = \left(T_{c,i}T_{c,j}\right)^{1/2}$$

Therefore, theses mixture model can easily be extended to components for which poor or even no experimental information is available for fitting the binary parameters of the reducing functions. The residual part of the reduced Helmholtz free energy of the mixture $\alpha^{\mathrm{r}}$ is given by:

$$\alpha^{\mathrm{r}}(\delta,\tau,x) = \sum_{i=1}^{N} x_i \alpha_i^{\mathrm{r}}(\delta,\tau) + \Delta\alpha^{\mathrm{r}}(\delta,\tau,x). \qquad (3.39)$$

In the equation, $\alpha_i^{\mathrm{r}}$ is the residual part of the reduced Helmholtz free energy of pure component *i* and $\Delta\alpha^{\mathrm{r}}$ is the so-called departure function that is dependent on the reduced variables $\delta$ and $\tau$, and the mixture composition *x*, accounts for the interaction of different species in the mixture. The reducing functions and the departure functions were developed to describe the behaviour of the mixture; in particular, the departure function was developed to improve the accuracy of the equation when the reducing functions are unable to reproduce highly accurate data. It is reported that in general the contribution of the departure function to the reduced residual Helmholtz free energy of the mixture is less than the contribution of the equations for the pure components. The general structure is used but the models of Lemmon and Lemmon and Jacobsen [355, 356]. In 1993, Tillner-Roth developed a departure function to describe the behaviour of individual binary mixtures for which a large amount of accurate experimental data are available. The binary specific departure function proposed was written in the form:

$$\Delta\alpha^{\mathrm{r}}(\delta,\tau,x) = f^{\Delta}(x_1,x_2)\cdot\alpha_{12}^{\mathrm{r}}(\delta,\tau) \qquad (3.40)$$

where $f^{\Delta}$ is called the composition-dependent factor. The term $\alpha_{12}^{\mathrm{r}}$ can be determined through the use of suitable structure optimisation procedures which gives the best representation of the thermodynamic properties of the mixture. Studies from Lemmon and co-workers [355, 356] reported a generalised departure function. The new generalised departure function can achieve an accurate description for a number of well-measured mixtures along with mixtures with limited data sets. The generalised function is given by:

$$\Delta\alpha^{\mathrm{r}}(\delta,\tau,x) = \sum_{i=1}^{N-1}\sum_{j=1}^{N} x_i x_j F_{ij}\alpha_{\mathrm{gen}}^{\mathrm{r}}(\delta,\tau) \qquad (3.41)$$

This structure is identical for all binary mixtures according to Equation (3.40), only the parameter $F_{ij}$ is binary mixture specific. The coefficients and exponents are obtained by non-linear regression to the experimental mixture data. To summarise, the development of the mixture models is based on a multi-fluid approximation that requires (1) equations of state for pure components, (2) composition-

dependant reducing functions and (3) departure functions depending on the reduced mixture density, the inverse reduced mixture temperature and mixture composition.

### 3.6.1 GERG-2004 and GERG-2008

The GERG EoS (Group Europeen de Recherche Gazieres) was adopted under the name GERG-2004 that was developed by Kunz *et al.* [38, 39] to predictive thermophysical properties of natural gases and other mixtures. The model uses accurate equations of state in the form of fundamental equations for each pure component in the mixture together with the functions developed for the binary mixtures of the components to take into account the residual mixture behaviour. Since it is explicit in the reduced Helmholtz energy, all thermodynamic properties can be calculated from combinations of the derivatives. It is based on a multi-fluid approximation and initially developed for mixtures that contain these 18 components: methane, nitrogen, carbon dioxide, ethane, propane, *n*-butane, iso-butane, *n*-pentane, iso-pentane, *n*-hexane, *n*-heptane, *n*-octane, hydrogen, oxygen, carbon monoxide, water, helium and argon. The development of GERG-2008 EoS [39] expands the number of components to 21 which include *n*-nonane, *n*-decane and hydrogen sulphide. The EoS was built based on accurate experimental thermodynamic property data and it is valid for describing the components mentioned above over the range $T$ = (60 to 700) K and at pressures up to 70 MPa. The equation is based on the multi-parameter Helmholtz energy expression, Equation (3.33). In their work, they developed binary specific departure functions enable a more accurate description of the thermodynamic properties of mixtures than the generalised formulations. It contains the sum of binary specific and generalised departure functions, which can be developed for single binary mixtures (binary specific) or for a group of binary mixtures (generalised). The overall departure function in GERG-2008 is given as:

$$\Delta a^{\mathrm{r}}(\delta,\tau,x) = \sum_{i=1}^{N-1}\sum_{j=1}^{N} \Delta\alpha_{ij}^{\mathrm{r}}(\delta,\tau,x) \tag{3.42}$$

with

$$\Delta a_{ij}^{\mathrm{r}}(\delta,\tau,x) = x_i x_j F_{ij}\alpha_{ij}^{\mathrm{r}}(\delta,\tau) \tag{3.43}$$

The departure function proposed by Kunz and Wagner can be implemented with well-characterised mixtures and mixtures that are characterised by poor or limited data. For mixtures with a binary specific departure function, $F_{ij}$ is set to unity; while for mixtures that covered by the generalised departure function, $F_{ij}$ is treated as an adjustable parameter. More details on the binary mixtures that are covered by the generalised departure function can be found in Kunz and Wagner [39]. To develop the reducing and departure functions, only binary mixtures data were used. However, departure functions were only developed for such binary mixtures for which accurate experimental data existed. For binary mixtures with insufficient data, no departure function was developed and $F_{ij}$ is set to zero,

only the parameters of the reducing functions $\rho_r(x)$ und $T_r(x)$ were fitted. The parameter $F_{ij}$ is used in a generalisation to relate the excess properties of one binary mixture to other binary mixtures. With this parameter, the same set of mixture coefficients can be used for several binary mixtures in the model. The function $\alpha_{ij}^r(\delta,\tau)$ which is part of the departure function that depends only on the reduced mixture variables $\delta$ and $\tau$ is given by:

$$\alpha_{ij}^r(\delta,\tau)=\sum_{k=1}^{K_{\mathrm{Pol},ij}} n_{ij,k}\delta^{d_{ij,k}}\tau^{t_{ij,k}}+\sum_{k=K_{\mathrm{Pol},ij}+1}^{K_{\mathrm{Pol},ij}+K_{\mathrm{Exp},ij}} n_{ij,k}\delta^{d_{ij,k}}\tau^{t_{ij,k}}\cdot\exp\left[-\eta_{ij,k}\left(\delta-\varepsilon_{ij,k}\right)^2-\beta_{ij,k}\left(\delta-\gamma_{ij,k}\right)\right] \tag{3.44}$$

where $K_{\mathrm{Pol},ij}$ is the number of 'polynomial' terms and $K_{\mathrm{Exp},ij}$ is the number of 'exponential' terms and $n_{ij,k}$, $\eta_{ij,k}$, $\varepsilon_{ij,k}$, $\beta_{ij,k}$ and $\gamma_{ij,k}$ are adjustable parameters used to model the shape of the term. For more information of the model, refer to the original publications [38, 39].

## 3.6.2 Multi-Fluid Helmholtz Energy Approximation (Optimisation)

Recently, Bell and Lemmon [357] developed an algorithm to optimise the binary interaction parameters in the multi-fluid Helmholtz-energy approximation. The formulation used in their work is the multi-fluid mixture property model that used in the state-of-the-art thermophysical property libraries REFPROP [358] and TREND [359]. The reducing parameters for a mixture in the model can be given by:

$$Y_r(x)=\sum_{i=1}^{N}x_i^2Y_{c,i}+\sum_{i=1}^{N-1}\sum_{j=i+1}^{N}2x_ix_j\frac{x_i+x_j}{\beta_{Y,ij}^2x_i+x_j}Y_{ij}\ , \tag{3.45}$$

where $Y$ is the parameter of interest, either given in the specific molar volume, $v$ or temperature, $T$. The necessary parameters are given in the following Table 3.2.

**Table 3.2** Parameters for the multi-fluid Helmholtz energy approximation model given by Bell and Lemmon.

| | **Temperature term** | **Specific molar volume term** |
|---|---|---|
| $Y_r$ | $T_{c,i}$ | $1/\rho_{c,i}$ |
| $Y_{c,i}$ | $\beta_{T,ij}\gamma_{T,ij}$ | $\beta_{v,ij}\gamma_{v,ij}$ |
| $\beta_{Y,ij}$ | $\beta_{T,ij}$ | $\beta_{v,ij}$ |
| $Y_{ij}$ | $\left(T_{c,i}T_{c,j}\right)^{1/2}$ | $1/8\left(1/\rho_{c,i}^{1/3}+1/\rho_{c,j}^{1/3}\right)^3$ |

In their study, they have fitted the binary interaction parameters for more than 1100 binary mixtures including cyclics, aromatics and refrigerants. Out of the four adjustable parameters, they chose to optimise only $\beta_T$ and $\gamma_T$ which they identified as the two most important for bubble-point data fitting; it was mentioned that changing these parameters had little effect on the single-phase properties. While

$\beta_T$ and $\gamma_T$ were optimised, the other adjustable parameters, $\beta_V$ and $\gamma_V$ were set to unity and $F_{ij}$ was set to zero. More details about the parameters and the optimisation are given in Bell and Lemmon.

## 3.7 Integration of Thermodynamic Properties

Speed-of-sound data are particularly useful for modelling in terms of its accuracy compared to other thermophysical properties that are directly measured. The speed-of-sound in a fluid depends primarily on the thermodynamic properties as a function of temperature and pressure; it can provide useful and very accurate information about thermodynamic quantities in either liquid or gas phase system. Thermodynamic integration allows the calculation of a complete spectrum of thermodynamic properties over the range of temperatures and pressures covered by experimental sound speed, density and isobaric heat capacity data, by means of a numerical integration technique. The derived thermophysical properties from the thermodynamic relations: isobaric thermal expansion coefficient, $\alpha$, the isothermal compressibility, $\beta$, the density, $\rho$, the sound velocity, $c$ and the isobaric heat capacity $c_p$. The relations are given by the following equations:

Isobaric thermal expansivity, $\alpha$:
$$\alpha = -\left(\frac{1}{\rho}\right)\left(\frac{\partial \rho}{\partial T}\right)_p \tag{3.46}$$

Isothermal compressibility, $\beta$:
$$\beta = \frac{1}{\rho}\left(\frac{\partial \rho}{\partial p}\right)_T = \frac{1}{\rho}\left(\frac{1}{c^2} + \frac{T\alpha_p^2}{c_p}\right) \tag{3.47}$$

Isentropic compressibility, $\beta_s$:
$$\beta_s = \frac{1}{\rho}\left(\frac{\partial \rho}{\partial p}\right)_S \tag{3.48}$$

The relationship between $\alpha$ and $\beta$:
$$\left(\frac{\partial \alpha}{\partial p}\right)_T = -\left(\frac{\partial \beta}{\partial T}\right)_p \tag{3.49}$$

Isobaric heat capacity, $c_p$:
$$\left(\frac{\partial c_p}{\partial p}\right)_T = -\frac{T}{p}\left[\alpha_p^2 + \left(\frac{\partial \alpha_p}{\partial p}\right)_p\right] \tag{3.50}$$

Density, $\rho$:
$$\left(\frac{\partial \rho}{\partial p}\right)_T = \frac{1}{c^2} + \frac{T\alpha^2}{c_p} \tag{3.51}$$

The method of determining thermodynamic properties indirectly from the speed-of-sound measurements was first devised by Davis and Gordon [48] for the study of mercury. Hereby, the calculation procedure which incorporates the explicit Euler method used by Davis and Gordon is discussed. It has been pointed out by Sun and co-workers [51, 74, 77] at the Van der Waals Laboratory that their method of the numerical differentiation and integration was inadequate, which resulted in systematic errors in the derived densities. Then Sun *et al.* [51] proposed a new method which modifies the method of Davis and Gordon for calculating thermodynamic properties of liquid hydrocarbons. The modification required extensive sound speed data across a range of temperatures and pressures to obtain an accurate function of $c$ vs $T$ and $p$ for the calculation of integrals. In

addition, it also required an accurate and smooth function of the atmospheric density data as input data for the numerical differentiation. To ease the integration process, they fitted all experimental data to suitable polynomial correlations. For this investigation, the speed-of-sound experimental data were fitted into an empirical correlation which was used by Sun *et al.* that covers the whole range of temperatures and pressures, given in the following form:

$$(p-p_0)=\sum_{i=1}^{3}\sum_{j=0}^{3}a_{ij}(c-c_0)^i\left(\frac{T_0}{T}\right)^j, \tag{3.52}$$

where $c_0$ denotes initial sound speed measured at an initial pressure and temperature, $p_0$ and , $T_0$, respectively (typically $p_0$ = 0.1 MPa and $T_0$ = 273.15 K). Later, another form of speed-of-sound correlation has been proposed by Daridon *et al.* [68] They suggested a rational function to correlate directly $1/c^2$ instead of $c$, given in the following form:

$$\begin{aligned}&\frac{1}{c^2}=\frac{A+Bp+Cp^2+Dp^3}{E+Fp}\\&A=A_0+A_1T+A_2T^2+A_3T^3\\&E=1+E_1T\end{aligned} \tag{3.53}$$

The correlation contains nine adjustable parameters which were able to correlate their experimental speed-of-sound data for *n*-hexane to 0.02 %. As the thermodynamic integration also requires as inputs the density and isobaric heat capacity along an isobar (usually at 0.1 MPa) over the full temperature range, the density and isobaric heat capacity data along one isobar were fitted to a polynomial equation as follows:

$$\rho_0=\sum_{i=0}^{3}a_i\left(\frac{T}{T_0}\right)^i \tag{3.54}$$

$$c_p=\sum_{i=0}^{3}a_i\left(\frac{T}{T_0}\right)^i \tag{3.55}$$

The accuracy of the thermodynamic integration depends heavily on the initial values; hence, the initial values of density must be sufficiently accurate to determine both the first and second temperature derivatives. Once the experimental data were fitted with polynomial equations, the mathematical procedure of the thermodynamic integration can begin. The thermodynamic properties of the compressed liquids were obtained by numerical integration of the following system of exact partial differential equations:

$$\begin{aligned}&c^2=\left[\left(\frac{\partial\rho}{\partial p}\right)_T-\frac{T}{\rho^2c_p}\left(\frac{\partial\rho}{\partial T}\right)_p^2\right]^{-1}\\&\left(\frac{\partial c_p}{\partial p}\right)=-\frac{T}{\rho^3}\left[2\left(\frac{\partial\rho}{\partial T}\right)_p^2-\rho\left(\frac{\partial^2\rho}{\partial T^2}\right)_p\right]\end{aligned} \tag{3.56}$$

The solution of Equation (3.56) is subject to the prescribed initial conditions on $\rho(T)$ and $c_p(T)$ at $p = p_0$ and a simple predictor-corrector algorithm was used to perform the integration with step lengths $\delta p = 0.1$ MPa and $\delta T$ = 10 K. In brief, starting at $p = p_0$, we calculated $(\partial\rho/\partial p)_T$ and $(\partial c_p/\partial p)_T$ at that pressure and each grid temperature from the above expression, making use of the correlations developed for sound speed, density and isobaric heat capacity Equations (3.52), (3.54) and (3.55) as well as the first two temperature derivatives of $\rho$. Then we estimated $\rho$ and $c_p$ at $p_1 = p_0 + \delta p$ and each grid temperature by means of the first-order expansions:

$$\rho(p_1) = \rho(p_0) + \delta p \cdot (\partial\rho/\partial p)_T\big|_{p=p_0} \tag{3.57}$$

$$c_p(p_1) = c_p(p_0) + \delta p \cdot (\partial c_p/\partial p)_T\big|_{p=p_0} \tag{3.58}$$

Returning to Equation (3.56), we then obtained estimates of $(\partial\rho/\partial p)_T$ and $(\partial c_p/\partial p)_T$ at $p = p_1$ and, in the corrector step, calculated final values of $\rho$ and $c_p$ at $p_1$ by means of the more accurate mid-point formulae:

$$\rho(p_1) = \rho(p_0) + \tfrac{1}{2}\delta p\{(\partial\rho/\partial p)_T\big|_{p=p_0} + (\partial\rho/\partial p)_T\big|_{p=p_1} \tag{3.59}$$

$$c_p(p_1) = c_p(p_0) + \tfrac{1}{2}\delta p\{(\partial c_p/\partial p)_T\big|_{p=p_0} + (\partial c_p/\partial p)_T\big|_{p=p_1} \tag{3.60}$$

This completed one predictor-corrector step and established all of the thermodynamic properties along the isobar at $p = p_1$ with temperature spacing $\delta T$. To begin the next step, density values at $p = p_1$ were then fitted by Equation (3.54) and the process restarted with $p_1$ as the initial pressure. Repetition of the procedure allowed the development of solution isobar-by-isobar until the upper limit in pressure is reached. The algorithm used in this work was tested by integration of the sound speed data reported by Sun *et al.* [51] for ethanol in the temperature range of (193.15 to 268.15) K with pressures up to 280 MPa. Therefore in conclusion, it can be seen that with knowledge of the speed-of-sound as a function of temperature and pressure, combined with density and isobaric heat capacity data at an initial pressure, typically atmospheric, can be solved to obtain all observable thermodynamic properties over the entire temperature and pressure for which speed-of-sound measurements have been made. The overall accuracy of derived thermophysical properties is generally governed by the accuracy of the initial values.

## 3.8 Excess Molar Volume

Volumetric properties of liquid binary mixtures provide important information for the characterization of the interactions between components. The excess molar volume $V_m^E$ as a function of composition,

temperature and pressure is one of the single-phase thermodynamic properties measured for mixtures. It is a quantitative measure of deviation in the behaviour of a liquid mixture from ideality. When the excess molar volume is not determined directly from experiments, it can be calculated from knowledge of density of the mixture as a function of composition. One would expect no volume change when mixing two ideal liquids to form a thermodynamically ideal solution at constant temperature and pressure. However, a change in volume may occur when real fluids/liquids are mixed. Generally, $V_m^{\mathrm{E}}$ can occur from three types of interactions between liquid mixtures: (1) physical interactions (mainly consist of dispersion forces or weak dipole-dipole interaction, resulting in a +ve contribution); (2) chemical or specific interactions (charge transfer, forming of hydrogen bonds and other complex forming interactions, resulting in a −ve contribution) and (3) structural contribution due to size and shape differences of the component of the mixtures (rearranging of molecules into each other's structure, reducing the volume and compressibility of the mixtures, resulting in a −ve contribution). For a binary mixture, $V^{\mathrm{E}}$ can be calculated by the following expression:

$$V_{\mathrm{m}}^{\mathrm{E}} = \frac{M_{\mathrm{mix}}}{\rho_{\mathrm{mix}}} - \left( \frac{xM_1}{\rho_1} + \frac{(1-x)M_2}{\rho_2} \right), \tag{3.61}$$

where $x$ denotes the mole fraction, $M$, the molar mass and $\rho$, the density. The subscripts mix, 1 and 2 represent the mixture and components 1 and 2, respectively. The excess molar volume data can be correlated with the Redlich-Kister polynomial [360], given as:

$$V_{\mathrm{m}}^{\mathrm{E}} = x_1(1-x_1)\sum_{i=1}^{n} A_i(2x_1-1)^i \tag{3.62}$$

Here, the correlation parameter can be found by regression with the experimental data. In this work, the excess molar volumes were determined for binary mixtures of $CO_2$ + hydrocarbons from compressed-liquid densities.

# 3.9 Modelling Approaches

In the present work, the compressed-liquid densities and the speeds-of-sound in $CO_2$ + hydrocarbon systems were used to test the predictive ability of the PPR78 EoS, SAFT-γ Mie EoS and the Helmholtz energy explicit EoSs. The parameters of all equations of state were applied directly without any fitting to experimental data.

In PPR78, the temperature-dependent binary interaction, $k_{ij}$, between each pair of components was calculated by the group-contribution scheme proposed by Jaubert *et al.* (Equation (3.18)). The critical temperature, critical pressure and acentric factor of each substance were obtained from the reference equations of state, and the values were taken from NIST REFPROP 9.1 software. The predictions calculations with the PPR78 were performed using Aspen Properties software package. The

comparisons will be discussed in detail in Chapter 6. Only the compressed-liquid densities were compared with the predictions from PPR78 as the speed-of-sound is generally poorly described by the cubic equations of state. Ye *et al.* [46, 361] conducted a study on the modelling capability of several equations of state for ultrasound velocity in pure hydrocarbons. In the study, they compared the performance of several equations of state including the SRK and PR EoSs for alkanes ($C_3$ – $C_{12}$), hexadecane, cyclohexane, benzene and methylbenzene. They mentioned the $\Delta_{AARD}$ between the experimental data and predictions from SRK and PR as 17.2 % and 13.8 %, respectively. Another study by Faradonbeh *et al.* also showed that speed-of-sound is poorly predicted by eight cEoS [362]. Therefore, PPR78 was not chosen for the speed-of-sound predictions in the present work.

Both the speed-of-sound and compressed-liquid density of pure and binary systems of $CO_2$ + hydrocarbon were tested with the predictions from SAFT-γ Mie EoS. The pure components parameters and cross-interaction parameters were taken directly from several publications. The calculations were performed with the gSAFT software. In the case of unsatisfactory fitting of the EoS, the cross-interaction parameters, $\varepsilon_{kl}$, the group dispersion interaction energies, and $\lambda_{kl}^{r}$, the repulsive exponents were optimised with the experimental data collected in this work. The results of the comparisons between the experimental data and predictions from the model will be described in Chapters 5 and 6.

The Helmholtz energy explicit equations of state were used to test the speed-of-sound and compressed-liquid density of pure and binary systems of $CO_2$ + hydrocarbon measured in this work. The predictions from the reference equations of state were compared with the pure components experimental data described in Chapter 5. Two Helmholtz energy explicit mixture models, GERG-2008 EoS and a multi-fluid approximation, were tested with the experimental density and speed-of-sound data for different binary mixtures and the results are shown in Chapter 6.

Lastly, the thermodynamic integration numerical method was applied to pure hydrocarbons where both the speed-of-sound and density across a wide temperature and pressure range were measured. As mentioned in Section 3.7 that the thermodynamic integration requires as inputs the isobaric heat capacity data along an isobar, the experimental heat capacity data were collected in the literature prior to the numerical integration. The derived properties including density, isobaric heat capacity, isothermal compressibility and isobaric expansivity were compared with the predictions from the reference equations of state. The results of the thermodynamic integration will be discussed in detail in Chapter 5.

## 3.10 Summary

The review presented in this chapter aims to summarise the equations of state that are considered relevant for this work. Three types of equations of state (PPR78 EoS, SAFT-γ Mie EoS and the Helmholtz energy explicit EoSs) were described and were chosen to be tested against the experimental data collected in this work. The predictive cubic PPR78 EoS and SAFT-γ Mie both are models that based on group contribution approaches and they have been proven to have good predictive capability for the thermophysical properties of hydrocarbon systems. Equations of state using the dimensionless Helmholtz energy have also been successfully employed to describe the thermophysical properties of pure and binary hydrocarbon systems over wide temperature and pressure ranges with high accuracy. Therefore it will be interesting to examine the predictive capabilities of such equations against data obtained for the binary mixtures studied in the present work. The comparisons between the experimental data and the predictions from these models will be shown in Chapters 5 and 6.

# Chapter 4: Apparatus Design and Experimental Methodology

## 4.1 Overview

In this chapter, the description of the experimental apparatus used for the speed-of-sound and density measurements is provided. The apparatus used throughout this research includes the liquid sound-speed apparatus and a high-pressure vibrating-tube densimeter. The calibration methods and procedures undertaken for both instruments have also been described. This incorporates the calibration of the acoustic path-length for the speed-of-sound ultrasonic cell and the calibration of the vibrating-tube densimeter. Detailed experimental procedures and uncertainty analysis are also presented in this chapter. In addition, this chapter details the experimental fluids used, including their stated purities, their sources and any further purification undertaken.

# 4.2 Speed-of-Sound Apparatus

The speed-of-sound apparatus was already in commission in the laboratory at the beginning of this project. It has been used successfully in the past for measurements on a variety of systems [47, 50, 81, 363]. The apparatus consisted of 5 MHz dual-path ultrasonic cell located inside a stainless-steel pressure vessel designed at a working pressure of 400 MPa that was immersed in a thermostatic bath. The temperature of the pressure vessel was measured with a platinum resistance thermometer. The fluid systems contained a high-pressure syringe pump rated for a maximum working pressure of 400 MPa, a pressure transducer, fill and drain valves and a bursting disc for the protection of the pressure vessel and the pressure transducer in the system.

## 4.2.1 Ultrasonic Cell

The ultrasonic cell was designed and built in-house and a schematic is shown in Figure 4.1. The metal part of the ultrasonic cell was made from stainless-steel type 316. The ultrasonic cell contained a 5 MHz thickness-mode piezo-transducer held between two stainless-steel clamping rings, two quartz spacer tubes with nominal lengths of 20 mm and 30 mm (18 mm inner diameter, 22 mm outer diameter) and a pair of stainless-steel reflectors. The fused quartz tubes were ground from solid pieces such that the lengths were accurate to ±10 μm. An advantage of using fused quartz as spacers is that its thermal expansion coefficient is very small so that corrections required to the path-lengths with the temperature change was minimised. The stainless-steel clamping rings have identical dimensions to ensure there is no difference between the path-lengths in the two parts of the cell at any temperature or pressure. The reflectors located at both ends of the ultrasonic cell, were 10 mm deep and 25 mm in diameter, each had a 90° conical cavity in the rear face. The reason for this cavity was to disperse sound that passed into the reflector and was then reflected from the rear face. The 5 MHz piezo-transducer is 10 mm in diameter and 0.4 mm thick, was made from lead zirconate titanate ($PbZrO_3/PbTiO_3$) coated with gold plated on both sides to provide electrical connections. Orifices around the outer circumferences of the reflectors and clamping rings permitted the filling, draining and evacuation of the ultrasonic cell. The ultrasonic cell components were held together by three 2 mm diameter threaded rods that were located at an angle $2/3\pi$ to each other in the reflectors, spacer tubes and clamping rings. Belleville washers were used to maintain the assembly in compression despite differential expansion/contraction of the cell components over a large range of temperatures. Figure 4.1 also shows a computer-generated picture for the ultrasonic cell used for the experimental work carried out in this thesis.

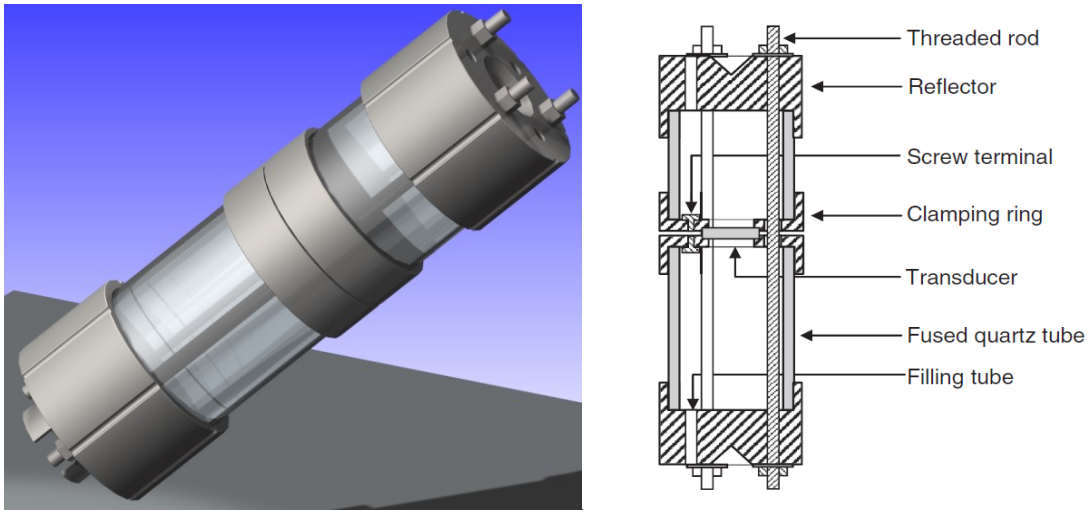



**Figure 4.1** Schematic of the 5 MHz ultrasonic cell of the speed-of-sound apparatus.

## 4.2.2 Pressure Vessel

The pressure vessel which contained the sound-speed ultrasonic cell was designed and manufactured by SITEC. The maximum working pressure of the pressure vessel was designed to be 400 MPa at 473.15 K. The body of the pressure vessel was fabricated with precipitation-hardening (PH) stainless-steel and the internal volume is approximately 50 $cm^3$. A vessel has one entry port in the cap which was for filling and also an entry for the lead wire from the transducer. A second port located at the bottom of the vessel was used for emptying and flushing the vessel. A thermowell was also created in the body of the pressure vessel for a platinum resistance thermometer (PRT). The pressure vessel was sealed by using the conventional Bridgman seal with two different types of compression rings, PTFE and PEEK followed by a metallic back-up ring. A copy of the engineering drawing of the pressure vessel can be found in the Appendix A.




**Figure 4.2** Schematic of the 4 kbar pressure vessel and plug of the speed-of-sound apparatus.

### 4.2.3 Temperature and Pressure Control

The pressure vessel and the ultrasonic cell were located in a thermostatic bath (Fluke model 6020) filled with a silicone oil (Dow Corning type 200/10) which can provide temperature stability and uniformity of ±0.005 K over the entire range of temperature from (263.15 to 473.15) K. The fluid circulation within the bath was provided by a stirrer and a baffle. The temperature was controlled by a proportional-integral-derivative (PID) temperature controller operating with a platinum resistance thermometer and a 100 W control heater. In order to achieve temperatures below ambient, a heat-exchanger device was used in the bath through which alcohol from an external refrigerated circulator was passed. The heat-exchanger device is cylindrical in shaped with a large heat-exchange surface area. The cooling fluid should be at a temperature approximately 10 K below the desired bath temperature. The temperature of the pressure vessel was measured with a platinum resistance thermometer (Fluke model 5615) which was inserted inside the thermowell in the wall of the pressure vessel. The PRT was calibrated at the temperature of the triple point of water and by comparison at temperatures up to 473 K with a standard platinum resistance thermometer having an expanded uncertainty of 0.002 K in the present temperature range. During measurements, some inconsistencies were discovered for the temperature control; the depth of the thermowell in the pressure vessel was insufficient to allow the thermometer to have appropriate immersion in the silicon oil for accurate temperature reading. To eliminate this temperature error, the PRT was instead placed directly next to the pressure vessel and a longer equilibrium time (1 to 2 hours) was allowed after each temperature change. In addition, it has to be noted that care should be taken when monitoring the oil-level in the oil bath. Due to the thermal expansion of the silicon oil, the oil-level increases during high temperatures and may cause overflow. It is necessary to remove an appropriate amount of oil to prevent overflow; however, the oil-level should always be at an optimum level at which it fully covers the surface of the pressure vessel.

The pressure transducer (Honeywell model TJE/60000) used to measure the system pressure was validated prior to this work at pressures up to 240 MPa against hydraulic pressure dead weight tester (DH-Budenberg model 580EHX) having a standard relative uncertainty of 0.004 %. The atmospheric pressure was measured with a digital barometer located in the same laboratory with an expanded uncertainty of 0.005 MPa. The overall uncertainty of the temperature and pressure control will be discussed in the following section.

### 4.2.4 Magnetic Circulating Pump

Between the injection pump and the pressure vessel, a magnetic circulating pump is installed. The magnetic circulating pump can provide re-mixing of the fluids to a homogeneous state inside the liquid sound-speed measurement apparatus. Typically, a homogeneous fluid is introduced into the initially-evacuated system, some flashing will take place and it is necessary to mix the contents by

means of circulation to restore the initial homogeneous state. Below shows a diagram of the magnetic circulating pump designed-in-house:

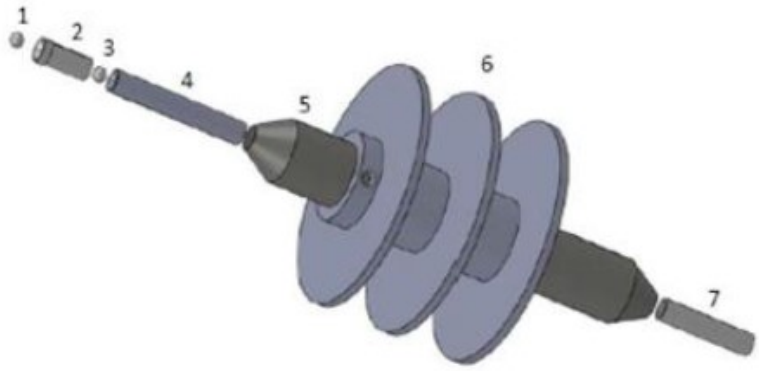



**Figure 4.3** Exploded view of the magnetic circulating pump, (1) check valve ball, (2) check valve body, (3) check valve ball, (4) magnet piston, (5) pump cylinder, (6) bobbin and (7) stainless-steel support. Reproduced from Lin and Trusler [81].

The pump cylinder was fabricated from a commercially available high-pressure nipple, 100 mm in length, with an outside diameter of 14.3 mm, and an initial inside diameter of 4.8 mm. The internal bore was honed to a final diameter of 5.0 mm so as to accommodate a cylindrical piston. The piston was fabricated from a magnetic stainless-steel, type 431, and was 32 mm in length and 4.97 mm in diameter. The piston was drilled through to create an internal bore of 2 mm diameter, the top end was machined to form a 90° conical seat, and a 3 mm diameter ruby sphere was inserted above to create a check valve. A second check valve was fabricated from a 5.5 mm outside diameter tube with a similar conical seat and ruby-sphere seal. This was inserted into the top end of the nipple, which was counter-bored to accept the close-fitting check valve. A tubular stainless-steel support was inserted below the piston to prevent it from falling to the bottom of the nipple. The piston was magnetically driven up and down by an external double solenoid coil, wound on an aluminium bobbin. The amplitude and the frequency of the sinusoidal driving current were regulated to obtain the desired flow rate.

## 4.2.5 Fluid Handling System

The fluid system contained a high-pressure syringe pump (SITEC-Sieber Engineering AG, model 750.1400) rated for a maximum working pressure of 400 MPa, fill and drain valves (for filling, draining and vacuum), an isolation valve (for re-injection and isolation) and a bursting disc safety device designed ($p_{\text{rupture}}$ = 440 MPa) for the protection of the pressure vessel and the pressure transducer in the system. A copy of the engineering drawing of the syringe pump can be found in the Appendix A. A feature of the fluid system is that it can be independently heated to up to a maximum

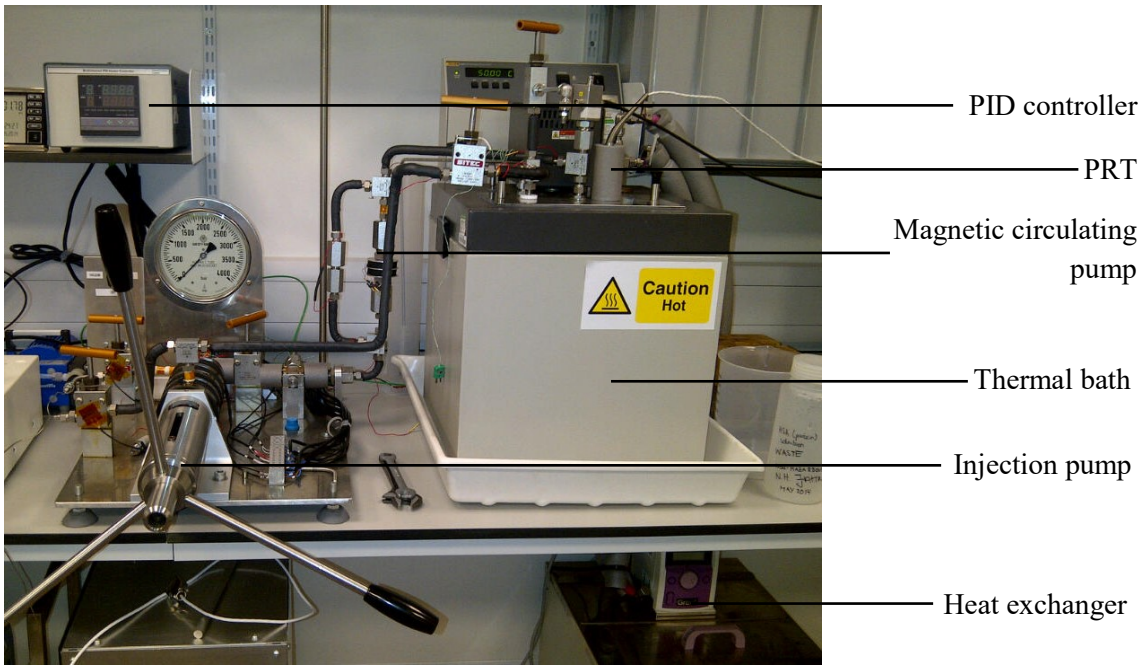
temperature of 323 K by means of a proportional-integral-differential (PID) process controller which can be useful with liquids that freeze under the application of high pressures.

### 4.2.6 Measurement Methodology

The speed-of-sound measurement begins with energising the transducer with a five-cycle tone burst of centre frequency 5 MHz and peak-to-peak amplitude 10 V produced by a function generator (Keysight Technologies 33120A). This caused a pair of ultrasonic pulses to propagate simultaneously in opposite directions through the liquid to either side of the transducer. After reflection at the end faces, the echoes returning to the transducer produced an output signal. Both the initiation pulse and the echo signals were captured by a high-speed digital oscilloscope (Keysight Technologies DSO6012A) operating with a bandwidth of 200 MHz and a sampling rate of 2 GHz. The resulting digital record was analysed in software to obtain the time difference, $(t_2 - t_1)$ between the round-trip times of flight on the long path, $L_2$, and short path, $L_1$, respectively. The speed-of-sound was then obtained based on the simple relation

$$c = 2\Delta L/\Delta t\,, \tag{4.1}$$

where $\Delta L = (L_2 - L_1)$, the path-length difference in the ultrasonic cell and $\Delta t = (t_2 - t_1)$, the flight time difference. A factor of two is required because the time recorded is for the signal to travel back and forward to the transducer. By calculating the difference in transit time, instead of absolute transit time, can reduce/eliminate errors such as diffraction and electronic delays.



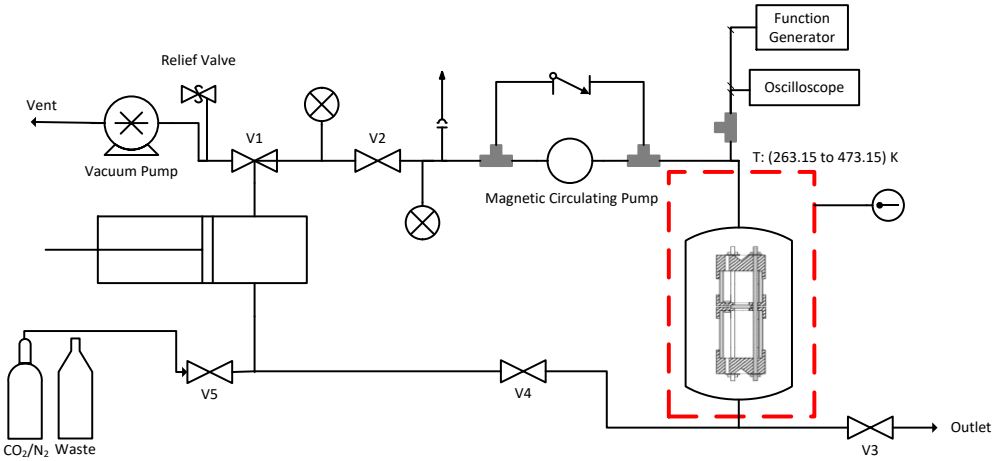



**Figure 4.4** P&ID for the liquid sound-speed apparatus. V1, V3, V5: inlet and out valves; V2, V4: isolation valves; analogue and digital pressure transducers; magnetic circulating pump; platinum resistance thermometer (Pt100); bursting disc safety device; injection pump.

Before filling the system with any liquid sample, it is highly important to completely drain and evacuate to ensure the cleanliness of the system. To create a vacuum in the system, close valves (V5 and V3) and open V1 fully. A dry diaphragm vacuum pump was used to evacuate the whole system and the apparatus should be then ready for filling. It has to be noted that no fluid should be in contact with the vacuum pump.

## 4.2.7 Assembly of the Ultrasonic Cell

The ultrasonic cell consists of several main components as mentioned above: two stainless-steel clamping rings, two stainless-steel reflectors, two unequal length quartz spacer tubes, a piezo-transducer disk and three threaded stainless-steel rods. Extra care should be paid during the assembly of the ultrasonic cell as imperfect arrangement/alignment of the ultrasonic cell may affect the repeatability of the measurements.

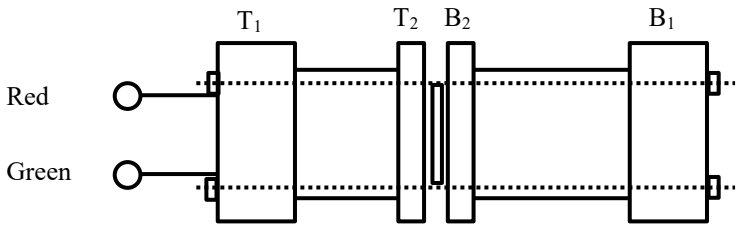



**Figure 4.5** Schematic of the assembly of the ultrasonic cell. $T_1$ & $B_1$: reflectors; $T_2$ & $B_2$: clamping rings; two unequal length quartz tubes; two lead wires (red and green) and a piezo-transducer.

The assembly procedures for the ultrasonic cell are as follows:

(1) Attach a lead wire to each of the clamping rings ($T_2$ & $B_2$). Attached a red wire to $B_2$ and a green wire to $T_2$. The wires should be long enough (about 10 cm) to pass through the quartz tube and the top reflector.

(2) Place the piezo-transducer disk between $T_2$ and $B_2$. The transducer should be centred and seated in the groove on the clamping rings.

(3) Attach the quartz tubes and the stainless-steel reflectors to the clamping rings as shown in Figure 4.5. During this step, guide the lead wires through the quartz tube and the top reflector.

(4) Insert the three threaded rods (120°) from the bottom reflector all-the-way-through to the top reflector (from $B_1$ to $T_1$). Place two Bellville washers at both ends of each of the threaded rods, and tighten the nuts equally across the three threaded rods.

(5) Solder a large-diameter soldering tag onto the red wire and a small-diameter soldering tag onto the green wire. Insulate the soldering tags and wires with heat-shrinks. Carry out a continuity test to confirm the tension of the nuts at both ends of the reflectors and the correct assembly of the ultrasonic cell. There should only be three complete paths: (i) $T_1$ & $B_1$, (ii) red & $B_2$ and (iii) green & $T_2$.

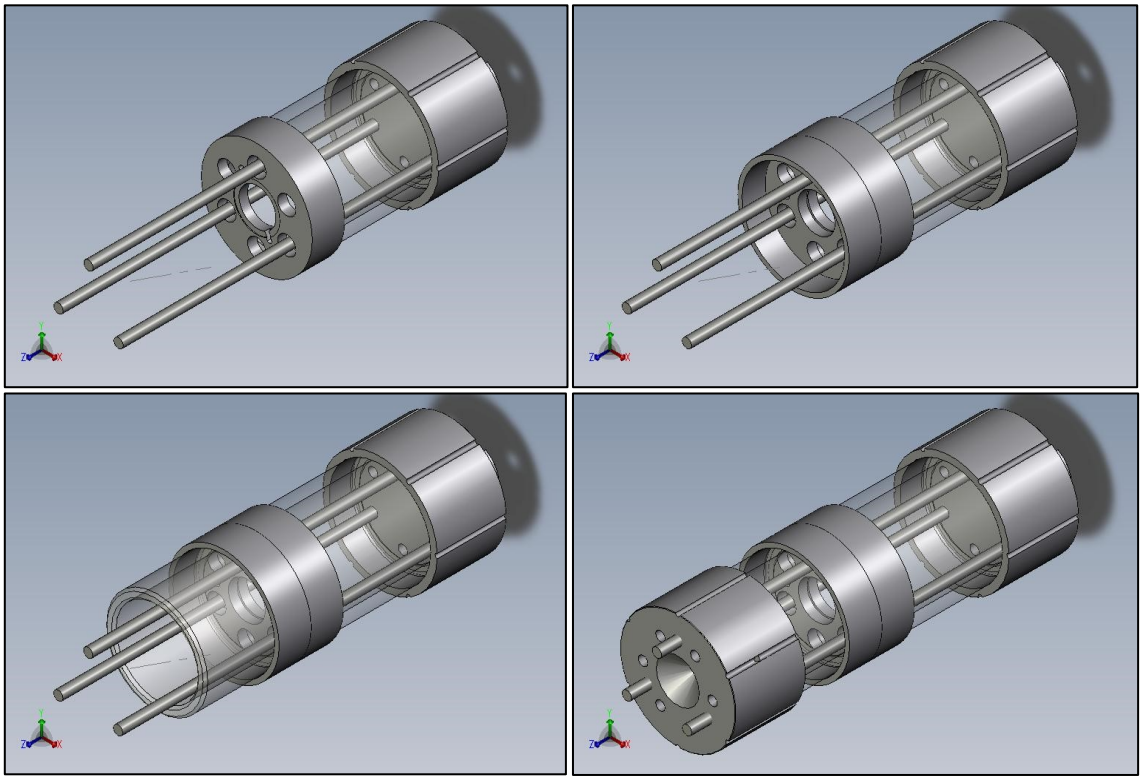


**Figure 4.6** Visualisation of the ultrasonic cell (nuts, washers and piezo-transducer not shown). Top left: bottom transducer clamping ring, quartz tube and reflector; the circular recess in which the transducer should be located can be seen in the centre of the clamping ring. Top right: addition of the top clamping ring. Bottom left: addition of the top quartz tube. Bottom right: fully assembled.

## 4.2.8 Calibration

*4.2.8.1 Temperature Calibration*

The platinum resistance thermometers (PRT) were calibrated in the range of (273.15 to 473.15) K at 50 K intervals in a thermal bath by comparison with a standard PRT which has an expanded uncertainty of 2 mK in the present temperature range. The standard PRT itself was calibrated on ITS-90 at the temperature of the triple point of water. The resistance-temperature data were used to determine the coefficients in the ITS-90 equation. Table 4.1 details the coefficients for the temperature calibration. The ITS-90 equation is given in the following form: (NIST ITS-90).

**Table 4.1** PRT calibration parameters for ITS-90 equation.

| | | |
|---|---|---|
| $R_{TPW}/\Omega$ = | 100.013961 | Directly measured value in triple point of water cell |
| $a_8$ = | -5.82957E-04 | (also known as 'a positive') |
| $b_8$ = | -2.94117E-04 | (also known as 'b positive') |

Taking all factors into account, the estimated overall standard uncertainty of the temperature measurement was 0.05 K.

*4.2.8.2 Pressure Calibration*

The pressure transducer (Honeywell model TJE/60000) was calibrated by a UKAS calibration company, Antech Calibration Services, prior to the experiments at pressures up to 400 MPa against a pressure balance with a relative uncertainty of 0.02 %. In the calibration, the transducer exhibited good linearity and a lack of hysteresis, leading to a standard uncertainty of 6 kPa. In order to compensate for sensor drift over time, the reading of the pressure transducer was zeroed periodically under vacuum. The pressure transducer was also validated against a hydraulic pressure dead weight tester (DH-Budenberg model 580EHX) having a standard relative uncertainty of 0.004 %. Taking all factors into account, the standard uncertainty of the experimental pressure, including the effects of non-repeatability, hysteresis and non-linearity, was estimated to be 50 kPa.

*4.2.8.3 Ultrasonic Cell Calibration*

It is essential to correctly determine the path-lengths of the ultrasonic cell to obtain an accurate speed-of-sound measurement. The liquid speed-of-sound system was calibrated using pure water at $T_0$ = 298.15 K and $p_0$ = 1 MPa. The pure water was obtained by means of an active resins filtering device (Millipore). The minimum purity of the pure water is specified to be 99.99% by volume with electrical resistivity ≥18 MΩ.cm at $T$ = 298.15 K. No further purification was carried out, but it was degassed under vacuum. The calibration was chosen to perform at 1 MPa rather than atmospheric pressure, to ensure that the ultrasonic cell inside the pressure vessel was completely filled with liquid water, free of air, even in the event of imperfect degassing. The path-length difference ($L_2 - L_1$) was

determined from the corrected acoustic path-lengths of the ultrasonic cell. The value of the speed-of-sound in water at the corresponding calibration temperature and pressure was taken the IAPWS-95 EoS [172] developed by Pruss and Span and is associated with an uncertainty of 0.005 %. The acoustic path-length measurement can be given in the form below:

$$\Delta L(T_0, p_0) = c_{\text{calibrate}} \Delta \tau_{\text{calibrate}}, \tag{4.2}$$

where $c_{\text{calibrate}}$ is the speed-of-sound value in water obtained from REFPROP 9.1 [358] which calculates using the equation of state of water (IAPWS-95) and $\Delta\tau_{\text{calibrate}}$ is the measured time delay between the echoes in the same fluid at calibration temperature $T_0$ and pressure $p_0$. The deviation in path-lengths $\Delta L$ can also be represented and calculated in the following form [364]:

$$\Delta L(T, p) = \Delta L_0(T_0, p_0)\left[1 + \langle\alpha\rangle(T - T_0) - \frac{1}{3}\langle\beta\rangle(p - p_0)\right], \tag{4.3}$$

where $T_0$ and $p_0$ are the initial calibration temperature and pressure, respectively. The linear thermal expansion coefficient of quartz was reported in several studies between (6 and 800) K [365-367]. The term $\alpha$ denotes the linear thermal expansivity of quartz [47], $\alpha = 5.5 \times 10^{-7}$ K$^{-1}$ (assumed independent of temperature and pressure) and $\beta$ denotes the isothermal compressibility of the quartz spacer tube in the ultrasonic cell. Lin and Trusler [50] reported a more accurate representation of both $\alpha$ and $\beta$ in their study of speed-of-sound in water. Based on the literature data on the measurement of the thermal expansivity of fused quartz, they developed an expression for $\alpha$ at 250 K $\leq T \leq$ 500 K based on a modified Einstein function, given in the following form:

$$10^6 \alpha / \text{K}^{-1} = \left[a_1 (\theta/T)^2 \exp(\theta/T) / \{\exp(\theta/T) - 1\}^2\right] - a_2, \tag{4.4}$$

where $a_1$ = 1.74, $a_2$ = 0.88, and $\theta$ = 535 K [50]. Similarly for isothermal compressibility, $\beta$ can be estimated through the following expression:

$$\frac{1}{\beta} / \text{MPa} = b_1 - b_2\{(T/298\text{K}) - 1\}^2 + b_3\{(T/298\text{K}) - 1\} + b_4\{(p/\text{MPa}) - 1\}^2, \tag{4.5}$$

with $b_1$ = 36898, $b_2$ = 1419, $b_3$ = 4568 and $b_4$ = 0.012. The value of the coefficients in $\beta$ was obtained from the data reported by McSkimin [368]. The detail of the ultrasonic cell was described previously in the above section. The following expressions for $\langle\alpha\rangle$ and $\langle\beta\rangle$ were used together with Equation (4.3).

$$\begin{aligned} \langle\alpha\rangle &= [\alpha(T) + \alpha(T_0)]/2 \\ \langle\beta\rangle &= [\beta(T, p) + \beta(T, p_0)]/2 \end{aligned} \tag{4.6}$$

It was mentioned by Lin & Trusler [50] that the ultrasonic cell may experience mechanical stability issues after assembly upon temperature and pressure cycling after calibrations, it was recommended to undergo several temperature and/or pressure cycles before carrying out the calibration of the path-length. For instance, the system was allowed to undergo several temperature and pressure cycles before starting the calibration and measurements. A different calibration approach has also been

investigated. In this case, the calibration of the ultrasonic cell was carried out at nine temperatures $T_{\mathrm{ref}}$, between (283.15 and 473.15) K and at 1 MPa. With this calibration approach, the temperature effect on the path-length difference can be experimentally determined and only correction of the pressure effect on the isothermal compressibility is required. The path-length determination expression, Equation (4.3) is reduced to the following form:

$$\Delta L(T,p) = \Delta L_0(T_{\mathrm{ref}}, p_0)\left[1 - \frac{1}{3}\langle\beta\rangle(p - p_0)\right]. \tag{4.7}$$

## 4.2.9 Uncertainty Analysis

The accuracy of experimental data depends on the uncertainty of the measurements; therefore it is very important to identify the potential sources of errors and determine the uncertainty precisely to have an understanding about the quality of the data. Throughout the research, the standard uncertainties for experimental quantities were determined by following the Guide to the Expression of Uncertainty in Measurements (GUM) [369]. The definition of the combined standard uncertainty $u_{\mathrm{c}}$ given by GUM, is the estimated standard deviation associated with the results and is equal to the positive square-root of the combined variance obtained from all variance and covariance components. The expanded uncertainty $U_{\mathrm{c}}$, is obtained by multiplying the combined standard uncertainty $u_{\mathrm{c}}$ by a coverage factor $k$. The parameter $k$ is normally chosen as 2 to represent the 95 % level of confidence. The combined standard uncertainty $U_{\mathrm{c}}(f)$ of quantities $f(x_1, x_2 \cdots x_n)$ that are independent can be estimated using the following function:

$$U_{\mathrm{c}}^2(f) = k^2 \sum_{i=1}^{n}\sum_{j=1}^{n} \frac{\partial f}{\partial x_i}\frac{\partial f}{\partial x_j} u(x_i, x_j), \tag{4.8}$$

where $x_i$ and $x_j$ represent pairs of input variables from the function $f$. The partial derivatives $(\partial f / \partial x_i)$ and $(\partial f / \partial x_j)$ are often called sensitivity coefficient which describe how the quantity $f$ changes with respect to $x_i$ and $x_j$. $u^2(x_i, x_j)$ is the covariance for variables $x_i$ and $x_j$ and normally only the variance terms ($i = j$) are considered in the uncertainty calculations. The overall sound-speed measurement uncertainty is composed of the contributions from the uncertainties of temperature, pressure, composition, calibration and repeatability of the measurement. The overall uncertainty of the sound-speed measurement was estimated from the following relation:

$$u_c^2 = \left[\left(\frac{\partial c}{\partial T}\right)u_T\right]^2 + \left[\left(\frac{\partial c}{\partial p}\right)u_p\right]^2 + \left[\left(\frac{\partial c}{\partial x}\right)u_x\right]^2 + [\delta c]^2 \tag{4.9}$$

where $u_T$, $u_p$ and $u_x$ are the standard uncertainties of temperature, pressure and mole fraction discussed in the calibration section. For pure component measurements, the mixing uncertainty was neglected. The partial derivatives were estimated using the surface fit correlation at each experimental point. The term $\delta c$ refers to the uncertainty that arises from the standard repeatability of the measurement

uncertainty which varies between (0.4 and 0.6) $m \cdot s^{-1}$ over the entire experimental range. The measurement range of the pressure sensor was up to 400 MPa with a standard uncertainty of 0.1 % of the full scale; this term has the highest impact on the overall speed-of-sound uncertainty at the high temperatures and low pressures. The estimated standard uncertainty of the temperature measurements was 0.05 K. For pure component measurements, the relative uncertainty $u_c/c$ varies from 0.02 % at low temperatures and high pressures, to approximately 0.04% at low pressures and high temperatures. Therefore, the overall expanded uncertainty is between (0.04 and 0.08) % with a coverage factor of 2 (for a 95 % confidence interval). As for binary mixtures measurements, the expanded relative uncertainties for of $CO_2$ + *n*-nonane and $CO_2$ + methylbenzene range from (0.04 to 0.14) % with a coverage factor of $k = 2$, across four compositions at all state points investigated. An example of the uncertainty budget for speed-of-sound measurement is shown in Table 4.2 for the case of the median temperature, pressure, and mole fraction.

**Table 4.2** Uncertainty budget for speed-of-sound in $CO_2$ + *n*-nonane at the median state point in terms of standard uncertainty $u$(y) of the dimensionless parameter (y) and arising contribution $u_r(c)$ to the overall standard relative uncertainty of speed-of-sound.

| Dimensionless parameter | Value | $u$(y) | $10^2 u_r(c)$ |
|---|---|---|---|
| $T$ / K | 373.15 | 0.05 | 0.02 |
| $p$ / MPa | 200 | 0.05 | 0.01 |
| $x$ | 0.4 | 0.00001 | 0.00 |
| $(c_{exp}\text{-}c_{EoS})$ / $(m \cdot s^{-1})$ | 1498.2 | 0.08 | 0.01 |
| $c$ / $(m \cdot s^{-1})$ | 1655.31 | 0.4 | 0.02 |
| Overall combined standard relative uncertainty | | | 0.06 |

## 4.3 Density Measurement Set-up

The vibrating-tube densimeter (Anton-Paar, DMA HP) is designed to measure the density of liquids and gases at pressures up to 70 MPa and temperatures between (283 and 473) K using a U-shaped vibrating-tube with an approximate 2 mL internal volume. Mainly the density set-up consisted of a vibrating-tube densimeter (Anton-Paar, DMA HP), a high-pressure syringe pump (DH Budenburg) with an internal volume of approximately 10 mL, a sample vessel, and temperature and pressure sensors. The components were connected via 1.6 mm o.d. stainless-steel tubing. The temperature of DMA HP was controlled and measured by an integrated Peltier thermostat with an accuracy of ± 0.01 K. A second calibrated Pt100 sensor was located inside a thermowell in the cellblock to verify the temperature readings. The DMA HP unit was connected to a master instrument (Anton-Paar, DMA 5000 M) that displays the measuring parameters including the temperature, pressure and the period of oscillation with a resolution of 0.01 μs. The master instrument is a vibrating tube densimeter but only limited for atmospheric pressure density measurement. The syringe pump was used for the injection

of fluids and to raise pressure during measurements. The pressure was measured using an external pressure transducer installed in the pump. The pressure transducer was rated for 70 MPa with an analogue signal output of (4 to 20) mA. An isolation valve (V2) in the system as shown in Figure 4.7, isolates the injection syringe pump and the VTD which allows the additional injection of fluid. The entire set-up was protected by a bursting disc with a bursting pressure of 80 MPa which is equivalent to about 110% of the maximum operating pressure. A pressure relief valve by Swagelok was connected to the vacuum inlet to protect the vacuum pump.

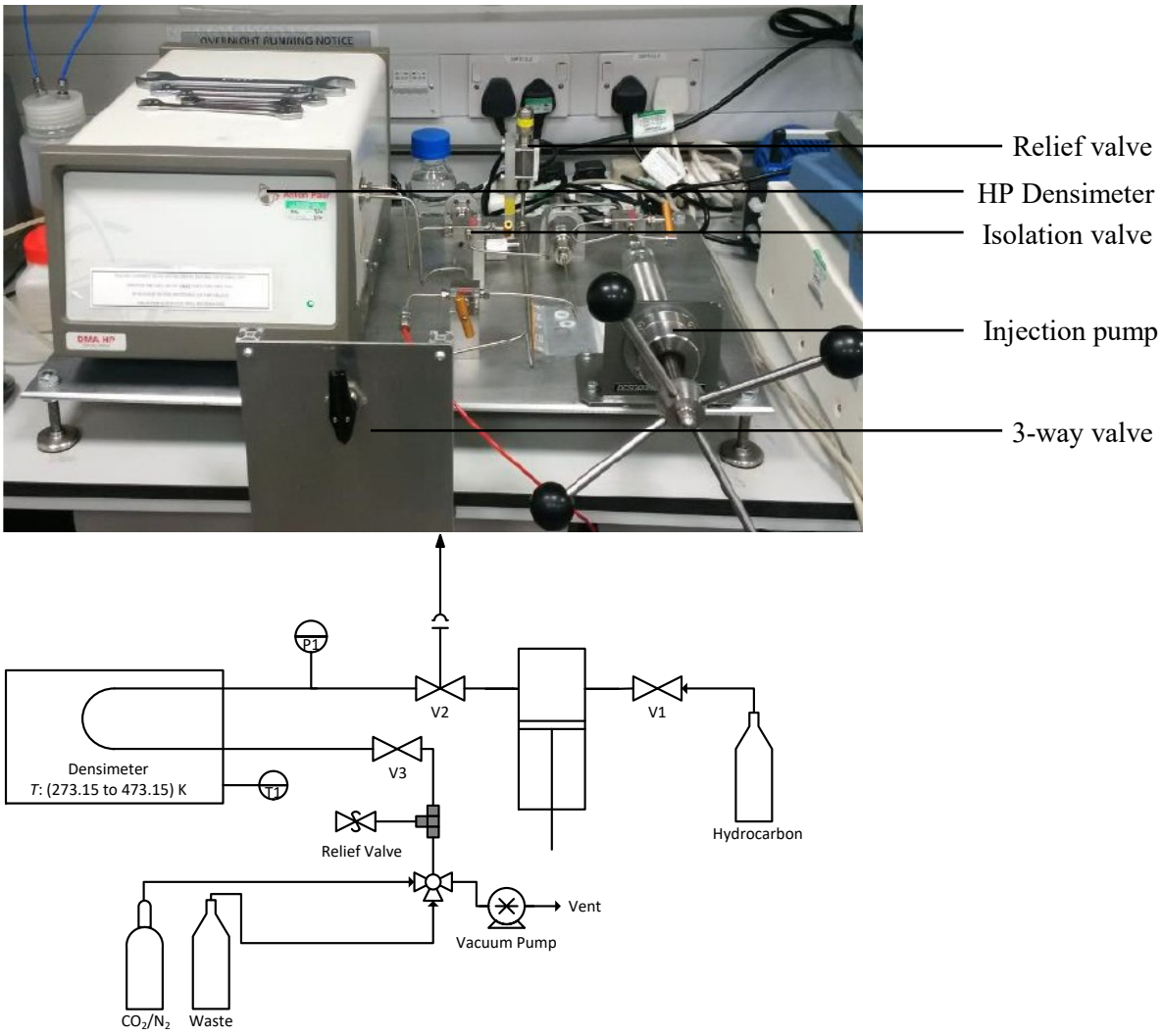



**Figure 4.7** P&ID for high-pressure density apparatus: densimeter; manual injection pump; V1 and V3: inlet and outlet valves; V2: isolation valve; T1: external PRT; P1: pressure transducer; pressure relief valve; injection pump.

## 4.3.1 Measurement Methodology

The density $\rho$ is related to the period of oscillation $\tau$ in a vibrating-tube densimeter is given by the relation:

$$\rho(p,T) = A(p,T)\tau^2 - B(p,T), \tag{4.10}$$

where $A$ and $B$ are known as the characteristic parameters that are determined by calibration with fluids of known density at each temperature and pressure.

## 4.3.2 Calibration

*4.3.2.1 Temperature and Pressure Calibration*

The temperature of DMA HP was measured by an internal integrated Peltier thermostat with an accuracy of ± 0.01 K. The temperature was verified with an external PRT which was calibrated in the range of (273.15 to 473.15) K at 50 K intervals in a thermal bath by comparison with a standard PRT which has an expanded uncertainty of 2 mK in the present temperature range. The pressure transducer was validated against a hydraulic pressure dead weight tester (DH-Budenberg model 580EHX) having a standard relative uncertainty of 0.004 %. During the validation, no hysteresis was discovered in the transducer when increasing/decreasing pressure, leading to a standard uncertainty of 6 kPa. Taking all factors into account, the standard uncertainty of the experimental pressure was estimated to be 20 kPa.

*4.3.2.2 VTD Calibration Models*

It is important and essential to calibrate the vibrating-tube densimeter in order to achieve highly accurate density measurement. In the past years, many authors reported different absolute and relative calibration methods for the VTDs, aiming to improve the accuracy of the measured density data. Typically, calibrations were carried out by measuring the temperature and pressure dependence of the period of oscillation at all considered $T$ and $p$ conditions. There are many reported ways, either based on underlying assumptions and/or on physical parameters, of experimental determination of density at elevated temperatures and pressures (the working coefficients $A$ and $B$ in Equation (4.10)). The classical calibration measurement usually consists of using two reference fluids of known density with accuracy typically better than 0.1 kg·m$^{-3}$. The calibration measurements cover a range of temperature and pressure and reference fluid density that covers the range of conditions to be measured for the unknown fluid. According to Anton Paar, the manufacturer of the densimeter used in this work, they suggested a power series expansion in temperature and pressure which are a common choice for the functional forms of $A$ and $B$, given in the following forms:

$$\begin{aligned} A &= \sum_{i=0}^{N}\sum_{j=0}^{M} a_{ij} T^i p^j \\ B &= \sum_{i=0}^{N}\sum_{j=0}^{M} b_{ij} T^i p^j \end{aligned} \tag{4.11}$$

Lagourette *et al.* [370] and Sousa *et al.* [371] proposed eliminating one of the calibration fluids in favour of determining the evacuated tube's resonance period as a function of temperature. Two assumptions were made regarding the pressure dependence of $A$ or $B$. One of the assumptions was that

only *B* varied with pressure and *A* varied only with temperature. Whereas in the second assumption, *A* and *B* were assumed to have the same pressure variations with pressure and the ratio *A*/*B* was independent of pressure. Lagourette *et al.* [370] concluded that the first set of assumption for *A* and *B* was able to represent the reference fluid density better than the second set of assumption. However, the second set of assumption contained a more physical basis. The characteristic parameters given in terms of density and period of oscillation can be calculated in the following form:

$$A(T,p)=\frac{\rho_{\mathrm{w}}(T,p)}{\tau_{\mathrm{w}}^2(T,p)-\tau_0^2(T)}$$
$$B(T,p)=\frac{\rho_{w}(T,p)\tau_0^2(T)}{\tau_{\mathrm{w}}^2(T,p)-\tau_0^2(T)} \tag{4.12}$$

Holcomb and Outcalt [168] presented a theoretically based calibration method of the VTD, in which *A* and *B* were linked with the Young's modules and the internal volume of the vibrating-tube as well as temperature and pressure. They measured the resonance periods under vacuum and for two reference fluids over the range of conditions. Bouchot and Richon [372, 373] recommended a calibration procedure that utilised measurements of vacuum and a single reference fluid at the same temperature as the intended sample measurements. Their approach was similar to the Holcomb and Outcalt's approach but contained more terms and allowed the pressure dependence of the tube's volume to be calculated from the elastic and geometrical properties of the tube. Their model contained two unknown parameters that were both determined at a constant temperature. However, the parameters were required to be re-determined when the VTD temperature was changed because the thermal variation of the apparatus parameters was not sufficiently repeatable. The hypothesis leads to the following expression:

$$\rho=\frac{\rho_{\mathrm{ref1}}\left(\tau^2-\tau_{\mathrm{ref2}}^2\right)-\rho_{\mathrm{ref2}}\left(\tau^2-\tau_{\mathrm{ref1}}^2\right)}{\left(\tau_{\mathrm{ref1}}^2-\tau_{\mathrm{ref2}}^2\right)}, \tag{4.13}$$

where $\tau_{\mathrm{ref1}}$ and $\tau_{\mathrm{ref2}}$ are the period of oscillation measured with well-studied calibration fluids 1 and 2 at given temperature and pressure, respectively. The terms $\rho_{\mathrm{ref1}}$ and $\rho_{\mathrm{ref2}}$ are the density of the reference fluids obtained from their equations of state. Therefore, the period of oscillation and the density as a function of temperature and pressure of the reference fluids are needed to be determined during the calibration process. Lampreia and Nieto de Castro [189] proposed an alternative method for relating the period of oscillation to density. In their approach, the spring constant was assumed to be independent of pressure. They also stated that the vacuum resonance periods could not be measured directly with sufficient accuracy in the vibrating-tube densimeter, and the use of two reference fluids at ambient pressure to calculate the vacuum resonance period at a given temperature was recommended. In addition, it was required for the measurements of a reference fluid over the measurement range to determine the variation of the tube volume with temperature and pressure. Recently in our group, May *et al.* [374] presented a new apparatus model for VTDs, developed by

extending the framework presented by Holcomb and Outcalt [168], and Bouchot and Richon [372, 373]. The model allows the apparatus parameters to be predicted via the following expression:

$$\rho_F = \frac{(\rho_M / S_{00})}{(1+\alpha_V t+\beta_V p)} \times \left[ \left( \frac{\tau}{\tau_{00}(1+\varepsilon_{\tau 1} t+\varepsilon_{\tau 2} t^2)} \right)^2 (1+\beta_\tau p) - 1 \right] \tag{4.14}$$

Here $t$ is the temperature degree Celsius. The equation above is related to the conventional apparatus parameters, $A$ and $B$ via the following relations:

$$A = \left( \frac{\rho_{\mathrm{M}}}{S_{00}\tau_{00}^2} \right) \left[ \frac{(1+\beta_\tau p)}{(1+\varepsilon_{\tau 1} t+\varepsilon_{\tau 2} t^2)^2 (1+\alpha_{\mathrm{V}} t+\beta_{\mathrm{V}} p)} \right]$$
$$B = \frac{\rho_{\mathrm{M}}}{S_{00}(1+\alpha_{\mathrm{V}} t+\beta_{\mathrm{V}} p)} \tag{4.15}$$

A summary of description and determination method of the seven apparatus parameters mentioned in the above calibration model are detailed in Table 4.3. It is vital to ensure the apparatus model and the parameters therein are well linked to quantities that are representative of the VTD's physical properties, as there are circumstances where extrapolation of the model used to describe the VTD is required beyond the range of the typical reference fluid (water) calibration [374]. For example, the measurement of brine densities [155, 156]. There are two major advantages of using a model with physically based parameters over the classical calibration approaches: one is the ability to extrapolate density beyond the calibration range with reduced uncertainty, and secondly the number of calibration measurements required to fully calibrate the densimeter can be reduced. To justify the advantages, May *et al.* [374] showed that the calibration result was similar when water was excluded during the calibration process. The extrapolated water density from helium contained an error of less than 0.4 kg·m$^{-3}$ when compared with the values from the IAPWS-95. To justify the second advantage, a constraint in the physical parameters of $\beta_V / \beta_\tau$ = -3.87 was applied and the use of only one reference fluid and vacuum was proposed for the calibration of the densimeter. This constraint was obtained from the results of several calibrations of different VTDs which used two calibration fluids through non-linear regression. Similar accuracy on density was achieved with the constraint and the methodology was described in detail in the paper.

**Table 4.3** Summary of the seven VTD apparatus parameters used in the calibration model reported by May *et al.* [374] and their determination methods.

| Symbol | Parameter | Determination method |
|---|---|---|
| $S_{00}$ | Geometric sensitivity factor of evacuated tube | Regression of reference fluid measurements |
| $\tau_{00}$ | Resonance period of evacuated tube | Regression of vacuum measurements |

| | | |
|---|---|---|
| $\varepsilon_{\tau 1}$ | Linear temperature response coefficient of spring constant | Regression of vacuum measurements / material properties estimates |
| $\varepsilon_{\tau 2}$ | Quadratic temperature response coefficient of spring constant | Regression of vacuum measurements / material properties estimates |
| $\beta_{\tau}$ | Pressure response coefficient of spring constant | Regression of reference fluid measurements |
| $\alpha_{V}$ | Temperature response coefficient of tube volume | Regression of reference fluid measurements |
| $\beta_{V}$ | Pressure response coefficient of tube volume | Regression of reference fluid measurements |

*4.3.2.3VTD Calibration Methodology*

It is understood that using two reference calibration fluids and vacuum over the required ($p$,$T$) range should sufficiently determine the working coefficients of the densimeter. For the choice of calibration fluids, as mentioned in Chapter 2, gas is sometimes used as a second calibration fluid besides water as the first one. The VTD used in this work was calibrated with helium, deionized water and vacuum at temperatures between (283.15 and 473.15) K and pressures up to 65 MPa before measurements. Both water and helium were chosen as the calibration fluids since they were studied extensively over a wide temperature and pressure range and their reference equations of state for density calculations have relatively low stated tolerances with 0.001 % and 0.05%, respectively [172, 175]. Another advantage of using helium as a calibration fluid is that the densities of helium can be measured at high pressures which provide the full scale of densities at the low end. The densities of the reference fluids were obtained from NIST REFPROP 9.1 [358] software package. The calibration was carried out in the full temperature and pressure range of interest. The calibration data are listed in Table A4.1 in Appendix A. Applying the density and period of oscillation obtained from the calibration data into Equation (4.10) and solving the boundary equations above simultaneously, expressions of $A$ and $B$ as a function of densities are obtained:

$$A = \frac{\left(\rho_{\mathrm{W}} - \rho_{\mathrm{H}}\right)}{\left(\tau_{\mathrm{W}}^{2} - \tau_{\mathrm{H}}^{2}\right)} \text{ and } B = \frac{\left(\rho_{\mathrm{W}}\tau_{\mathrm{H}}^{2} - \rho_{\mathrm{H}}\tau_{\mathrm{W}}^{2}\right)}{\left(\tau_{\mathrm{W}}^{2} - \tau_{\mathrm{H}}^{2}\right)} \tag{4.16}$$

Substituting expression $A$ and $B$ into the working equation, the density expression in terms of helium-water density and period of oscillation is given as:

$$\rho = \frac{\rho_{\mathrm{W}}\left(\tau^{2} - \tau_{\mathrm{H}}^{2}\right) - \rho_{\mathrm{H}}\left(\tau^{2} - \tau_{\mathrm{W}}^{2}\right)}{\left(\tau_{\mathrm{W}}^{2} - \tau_{\mathrm{H}}^{2}\right)}, \tag{4.17}$$

where $\tau_{\mathrm{W}}$ and $\tau_{\mathrm{H}}$ are the periods of oscillation for water and helium. $\rho_{\mathrm{W}}$ is the density for calibration with water at given pressure and temperature. In this case, $\rho_{\mathrm{W}}$ was taken from the IAPWS-95 developed by Pruss and Wagner and is associated with a relative uncertainty of 0.01 %. The mechanical part of the VTD may experience changes over time, to validate the calibration data of the VTD, the period of oscillation readings under vacuum at temperatures could be checked for

indication. The vacuum readings would also provide information about the cleanliness of the VTD once the measuring fluid was rejected. Table 4.4 below shows the period of oscillation readings under vacuum measured at temperatures from (283.15 to 473.15) K. In the following section, we will explore the two different calibration models: (1) The polynomial model and (2) the physical model. We have applied the calibration data to both sets of models and compared the accuracy and the difference in density between the two models.

**Table 4.4** Period of oscillation readings, $\tau_0$ under vacuum at temperatures from (283.15 to 473.15) K

| $T$ / K | $\tau_0$ / μs |
|---|---|
| 283.15 | 2441.80 |
| 298.15 | 2446.52 |
| 323.15 | 2454.52 |
| 348.15 | 2462.68 |
| 373.15 | 2470.98 |
| 398.15 | 2479.44 |
| 423.15 | 2488.07 |
| 448.15 | 2496.81 |
| 473.15 | 2505.68 |

**Polynomial Calibration Model:** Calibration with the two fluids at each temperature and pressure yielded values of $A$ and $B$ which were subsequently represented as functions of temperature and pressure by means of empirical polynomials [155, 156]. The parameters of $A$ and $B$ were obtained by linear regression against the calibration fluids densities. The objective function was set such that the deviations between the experimental densities from all the isotherms are minimised from the predicted data calculated with the equations of state. It has been found out that both $A$ and $B$ depend linearly on pressure and quadratically with temperature, the expressions for $A$ and $B$ are displayed as below:

$$\begin{aligned} A/\left(\mathrm{kg}\cdot\mathrm{m}^{-3}\cdot\mu\mathrm{s}^{-2}\right) &= \sum_{i=0}^{1}\sum_{j=0}^{2} a_{ij}\left(p/\mathrm{MPa}\right)^{i}\left(T/\mathrm{K}\right)^{j} \\ B/\left(\mathrm{kg}\cdot\mathrm{m}^{-3}\right) &= \sum_{i=0}^{1}\sum_{j=0}^{2} b_{ij}\left(p/\mathrm{MPa}\right)^{i}\left(T/\mathrm{K}\right)^{j} \end{aligned}, \tag{4.18}$$

where $a_{ij}$ and $b_{ij}$ are determined from a regression of the experimental data. Equation (4.18) was represented in the dimensionless form such that the coefficients are dimensionless. In Figure 4.8, the deviation plots between the experimental density values (obtained from the calibration correlations) and the values calculated from the equations of state are shown. It can be seen that the deviations between the reference densities and experimental densities of the calibration fluids lie within a band of ±0.1 kg·m$^{-3}$ for most isotherms investigated. The parameters of Equation (4.18) are listed in Table 4.5.

**Table 4.5** Coefficients of the polynomial calibration model, Equation (4.18) for the vibrating-tube densimeter, DMA HP. The calibration was carried out under vacuum, helium and water at $T$: (283.15 to 473.15) K and $p$: (0.1 to 65) MPa.

| Parameter | Value | Parameter | Value |
|---|---|---|---|
| $a_{00}$ | $1.040\times10^{-3}$ | $b_{00}$ | $-5.791\times10^{3}$ |
| $a_{10}$ | $-1.544\times10^{-9}$ | $b_{10}$ | 0.000 |
| $a_{11}$ | $-2.202\times10^{-11}$ | $b_{11}$ | $1.335\times10^{-4}$ |
| $a_{12}$ | $2.558\times10^{-14}$ | $b_{12}$ | $-1.438\times10^{-7}$ |
| $a_{01}$ | $-2.545\times10^{-7}$ | $b_{01}$ | $1.260\times10^{-1}$ |
| $a_{02}$ | $-4.551\times10^{-11}$ | $b_{02}$ | $1.102\times10^{-4}$ |

**Physical Calibration Model:** Parameters in the physical calibration model are linked to quantities that are representative of the VTD's physical properties [374]. The seven parameters in the physical model were determined in two stages. First $\tau_{00}$, $\varepsilon_{\tau1}$ and $\varepsilon_{\tau2}$ were calculated by a linear least square regression of vacuum resonance periods measured at different temperatures. In the second stage, the remaining four parameters $S_{00}$, $\alpha_V$, $\beta_V$ and $\beta_\tau$ were determined by a non-linear regression of resonance periods measured with reference fluids to densities calculated from the experimental pressure and temperature using the reference equation of state for the fluids. The comparison between the reference densities and the values calculated from the physical model is shown in Figure 4.9. The values of the parameter as shown in Equation (4.14) are given in Table 4.6.

**Table 4.6** Coefficients of the physical calibration model, Equation (4.14) for the vibrating-tube densimeter, DMA HP. The calibration was carried out under vacuum, helium and water at $T$: (10 to 200) °C and $p$: (0.1 to 65) MPa.

| Parameter | Value | Parameter | Value |
|---|---|---|---|
| $S_{00}$ | 1.546 | $\rho_M$ / kg·m$^{-3}$ | 889.0 |
| $\tau_{00}$ / μs | 2438.664 | $\beta_\tau$ / MPa$^{-1}$ | $3.947\times10^{-5}$ |
| $\varepsilon_{\tau1}$ / °C$^{-1}$ | $1.277\times10^{-4}$ | $\alpha_V$ / °C$^{-1}$ | $5.325\times10^{-5}$ |
| $\varepsilon_{\tau2}$ / °C$^{-1}$ | $4.884\times10^{-8}$ | $B_V$ / MPa$^{-1}$ | $-1.376\times10^{-5}$ |

**Evaluation of the Two Calibration Models:** Further investigation regarding the effect of using the two calibration models described above was carried out. The results suggested that the difference in absolute density when different calibration approaches are used is small. When comparing between

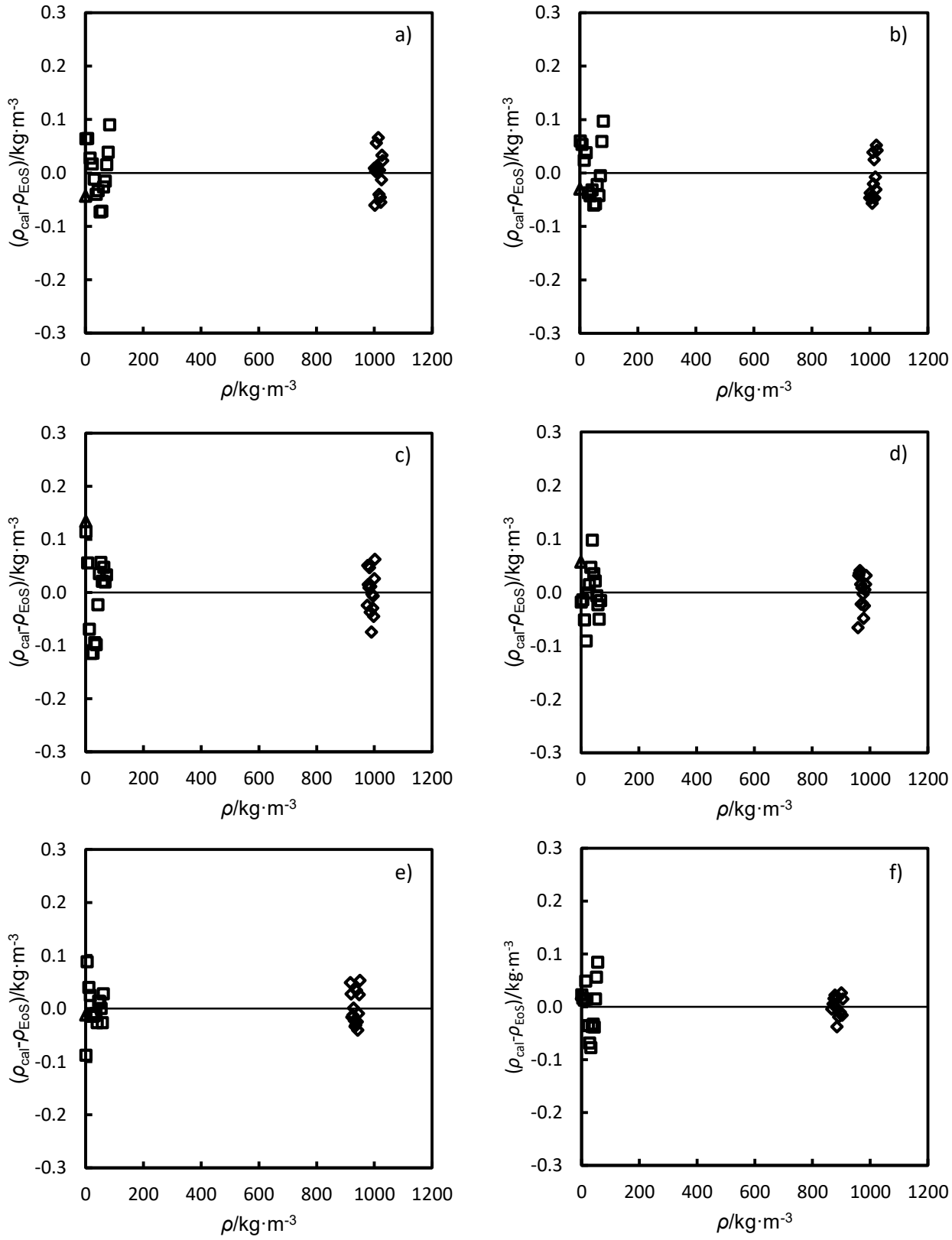



**Figure 4.8** Polynomial model: Comparison between the experimental data calculated from the calibration curve and the predictions from the equations of state across six isotherms: a) 283.15 K, b) 298.15 K, c) 348.15 K, d) 373.15 K e) 423.15 K, f) 473.15 K. Symbols: ◇, water; △, vacuum; □, helium.

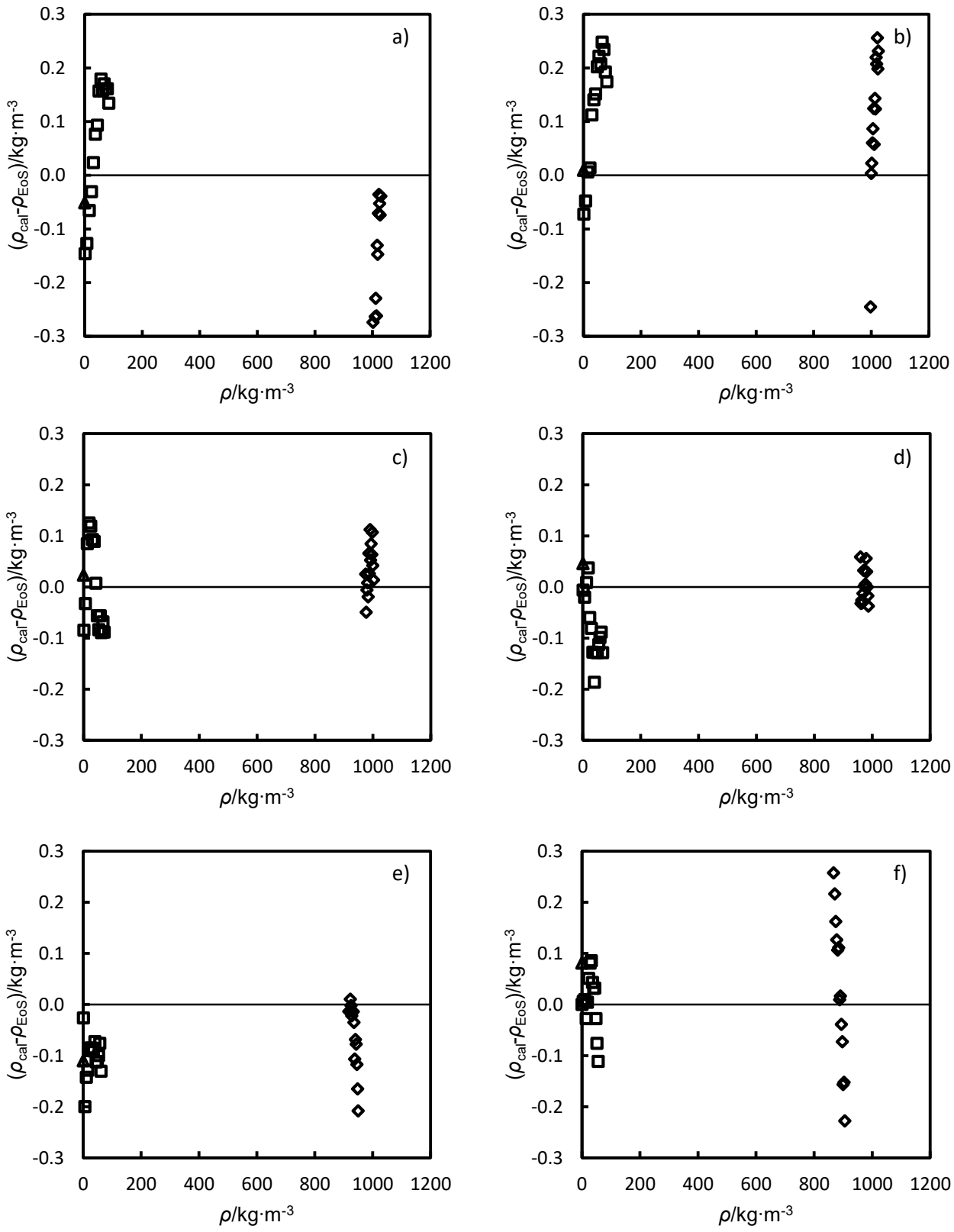



**Figure 4.9** Physical model: Comparison between the experimental data calculated from the calibration curve and the predictions from the equations of state across six isotherms: a) 283.15 K, b) 298.15 K, c) 348.15 K, d) 373.15 K e) 423.15 K, f) 473.15 K. Symbols: ◇, water; △, vacuum; □, helium.

It can be seen in Figures 4.8 and 4.9 that on selected isotherms, the difference between two calibration models is approximately 0.1 kg·m$^{-3}$ throughout the calibration temperature and pressure range. The density difference between two models is insignificant compared with the estimated uncertainty of the density measurement. Therefore both models were considered to be valid for the calibration of the vibrating-tube densimeter.

### 4.3.3 Uncertainty Analysis

Based on the Guide to the Expression of Uncertainty in Measurements (GUM), Equation (4.8), the combined standard uncertainty of the density $U_c(\rho)$ is obtained. The calculation for the overall standard uncertainty for density measurements was divided into two parts: (1) calibration uncertainty (uncertainties arise during the calibration of the VTD, these mainly come from the period of oscillation for each reference fluid and reference fluids density from the equations of state); (2) experimental uncertainty (uncertainty arise during experiments, including period of oscillation, temperature and pressure). Combining both contributions of uncertainties from calibration and experiments, the expression for the expanded uncertainty of density measurement is given in the following form:

$$U_c^2(\rho) = k^2\left\{\left[\left(\frac{\partial\rho}{\partial\tau_w}\right)u(\tau_w)\right]^2 + \left[\left(\frac{\partial\rho}{\partial\tau_H}\right)u(\tau_H)\right]^2 + \left[\left(\frac{\partial\rho}{\partial\rho_w}\right)u(\rho_w)\right]^2 + \left[\left(\frac{\partial\rho}{\partial\rho_H}\right)u(\rho_H)\right]^2 + \left[\left(\frac{\partial\rho}{\partial\tau}\right)_T u(\tau)\right]^2 + \left[\left(\frac{\partial\rho}{\partial p}\right)_T u(p)\right]^2 + \left[\left(\frac{\partial\rho}{\partial T}\right)_p u(T)\right]^2\right\} \quad (4.19)$$

Here $k$ is a coverage factor, which is the multiplier of the combined standard uncertainty in order to obtain the expanded uncertainty. The standard uncertainties from temperature, pressure and period of oscillation have been discussed above. An example of the various contributions to the uncertainty of the density measurement are given in Table 4.7 for $CO_2$ + methylbenzene at $T$ = 373.15 K, $p$ = 30 MPa and $x_{CO2}$ = 0.4. For binary mixtures measurements, the mixing uncertainty in the mole fraction was considered. The results for the pure components and binary mixtures are very similar. The standard relative uncertainty increases as temperature increases, but decreases as pressure increases, hence the largest uncertainty occurs at the highest temperature, and lowest pressure. Estimated uncertainties at 95% confidence ($k$ =2) were 0.05 K for temperature, 0.01 MPa for pressure, and 0.001$\rho$ for density. Again, the estimated uncertainty excludes the unknown effects of any sample decomposition that might have occurred during the course of the measurements.

**Table 4.7** Uncertainty budget for density for $CO_2$ + methylbenzene at the median state point in terms of standard uncertainty $u$(y) of the dimensionless parameter (y) and arising contribution $u_r(\rho)$ to the overall standard relative uncertainty of density.

| Dimensionless parameter | Value | $u$(y) | $10^2u_r(\rho)$ |
|---|---|---|---|

| | | | |
|---|---|---|---|
| $T$ / K | 373.15 | 0.03 | 0.002 |
| $p$ / MPa | 30 | 0.02 | 0.002 |
| $x$ | 0.4 | 0.00001 | 0.000 |
| $\tau$ / μs | 2615.64 | 0.01 | 0.006 |
| $(\rho_{VTD}-\rho_{EoS})_{r.m.s}$ / (kg·m$^{-3}$) | | 0.21 | 0.025 |
| Overall combined standard relative uncertainty | | | 0.035 |

# 4.4 Variable Volume Cell

A variable cell was designed and manufactured for the preparation of mixtures with fluids that are not liquid under ambient conditions. The variable volume cell acts as a high-pressure vessel which allows the preparation of a homogeneous mixture under high-pressure. It was designed according to the sound engineering practice (SEP) described in BS5500 and consists of a high-pressure vessel with the maximum working pressure of 18 MPa at temperatures up to 323.15 K. A diagram of the variable volume cell is shown in Figure 4.10. It was constructed with stainless-steel type 316 to withstand high-pressure and corrosion. The external dimensions of the vessel were 21 cm and a diameter of 6.9 cm, the maximum internal volume of the sample chamber was about 150 cm$^3$. A movable piston was located in the cylinder vessel which was divided into two compartments: one for fluid sample and the other for pressurising medium, in this case, nitrogen. Two ports, the sample injection port and the gas inlet port, are located at the top and bottom of the vessel. The gas inlet port provides a path for nitrogen to be injected and pushes the piston inside the vessel upwards, compressing the mixture at a high pressure. A magnetic stirrer bar was placed in the sample compartment to aid the mixing of the fluid sample. The variable volume cell contains three elastomer o-rings, two on the movable piston and one at the cover cap. The specifications of the o-rings are summarised in Table 4.8 below.

**Table 4.8** Specifications of the o-rings in the variable volume cell.

| | **Dimensions** | **Materials** | **Hardness** |
|---|---|---|---|
| Piston | 41.66 mm (id) x 2.40 mm (cs) | Floroelastomers (FKM) | Shore 75 |
| Cover cap | 57.60 mm (id) x 2.40 mm (cs) | Floroelastomers (FKM) | Shore 75 |

The variable volume cell was pressure-tested with water at 1.5 times of the maximum working pressure and the engineering drawings of the variable volume cell can be found in Appendix A. A schematic of the assembly of the variable volume cell is shown below:

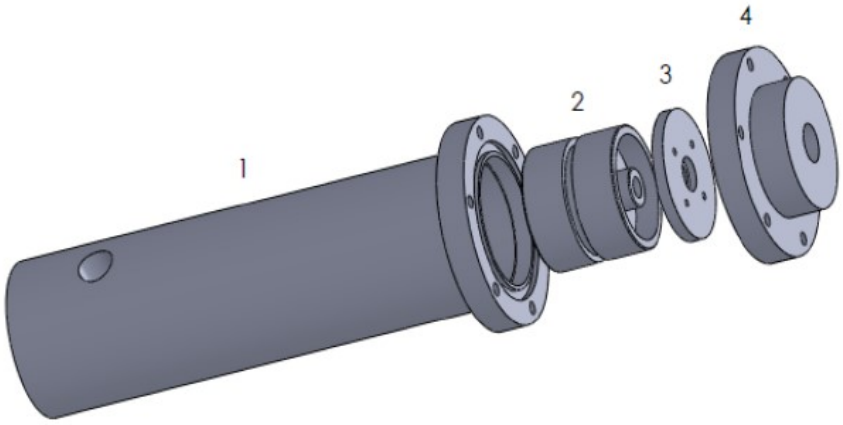



**Figure 4.10** Schematic of the variable volume cell, (1) a cylindrical body, (2) an internal piston, (3) a piston resisted screw disk and (4) a bolted cover cap. The function requires two ports which are inlet gas port and sample inlet/outlet port. Reproduced from Lin and Trusler [81].

## 4.4.1 Liquid Mixture Preparation

Preparing liquid mixtures of known composition gravimetrically is considered to provide most accurate mixtures. For liquid mixtures, the sample fluids must be maintained above bubble pressure during the preparation, for this, phase envelope or equation of state is required. Prior to any experiments, the variable volume cell was cleaned with solvent and dried under vacuum. Then, the hydrocarbon was first injected into the cell by using an HPLC pump (Knauer). After that, $CO_2$ was expanded into the cell from a high-pressure dip-tube cylinder. The mass of each component in the cell was weighed using an analytical balance (Mettler Toledo, model PR5003) with 0.005 g resolution. The mole fraction of the composition can be calculated using the following expression:

$$x_i = \left(\frac{m_i}{M_i}\right) / \left(\frac{m_i}{M_i} + \frac{m_j}{Mj}\right), \tag{4.20}$$

where $m$ is the mass and $M$ the molar mass. Subscripts $i$ and $j$ denote component 1 and 2 respectively. Since the weightings for each mixture preparation were completed within a short period during which the ambient air density was constant, buoyancy corrections have been neglected. Once the two fluids were injected into the cell, the mixture was pressurised by moving the piston with compressed nitrogen and the sample was stirred at room temperature for approximately 2 hours. Meanwhile, the measuring apparatus was cleaned with solvents, evacuated and flushed with $N_2$ several times. During transfer process from the variable volume cell to the measurement apparatus, in order to maintain the homogeneous mixture, the pressure in the variable-volume cell was kept constant by moving the piston.

### 4.4.2 Uncertainty Analysis

The experimental uncertainty that is associated with the mixture preparation is influenced by weighing errors. The binary mixtures were prepared gravimetrically, and the standard uncertainty $u_x$ of the mole fraction was calculated from the equation:

$$u_x^2 = \left[\left(\frac{\partial x}{\partial m_1}\right)u_m\right]^2 + \left[\left(\frac{\partial x}{\partial m_2}\right)u_m\right]^2, \tag{4.21}$$

where $u_m$ is the standard uncertainty of the measured mass, which is ±5 mg. Since the final mass was averaged between two weighing, $u_m = 5 \times \sqrt{2} = 7\,\text{mg}$. Only the repeatability error from the balance is considered. The calibration errors from the balance were cancelled out from subsequent weighing. From the analysis, the standard uncertainty $u_x$ was found to be $10^{-5}$.

## 4.5 Materials

The chemicals used in this work is summarised in this section. Pure deionized water used for the calibration of the speed-of-sound apparatus and the vibrating-tube densimeter was obtained from Millipore. The minimum purity of the pure water is specified to be 99.99 % by volume with an electrical resistivity of 18 MΩ.cm at $T$ = 298.15 K. Carbon dioxide and helium were supplied by BOC with a mole fraction purity higher than 0.99995 and 0.99999, respectively, and were used as supplied. All liquid hydrocarbon components were supplied by Sigma Aldrich (UK). The specified purity for *n*-pentane, *n*-heptane, *n*-nonane and methylbenzene were $x \geq 0.99$, $x \geq 0.99$, $x \geq 0.99$ and $x \geq 0.999$, respectively. The chemicals were used as supplied and no purification was attempted. The samples were degassed with and dried using molecular sieves (4Å) before the experiments. The degassing and drying methods are detailed in section 4.6 below.

**Table 4.13** Description of chemical samples, where $x$ denotes mole fraction and $\rho_e$ denotes electrical resistivity.

| Chemical | Source | Purity | Additional purification |
|---|---|---|---|
| Water | Millipore Direct-Q UV3 apparatus | $\rho_e \geq 18$ MΩ.cm at $T$ = 298.15 K | Degassed |
| Carbon dioxide | BOC (UK) | $x \geq 0.99995$ | None |
| Helium | BOC (UK) | $x \geq 0.99999$ | None |
| *n*-Pentane | Sigma Aldrich (UK) | $x \geq 0.99$ | Degassed |
| *n*-Heptane | Sigma Aldrich (UK) | $x \geq 0.99$ | Degassed |
| *n*-Nonane | Sigma Aldrich (UK) | $x \geq 0.99$ | Dried and degassed |
| Methylbenzene | Sigma Aldrich (UK) | $x \geq 0.999$ | Degassed |

## 4.6 Sample Preparation (Degassing & Drying)

The samples were ensured gas-free before introducing into the measuring apparatus. The present of gas in the samples may affect the pressure reading of the measurement. Three different types of degassing were carried out for the preparation of the samples: (1) vacuum degassing, (2) ultrasonic degassing and (3) freeze-thaw degassing. The procedures of the methods are described below. Methods (1) and (2) were generally used throughout this work, however in the case of volatile component (*n*-pentane), method (3) was used. It is also important to remove the water content present in the samples. The drying process was achieved by using molecular sieves. The molecular sieves (4 Å) were supplied by Sigma-Aldrich. Before and after use, the saturated molecular sieves were regenerated by heating to 473.15 K using a Thermo-oven.

**Vacuum Degassing:** Degassing under vacuum is suitable for non-volatile samples. The standard operating procedure is as follows: Transfer solvent in a glass bottle with a close-fitting screw cap and a dip tube through which sample could be drawn. Connect the vacuum pump via another tube through the screw cap. The end of the tube should be above the liquid level in the reservoir. Turn on vacuum and keep the reservoir under stirring for approximately 10 minutes.

**Ultrasonic Degassing:** Ultrasonic degassing is an efficient method of removing dissolved gases and entrained gas bubbles from a variety of liquids. To carry out: Fill the ultrasonic bath with de-ionised water and set at constant room temperature. Place the sample in a closed bottle and make sure the water-level in the ultrasonic bath is higher than the sample level. Turn on the ultrasound and let the sample degas for 20 minutes.

**Freeze-Thaw Degassing:** The Freeze-Thaw degassing technique is one of the most effective degassing methods and it is suitable for degassing of volatile solvents. The standard operating procedure is detailed as follows: Transfer solvent into a thick-wall sealed cylinder. Immerse the cylinder into liquid $N_2$ and allow it to freeze for about 20 minutes. Extra care should be taken as the cylinder will cause the liquid $N_2$ to boil. When the solvent is completely frozen (temperature equilibrium), connect the cylinder under vacuum for about 10 minutes with the cylinder still immersed in liquid $N_2$. Disconnect the vacuum and place the cylinder in a water bath to accelerate the melting process. Repeat the process three times.

## 4.7 Summary

This chapter summarises the apparatus used throughout this research. The experimental procedures for each experiment and the sample preparation for the binary mixtures were also described in detail. The experimental results are presented in Chapters 5, 6 and 7.

# Chapter 5: Measurements on Pure Hydrocarbons and Pure $CO_2$

## 5.1 Overview

In this chapter, the experimental results of pure hydrocarbon and pure $CO_2$ are presented. The systems studied include *n*-pentane, *n*-heptane, *n*-nonane, methylbenzene and $CO_2$. The speed-of-sound measurements for (*n*-pentane, *n*-heptane, *n*-nonane and methylbenzene) were carried out at a wide temperature and pressure range by means of an ultrasonic cell which utilises the double-path pulse-echo technique, and the density measurements for (*n*-heptane, *n*-nonane, methylbenzene and $CO_2$) were performed using a vibrating-tube densimeter. The collected experimental data were fitted with empirical correlations to within the experimental uncertainties for most of the data. The experimental data were compared with the available literature data, and comparisons with values predicted from the reference equations of state were also made. The uncertainty of each measurement has also been estimated following the guidelines from Guide to the Expression of Uncertainty to Measurement (GUM). In the cases where both speed-of-sound and density were measured for a system, a thermodynamic integration was carried out to derive a full spectrum of the observable thermophysical properties. Sound-speed and density data were combined with isobaric heat capacity data which were obtained from the literature to implement the thermodynamic integration. The thermophysical properties including density, isobaric heat capacity, isothermal compressibility and isobaric expansivity were derived up to the pressure at which sound-speed measurements were made. The derived data were compared with the predictions from the reference equations of state. This chapter should provide new experimental data which will be beneficial in improving the current reference equations of state.

## 5.2 Introduction

Although the thermophysical properties of hydrocarbons have been studied extensively, there remain significant gaps in the literature for high-temperature and high-pressure (HTHP) conditions. Experimental thermophysical properties data provided in this work not only will help to fill in knowledge gaps in academic research, but they are also essential in the development of better theoretical models. Experimental data collected over a wide temperature and pressure range of interest are used to validate existing thermodynamic models, which then can be used to predict thermophysical properties for all conditions for different applications. It is of great importance to have reliable data in order to develop accurate models. By utilising new and highly accurate experimental data, current equations of state and thermodynamic models can be improved through optimisation.

## 5.3 Experimental Uncertainty

The uncertainty of the density and speed-of-sound measurements was estimated following the approach suggested by the Guide to the Expression of Uncertainty in Measurement (GUM) [369] given by the expression below:

$$u_c^2(f) = \sum_{i=1}^{n}\sum_{j=1}^{n} \frac{\partial f}{\partial x_i}\frac{\partial f}{\partial x_j} u(x_i, x_j). \tag{5.1}$$

This expression takes into account both uncertainties rose during calibration and experiment. The explanation of the uncertainty calculation and examples of the uncertainty budget are provided in Chapter 4. For density, the expanded uncertainties at 95 % confidence for density measurements, $U_c(\rho)$ was calculated to be approximately 0.6 $kg \cdot m^{-3}$ over the region of temperature and pressure investigated for the pure hydrocarbons measurements. The expanded uncertainty for $CO_2$ measurements was found to be slightly higher with a value of approximately 0.9 $kg \cdot m^{-3}$. Therefore the expanded relative uncertainty for *n*-heptane, *n*-nonane and methylbenzene ranges from (0.06 to 0.12) % and (0.1 to 0.3) % for $CO_2$, respectively. For speed-of-sound measurements, the expanded standard uncertainty $U_c(c)$ varies between (0.4 and 0.8) $m \cdot s^{-1}$ over the temperature and pressure range investigated with a coverage factor of $k = 2$. Therefore the expanded relative standard uncertainty ranges from (0.04 to 0.12) % for speed-of-sound measurements for *n*-pentane, *n*-heptane, *n*-nonane and methylbenzene. The relative uncertainties increase as temperature increases, but decrease as pressure increases; hence the largest uncertainty state points occur at the highest temperature and lowest pressure.

# 5.4 *n*-Pentane

This section gives the results of the speed-of-sound measurements made over the temperature range of (263.20 to 473.15) K at pressures up to 390 MPa. The experimental data were fitted by a pressure-explicit correlation which covers a wide range of temperatures and pressures. A comparison between the present speed-of-sound data and the literature data is given. The experimental results were also compared with the predictions from SAFT-γ Mie equation of state.

## 5.4.1 Literature Review

Most speed-of-sound data for *n*-pentane reported in the literature are restricted to atmospheric pressure. One of the earliest studies was carried out by Richardson and Tait [138] who conducted the sound-speed measurements in liquid *n*-pentane at temperatures between (288 and 317) K and at pressures up to 55 MPa. The study of Otpushchennikov *et al.* [107] extends over a wider temperature range of (303 to 393) K with pressures up to 196 MPa. Lainez *et al.* [72] further extend the experimental range with pressures up to 210 MPa and at temperatures between (263 and 433) K using a pulse-echo-overlap method operated at 3 MHz. The highest pressure sound-speed data were reported by Zotov *et al.* [109], they measured at temperatures between (303 and 433) K at pressures up to 500 MP. Ding *et al.* [110] obtained sound-speeds on five isotherms between (293 and 373) K and pressures up to 100 MPa. The latest study on the speed-of-sound in *n*-pentane was carried out by Tahani [111], he measured the sound-speed from (298 to 333) K and at pressures up to 35 MPa. Details of other studies reporting the speed-of-sound in *n*-pentane can be found in Table 2.1 in Chapter 2. The current reference equation of state for *n*-pentane was developed by Span and Wagner and the specified uncertainty for the speed-of-sound predictions is 2% up to 100 MPa.

## 5.4.2 Experimental Speed-of-Sound Results and Discussion

Speed-of-sound measurements in *n*-pentane were made across eleven isotherms: $T$ = (263.20, 273.15, 283.15, 298.15, 323.15, 348.15, 373.15, 398.15, 423.15, 448.15, and 473.15) K and at pressures up to 390 MPa. The experimental data were tabulated in Table B.1 in Appendix B and sound-speeds as a function of pressure is shown in Figure 5.1. Due to a wide range of temperatures and pressures studied for the speed-of-sound measurements, it was essential to have knowledge of the phase envelopes of *n*-pentane to avoid any phase change before the experiments. It was important to verify both the saturation and freezing phase boundaries in order to determine if they impacted on the overall measurement range. The saturation and freezing curves were predicted using the reference equation of state for *n*-pentane, and the calculations were performed in NIST REFPROP 9.1 software [358]. The starting measurement points were pushed to 10 MPa at higher temperature isotherms to avoid phase change in the sample. Similarly, the maximum pressure was limited to 300 MPa for isotherms below 273.15 K to avoid freezing of the sample.

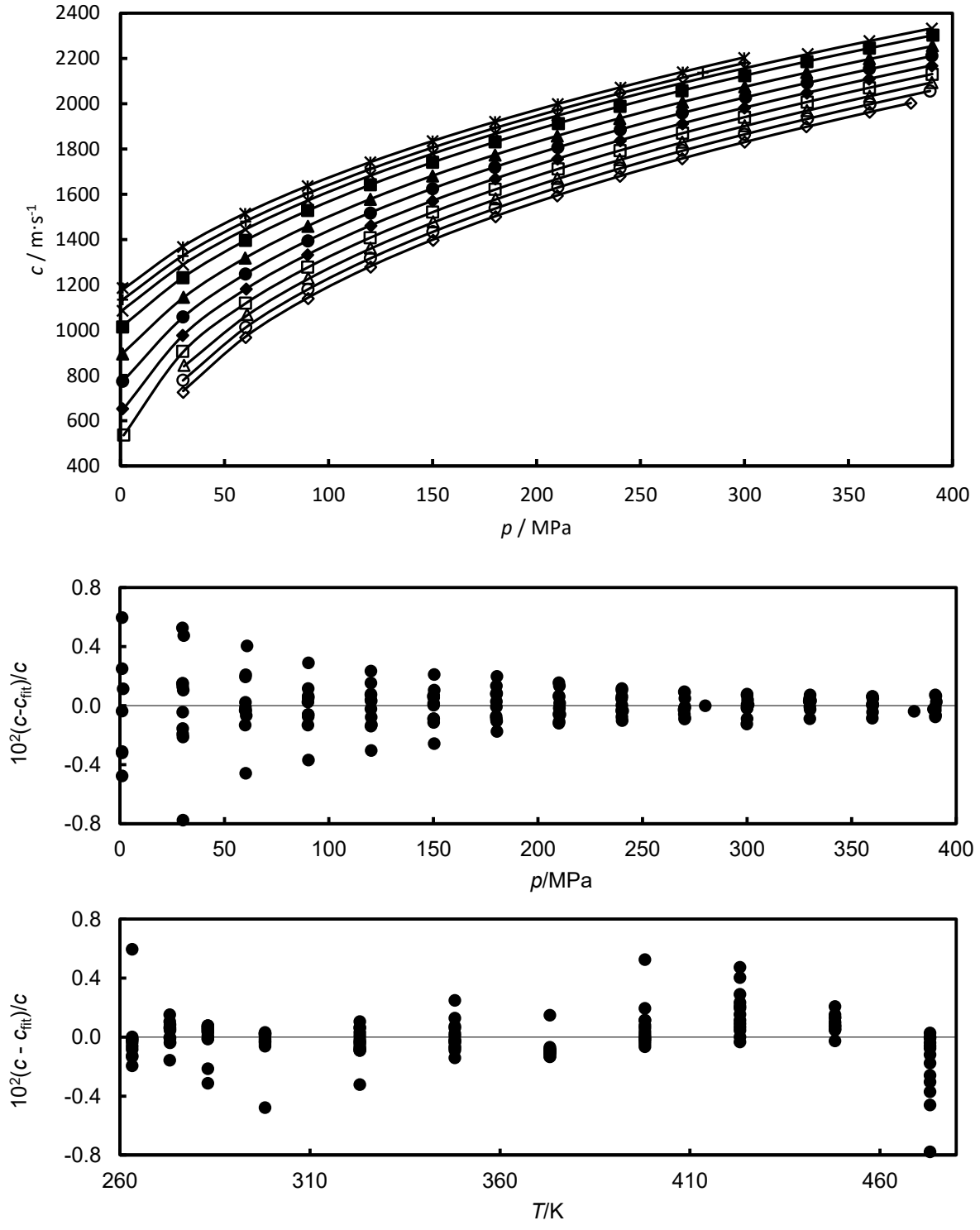



**Figure 5.1** (*top*) Experimental sound-speed $c$ in *n*-pentane as a function of pressure across 11 isotherms: ∗, 263.20 K; +, 273.15 K; ×, 283.15 K; ■, 298.15 K; ▲, 323.15 K; ●, 348.15 K; ◆, 373.15 K; □, 398.15 K; △, 423.15 K; ○, 448.15 K; ◇, 473.15 K. Solid lines represent sound-speeds calculated from the empirical correlation. (*bottom*) Deviations of the experimental speed-of-sound in *n*-pentane from the values $c_{fit}$ calculated from the empirical correlation as a function of pressure and temperature.

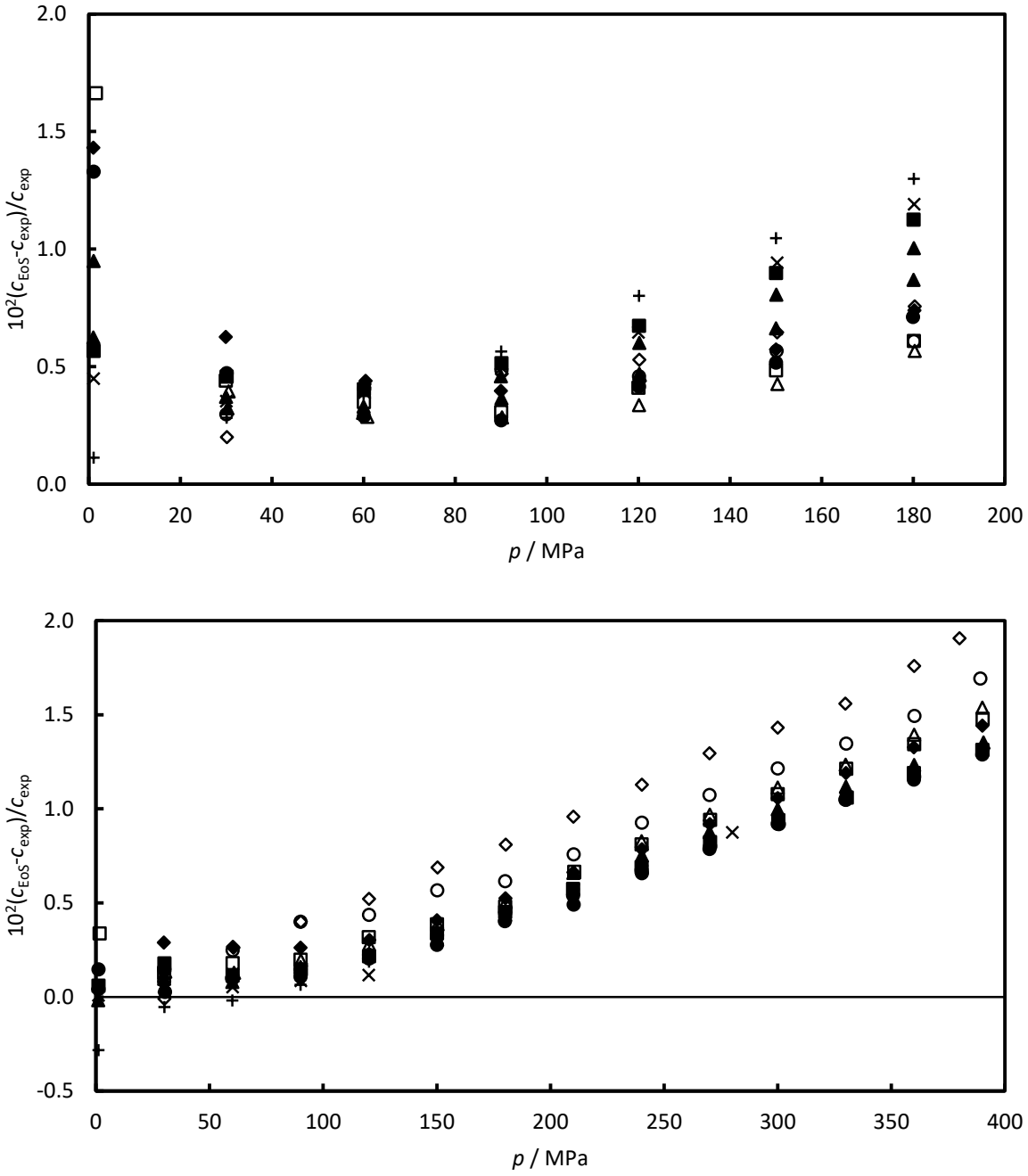



**Figure 5.2** Deviations between the experimental sound-speed $c_{exp}$ in *n-p*entane and predictions calculated from two equations of state $c_{EoS}$. (*top*) Original EoS developed by Span and Wagner [375-377]; (*bottom*) New EoS. Symbols represent experimental data: ＋, 273.15 K; ×, 283.15 K; ■, 298.15 K; ▲, 323.15 K; ●, 348.15 K; ◆, 373.15 K; □, 398.15 K; △, 423.15 K; ○, 448.15 K; ◇, 473.15 K.

The experimental sound-speed in *n*-pentane was compared with the values calculated from two sets of equations of state. The first one was developed by Span and Wagner [375-377] for *n*-pentane and the predictions were limited to 180 MPa. The second reference equation of state was taken from an on-going work carried out the Span and co-workers. Hereby, we refer the second EoS as the new EoS. The deviations between the experimental data and the calculated values using both equations of state are shown in Figure 5.2. It can be seen that the new EoS is able to predict the sound-speed more accurately at the low-pressure region compared to the predictions from the original EoS; the deviations of the experimental data are within 0.5 % up to 100 MPa. The average absolute relative deviation ($\Delta_{AARD}$) was calculated to be 0.6 % between the experimental data and the predictions. The speeds-of-sound in *n*-pentane measured in this work were also compared with the datasets reported by several authors in the literature as shown in Figure 5.3. Most sound-speed data were published at pressures below 100 MPa, and hereby a brief comparison was made only with the high-pressure data reported by four authors. It can be seen in Figure 5.3 that the present data have better agreements with the literature data at low temperatures. Our data have the best agreement with the experimental data reported by Otpushchennikov *et al.* and Lainez *et al.* [72, 107], both with an $\Delta_{AARD}$ of less than 0.2 %.

**Correlation:** The speeds-of-sound in *n*-pentane were fitted into an empirical correlation which covers the whole range of temperatures and pressures investigated. The pressure explicit sound-speed correlation is given in the following form:

$$(p - p_0)/\mathrm{MPa} = \sum_{i=1}^{3}\sum_{j=0}^{3} a_{ij} \left\{(c - c_0)/\left(\mathrm{m \cdot s^{-1}}\right)\right\}^i \left(\frac{T_0}{T}\right)^j , \tag{5.2}$$

where $p_0$, $T_0$ and $c_0$ are the initial pressure, temperature and sound-speed, respectively. The terms $p_0$ and $T_0$ were set to 0.1 MPa and 273.15 K, respectively. The quantity $c_0$ was then correlated as a function of temperature as follows:

$$c_0 \,/\left(\mathrm{m \cdot s^{-1}}\right) = \sum_{i=0}^{3} b_i \left(\frac{T}{T_0}\right)^i \tag{5.3}$$

The goodness of the surface fit was measured by means of the absolute average relative deviation ($\Delta_{AARD}$) and the maximum absolute relative deviation ($\Delta_{MARD}$) in the following forms:

$$\Delta_{AARD,X} = \frac{1}{N}\sum_{i=1}^{N}\left|\frac{X_i - X_{i,\mathrm{fit}}}{X_i}\right| \times 100 \qquad \text{and} \qquad \Delta_{MARD,X} = \mathrm{MAX}\left(\frac{1}{N}\sum_{i=1}^{N}\left|\frac{X_i - X_{i,\mathrm{fit}}}{X_i}\right| \times 100\right) \tag{5.4}$$

Here $X_i$ denotes the experimental data, $X_{fit}$ the value obtained from the correlation at the corresponding state point and $N$ is the number of points.

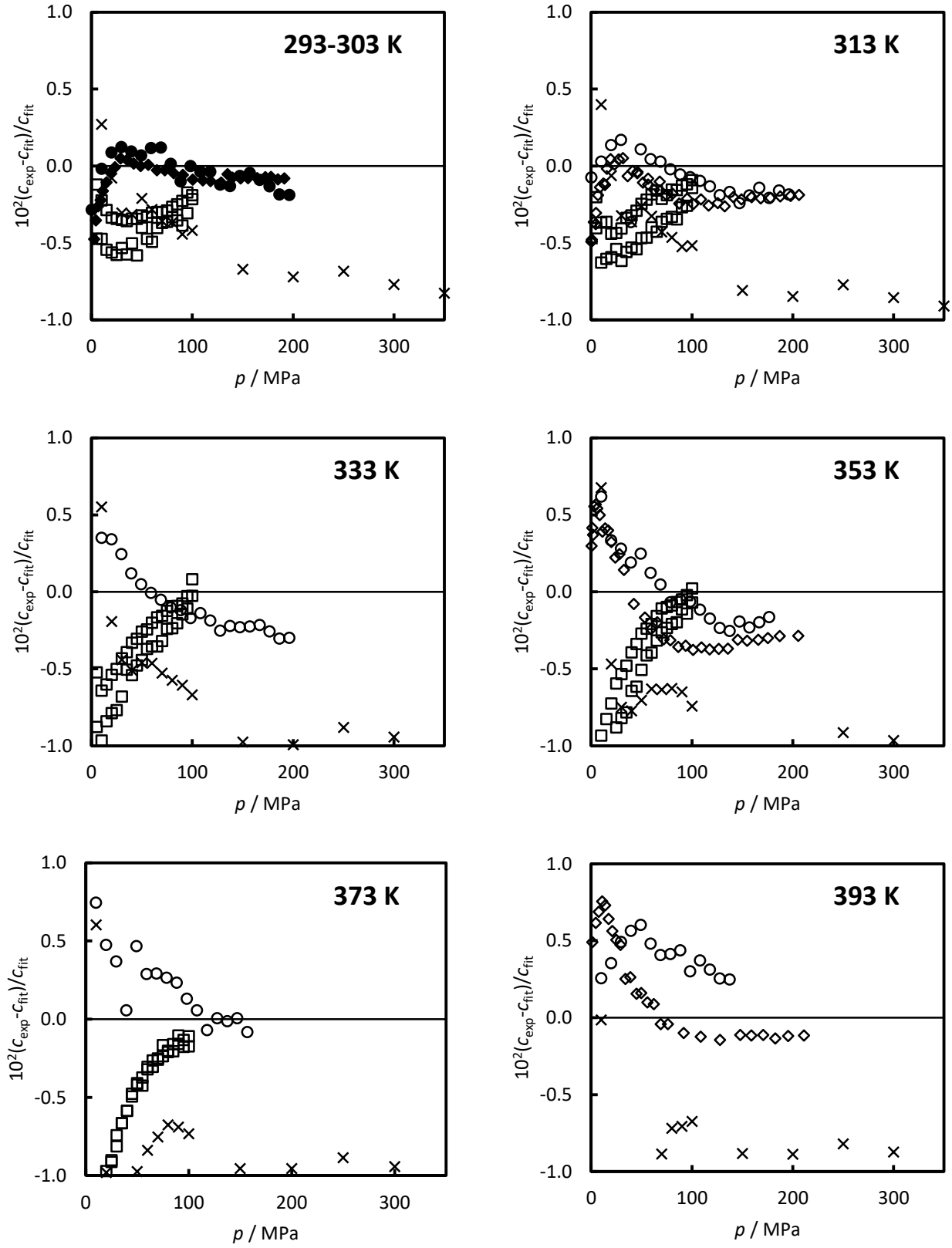



**Figure 5.3** Comparison between experimental sound-speed from literature $c_{exp}$ in *n*-pentane and values calculated from the empirical correlation, Equation (5.2) $c_{fit}$ at six isotherms. Symbols represent experimental data: □, Ding *et al.* [110]; ○ and ●, Otpushchennikov *et al.* [107]; ×, Zotov *et al.* [109]; ◇ and ◆, Lainez *et al.* [72]

The statistical measures, $\Delta_{AARD}$ and $\Delta_{MARD}$ between the experimental data and the values calculated with the correlation were found to be 0.1 % and 0.9 %, respectively. The deviation plots as a function of temperature and pressure are shown in Figure 5.1. In general, the correlation is able to correlate most of the experimental sound-speed data across a wide range of temperature and pressure within the overall standard uncertainty. The outliers are mostly in the low-pressure region, where speeds-of-sound exhibit a non-linear behaviour. The parameters in equations (5.2) and (5.3) are given in Table 5.1.

**Table 5.1** Fitting parameters of the empirical correlation, Equation (5.2) for the speed-of-sound measurements in *n*-pentane together with the statistical parameters, average absolute relative deviation $\Delta_{AARD}$ and maximum absolute relative deviation $\Delta_{MARD}$.

| | | | | | | | | | |
|---|---|---|---|---|---|---|---|---|---|
| $a_{10}$ | $5.834\times10^{-1}$ | $a_{20}$ | $-1.152\times10^{-3}$ | $a_{30}$ | $5.583\times10^{-7}$ | $b_0$ | $1340\times10^{-3}$ | $\Delta_{AARD}$ | 0.10% |
| $a_{11}$ | -2.716 | $a_{21}$ | $4.504\times10^{-3}$ | $a_{31}$ | $-2.179\times10^{-6}$ | $b_1$ | $1.301\times10^{3}$ | | |
| $a_{12}$ | 4.000 | $a_{22}$ | $-5.554\times10^{-3}$ | $a_{32}$ | $2.933\times10^{-6}$ | $b_2$ | $-2.009\times10^{3}$ | $\Delta_{MARD}$ | 0.88% |
| $a_{13}$ | -1.747 | $a_{23}$ | $2.333\times10^{-3}$ | $a_{33}$ | $-1.290\times10^{-6}$ | $b_3$ | $4.952\times10^{2}$ | | |

## 5.4.4 Modelling

Predicting second derivative property such as the speed-of-sound is a rigorous test for any thermodynamic model, and high deviations are to be expected with most equations of state. In this work, the predictive capability of SAFT-γ Mie on the speed-of-sound was tested with the experimental data for *n*-pentane. The structure and method of SAFT-γ Mie have been described previously in Chapter 3 and only a brief reference is made here for the particular function groups of the *n*-pentane system. As mentioned in Papaioannou *et al.* [351], the parameters for the *n*-alkanes chemical family which includes methyl ($CH_3$) and methylene ($CH_2$) functional groups, were estimated from experimental data for vapour pressure, saturated-liquid density and single-phase density of linear alkanes from ethane to *n*-decane. The parameters for the function groups $CH_3$ and $CH_2$ are summarised in Table 5.2. The deviation plot between the experimental data and the predictions is shown in Figure 5.4. The deviations increase with pressure and the $\Delta_{AARD}$ between the predictions and the experimental data was calculated to be 1.6 % across all temperatures and pressures.

**Table 5.2** SAFT-γ Mie like parameters for functional groups $CH_3$ and $CH_2$, $v_k^*$ the number of segments, $S_k$ the shape factor, $\varepsilon_{kk}$ the interaction energy, $\sigma_{kk}$ the segment diameter, and $\lambda_{kk}^{r}$ and $\lambda_{kk}^{a}$ the repulsive and attractive exponents, respectively.

| Functional Group | $v_k^*$ | $S_k$ | $(\varepsilon_{kk}/k_B)$/K | $\sigma_{kk}\times10^{10}$/m | $\lambda_{kk}^{r}$ | $\lambda_{kk}^{a}$ | Ref. |
|---|---|---|---|---|---|---|---|
| $CH_3$ | 1 | 0.5725 | 256.77 | 4.077 | 15.050 | 6.000 | [350] |
| $CH_2$ | 1 | 0.2293 | 473.39 | 4.880 | 19.871 | 6.000 | [350] |

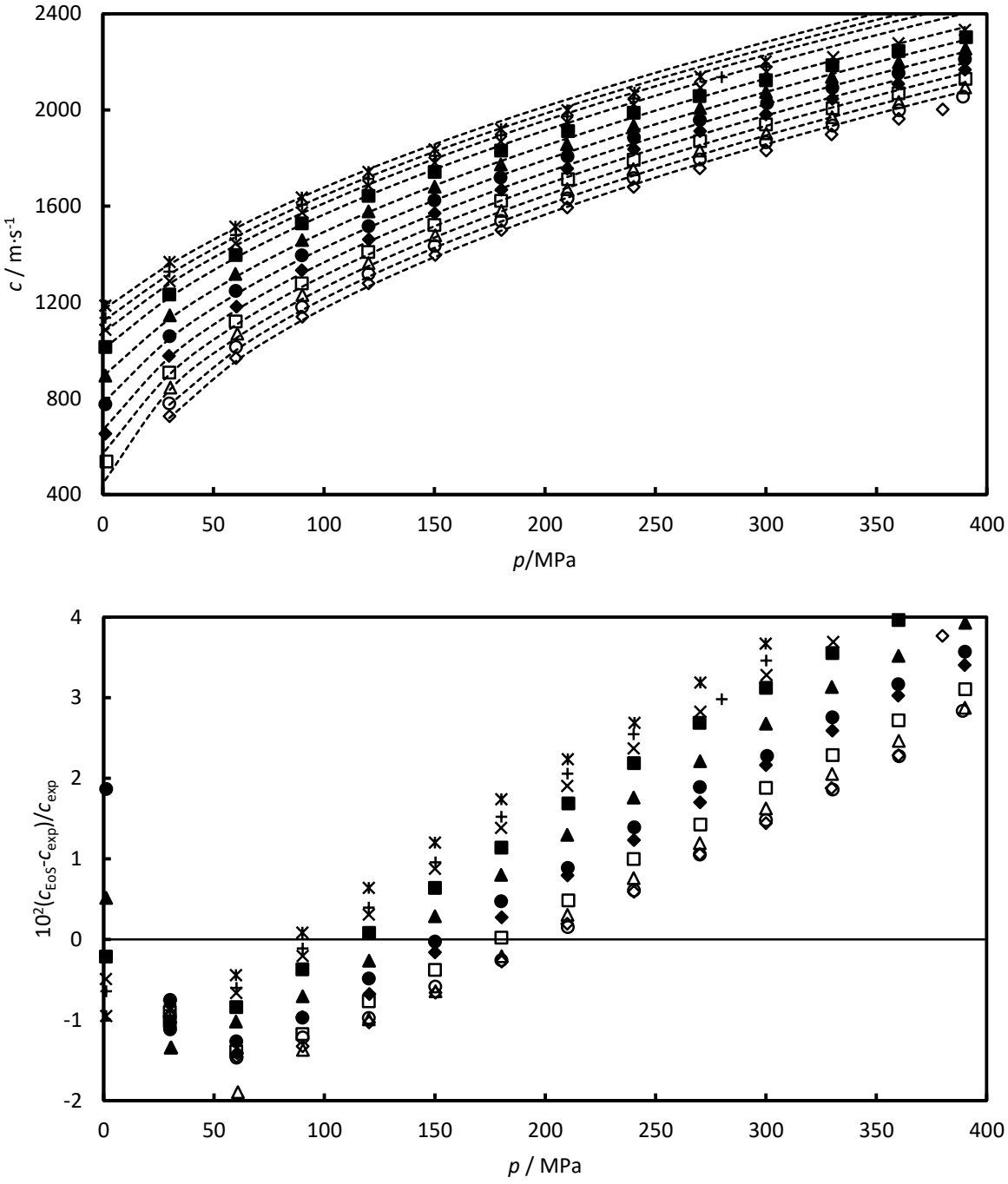



**Figure 5.4** (*top*) Comparison between experimental speed-of-sound in *n*-pentane and values calculated with SAFT-γ Mie EoS. Dotted lines represent predictions. (*bottom*) Deviations between the experimental speed-of-sound $c_{exp}$ and predictions from SAFT-γ Mie EoS $c_{EoS}$ across ten isotherms. Symbols: ∗, 263.20 K; +, 273.15 K; ×, 283.15 K; ■, 298.15 K; ▲, 323.15 K; ●, 348.15 K; ◆, 373.15 K; □, 398.15 K; △, 423.15 K; ○, 448.15 K; ◇, 473.15 K.

# 5.5 *n*-Heptane

This section gives the results of the density measurements made for *n*-heptane over a temperature range of (283.15 to 473.15) K and for pressures up to 68 MPa. In conjunction, the results of the speed-of-sound measurements made over temperature ranges of (283.15 to 473.15) K at pressures up to 180 MPa are also presented. A comparison between the present density and speed-of-sound data and literature data was made. The experimental results were also compared with the predictions from the reference equation of state and the SAFT-γ Mie model. In the final part of this section, the experimental sound-speed and density data were combined with isobaric heat capacities to obtain a full spectrum of thermophysical properties via thermodynamic integration.

## 5.5.1 Literature Review

An extensive literature review on the density and speed-of-sound in *n*-heptane has been carried out and hereby the results of the review are presented. Many authors have reported the density of *n*-heptane and the amount of available data is abundant in the literature. In this work, a brief comparison of the new densities of *n*-heptane with the available measurements of several experimental groups is presented. Schillings *et al.* [209] measured the density of *n*-heptane at temperatures between (233.15 and 473.15) K and at pressures up to 30 MPa using a single-sinker densimeter. Lampreia and Nieto de Castro [189] measured the density of *n*-heptane at temperatures between (283.15 and 323.15) K at pressures up to 60 MPa using a vibrating-tube densimeter. Alaoui *et al.* [202] reported density data at pressures up to 140 MPa and at temperatures from (298.15 to 393.15) K. Other studies reporting the densities of *n*-heptane can be found in Table 2.4 in Chapter 2. Several authors have reported the speed-of-sound in *n*-heptane at atmospheric temperature and pressure. Examples of the atmospheric speed-of-sound datasets of *n*-heptane can be found in these studies [109, 378]. Boelhouwer [86] studied the largest temperature range ranging from (253.15 to 453.15) K and at pressures up to 140 MPa using a pulse technique. Daridon *et al.* [69] extended the studied pressure range to 150 MPa and at temperatures ranging from (293 to 373) K. Dzida *et al.* [124] reported the sound-speed in *n*-heptane at temperatures between (293 and 318) K at pressures up to 90 MPa. Muringer *et al.* [93] measured the sound-speed in *n*-heptane at elevated pressures between (185 and 310) K. The most recent data was published by Hasonov [128] who studied the speed-of-sound at pressures up to 60 MPa and temperatures up to 523.15 K. Other speed-of-sound studies are also listed in Table 2.1 in Chapter 2. *n*-Heptane shares the same reference equation of state as *n*-pentane which was developed by Span and Wagner for several non-polar fluids [375-377]. The specified uncertainties for the liquid density and speed-of-sound are 0.5 %and 2 %, respectively at temperatures up to 600 K and at pressures up to 100 MPa.

## 5.5.2 Experimental Density Results and Discussion

The compressed-liquid density of *n*-heptane has been measured at temperatures between (283.15 and 473.15) K at pressures up to 68 MPa. Experimental density as a function of pressure is given in Table B.2 in Appendix B and illustrated in Figure 5.5. All of the measurements were made in the liquid phase, hence the starting pressures at which the density measurements were made increased with increasing temperature. As expected, the results show a standard behaviour for the liquid state density: the densities increase with pressure and decrease with temperature. The experimental results were compared with the predictions from the reference equation of state developed by Span and Wagner [375-377], and deviation plot is shown in Figure 5.6. It can be seen that our data agree well with the predictions to within ±0.4 % which is smaller than the specified tolerance of the EoS of 0.5 % at high temperatures. There are many sets of reported density data for *n*-heptane, only a brief comparison of our new experimental data and the available measurements of other experimental groups is presented. The deviation plots between the experimental measurements collected in this work and literature data can be found in Figure 5.7. Most of the new density data agree with the literature data to within ±0.1 % at temperatures up to 393.15 K. The new experimental data has the best agreement with the data reported by Schilling *et al.* [209] which is considered as the most reliable dataset with the specified uncertainty of 0.02 %; the $\Delta_{AARD}$ between both datasets was calculated to be 0.05 %.

**Correlation:** The modified Tait equation was chosen to represent experimental density due to the fact that it is widely used and it can accurately describe density over a wide temperature and pressure range [176-178]. It also has the advantage of being accurate for extrapolation of densities to pressures greater than the experimental range. The modified Tait equation is given in the following form:

$$\rho = \rho_0 \left[ 1 - C \log_{10} \left( \frac{p + B}{p_0 + B} \right) \right]^{-1}, \tag{5.5}$$

where $\rho_0$ is the density at a reference pressure, $p_0$ = 0.1 MPa; $C$ is a temperature-independent constant and $B$ is a temperature-dependent parameter. Parameters $\rho_0$, $B$ and $C$ were adjusted such that the absolute difference between the experimental data and the ones calculated by the correlations was minimised. To allow interpolation between temperatures, $\rho_0$ and $B$ were further correlated as functions of temperature as follows:

$$\rho_0 \,/\left(\mathrm{kg \cdot m^{-3}}\right) = \sum_{i=0}^{3} a_i \left( \frac{T}{T_0} \right)^i, \tag{5.6}$$

$$B \,/\,\mathrm{MPa} = \sum_{i=0}^{3} b_i \left( \frac{T}{T_0} \right)^i, \tag{5.7}$$

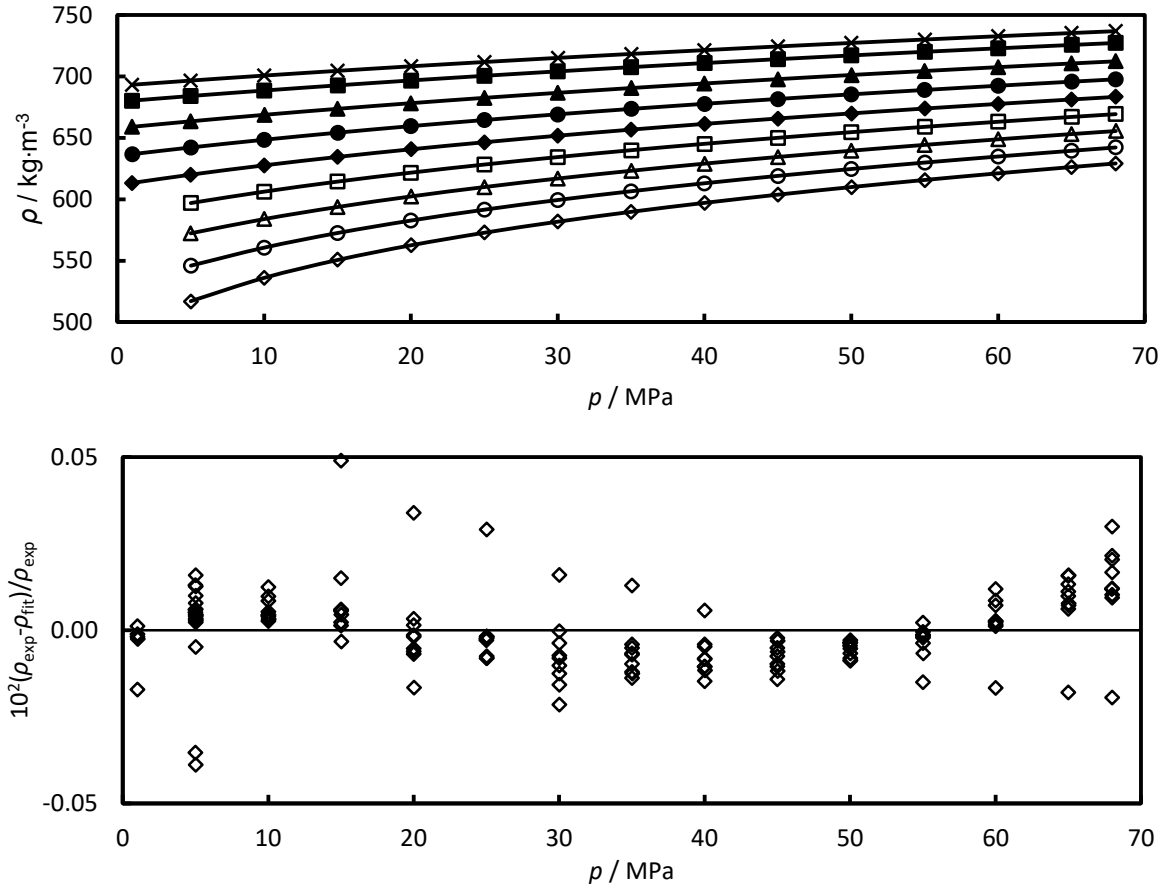



**Figure 5.5** (*top*) Experimental density $\rho$ of *n*-heptane as a function of pressure across nine isotherms: ×, 283.15 K; ■, 298.15 K; ▲, 323.15 K; ●, 348.15 K; ◆, 373.15 K; □, 398.15 K; △, 423.15 K; ○, 448.15 K; ◇, 473.15 K. Solid lines represent densities calculated from the modified Tait equation. (*bottom*) Deviations between the experimental densities $\rho_{exp}$ and the values calculated using the Tait equation $\rho_{fit}$.

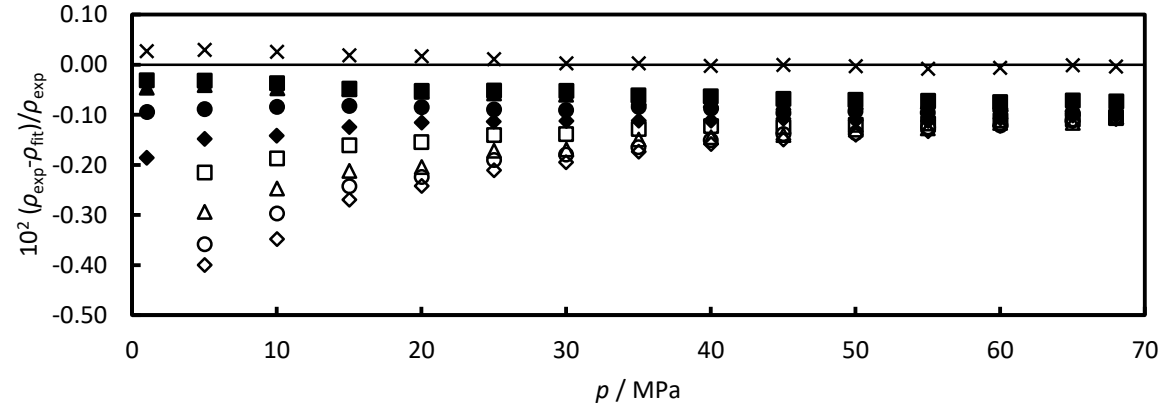



**Figure 5.6** Deviations between the experimental densities $\rho_{exp}$ from the calculated densities using the *n*-heptane equation of state $\rho_{EoS}$ across nine isotherms. Symbols: ×, 283.15 K; ■, 298.15 K; ▲, 323.15 K; ●, 348.15 K; ◆, 373.15 K; □, 398.15 K; △, 423.15 K; ○, 448.15 K; ◇, 473.15 K.

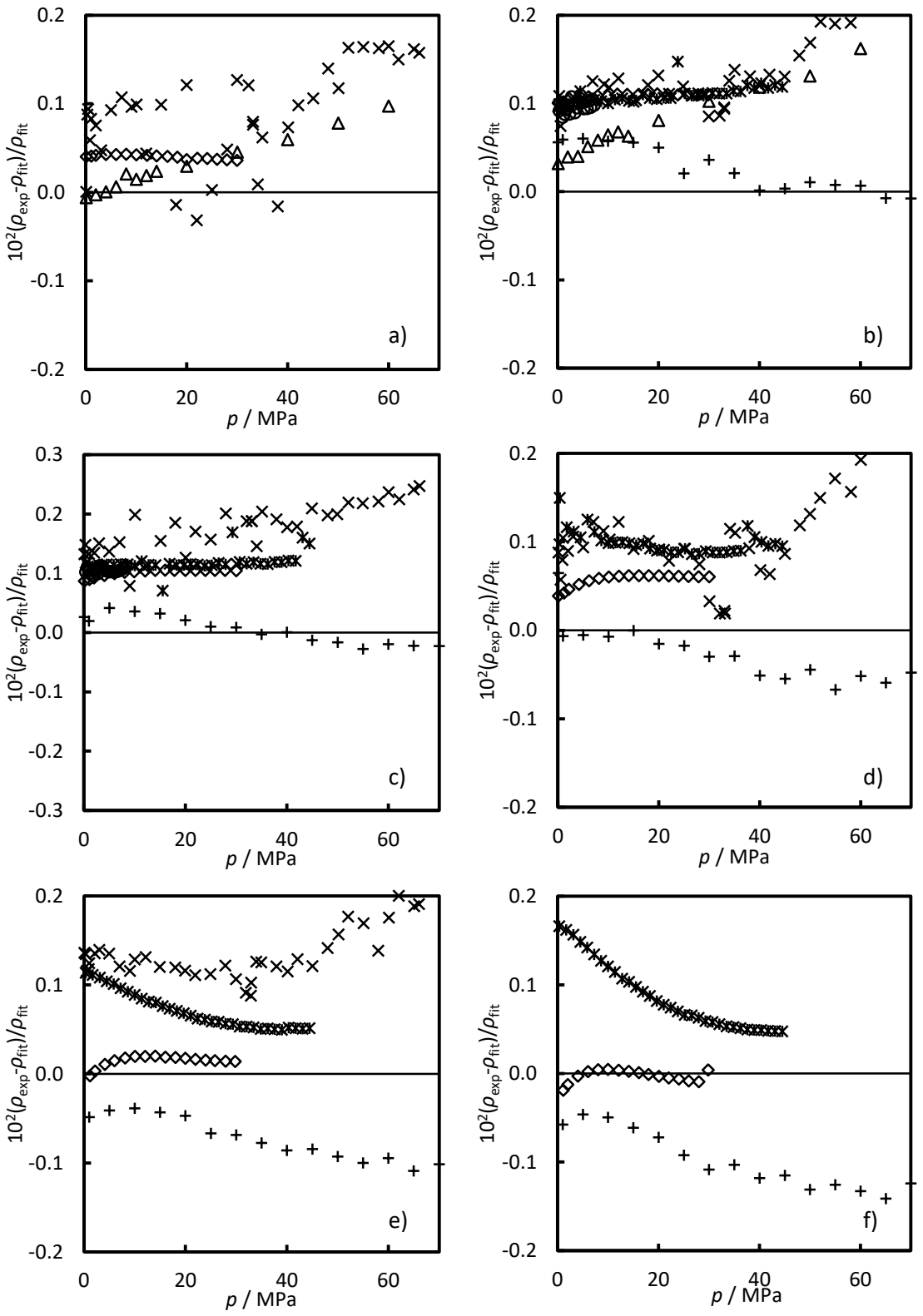



**Figure 5.7** Deviation plots between the experimental density from the literature $\rho_{exp}$ and values calculated using the modified Tait equation, Equation (5.5) $\rho_{fit}$ for $CO_2$ + *n*-heptane. a) 293.15 K; b) 313.15 K; c) 333.15 K; d) 353.15 K; e) 373.15 K; f) 393.15 K. Symbols represent literature data: ◇, Schilling *et al.* [209]; △, Lampreia and Nieto de Castro [189]; ×, Iglesias *et al.* [201]; ∗, Haghbakhsh *et al.* [200]; □, Alaoui *et al.* [202]

where $T_0$ is the reference temperature, which was set at 273.15 K in this work. At temperatures above 373.15 K, $\rho_0$ is a hypothetical liquid density when the temperature exceeds the boiling temperature at $p$ = 0.1 MPa. The goodness of the surface fit was measured by means of the $\Delta_{AARD}$ and $\Delta_{MARD}$. The statistical measures and the parameters of the modified Tait equation are given in Table 5.3; they compare favourably with the relative uncertainty of the data. Equation (5.5) fitted the experimental data to approximately ±0.1 kg·m$^{-3}$ which is equivalent to an $\Delta_{AARD}$ of about 0.01 %, and the $\Delta_{MARD}$ was found to be 0.05 %.

**Table 5.3** Fitting parameters of the modified Tait equation, Equation (5.5) for the compressed-liquid density measurements of *n*-heptane together with the statistical parameters, $\Delta_{AARD}$ and $\Delta_{MARD}$.

| | | | | | |
|---|---|---|---|---|---|
| $a_0$ | 1212.54 | $b_0$ | 345.81 | $C$ | 0.20 |
| $a_1$ | -955.23 | $b_1$ | -405.92 | | |
| $a_2$ | 626.96 | $b_2$ | 151.87 | $\Delta_{AARD}$ | 0.01% |
| $a_3$ | -182.66 | $b_3$ | -17.82 | $\Delta_{MARD}$ | 0.05% |

## 5.5.3 Experimental Speed-of-Sound Results and Discussion

Experimental sound-speed in *n*-heptane was measured at temperatures between (283.15 and 473.15) K and pressures up to 180 MPa and is given in Table B.3 in Appendix B. Figure 5.8 shows the experimental sound-speed across nine isotherms as a function of pressure. The collected sound-speed data were also compared with the predictions from the reference equation of state developed by Span and Wagner [375-377]. It can be seen in Figure 5.8 that most of the predictions from EoS deviate from the experimental data within a band of ±0.5 %. However, the deviations are consistent with the specified tolerance in the EoS of 2 % at pressures up to 100 MPa. The experimental sound-speed data were also compared with the available literature data as shown in Figure 5.9. It can be noticed that our data have the best agreement with data from Daridon *et al.* [69] with an $\Delta_{AARD}$ of 0.10 % who measured the sound-speed in *n*-heptane with a single-path pulse technique and the data were considered accurate up to 0.10 %.

**Correlation:** The sound-speed experimental data were fitted by a least squares analysis to an empirical correlation which covers the whole range of temperatures and pressures, given by Equation (5.2). The term $c_0$ was also correlated with a polynomial equation as a function of temperature, Equation (5.3). The parameters in Equations (5.2) and (5.3) and the statistical measures $\Delta_{AARD}$ and $\Delta_{MARD}$ are tabulated in Table 5.4. The deviation plot of experimental data against values calculated from the correlation is illustrated in Figure 5.8. In general, the correlation describes the sound-speed experimental data well across a wide range of temperatures and pressures with the $\Delta_{AARD}$ consistent with the overall standard uncertainty.

**Table 5.4** Fitting parameters of the empirical correlation, Equation (5.2) for the speed-of-sound measurements in *n*-heptane together with the statistical parameters, average absolute deviation, $\Delta_{AARD}$ and maximum absolute deviation $\Delta_{MARD}$.

| | | | | | | | | | |
|---|---|---|---|---|---|---|---|---|---|
| $a_{10}$ | -1.229 | $a_{20}$ | $1.055\times10^{-3}$ | $a_{30}$ | $-1.111\times10^{-6}$ | $b_0$ | $4.029\times10^{3}$ | $\Delta_{AARD}$ | 0.05% |
| $a_{11}$ | 4.491 | $a_{21}$ | $-4.343\times10^{-3}$ | $a_{31}$ | $4.709\times10^{-6}$ | $b_1$ | $-4.938\times10^{3}$ | | |
| $a_{12}$ | -5.284 | $a_{22}$ | $6.266\times10^{-3}$ | $a_{32}$ | $-6.416\times10^{-6}$ | $b_2$ | $2.866\times10^{3}$ | $\Delta_{MARD}$ | 0.26% |
| $a_{13}$ | 2.184 | $a_{23}$ | $-2.872\times10^{-3}$ | $a_{33}$ | $2.876\times10^{-6}$ | $b_3$ | $-7.120\times10^{2}$ | | |

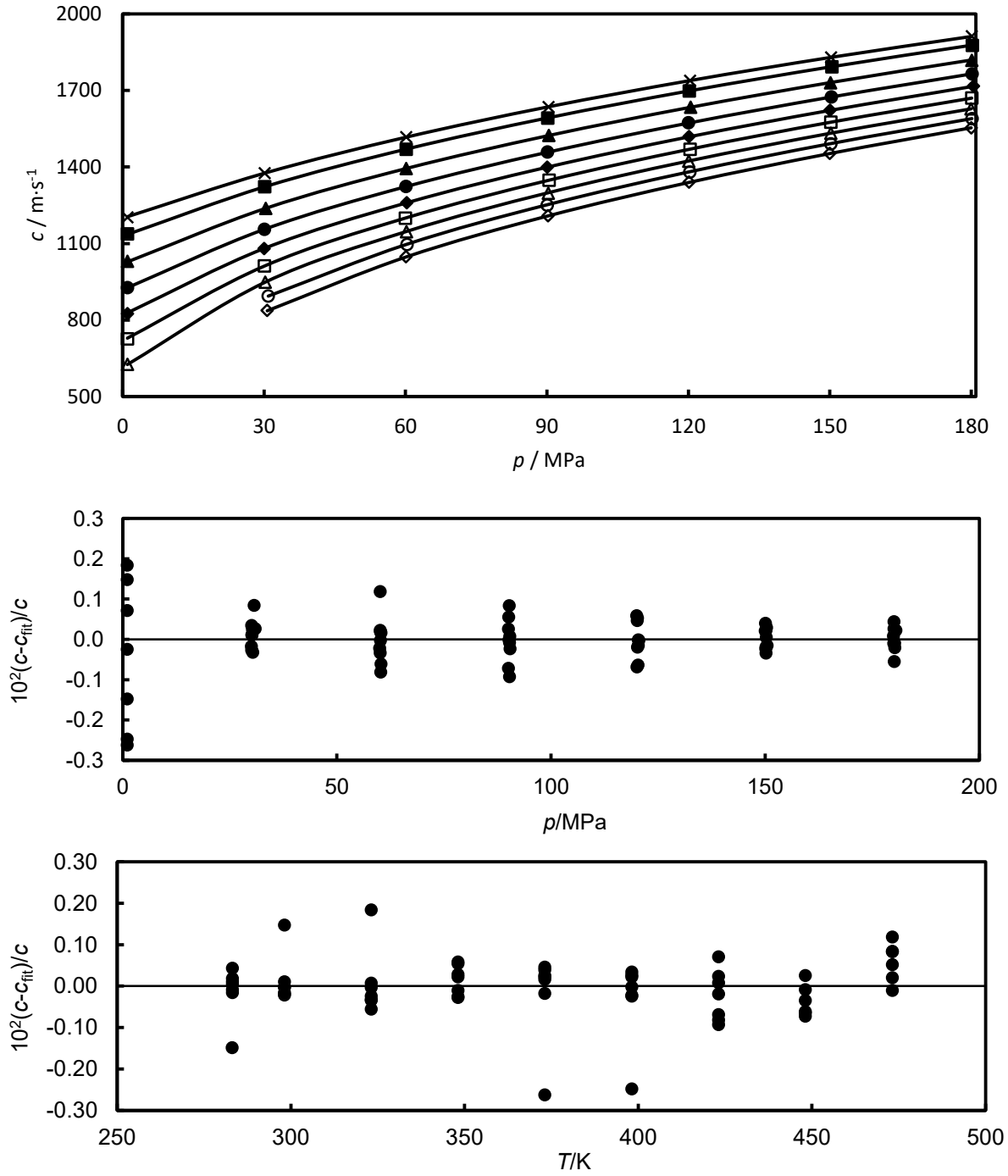



**Figure 5.8** (*top*) Experimental sound-speeds $c$ in *n*-heptane as a function of pressure across nine isotherms: ×, 283.15 K; ■, 298.15 K; ▲, 323.15 K; ●, 348.15 K; ◆, 373.15 K; □, 398.15 K; △, 423.15 K; ○, 448.15 K; ◇, 473.15 K. Solid lines represent sound-speeds calculated from the pressure-explicit correlation, Equation (5.2). (*bottom*) Deviations of the experimental speed-of-sound in *n*-heptane from the values $c_{fit}$ calculated from the empirical correlation as a function of pressure and temperature.

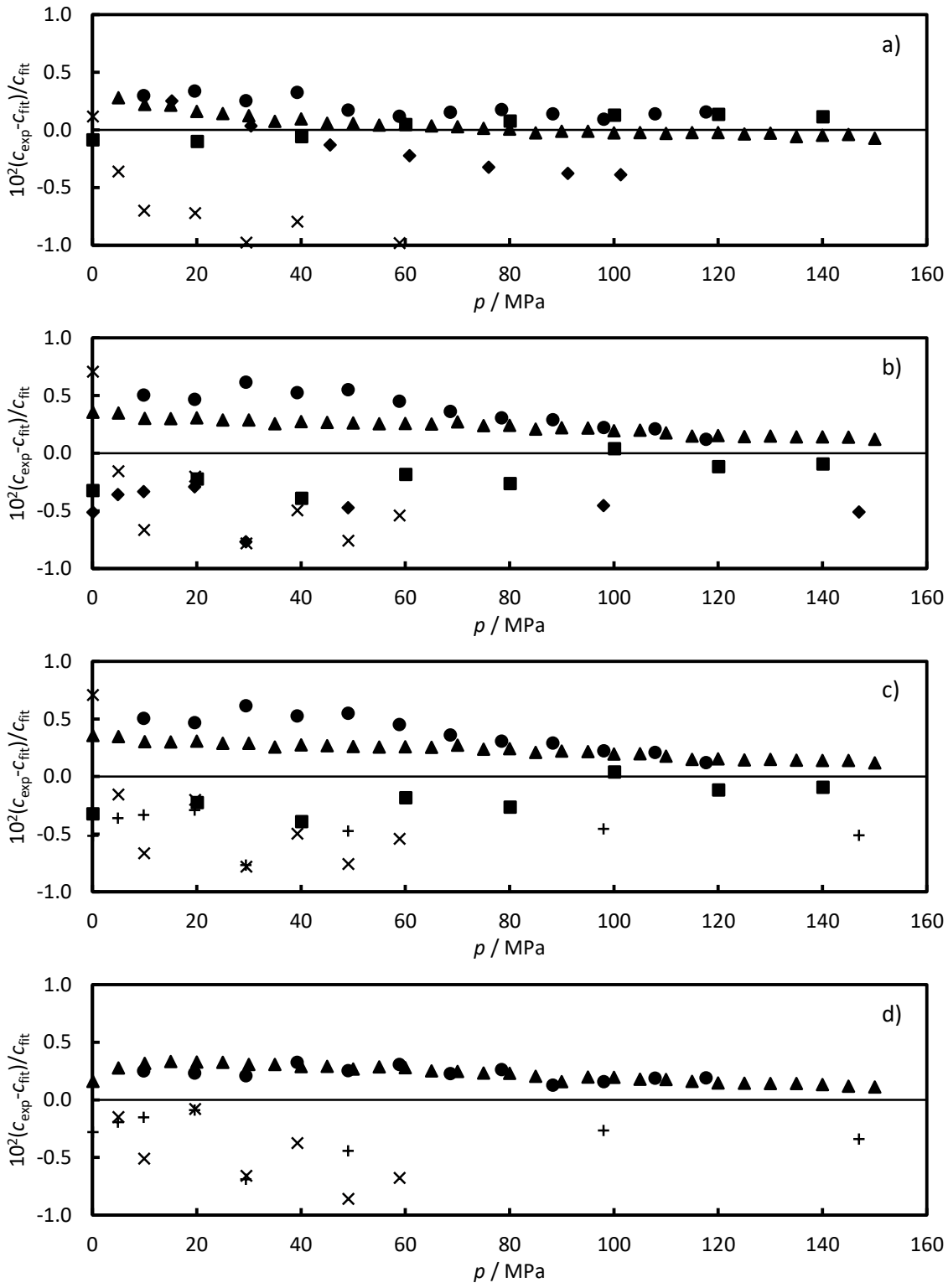



**Figure 5.9** Comparison between the experimental literature data $c_{exp}$ and sound-speed calculated from the correlation $c_{fit}$ for *n*-heptane. a) 298.15 K, b) 323.15 K, c) 348.15 K, d) 373.15 K. Symbols represent literature data by several authors: ▲, Daridon *et al.* [69] (303, 313, 343 and 373) K; ■, Boelhower [86] (293, 313, 323 and 353) K; ×, Hassanov [128] (298, 323, 348 and 373) K; ◆, Dzida *et al.* [124] (298 and 313) K; +, Golik *et al.* [122] (353 and 373) K; ●, Badalyan *et al.* [116] (303, 323, , 353 and 363) K.

### 5.5.5 Modelling

The experimental compressed-liquid density and speed-of-sound data for *n*-heptane have been compared with the predictions from SAFT-γ Mie EoS. The functional groups parameters in SAFT-γ Mie used for *n*-heptane are the same as *n*-pentane (refer to Table 5.2). The deviations between the experimental data and the predictions are shown in Figure 5.10. The predictions from SAFT-γ Mie are accurate up to ±0.9 % for compressed-liquid densities with an $\Delta_{AARD}$ of 0.4 %. For sound-speed predictions, the deviations for most points lie within a band of ±2 %, and the $\Delta_{AARD}$ between the experimental data and the predictions was estimated to be approximately 0.9 %.

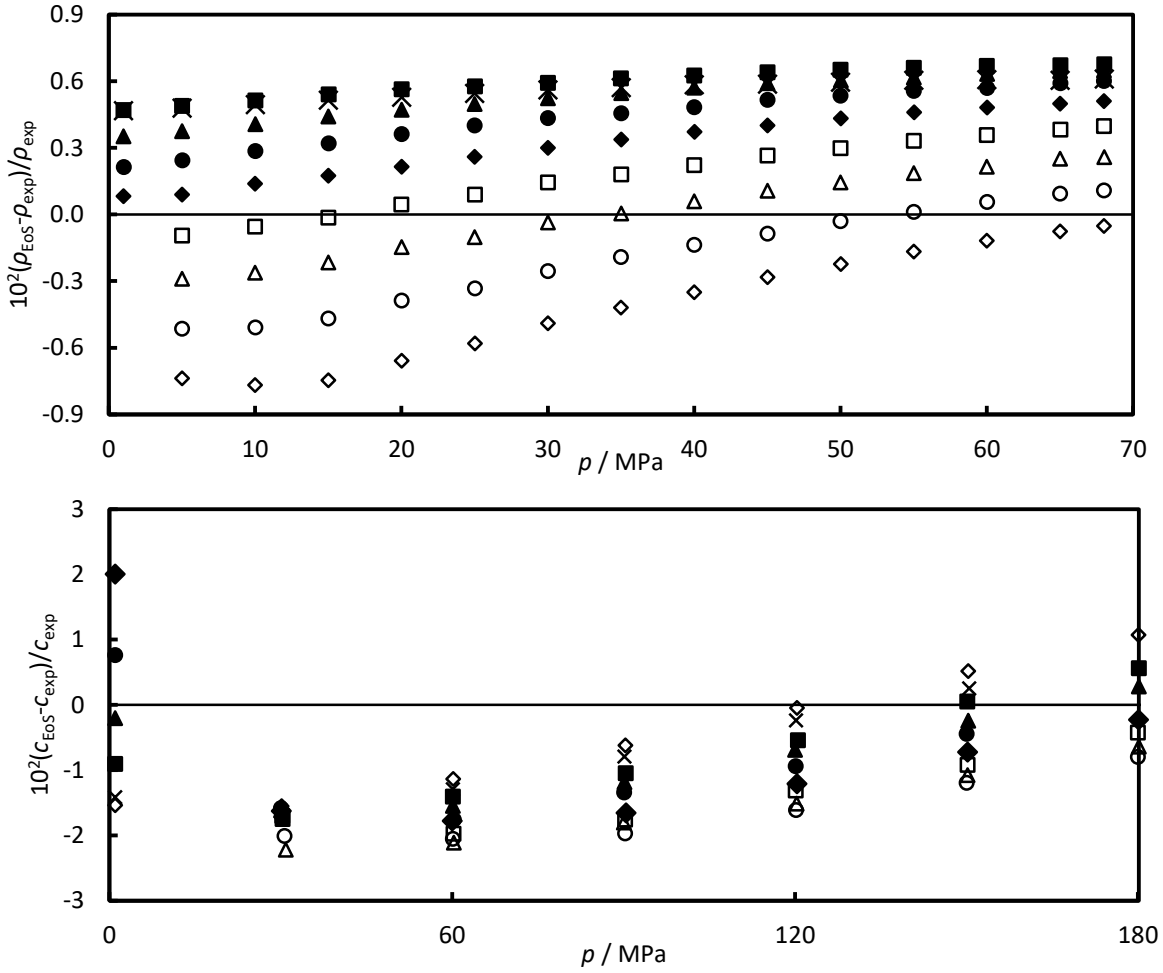



**Figure 5.10** (*top*) Deviations of the experimental density $\rho_{exp}$ in *n*-heptane from the values calculated from SAFT-γ Mie EoS $\rho_{EoS}$ across nine isotherms. (*bottom*) Deviations of the experimental speed-of-sound $c_{exp}$ in *n*-heptane from the values calculated from SAFT-γ Mie EoS $c_{EoS}$ across nine isotherms: ×, 283.15 K; ■, 298.15 K; ▲, 323.15 K; ●, 348.15 K; ◆, 373.15 K; □, 398.15 K; △, 423.15 K; ○, 448.15 K; ◇, 473.15 K.

## 5.5.6 Derived Thermophysical Properties

To obtain a full range of thermophysical properties using the sound-speed and density measurements, isobaric heat capacity data along one isobar (normally the lowest pressure) is needed. The thermophysical properties were derived by means of the thermodynamic integration; the theory and derivation method were described in Chapter 3. The algorithm was tested by work carried out in our group for the thermophysical properties of water. It confirmed that the purely numerical integration errors are negligible in the derivation. Before carrying out the thermodynamic integration, a literature review of the available heat capacity data was conducted; there are several studies which contain the isobaric heat capacity of *n*-heptane up to 520 K. Examples of the experimental studies of the isobaric heat capacity of *n*-heptane can be found in the works of Ginning and Furukawa [379], Cerdeirina *et al.* [380], Zhao *et al.* [381] and Vega-Maza *et al.* [382] A brief summary of literature data reported between is given in Table 5.5 and is shown in Figure 5.11. The $c_{p,\mathrm{EoS}}$ values calculated from the reference EoS [375-377] for *n*-heptane which associated with an uncertainty of 2 %, have also been added in Figure 5.11 for comparison purpose.

**Table 5.5** Isobaric heat capacities $c_p$ studies of *n*-heptane; $T$ and $p$ refer to the temperature and pressure ranges examined, respectively.

| Author (Year) | $T$ / K | $p$ / MPa |
|---|---|---|
| Ginnings and Furukawa (1953) [379] | 182.56 – 520.00 | saturated |
| Cerdeirina *et al.* (2001) [380] | 288.15 – 333.15 | 0.1 |
| Span and Wagner (2003) (EoS) [375-377] | 182.00 – 600.00 | up to 100 |
| Zhao *et al.* (2006) [381] | 278.13 – 353.42 | saturated |
| Vega-Maza *et al.* (2011) [382] | 273.15 – 333.15 | 0.1 – 20 |

In the present work, the isobaric heat capacity data were collected from Ginnings and Furukawa who reported the isobaric heat capacity of *n*-heptane from (182 to 520) K at saturation pressure using an adiabatic calorimeter. Their heat capacity data were reported at the widest temperature range in the literature. Their data were considered accurate up 0.2 %. A polynomial correlation was used to correlate the isobaric heat capacity data to aid the numerical integration process. The correlation is defined in the following form:

$$c_p \,/\left(\mathrm{kJ}\cdot\mathrm{kg}^{-1}\cdot\mathrm{K}^{-1}\right)=\sum_{i=0}^{3} e_i\left(\frac{T}{T_0}\right)^i \,, \tag{5.8}$$

where $T_0$ is the reference temperature, was set to 273.15 K. The parameters were obtained by regression of the experimental data. Figure 5.11 shows the deviation plot of the experimental data from the values calculated using Equation (5.8). It can be seen that most of the values calculated with the correlation are within ±0.05 % to the experimental data. The parameters of Equation (5.8) are listed in Table 5.6.

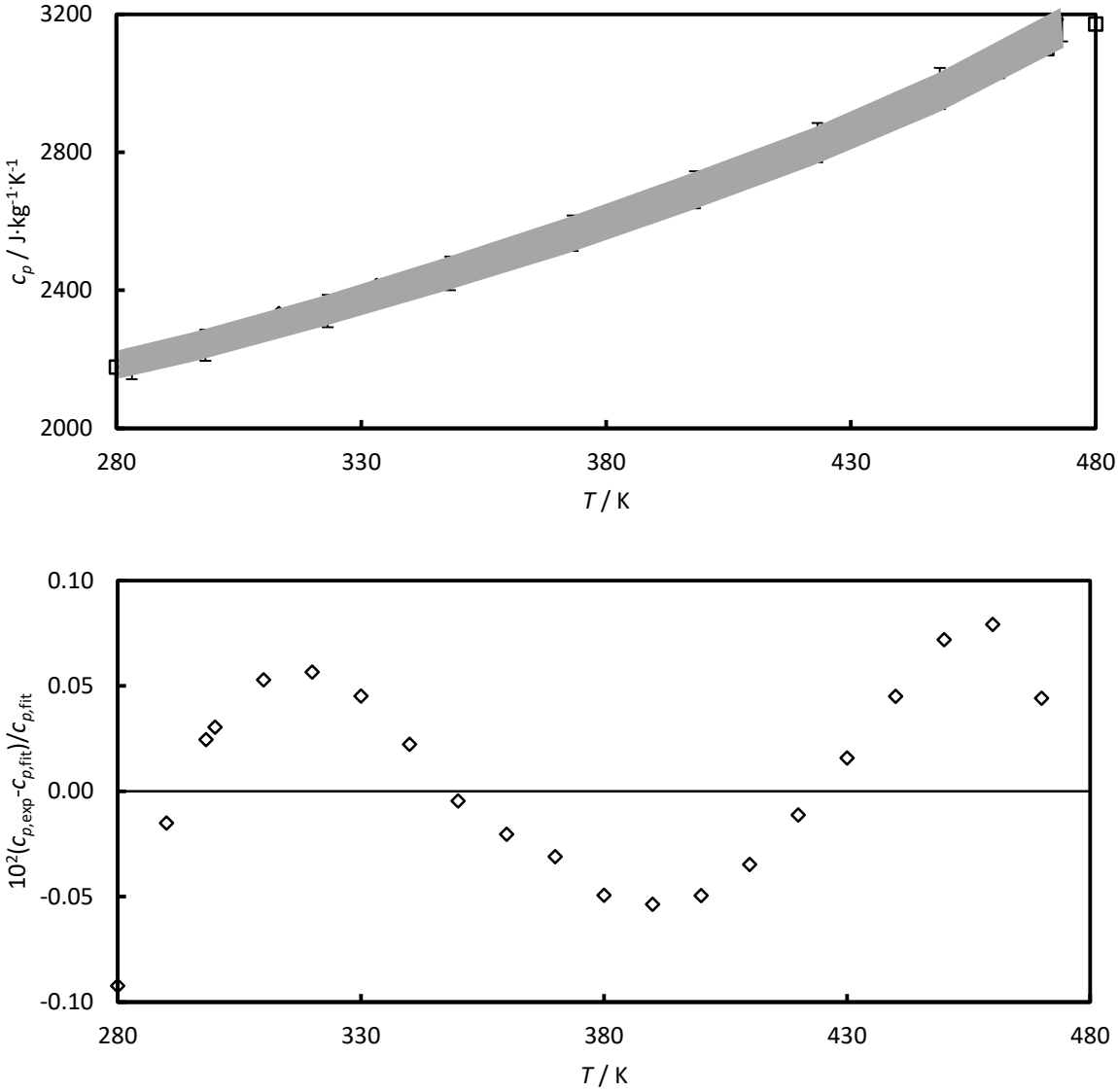



**Figure 5.11** (*top*) Experimental isobaric heat capacity data $c_{p,\mathrm{exp}}$ for *n*-heptane taken from literature. Symbols: □, Ginnings and Furukawa [379]; ○, Cerdeirina *et al.* [380]; ▲, Zhao *et al.* [381]; ◆, Vega-Maza *et al.* [382] Line represent values calculated from the reference equation of state developed by Span and Wagner. (*bottom*) Deviations between the experimental isobaric heat capacity data $c_{p,\mathrm{exp}}$ taken from (Ginnings and Furukawa) for *n*-heptane and values calculated from the polynomial correlation, Equation (5.8) $c_{p,\mathrm{fit}}$.

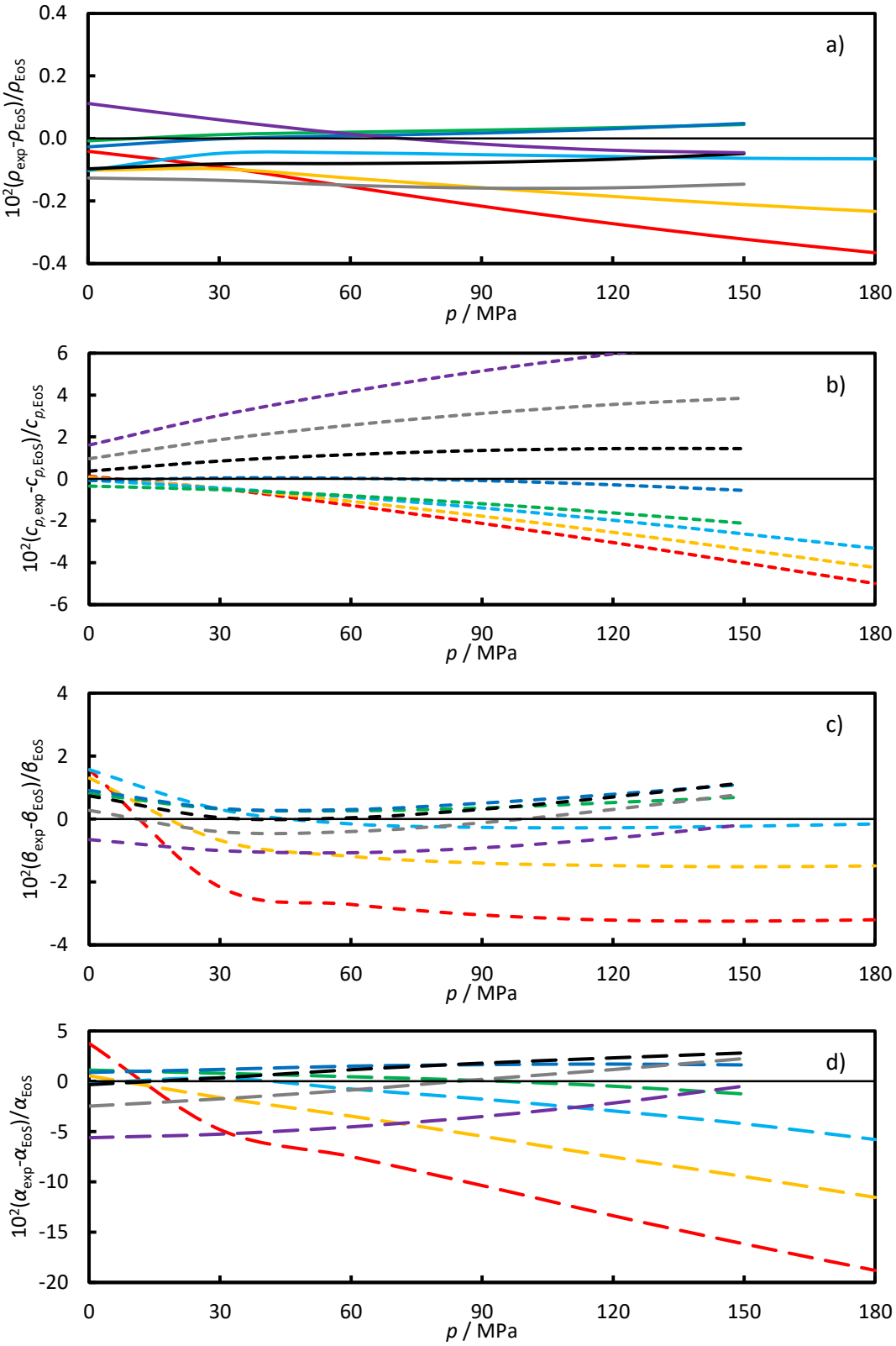



**Figure 5.12** Deviations between the derived density $\rho_{exp}$, isobaric heat capacity $c_{p,exp}$, isothermal compressibility $\beta_{exp}$ and isobaric expansivity $\alpha_{exp}$ and values calculated from the EoS across eight isotherms. Lines denote predictions from EoS: (red), 298.15 K; (orange), 323.15 K; (light blue), 348.15 K; (green), 373.15 K; (blue), 398.15 K; (black), 423.15 K; (grey), 448.15 K; (purple), 473.15 K.

**Table 5.6** Parameters of the isobaric heat capacity correlation, Equation (5.8) for *n*-heptane.

| | | | | | | | | | |
|---|---|---|---|---|---|---|---|---|---|
| $e_0$ | $1.250\times10^3$ | $e_1$ | $1.055\times10^3$ | $e_2$ | $-3.862\times10^2$ | $e_3$ | $2.313\times10^2$ | $\Delta_{AARD}$ | 0.04% |

The density, isobaric heat capacity, isothermal compressibility and isobaric expansivity have been derived up to 180 MPa. The derived data are listed in Table B.4 in Appendix B. Figure 5.12 shows the difference between the derived properties and the calculated values using the reference EoS for *n*-heptane. It can be seen that most of the derived density values agree with the predictions to within ±0.2 %. The highest deviations occur at the lowest isotherm. For derived $c_p$ values, most of the values deviate within ±3 % from the predictions of EoS up to 150 MPa. The average absolute relative deviation was 0.9 % for isothermal compressibility across all temperatures and pressures. The $\Delta_{AARD}$ for isobaric expansivity was higher with a value of 3.6 %.

The error in the derived values of all thermodynamic properties can be estimated by introducing perturbation on the input data and recording their effects on the final results. To do that, we perturbed, in turn, each set of data provided for the integration process, $c$, $\rho_0$ and $c_{p,0}$ at their calculated uncertainty. First, we perturbed the experimental sound-speed data by 0.1 % (the experimental uncertainty and the errors in the surface fit for speed-of-sound) to look at the effect on the derived properties. The effect on the derived values of density is small, with the percentage change varying from 0 % at low temperature to approximately 0.04 % at the highest isotherm. Similarly, the change in $c_p$ is ranging from (0 to 0.1) % with the biggest change occurred at the highest temperature. The changes in isothermal compressibility and isobaric expansivity are slightly larger, ranging from (0.1 to 0.2) % and (0 to 0.3), respectively, at all temperatures and pressures. Then we looked at the effect of changing $\rho_0$ by 0.1 % which is equivalent to the uncertainty of the measurement. The change in $c_p$ is tiny, with an $\Delta_{AARD}$ of less than 0.1 %. The derived values of $\alpha$ and $\beta$ are changed by an average of 0.09 % and 0.07 %, respectively. Lastly, the initial values of $c_p$ were perturbed by 0.2 %. The changes in $\rho$ and $\beta$ were minimal with the largest relative changes for density and isothermal compressibility being 0.01 % and 0.04 %, respectively. The average relative change in isobaric expansivity is 0.02 % from perturbing the initial values of $c_p$ by 0.2 %. Considering the combined effects of the input data, we estimate that the relative uncertainties of the derived properties are approximately 0.2 % for $\rho$, 2 % for $c_p$, 1 % for $\beta$ and 2% for $\alpha$ at all state points.

# 5.6 *n*-Nonane

This section gives the results of the density measurements made for *n*-nonane over a temperature range of (283.15 to 473.15) K and for pressures up to 68 MPa. In conjunction, the results of the speed-of-sound measurements made over temperature ranges of (283.15 to 473.15) K at pressures up to 390 MPa are also presented. A comparison of the present density and speed-of-sound data to literature data is given. The experimental data were compared with the values calculated with the reference EoS and SAFT-γ Mie. At the end of the measurements, the experimental sound-speed and density data were combined with isobaric heat capacity data to obtain a full spectrum of thermophysical properties via thermodynamic integration.

## 5.6.1 Literature Review

Currently, high *T*, *p* density data are scarce in the literature with most of the available density data reported at atmospheric pressure. Doolittle [383] reported the density of *n*-nonane from (323 to 473) K up to 50 MPa, Brostow *et al.* [384] measured at temperatures between (323 and 423) K and Grindley and Lind [385] reported the density in the largest pressure range from (20 to 620) MPa at temperatures between (373 and 423) K. Data reported from theses three studies were measured with a piezometer. In addition to these studies, Valencia *et al.* [191], Moravkova *et al.* [223] and Banipal *et al.* [386] all measured the density of *n*-nonane with a vibrating-tube densimeter and reported the densities at temperatures between (283 and 373) K and pressures up to 60 MPa. The most accurate dataset with given uncertainty of 0.01 % was reported by Schilling *et al.* [209] who measured at pressures up to 30 MPa and at temperatures between (233 and 373) K with a single-sinker densimeter. Other studies reporting the densities of *n*-nonane can be found in Table 2.4 in Chapter 2. Most speed-of-sound experimental data for *n*-nonane in the literature are restricted to atmospheric pressure, and within a temperature range of (288 to 423) K. Examples of atmospheric sound-speed studies can be found in the works of Casas *et al.*, Pereira *et al.*, and Aminabhavi and Gopalkrishna [387-389]; they all reported the speed-of-sound in *n*-nonane at temperatures between (288 and 343) K and at atmospheric pressure conditions. There are only four authors that measured the speed-of-sound in *n*-nonane at elevated pressures. The most recent data were presented by Lago *et al.* [130] who measured the sound-speed using the double path pulse-echo technique at temperatures between (293.15 and 393.15) K in the pressure range from (0.11 to 99.9) MPa. Data were considered accurate up to 0.2 %. Boelhouwer [86] made measurements using a single-pulse transient apparatus. Sound-speed data were presented at temperatures between (253 and 412) K and at pressures up to approximately 140 MPa. It was reported that the results were considered accurate to approximately 0.2 %. Zotov *et al.* [109] reported at the widest temperature and pressure range; they measured at temperatures between (303 and 433) K and pressures up to 600 MPa. However, their data also contained the highest specified uncertainty of 0.3 %. Badalyan *et al.* [116] measured at pressures up to 118 MPa and temperatures

ranging from (303 to 393) K in 10 K intervals. The reference equation of state of *n*-nonane was developed by Lemmon and Span [40] in 2006, and the specified standard uncertainties for liquid-phase density and speed-of-sound were 0.3 % and 1 %, respectively at pressures up to 100 MPa and temperatures below 430 K.

## 5.6.2 Experimental Density Results and Discussion

The density of *n-n*onane was measured along nine isotherms at $T$ = (283.15, 298.15, 323.15, 348.15, 373.15, 398.15, 423.15, 448.15 and 473.15) K and at pressures between (0.1 and 65) MPa. The experimental density as a function of pressure is shown in Figure 5.13. The experimental densities together with the estimated uncertainty are tabulated in Table B.5 in Appendix B. At temperatures above 423.15 K, the starting measurement points were adjusted to 1 MPa to avoid phase separation and loss of volatile components at higher temperatures. The experimental density data obtained were compared with the reference equation of state for *n*-nonane developed by Lemmon and Span [40]. The values calculated from this equation show systematic deviations from the new data between (-0.1 and 0.3) % throughout the experimental range as illustrated in Figure 5.14. The deviations of the experimental data were consistent with the tolerance specified for the EoS of *n*-nonane of 0.3 %. In addition, the experimental data has been compared with the available literature sources. The comparison plots of the literature data across nine isotherms are shown in Figure 5.15. The predictions calculated from the EoS have also been added to the plots for comparison. It can be noticed that the deviations between our data and the literature data scatter across ±0.1 % for most temperatures, but the deviations increase at the higher temperatures. Our data have the best agreement with data reported by Schilling *et al.* [209] which is considered as the most reliable with an uncertainty of 0.02 %.

**Correlation:** In the present case, the experimental density data for *n*-nonane over the entire temperature and pressure range were fitted with the modified Tait equation, Equation (5.5). The parameters were determined using the sum of the least square method. The terms $\rho_0$ and $B$ were further correlated as functions of temperature as shown in Equations (5.5) and (5.6). At temperatures above 423.15 K, $\rho_0$ was a hypothetical liquid density when the temperature exceeded the boiling temperature at $p$ = 0.1 MPa. The parameters of the modified Tait equation were tabulated in Table 5.7. Equation (5.5) fitted the experimental data within ±0.4 kg·m$^{-3}$ which is equivalent to the percentage deviation of about 0.1 %. Figure 5.13 shows the deviations between the experimental density data and densities calculated from the Tait equation. The $\Delta_{AARD}$ was found to be 0.01 %, and the $\Delta_{MARD}$ was determined to be 0.03 % at all temperatures and pressures.

**Table 5.7** Fitting parameters of the modified Tait equation, Equation (5.5) for the compressed-liquid density measurements of *n*-nonane together with the statistical parameters, $\Delta_{AARD}$ and $\Delta_{MARD}$

| | | | | | |
|---|---|---|---|---|---|
| $a_0$ | 1012.13 | $b_0$ | 399.79 | $C$ | 0.20 |
| $a_1$ | -403.77 | $b_1$ | -482.84 | | |
| $a_2$ | 184.47 | $b_2$ | 201.61 | $\Delta_{AARD}$ | 0.01% |
| $a_3$ | -59.31 | $b_3$ | -29.88 | $\Delta_{MARD}$ | 0.03% |

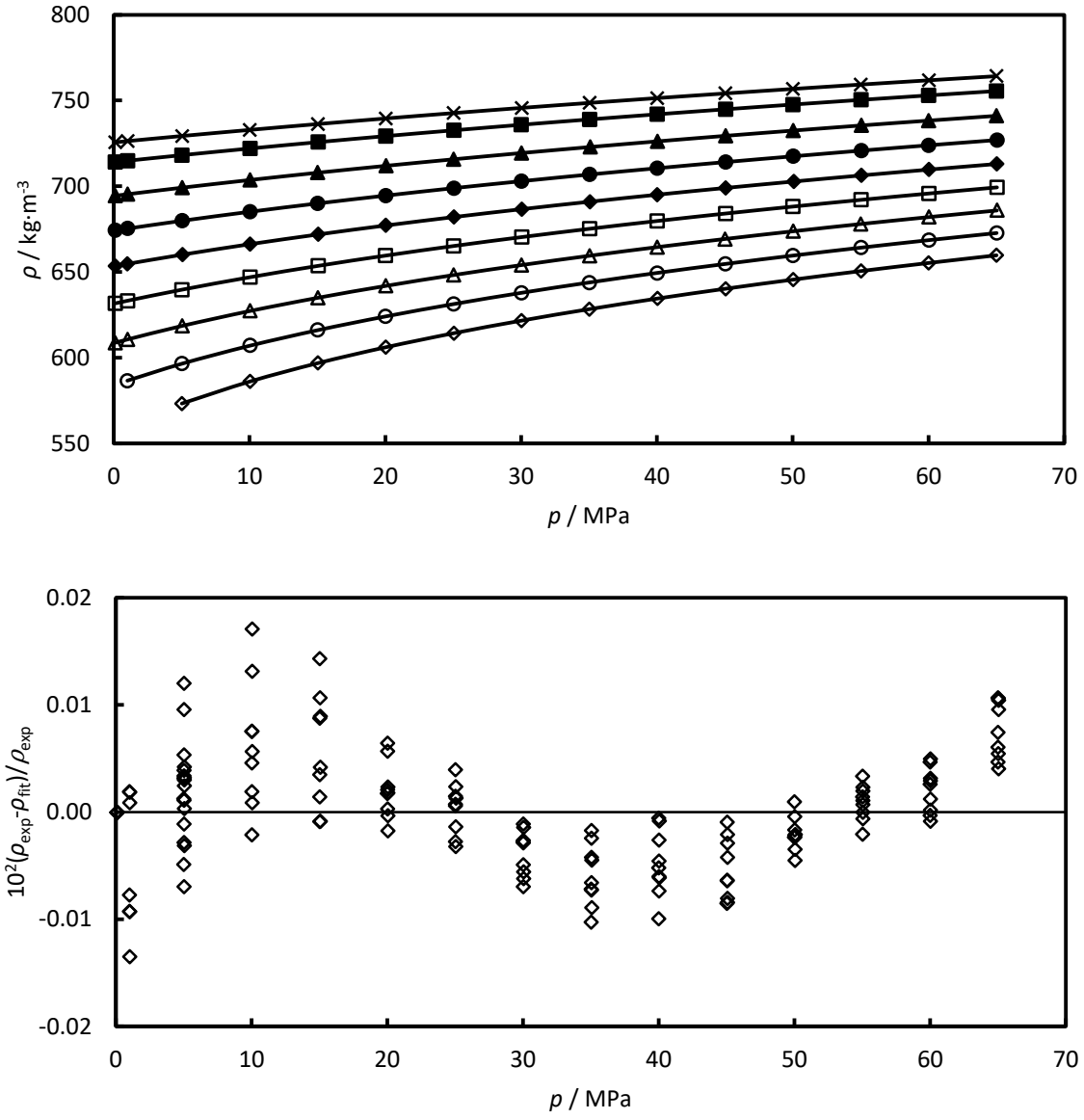



**Figure 5.13** (*top*) Experimental density $\rho$ of *n*-nonane as a function of pressure across nine isotherms: ×, 283.15 K; ■, 298.15 K; ▲, 323.15 K; ●, 348.15 K; ◆, 373.15 K; □, 398.15 K; △, 423.15 K; ○, 448.15 K; ◇, 473.15 K. Solid lines represent densities calculated from the modified Tait equation. (*bottom*) Deviations between experimental densities $\rho_{exp}$ and the values calculated using the modified Tait equation $\rho_{fit}$.

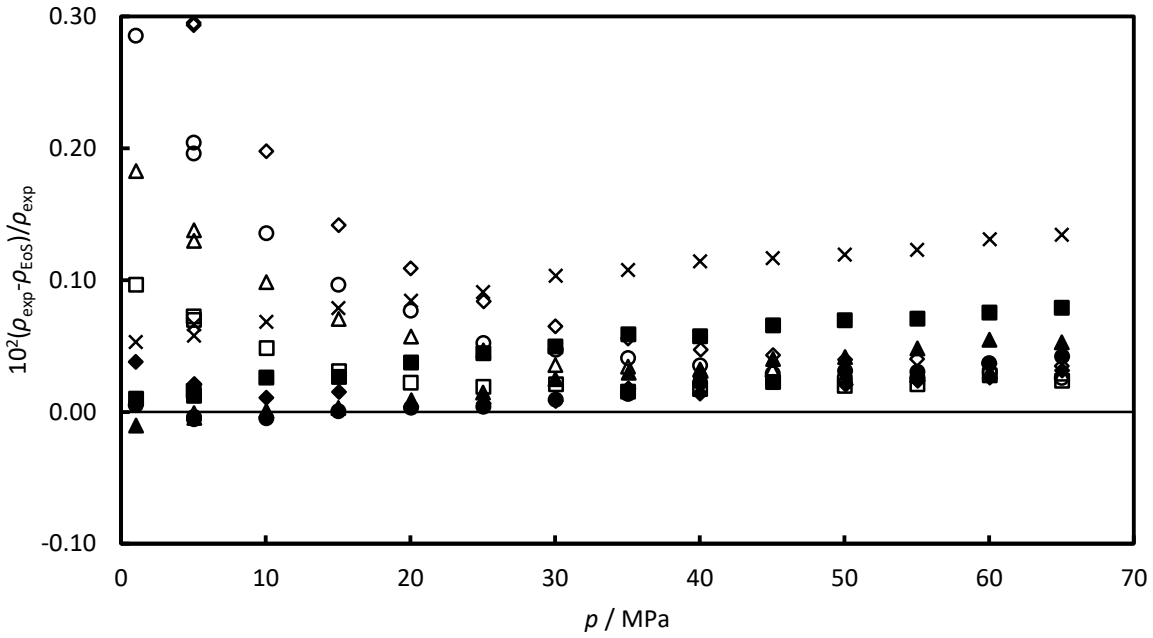



**Figure 5.14** Deviations between the experimental densities $\rho_{exp}$ of *n*-nonane and the values calculated using the EoS developed by Lemmon and Span across nine isotherms: ×, 283.15 K; ■, 298.15 K; ▲, 323.15 K; ●, 348.15 K; ◆, 373.15 K; □, 398.15 K; △, 423.15 K; ○, 448.15 K; ◇, 473.15 K.

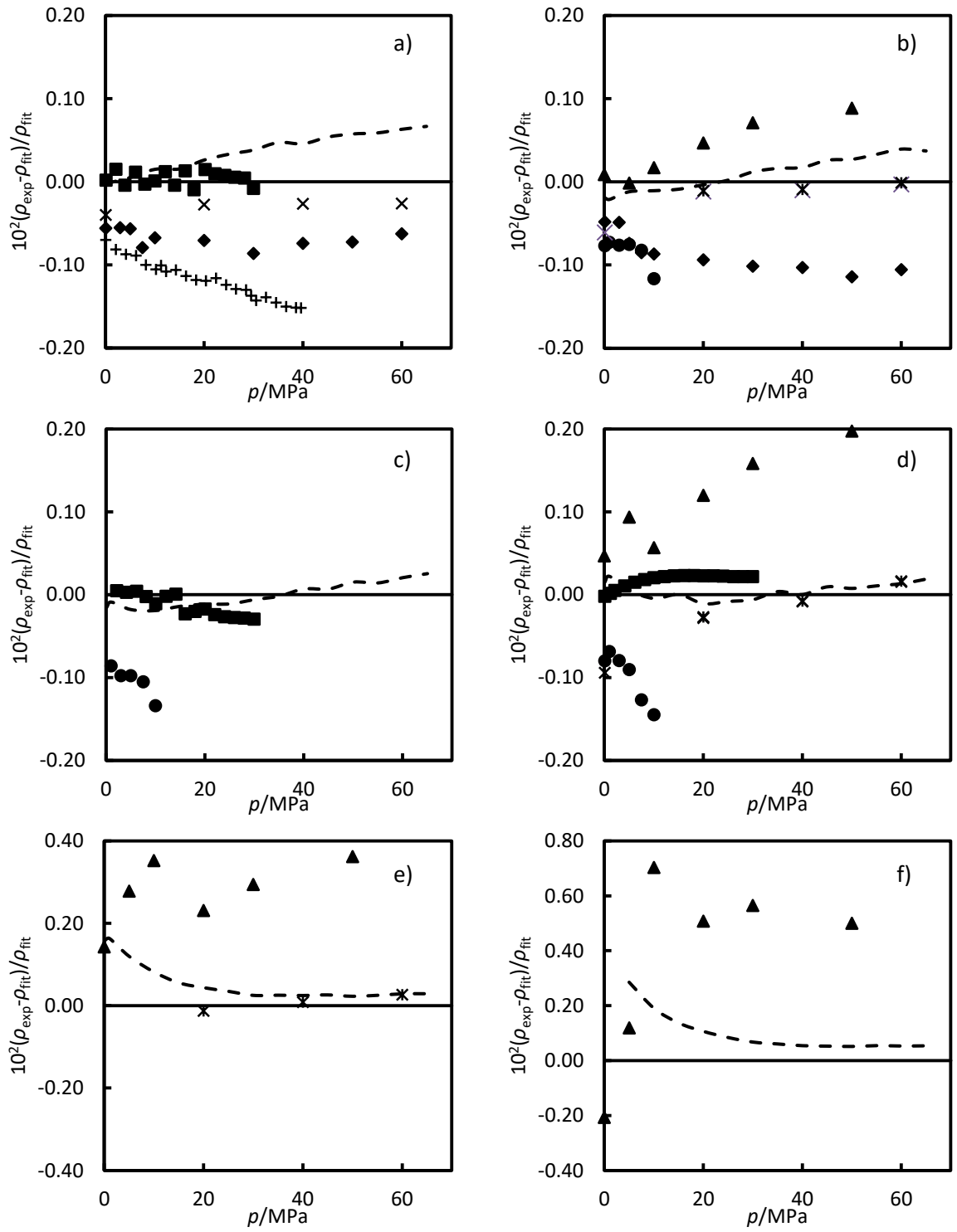



**Figure 5.15** Deviation plots between the experimental densities obtained from the literature $\rho_{exp}$ and the values calculated using Equation (5.5) at six temperatures. a) 298.15 K; b) 323.15 K; c) 348.15 K; d) 373.15 K; e) 423.15 K; f) 473.15 K. Symbols represent literature data: ◆, Valencia *et al.* [191]; ●, Banipal *et al.* [386]; ■, Schilling *et al.* [209]; ▲, Doolittle [383]; +, Moravkova *et al.* [223]; ×, Grindley and Lind [379]; ∗, Brostow *et al.* [384] Dotted lines denote predictions from the reference EoS [40].

## 5.6.3 Experimental Speed-of-Sound Results and Discussion

The speed-of-sound measurement for *n*-nonane along nine isotherms ($T$ = 283.15, 298.15, 323.15, 348.15, 373.15, 398.15, 423.15, 448.15 and 473.15) K at pressures up to 390 MPa was carried out. In all cases, the deviations between the initial measurement and the final check measurement at the same temperature and pressure were less than 0.01 %. The absolute difference between the initial and check measured was always less than 0.4 $m \cdot s^{-1}$ over the entire temperature, which was taken as the repeatability uncertainty in the overall uncertainty calculation. The measurement results are reported in Table B.6 in Appendix B. Figure 5.16 shows the experimental speed-of-sound data as a function of pressure. In the measurement region, the speed-of-sound in *n*-nonane ranges from approximately 570 $m \cdot s^{-1}$ to 2380 $m \cdot s^{-1}$. In Figure 5.17, we compared the speed-of-sound with the values calculated from the EoS. Most deviations between the predictions and the experimental data are within ±0.5 %. These deviations are smaller than the tolerances of 1 % specified for the EoS of *n*-nonane in the temperature and pressure ranges of the present study but larger than the uncertainty of the present results. The speed-of-sound experimental data have also been compared with the available literature reported data. Since the reported data points were measured at different isotherms, the developed correlation, Equation (5.2), was used to interpolate our experimental data in order to have a more accurate comparison. Experimental data across six isotherms (293.15 K, 313.15 K, 333.15 K, 353.15 K, 373.15 K and 393.15 K) have been compared, and the deviation plots are shown in Figure 5.18. It can be seen that the deviations between our data and the literature scatter around ±0.2 % at most of the isotherms. There is only one set of data reported at pressures above 200 MPa, and the comparisons showed that our data agree with the high-pressure data to within ±0.2 %. Our experimental data have the best agreement with data from Lago *et al.* [130] and Boelhouwer [86] with an $\Delta_{AARD}$ of 0.05 % and 0.1 %, respectively.

**Correlation:** The sound-speed experimental data were fitted into a pressure-explicit correlation as shown in Equation (5.2). The reference speed-of-sound, $c_0$ was then correlated as a function of temperature, given in Equation (5.2). Similarly, the goodness of the fit is determined by statistical functions, $\Delta_{AARD}$ and $\Delta_{MARD.}$ The $\Delta_{AARD}$ for the surface fit of speed-of-sound data was found to be 0.04 %, and the $\Delta_{MARD}$ was 0.4 %. The deviation plot of experimental data against values calculated from the correlation is shown in Figure 5.16. In general, the correlation describes the sound-speed experimental data well across a wide range of temperature and pressure and with the $\Delta_{AARD}$ consistent with the overall standard uncertainty. The highest deviation point occurs at 473.15 K and 1 MPa, where the state point was measured very close to the bubble pressure of *n*-nonane with less clear signals during measurement. The parameters in equations (5.2) and (5.2) are tabulated in Table 5.8 below.

**Table 5.8** Fitting parameters of the empirical correlation, Equation (5.2) for the speed-of-sound measurements in *n*-nonane together with the statistical parameters, average absolute deviation, $\Delta_{AARD}$ and maximum absolute deviation $\Delta_{MARD}$.

| | | | | | | | | | |
|---|---|---|---|---|---|---|---|---|---|
| $a_{10}$ | $3.379\times10^{-1}$ | $a_{20}$ | $-1.631\times10^{-3}$ | $a_{30}$ | $9.061\times10^{-7}$ | $b_0$ | $2.659\times10^{3}$ | $\Delta_{AARD}$ | 0.04% |
| $a_{11}$ | -1.650 | $a_{21}$ | $6.821\times10^{-3}$ | $a_{31}$ | $-3.652\times10^{-6}$ | $b_1$ | $-1.599\times10^{3}$ | | |
| $a_{12}$ | 2.743 | $a_{22}$ | $-8.887\times10^{-3}$ | $a_{32}$ | $4.963\times10^{-6}$ | $b_2$ | $2.843\times10^{2}$ | $\Delta_{MARD}$ | 0.38% |
| $a_{13}$ | -1.273 | $a_{23}$ | $3.859\times10^{-3}$ | $a_{33}$ | $-2.199\times10^{-6}$ | $b_3$ | $-3.486\times10^{1}$ | | |

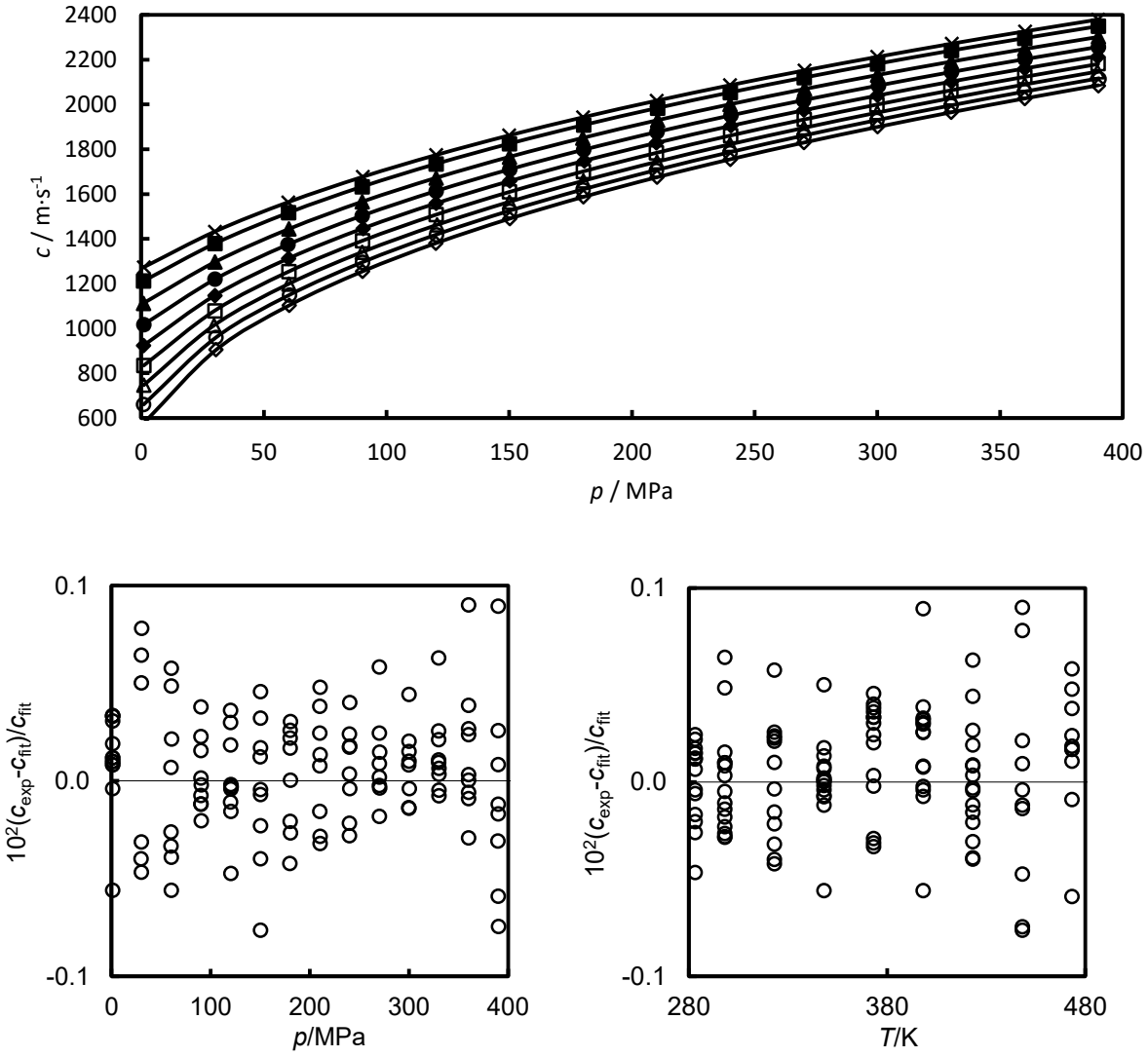



**Figure 5.16** (*top*) Experimental sound-speed $c$ in *n*-nonane along nine isotherms: ×, 283.15 K; ■, 298.15 K; ▲, 323.15 K; ●, 348.15 K; ◆, 373.15 K; □, 398.15 K; △, 423.15 K; ○, 448.15 K; ◇, 473.15 K. Symbols and lines represent experimental data and values calculated from the correlation, respectively. (*bottom*) Deviations of the experimental speed-of-sound in *n*-nonane $c_{exp}$ from the values calculated from the empirical correlation $c_{fit}$ as a function of pressure and temperature.

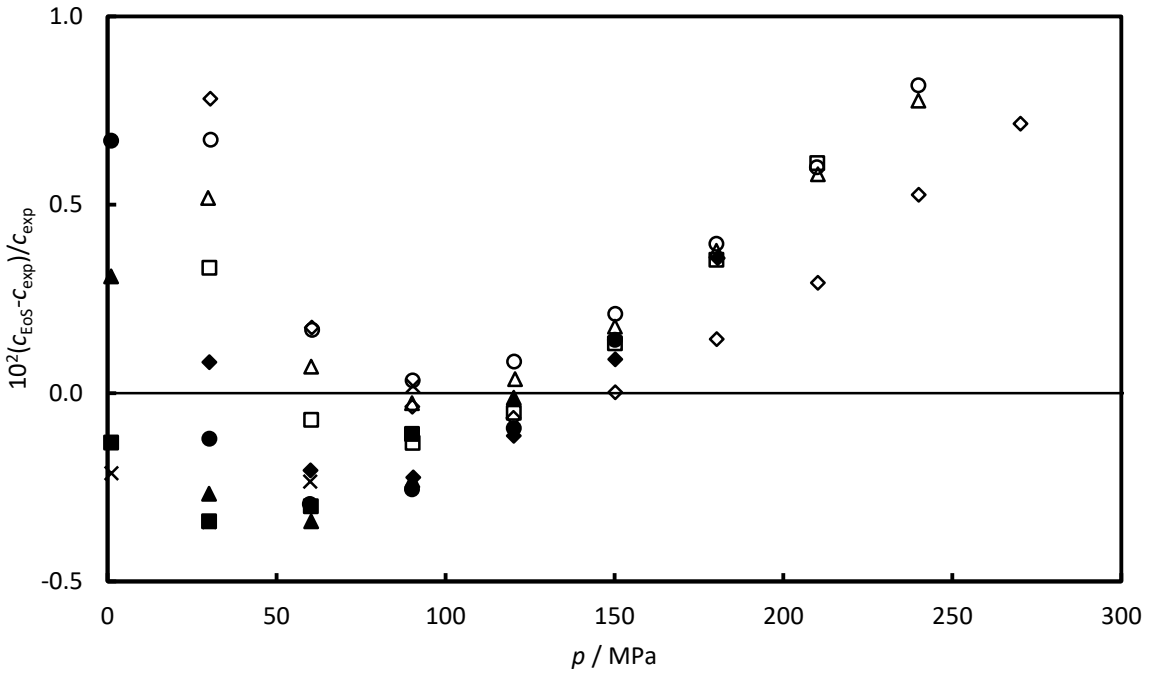



**Figure 5.17** Deviations of the experimental speed-of-sound $c_{exp}$ in *n*-*n*onane from the values calculated from EoS $c_{EoS}$. Symbols represent experimental data: ×, 283.15 K; ■, 298.15 K; ▲, 323.15 K; ●, 348.15 K; ◆, 373.15 K; □, 398.15 K; △, 423.15 K; ○, 448.15 K; ◇, 473.15 K.

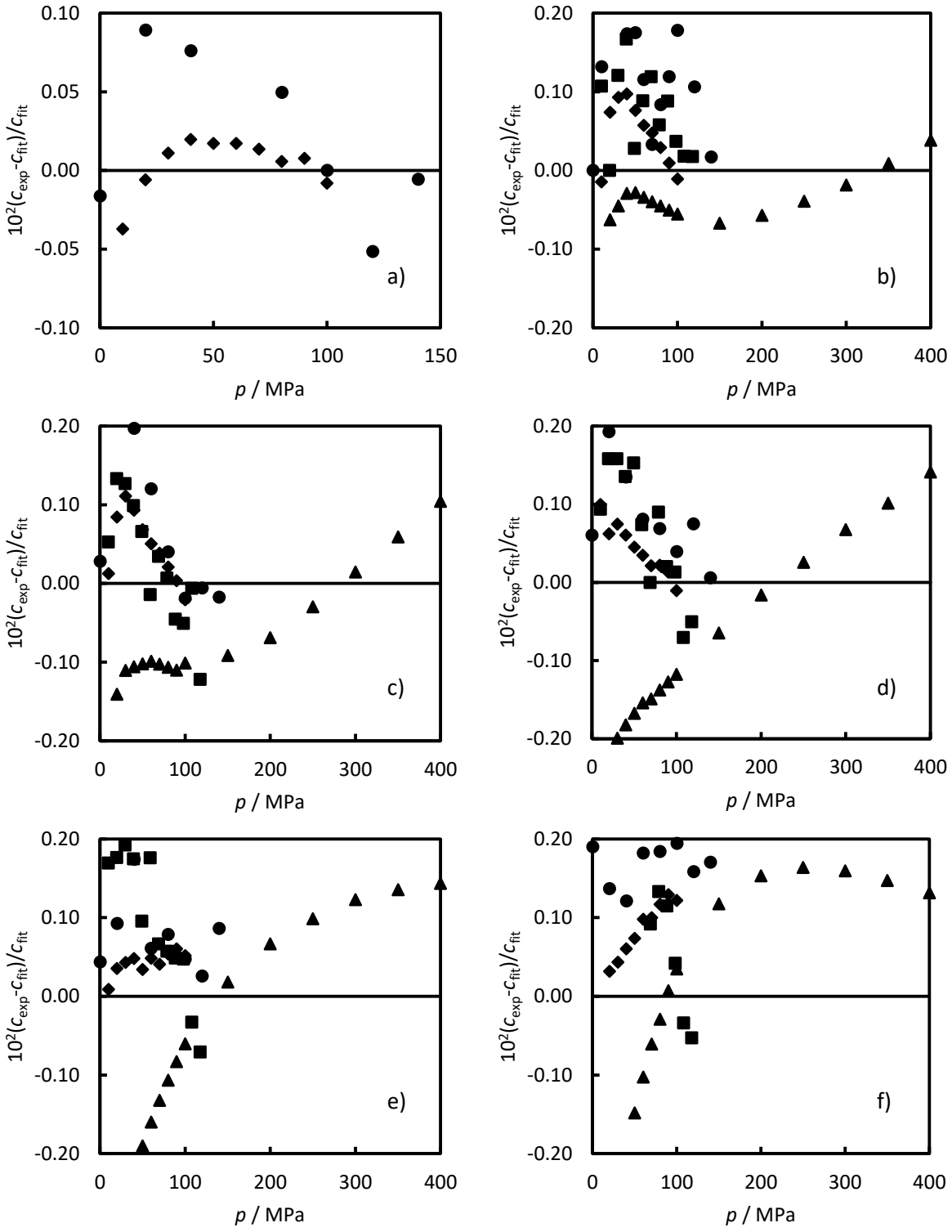



**Figure 5.18** Comparison between the literature data $c_{exp}$ and sound-speed calculated from the correlation, Equation (5.2) $c_{fit}$. a) 293.15 K, b) 313.15 K, c) 333.15 K, d) 353.15 K, e) 373.15 K, f) 393.15 Symbols represent literature data by several authors: ■, Badalyan *et al.* [116]; ▲, Zotov *et al.* [109]; ●, Boelhouwer [86]; ◆, Lago *et al.* [129, 130]

## 5.6.5 Modelling

The experimental density and sound-speed data for *n*-nonane were compared with the predictions from SAFT-γ Mie EoS. The functional groups parameters in SAFT-γ Mie used for *n*-heptane are the same as *n*-pentane (Table 5.2). The comparison between experimental density data and predictions from SAFT-γ Mie gave an average absolute relative deviation $\Delta_{AARD}$ of 0.4 % for all isotherms and pressures. For sound-speed predictions, the deviations for most points lie within a band of ±2 %, and the $\Delta_{AARD}$ between the experimental data and the predictions was estimated to be approximately 0.9 %. The deviation plots are shown in Figure 5.19.

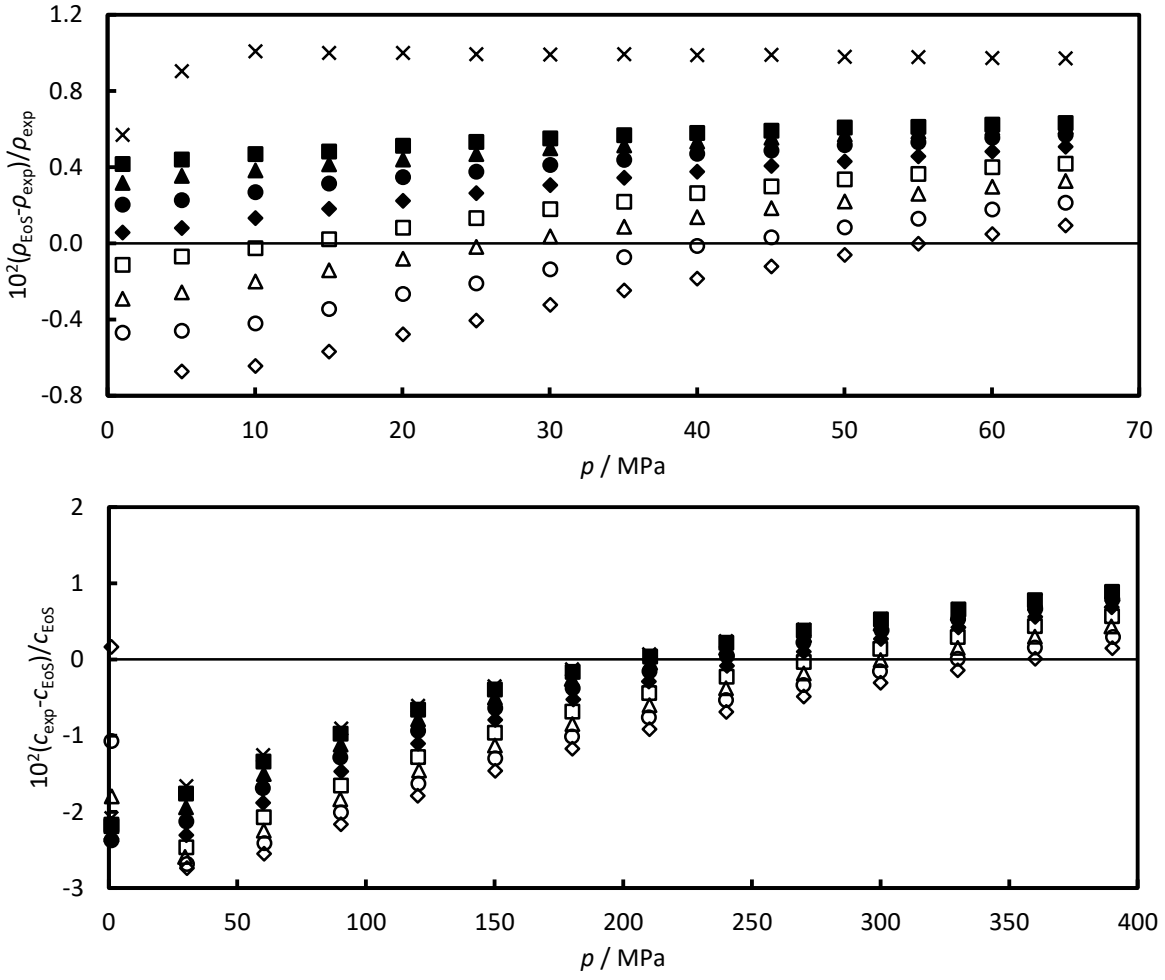



**Figure 5.19** (*top*) Deviations between the experimental density $\rho_{exp}$ in *n*-nonane from the values calculated from SAFT-γ Mie EoS $\rho_{EoS}$ across nine isotherms. (*bottom*) Deviations of the experimental speed-of-sound $c_{exp}$ in *n*-nonane from the values calculated from SAFT-γ Mie $c_{EoS}$ across nine isotherms: ×, 283.15 K; ■, 298.15 K; ▲, 323.15 K; ●, 348.15 K; ◆, 373.15 K; □, 398.15 K; △, 423.15 K; ○, 448.15 K; ◇, 473.15 K.

## 5.6.6 Derived Thermodynamic Properties

In this work, the collected speed-of-sound data for *n*-nonane at temperatures ranging from (283.15 to 473.15) K and at pressures up to 390 MPa, combined with density and isobaric heat capacity data along an isobar (saturation line), have been applied to a thermodynamic integration to obtain other observable thermophysical properties. The isobaric heat capacity data of *n*-nonane was not measured in this work. In order to get the data in the literature, an extensive literature review was carried out. To our knowledge, the experimental data available are scarce in the literature. Most experimental data were reported below 373.15 K, and only one literature source contained isobaric heat capacity experimental data for liquid over 373.15 K. In Table 5.9, all experimental $c_p$ data available in the literature are summarised with the reported temperature and pressure range. For the required temperature range (283.15 to 473.15) K, the experimental isobaric heat capacity data were collected from three literature sources. The low-temperature data were obtained from Osborne, and Ginnings [390] who measured $c_p$ at temperatures from (278.15 to 318.15) K. Mid-temperature data were taken from Banipal.*et al.* [386] who measured the isobaric heat capacity of *n*-nonane from temperatures (318.15 to 373.15) K and at pressures up to 10 MPa. Their heat capacity measurements were carried out using a commercial DSC calorimeter which based on the Tian-Calvert measurement principle which had an uncertainty of 0.5%. The high-temperature data were taken from Kuznetsov *et al.* [391] who reported the isobaric heat capacity at temperatures between (323.80 and 589.59) K and at pressures between (5 and 60) MPa and their data were associated with 0.5% uncertainty. A linear extrapolation was carried out on Kuznetsov *et al.* data to obtain isobaric heat capacity of *n*-nonane along the saturation curve. The combined literature data were then fitted with a polynomial equation, Equation (5.8) and the parameters are listed in Table 5.10. The $c_{p,\mathrm{EoS}}$ values calculated from the EoS [40] which associated with an uncertainty of 2 %, have also been added in Figure 5.20 for comparison purpose. Figure 5.21 shows the comparison between the experimental data obtained from literature and the values calculated using the developed heat capacity correlation shown in Equation (5.8), it can be seen that the deviations are within ±0.3 %.

**Table 5.9** Isobaric heat capacities $c_p$ studies of *n*-nonane; $T$ and $p$ refer to the temperature and pressure ranges examined, respectively.

| Author (Year) | $T$ / K | $p$ / MPa |
|---|---|---|
| Osborne and Ginnings (1947) [390] | 278.15 – 318.15 | saturated |
| Finke *et al.* (1954) [392] | 225.03 – 313.88 | saturated |
| Kuznetsov *et al.* (1988) [391] | 323.80 – 589.59 | 5 – 60 |
| Banipal *et al.* (1991) [386] | 318.15 – 373.15 | 0.1 – 10 |
| Lemmon and Span (2006) (EoS) [40] | 219.70 – 600.00 | up to 800 |

**Table 5.10** Parameters of the isobaric heat capacity correlation, Equation (5.8) for *n*-nonane.

| | | | | | | | | | |
|---|---|---|---|---|---|---|---|---|---|
| $e_0$ | $1.533\times10^3$ | $e_1$ | $2.868\times10^2$ | $e_2$ | $3.431\times10^2$ | $e_3$ | $-3.008\times10^1$ | $\Delta_{AARD}$ | 0.12% |

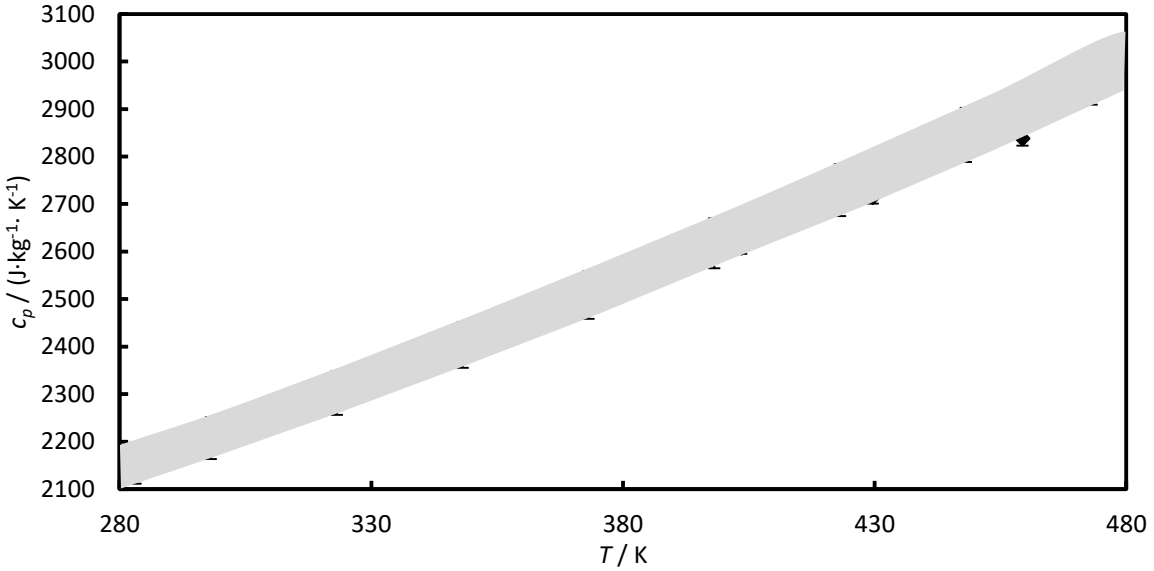



**Figure 5.20** Experimental isobaric heat capacity data $c_p$ for *n*-nonane taken from the literature. Symbols represent literature data: ●, Osborne and Ginnings; ▲, Banipal *et al.*; ◆, Kuznetsov *et al.* and the line represents values calculated from EoS developed by Lemmon and Span.

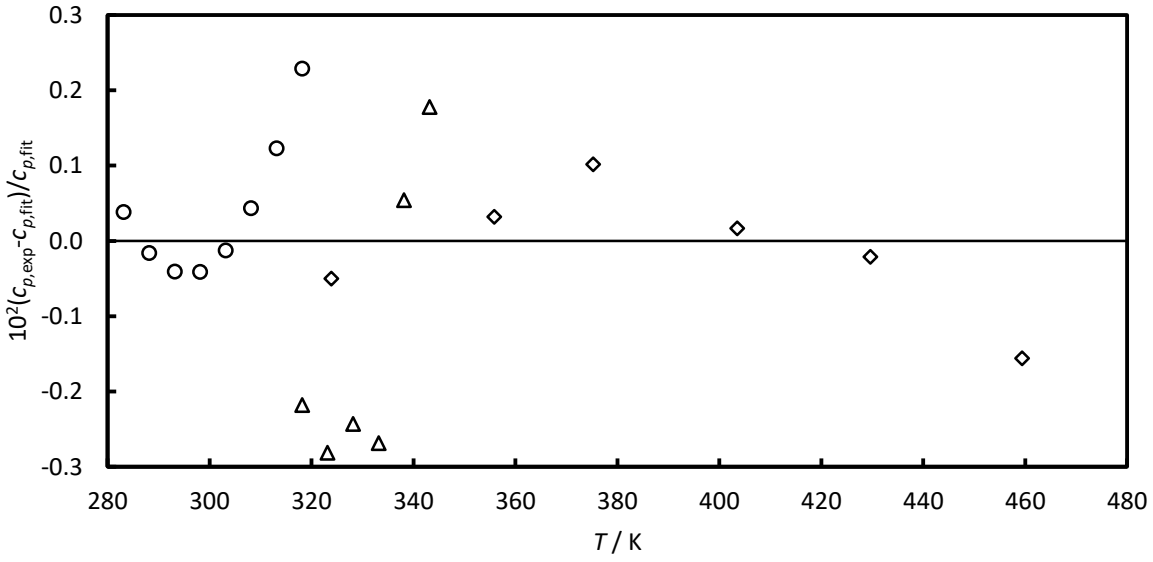



**Figure 5.21** Deviations between the isobaric heat capacity data from the literature $c_{p,exp}$ and the values calculated using the polynomial correlation, Equation (5.8) $c_{p,fit}$ at saturated pressure from temperatures of (283 to 473) K.

The derived thermophysical properties up to 390 MPa and were compared with the calculated values using the EoS for *n*-nonane. Figure 5.22 shows the comparison of the derived properties. It can be seen that the derived density data agreed with the predictions from the EoS within ±0.2 %. The maximum deviation occurs at the highest temperature with an $\Delta_{AARD}$ of 0.12 % which is less than the stated uncertainty of the model. For the derived $c_p$ values, they deviate up to approximately 2 % from the predictions of EoS. Deviation plots of the derived isothermal compressibility and isobaric expansivity were also shown in Figure 5.22. All derived thermophysical properties are tabulated in Table B.7 in Appendix B.

It is hard to perform an uncertainty calculation for the derived properties as they depend on multiple functions. Thus, a sensitivity analysis was carried out to estimate the uncertainties in the derived properties, which arose from the separate contributions of uncertainties in the experimental sound-speed data and the initial values of density and isobaric heat capacity. To do that, we perturbed in turn, each set of data provided by the integration process, $c$, $\rho_0$ and $c_{p,0}$ at their calculated uncertainty. First for $c$, given the experimental uncertainty and the errors in the surface fit for speed-of-sound, we perturbed the experimental sound-speed data by 0.1 % to look at the effect on the derived properties. This has only a very small effect on the derived values of density, varying from 0 % at low temperature to approximately 0.04% at the highest isotherm. Similarly, the change in $c_p$ is ranging from (0 to 0.1) % with the biggest change occurred at the highest temperature. Isothermal compressibility changes from (0.1 to 0.2) % and for isobaric expansivity, the relative changes are within approximately 0.3 % across all temperatures and pressures. We also considered the effect of a relative perturbation to $c$ given by cosinusoidal functions of $T$ and $p$ in the following expressions:

$$\frac{1}{c^2} \rightarrow \frac{1+\varepsilon f}{c^2} \text{ and } f(T,p) = A\cos(k_1 T)\cos(k_2 p). \tag{5.9}$$

Here, $\varepsilon$ is a dimensionless parameter, $\varepsilon << 1$, $f$ is a dimensionless function of temperature and pressure and $A$ is the amplitude. This equation allows variable perturbations to be applied on to the sound-speed data. We explored different scenarios in which $k_1$ = (0.05, 0.1 or 0.2) $K^{-1}$ with $k_2$ = (0 or 0.02) $MPa^{-1}$. It has been noticed that the effect of the sound-speed perturbation on other properties is reduced when $k_2 > 0$. The effects of different values of $k_1$ and $k_2$ on the derived properties are shown in Figures 5.23 and 5.24. Then we looked at the effect of changing $\rho_0$ by 0.1 % which is the uncertainty of the measurement. The change in $c_p$ and $\beta$ are very small, both with an average absolute relative deviation of less than 0.1 %. The derived values of $\alpha$ are changed by an average of 0.09%. Lastly, the initial values of $c_p$ were perturbed by 0.2 %. The changes in $\rho$ and $\beta$ were minimal with the largest relative changes for density and isothermal compressibility being 0.01 % and 0.04 %, respectively. The average relative change in isobaric expansivity was 0.03 % from changing the initial values of $c_p$. Considering the combined effects of the input data, we estimate that the relative uncertainties of the

derived properties are approximately 0.1 % for $\rho$, 2 % for $c_p$, 1% for $\beta$ and 2% for $\alpha$ at all state points with 283.15 K ≤ $T$ ≤ 473.15 K.

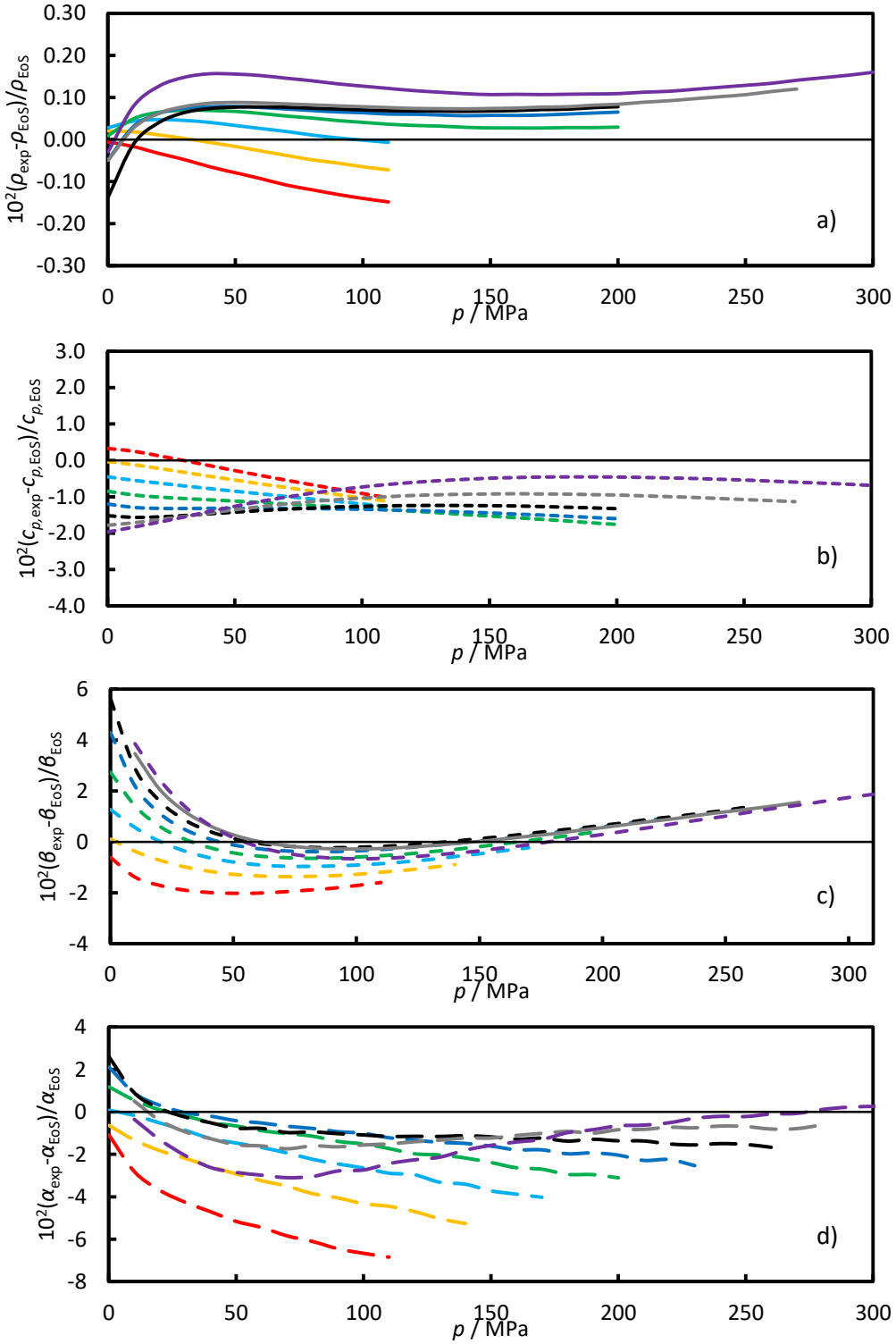



**Figure 5.22** Deviations between derived density $\rho$, isobaric heat capacity $c_p$, isothermal compressibility $\beta$ and isobaric expansivity $\alpha$ and values calculated from the reference EoS up to 390 MPa across eight isotherms. Lines denote predictions from EoS: (red), 298.15 K; (orange), 323.15 K; (light blue), 348.15 K; (green), 373.15 K; (blue), 398.15 K; (black), 423.15 K; (grey),448.15 K; (purple), 473.15 K.

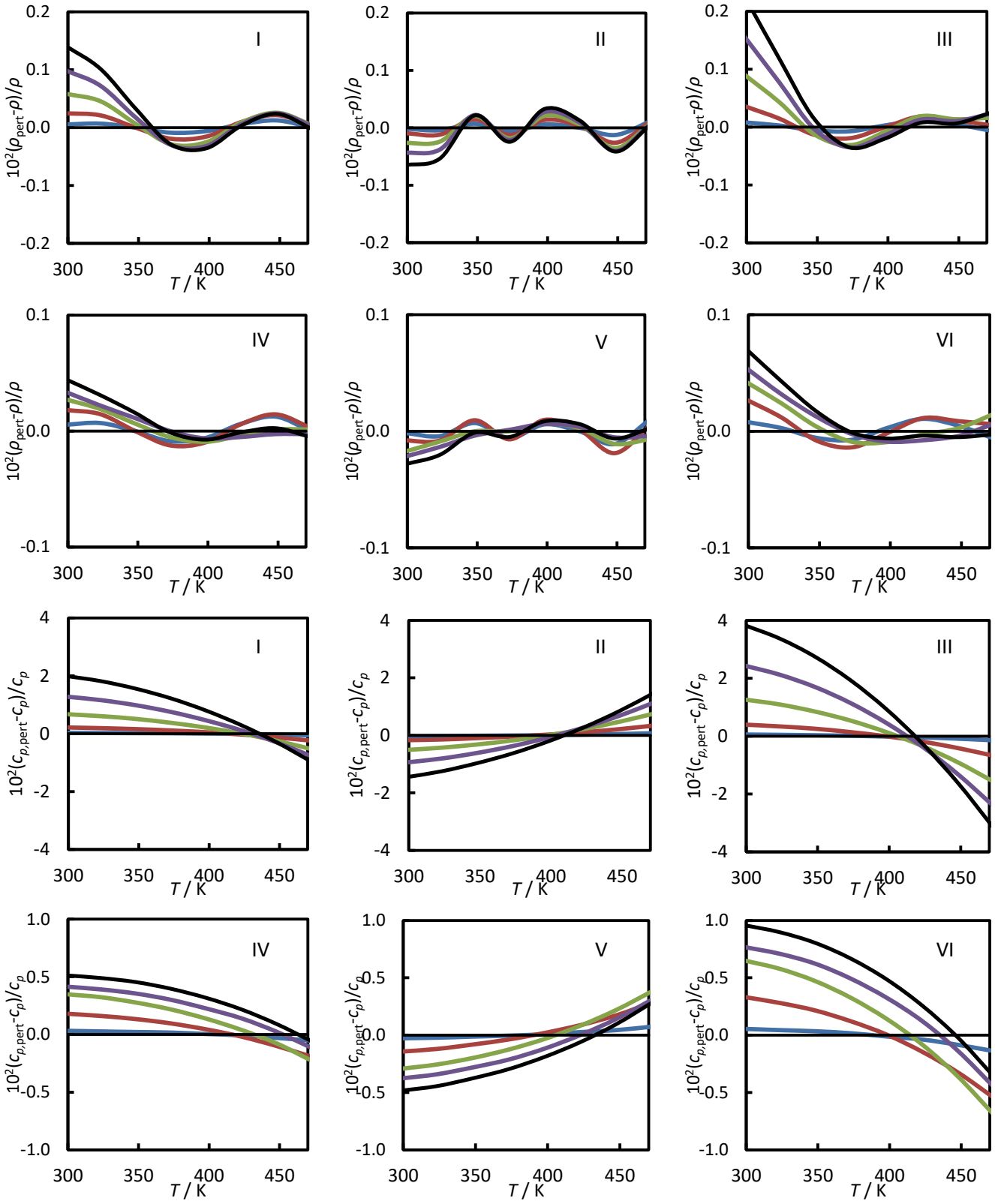



**Figure 5.23** Change in density and isobaric heat capacity, arising from sound-speed cosinusodal perturbation with amplitude of 0.1 %: (I) $k_1 = 0.05$, $k_2 = 0$; (II) $k_1 = 0.1$, $k_2 = 0$; (III) $k_1 = 0.2$, $k_2 = 0$; (IV) $k_1 = 0.05$, $k_2 = 0.02$; (V) $k_1 = 0.1$, $k_2 = 0.02$; (VI) $k_1 = 0.2$, $k_2 = 0.02$. Curves: blue, $p = 30$ MPa; red, $p = 90$ MPa; green, $p = 180$ MPa; purple, $p = 270$ MPa; black, $p = 360$ MPa.

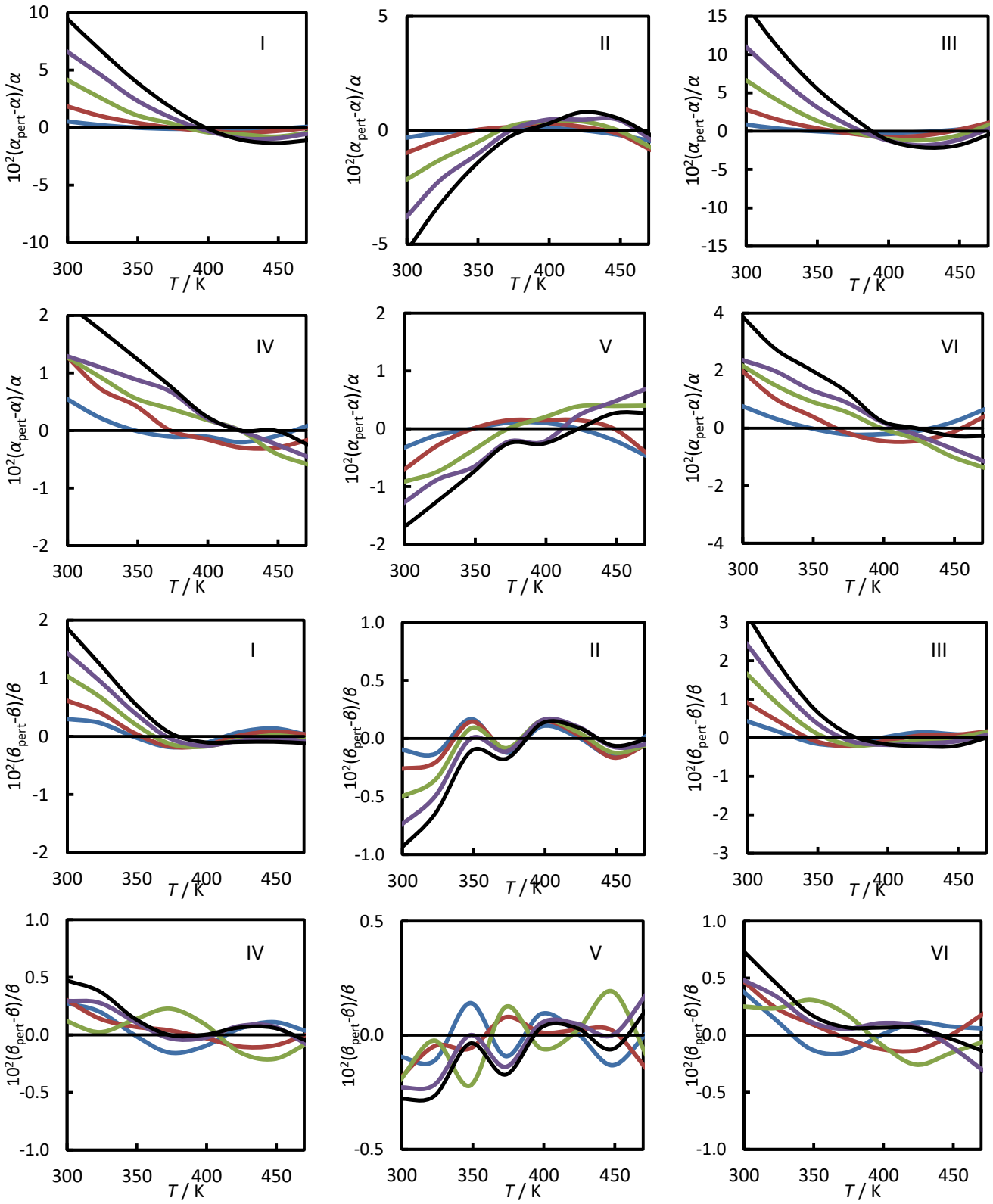



**Figure 5.24** Change in isobaric expansivity and isothermal compressibility, arising from sound-speed cosinusodal perturbation with amplitude of 0.1 %: (I) $k_1 = 0.05$, $k_2 = 0$; (II) $k_1 = 0.1$, $k_2 = 0$; (III) $k_1 = 0.2$, $k_2 = 0$; (IV) $k_1 = 0.05$, $k_2 = 0.02$; (V) $k_1 = 0.1$, $k_2 = 0.02$; (VI) $k_1 = 0.2$, $k_2 = 0.02$. Curves: blue, $p$ = 30 MPa; red, $p$ = 90 MPa; green, $p$ = 180 MPa; purple, $p$ = 270 MPa; black, $p$ = 360 MPa.

# 5.7 Methylbenzene

This section gives the results of the density measurements made for methylbenzene over a temperature range of (283.15 to 473.15) K and for pressures up to 68 MPa. In conjunction, the results of the speed-of-sound measurements made over temperature ranges of (283.15 to 473.15) K at pressures up to 390 MPa are also presented. A comparison of the present density and speed-of-sound data to literature data is given. The experimental data were compared with the predictions from the reference EoS and the SAFT-γ Mie model. Lastly, the experimental sound-speed and density data were combined with isobaric heat capacities to obtain a full spectrum of thermophysical properties via thermodynamic integration.

## 5.7.1 Literature Review

Experimental density data of methylbenzene are plentiful, but most of these experimental data are only restricted to the relatively low-pressure range. Examples of these studies can be found in works such as Fandino *et al.* [171] who studied the system at pressures up to 60 MPa at temperatures between (298 and 398) K; Zeberg-Mikkelsen *et al.* [256] studied the same system at temperatures between (283.15 and 353.15) K and pressures up to 45 MPa; both Segovia *et al.* [227] and Valencia *et al.* [191] reported density of methylbenzene at temperatures between (283 and 398) K at pressures up to 70 MPa. Moravkova *et al.* [221] measured the density at temperatures from (298 to 328) K and pressures up to 40 MPa. All of the works mentioned above used a vibrating-tube densimeter for the density measurements. Avelino *et al.* reported the densities at temperatures between (222 and 348) K and pressures up to 80 MPa using the vibrating-wire technique. McLinden and Splett [253]measured pure methylbenzene density at *T*: (263 to 473) K with pressures up to 35 MPa. Sommer *et al.* [250] measured at a temperature range of (233 to 473) K with pressures up to 30 MPa. Glen and Johns [252] reported at pressures up to 30 MPa at temperatures between (293 and 373) K. All of these measurements were carried out with a double-sinker densimeter. There are fewer experimental sound-speed data compared to density in the literature. The most recent dataset was reported by Meier and Kabelac [147] who measured the speed-of-sound in methylbenzene at temperatures between (280 and 420) K and at pressures up to 100 MPa using the double path-echo technique. Muringer *et al.* [93] made measurements at temperatures between (173 and 320) K and pressures up to 263 MPa, also using a pulse-echo overlap device. The work from Okhotin *et al.* [393] covered the largest part of the liquid region, who reported the sound-speeds in the temperature range of (183 to 523) K and pressures up to 60 MPa. Zotov *et al.* [109] reported at temperatures between (313.15 and 433.15) K. The aim of this work is to extend the current pressure range of the data and provide new accurate experimental thermophysical properties measurement of methylbenzene in wide temperature range. The reference equation of state of methylbenzene was developed by Lemmon and Span [40], and the specified standard uncertainties for liquid-phase density and speed-of-sound were up to 0.3 % and 1 %,

respectively at pressures up to 100 MPa and temperatures below 430 K. Other studies on speed-of-sound are listed in Table 2.4 in Chapter 2.

## 5.7.2 Experimental Density Results and Discussion

The density of methylbenzene along nine isotherms was measured $T$ = (283.15, 298.15, 323.15, 348.15, 373.15, 398.15, 423.15, 448.15 and 473.15) K and at pressures up to 65 MPa. The experimental density data are tabulated in Table B.8 in Appendix B. Figure 5.25 shows the experimental density in methylbenzene as a function of pressure across nine temperatures. In Figure 5.26, we showed the comparison between the experimental densities and the values calculated from the reference EoS developed by Lemmon and Span [40]. Our data agree with the predictions from the EoS and most of the deviations are within ±0.05 % which is consistent with the specified tolerance for the EoS in the temperature and pressure ranges of the present study. The experimental density data of methylbenzene as a function of pressure were compared with nine literature source. Figure 5.27 shows the deviation plots between the literature data and the experimental density data as a function of pressure. It can be seen that the experimental data presented in this work have good agreement with the literature data to within ±0.1 %.

**Correlation:** The isothermal experimental density data of pure methylbenzene was correlated by the modified Tait equation given in Equation (5.5). At temperatures above 398.15 K, the calculated density, $\rho_0$ at 0.1 MPa, were "pseudo" liquid densities as methylbenzene was below the saturation curve for those particular temperatures. The statistical measures and the parameters of Equations (5.5) and (5.6) are given in Table 5.9. The relative deviations of the experimental density from the Tait equation were all within ±0.02 % as shown in Figure 5.25. The calculated statistical parameters, $\Delta_{AARD}$ and $\Delta_{MARD}$ were found to be 0.01 % and 0.04 %, respectively in the entire temperature and pressure range.

**Table 5.11** Fitting parameters of the modified Tait equation (5.5) for the compressed-liquid density measurements of methylbenzene together with the statistical parameters, $\Delta_{AARD}$ and $\Delta_{MARD}$.

| | | | | | |
|---|---|---|---|---|---|
| $a_0$ | 1267.77 | $b_0$ | 481.23 | $C$ | 0.20 |
| $a_1$ | -599.78 | $b_1$ | -559.94 | | |
| $a_2$ | 311.76 | $b_2$ | 223.84 | $\Delta_{AARD}$ | 0.01% |
| $a_3$ | -94.31 | $b_3$ | -31.92 | $\Delta_{MARD}$ | 0.04% |

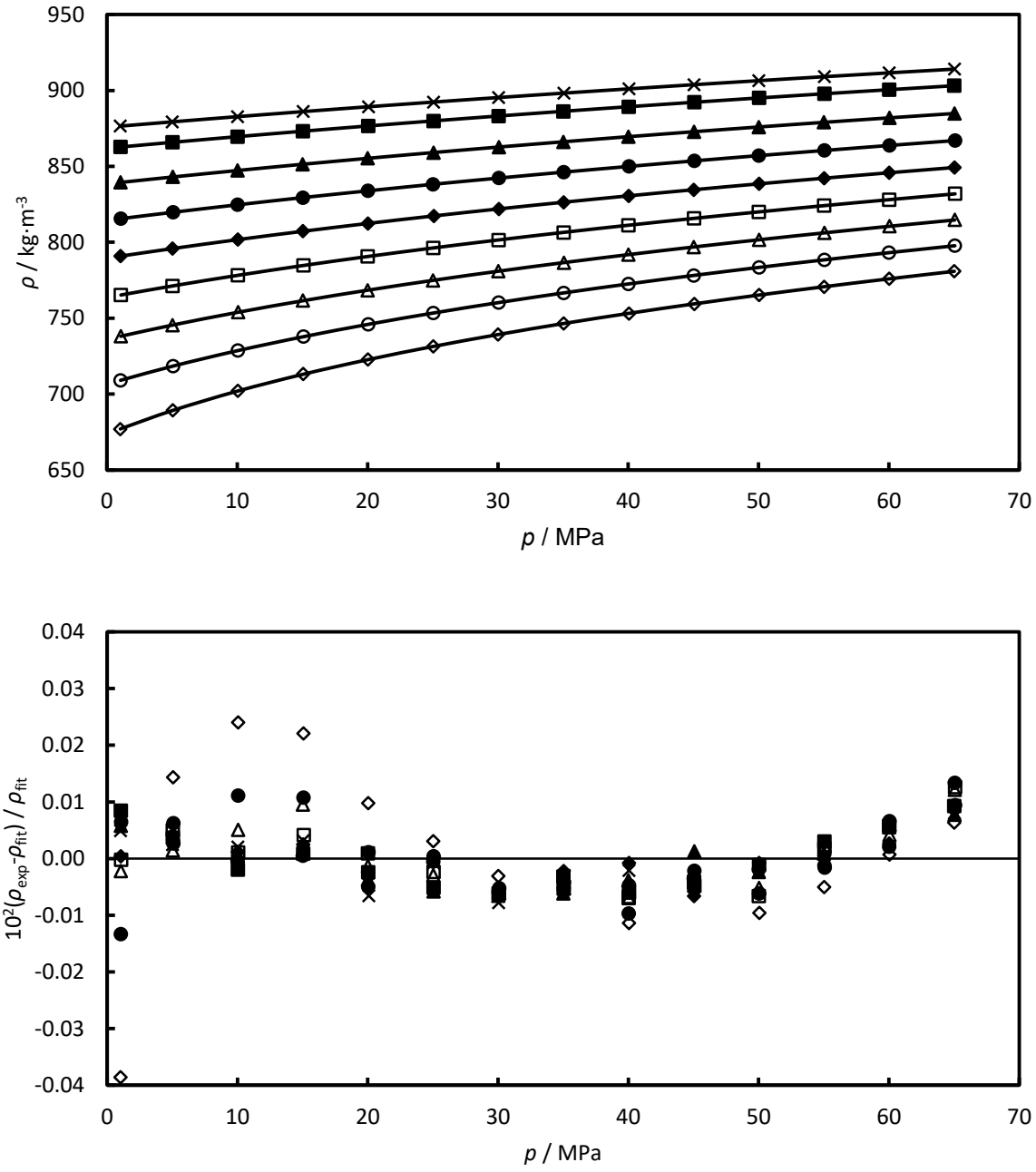



**Figure 5.25** (*top*) Experimental density of methylbenzene as a function of pressure across nine isotherms: ×, 283.15 K; ■, 298.15 K; ▲, 323.15 K; ●, 348.15 K; ◆, 373.15 K; □, 398.15 K; △, 423.15 K; ○, 448.15 K; ◇, 473.15 K. Solid lines: densities calculated from the modified Tait equation, Equation (5.5). (*bottom*) Deviations of experimental densities $\rho_{exp}$ from the calculated densities using the modified Tait equation $\rho_{fit}$.

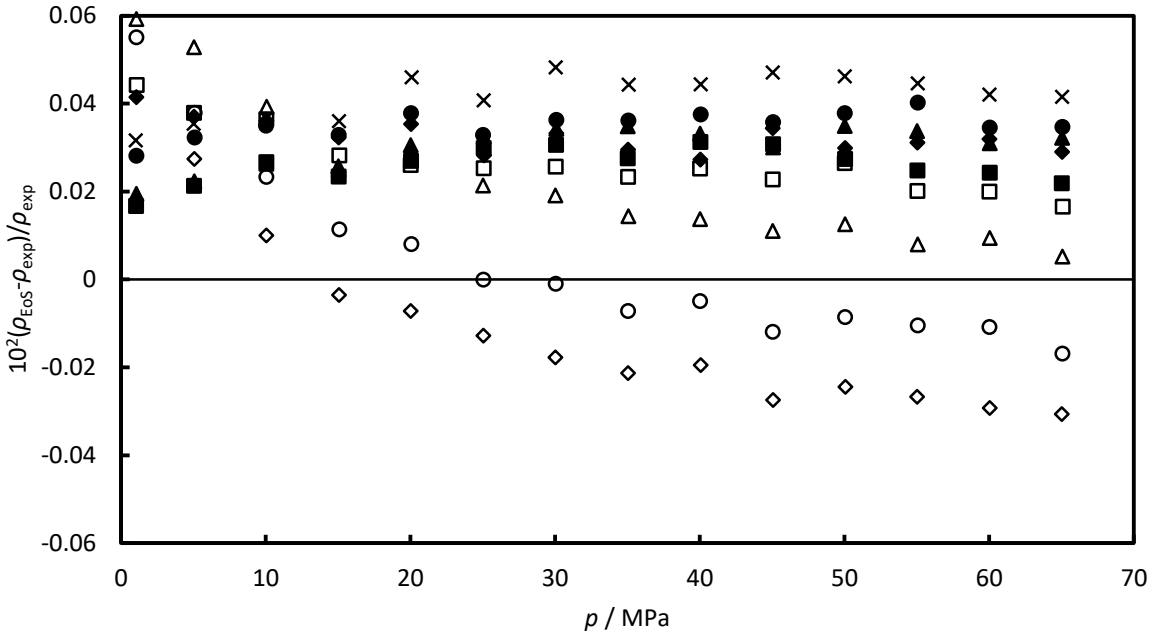



**Figure 5.26** Deviations of experimental densities $\rho_{exp}$ of methylbenzene from the values calculated from the reference EoS $\rho_{EoS}$ across nine isotherms: ×, 283.15 K; ■, 298.15 K; ▲, 323.15 K; ●, 348.15 K; ◆, 373.15 K; □, 398.15 K; △, 423.15 K; ○, 448.15 K; ◇, 473.15 K.

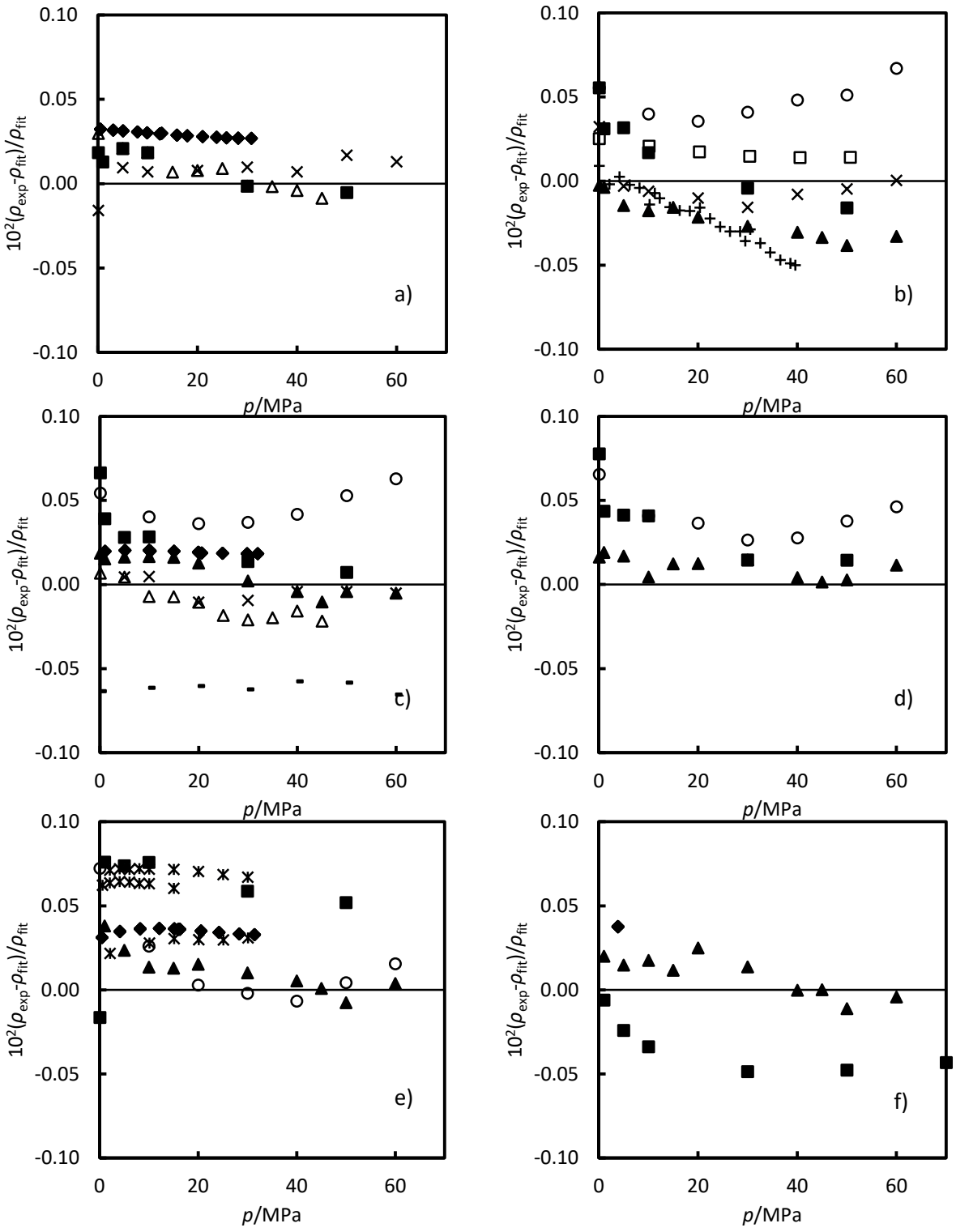



**Figure 5.27** Deviation plots of the literature data $\rho_{exp}$ and the values calculated using the modified Tait equation, Equation (5.5) $\rho_{fit}$. a) 283.15 K; b) 298.15 K; c) 323.15 K; d) 348.15 K; e) 373.15 K; f) 398.15 K. Symbols represent literature data: ■, Segovia *et al.* [227]; ◆, McLinden and Splett [253]; ▲, Fandino *et al.* [171]; ✖, Valencia *et al.* [191]; ○, Avelino *et al.* [257]; □, Muringer *et al.* [93]; ✱, Glen and Johns [252]; △, Zeberg-Mikkelsen *et al.* [256]; ✚, Moravkova *et al.* [221]

## 5.7.3 Experimental Speed-of-Sound Results and Discussion

The speed-of-sound measurement in methylbenzene along nine isotherms: $T$ = (283.15, 298.15, 323.15, 348.15, 373.15, 398.15, 423.15, 448.15 and 473.15) K and at pressures up to 390 MPa, were carried out. The experimental data are given in Table B.9, and Figure 5.28 shows the sound-speed as a function of pressure. In Figure 5.29, we compared the speed-of-sound in methylbenzene with values calculated using the reference EoS [40]. A clear trend emerges with the predicted values generally being too high; the deviations are within 0.5 % at $p$ < 100 MPa and within 2 % at $p$ > 100 MPa. These deviations are consistent with the specified tolerances of for the EoS of methylbenzene in the temperature and pressure ranges of the present study but larger than the uncertainty of the present results. The specified uncertainty from the equation of state, sound-speed is 1 % up to 500 K and 100 MPa and rises to 2 % at higher pressures and temperatures. The experimental sound-speed has also been compared with the available literature data. Figure 5.30 shows the comparison across six temperature ranges between our data and the literature data. The speed-of-sound values calculated from the equation of state have also been added to the plots for comparison. Our data have the best agreement with the literature data reported by Meier and Kabelac [147] which is considered as the most reliable dataset which contained the specified uncertainty of 0.05 %.

**Correlation:** An empirical pressure-explicit correlation, Equation (5.2) was developed to represent the experimental sound-speed data over the studied temperature and pressure range. The parameters were determined by minimising the sum square error between the experimental data and the values calculated by the correlation across all temperatures and pressures. The reference speed-of-sound, $c_0$ was then correlated as a function of temperature, given in Equation (5.2). In general, the correlation describes the sound-speed experimental data well across a wide range of temperature and pressure and with the $\Delta_{AARD}$ consistent with the overall standard uncertainty. The $\Delta_{AARD}$ for the surface fit of speed-of-sound correlation was 0.02 %, and the $\Delta_{MARD}$ was 0.25 % which occurred at the state point ($T$ = 423.15 K and $p$ = 30 MPa). The parameters in equations (5.2) and (5.2) are tabulated in Table 5.10.

**Table 5.12** Fitting parameters of the empirical correlation, Equation (5.2) for the speed-of-sound measurements in methylbenzene together with the statistical parameters, average absolute relative deviation, $\Delta_{AARD}$ and maximum absolute relative deviation $\Delta_{MARD}$.

| | | | | | | | | | |
|---|---|---|---|---|---|---|---|---|---|
| $a_{10}$ | $-4.173\times10^{-1}$ | $a_{20}$ | $-1.088\times10^{-4}$ | $a_{30}$ | $-1.166\times10^{-7}$ | $b_0$ | $3.238\times10^{3}$ | $\Delta_{AARD}$ | 0.02% |
| $a_{11}$ | 1.286 | $a_{21}$ | $5.969\times10^{-4}$ | $a_{31}$ | $5.518\times10^{-7}$ | $b_1$ | $-2.602\times10^{3}$ | | |
| $a_{12}$ | $-9.567\times10^{-1}$ | $a_{22}$ | $-4.621\times10^{-4}$ | $a_{32}$ | $-6.522\times10^{-7}$ | $b_2$ | $9.934\times10^{2}$ | $\Delta_{MARD}$ | 0.25% |
| $a_{13}$ | $3.047\times10^{-1}$ | $a_{23}$ | $1.588\times10^{-4}$ | $a_{33}$ | $2.577\times10^{-7}$ | $b_3$ | $-2.125\times10^{2}$ | | |

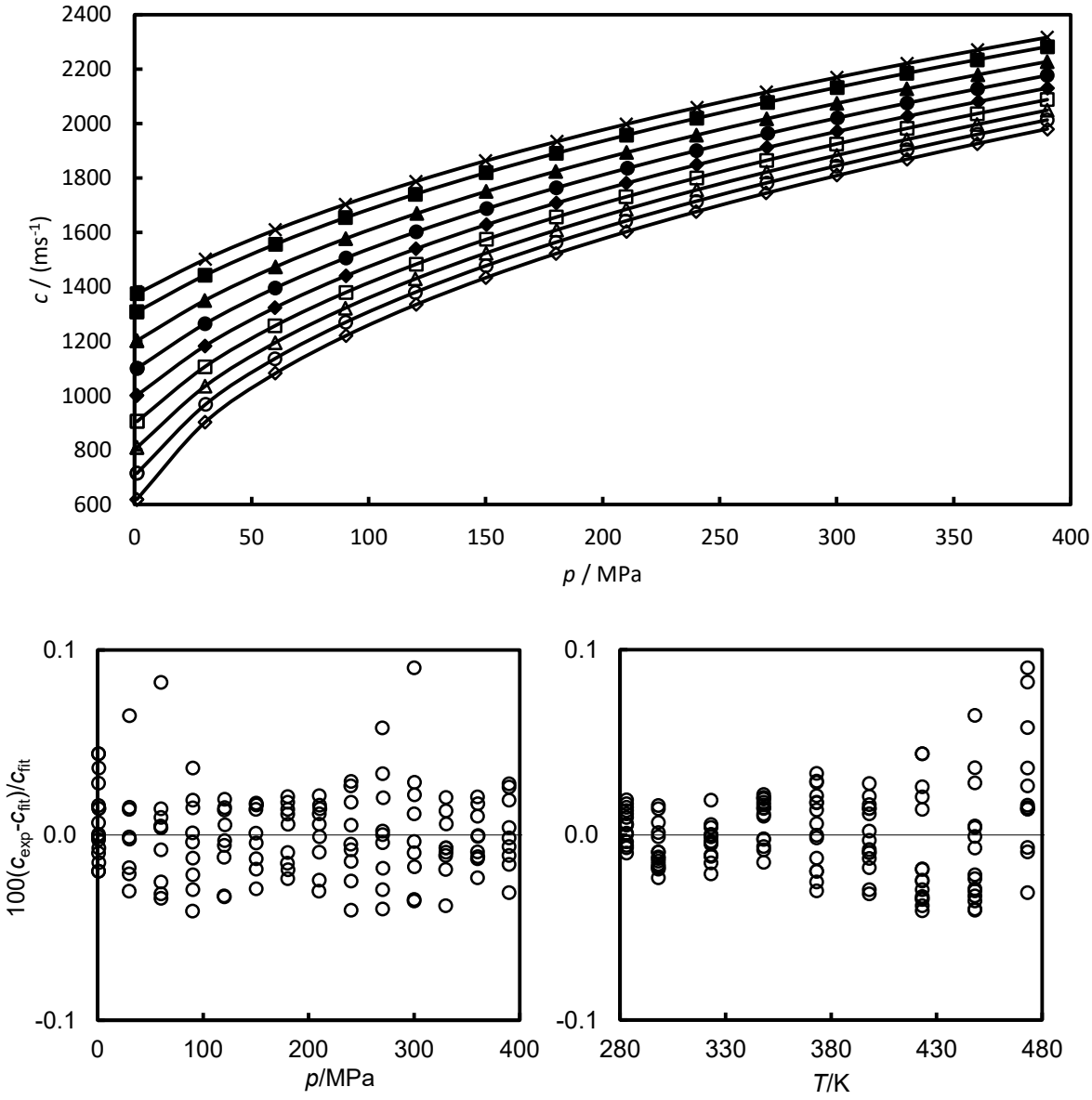



**Figure 5.28** (*top*) Experimental sound-speed data in methylbenzene along nine isotherms: ×, 283.15 K; ■, 298.15 K; ▲, 323.15 K; ●, 348.15 K; ◆, 373.15 K; □, 398.15 K; △, 423.15 K; ○, 448.15 K; ◇, 473.15 K. Symbols represent experimental data and lines denote correlation, respectively. (*bottom*) Deviations of the experimental speed-of-sound in methylbenzene $c_{exp}$ from the values $c_{fit}$ calculated from the empirical correlation with parameters fitted to the experimental data a function of pressures and temperatures.

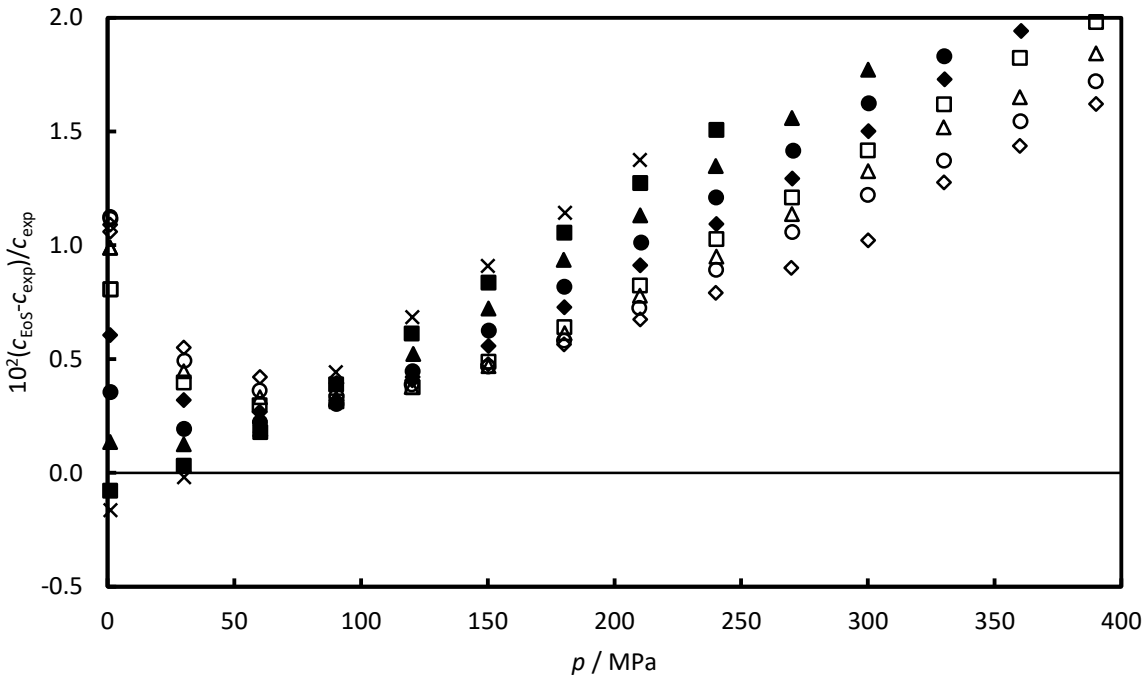



**Figure 5.29** Deviations of experimental speed-of-sound $c_{exp}$ of methylbenzene from the values calculated from the reference EoS $c_{EoS}$ across nine isotherms: ×, 283.15 K; ■, 298.15 K; ▲, 323.15 K; ●, 348.15 K; ◆, 373.15 K; □, 398.15 K; △, 423.15 K; ○, 448.15 K; ◇, 473.15 K.

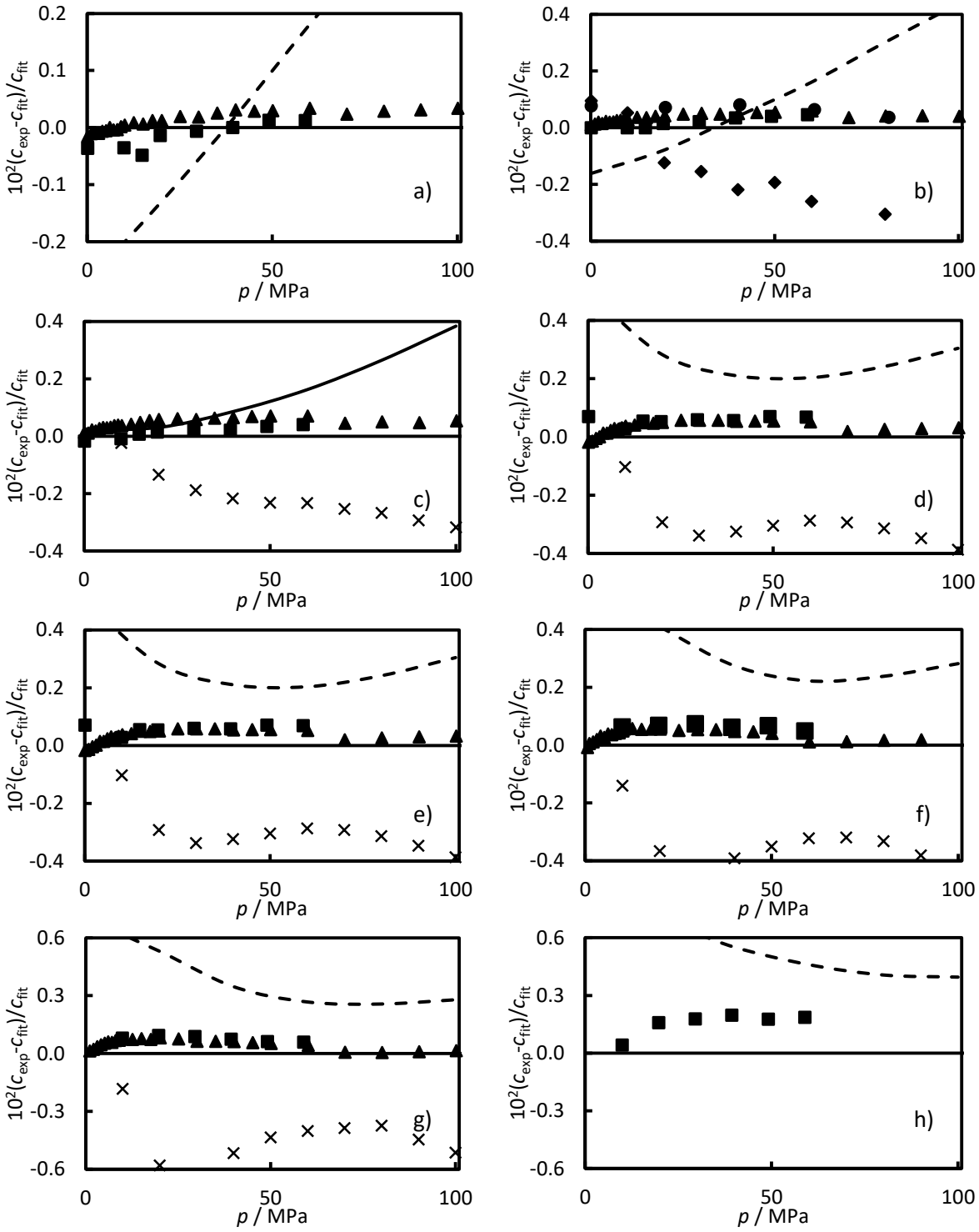



**Figure 5.30** Comparison between the literature data $c_{exp}$ and sound-speeds calculated from the empirical correlation, Equation (5.2) $c_{fit}$. a) 283.15 K, b) 298.15 K, c) 323.15 K, d) 348.15 K, e) 373.15 K, f) 398.15, g) 423.15 K, h) 473.15 K .Symbols represent literature data from several workers: ▲, Meier and Kabelac [147] (280, 300, 320, 340, 380, 400 and 420) K; ■, Okhotin *et al.* [393] (283, 303, 323, 343, 373, 403, 423 and 473) K; ×, Zotov *et al.* [109] (353, 373, 393, 413 and 433) K; ◆, Muringer *et al.* [93] (298) K. Dotted lines represent predictions from the reference EoS [40].

## 5.7.5 Modelling

The experimental compressed-liquid density and speed-of-sound data for methylbenzene have been compared with the predictions from SAFT-γ Mie EoS. The structure and method of SAFT-γ Mie have been described previously in Chapter 3, and only a brief reference is made here for the particular function groups. To characterise methylbenzene, functional groups (aCH) and ($aCCH_3$) are used. The parameters of these functional groups were optimised by Papaioannou *et al.* [351] with experimental data. The parameters for the function groups aCH and $aCCH_3$ are summarised in Table 5.13. The deviation plot between the experimental data and the predictions is shown in Figure 5.31. The $\Delta_{AARD}$ between the experimental data and the predictions were 0.1 % and 1.4 % for density and sound-speed, respectively.

**Table 5.13** SAFT-γ Mie like parameters for functional groups aCH and $aCCH_3$, $v_k^*$ the number of segments, $S_k$ the shape factor, $\varepsilon_{kk}$ the interaction energy, $\sigma_{kk}$ the segment diameter, and $\lambda_{kk}^{r}$ and $\lambda_{kk}^{a}$ the repulsive and attractive exponents, respectively.

| Functional Group | $v_k^*$ | $S_k$ | $(\varepsilon_{kk}/k_B)$/K | $\sigma_{kk}\times10^{10}$/m | $\lambda_{kk}^{r}$ | $\lambda_{kk}^{a}$ | Ref. |
|---|---|---|---|---|---|---|---|
| aCH | 1 | 0.3218 | 371.53 | 4.058 | 14.756 | 6.000 | [394] |
| $aCCH_3$ | 1 | 0.3166 | 651.41 | 5.487 | 23.627 | 6.000 | [351] |

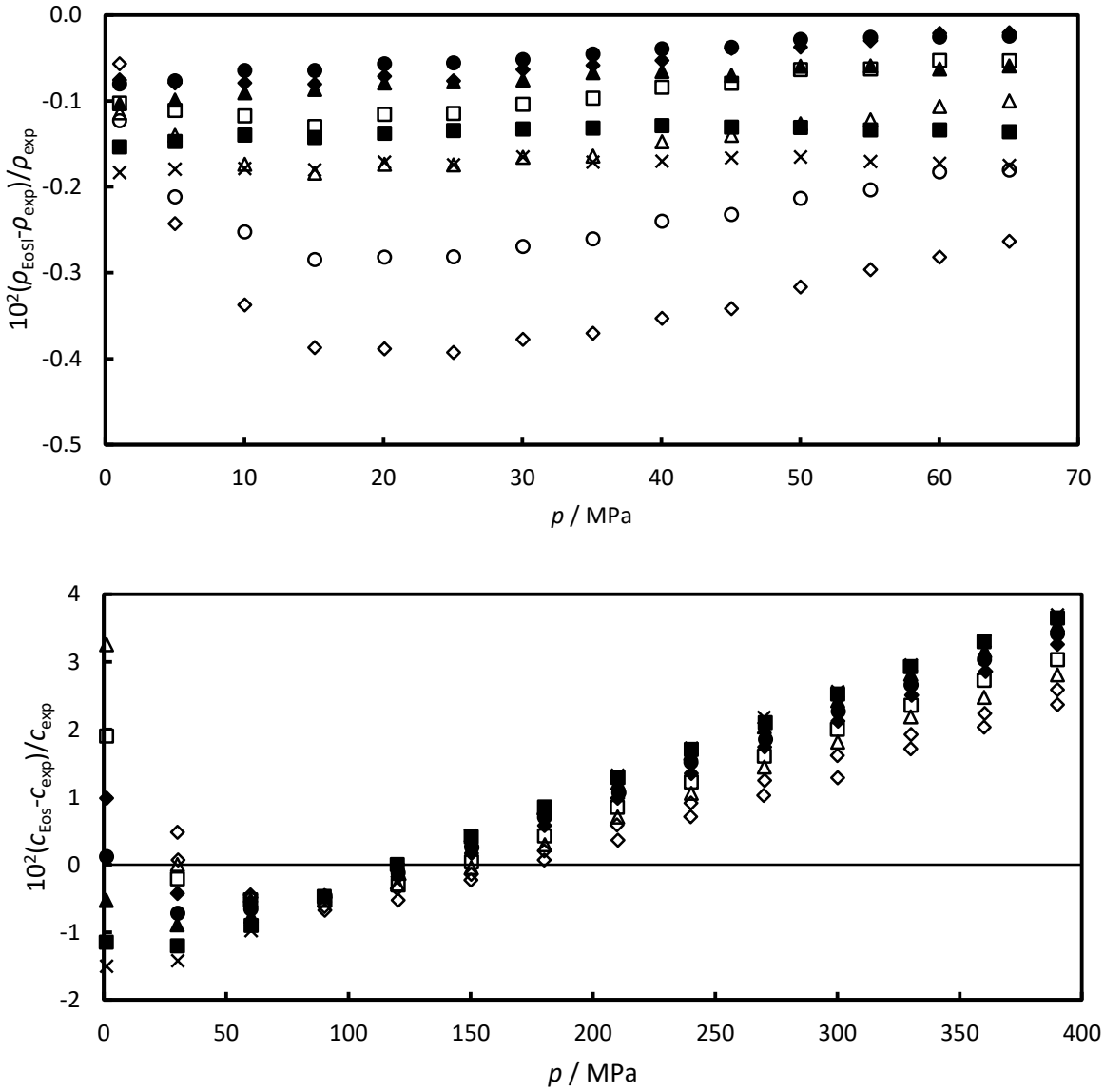



**Figure 5.31** (*top*) Deviations of the experimental density $\rho_{exp}$ in methylbenzene from the values calculated from SAFT-γ Mie $\rho_{EoS}$. (*bottom*) Deviations of the experimental speed-of-sound in methylbenzene, $c_{exp}$ from the values $c_{EoS}$ calculated from SAFT-γ Mie across nine isotherms: ×, 283.15 K; ■, 298.15 K; ▲, 323.15 K; ●, 348.15 K; ◆, 373.15 K; □, 398.15 K; △, 423.15 K; ○, 448.15 K; ◇, 473.15 K.

## 5.7.6 Derived Thermophysical Properties

The experimental sound-speed data combined with isobaric heat capacities and density along one isobar, by means of thermodynamic integration, density and isobaric heat capacity alongside with other thermophysical properties such isothermal compressibility, $\beta$ and isobaric expansivity, $\alpha$ have been derived up to the 390 MPa. The accuracy of the derived data was governed by the experimental uncertainty of the input properties. This method was first proposed by Davis and Gordon [48], and the method has been described in detail in Chapter 3. Similarly, the isobaric heat capacity data of methylbenzene along an isobar was obtained from the literature. According to our literature review, several workers have reported the isobaric heat capacity of methylbenzene at temperatures between (223 and 620) K at different pressures. In our case, for the thermodynamic integration, only isobaric heat capacity data along one isobar was required (saturation curve). The required temperature range of the isobaric heat capacity data would be between (283.15 and 473.15) K. The available literature data are tabulated in Table 5.14 and shown in Figure 5.32. The $c_{p,\mathrm{EoS}}$ values calculated from the EoS have also been added to Figure 5.32 for comparison.

**Table 5.14** Isobaric heat capacities $c_p$ studies of methylbenzene; $T$ and $p$ refer to the temperature and pressure ranges examined, respectively.

| Author (Year) | $T$ / K | $p$ / MPa |
|---|---|---|
| Okhotin *et al.* (1987) [145] | 181.45 – 380.40 | saturated |
| Chirico and Steele (1994) [395] | 300.00 – 570.00 | saturated |
| Becker *et al.* (2000) [396] | 288.13 – 353.20 | saturated |
| Cerdeirina *et al.* (2002) [397] | 278.15 – 338.15 | saturated |
| Lemmon and Span (2006) (EoS) [40] | 178.00 – 700.00 | 0.1 – 500 |
| Segovia *et al.* (2008) [398] | 273.15 – 333.15 | 0.1 – 20 |

The $c_p$ data along the saturated curve were obtained from two literature datasets: Cerdeirina *et al.* [397] and Chirico and Steele [395]. Cerdeirina *et al.* reported $c_p$ at temperatures between (278.15 and 338.15) K using a differential scanning calorimeter Micro DSC II from Setaram, with an associated uncertainty of 0.5 % and Chirico and Steele reported the isobaric heat capacity at temperatures from (300 to 570) K with a differential scanning calorimeter Perki*n*-Elmer DSC II. To facilitate the thermodynamic integration, the literature data were correlated by a polynomial equation, Equation (5.8). Figure 5.33 shows the deviation between the literature data and the values calculated from the polynomial correlation. Most deviations are within a band of ±0.1 %.

**Table 5.15** Parameters of the isobaric heat capacity correlation, Equation (5.8) for methylbenzene.

| | | | | | | | | | |
|---|---|---|---|---|---|---|---|---|---|
| $e_0$ | $1.575\times10^{3}$ | $e_1$ | $-8.072\times10^{2}$ | $e_2$ | $1.045\times10^{3}$ | $e_3$ | $-1.808\times10^{2}$ | $\Delta_{\mathrm{AARD}}$ | 0.05% |

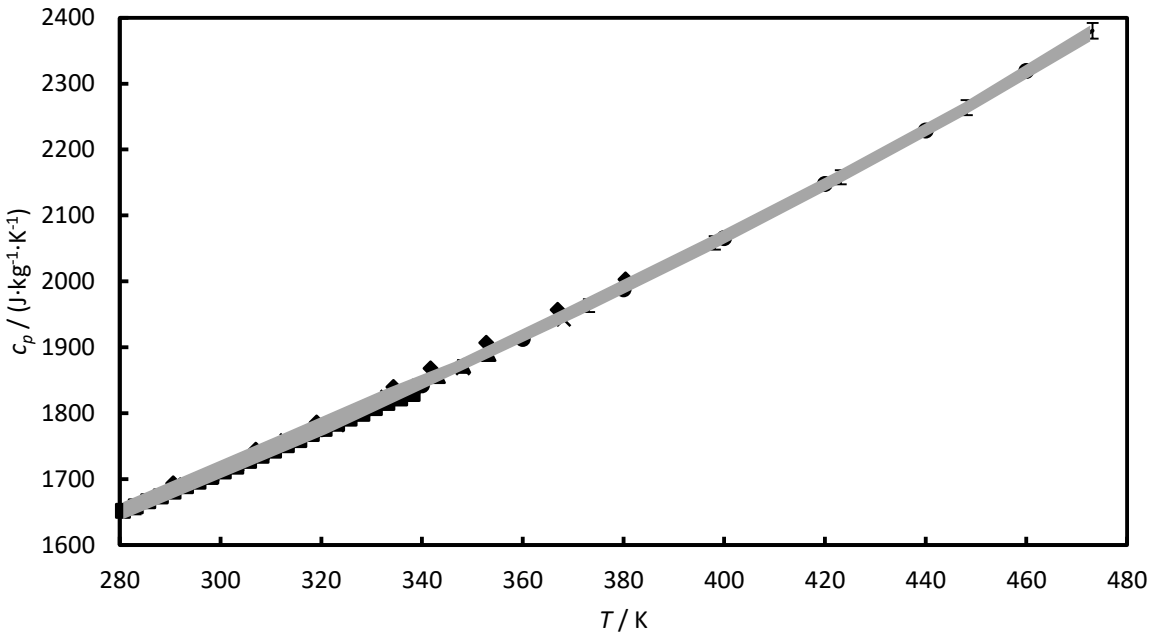



**Figure 5.32** Experimental isobaric heat capacities $c_p$ of methylbenzene in the literature from (283.15 to 473.15) K. Symbols represent literature data : ●, Chirico and Steele [395]; ▲, Becker *et al.* [396]; ■, Cerdeirina *et al.* [397]; ◆, Okhotin *et al.* [145]; ×, Segovia *et al.* [398]Line represent predictions from the reference EoS [40].

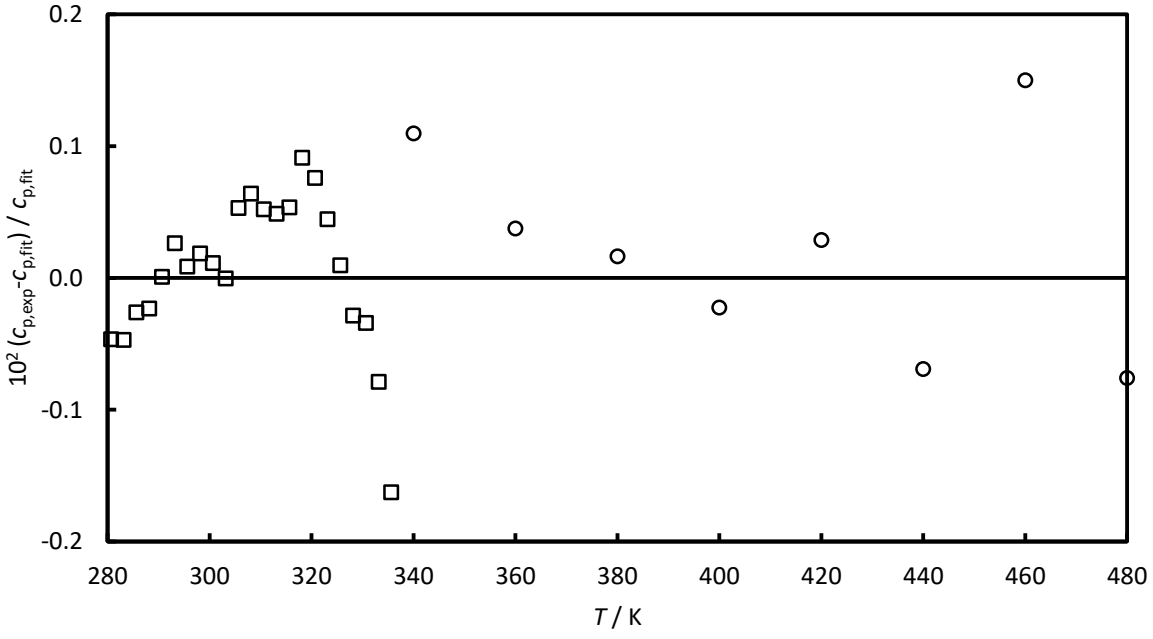



**Figure 5.33** Deviations of the experimental isobaric heat capacity of methylbenzene in literature $c_{p,exp}$ from the values calculated from the polynomial correlation, Equation (5.8) $c_{p,fit}$. Symbols: □, Cerdeirina *et al.* [397]; ○, Chirico and Steele [395].

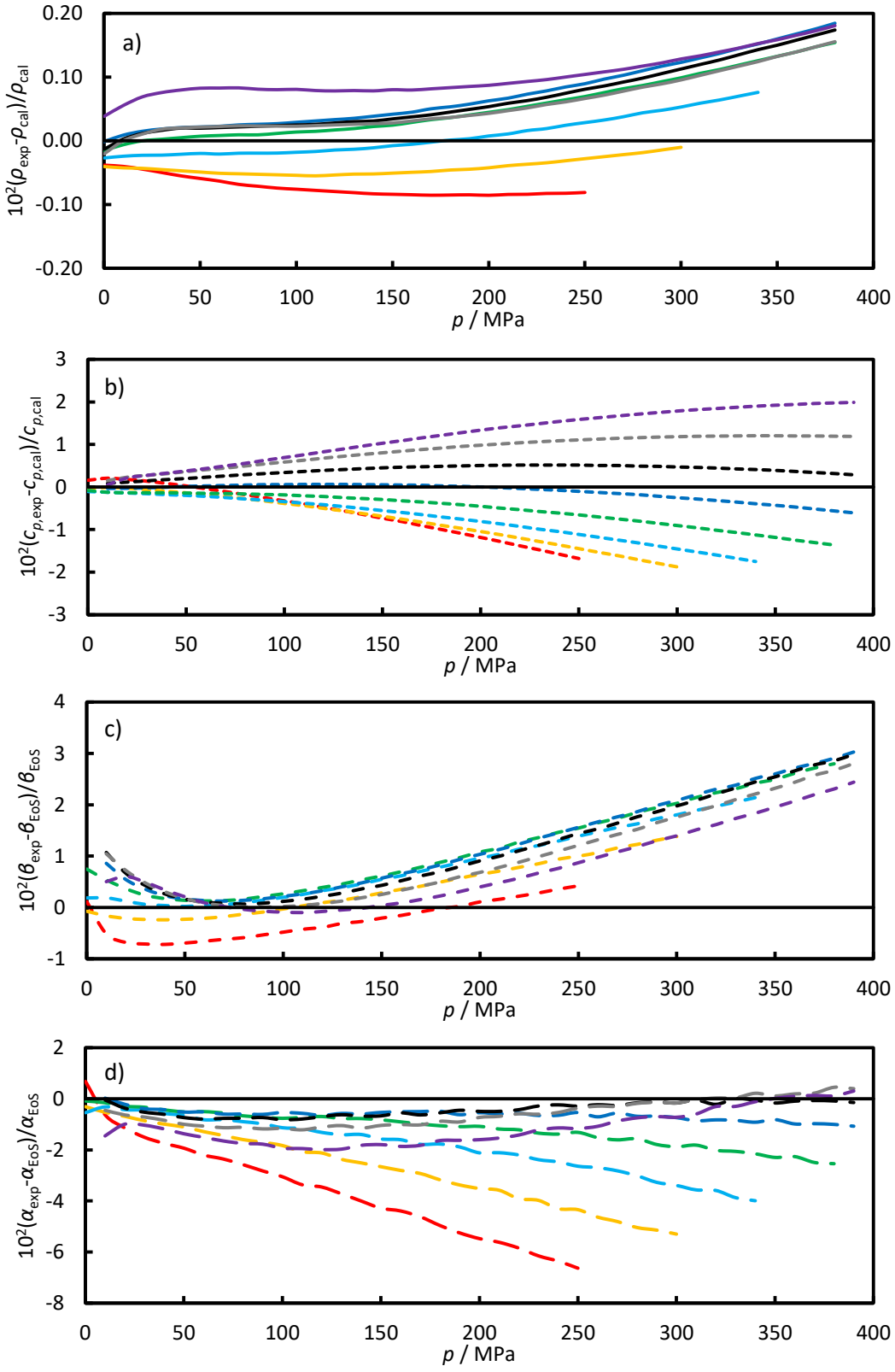



**Figure 5.34** Deviations between derived density $\rho$, isobaric heat capacity $c_p$, isothermal compressibility $\beta$ and isobaric expansivity $\alpha$ and values calculated from the EoS up to 390 MPa across eight isotherms. Lines denote predictions from EoS: (red), 298.15 K; (orange), 323.15 K; (light blue), 348.15 K; (green), 373.15 K; (blue), 398.15 K; (black), 423.15 K; (grey),448.15 K; (purple), 473.15 K.

A full spectrum of thermophysical properties has been derived up to 390 MPa, and they were compared with the calculated values using the reference EoS for methylbenzene developed by Lemmon and Span. The deviation plots are shown in Figure 5.34. It can be seen that most of the derived densities agree with the predictions from the EoS to within ±0.1 % up to 390 MPa. For isobaric heat capacity, most of our data agree to about a band of ±2 % with the EoS predictions. Comparisons of the isobaric expansivity and isothermal compressibility with the predictions from EoS can also be found in Figure 5.34. The derived thermophysical properties are tabulated in Table B.10 in Appendix B.

The true uncertainty of the derived properties is difficult to estimate; however, to quantify the uncertainty of the derived properties, perturbation of initial values of density and heat capacity data, and sound-speed experimental data has been carried out, in turn, to see the effect on the derived thermophysical properties up to 390 MPa. Given the experimental uncertainty and the errors in the surface fit for speed-of-sound, we perturbed the sound-speed data by 0.1 %; this changed the derived values of density between (0 and 0.03) % with the largest changes occurred at the highest isotherm. The change in $c_p$ was ranging from (0 to 0.07) % with the biggest change also took place at the highest isotherm. The relative changes for Isothermal compressibility were within 0.1 %. Isobaric expansivity had the largest change of approximately 0.2 % throughout all temperatures and pressures. We also considered the effect of a relative perturbation to $c$ given by a cosinusoidal function of $T$ and $p$, given by Equation (5.9). This expression allows variable perturbations to be applied on to the sound-speed data. We explored different scenarios in which $k_1$ = (0.05, 0.1 or 0.2) $K^{-1}$ with $k_2$ = (0 or 0.02) $MPa^{-1}$. It has been noticed that the effect of the sound-speed perturbation on other properties is reduced when $k_2 > 0$. The effects of different values of $k_1$ and $k_2$ on the derived properties are shown in Figures 5.35 and 5.36. Then we looked at the effect of changing $\rho_0$ by 0.1 % which is the uncertainty of the measurement. The change in $c_p$ was insignificant with the largest change being 0.03 %. $\beta$ were changed within (0.03 to 0.15) %, and the derived values of $\alpha_p$ were changed by an average of 0.09%. Lastly, we increased the initial values of $c_p$ by 0.2 %. The changes in $\rho$ and $\kappa$ were very small with the largest relative changes for density and isothermal compressibility being 0.01 % and 0.05 % respectively. The average relative change in isobaric expansivity was 0.03 % from changing the initial values of $c_p$. Considering the combined effects of the input data, we estimate that the relative uncertainties of the derived properties are approximately 0.1 % for $\rho$, 2 % for $c_p$, 1 % for $\beta$, and 2 % for $\alpha$ at all state points with 283.15 K $\leq T \leq$ 473.15 K.

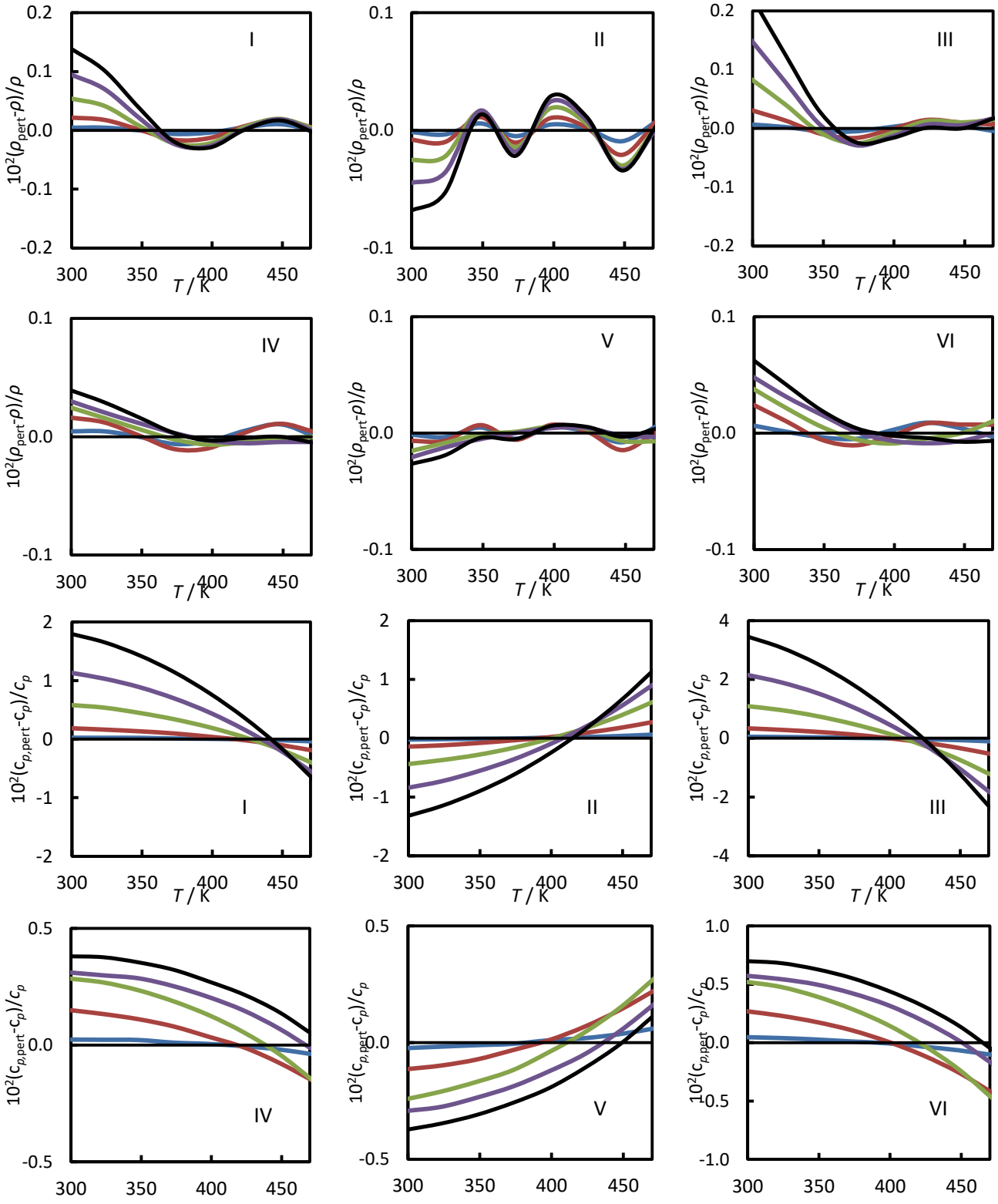



**Figure 5.35** Change in density and isobaric heat capacity, arising from sound speed cosinusodal perturbation with amplitude of 0.1 %: (I) $k_1 = 0.05$, $k_2 = 0$; (II) $k_1 = 0.1$, $k_2 = 0$; (III) $k_1 = 0.2$, $k_2 = 0$; (IV) $k_1 = 0.05$, $k_2 = 0.02$; (V) $k_1 = 0.1$, $k_2 = 0.02$; (VI) $k_1 = 0.2$, $k_2 = 0.02$. Curves: blue, $p = 30$ MPa; red, $p = 90$ MPa; green, $p = 180$ MPa; purple, $p = 270$ MPa; black, $p = 360$ MPa.

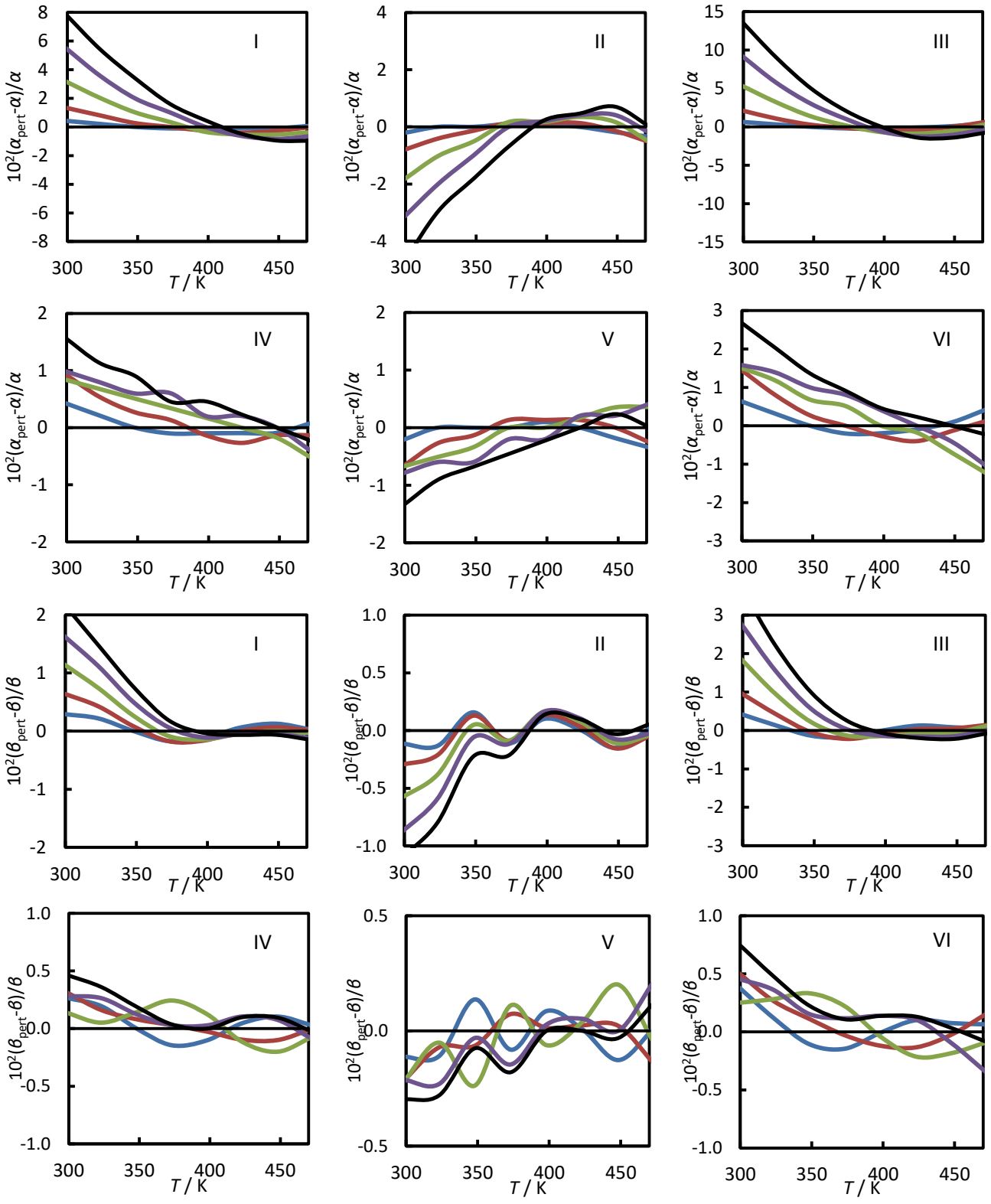



**Figure 5.36** Change in isobaric expansivity and isothermal compressibility, arising from sound speed cosinusodal perturbation with amplitude of 0.1 %: (I) $k_1 = 0.05$, $k_2 = 0$; (II) $k_1 = 0.1$, $k_2 = 0$; (III) $k_1 = 0.2$, $k_2 = 0$; (IV) $k_1 = 0.05$, $k_2 = 0.02$; (V) $k_1 = 0.1$, $k_2 = 0.02$; (VI) $k_1 = 0.2$, $k_2 = 0.02$. Curves: blue, $p$ = 30 MPa; red, $p$ = 90 MPa; green, $p$ = 180 MPa; purple, $p$ = 270 MPa; black, $p$ = 360 MPa.

# 5.8 Carbon Dioxide

This section gives the results of the compressed-liquid density measurements made for pure carbon dioxide over a temperature range of (283.15 to 473.15) K, and pressures up to 65 MPa. The experimental data were compared with the predictions from the reference equation of state and SAFT-γ Mie.

## 5.8.1 Literature Review

Most of the available literature density data were measured below the critical temperature, examples of these works can be found in Table 2.6 in Chapter 2. The study carried out by Klimeck *et al.* [272] covered the largest temperature range from (240 to 430) K and at pressures up to 30 MPa. They measured the density of $CO_2$ with a single-sinker densimeter, and their data were considered accurate up to 0.03 %. A reference equation of state was developed by Span and Wagner [174] for $CO_2$ which is capable of calculating the thermophysical properties of $CO_2$ from the triple point temperature to 1100 K at pressures up to 800 MPa. The density predictions from the equation of state are associated with an uncertainty of 0.05 % at pressures up to 30 MPa and temperatures up to 523 K.

## 5.8.2 Experimental Density Results and Discussion

Liquid-phase density was measured for pure $CO_2$ across nine isotherms $T$ = (283.15, 298.15, 348.15, 373.15, 398.15, 423.15, 448.15 and 473.15) K at pressures up to 65 MPa. At each isotherm, the measurement started at 10 MPa to ensure $CO_2$ is a single-liquid-phase fluid. In the measurement range, $CO_2$ behaved both as a sub-critical and a supercritical fluid. Experimental density as a function of pressure is shown in Figure 5.37 and is given in Table B.11 in Appendix B. The $CO_2$ density results showed a typical trend for liquids where the density increases with pressure and decreases with temperature. At 323.15 K, the starting measurement point was measured very close to the critical region and there shows a large density increment from (10 to 15) MPa. On the same isotherm, the change in density as a function of pressure was the largest amongst all the isotherms and ranges from approximately (388 to 1006) $kg \cdot m^{-3}$. The density is very pressure-sensitive near the critical region, as shown in Figure 5.37, a small change in pressure results in a large change in the density of $CO_2$. The collected experimental data were compared with the predictions from the equation of state developed for $CO_2$ by Span and Wagner. The deviation plot is shown in Figure 5.38 and most of our data agree to within ±0.10 % with the predictions and the $\Delta_{AARD}$ was found to be 0.1 %.

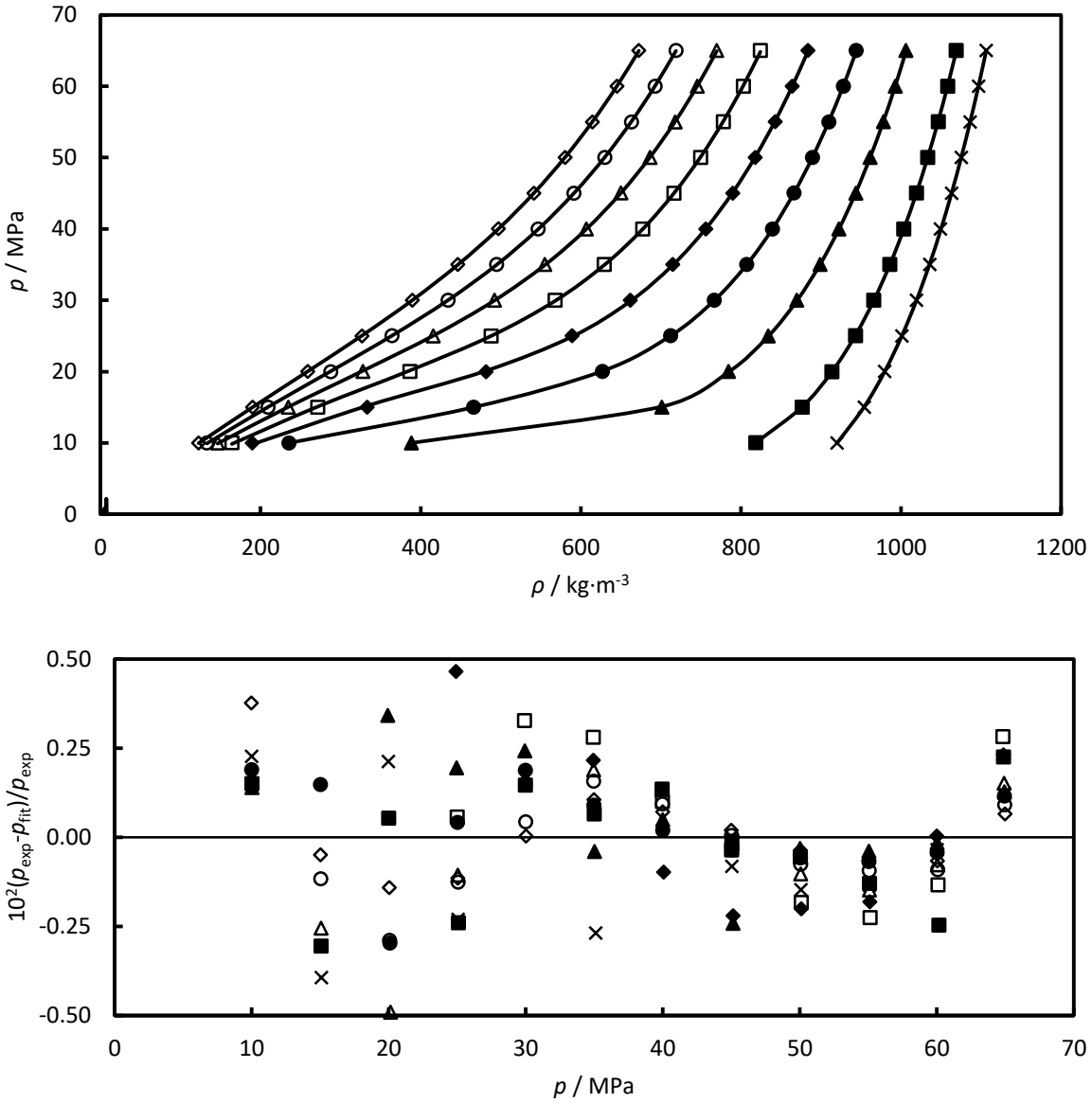



**Figure 5.37** (*top*) Pressure as a function of experimental density $\rho$ of carbon dioxide across nine isotherms: ×, 283.15 K; ■, 298.15 K; ▲, 323.15 K; ●, 348.15 K; ◆, 373.15 K; □, 398.15 K; △, 423.15 K; ○, 448.15 K; ◇, 473.15 K. Solid lines: densities calculated from the new empirical equation, Equation (5.10). (*bottom*) Deviations between the experimental densities $\rho_{exp}$ and the calculated densities using Equation (5.10) $\rho_{fit}$.

**Correlation:** The compressed-liquid density data of $CO_2$ were first correlated with the modified Tait equation, Equation (5.5) described earlier. However, due to the high compressibility of $CO_2$ and the non-linearity in density around the critical region, the equation was not able to correlate the experimental data to a high accuracy over the measured range. An empirical correlation was hence developed the compressed-liquid density of $CO_2$ across the sub- and supercritical regions. The developed correlation is given as follows:

$$p = A\rho + B\rho^2 + C\frac{(\rho - \rho_r)^\delta}{\delta}, \tag{5.10}$$

where $\rho_r$ refers to the reference density at each isotherm which is a floating parameter. To account for the non-linearity of the densities around the critical region, a non-linear term $(\rho - \rho_r)^\delta / \delta$ was added into the equation. The term $\delta$ is a universal critical exponent whose value was set to be 4.82. Parameters $A$, $B$, $C$ and $\rho_r$, are all adjustable parameters which were optimised using the Lenvenberg-Marquardt optimisation method. Figure 5.37 shows the calculated densities using empirical equation and the experimental measurements. The parameters of Equation (5.10) are summarised in Table B.12 in Appendix B. It was estimated that the $\Delta_{AARD}$ between the experimental data and the predictions from the empirical correlation is approximately 0.2 % and the deviation plot can be found in Figure 5.38.

## 5.8.4 Modelling

The experimental density was compared with the predictions from SAFT-γ Mie, and the description of the SAFT-γ Mie model has been described previously in Chapter 3. The parameters for the $CO_2$ molecular group were estimated in the work of Papaioannou *et al.* [350, 351], using vapour pressure and saturated liquid density data. The like parameters for functional group $CO_2$ are given in Table 5.16. In Figure 5.38, we compared the predictive ability of the SAFT-γ Mie EoS and the reference EoS on the compressed-liquid density of $CO_2$. The predictions from the reference EoS have better agreement with the experimental data and SAFT-γ Mie EoS generally under-predicts the density throughout the experimental range. The $\Delta_{AARD}$ between the experimental data and the predictions from SAFT-γ Mie was found to be 3.7 %.

**Table 5.16** SAFT-γ Mie like parameters for functional group $CO_2$, $v_k^*$ the number of segments, $S_k$ the shape factor, $\varepsilon_{kk}$ the interaction energy, $\sigma_{kk}$ the segment diameter, and $\lambda_{kk}^r$ and $\lambda_{kk}^a$ the repulsive and attractive exponents, respectively.

| Functional Group | $v_k^*$ | $S_k$ | $(\varepsilon_{kk}/k_B)$/K | $\sigma_{kk}\times10^{10}$/m | $\lambda_{kk}^r$ | $\lambda_{kk}^a$ | Ref. |
|---|---|---|---|---|---|---|---|
| $CO_2$ | 2 | 0.8468 | 207.89 | 3.050 | 26.408 | 5.055 | [351] |

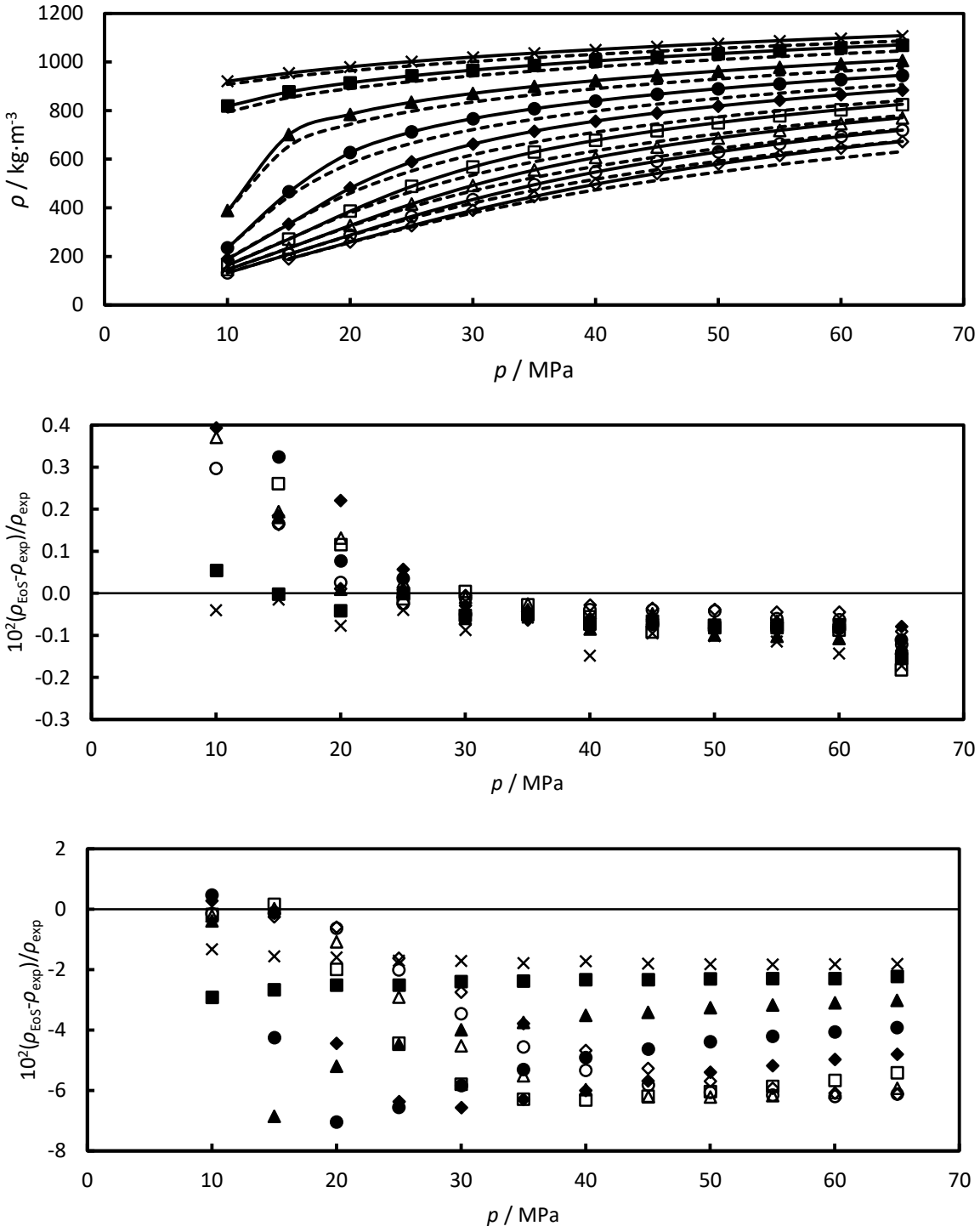



**Figure 5.38** (*top*) Comparison between experimental density of $CO_2$ and the predictions from the reference EoS and SAFT-γ Mie EoS. (*middle*) Deviations of the experimental density $\rho_{exp}$ of $CO_2$ from the values calculated from the reference EoS $\rho_{EoS}$. (*bottom*) Deviations of the experimental speed-of-sound in $CO_2$, $c_{exp}$ from the values $c_{EoS}$ calculated from SAFT-γ Mie across nine isotherms: ×, 283.15 K; ■, 298.15 K; ▲, 323.15 K; ●, 348.15 K; ◆, 373.15 K; □, 398.15 K; △, 423.15 K; ○, 448.15 K; ◇, 473.15 K.

## 5.9 Summary

The compressed-liquid density has been measured precisely for (*n*-heptane, *n*-nonane, methylbenzene and $CO_2$) at nine isotherms with temperatures between (283.15 and 473.15) K and pressures up to 68 MPa. The expanded relative uncertainties at 95% confidence were calculated to be approximately 0.1 % for the density measurements. The experimental results were compared with the predictions from the reference equations of state, and deviations are within the specified tolerances of the equations. To allow interpolation with respect to $T$ and $p$, the experimental density data for all systems measured apart from $CO_2$, were correlated with the modified Tait equation. The $\Delta_{AARD}$ between the experimental data and the values calculated with the correlations is approximately 0.01 %. For $CO_2$, a new empirical correlation has been developed. The experimental data, in general, are in good agreement with the literature data. The speed-of-sound measurements were carried out for (*n*-pentane, *n*-heptane, *n*-nonane and methylbenzene) at temperatures between (263.21 and 473.15) K and pressures up to 390 MPa. The estimated expanded relative uncertainties at 95% confidence are less than 0.1 % for speed-of-sound measurement throughout the experimental conditions. The experimental data are in good agreement with the predictions from the reference equations of state. Similarly, the speed-of-sound data were correlated with an empirical equation, and the $\Delta_{AARD}$ was calculated to be 0.05 % which is lower than the specified uncertainty of the measurements. The experimental results were also compared with the available literature data. Both density and speed-of-sound experimental data were compared with the predictions from the SAFT-$\gamma$ Mie EoS.

In the final part of this work, in the cases where both density and speed-of-sound were measured, the thermodynamic integration technique was used to derive thermophysical properties up to 390 MPa. As the thermodynamic integration requires isobaric heat capacity as input, experimental data along the saturation curve were obtained from the literature. The isobaric heat capacity data were fitted with a polynomial correlation for the purpose of the numerical integration. The derived properties were compared with the values calculated from equations of state. A perturbation analysis of the experimental data has been investigated to estimate the uncertainty of the derived properties. From the sensitivity analysis, we estimated the relative uncertainties of derived properties are approximately 0.1 % for $\rho$, 2 % for $c_p$, 1% for $\beta$ and 2% for $\alpha$ at all state points. The speed-of-sound data provided in this work extends experimental range in the literature, and the data should make a useful contribution to the development of the reference equation of state.

# Chapter 6: Measurements on Binary Mixtures of Hydrocarbons and $CO_2$

## 6.1 Overview

In this chapter, the thermophysical properties of three binary systems are reported. New experimental speed-of-sound, compressed-liquid density data for binary systems over wide ranges of temperatures, pressures and compositions were collected and are presented. The systems investigated include ($CO_2$ + *n*-heptane), ($CO_2$ + *n*-nonane) and ($CO_2$ + methylbenzene). The experimental results were fitted with new empirical correlations. The excess molar volumes were calculated from the compressed-liquid densities measured across four compositions and were fitted with the Redlich-Kister correlation. In the cases of a binary system with available literature data, comparisons were made between the experimental data and the literature data. In the binary systems ($CO_2$ + *n*-heptane) and ($CO_2$ + methylbenzene), the collected compressed-liquid densities were combined with saturated-phase densities to obtain bubble-pressures. Lastly, the experimental data were implemented to test the predictive capability of several thermodynamic models which include PPR78 EoS, SAFT-γ Mie EoS and Helmholtz energy explicit EoSs. The results of this chapter will make a meaningful contribution to filling in the literature gaps and the testing and development of various thermodynamic models.

## 6.2 Introduction

The understanding of the thermophysical properties of $CO_2$ + hydrocarbons systems at reservoir conditions is paramount for the correct design and optimisation of processes such as EOR and carbon storage. The available compressed-liquid densities and speed-of-sound data for these mixtures are limited, especially under high pressures above the bubble pressure in the single-liquid-phase region. These thermophysical properties help to develop tools that can determine the potential amount of $CO_2$ to be stored in active/depleted oil reservoirs as well as to understand the convective transport through the reservoir. Moreover, such experimental data are also valuable in a wide range of industrial applications such as supercritical extraction or process separation. Since these processes cover an extensive range of operation conditions and involve multicomponent systems, reservoir/process simulations are employed in the design of these engineering applications. A robust and safe process can only be achieved if the thermodynamic models used for these simulations are optimised and/or validated with accurate experimental data.

## 6.3 Experimental Uncertainty

The overall standard uncertainty calculation for the experimental compressed-liquid density and speed-of-sound measurements was performed following the guidelines described by GUM [369]. The overall uncertainty calculation for both sets of measurements is composed of the contributions from the uncertainties of temperature, pressure, composition, calibration and repeatability of the measurement. The combined standard uncertainty for compressed-liquid density measurements was estimated to be less than 1 $kg \cdot m^{-3}$. Therefore the expanded relative uncertainty for ($CO_2$ + *n*-heptane), ($CO_2$ + *n*-nonane) and ($CO_2$ + methylbenzene) measurements was calculated to be approximately 0.1 % over the entire temperature and pressure range. The expanded relative uncertainties for speed-of-sound measurement of ($CO_2$ + *n*-nonane) and ($CO_2$ + methylbenzene) were found to be ranging from (0.04 to 0.10) % and (0.04 to 0.14) %, respectively with a coverage factor of $k = 2$, across four compositions at all state points investigated. The uncertainty of the measurement increases with the mole fraction of $CO_2$ in the mixture. The standard uncertainty of the mixing procedure was calculated to be less than $10^{-5}$ which has a minimal contribution towards the overall uncertainty. Examples of the uncertainty budget and the formulas used for speed-of-sound and density measurements can be found in Chapter 4.

# 6.4 $CO_2$ + *n*-Heptane

This section details the results of the compressed-liquid density measurements made for ($CO_2$ + *n*-heptane) over a temperature range of (283.15 to 473.15) K and for pressures up to 68 MPa. An empirical correlation was developed to correlate the experimental densities, and the results were compared with the literature data. The results of the compressed-liquid densities were used to calculate the excess molar volumes. In the final part of this section, the experimental data were tested with the predictive abilities of PPR78 EoS, SAFT-γ Mie EoS and GERG-2008 EoS. An optimisation of the SAFT-γ Mie parameters using the present experimental data was also carried out.

## 6.4.1 Literature Review

To ensure the homogeneity of the mixture throughout the measurement, the experimental conditions were chosen based on the VLE data estimated using Aspen Properties software package. In the literature, the amount of available literature data is limited, and only two authors have reported the compressed-liquid densities of $CO_2$ + *n*-heptane as a function of temperature and pressure. The most recent study on the densities $CO_2$ + *n*-heptane was carried out by Medina-Bermudez *et al.* [286] They made the density measurements at temperatures between (313 and 363) K with a vibrating-tube densimeter. The composition of $CO_2$ in the binary mixture studied was $x$ = (0.02, 0.31, 0.51, 0.75 and 0.95). Fenghour *et al.* [285] also measured the compressed-liquid densities of the same mixture at a temperature range of (302 to 459) K and pressures up to 55 MPa at four predetermined compositions. Details of other studies reporting the saturated-phase densities of $CO_2$ + *n*-heptane can be found in Table 2.7 in Chapter 2. The present study aims to expand the current database to wider ranges of $p$ and $T$ by carrying out precise measurements.

## 6.4.2 Experimental Results and Discussion

Compressed-liquid density measurement was carried out as a function of pressure along nine isotherms: (283.15, 298.15, 323.15, 348.15, 373.15, 398.15, 423.15, 448.15 and 473.15) K at pressures up to 68 MPa. The four nominal carbon dioxide mole fractions of the binary mixture studied were 0.2, 0.4, 0.6 and 0.8. The experimental densities and the actual mole fractions of $CO_2$ in the mixtures together with the standard uncertainty are listed in Table C.1 in Appendix C. In Figure 6.1, selected experimental densities at four different mole fractions as functions of pressure and temperature are shown. As expected, the density increases with decreasing temperature and increasing pressure at constant composition. At temperatures below 323.15 K, the density increases with the concentration of $CO_2$ in the mixture. It can be noticed that a crossover effect in the mixture densities occurs at temperatures higher than 323.15 K. As temperature increases, the crossover pressure point shifts towards higher pressure. The effect can be explained by the difference in densities between pure components, $CO_2$ and *n*-heptane, as shown in Figure 6.1. The density crossover behaviour in mixtures

of hydrocarbons with $CO_2$ has also been reported by Medina-Bermudez *et al.* [286] who measured the compressed-liquid densities of the same binary mixture between (313 and 363) K and at pressures up to 25 MPa using a vibrating-tube densimeter. Their study contained $CO_2$ mole fractions that range from 0.02 to 0.95. The experimental data at 323.15 K and 348.15 K measured in this work were compared with the data reported by Medina-Bermudez *et al.* A linear interpolation in pressure was performed in our data for the purpose of comparison. Figure 6.2 shows the comparison between experimental data measured in this work and the literature data. Both datasets are in good agreement with an average absolute relative deviation, $\Delta_{AARD}$, of 0.7% and average absolute deviation, $\Delta_{AAD}$ of 4.0 $kg \cdot m^{-3}$. As mentioned Fenghour *et al.* [285] also measured the compressed-liquid densities of the same mixture; however, a direct comparison with their reported data has not been carried out since these data were reported at different compositions, temperatures and pressures. A three-way interpolation on $T$, $p$ and $x$ would not be accurate enough for comparison in this case.

**Correlation:** To verify the consistency of the experimental data, a new empirical correlation for the data was developed. In addition, we made use of the correlation and determined the bubble-pressures of $CO_2$ + *n*-heptane at different temperatures, using both compressed-liquid and saturated phase densities; this will be discussed in detail later. The empirical correlation developed to describe the compressed-liquid densities of the $CO_2$ + *n*-heptane mixtures was given in a pressure-explicit form. The correlation describes pressure as a function of density at each temperature and composition, given as [399, 400]:

$$p = A\rho + B\frac{(\rho - \rho_r)^{\delta}}{\delta} \,. \tag{6.1}$$

Here $\rho_r$ denotes the reference density which is a floating parameter. A non-linear term was introduced into the equation to describe the non-linearity of the densities around the critical region. Delta is a universal critical exponent whose value was set to be 4.82. Parameters $A$, $B$ and $\rho_r$, are all adjustable parameters which were optimised using the Lenvenberg-Marquardt optimisation method. Figure 6.1 shows the calculated densities using Equation (6.1) for four compositions. The parameters are summarised in Table C.2, and the deviation plots between the calculated values and experimental compressed-liquid densities are shown in Figure 6.3. The $\Delta_{AAD}$ and $\Delta_{AARD}$ of the correlation were about 0.05 MPa and 0.3 %, respectively. The performance of the correlation decreases with increasing $CO_2$ mole fraction in the binary mixtures due to the non-linearity behaviour in densities around the critical region.

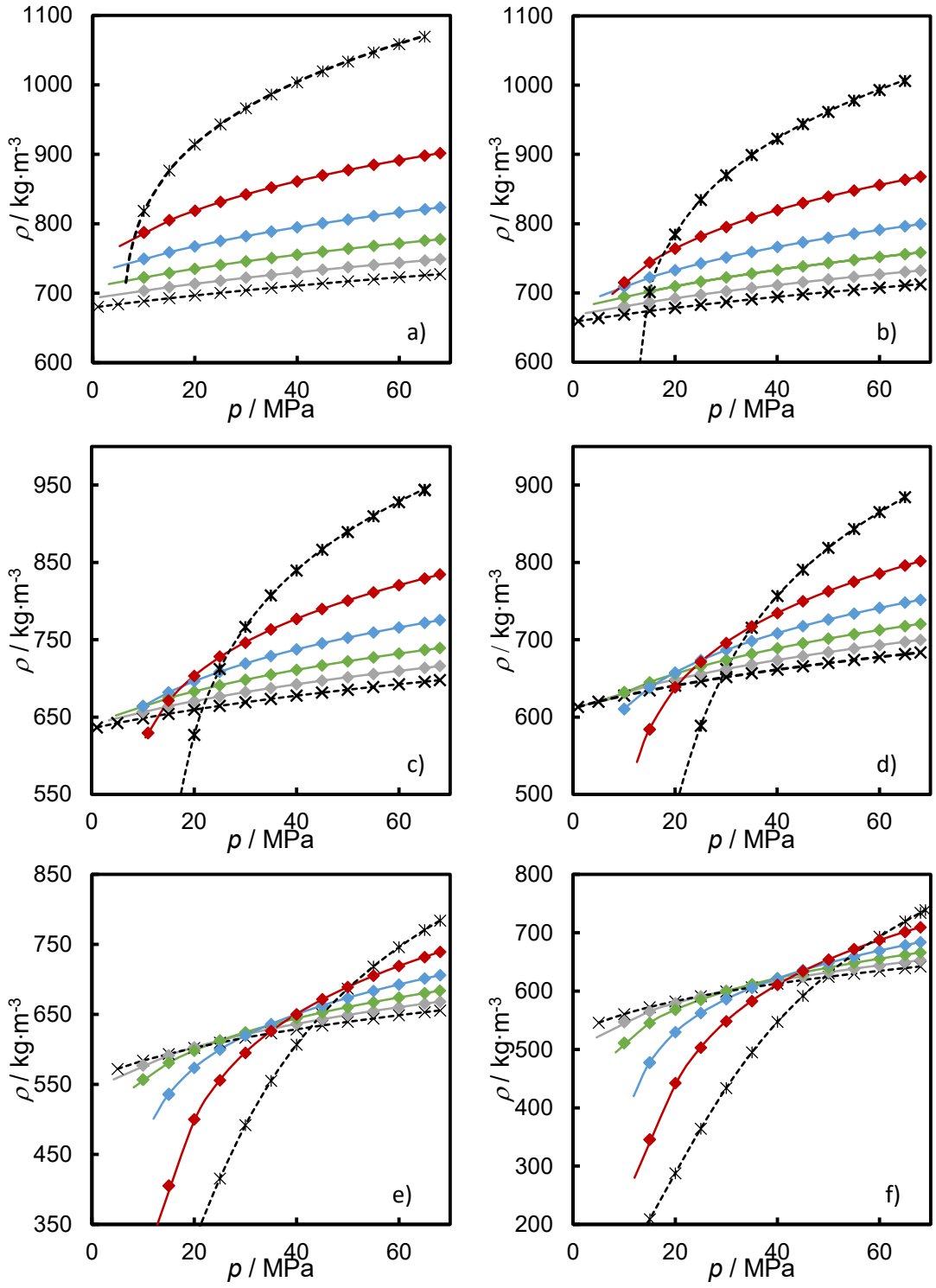



**Figure 6.1** Compressed-liquid densities $\rho$ (coloured diamond) against pressure for $CO_2$ + *n*-heptane system at four mole fractions of $CO_2$: ×, 0; (green), 0.2; (orange), 0.4; (blue),0.6; (red), 0.8; ∗,1; at six temperatures: a) 298 K, b) 323 K, c) 348 K, d) 398 K, e) 423 K and f) 473 K. Coloured lines represent values calculated with the empirical correlation, Equation (6.1).

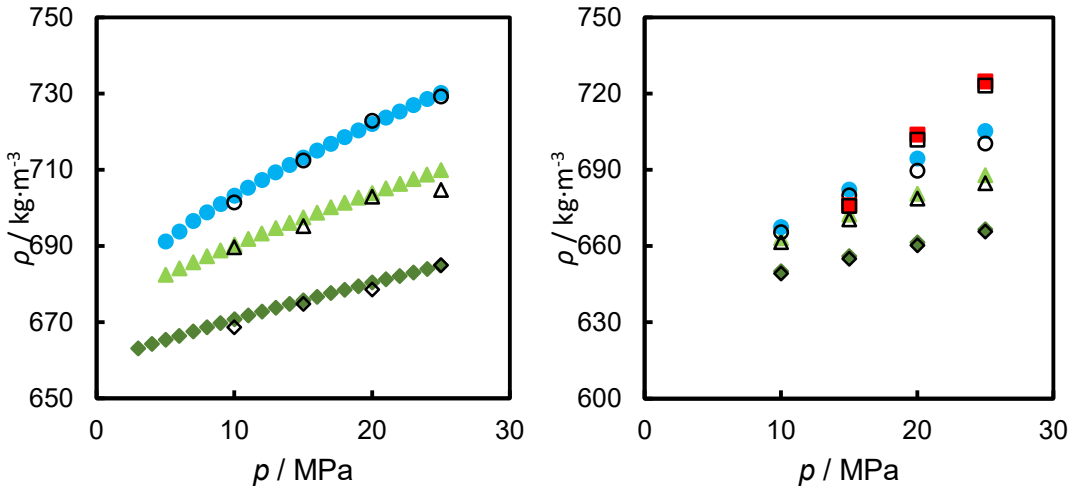



**Figure 6.2** Comparison of compressed-liquid densities $\rho$ of $CO_2$ + *n*-heptane at (*left*) 323 K and (*right*) 348 K between our work and literature data. Unfilled symbols represent data interpolated from our measurement and filled symbols represent the work by Medina-Bermudez *et al.* [286], respectively. Mole fraction of $CO_2$ in the mixture: ◆, 0.02; ▲, 0.31; ●, 0.51; ■, 0.75.

**Excess Molar Volume:** Excess molar volume ($V_m^E$) can provide a measure of the non-ideal mixing of binary and multi-components mixtures. We calculated the $V_m^E$ for $CO_2$ (1) + *n*-heptane (2) system from the experimental compressed-liquid density data using the following relation:

$$V_m^E = \frac{M_{mix}}{\rho_{mix}} - \left( \frac{xM_1}{\rho_1} + \frac{(1-x)M_2}{\rho_2} \right), \tag{6.2}$$

where $x$ is the $CO_2$ mole fraction, $M$, the molar mass and $\rho$ the density. The subscripts mix, 1 and 2 represent the mixture, carbon dioxide and *n*-heptane, respectively. The density of the pure components, both $CO_2$ and *n*-heptane, were measured using the vibrating-tube densimeter mentioned in Chapter 5. Figure 6.4 shows the plots of $V_m^E$ as a function of mole fraction of $CO_2$ across six isotherms. The excess molar volume is slightly positive at 283.15 K for all isobars and at 298.15 K for pressures above 15 MPa. At 323.15 K, the excess volume displays a sigmoidal pattern at pressures higher than 10 MPa. At temperatures above 373.15 K, the excess molar volume is negative over the entire range of composition for all isobars and becomes more negative with increasing temperature and decreasing pressure. The variations of excess volume with pressure or temperature might be due to an increase or decrease of the pure $CO_2$ density with pressure or temperature, respectively. It can be noticed that the maximum/minimum excess molar volume always occurs around $x_{CO2}$ = 0.6/0.7 at all temperatures. The negative values of the excess molar volume are observed when $CO_2$ behaves as a gas-like fluid and mixes with liquid *n*-heptane.

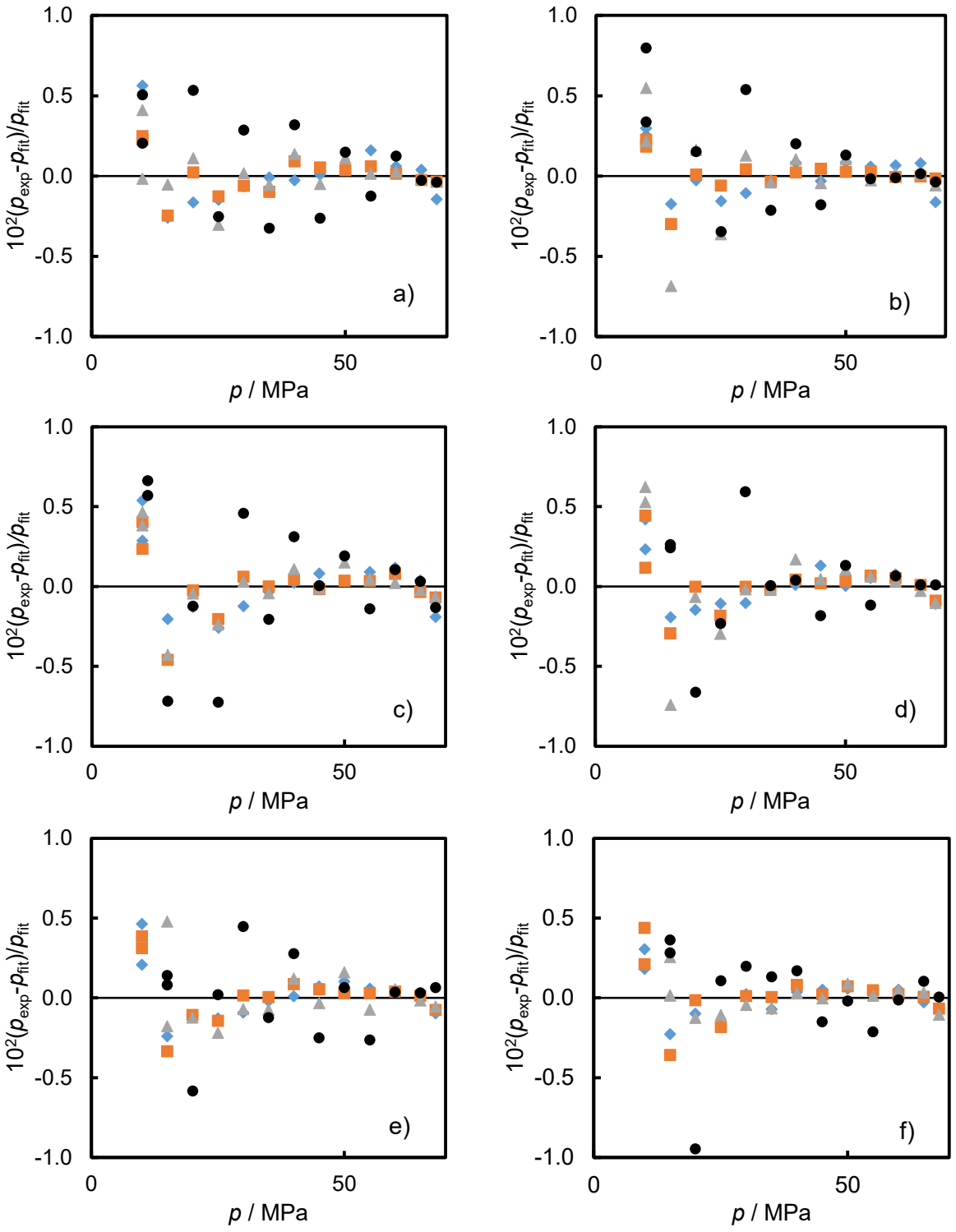



**Figure 6.3** Deviations of the experimental pressure $p_{exp}$ from values calculated with the empricial correlation, Equation (6.1) $p_{fit}$ and at a) 298 K, b) 323 K, c) 348 K, d) 373 K, e) 423 K and f) 448 K. Symbols denote different mole fraction of $CO_2$ in the binary mixture: ▲, 0.2; ■, 0.4; ●, 0.6; ◆, 0.8.

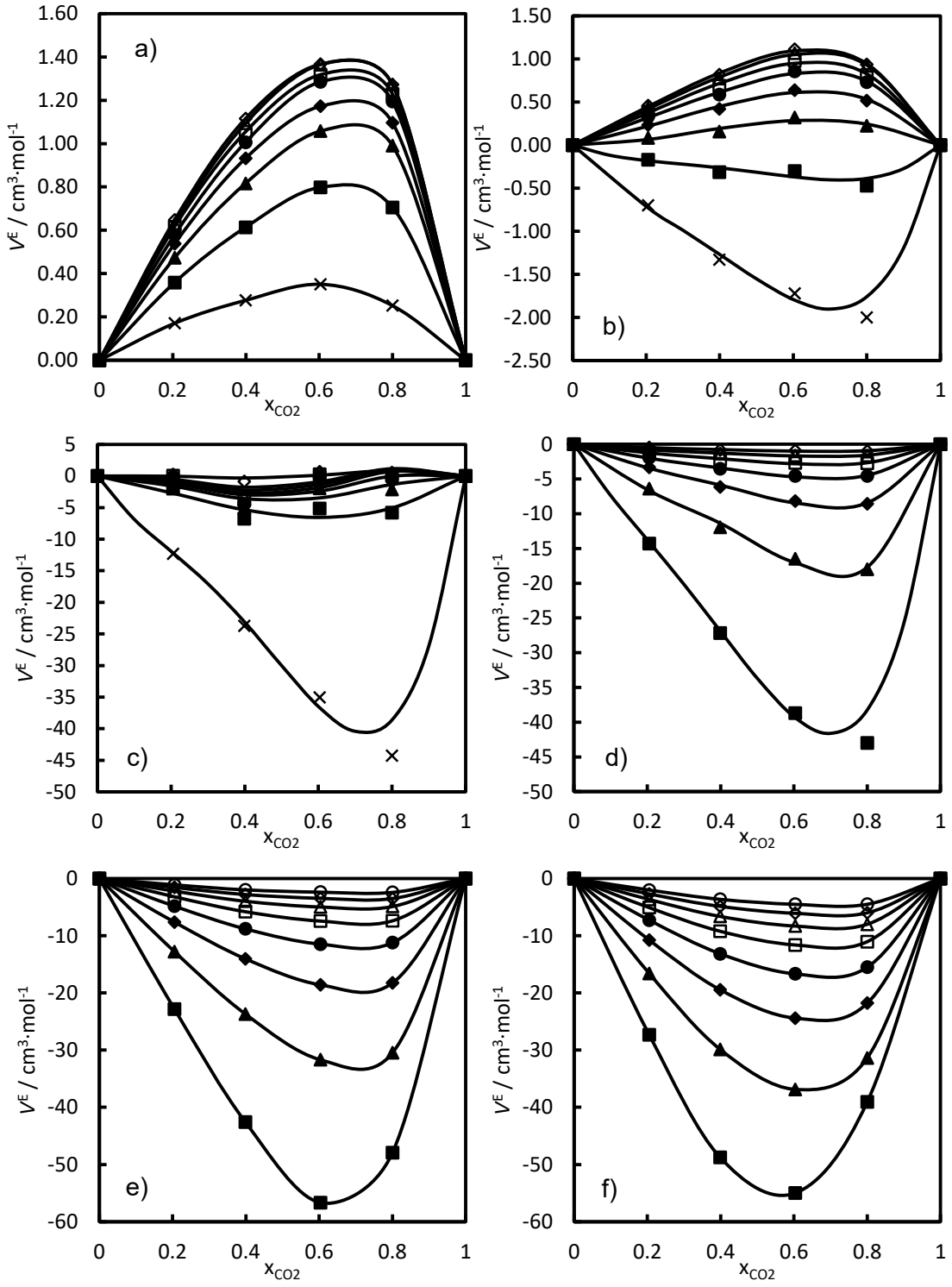



**Figure 6.4** Excess molar volume $V_m^E$ of $CO_2$ + *n*-heptane system versus the molar fraction of $CO_2$ at six temperatures: a) 283 K; b) 298 K; c) 323 K; d) 373 K; e) 423 K; f) 473 K and at nine isobars: ✖,10 MPa; ■, 15 MPa; ▲, 20 MPa; ◆, 25 MPa; ●, 30 MPa; □, 35 MPa; △, 40 MPa; ◇, 45 MPa; ○, 50 MPa. Solid lines represent values calculated from the Redlich-Kister correlation, Equation (6.3) with parameters from Table C.3.

These large negative values relate to the change in volume of carbon dioxide, from a low-density fluid to a liquid-mixture component. When $CO_2$ and *n*-heptane are mixed at particular conditions where $CO_2$ is a liquid-like fluid and the resulting mixture is a liquid; the excess volume shows moderate values. The observed moderate negative values of $V_m^E$ may be because $CO_2$ molecules rearrange themselves into the free volume space in-between the *n*-heptane chains hence reducing the overall volume. The excess molar volume has been correlated with the Redlich-Kister equation which is given in the following form [360]:

$$V_m^E = x(1-x)\sum_{i=1}^{3} A_i (2x-1)^{i-1}, \tag{6.3}$$

where $V_m^E$ and $x$ is the excess molar volume and mole fraction of $CO_2$, respectively. $A_i$ is the correlation parameter which was found by regression with the experimental data. The calculated excess molar volumes have been fitted to each isotherm and isobar individually. The results of the correlation are shown in Figure 6.4, and the goodness of the fit was given by the $\Delta_{AAD}$, which is 0.03 $cm^{-3}\cdot mol$ across all isotherms and isobars. The parameters determined are shown in Table C.3 in Appendix C.

## 6.4.3 Bubble Pressure Determination

In this work, we presented a novel way of determining the bubble pressures from two sets of densities data (saturated-phase density and compressed-liquid density) measured across the sub-critical and supercritical regions. The saturated-phase densities were measured by Yolanda Sanchez-Vicente using a two-phase density apparatus in the group. More details about the saturated-phase density measurements can be found in Sanchez-Vicente *et al.* [399] By combining both sets of experimental density data, the bubble pressures and compositions at each isotherm were determined. The bubble pressures were calculated by finding the intercepts between the two sets of experimental density data, as shown in Figure 6.5. To achieve that, the compressed-liquid density data were extrapolated using the developed correlation, Equation (6.1), down to the pressures where they intercept with the saturated-phase density. The composition of the bubble point corresponds to the composition of the compressed-liquid density mixture. The calculated bubble pressures have been determined for four isotherms $T$ = (298, 323, 373 and 423) K in this way and are given in Table 6.1. In Figure 6.6, we compared the calculated bubble pressures with data obtained by the directly VLE measurements which were carried out by Saif Al-Ghafri. The experimental apparatus and procedures can also be found in Sanchez-Vicente *et al.* Our calculated bubble pressures agree well with the experimental bubble pressures to within ±0.1 MPa. The uncertainty for the calculated bubble pressure points was difficult to calculate precisely.

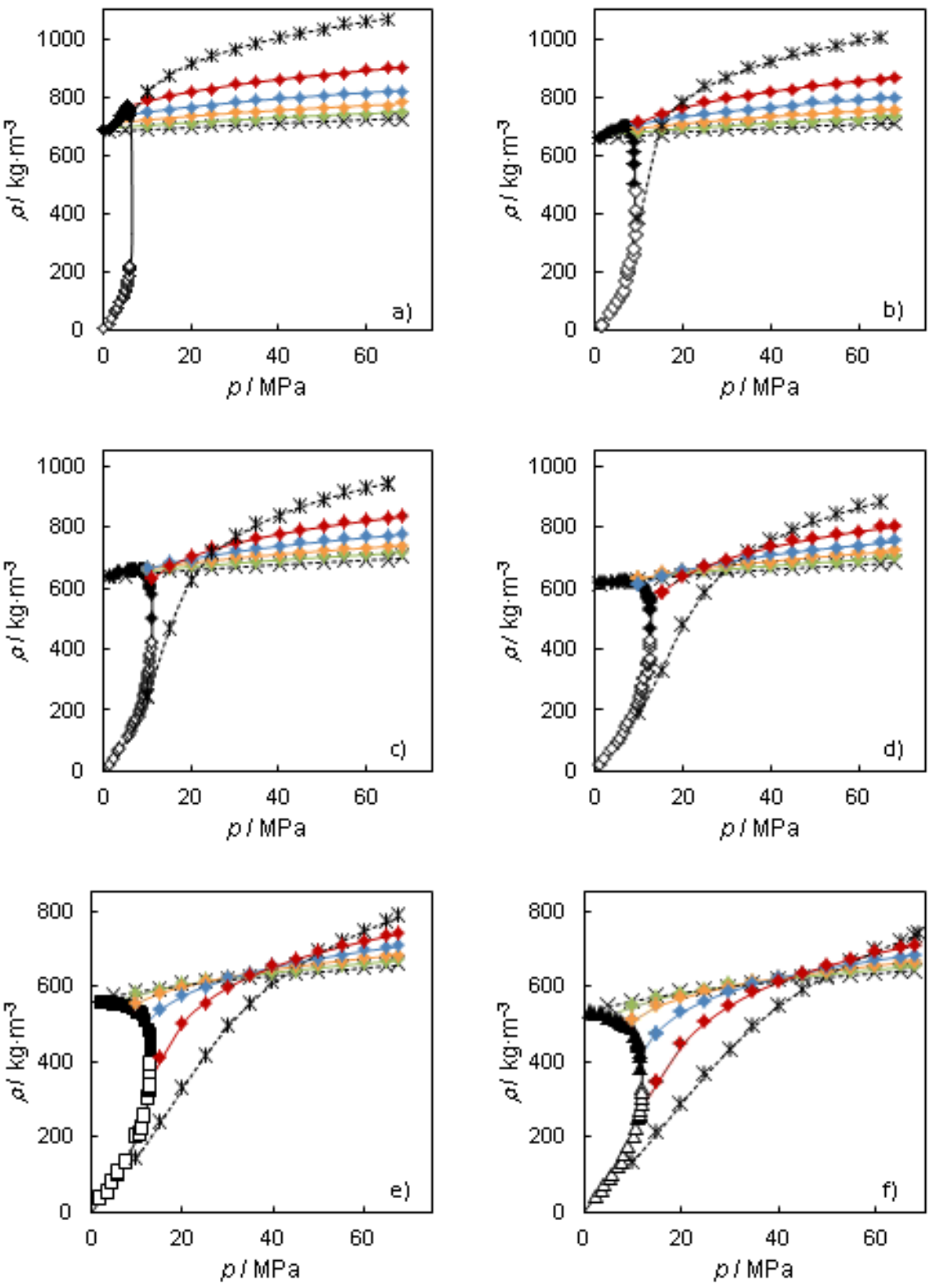



**Figure 6.5** Compressed-liquid densities $\rho$ (coloured diamond) and saturated-phase densities (black and white symbols) versus pressure for $CO_2$ + *n*-heptane system at four mole fractions of $CO_2$: ×, 0; (green), 0.2; (orange), 0.4; (blue),0.6;(red), 0.8; ∗,1; at six temperatures: a) 298 K, b) 323 K, c) 348 K, d) 398 K, e) 423 K and f) 473 K. Coloured lines represent values calculated with the empricial correlation, Equation (6.1).

However, the absolute uncertainty of the calculated bubble pressure was estimated to be about 0.1 MPa by the comparison with the experimental data obtained by the VLE apparatus. This bubble point calculation using density data represents a novel way of determining the bubble pressures of a binary system, and it has the potential of calculating the bubble pressure accurately for a complex system where direct observation of phase equilibrium is difficult. This method also provides the confidence in both sets of density data.

**Table 6.1** Bubble pressures $p_b$ for ($CO_2$ + *n*-heptane) system at temperatures and $CO_2$ mole fractions $x$ determined from the intersection between the compressed-liquid densities and the saturated-phase densities[a]. Experimental bubble pressure data obtained from the direct observation of VLE[b].

| $T$/ K | $x$ | [a]$p_b$ / MPa | [b]$p_b$ / MPa |
|---|---|---|---|
| 298.15 | 0.2053 | 1.52 | 1.55 |
| | 0.3989 | 3.06 | 3.08 |
| | 0.6037 | 4.28 | 4.37 |
| | 0.8001 | 5.26 | 5.23 |
| 323.15 | 0.2053 | 1.97 | 2.16 |
| | 0.3989 | 4.06 | 4.19 |
| | 0.6037 | 6.37 | 6.31 |
| | 0.8001 | 7.73 | 7.83 |
| 373.15 | 0.2053 | 3.35 | 3.38 |
| | 0.3989 | 6.68 | 6.48 |
| | 0.6037 | 9.76 | 9.88 |
| | 0.8001 | 12.55 | 12.45 |
| 423.15 | 0.2053 | 4.41 | 4.38 |
| | 0.3989 | 8.16 | 8.41 |
| | 0.6037 | 12.34 | 12.22 |
| | 0.8001 | 13.00 | 12.39 |

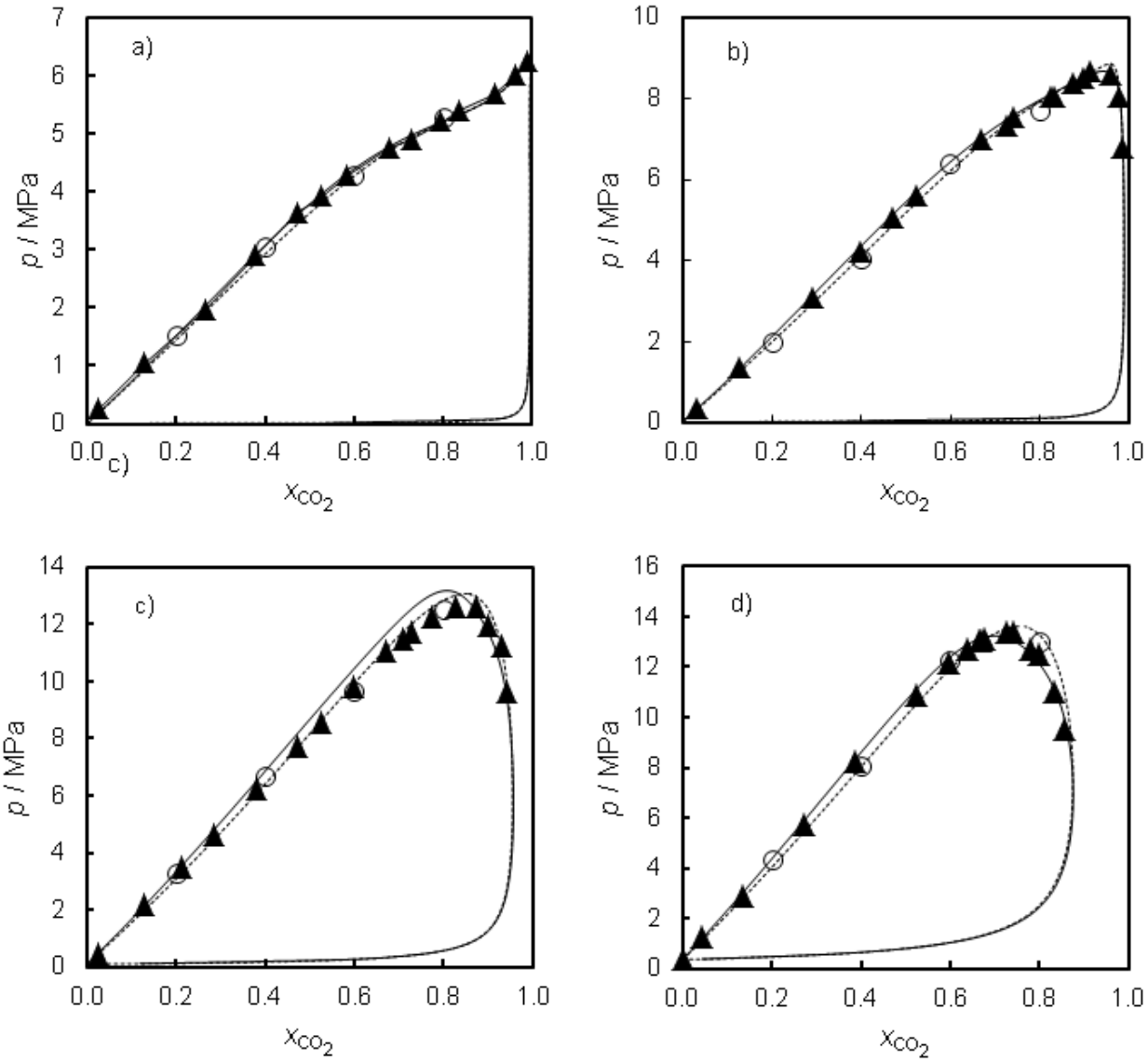



**Figure 6.6** Bubble pressures $p_b$ for ($CO_2$ + *n*-heptane) as a function of the $CO_2$ mole fraction at four temperatures: a) 298 K, b) 323 K, c) 373 K, d) 423 K. Symbols: ▲, experimental data from direct observation of VLE and, ○, experimental data obtained from densities. Solid and dotted lines represent predictions from PPR78 and SAFT-γ Mie, respectively.

## 6.4.4 Modelling

In this work, the predictive capability of PPR78, SAFT-γ Mie and GERG-2008 was tested with the compressed-liquid densities data for the binary mixture of $CO_2$ + *n*-heptane. No parameters were adjusted for the equations of state during the density calculations. First, the experimental data for the $CO_2$ + *n*-heptane binary system were predicted using the Peng-Robinson EoS (PR78) [306] and the classical mixing rule is given by:

$$a = \sum_{i=1}^{N}\sum_{j=1}^{N} x_i x_j \sqrt{a_i a_j}\left[1 - k_{ij}(T)\right]$$
$$b = \sum_{i=1}^{N} x_i b_i \tag{6.4}$$

where $x_i$ is the mole fraction of component $i$, $k_{ij}(T) = k_{ji}(T)$ are the temperature-dependent binary interaction parameter to components $i$ and $j$. The $k_{ij}$ for the pair $CO_2$ and $n$-heptane was calculated using the group contribution approach proposed by Jaubert and co-workers [316-319], as shown in Equation (3.18). The group contribution approach method to the Peng-Robinson EoS has been described in detail in Chapter 3. The critical properties such as the critical temperature, $T_c$ and pressure, $p_c$ and the acentric factor, $\omega$ were obtained from the reference equations of state with the NIST REFPROP 9.1 software [358]. The density predictions of PPR78 were calculated with the Aspen Properties software package. In the SAFT-γ Mie model, the thermophysical properties of a compound are described by different functional groups which contain both like and un-like parameters. These functional groups specific parameters and cross-interaction parameters are typically determined from experimental data across a wide temperature and pressure range. The structure and method of SAFT-γ Mie have been described previously in Chapter 3. A brief reference is made here for the particular compounds of the ($CO_2$ + $n$-heptane) system and their cross-interaction parameters. The like parameters of functional groups $CH_3$, $CH_2$ and $CO_2$, were described previously in Chapter 5. The group parameters for the description of the $CO_2$ + $n$-heptane mixture were reported by Galindo and co-workers recently. With this SAFT-γ Mie group contribution approach, properties of carbon dioxide + $n$-alkane binary mixtures can be estimated from the determination of just two un-like cross-interaction parameters, the group dispersion energies, $\varepsilon_{kl}$ and the repulsive component, $\lambda_{kl}$ in the $CH_3$-$CO_2$ and $CH_2$-$CO_2$ groups. Among the two cross- interaction parameters of $CO_2$-$CH_3$ and $CO_2$-$CH_2$ groups, only $\varepsilon_{kl}$ was estimated from experimental VLE data for $CO_2$ + $n$-decane and $CO_2$ + $n$-pentane at temperatures from (344.59 to 377.59) K. Whereas, the other parameter $\lambda_{kl}$ was obtained using the combining rules. The computations of SAFT-γ Mie predictions were carried out in gSAFT software developed by PSE Ltd. Lastly, the compressed-liquid density for $CO_2$ + $n$-heptane was tested with the predictions from the GERG-2008 EoS. Components, $CO_2$ and $n$-heptane, are specified by the GERG-2008 EoS; therefore the parameters for this binary system were optimised with experimental thermodynamic data by Kunz and Wagner [39]. The parameters used in the three models are listed in Table 6.2.

**Table 6.2** Experimental parameters for three equations of state for the compressed-liquid density predictions of $CO_2$ + *n*-heptane: PPR78 (the binary interaction parameter, *kij* determined from the critical components $p_c$ and $T_c$ and acentric factor $\omega$); SAFT-γ Mie (un-like functional group parameters and cross-interaction parameters) and GERG-2008 (four adjustable parameters).

| | | | | | | | | |
|---|---|---|---|---|---|---|---|---|
| PPR78 | Component | $\omega$ | | $p_c$ / MPa | | $T_c$ / K | | Ref. |
| | *n*-heptane | 0.349 | | 2.74 | | 540.13 | | [376] |
| | carbon dioxide | 0.224 | | 7.38 | | 304.13 | | [174] |
| | System | $T$ / K | $k_{ij}$ | $T$ / K | $k_{ij}$ | $T$ / K | $k_{ij}$ | |
| | $CO_2$ + *n*-heptane | 283.15 | 0.1280 | 348.15 | 0.1281 | 423.15 | 0.1332 | - |
| | | 298.15 | 0.1275 | 373.15 | 0.1293 | 448.15 | 0.1358 | - |
| | | 323.15 | 0.1275 | 398.15 | 0.1310 | 473.15 | 0.1388 | - |
| SAFT-γ Mie | Functional Group | $v_k^*$ | $S_k$ | $(\varepsilon_{kk}/k_B)$/K | $\sigma\times10^{10}$/m | $\lambda_{kk}^r$ | $\lambda_{kk}^a$ | |
| | $CO_2$-$CH_3$ | - | - | 205.70 | - | CR | - | [351] |
| | $CO_2$-$CH_2$ | - | - | 276.45 | - | CR | - | [351] |
| GERG-2008 | System | $\beta_T$ | | $\gamma_T$ | $\beta_v$ | $\gamma_v$ | $F_{ij}$ | |
| | $CO_2$ + *n*-heptane | 1.0118 | | 1.0462 | 1.2055 | 1.1646 | 0 | [39] |

The compressed-liquid density predictions of the PPR78, SAFT-γ Mie and GERG-2008 EoSs, are shown in Figures 6.7 and 6.9. Figure 6.8 shows the deviation plots of the experimental compressed-liquid density against the predictions from PPR78 and SAFT-γ Mie EoSs. From Figure 6.7, it can be seen that the predictions from both models are quite similar; the models generally over-predict the densities at low temperatures and under-predict them at high temperatures regardless of the composition. Overall, the compressed-liquid densities are quite similarly predicted by both equations with $\Delta_{AARD}$ about 1.7 % and 1.6 % for SAFT-γ Mie and PPR78 EoSs, respectively. The predictions from GERG-2008 are the worst among the three equations of state tested. The predictions are under-estimated for all temperatures and pressures across four compositions. The $\Delta_{AARD}$ between the predictions and the experimental data was found to be 2.5 %. It is expected to have a high deviation with the GERG-2008 model since the model is designed for natural gas mixtures with a small amount of hydrocarbons. In addition, it was mentioned in Kunz and Wagner that the experimental data used by GERG-2008 for parameters optimisations were limited [39]; hence there is still room for improvement in the model.

**PPR78 with Volume Translation:** The idea of volume translation is to correct the liquid density predictions by improving the liquid volume estimation of the cubic equation of state. The volume translation method was developed by Peneloux *et al.* [314] who introduced a shift factor to improve the accuracy of the liquid volume predictions. The method was described earlier in Chapter 3. Generally, the volume translation method is applied to hydrocarbon mixtures only. The volume translation was tested on the density predictions of the PPR78 EoS for $CO_2$ + *n*-heptane. As expected,

the translation did not give an overall improvement on the compressed-liquid density predictions, and the results were very similar to the predictions before the volume translation applied. The new $\Delta_{AARD}$ across four compositions was calculated to be 1.8 %. The $\Delta_{AARD}$ and the $\Delta_{AARD,overall}$ between the experimental compressed-liquid density and the predictions from PPR78, SAFT-γ Mie and GERG-2008 EoSs for $CO_2$ + *n*-heptane at four compositions are summarised in Table 6.3 below.

**Table 6.3:** Average absolute relative deviations $\Delta_{AARD}$ between the experimental compressed-liquid density and the predictions from PPR78, SAFT-γ Mie and GERG-2008 EoSs for $CO_2$ + *n*-heptane at four compositions, and the overall average absolute relative deviations $\Delta_{AARD,overall}$. VT represents volume translation.

| Equation of state | Property | $\Delta_{AARD,overall}$ | $x_{CO2}$ | $\Delta_{AARD}$ |
|---|---|---|---|---|
| PPR78 (VT) | Compressed-liquid density | 1.6% (1.8%) | 0.2 | 1.3% (1.3%) |
| | | | 0.4 | 1.3% (1.5%) |
| | | | 0.6 | 1.6% (1.8%) |
| | | | 0.8 | 2.4% (2.5%) |
| SAFT-γ Mie | Compressed-liquid density | 1.7% | 0.2 | 0.7% |
| | | | 0.4 | 1.1% |
| | | | 0.6 | 1.6% |
| | | | 0.8 | 3.3% |
| GERG-2008 | Compressed-liquid density | 2.5% | 0.2 | 2.5% |
| | | | 0.4 | 1.4% |
| | | | 0.6 | 2.0% |
| | | | 0.8 | 2.5% |

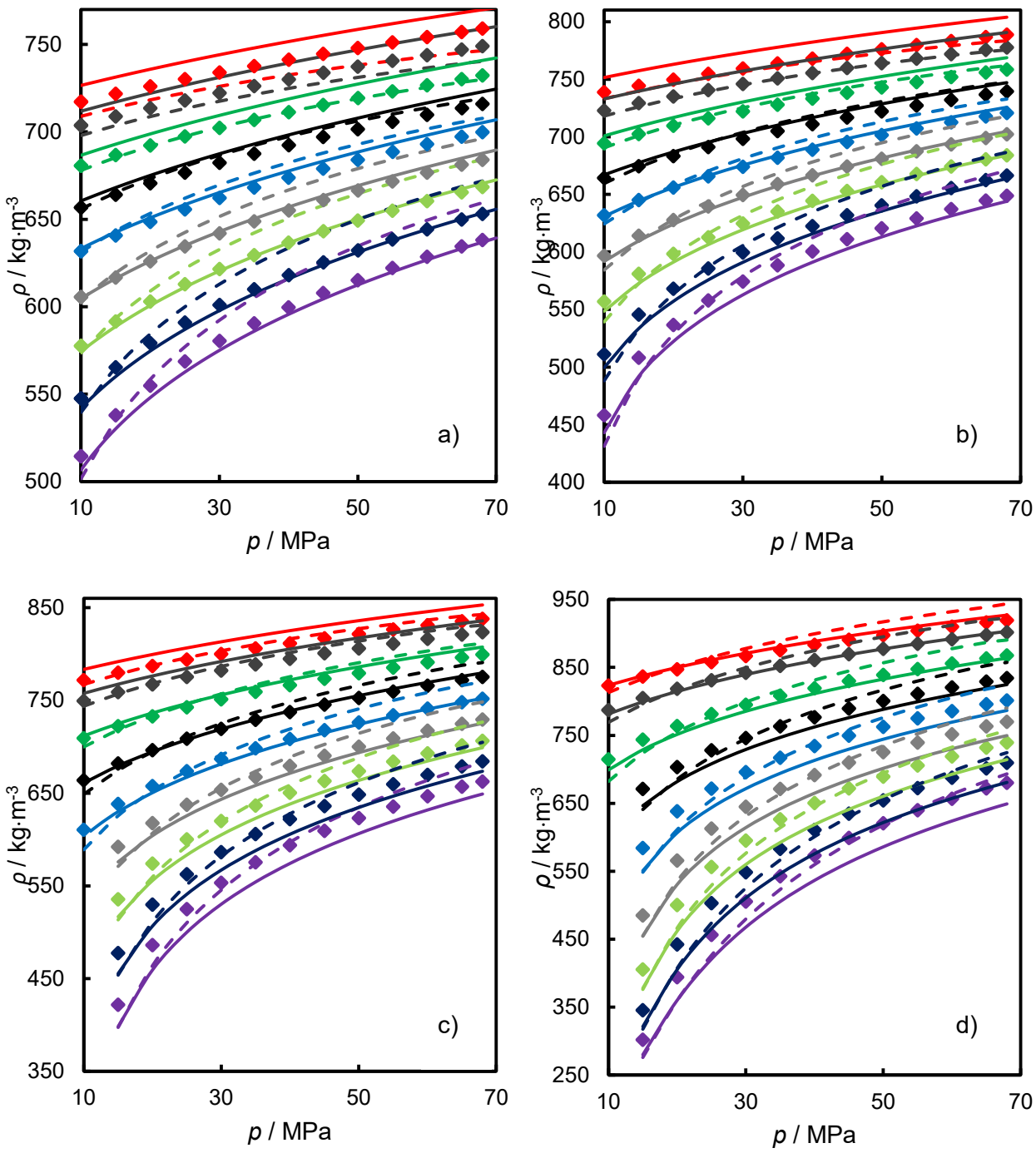



**Figure 6.7** Comparisons between the experimental compressed-liquid density of $CO_2$ + *n*-heptane and the predictions from SAFT-γ Mie and PPR78 EoS at nine temperatures: (red), 283 K; (yellow), 298 K; (green), 323 K; (black), 348 K; (blue), 373 K; (grey), 398 K; (dark red), 423 K; (dark blue), 448 K; (purple), 473 K and at four mole fractions of $CO_2$: a) $x$ = 0.2; b) $x$ = 0.4; c) $x$ = 0.6; d) $x$ = 0.8. Solid and dotted lines represent predictions from SAFT-γ Mie and PPR EoS, respectively.

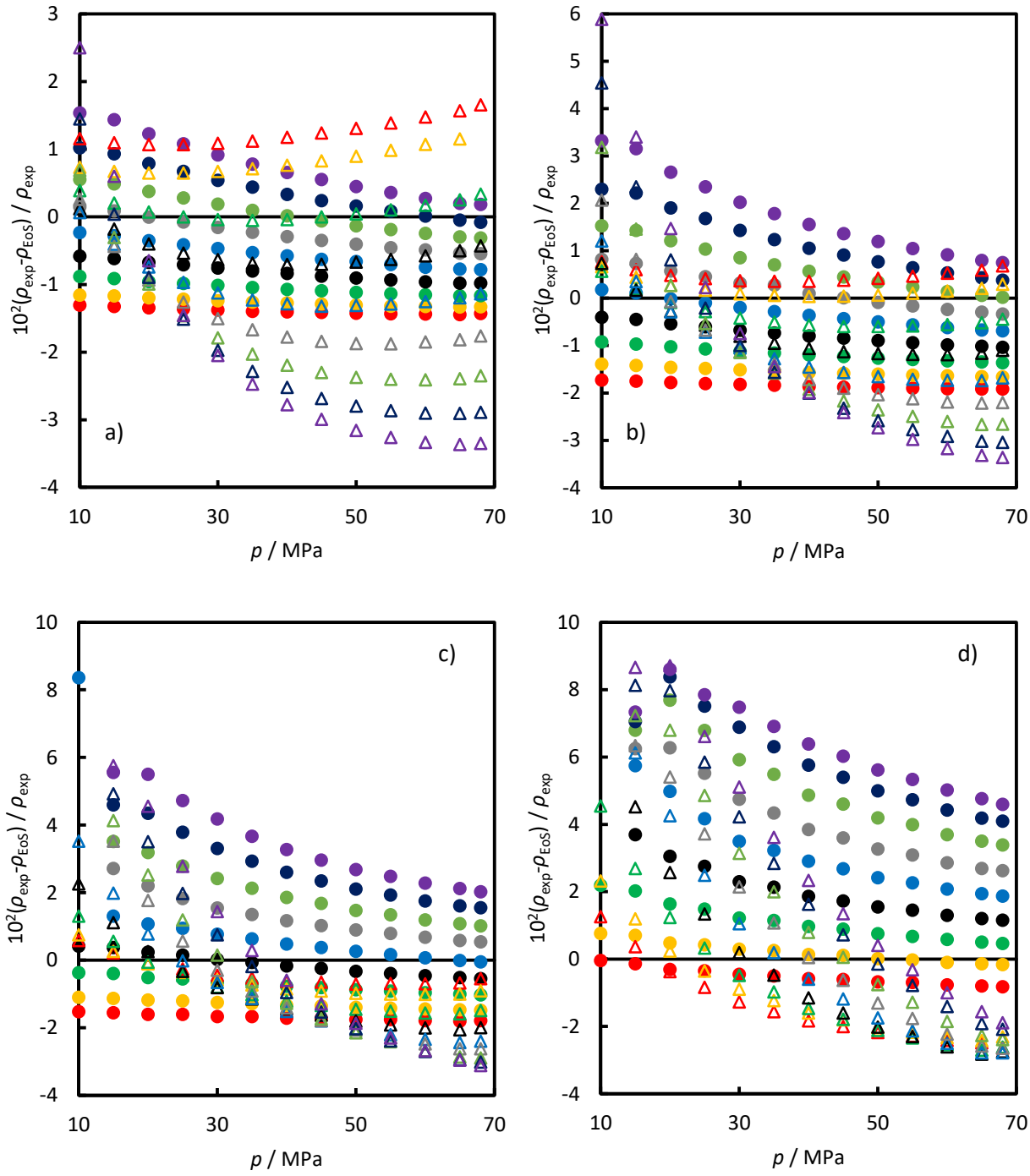



**Figure 6.8** Deviation plots between the experimental compressed-liquid density $\rho_{exp}$ and the predictions from SAFT-γ Mie and PPR78 EoS $\rho_{EoS}$ for $CO_2$ + *n*-heptane at nine isotherms: (red), 283 K; (yellow), 298 K; (green), 323 K; (black), 348 K; (blue), 373 K; (grey), 398 K; (dark red), 423 K; (dark blue), 448 K; (purple), 473 K and at four mole fractions of $CO_2$: a) $x = 0.2$; b) $x = 0.4$; c) $x = 0.6$; d) $x = 0.8$. Symbols: ●, SAFT-γ Mie and △, PPR78 EoS.

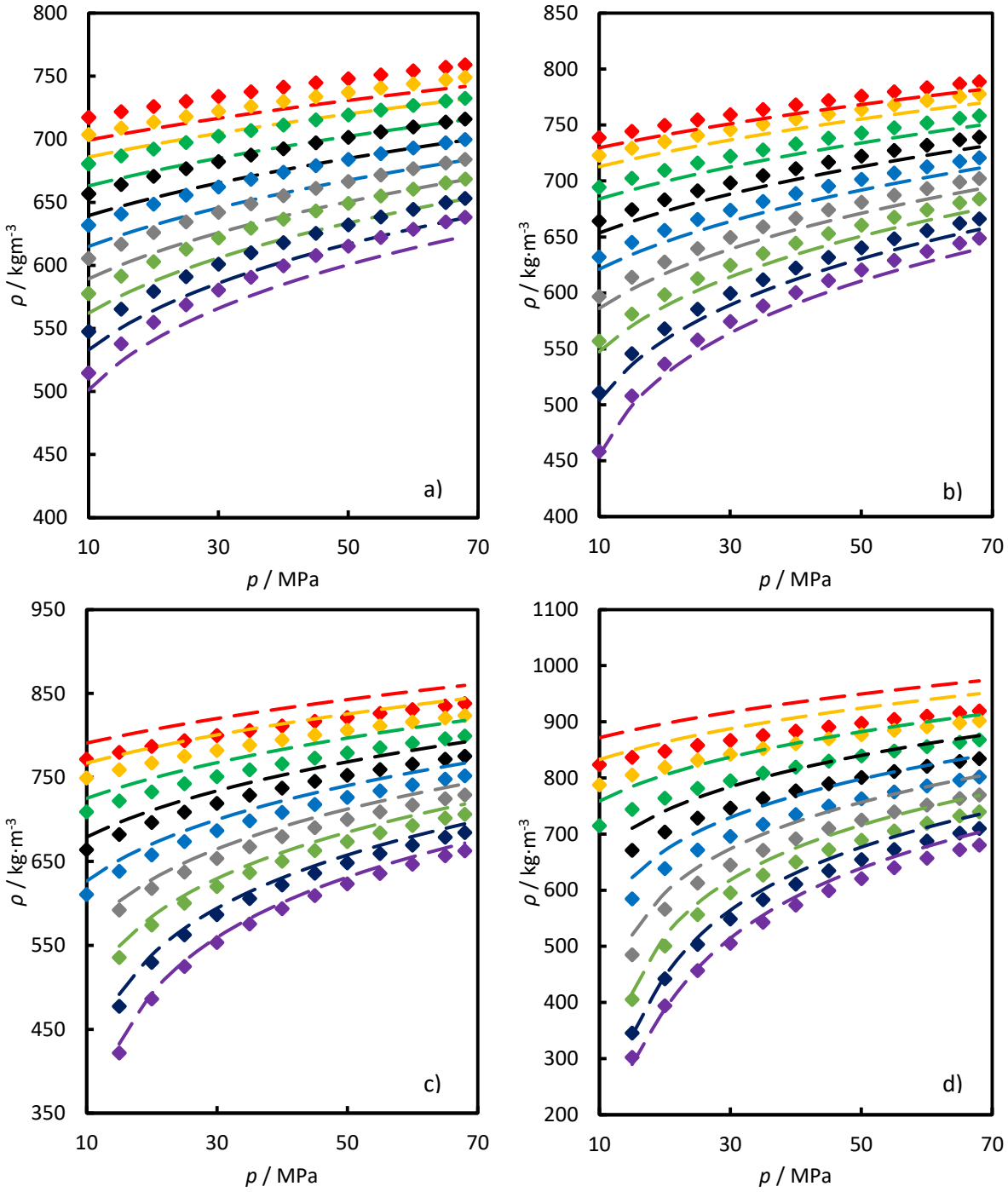



**Figure 6.9** Comparisons between the experimental compressed-liquid density of $CO_2$ + *n*-heptane and the predictions from GERG-2008 EoS at nine temperatures: (red), 283 K; (yellow), 298 K; (green), 323 K; (black), 348 K; (blue), 373 K; (grey), 398 K; (dark red), 423 K; (dark blue), 448 K; (purple), 473 K and at four mole fractions of $CO_2$: a) $x$ = 0.2; b) $x$ = 0.4; c) $x$ = 0.6; d) $x$ = 0.8. Dash lines represent predictions from GERG-2008 EoS.

## 6.4.5 Optimisation of SAFT-γ Mie

From the previous section, it can be seen that the compressed-liquid density predictions from SAFT-γ Mie EoS generally over-estimates the binary mixture density at low temperatures and under-estimates at high temperature. This trend was observed across the four compositions of the binary mixture studied. It has been mentioned that the strength of the SAFT-γ Mie approach is the accuracy of single-phase and second-derivative properties from parameters estimated using VLE data. Therefore there may be room for improvement through parameters optimisation. Papaioannou and co-workers [351, 394] suggested that optimising the un-like cross-interaction parameters may improve the prediction of SAFT-γ Mie. The un-like parameters that they identified to be important were the group dispersion interaction energies, $\varepsilon_{kl}$ and the repulsive exponent, $\lambda_{kl}^{r}$. As mentioned earlier in section 6.3.5, only $\varepsilon_{kl}$ was optimised using literature data and $\lambda_{kl}^{r}$ was calculated using the combing rules, therefore suggesting that the group parameters may not be fully optimised. The combining rule for $\lambda_{kl}^{r}$ is given in the following form:

$$\lambda_{kl} = 3 + \sqrt{(\lambda_{kk} - 3)(\lambda_{ll} - 3)} \tag{6.5}$$

where $\lambda_{kk}$ and $\lambda_{ll}$ are the repulsive exponents of the functional group $k$ and $l$. For details about these parameters and the structure of the SAFT-γ Mie, see Chapter 3. Compressed-liquid density and VLE data of ($CO_2$ + *n*-heptane) were included as well as the VLE data of ($CO_2$ + *n*-decane) and ($CO_2$ + *n*-pentane) during the optimisation for the parameters $\varepsilon_{kl}$ and $\lambda_{kl}^{r}$ of functional groups $CO_2$-$CH_2$ and $CO_2$-$CH_3$. The optimisation was carried out using the SAFT Material Modeller (gSAFTmm) developed by PSE Ltd. The objective function used in the estimation of molecular group parameter was given in the following form:

$$\min f_{obj} = w_{\mathrm{p}} \sum_{i=1}^{Nc} \sum_{j=1}^{Np} \left[ \frac{X_{b,i}^{\exp}(T_j, x_j) - X_{b,i}^{\mathrm{calc}}(T_j, x_j, \Omega)}{X_{bi}^{\exp}(T_j, x_j)} \right]^2 \tag{6.6}$$

where $X$ denotes the examined property, Ω denotes the vector of estimated parameters, $w_{\mathrm{p}}$ is the weighting factor for the experimental data and $N_{\mathrm{P}}$ is the number of experimental points. A multi-start gradient based algorithm was used for the parameter optimisation. To explore the ability of the software and predictive ability of SAFT-γ Mie, we have carried out a series of optimisation for the un-like interaction parameters. Table 6.4 summarises the sets of optimisation performed in this work. (Option A) First, equal weight factors for VLE and compressed-liquid density data were employed, and parameter, $\varepsilon_{kl}$ for groups $CO_2$-$CH_2$ and $CO_2$-$CH_3$ was optimised simultaneously. There was almost no change in the density predictions with the new optimised parameters. (Option B) Then, we tried to optimise with two parameters, both $\varepsilon_{kl}$ and $\lambda_{kl}^{r}$ simultaneously and the results showed that the optimisation gave a small improvement on the compressed-liquid densities at lower temperatures while maintaining the accuracy of the prediction of VLE and saturated density data. The $\Delta_{\mathrm{AARD}}$ for the

compressed-liquid density decreased from 1.7 % to 1.6 %. (Option C) Finally, we have decided to increase the weight ratio of the compressed-liquid density dataset to VLE datasets to 1000:1, meaning that there was a strong bias towards our compressed-liquid density dataset. The results of the three optimisations are shown in Figure 6.10. It can be seen that the accuracy of the compressed-liquid densities has significantly improved especially in the low-pressure region compared to the first optimisation. However, when predicting VLE and saturated-phase densities with the same parameters, the fittings did not have good agreement with both properties compared to the original parameters. It needs to be kept in mind that the compressed-liquid density predictions should not be improved at the expense of significant deterioration of vapour pressure and saturated-phase density predictions. Therefore, the optimisation could not be considered valid in this case.

In conclusion, the optimisation results demonstrated that the model did not have a significant improvement in the predictive ability on compressed-liquid density by changing only the un-like cross-interaction group parameters while keeping the pure components parameters unchanged. The results also suggested that the SAFT-γ Mie model seemed to be unable to predict VLE and saturated-phase density accurately without compromising the accuracy on the compressed-liquid density at the same time.

**Table 6.4** Optimisation of SAFT-γ Mie cross-interaction parameters: the values for the group dispersion energies, $\varepsilon_{kl}$ and the repulsive component, $\lambda_{kl}$, the experimental dataset and the weight factor used for each optimisation.

| | Parameters | | | | Data used during optimisation | Weight factor |
|---|---|---|---|---|---|---|
| | $CH_3$-$CO_2$ | | $CH_2$-$CO_2$ | | | |
| | $\varepsilon_{kl}$ | $\lambda_{kl}$ | $\varepsilon_{kl}$ | $\lambda_{kl}$ | | |
| Original | 205.70 | CR | 276.45 | CR | VLE: ($CO_2$ + *n*-pentane), ($CO_2$ + *n*-decane) | - |
| | $\varepsilon_{kl}$ | $\lambda_{kl}$ | $\varepsilon_{kl}$ | $\lambda_{kl}$ | VLE: ($CO_2$ + *n*-pentane), ($CO_2$ + *n*-decane), | |
| Option A | 208.55 | CR | 277.69 | CR | ($CO_2$ + *n*-heptane) Compressed-liquid density: ($CO_2$ + *n*-heptane) | *w* = 1:1 |
| | $\varepsilon_{kl}$ | $\lambda_{kl}$ | $\varepsilon_{kl}$ | $\lambda_{kl}$ | VLE: ($CO_2$ + *n*-pentane), ($CO_2$ + *n*-decane), | |
| Option B | 220.25 | 22.88 | 241.57 | 16.05 | ($CO_2$ + *n*-heptane) Compressed-liquid density: ($CO_2$ + *n*-heptane) | *w* = 1:1 |
| | $\varepsilon_{kl}$ | $\lambda_{kl}$ | $\varepsilon_{kl}$ | $\lambda_{kl}$ | VLE: ($CO_2$ + *n*-pentane), ($CO_2$ + *n*-decane), | |
| Option C | 215.44 | 15.05 | 225.56 | 14.33 | ($CO_2$ + *n*-heptane) Compressed-liquid density: ($CO_2$ + *n*-heptane) | *w* = 1:1000 |

Special thanks to Lorena Souza and Sultan Al Habsi for assistance in the gSAFTmm optimisation.

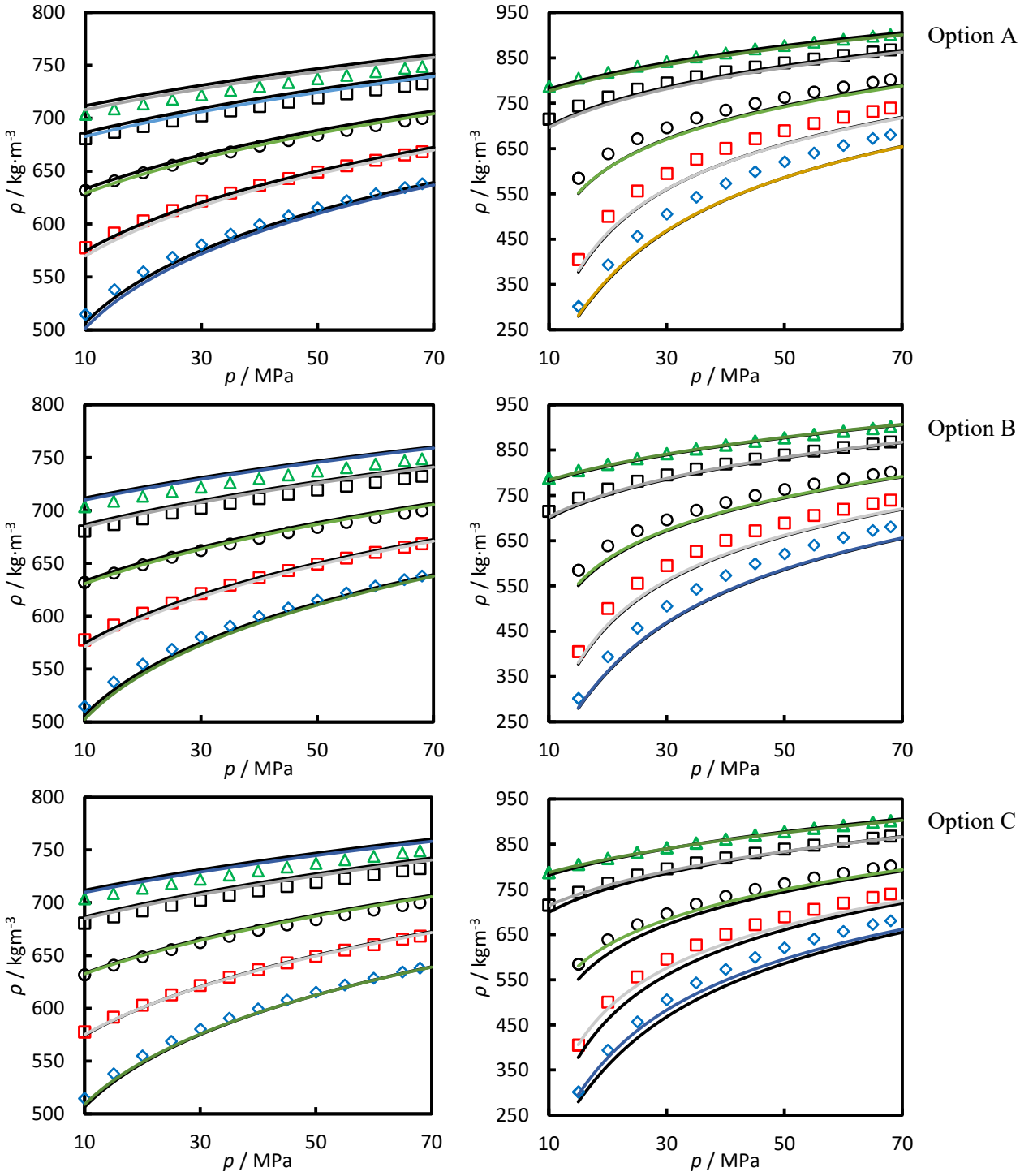



**Figure 6.10** Comparison of the compressed-liquid density predictions with the optimised and un-optimised parameters $\varepsilon_{kl}$ and $\lambda_{kl}^{r}$ of SAFT-γ Mie for $CO_2$ + *n*-heptane at two mole fractions of $CO_2$ at three scenarios: (1st column), $x$ = 0.2; (2nd column), $x$ = 0.8. Symbols represent experimental data: △, 298 K; □, 323 K; ○, 373 K; □, 423 K; ◇, 473 K. Black and coloured lines represent predictions with un-optimised and optimised parameters, respectively.

# 6.5 $CO_2$ + *n*-Nonane

This section gives the results of the compressed-liquid density measurements made for ($CO_2$ + *n*-nonane) over a temperature range of (283.15 to 473.15) K and for pressures up to 68 MPa. In conjunction, the results of speed-of-sound measurements made over temperature ranges of (283.15 to 473.15) at pressures up to 390 MPa are also presented. Both sets of experimental data were fitted with empirical correlations which permit interpolations with respect to *T* and *p.* Finally, the experimental data were also used to test the predictive abilities of several thermodynamic models.

## 6.5.1 Literature Review

Due to a wide range of temperatures and pressures studied for the speed-of-sound and density measurements, it was essential to have knowledge of the phase envelopes of the binary mixtures before carrying out the experiments. Both the density and speed-of-sound measurements were performed in the single-liquid-phase region. It was important to verify both the saturation and freezing pressures phase boundaries in order to determine if they impacted on the overall measurement range. Unfortunately, no data could be found in the literature relating to the freezing pressure of this binary mixture. Therefore, the freezing pressures of $CO_2$ + *n*-nonane were estimated in the NIST REFPROP 9.1 software [358]. Whereas, the saturation pressures are reported by several authors who carried out VLE measurements on $CO_2$ + *n*-nonane system [401-403]. The most recent study was conducted by Camacho-Camacho *et al.* [401] They studied the largest temperature range among all the other studies across four isotherms: $T$ = (315, 344, 373 and 418) K. For the rest of the measured temperatures, the phase envelopes were estimated using the PR78 EoS using the Aspen Properties software package. It is generally understood that PR78 EoS can predict VLE of $CO_2$ + hydrocarbon systems to a high accuracy. The experimental conditions were chosen such that the mixtures always stayed as a single-phase liquid based on these VLE results.

There are no reported experimental data on the compressed-liquid density of $CO_2$ + *n*-nonane in the literature. For density measurement of $CO_2$ + *n*-nonane system, only one study was found in the literature. Ashcroft and Isa [404] studied the effect of dissolved $CO_2$ on the densities of *n*-nonane. They measured the saturated liquid-phase density of $CO_2$ + *n*-nonane with a vibrating-tube densimeter. However, the measurements were only carried out on one isotherm, $T$ = 298.15 K and at pressure 1.01 MPa. Similarly, no sound-speed data for this binary system can be found in the literature; therefore no comparison could be made with our experimental data. The measurements reported here hence represent a significant contribution to the experimental thermodynamics of this system.

## 6.5.2 Experimental Density Results and Discussion

Compressed-liquid density measurement of $CO_2$ + *n*-nonane was carried out as a function of pressure along nine isotherms: $T$ = (283.15, 298.15, 323.15, 348.15, 373.15, 398.15, 423.15, 448.15 and 473.15) K at pressures up to 68 MPa. The four nominal mole fractions of $CO_2$ in the binary mixture studied were 0.2, 0.4, 0.6 and 0.8. The collected density data are given in Table C.4. In Figure 6.11, selected experimental densities measured at six isotherms across four different mole fractions of $CO_2$ as a function of pressure are shown. The density of pure *n*-nonane and $CO_2$ has also been added to the plots (results presented in Chapter 5). A similar analysis which was performed for the compressed-liquid density of $CO_2$ + *n*-heptane has been carried out. It has been noticed that at constant pressure, the dissolution of $CO_2$ in *n*-nonane both increases and decreases the density of the overall mixtures at different temperatures. At temperatures below 323.15 K, the overall density of the mixture increases with the concentration of $CO_2$ in the mixture. A crossover effect in the mixture densities was observed at temperatures between (348.15 and 473.15) K. As temperature increases, the crossover pressure point shifts towards a higher pressure. The crossover pressure is approximately 20 MPa at 373.15 K, and it shifts to about 60 MPa at the highest temperature. The density of the mixture was no longer higher than the pure components at high-temperature isotherms. The density crossover behaviour in mixtures of hydrocarbons with $CO_2$ has also been observed in the literature and also in our earlier work with $CO_2$ + *n*-heptane system. Since the measurements from Ashcroft and Isa [404] were restricted to one isotherm, $T$ = 298.15 K and at pressure 1.01 MPa; no comparison were made in this work.

**Correlation:** The compressed-liquid densities of $CO_2$ + *n*-nonane mixtures were fitted with the same empirical correlation that we used for the $CO_2$ + *n*-heptane data. The correlation is based on a polynomial function which describes pressure as a function of density at each composition, Equation (6.1). The density calculations using Equation (6.1) are represented in Figure 6.11. The correlation parameters combined with the $\Delta_{AAD}$ and $\Delta_{AARD}$ of the fitting are summarised in Table C.5 in the Appendix. The deviation plots between the calculated values and experimental compressed-liquid densities are shown in Figure 6.12. From the fitting procedure, it was found that the empirical correlation represented all of the compressed-liquid density data with the $\Delta_{AAD}$ and $\Delta_{AARD}$ about 0.03 MPa and 0.1 %, respectively. The fit of the empirical correlation decreases with increasing mole fraction of $CO_2$ in the mixture; this is because the change in density as a function of pressure was large with a range of approximately (420 to 920) kg·m$^{-3}$ at pressures between (10 and 65) MPa.

**Excess Molar Volume:** The excess molar volume ($V_m^E$) has been determined for the $CO_2$ + *n*-nonane system from the experimental compressed-liquid density data using Equation (6.2). The density measurement of the pure components, both $CO_2$ and *n*-nonane, were carried out prior to the

measurement of the binary mixture using the vibrating-tube densimeter which was described in Chapter 5. The pure components densities for *n*-nonane and $CO_2$ are reported in Tables B.5 and B.11 in the Appendix. In Figure 6.13, we show the plots of $V_m^E$ as a function of mole fraction of $CO_2$ across six isotherms: $T$ = (283.15, 298.15, 348.15, 373.15, 423.15 and 473.15) K. In the composition range investigated, $V_m^E$ of $CO_2$ + *n*-nonane system behaves similarly to other $CO_2$ + hydrocarbon systems. The excess molar volume becomes more negative with increasing temperature but less negative with increasing pressure. The excess molar volume displayed a sigmoidal variation with the composition at $T$ = (283.15 and 298.15) K. The mixtures display a maximum excess molar volume at $x$ = 0.2 and a minimum at around $x$ = 0.8. At temperatures above 373.15 K, the excess molar volume is negative over the entire range of composition for all pressures and becomes more negative with increasing temperature and decreasing pressure. The negative values of excess molar volume were observed when $CO_2$ behaved as a gas-like fluid. To allow interpolation between compositions, the excess molar volume has been correlated with Redlich-Kister equation [360], Equation (6.3). The correlation parameters were determined by minimising the absolute difference between the experimental data and the correlated values. The calculated excess molar volumes have been fitted to each isotherm and isobar individually. The results of the correlation are shown in Figure 6.11, and the goodness of the fit was given by the $\Delta_{AAD}$, which is 0.163 $cm^{-3}\cdot mol$ across all isotherms and isobars. The parameters determined are listed in Table C.6 shown in Appendix C.

## 6.5.3 Experimental Speed-of-Sound Results and Discussion

Experimental sound-speed data in the binary mixture $CO_2$ + *n*-nonane were collected as a function of pressure along nine isotherms at $T$ = (283.15, 298.15, 323.15, 348.15, 373.15, 398.15, 423.15, 448.15 and 473.15) K and at pressures up to 390 MPa. On each isotherm, the measurements started at approximately 10 MPa and increased to the highest pressure in increments of approximately 40 MPa. The four nominal mole fractions of $CO_2$ in the binary mixtures were 0.2, 0.4, 0.6 and 0.8. The experimental sound-speed data together with the mole fractions were given in Table C.7. Figure 6.14 shows the sound-speed as a function of pressure across nine temperatures at four different compositions. At constant composition, it can be seen that the speed-of-sound in the binary mixture increases non-linearly with pressure and decreases with temperature. At constant temperatures and pressures, the sound-speeds decrease with increasing $CO_2$ mole fraction in the mixture. To our knowledge, there are no available sound-speed data for this binary system in the literature; therefore no comparison could be made with our experimental data.

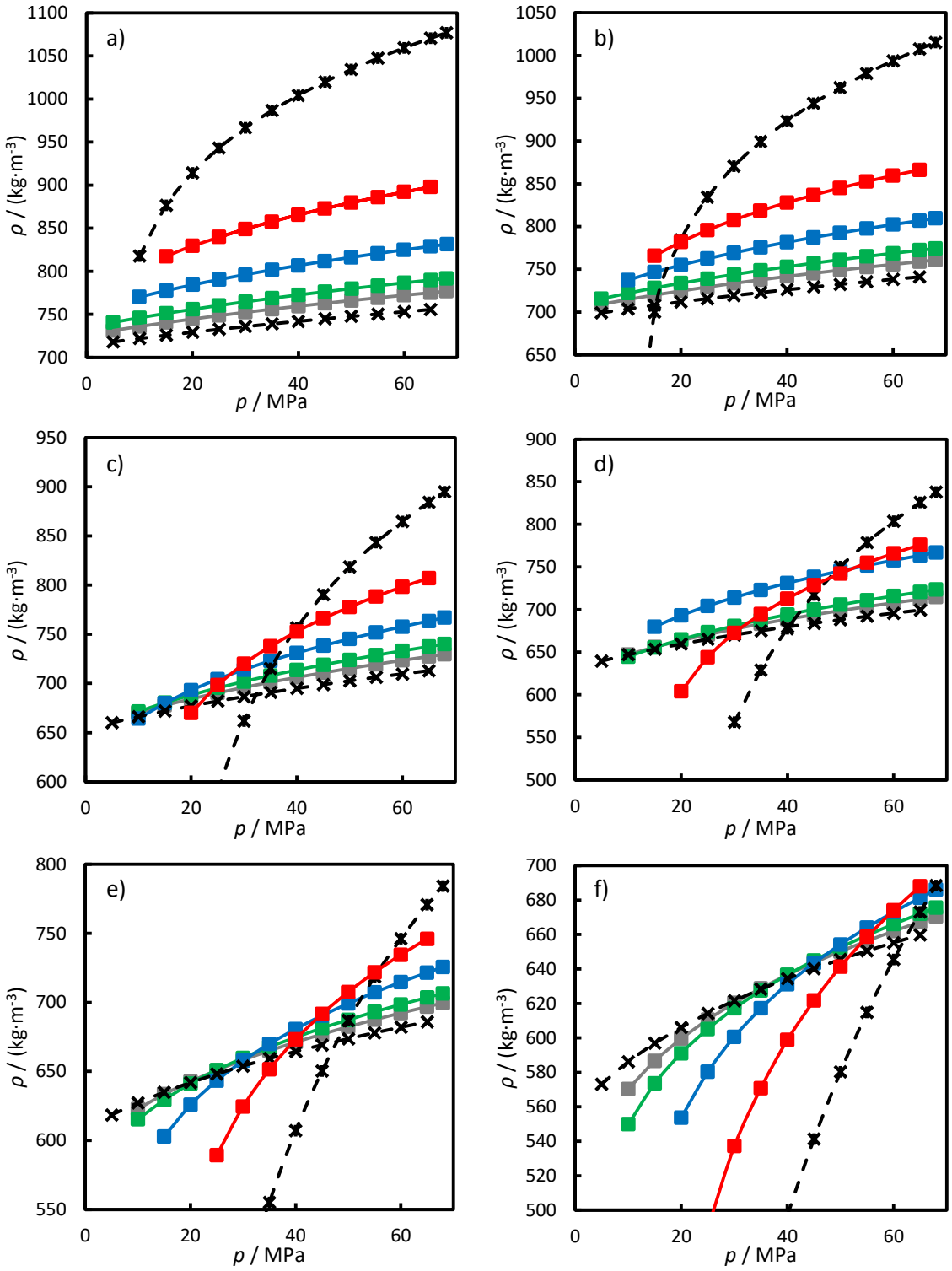



**Figure 6.11** Compressed-liquid densities $\rho$ (coloured square) against pressure for $CO_2$ + *n*-nonane system at four mole fractions of $CO_2$: ∗, 0; (grey), 0.2; (green), 0.4; (blue),0.6; (red), 0.8;×,1; at six temperatures: a) 298 K, b) 323 K, c) 348 K, d) 398 K, e) 423 K and f) 473 K. Coloured lines represent values calculated with the empirical correlation, Equation (6.1).

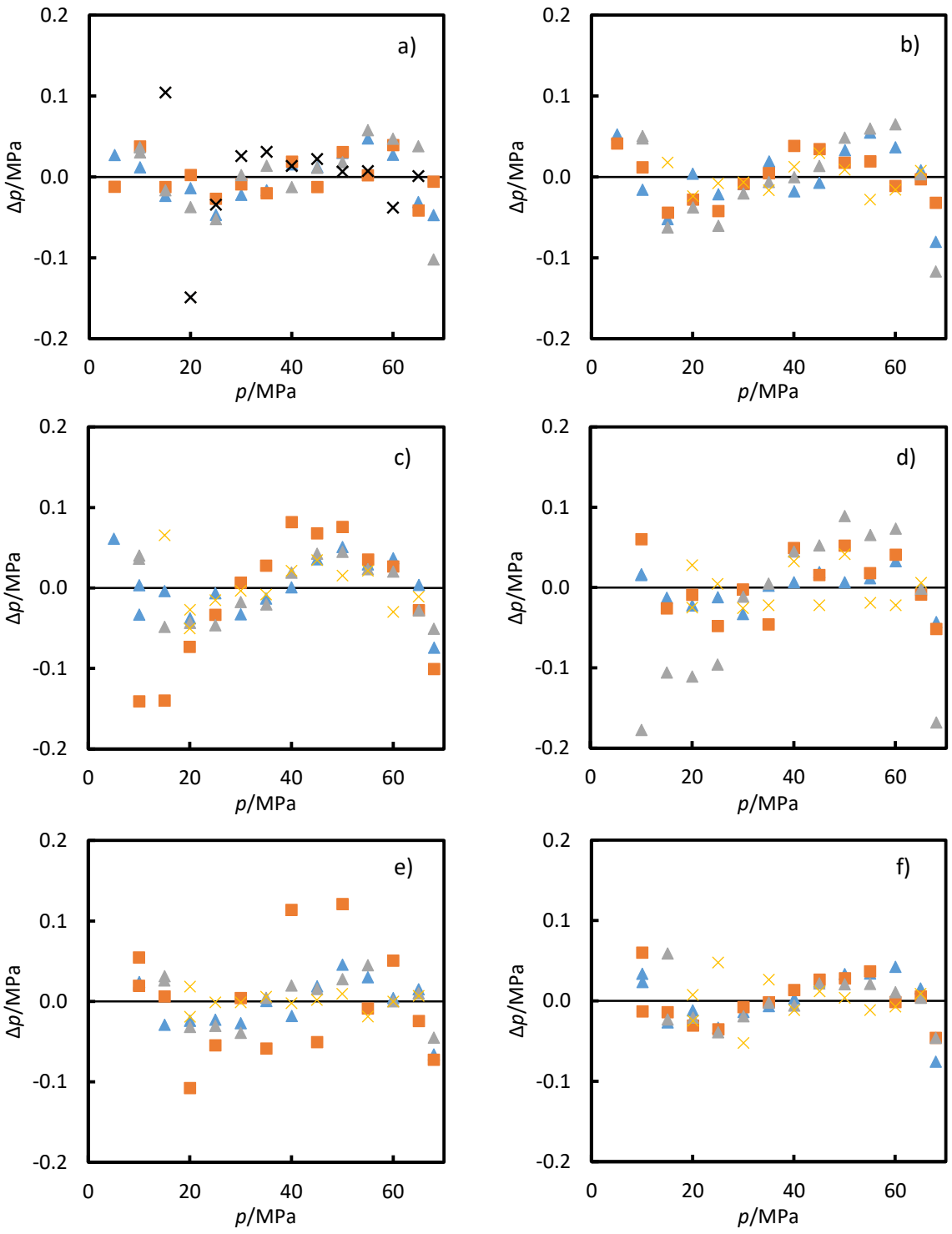



**Figure 6.12** Deviations between the experimental pressure $p_{exp}$ and values calculated from the empirical correlation $p_{fit}$, $\Delta p = p_{exp} - p_{fit}$ for $CO_2$ + *n*-nonane at six temperatures: a) 298 K, b) 323 K, c) 348 K, d) 373 K, e) 423 K and f) 448 K. Symbols denote different mole fraction of $CO_2$ in the binary mixture: ▲, 0.2; ■, 0.4; ● , 0.6; ◆, 0.8.

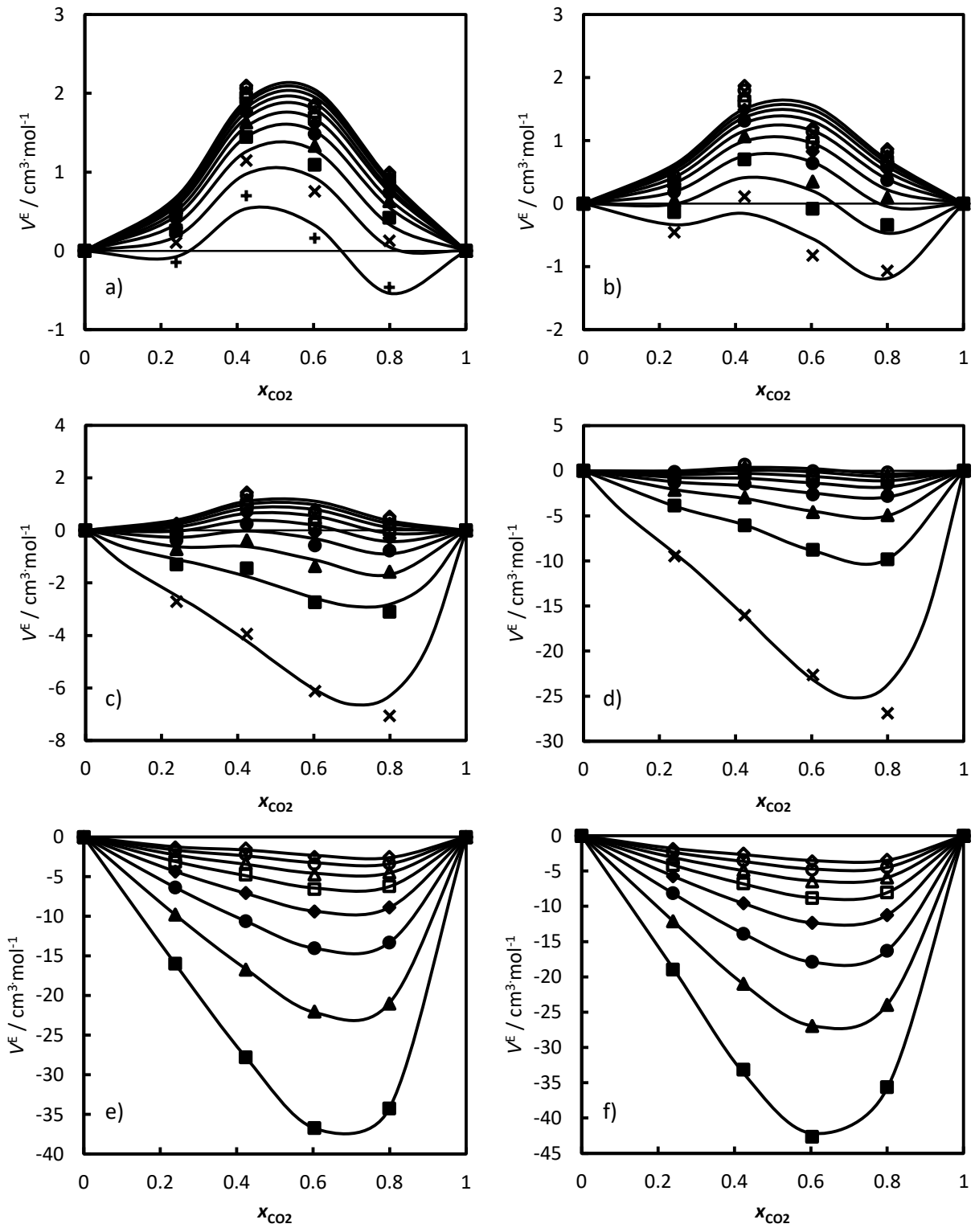



**Figure 6.13** Excess molar volume $V_m^E$ of $CO_2$ + *n*-nonane system versus the molar fraction of $CO_2$ at six temperatures: a) 283 K; b) 298 K; c) 323 K; d) 373 K; e) 423 K; f) 448 K and at ten isobars: +, 10 MPa; ✖,15 MPa; ■, 20 MPa; ▲, 25 MPa; ●, 30 MPa; ◆, 35 MPa; □, 40 MPa; △, 45 MPa; ○, 50 MPa; ◇, 55 MPa. Solid lines represent values calculated from the Redlich-Kister correlation, Equation (6.3) with parameters from Table C.6.

**Correlation:** The experimental sound-speed data for $CO_2$ + *n*-nonane at each composition were fitted by an empirical correlation which covers the whole range of temperatures and pressures. The correlation allows testing of smoothness of the experimental data and at the same time permits interpolation with respect to *T* and *p*. The sound-speed correlation is given in the following pressure-explicit form:

$$(p - p_0)/\,\mathrm{MPa} = \sum_{i=1}^{3}\sum_{j=0}^{3} a_{ij}\left\{(c - c_0)/(\mathrm{m\cdot s^{-1}})\right\}^i \left(\frac{T_0}{T}\right)^j , \tag{6.7}$$

where $p_0$ and $T_0$ are the reference values of pressure and temperature: $T_0$ was set to 273.15 K, and $p_0$ was set at different values ranging from (0.1 to 20) MPa depending on the composition of the mixture. The quantity $c_0 = c(T_0, p_0)$ was then correlated as a function of reduced temperature as follows:

$$c_0\,/(\mathrm{m\cdot s^{-1}}) = \sum_{i=0}^{3} b_i \left(\frac{T}{T_0}\right)^i . \tag{6.8}$$

The goodness of the fit was determined by the average absolute deviation $\Delta_{AARD.}$ The $\Delta_{AARD}$ for the surface fit of speed-of-sound data for $CO_2$ + *n*-nonane at each composition ranges from (0.07 to 0.34) % across the four compositions. The deviation plots as a function of temperature and pressure are shown in Figure 6.15. The $\Delta_{AARD}$ across four compositions was calculated to be 0.1 % which is comparable to the expanded uncertainty of 0.1 %. The $\Delta_{AARD}$ increases with the amount of $CO_2$ in the binary mixture; this is because the speeds-of-sound vary greatly from the normal liquid region to the supercritical region in the wide temperature and pressure range measured. The highest deviation points normally occurred at the highest isotherm and the lowest pressure, where the state points were measured very close to the bubble curve with less sensitive signals during the measurements. The parameters of Equations (6.7) and (6.8), together with the $\Delta_{AARD}$ for the binary mixture are given in Table C.8 in Appendix C.

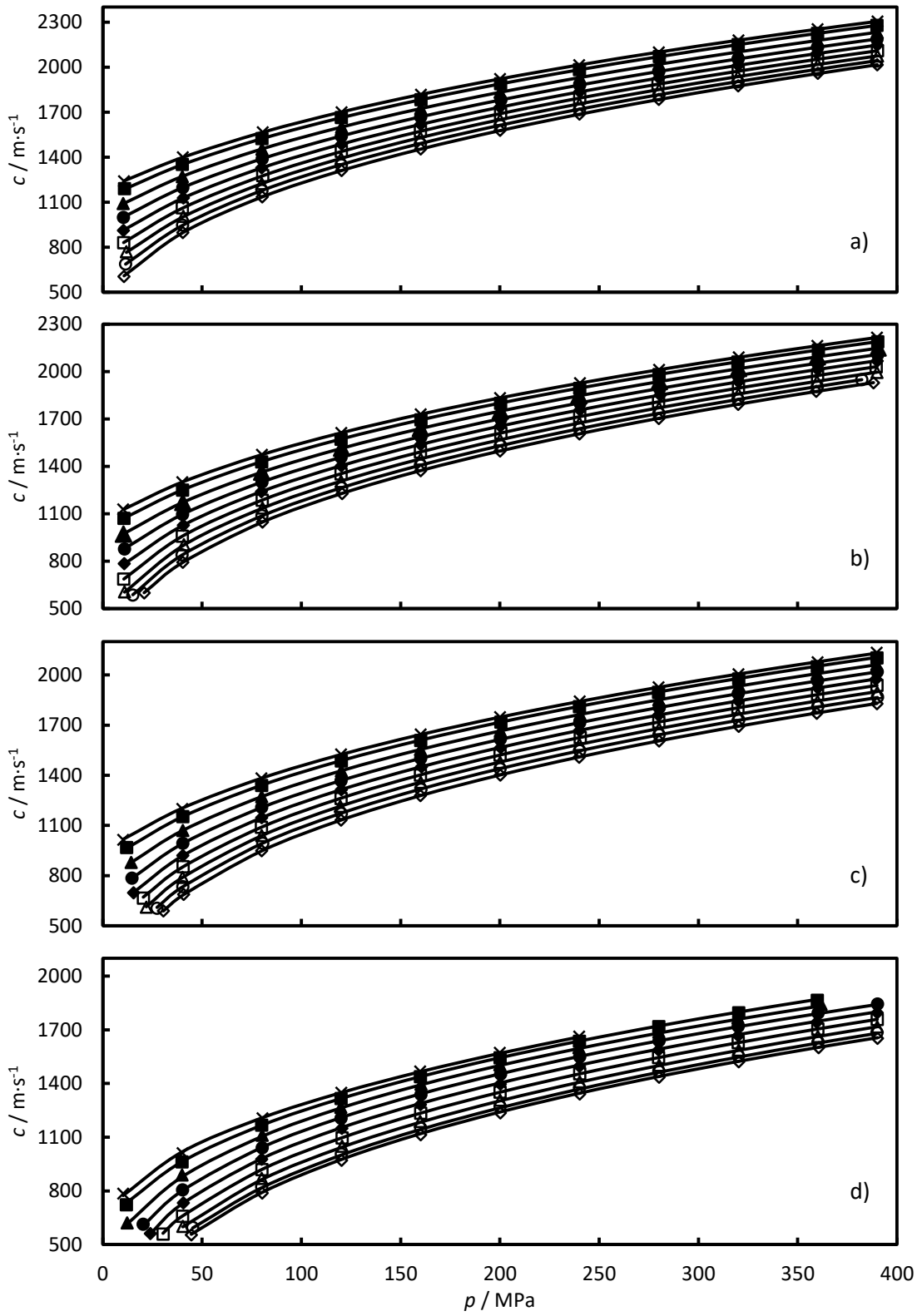



**Figure 6.14** Experimental sound-speed $c$ in $CO_2$ + $n$-nonane across nine isotherms as a function of pressure at four compositions. Symbols represent experimental data: ×, 283.15 K; ■, 298.15 K; ▲, 323.15 K; ●, 348.15 K; ◆, 373.15 K; □, 398.15 K;△, 423.15 K; ○, 448.15 K; ◇, 473.15 K. a) $x$ = 0.2; b) $x$ = 0.4; c) $x$ = 0.6 d) $x$ = 0.8. Lines represent sound-speed values calculated from the empirical correlation, Equation (6.7).

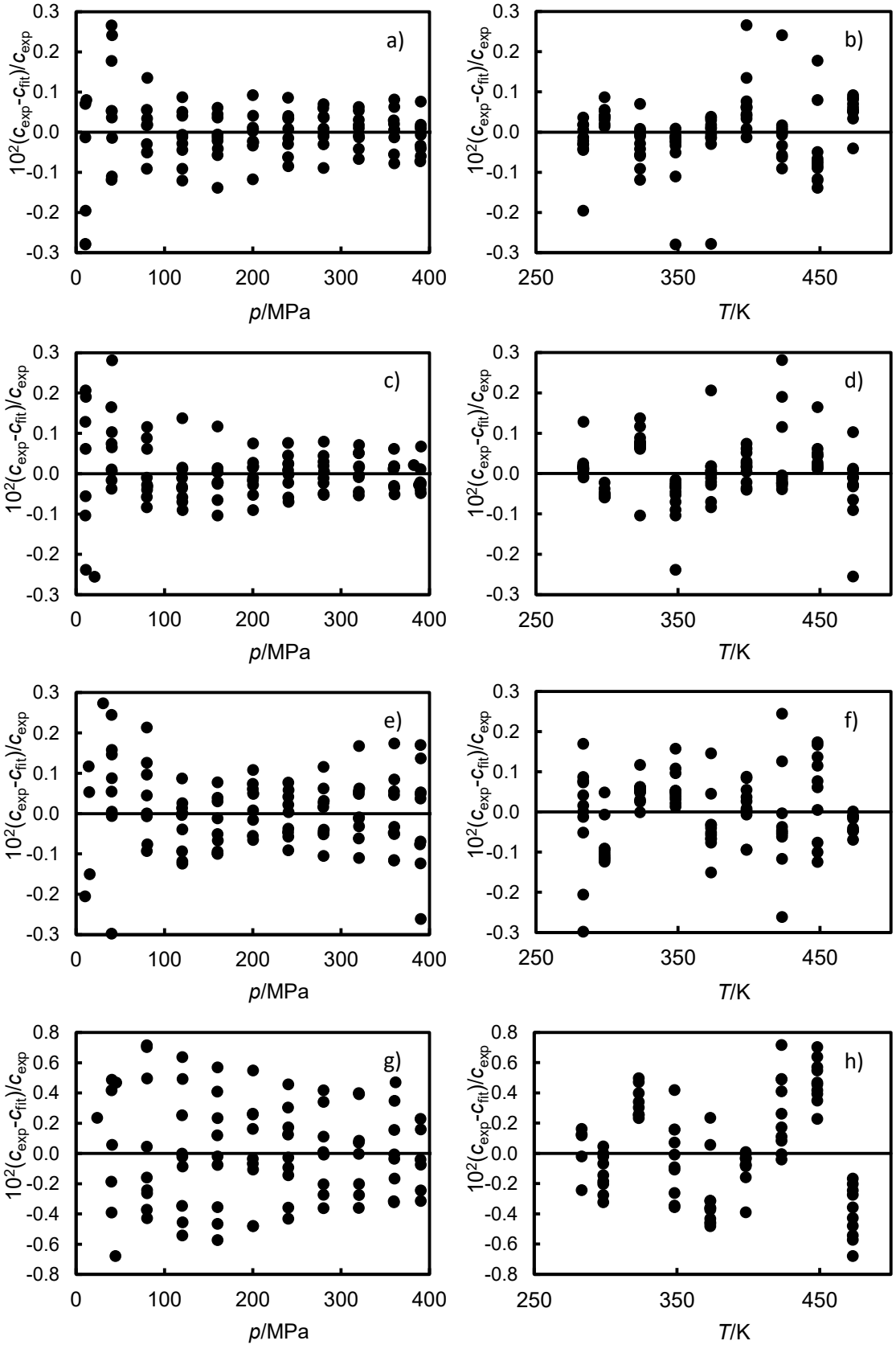



**Figure 6.15** Deviations of the experimental speed-of-sound $c_{exp}$ in $CO_2$ + *n*-nonane from the values calculated from the empirical correlation $c_{fit}$ as a function of pressure and temperature. (1st row), $x$ = 0.2; (2nd row), $x$ = 0.4; (3rd row), $x$ = 0.6; (4th row), $x$ = 0.8.

## 6.5.4 Modelling

The experimental compressed-liquid densities have been compared with the predictions from the PPR78, SAFT-γ Mie, and GERG-2008 EoSs. Similarly, the temperature-dependent binary interaction parameter $k_{ij}$ in PPR78 EoS between $CO_2$ and *n*-nonane was calculated by the group-contribution scheme [316-319], Equation (3.18). In the SAFT-γ Mie EoS, the functional groups $CH_2$ and $CH_3$ were required to characterise *n*-nonane. The descriptions of the cross-interaction parameters for functional groups ($CO_2$-$CH_3$) and ($CO_2$-$CH_2$) can be found in Table 6.5. Lastly, the compressed-liquid densities have also been tested with the GERG-2008 EoS, the binary interaction parameters were taken directly from Kunz and Wagner [39], and the calculations were performed without any adjustment. The parameters implemented in the three thermodynamic models for this binary system $CO_2$ + *n*-nonane are tabulated in Table 6.5.

**Table 6.5** Experimental parameters for two equations of state: PPR78 (the binary interaction parameter, *kij* determined from the critical components $p_c$ and $T_c$ and acentric factor $\omega$) and GERG-2008 (four adjustable parameters).

| | | | | | | | | |
|---|---|---|---|---|---|---|---|---|
| PPR78 | Component | $\omega$ | | $p_c$ / MPa | | $T_c$ / K | | Ref |
| | *n*-nonane | 0.443 | | 2.28 | | 594.55 | | [40] |
| | carbon dioxide | 0.224 | | 7.38 | | 304.13 | | [174] |
| | System | $T$ / K | $k_{ij}$ | $T$ / K | $k_{ij}$ | $T$ / K | $k_{ij}$ | |
| | $CO_2$ + *n*-nonane | 283.15 | 0.1280 | 348.15 | 0.1281 | 423.15 | 0.1332 | - |
| | | 298.15 | 0.1275 | 373.15 | 0.1293 | 448.15 | 0.1358 | - |
| | | 323.15 | 0.1275 | 398.15 | 0.1310 | 473.15 | 0.1388 | - |
| GERG-2008 | System | $\beta_T$ | | $\gamma_T$ | $\beta_v$ | $\gamma_v$ | $F_{ij}$ | |
| | $CO_2$ + *n*-nonane | 1.0077 | | 1.1407 | 1.0000 | 0.9794 | 0 | [39] |

As shown in Figure 6.16, the compressed-liquid density predictions from PPR78 are generally lower than the experimental data, and the overall $\Delta_{AARD}$ across four compositions is 2.5 %. For the case of SAFT-γ Mie EoS, it was observed that the model generally over-predicts the densities at low-temperatures and under-predicts at high temperatures. The trend across the four compositions of the mixture is similar and the overall $\Delta_{AARD}$ is 1.5 %. The deviation plots for the two thermodynamic models are shown in Figure 6.17. No optimisation of the cross-interaction parameters of SAFT-γ Mie was carried out for this system. Lastly, the experimental results were compared with the predictions from GERG-2008 EoS. As shown in Figure 6.18, the predictions are significantly higher than the experimental density with an $\Delta_{AARD}$ of 8.4% across four compositions.

**PPR78 with Volume Translation:** The method was described earlier in Chapter 3. We applied the volume translation to the predictions of the PPR78 EoS. In this case, the predictions with volume translation are closer to the experimental data, and the new $\Delta_{AARD}$ across four compositions was

calculated to be 1.8 %. The effect of the volume translation was greater on the compressed-liquid densities of $CO_2$ + *n*-nonane compared to $CO_2$ + *n*-heptane, as seen earlier.

**Table 6.6** Average absolute relative deviations $\Delta_{AARD}$ between the experimental compressed-liquid density, speed-of-sound and the predictions from PPR78, SAFT-γ Mie and GERG-2008 EoSs for $CO_2$ + *n*-nonane at four compositions, and the overall average absolute relative deviations $\Delta_{AARD,overall}$.

| Equation of state | Property | $\Delta_{AARD,overall}$ | $x_{CO2}$ | $\Delta_{AARD}$ |
|---|---|---|---|---|
| PPR78 (VT) | Compressed-liquid density | 2.5% (1.8%) | 0.2 | 3.0% (1.5%) |
| | | | 0.4 | 2.4% (1.4%) |
| | | | 0.6 | 2.4% (2.0%) |
| | | | 0.8 | 2.0% (2.4%) |
| SAFT-γ Mie | Compressed-liquid density | 1.5% | 0.2 | 0.7% |
| | | | 0.4 | 1.6% |
| | | | 0.6 | 1.7% |
| | | | 0.8 | 2.1% |
| GERG-2008 | Compressed-liquid density | 8.4% | 0.2 | 4.9% |
| | | | 0.4 | 8.5% |
| | | | 0.6 | 10.3% |
| | | | 0.8 | 10.0% |

Experimental sound-speed data in the binary mixture $CO_2$ + *n*-nonane were also compared with the values calculated using GERG-2008 and SAFT-γ Mie. The calculations of the GERG-2008 predictions of $CO_2$ + *n*-nonane were carried out using the NIST REFPROP 9.1 software. These calculated values were based on reference-quality equations of state for $CO_2$ and *n*-nonane, combined with the GERG-2008 mixture model. It has to be noted that the predicted values in REFPROP 9.1 software are similar but not identical to those of GERG-2008 because the pure-component equations of state used in REFPROP 9.1 software are different to those specified in GERG-2008. In addition, with the limitation of the pressure in the equation of state built for *n*-nonane, high-pressure sound-speed values could only be obtained at high-temperature isotherms. The predictive ability of SAFT-γ Mie on second derivative properties has been tested with pure alkanes systems, and the results were detailed in Papaioannou and co-workers [350, 394]. In Figure 6.20, comparisons between the experimental sound-speeds in $CO_2$ + *n*-nonane across five isotherms and the predictions obtained from the two equations of state are shown. We have included the sound-speed data for pure nonane and pure $CO_2$ data which are taken from Tay and Trusler [405] and Lin and Trusler [81], respectively.

In comparison with GERG-2008, a trend emerges with the predicted values generally being too low across the measured pressure range. The deviations increase at pressures above 80 MPa. At $x$ = 0.2, most of the deviations are within ±1.3 % across the entire pressure range. These deviations increase with increasing mole fraction of $CO_2$, with the $\Delta_{AARD}$ at $x$ = 0.8 being 5.5 %. The $\Delta_{AARD}$ for state points below 100 MPa is 2.5 % across four compositions. It has to be noted that the intended temperature and pressure ranges for the GERG-2008 EoS were $T \leq 700$ K and respectively. The high

deviations could be explained by the fact that the measurements exceeded the specified pressure range of the pure components equations of state and GERG-2008. Since the structure and properties of $CO_2$ and nonane are different, the departure function in the Helmholtz mixture model may be important to describe this binary system accurately [38, 39].

In GERG-2008, the development of the departure functions for binary pairs were developed only for those systems for which adequate experimental data existed in the literature. Due to the lack of accurate data for this system, a departure function was not optimised for the $CO_2$ + *n*-nonane system. The SAFT-γ Mie predictions are generally higher compared to the experimental data throughout the experimental temperature, pressure and composition range with the $\Delta_{AARD}$ ranging from (1.7 to 2.8) % across the four compositions. The predictions from SAFT-γ Mie have a better agreement with the experimental data than seen with GERG-2008 and the overall $\Delta_{AARD}$ were 2.1 % and 3.9 % for the predictions from SAFT-γ Mie and GERG-2008, respectively. The deviations between the experimental data for $CO_2$ + *n*-nonane and the predicted data calculated from the two models are plotted in Figures 6.20 and 6.21.

**Table 6.7:** Average absolute relative deviations $\Delta_{AARD}$ between the experimental compressed-liquid density, speed-of-sound and the predictions from PPR78, SAFT-γ Mie and GERG-2008 EoSs for $CO_2$ + *n*-nonane at four compositions, and the overall average absolute relative deviations $\Delta_{AARD,overall}$.

| Equation of state | Property | $\Delta_{AARD,overall}$ | $x_{CO2}$ | $\Delta_{AARD}$ |
|---|---|---|---|---|
| SAFT-γ Mie | Speed-of-sound | 2.1% | 0.2 | 1.7% |
| | | | 0.4 | 1.7% |
| | | | 0.6 | 2.0% |
| | | | 0.8 | 2.8% |
| GERG-2008 | Speed-of-sound | 3.9% | 0.2 | 1.3% |
| | | | 0.4 | 3.2% |
| | | | 0.6 | 5.6% |
| | | | 0.8 | 5.5% |

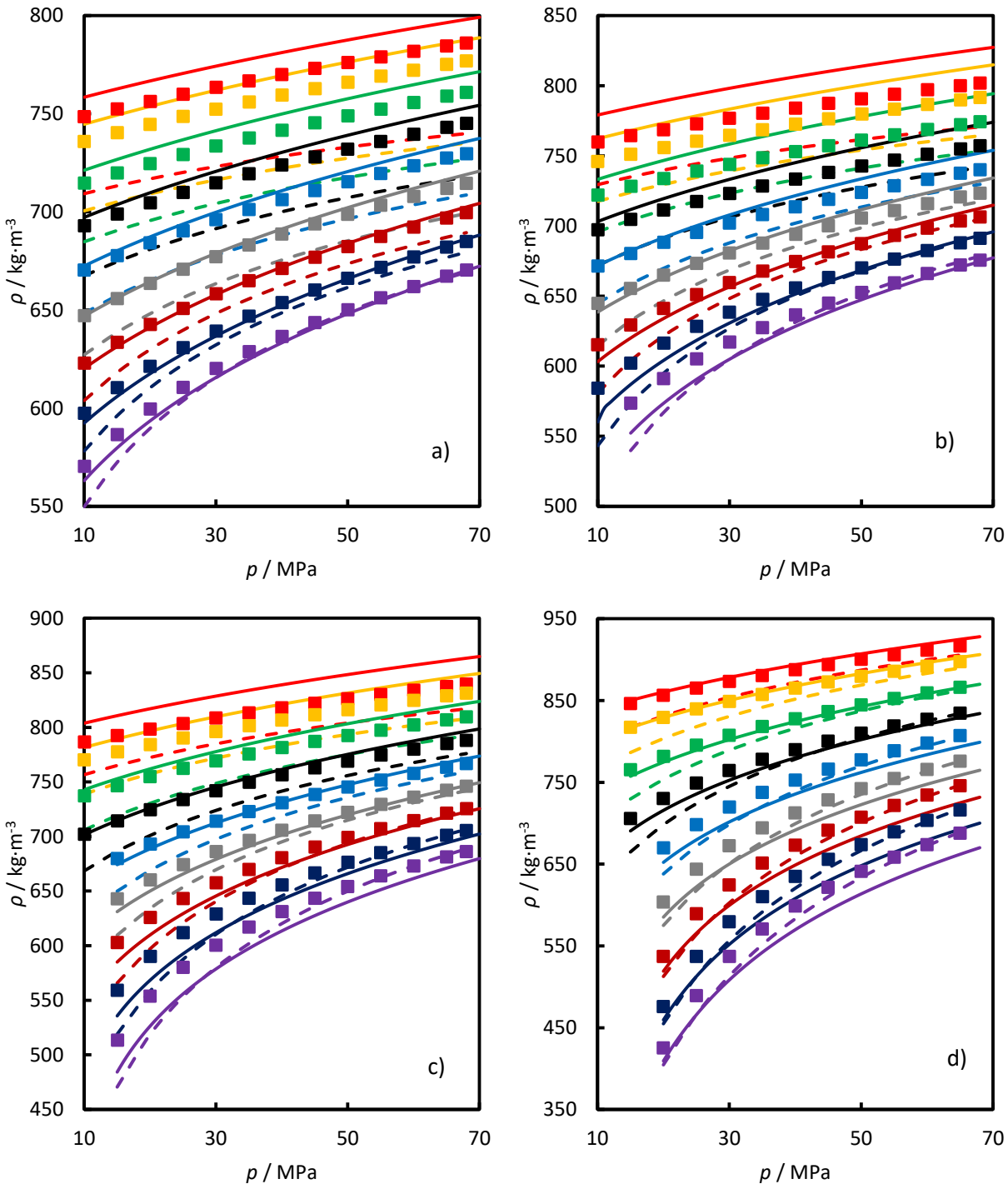



**Figure 6.16** Comparisons between experimental compressed-liquid density of $CO_2$ + *n*-nonane and the predictions from SAFT-γ Mie and PPR78 EoS at nine temperatures: (red), 283 K; (yellow), 298 K; (green), 323 K; (black), 348 K; (blue), 373 K; (grey), 398 K; (dark red), 423 K; (dark blue), 448 K; (purple), 473 K and at four mole fractions of $CO_2$: a) $x$ = 0.2; b) $x$ = 0.4; c) $x$ = 0.6; d) $x$ = 0.8. Solid and dotted lines represent predictions from SAFT-γ Mie and PPR EoS, respectively.

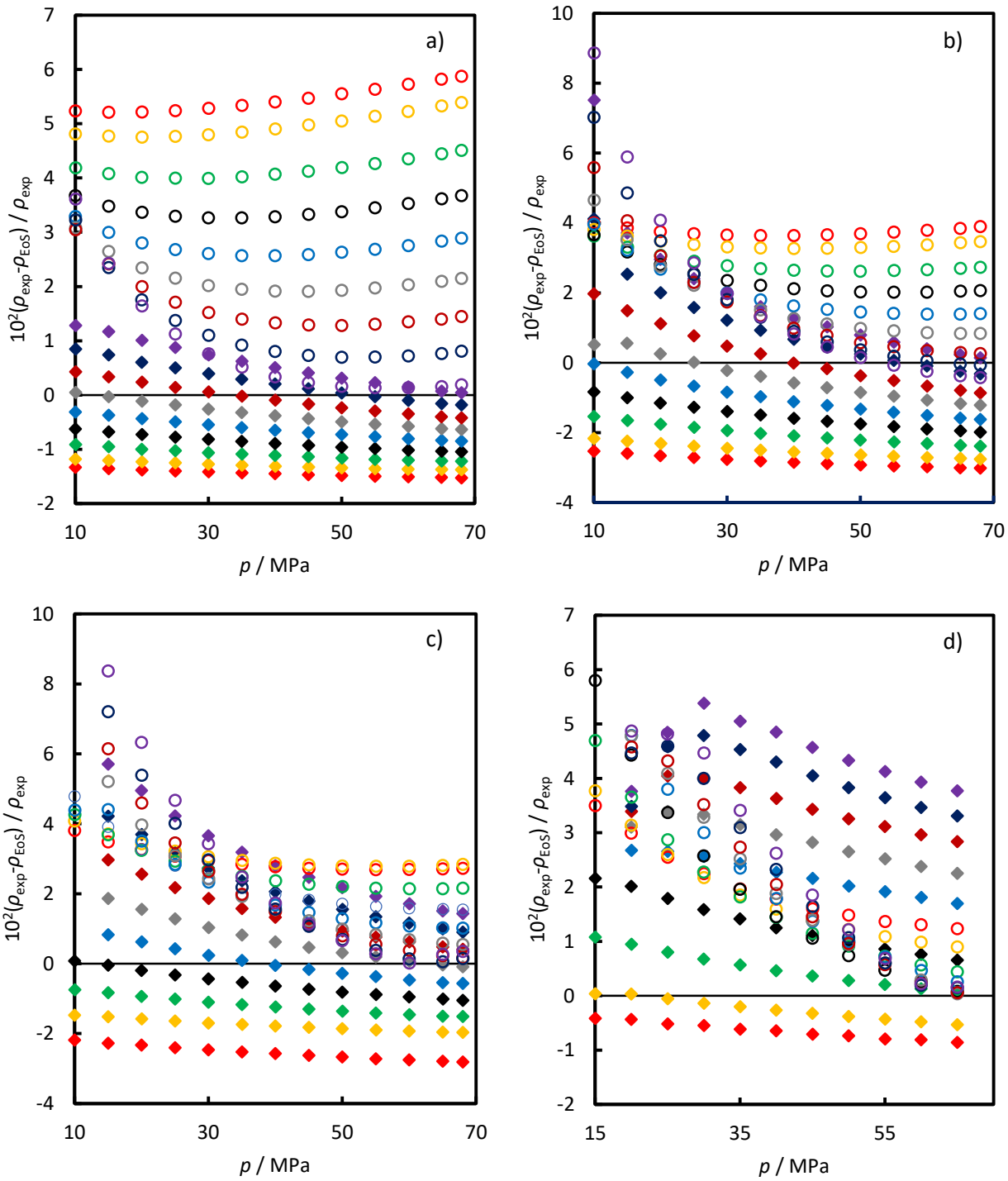



**Figure 6.17** Deviation plots between the experimental compressed-liquid density $\rho_{exp}$ for $CO_2$ + *n*-nonane and the predictions from SAFT-γ Mie and PPR78 EoS $\rho_{EoS}$ at nine isotherms: (red), 283 K; (yellow), 298 K; (green), 323 K; (black), 348 K; (blue), 373 K; (grey), 398 K; (dark red), 423 K; (dark blue), 448 K; (purple), 473 K. Symbols: ◆, SAFT-γ Mie and ○, PPR78 EoS.

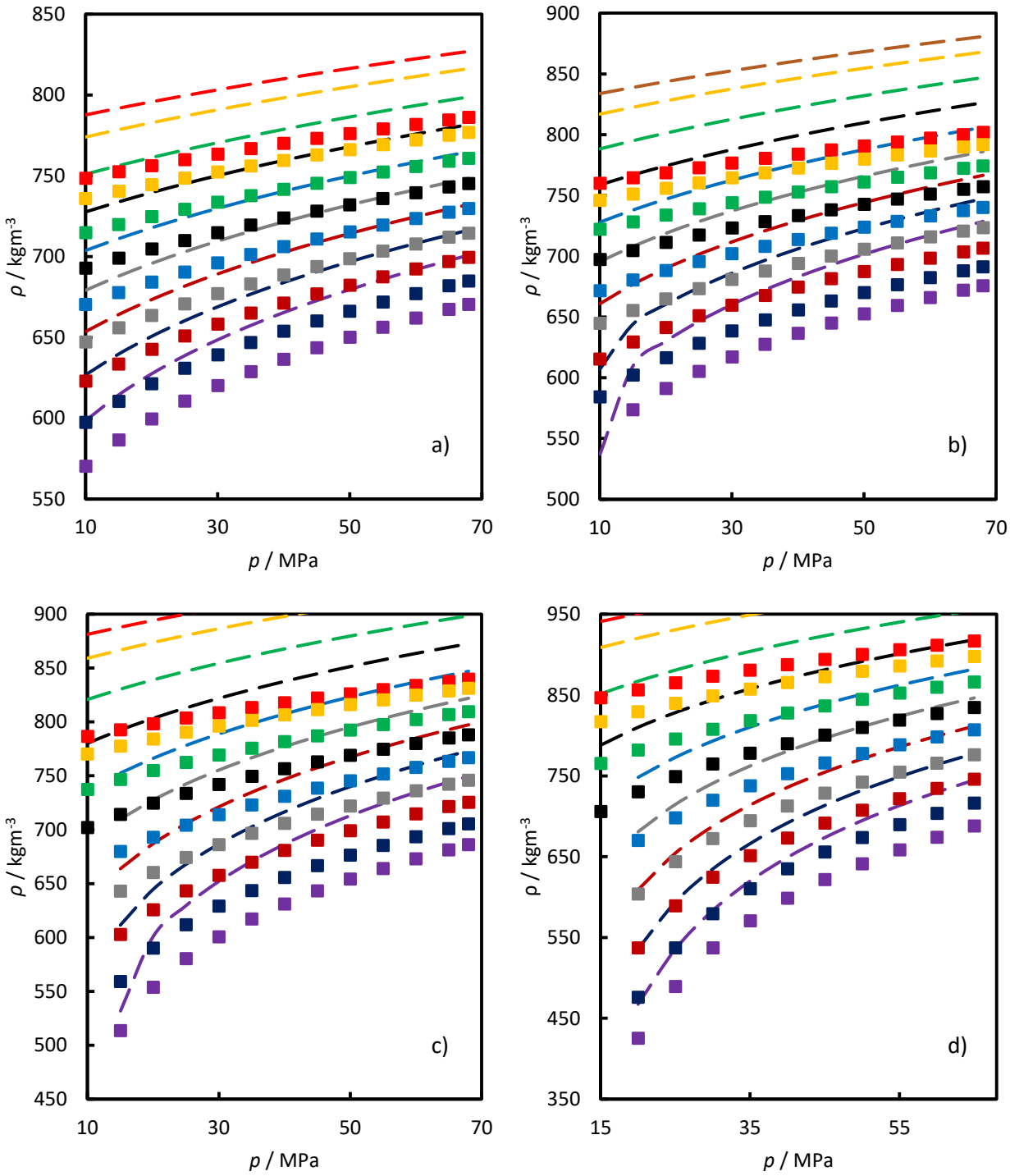



**Figure 6.18** Comparisons between the experimental compressed-liquid density of $CO_2$ + *n*-nonane and the predictions from GERG-2008 EoS at nine temperatures: (red), 283 K; (yellow), 298 K; (green), 323 K; (black), 348 K; (blue), 373 K; (grey), 398 K; (dark red), 423 K; (dark blue), 448 K; (purple), 473 K and at four mole fractions of $CO_2$: a) $x$ = 0.2; b) $x$ = 0.4; c) $x$ = 0.6; d) $x$ = 0.8 and the predictions from GERG-2008 EoS. Dash lines represent predictions from GERG-2008 EoS.

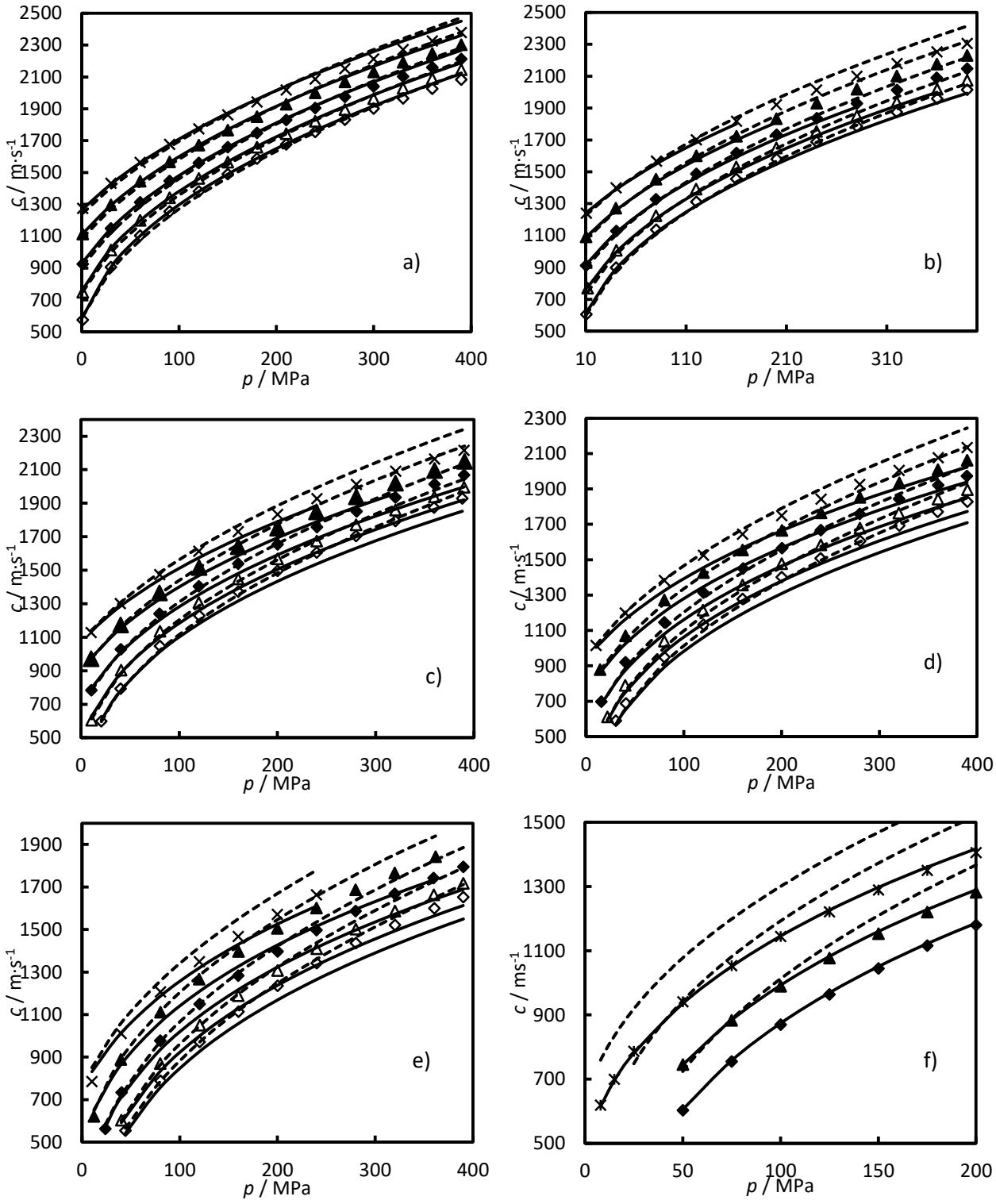



**Figure 6.19** Comparison between experimental sound-speed in $CO_2$ + *n*-nonane and predictions from SAFT-γ Mie and GERG-2008 across nine isotherms as a function of pressure. Symbols represent experimental data: ∗, 273.15 K;×, 283.15 K; ▲, 323.15 K; ◆, 373.15 K; △, 423.15 K; ◇, 473.15 K. a) $x = 0$; b) $x = 0.2$; c) $x = 0.4$; d) $x = 0.6$; e) $x = 0.8$; f) $x = 1$. Pure $CO_2$ data are taken from Lin and Trusler [81]. Solid and dotted lines represent sound-speed values calculated from the GERG-2008 and SAFT-γ Mie, respectively.

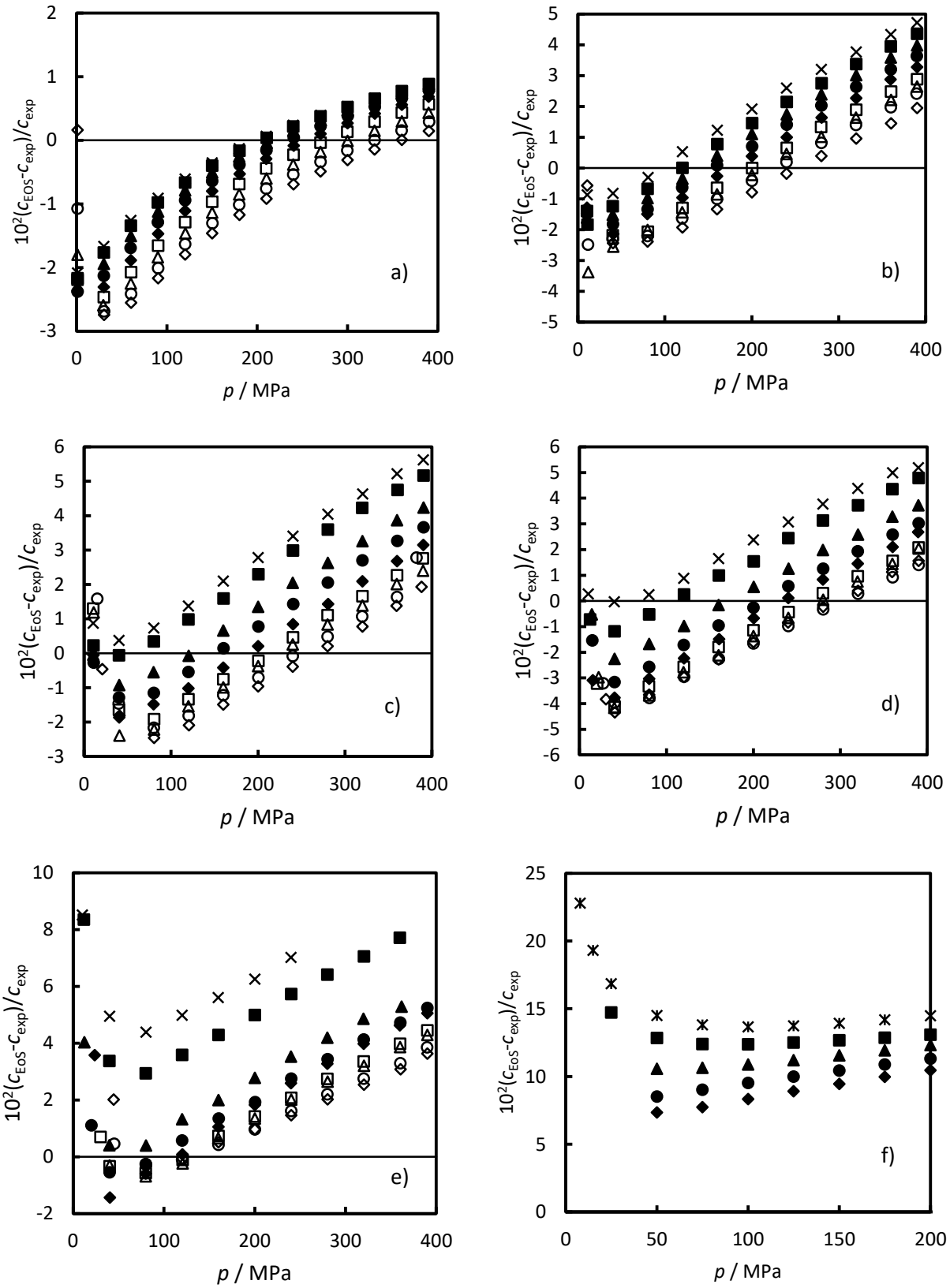



**Figure 6.20** Deviations between experimental sound-speed $c_{exp}$ and predictions from SAFT-γ Mie $c_{EoS}$ of $CO_2$ + *n*-nonane across nine isotherms as a function of pressure. Symbols represent experimental data: ×, 283.15 K; ■, 298.15 K; ▲, 323.15 K; ●, 348.15 K; ◆, 373.15 K; □, 398.15 K;△, 423.15 K; ○, 448.15 K; ◇, 473.15 K. a) $x$ = 0; b) $x$ = 0.2; c) $x$ = 0.4; d) $x$ = 0.6; e) $x$ = 0.8; f) $x$ = 1.

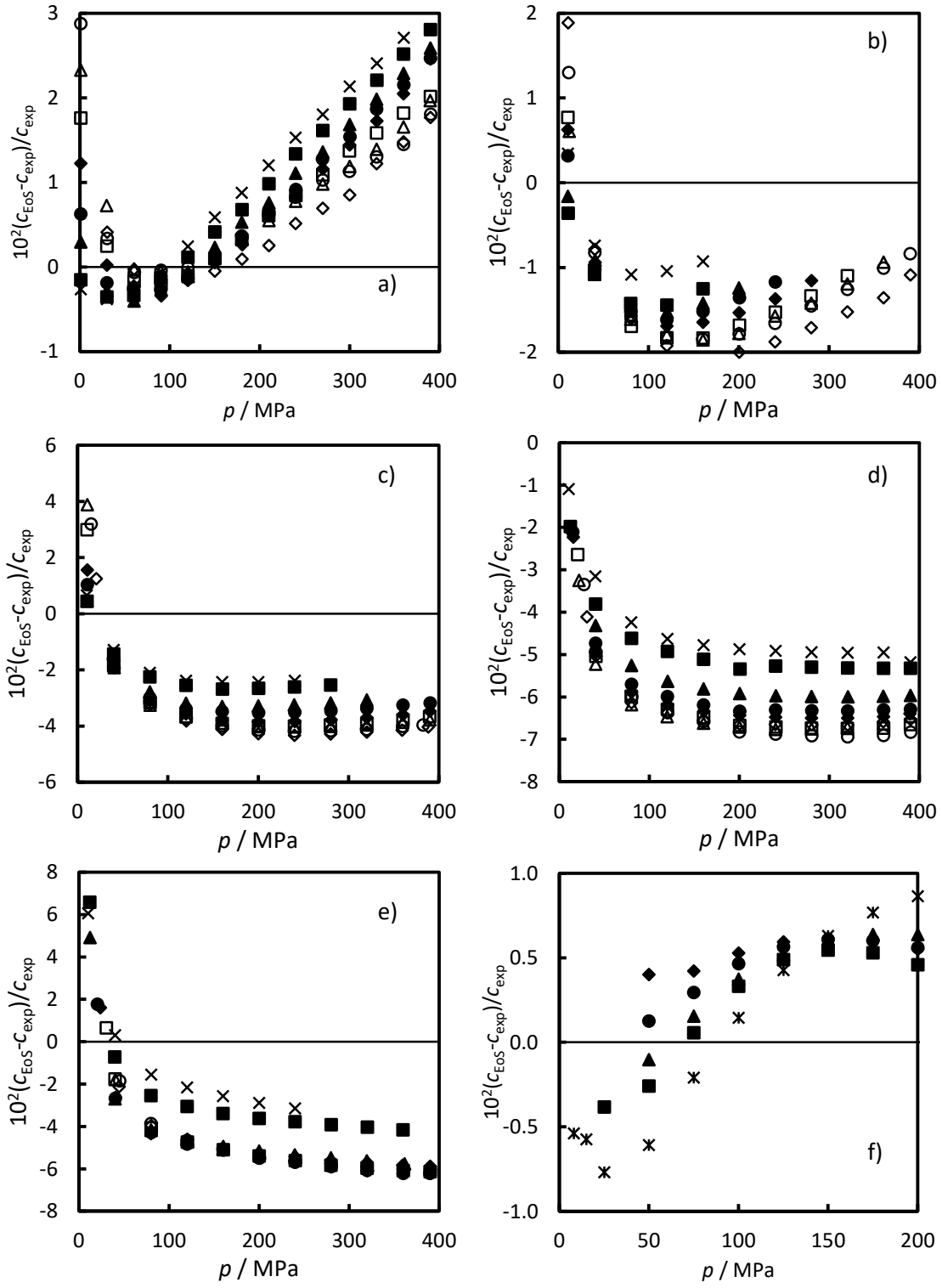



**Figure 6.21** Deviations between experimental sound-speed $c_{exp}$ and predictions from GERG-2008 $c_{EoS}$ of $CO_2$ + *n*-nonane across nine isotherms as a function of pressure. Symbols represent experimental data: ×, 283.15 K; ■, 298.15 K; ▲, 323.15 K; ●, 348.15 K; ◆, 373.15 K; □, 398.15 K;△, 423.15 K; ○, 448.15 K; ◇, 473.15 K. a) $x = 0$; b) $x = 0.2$; c) $x = 0.4$; d) $x = 0.6$; e) $x = 0.8$; f) $x = 1$.

# 6.6 $CO_2$ + Methylbenzene

This section gives the results of the density measurements made for ($CO_2$ + methylbenzene) at four compositions over a temperature range of (283.15 to 473.15) K and for pressures up to 68 MPa. In conjunction, the results of speed-of-sound measurements made at four compositions over temperature ranges of (283.15 to 473.15) K at pressures up to 390 MPa are also presented. A comparison of the present density and speed-of-sound data to literature data if present is given. Finally, the experimental data were also used to test the predictive abilities of several thermodynamic models.

## 6.6.1 Literature Review

Due to a wide range of temperatures and pressures studied for the speed-of-sound and density measurements, it was essential to have knowledge of the phase envelopes of the binary mixtures before carrying out the experiments. Both the density and speed-of-sound measurements were carried out in the single-liquid-phase region, so the starting measurement pressures varied according to the vapour pressure curves. It was important to verify both the saturation and freezing pressures phase boundaries in order to determine if they impacted on the overall measurement range. No data could be found in the literature relating to the freezing pressure of any of the mixtures. Therefore, the freezing curve was estimated in NIST REFPROP 9.1 software. For the saturation curve of $CO_2$ + methylbenzene system, there are more reported data compared to the $CO_2$ + *n*-nonane system in the literature. Examples of the phase behaviour study of $CO_2$ + methylbenzene can be found in the works of Lay [406], Chang [407] and Wu *et al.* [408] However, some of the reported isotherms were different to the isotherms measured in this work. Therefore, PR78 EoS was used to predict the bubble pressures for most isotherms measured. To our knowledge, there is only one study on the compressed-liquid density of $CO_2$ + methylbenzene. Pohler and Kiran [264] measured the compressed-liquid density using a variable volume view cell. Compressed-liquid density data were reported at pressures up to 70 MPa and temperatures between (323 and 423) K in 25 K intervals at three compositions. Two authors have reported the saturated-phase densities of $CO_2$ + methylbenzene; Chang *et al.* [300] reported data at pressures up to 7 MPa at three temperatures (290.8, 300.9 and 310.1) K using a vibrating-tube densimeter and Park *et al*. [301] reported data up to 15.4 MPa and temperatures between (333.2 and 393.2) K. Unfortunately, no sound-speed data for this binary system were found in the literature; therefore no comparison could be made with our experimental data.

## 6.6.2 Experimental Density Results and Discussion

Compressed-liquid density measurement was carried out as a function of pressure along nine isotherms: $T$ = (283.15, 298.15, 323.15, 348.15, 373.15, 398.15, 423.15, 448.15 and 473.15) K at pressures up to 65 MPa. The four nominal mole fractions of $CO_2$ in the binary mixture studied were 0.2, 0.4, 0.6 and 0.8. The experimental densities together with the standard uncertainty for these

mixtures are listed in Table C.9 in Appendix C. In Figure 6.22, selected experimental densities at four different mole fractions as functions of pressure and temperature are shown. At these conditions, the mixtures either are in the supercritical region or exist as a single-phase liquid. As expected at constant composition, the density increases with increasing pressures, but decreases with increasing temperatures. At low temperatures (283.15, 298.15 and 323.15) K, the overall density increases with the concentration of $CO_2$ in the mixture. A crossover in density has been observed at temperatures between (323.15 and 423.15) K. As temperature increases, the crossover pressure point shifts towards a higher pressure. The effect can be explained by the difference in compressibility between pure components, $CO_2$ and methylbenzene, with methylbenzene being less compressible as shown in Figure 6.23. At temperatures above 423.15 K, the mixture density decreases with the concentration of $CO_2$ in the mixture. The density crossover behaviour in mixtures of hydrocarbons with $CO_2$ has also been observed in our earlier work with $CO_2$ + *n*-heptane and $CO_2$ + *n*-nonane systems. The experimental results were compared with the date reported by Pohler and Kiran. Pohler and Kiran [264] reported the densities at temperatures between (323 and 423) K and at pressures up to 70 MPa using a variable volume view cell. The studied compositions range from $x_{CO2}$ = (0.74 to 0.94). Their reported density and excess molar volume data are considered to be accurate up to 1.2 % and 11 %, respectively. We only compared our experimental data measured at $x_{CO2}$ = 0.8 with their data at the temperatures reported in their work. To have a direct comparison, a linear interpolation in composition and pressure was performed in their data. Figure 6.23 shows the comparison with their reported data. The literature data are systemically higher than our data across all isotherms and the $\Delta_{AARD}$ between our data is 1.8%. No further comparison with other compositions was carried out.

**Correlation:** The compressed-liquid densities of $CO_2$ + methylbenzene mixtures were fitted with the empirical correlation, Equation (6.1). The parameters $A$, $B$ and $\rho_r$, are optimised using the Lenvenberg-Marquardt optimisation method. Figure 6.22 shows the calculated densities using Equation (6.1). The parameters combined with the $\Delta_{AAD}$ and $\Delta_{AARD}$ of the fitting are summarised in Table C.10. The deviation plots between the calculated values and experimental compressed-liquid densities are shown in Figure 6.24. From the fitting procedure, it was found that the empirical correlation represented all of the compressed-liquid density data with the $\Delta_{AAD}$ and $\Delta_{AARD}$ about 0.05 MPa and 0.3%, respectively. Similarly, the fit of the empirical correlation to the experimental data decreases when the mole fraction of $CO_2$ increases.

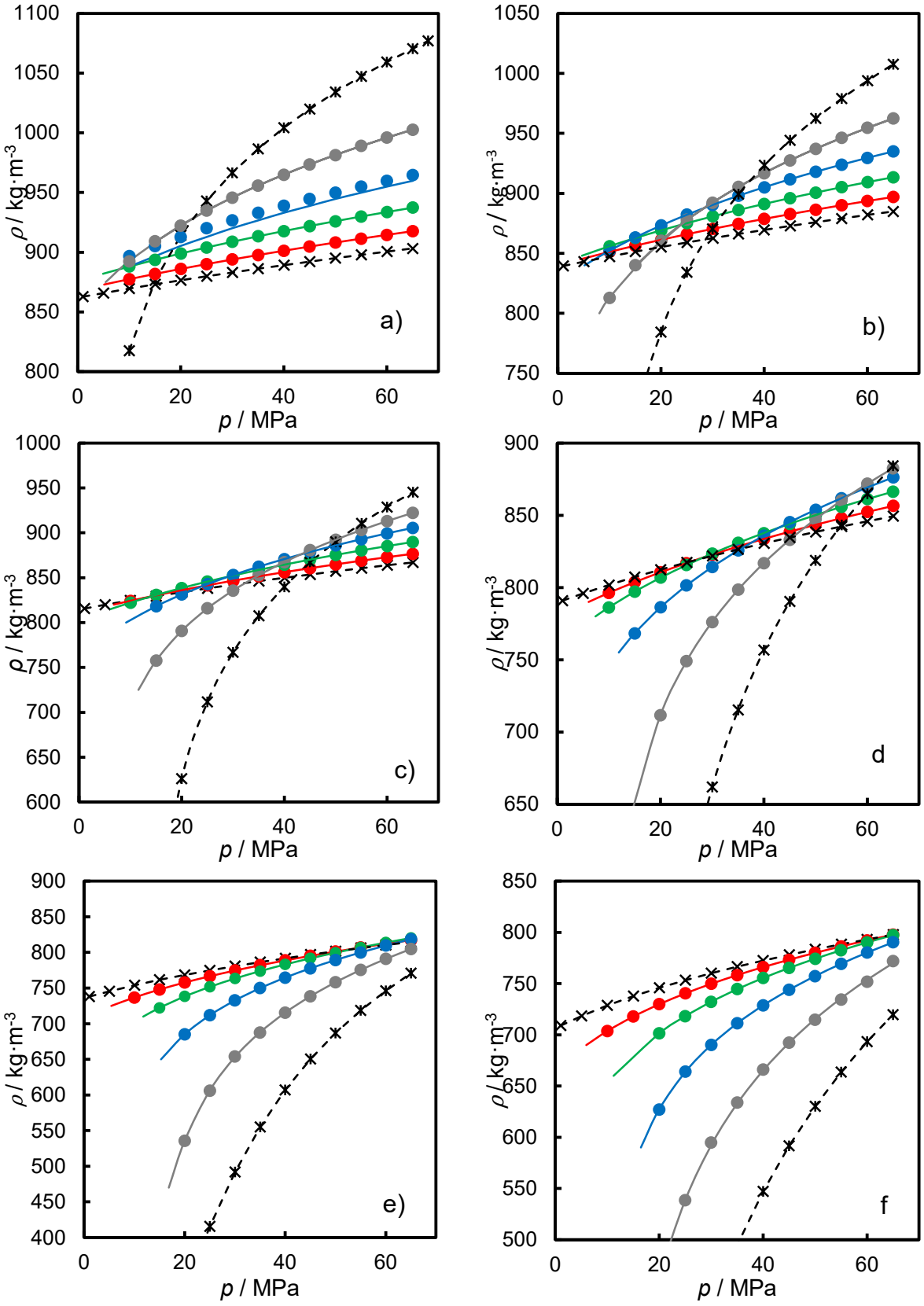



**Figure 6.22** Compressed-liquid densities $\rho$ (coloured square) against pressure for $CO_2$ + methylbenzene system at four mole fractions of $CO_2$: ×, 0; (red), 0.2; (green), 0.4; (blue), 0.6; (grey), 0.8; ✱,1; and at nine temperatures: a) 298 K, b) 323 K, c) 348 K, d) 398 K, e) 423 K and f) 473 K. Coloured lines represent values calculated with the empirical correlation, Equation (6.1).

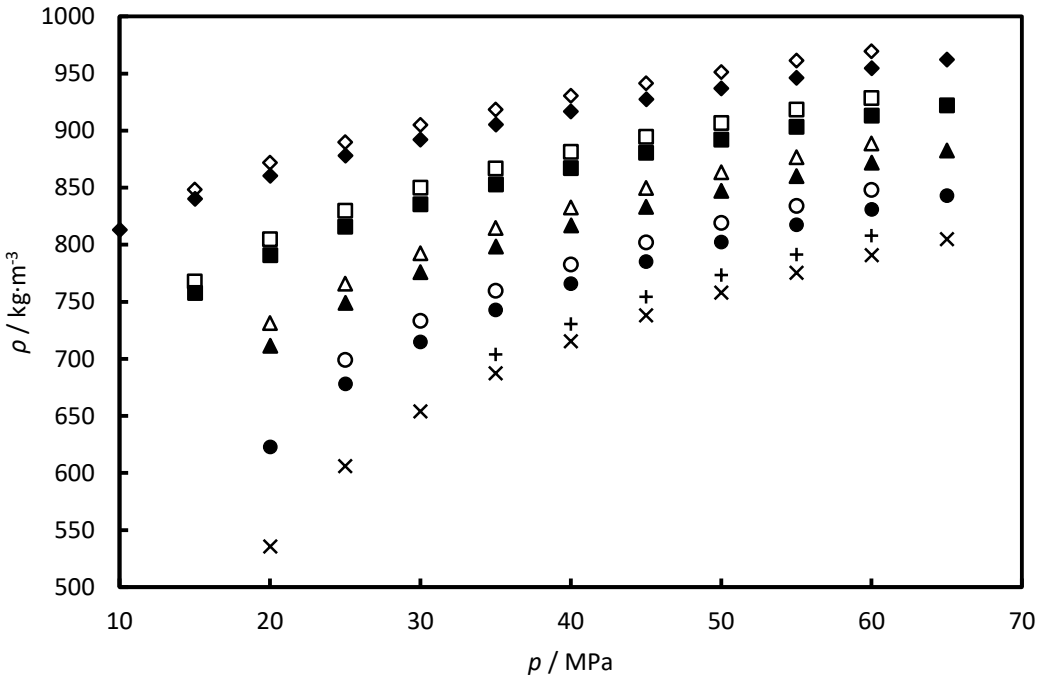



**Figure 6.23** Comparison of the compressed-liquid densities of $CO_2$ + methylbenzene measured in this work and Pohler and Kiran [264] across five isotherms: ◆, 323.15 K; ■, 348.15 K; ▲, 373.15 K; ●, 398.15 K; ×, 423.15 K. Filled symbols and × represent data from our work and unfilled symbols and + represent data interpolated from the work by Pohler and Kiran, respectively.

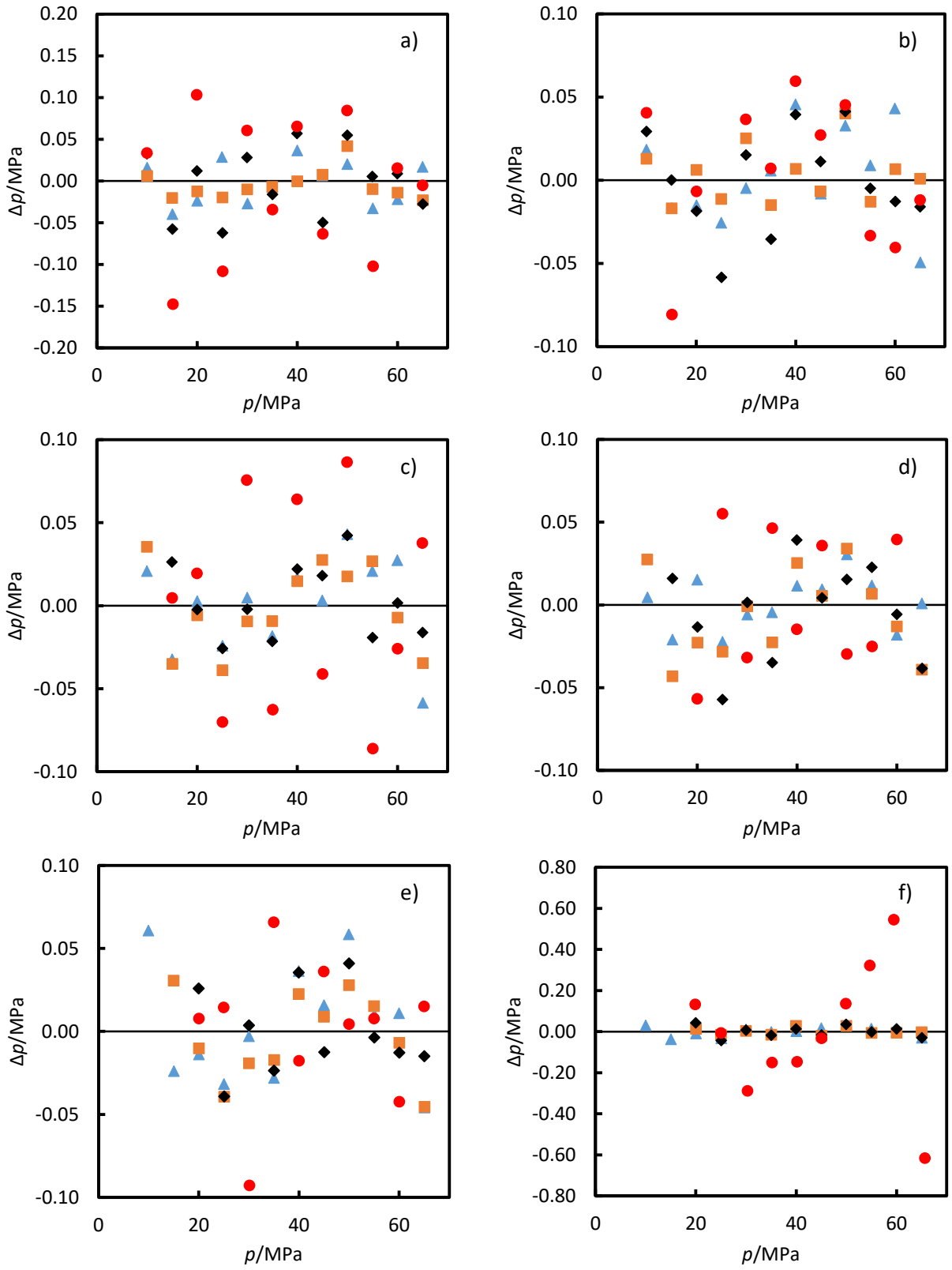



**Figure 6.24** Deviations between the experimental pressure $p_{exp}$ for $CO_2$ + methylbenzene and the values calculated with the empirical correlation, Equation (6.1) $p_{fit}$, $\Delta p = p_{exp} - p_{fit}$ at a) 298 K, b) 323 K, c) 348 K, d) 373 K, e) 423 K and f) 448 K. Symbols denote different mole fraction of $CO_2$ in the binary mixture: ▲, 0.2; ■, 0.4; ◆, 0.6; ●, 0.8.

**Excess Molar Volume:** The excess molar volume ($V_m^E$) was also calculated for the $CO_2$(1) + methylbenzene(2) system from the experimental compressed-liquid density data. The density measurement of the pure components, both $CO_2$ and methylbenzene, were carried out prior to the measurement of the binary mixture using the same vibrating-tube densimeter. For more details, please refer to Chapter 5. Figure 6.25 shows the plots of $V_m^E$ as a function of mole fraction of $CO_2$ across six isotherms: $T$ = (283.15, 298.15, 348.15, 373.15, 423.15 and 473.15) K. In the composition range investigated, $V_m^E$ becomes more negative with increasing temperature, but less negative with increasing pressure. The negative excess volumes for these mixtures indicated that the overall volume of the mixture decreased upon mixing compared to simple additions. The excess molar volume displayed a sigmoidal variation with the composition at low temperatures. At 298.15 K, mixtures displayed a negative excess volume which then became positive and went through a maximum at around 0.8 mole fraction of $CO_2$ at the higher pressure isobars. At temperatures above 348.15 K, the excess molar volume was negative over the entire range of composition for all pressures and became more negative with increasing temperature and decreasing pressure. The maximum/minimum excess molar volume occurs mostly around $x$ = (0.6 to 0.8) across all temperatures. The densities of pure components in relation to the mixture densities are presented in Figure 6.23. To allow interpolation between compositions, the excess molar volume has been correlated with Redlich-Kister equation, Equation (6.3). $A_i$ is the correlation parameter which was determined by minimising the absolute difference between the experimental data and the correlated values. The calculated excess molar volumes have been fitted to each isotherm and isobar individually. The results of the correlation are shown in Figure 6.26, and the goodness of the fit was given by the $\Delta_{AAD}$, which is 0.198 $cm^{-3}\cdot mol$ across all isotherms and isobars. The parameters determined are listed in table C.11 shown in Appendix C.

## 6.6.3 Bubble Pressure Determination

In this work, we also determined the bubble pressures of the $CO_2$ + methylbenzene system by combining the compressed-liquid densities with the saturated-phase densities. This method has been verified by our previous work on $CO_2$ + *n*-heptane system. Similarly, the saturated-phase densities were measured using a two-phase density apparatus in the group by Yolanda Sanchez-Vicente. The experimental apparatus and procedures can be found in Tay *et al.* [400] As mentioned in Section 6.3.3, the bubble pressure was found by locating the interception point between the two sets of experimental density data, as shown in Figure 6.26. The compositions of the four bubble points across an isotherm would be the same as the compositions of the compressed-liquid density mixtures. Bubble pressures have been determined for four isotherms $T$ = (298.15, 323.15, 373.15 and 423.15) K.

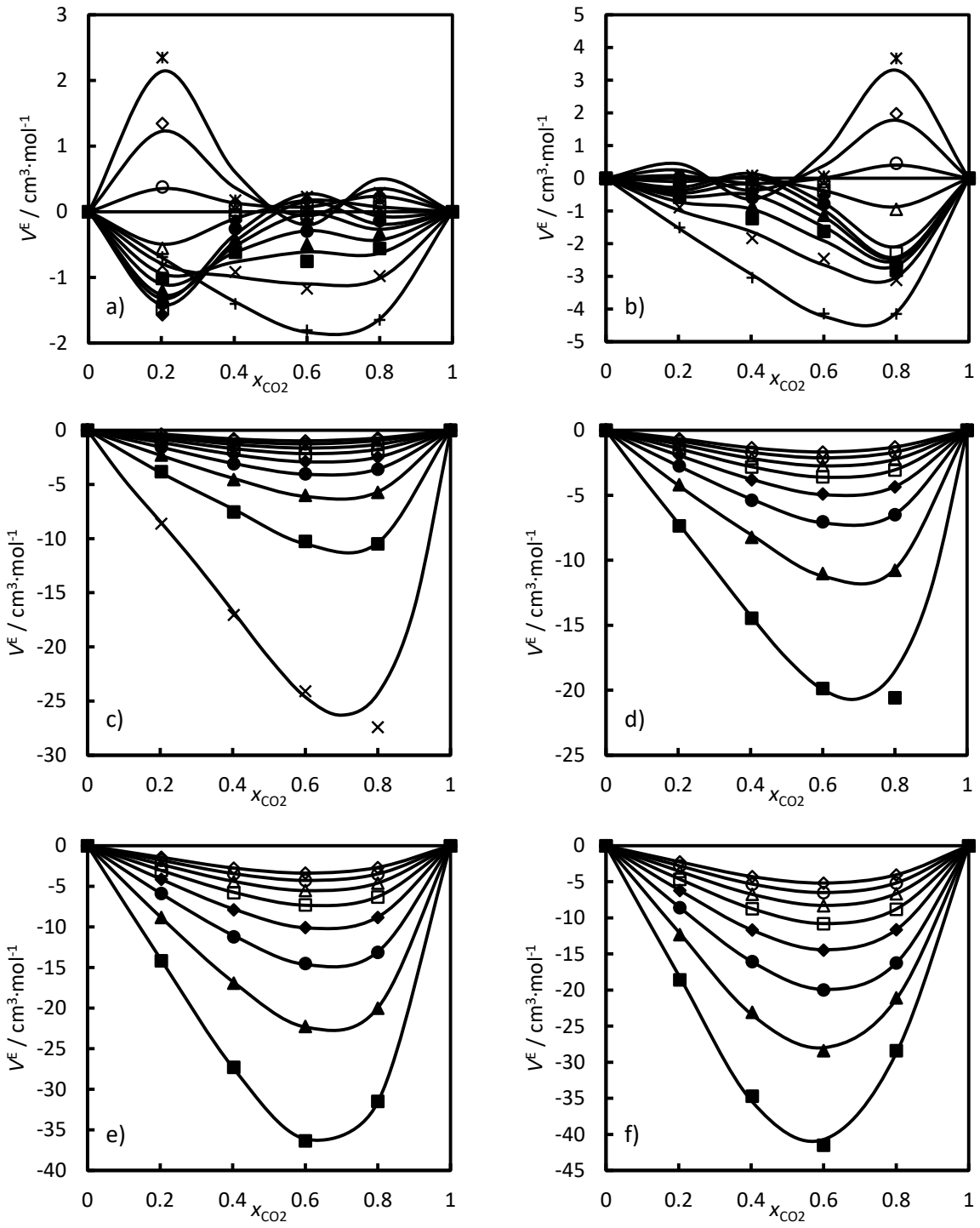



**Figure 6.25** Excess molar volume $V_m^E$ of $CO_2$ + methylbenzene system versus the molar fraction of $CO_2$ at six temperatures: a) 283 K; b) 298 K; c) 323 K; d) 373 K; e) 423 K; f) 473 K and at ten isobars: ✚, 10 MPa; ✖,15 MPa; ■, 20 MPa; ▲, 25 MPa; ●, 30 MPa; ◆, 35 MPa; □, 40 MPa; △, 45 MPa; ○, 50 MPa; ◇, 55 MPa. Solid lines represent values calculated from the Redlich-Kister equation, Equation (6.3) with parameters from Table C.11.

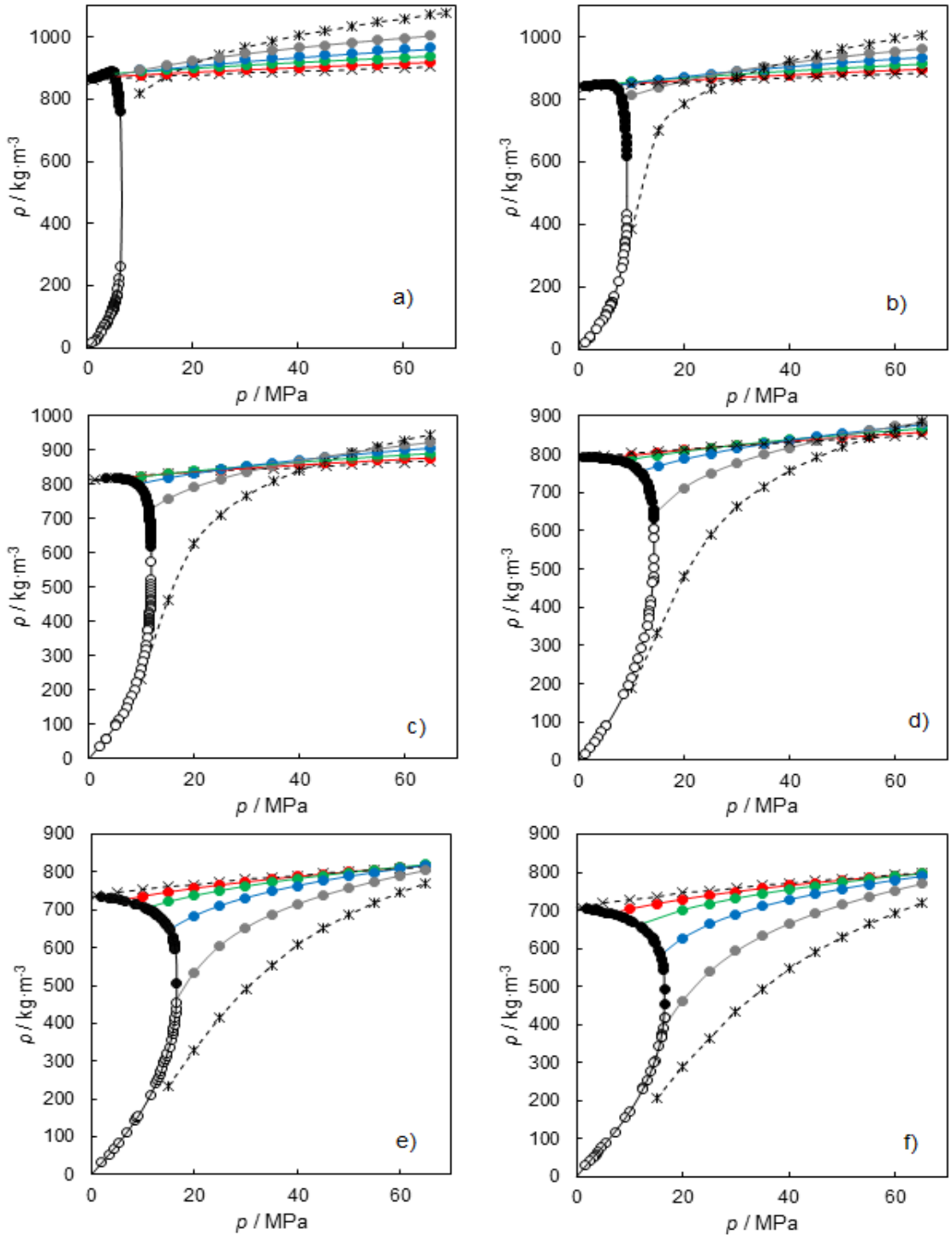



**Figure 6.26** Compressed-liquid densities $\rho$ (coloured circles) and saturated-phase densities (black and white symbols) versus pressure for $CO_2$ + methylbenzene system with a mole fraction of $CO_2$: ×, 0; (red), 0.2; (green), 0.4; (blue), 0.6; (grey), 0.8; ∗,1; at temperatures: a) 298 K, b) 323 K, c) 348 K, d) 398 K, e) 423 K and f) 473 K. Coloured lines represent values calculated with the empirical correlation, Equation (6.1).

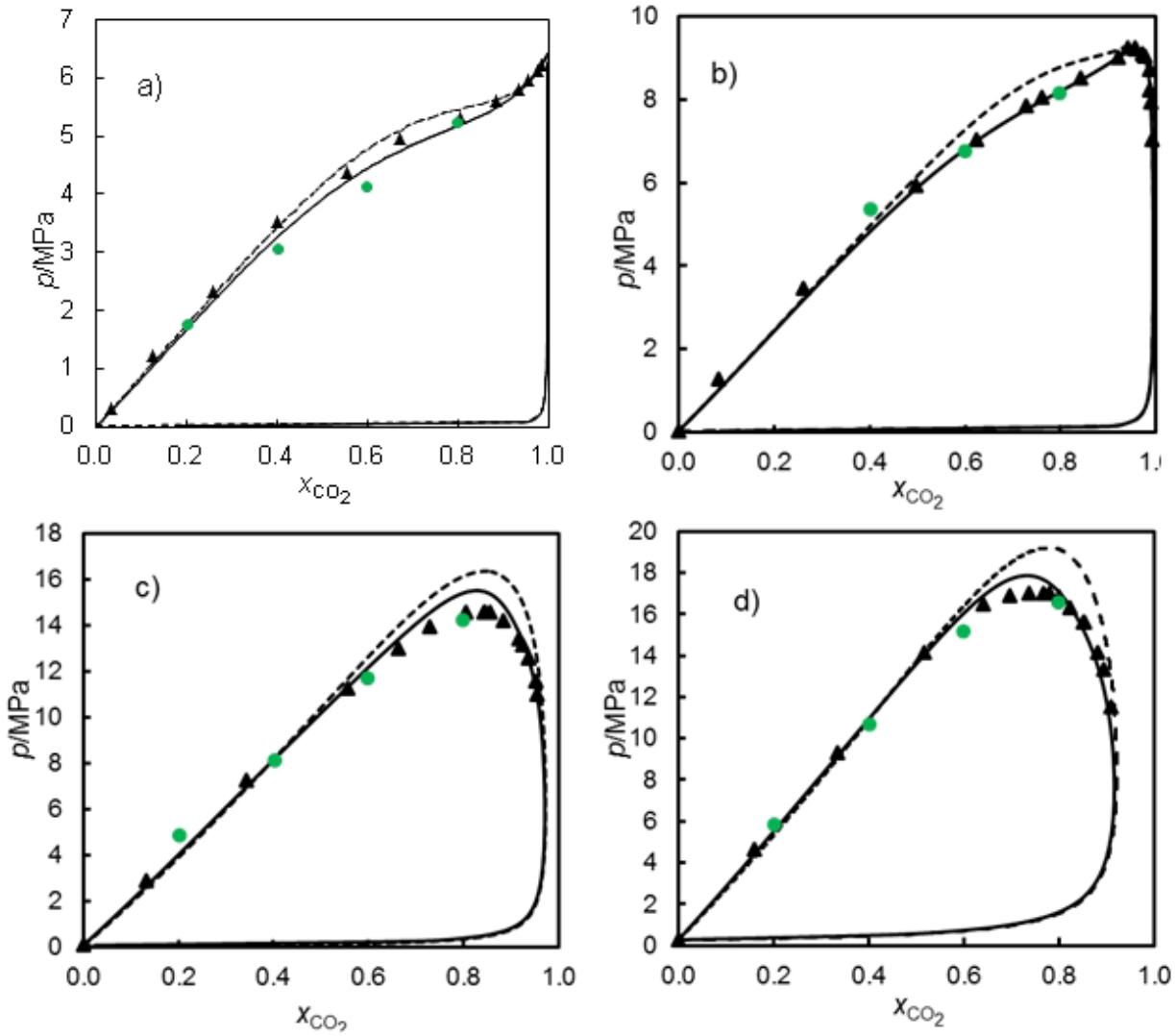



**Figure 6.27** Bubble pressures $p_b$ for $CO_2$ + methylbenzene as a function of the $CO_2$ mole fraction at four temperatures: a) 298.15 K, b) 323.15 K, c) 373.15 K, d) 423.15.15 K. In this work, ▲, the experimental data from direct observation of VLE and, ○, the experimental data obtained from densities.

**Table 6.8** Bubble pressures $p_b$ for $CO_2$ + methylbenzene system at temperatures and $CO_2$ mole fractions $x$ determined from the intersection between the compressed-liquid densities and the saturated-phase densities[a]. Experimental bubble pressure data obtained from the direct observation of VLE[b].

| $T$/ K | $x$ | [a]$p_b$/ MPa | [b]$p_b$/MPa |
|---|---|---|---|
| 298.15 | 0.2030 | 1.75 | 1.87 |
| | 0.4030 | 3.04 | 3.57 |
| | 0.5999 | 4.11 | 4.60 |
| | 0.7999 | 5.21 | 5.31 |
| 323.15 | 0.2030 | - | 2.74 |
| | 0.4030 | 5.35 | 4.94 |

| | | | |
|---|---|---|---|
| | 0.5999 | 6.75 | 6.82 |
| | 0.7999 | 8.13 | 8.28 |
| 373.15 | 0.2030 | 4.85 | 4.35 |
| | 0.4030 | 8.08 | 8.37 |
| | 0.5999 | 11.66 | 11.95 |
| | 0.7999 | 14.22 | 14.52 |
| 423.15 | 0.2030 | 5.83 | 5.79 |
| | 0.4030 | 10.64 | 11.14 |
| | 0.5999 | 15.14 | 15.71 |
| | 0.7999 | 16.52 | 16.83 |

The calculated bubble points can be found in Table 6.9. In Figure 6.27, we compared the calculated bubble pressures with the data collected by direct VLE measurement. More detail about the VLE measurements can be found in Tay *et al.* [400] Our calculated bubble pressures are in good agreement with the experimental bubble pressures.

## 6.6.4 Experimental Speed-of-Sound Results and Discussion

Speeds-of-sound in the binary mixture $CO_2$ + methylbenzene were measured isothermally as a function of pressure along nine isotherms at $T$ = (283.15, 298.15, 323.15, 348.15, 373.15, 398.15, 423.15, 448.15 and 473.15) K and pressures up to 390 MPa, in steps of approximately 40 MPa. The four nominal mole fractions studied of $CO_2$ in the binary mixtures were 0.2, 0.4, 0.6 and 0.8. The experimental sound-speed data together with the mole fractions are given in Table C.12. In Figure 6.28, we showed the sound-speed in $CO_2$ + methylbenzene as a function of pressure across nine temperatures at the four different compositions. The sound-speed in $CO_2$ + methylbenzene shows similar trends as $CO_2$ + *n*-nonane. To our knowledge, the speed-of-sound values presented in this study are the first to be reported for the $CO_2$ + methylbenzene system.

**Correlation:** The sound-speed experimental data were fitted individually for each composition into an empirical correlation, Equation (6.7) which covers the whole range of temperatures and pressures. Similarly, the quantity $c_0 = c(T_0, p_0)$ was then correlated in a polynomial form as a function of temperature as shown in Equation (6.8). The correlation fitted the experimental data with $\Delta_{AARD}$ of 0.04 % for the lowest $CO_2$ mole fraction mixture. However, the highest $CO_2$ mole fraction mixture has an $\Delta_{AARD}$ of 0.6 %. The average across four compositions was 0.2 % which is comparable to the experimental uncertainty. The deviation plots as a function of temperature and pressure can be found in Figure 6.29. The applicability of the correlation to the experimental data decreases with low pressures and high $CO_2$ mole fractions in the mixture. Large differences can be observed at the high temperatures and low pressures, where state points were measured very close to the bubble curve with

less sensitive signals during the measurements. The parameters of Equations (6.7) and (6.8), together with the $\Delta_{AARD}$ are given in Table C.13 in the Appendix.

A different sound-speed correlation was proposed by Lin *et al.* [363] that can correlate the speed-of-sound measured over wide ranges of temperature and pressure. It was reported that $c^3$ has a nearly linear relationship with $p$ for a liquid at low reduced temperatures.

$$c = \left(A_0 + A_1 p + A_2 p^2 + A_3 p^3\right)^{1/n}, \tag{6.10}$$

where $A_0$, $A_1$, $A_2$, $A_3$, and the exponent $n$ are adjustable parameters. The optimal values of $n$ were found to be between 2 and 3 in the temperature range investigated. To represent the entire data set the equation was generalised to the following form:

$$c = \left( \sum_{i=0}^{4} \sum_{j=0}^{3} a_{ij} T^i p^j \right)^{1/n} \tag{6.11}$$

The experimental sound-speed data of $CO_2$ + methylbenzene were fitted with this correlation with the parameters determined by the sum of lease square method. The results of the two correlations were very similar.

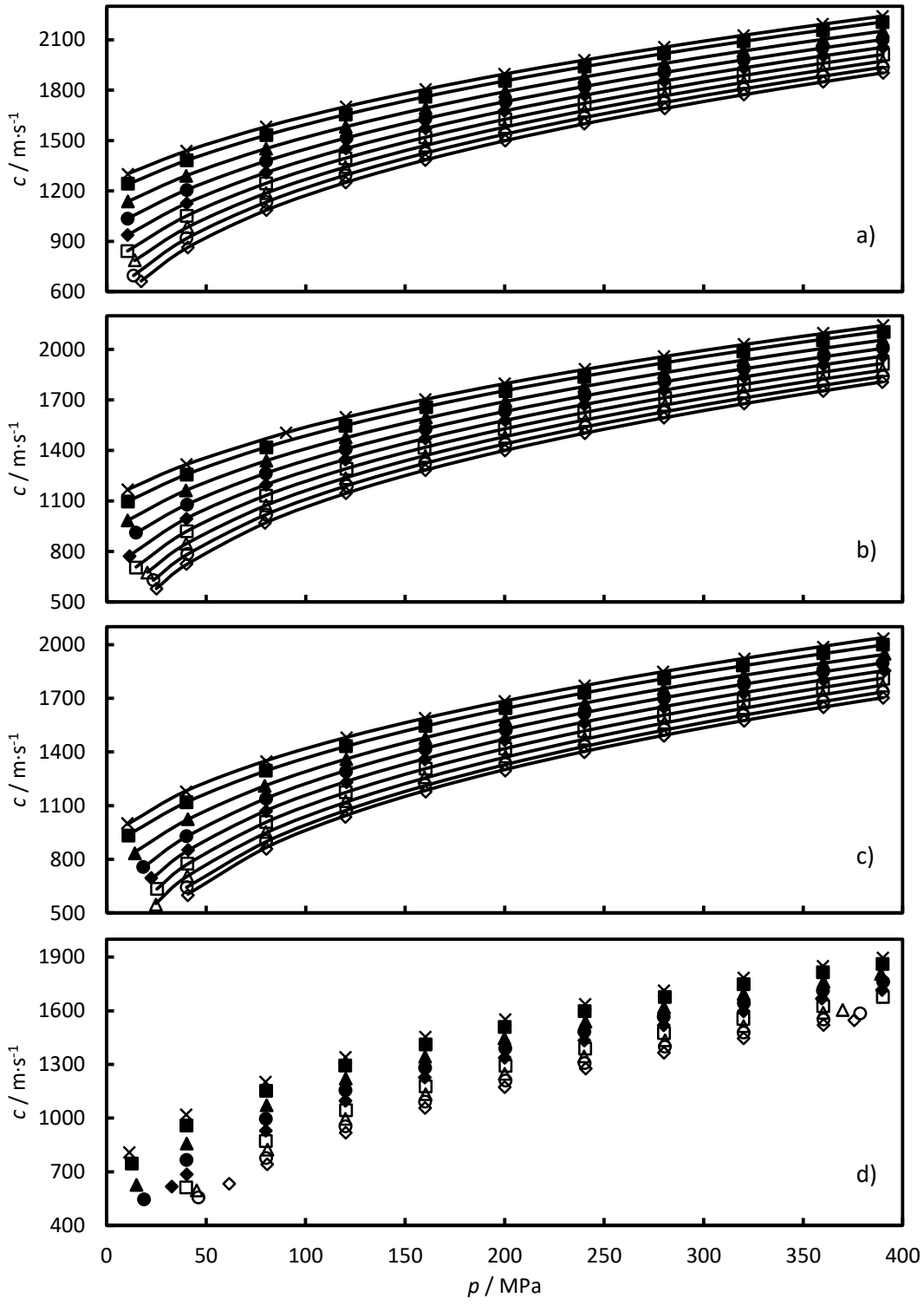



**Figure 6.28** Experimental sound-speed $c$ in $CO_2$ + methylbenzene across nine isotherms as a function of pressure at four compositions a) $x$ = 0.2, b) $x$ = 0.4, c) $x$ = 0.6, d) $x$ = 0.8. Symbols represent experimental data: ×, 283.15 K; ■, 298.15 K; ▲, 323.15 K; ●, 348.15 K; ◆, 373.15 K; □, 398.15 K; △, 423.15 K; ○, 448.15 K; ◇, 473.15 K. Lines represent sound-speed values calculated from the empirical correlation.

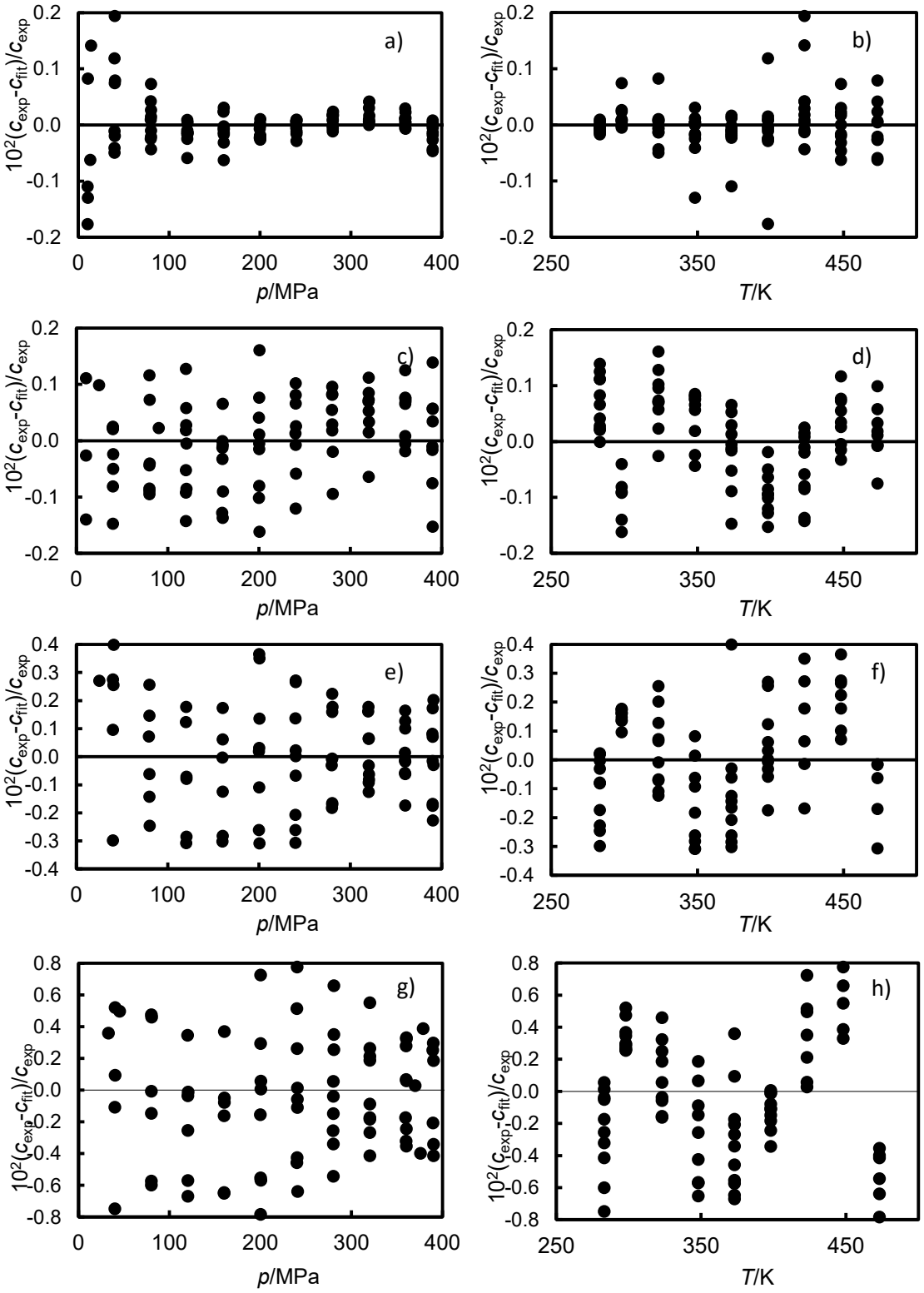



**Figure 6.29** Deviations of the experimental speed-of-sound $c_{exp}$ in $CO_2$ + methylbenzene from the values calculated from the empirical correlation $c_{fit}$ as a function of pressure and temperature. (1st row), $x = 0.2$; (2nd row), $x = 0.4$; (3rd row), $x = 0.6$; (4th row), $x = 0.8$.

## 6.6.5 Modelling

The performance of the PPR78, SAFT-γ Mie and a multi-fluid Helmholtz energy approximation model in predicting the compress-liquid densities and speeds-of-sound in the binary mixtures was examined. The performance of PPR78 on compressed-liquid density predictions was tested, and the binary interaction parameters were first calculated based on Equation (3.18). SAFT-$\gamma$-Mie model has been described in detail previously, and here only the nature and source of the parameters involved are summarised. For $CO_2$ + methylbenzene system in SAFT-γ Mie, the cross-interaction parameters for functional groups $CO_2$-aCH and $CO_2$-a$CCH_3$, were optimised in Al Ghafri *et al.* [409] using VLE data of $CO_2$ + benzene and $CO_2$ + methylbenzene at temperatures between (298.15 and 423.15) K. For the determination of $CO_2$ group parameters, its vapour pressure and saturated-phased liquid density data were used. The computations of SAFT-γ Mie were carried out in gProms software with the gSAFT package (PSE Ltd). As mentioned in Chapter 3, methylbenzene is not a component included in the GERG-2008 model [38, 39] and therefore no parameters were specified. Recently, Bell and Lemmon [357] developed an algorithm to optimise the binary interaction parameters in the multi-fluid Helmholtz-energy approximation in which they have fitted the binary interaction parameters for more than 1100 binary mixtures including $CO_2$ + methylbenzene. The model was described in detail in Chapter 3. The parameters for $CO_2$ + methylbenzene were estimated from VLE data of $CO_2$ + methylbenzene reported by 32 authors at temperatures ranging from (283 to 572) K and pressures from (0.101 to 15.3) MPa. The calculations of sound-speed from the optimised parameters were carried out in REFPROP 9.1 software. The parameters of the equations of state are tabulated in Table 6.9 below.

**Table 6.9** Experimental parameters for three equations of state: PPR78 (the binary interaction parameter, *kij* determined from the critical components $p_c$ and $T_c$ and acentric factor $\omega$) SAFT-γ Mie (un-like functional group parameters and cross-interaction parameters) and Multi-fluid Approximation (four adjustable parameters).

| | | | | | | | | |
|---|---|---|---|---|---|---|---|---|
| PPR78 | Component | $\omega$ | | $p_c$ / MPa | | $T_c$ / K | | Ref |
| | methylbenzene | 0.266 | | 4.13 | | 591.75 | | [40] |
| | carbon dioxide | 0.224 | | 7.38 | | 304.13 | | [174] |
| | System | $T$ / K | $k_{ij}$ | $T$ / K | $k_{ij}$ | $T$ / K | $k_{ij}$ | |
| | $CO_2$ + methylbenzene | 283.15 | 0.1082 | 348.15 | 0.0997 | 348.15 | 0.0997 | - |
| | | 298.15 | 0.1049 | 373.15 | 0.0990 | 373.15 | 0.0990 | - |
| | | 323.15 | 0.1015 | 398.15 | 0.0989 | 398.15 | 0.0989 | - |
| SAFT-γ Mie | Functional Group | $v_k^*$ | $S_k$ | $(\varepsilon_{kk}/k_B)$ / K | $\sigma\times10^{10}$ / m | $\lambda_{kk}^r$ | $\lambda_{kk}^a$ | |
| | $CO_2$-aCH | - | - | 221.18 | - | 13.547 | - | [409] |
| | $CO_2$-a$CCH_3$ | - | - | 284.66 | - | 21.319 | - | [409] |
| Multi-fluid Approximation | System | $\beta_T$ | | $\gamma_T$ | $\beta_v$ | $\gamma_v$ | $F_{ij}$ | |
| | $CO_2$ + methylbenzene | 1.0050 | | 1.0668 | 1.0000 | 1.0000 | 0 | [357] |

The compressed-liquid density predictions of the PPR78, SAFT-γ Mie and the multi-fluid Helmholtz-energy approximation, are shown in Figures 6.30 and 6.32. In Figure 6.31, we showed the deviation plots of the experimental compressed-liquid density against the predictions from the two predictive models. The PPR78 EoS generally over-predicts the density for most isotherms. There isn't a clear trend about the deviations, but it can be noticed that the predictions are better at low pressures. The comparison between the experimental data and predictions from PPR78 gives an $\Delta_{AARD}$ of 1.4 % across all isotherms and compositions. For SAFT-γ Mie, the predictions of density are better at mixtures with a low mole fraction of $CO_2$. Unlike the predictions of PPR78, SAFT-γ Mie EoS generally under-predicts the density for most isotherms. The $\Delta_{AARD}$ for the predictions of SAFT-γ Mie EoS from the experimental data was 1.1 % over the entire measurement range. In absolute term, SAFT-γ Mie predicts the compressed-liquid density of $CO_2$ + methylbenzene slightly more accurate compared to PPR78. The comparison with the calculations from the multi-fluid Helmholtz-energy approximation gave an $\Delta_{AARD}$ of 4.1 % across four compositions which have the worst agreement with the experimental data among the three equations of state tested.

**PPR78 with Volume Translation:** We applied the volume translation to the predictions of the PPR78 EoS, however, the results indicated that the volume translation did not improve the predictions of PPR78 on the compressed-liquid densities. The new $\Delta_{AARD}$ across four compositions was calculated to be 2.2 %

Figure 6.33 shows the comparison between the experimental sound-speed data and the predictions of SAFT-γ Mie and the multi-fluid approximation models for $CO_2$ + methylbenzene. Similarly, we have included the sound-speed data for pure methylbenzene and pure $CO_2$ which are taken from Tay and Trusler [410] and Lin and Trusler [81]. It can be seen that on most isotherms, SAFT-γ Mie generally over-predicts the sound-speeds. The errors increase with increasing compositions and decrease with increasing temperatures. For the multi-fluid Helmholtz energy approximation model, the predictions have mostly good agreement at low $CO_2$ composition, but it under-predicts the sound-speed values at higher mole fractions of $CO_2$. The $\Delta_{AARD}$ at $x$ = (0.2 and 0.8) are 0.4 % and 1.7 %, respectively. It can be seen from Figure 6.33 that the overall predictions of the multi-fluid Helmholtz energy approximation were better than those of SAFT-γ Mie across all isotherms and compositions. The $\Delta_{AARD}$ for the predictions of all temperatures, pressures and compositions for the multi-fluid Helmholtz energy approximation model and SAFT-γ Mie were 1.2 % and 3.5 %, respectively. The deviation plots of the two models are shown in Figures 6.34 and 6.35.

**Table 6.10** Average absolute relative deviations $\Delta_{AARD}$ between the experimental compressed-liquid density, speed-of-sound and the predictions from PPR78, SAFT-γ Mie and Multi-fluid approximation

EoSs for $CO_2$ + methylbenzene at four compositions, and the overall average absolute relative deviations $\Delta_{AARD,overall}$.

| Equation of state | Property | $\Delta_{AARD,overall}$ | $x_{CO2}$ | $\Delta_{AARD}$ |
|---|---|---|---|---|
| PPR78 (VT) | Compressed-liquid density | 1.4% (2.2%) | 0.2 | 1.0% (2.4%) |
| | | | 0.4 | 1.0% (2.2%) |
| | | | 0.6 | 1.4% (2.0%) |
| | | | 0.8 | 2.2% (2.0%) |
| SAFT-γ Mie | Compressed-liquid density | 1.1% | 0.2 | 0.4% |
| | | | 0.4 | 0.6% |
| | | | 0.6 | 1.1% |
| | | | 0.8 | 2.4% |
| Multi-fluid approximation | Compressed-liquid density | 4.1% | 0.2 | 2.4% |
| | | | 0.4 | 4.1% |
| | | | 0.6 | 5.1% |
| | | | 0.8 | 4.7% |
| SAFT-γ Mie | Speed-of-sound | 3.5% | 0.2 | 1.5% |
| | | | 0.4 | 3.0% |
| | | | 0.6 | 4.0% |
| | | | 0.8 | 5.7% |
| Multi-fluid approximation | Speed-of-sound | 1.2% | 0.2 | 0.4% |
| | | | 0.4 | 1.0% |
| | | | 0.6 | 1.8% |
| | | | 0.8 | 1.7% |

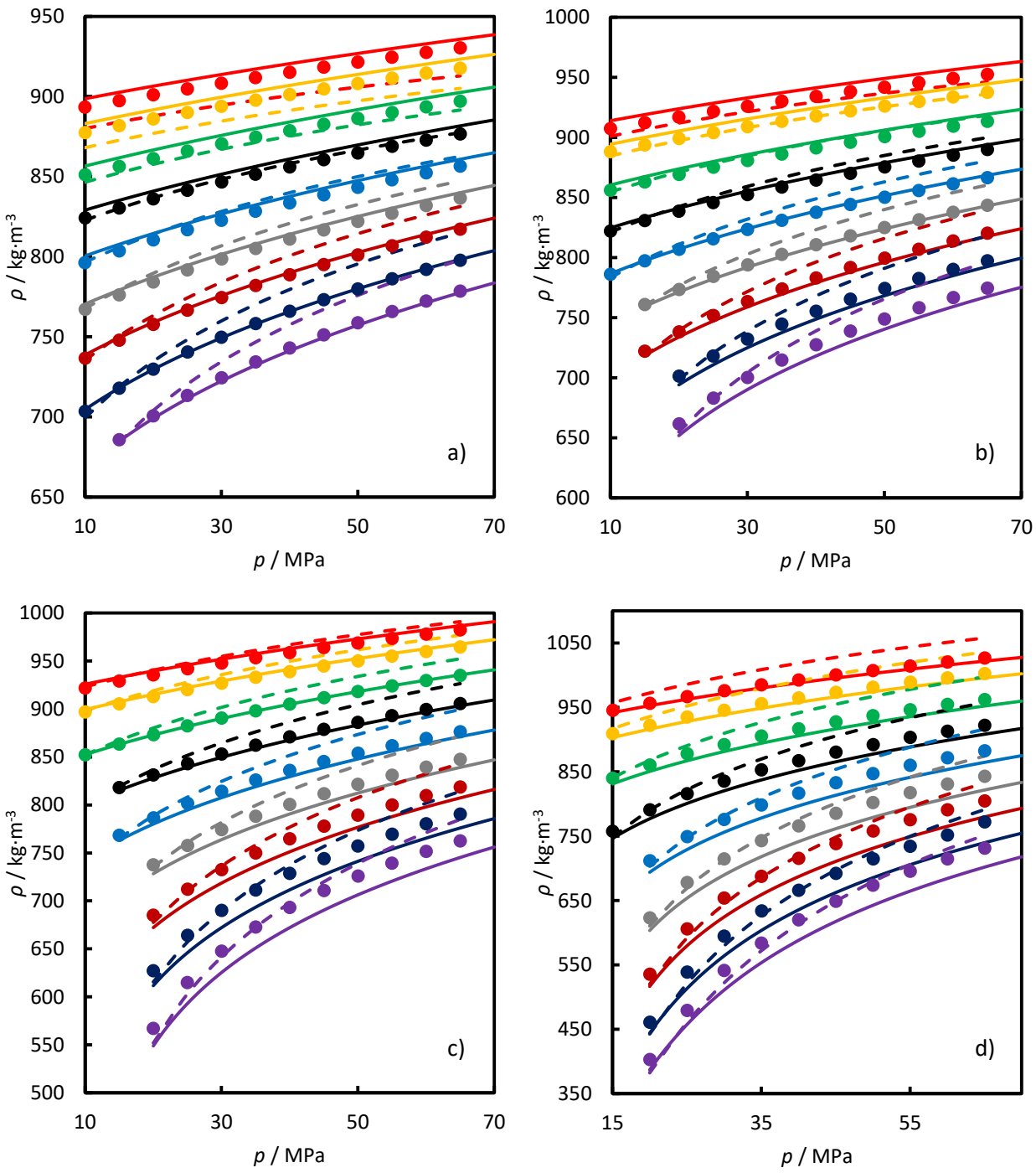



**Figure 6.30** Comparisons between the experimental compressed-liquid density $\rho_{exp}$ of $CO_2$ + methylbenzene and the predictions from SAFT-γ Mie and PPR78 EoS at nine temperatures: (red), 283 K; (yellow), 298 K; (green), 323 K; (black), 348 K; (blue), 373 K; (grey), 398 K; (dark red), 423 K; (dark blue), 448 K; (purple), 473 K and at four mole fractions of $CO_2$: a) $x_{CO2}$ = 0.2; b) $x_{CO2}$ = 0.4; c) $x_{CO2}$ = 0.6; d) $x_{CO2}$ = 0.8. Solid and dotted lines represent predictions from SAFT-γ Mie and PPR EoS, respectively.

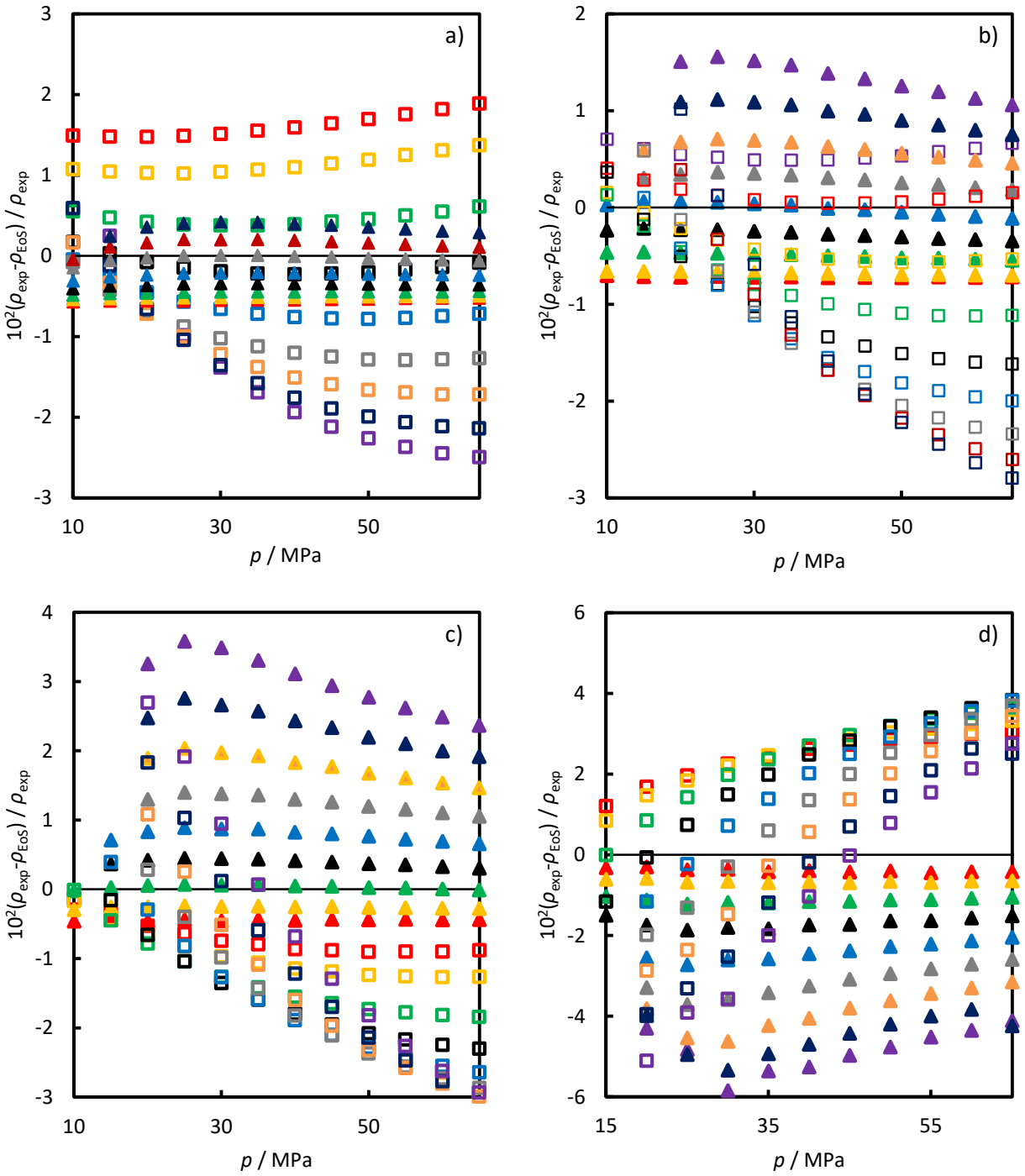



**Figure 6.31** Deviation plots between the experimental compressed-liquid density $\rho_{exp}$ for $CO_2$ + methylbenzene and the predictions from SAFT-γ Mie and PPR78 EoS $\rho_{EoS}$ at nine isotherms: (red), 283 K; (yellow), 298 K; (green), 323 K; (black), 348 K; (blue), 373 K; (grey), 398 K; (dark red), 423 K; (dark blue), 448 K; (purple), 473 K. Symbols: ▲, SAFT-γ Mie and □, PPR78 EoS.

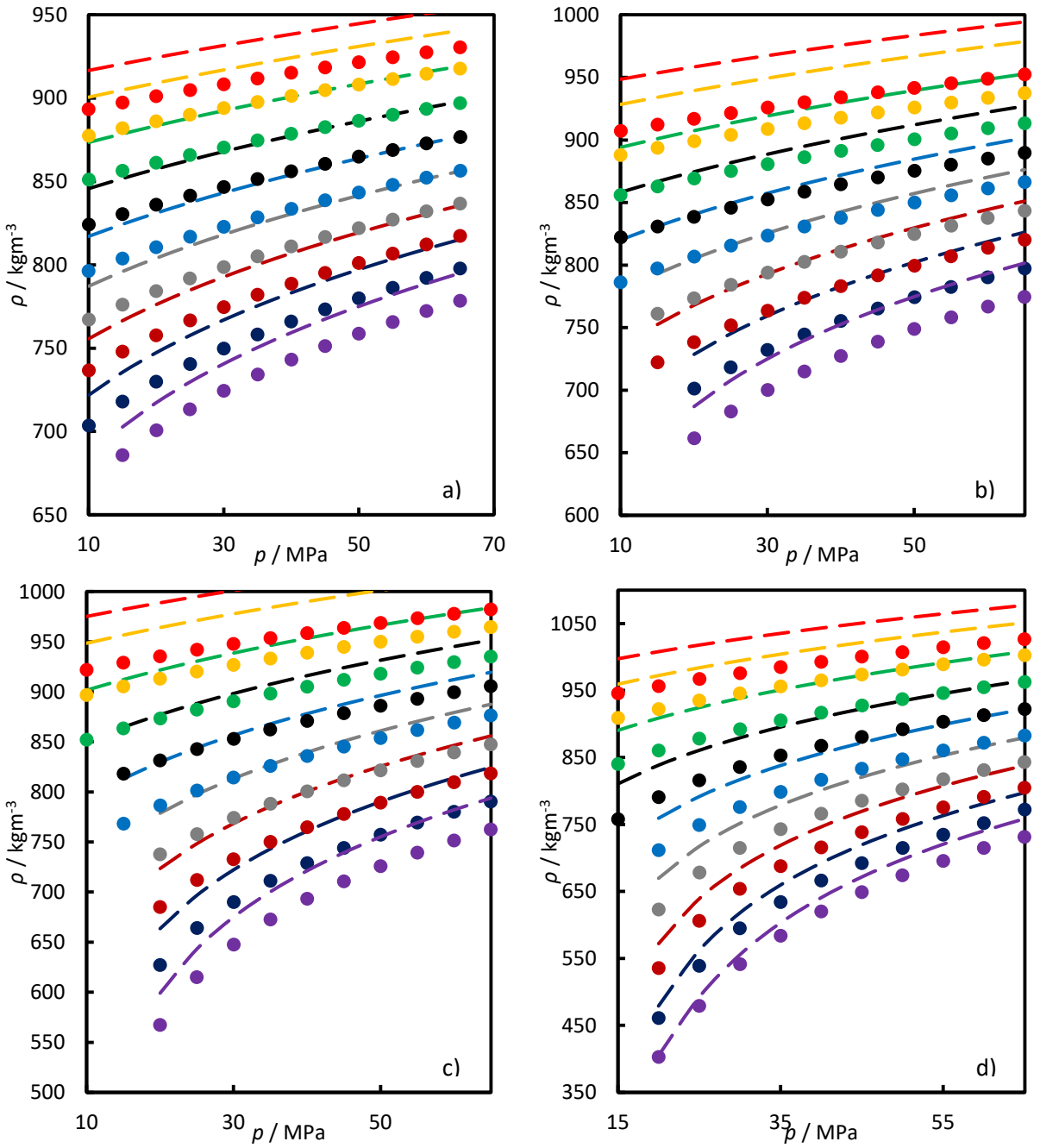



**Figure 6.32** Comparisons between the experimental compressed-liquid density $\rho$ of $CO_2$ + methylbenzene at temperatures: (red), 283 K; (yellow), 298 K; (green), 323 K; (black), 348 K; (blue), 373 K; (grey), 398 K; (dark red), 423 K; (dark blue), 448 K; (purple), 473 K at 4 mole fractions of $CO_2$: a) $x_{CO2}$ = 0.2; b) $x_{CO2}$ = 0.4; c) $x_{CO2}$ = 0.6; d) $x_{CO2}$ = 0.8 and the predictions from multi-fluid Helmholtz energy approximation. Dash lines represent predictions from multi-fluid Helmholtz energy approximation.

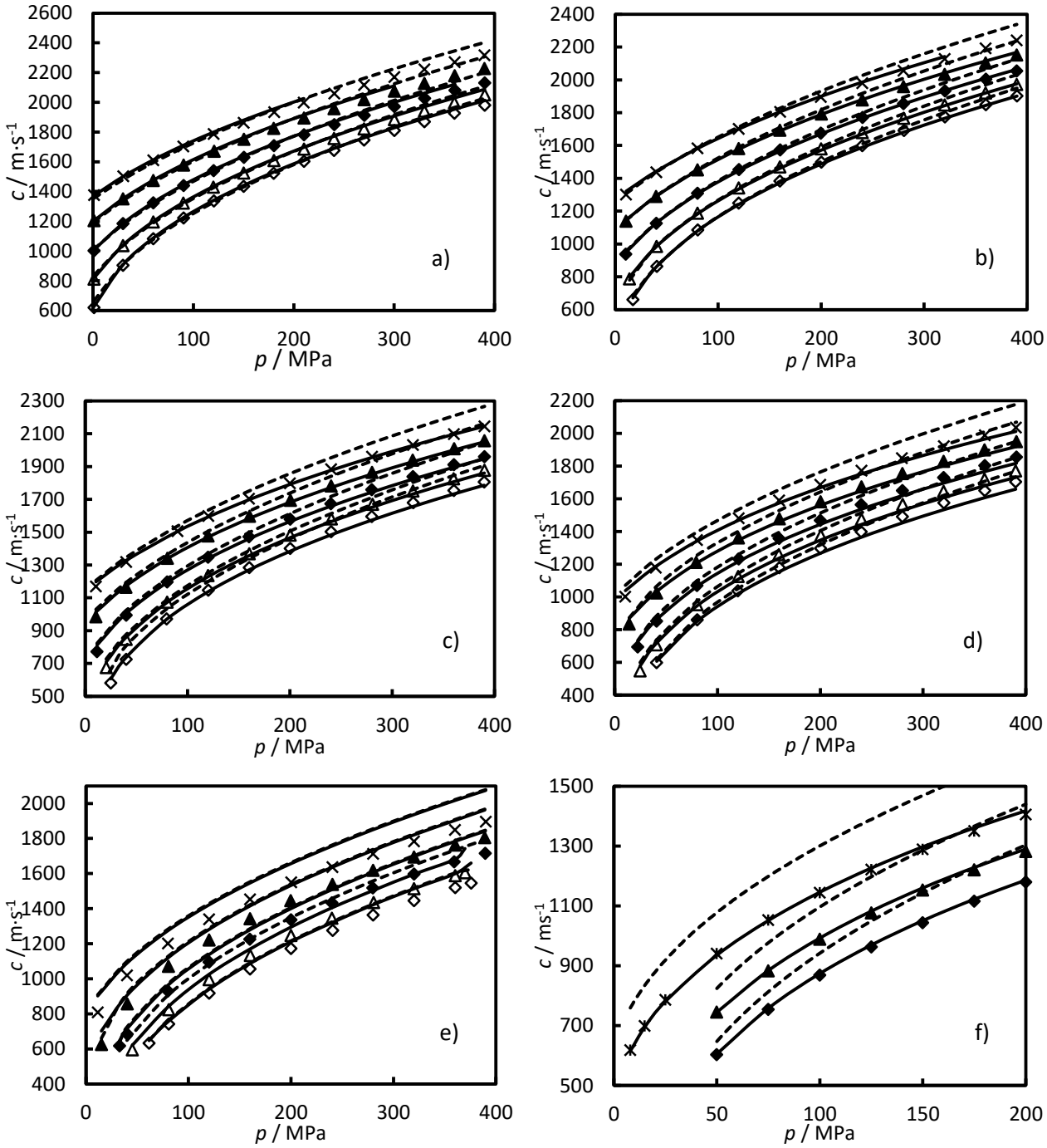



Figure **6.33** Comparison between the experimental sound-speed in $CO_2$ + methylbenzene and predictions from SAFT-γ Mie and multi-fluid Helmholtz energy approximation model developed by Bell and Lemmon across nine isotherms as a function of pressure. Symbols represent experimental data: ∗, 273.15 K; ×, 283.15 K; ▲, 323.15 K; ◆, 373.15 K; △, 423.15 K; ◇, 473.15 K. a) $x = 0$; b) $x = 0.2$; c) $x = 0.4$; d) $x = 0.6$; e) $x = 0.8$; f) $x = 1$. Solid and dotted lines represent sound-speed values calculated from the multi-fluid Helmholtz energy approximation model and SAFT-γ Mie, respectively.

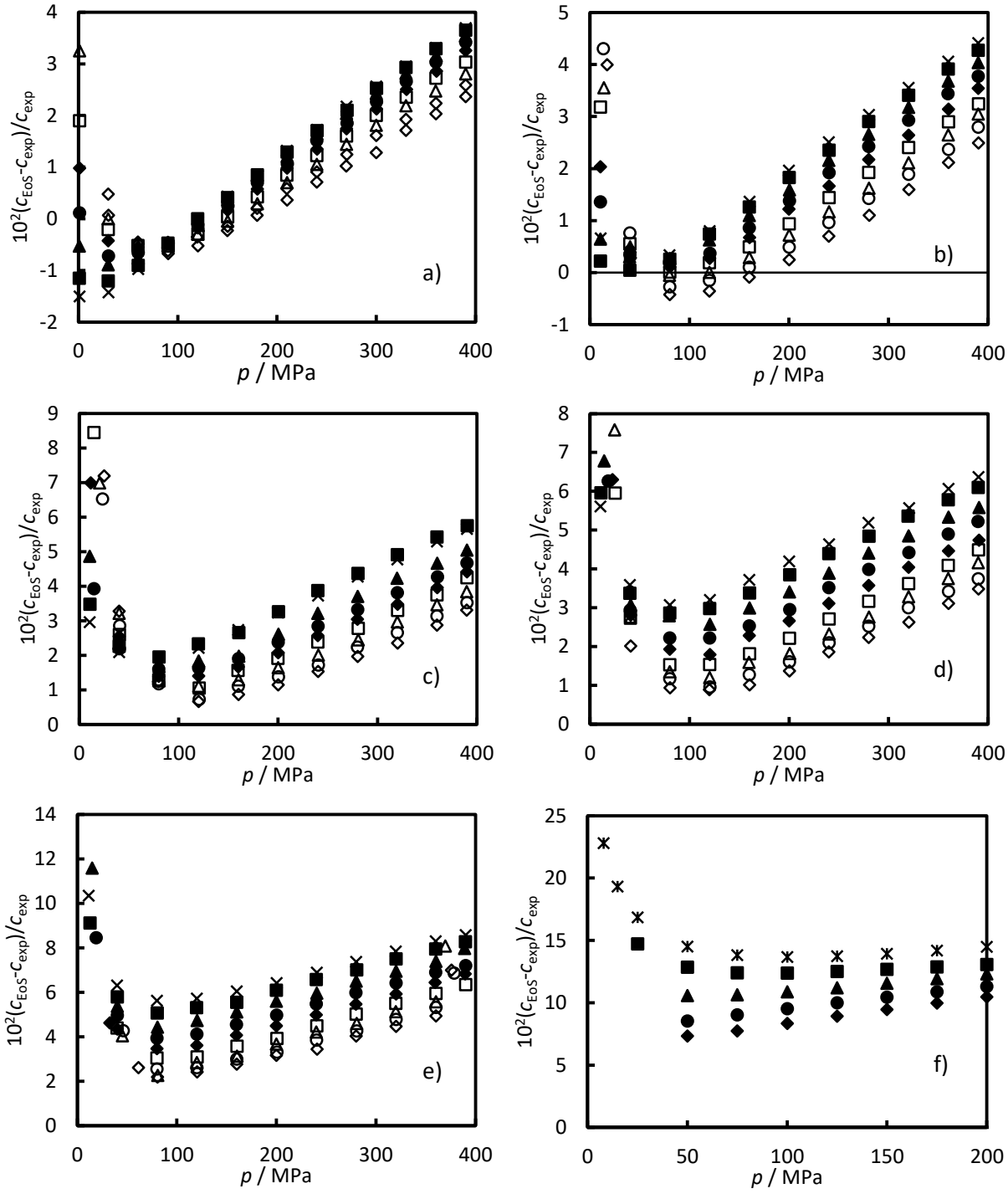



**Figure 6.34** Deviations between the experimental sound-speed $c_{exp}$ and the predictions from SAFT-γ Mie $c_{EoS}$ of $CO_2$ + methylbenzene across nine isotherms as a function of pressure. Symbols represent experimental data: ×, 283.15 K; ■, 298.15 K; ▲, 323.15 K; ●, 348.15 K; ◆, 373.15 K; □, 398.15 K; △, 423.15 K; ○, 448.15 K; ◇, 473.15 K. a) $x$ = 0; b) $x$ = 0.2; c) $x$ = 0.4; d) $x$ = 0.6; e) $x$ = 0.8; f) $x$ = 1.

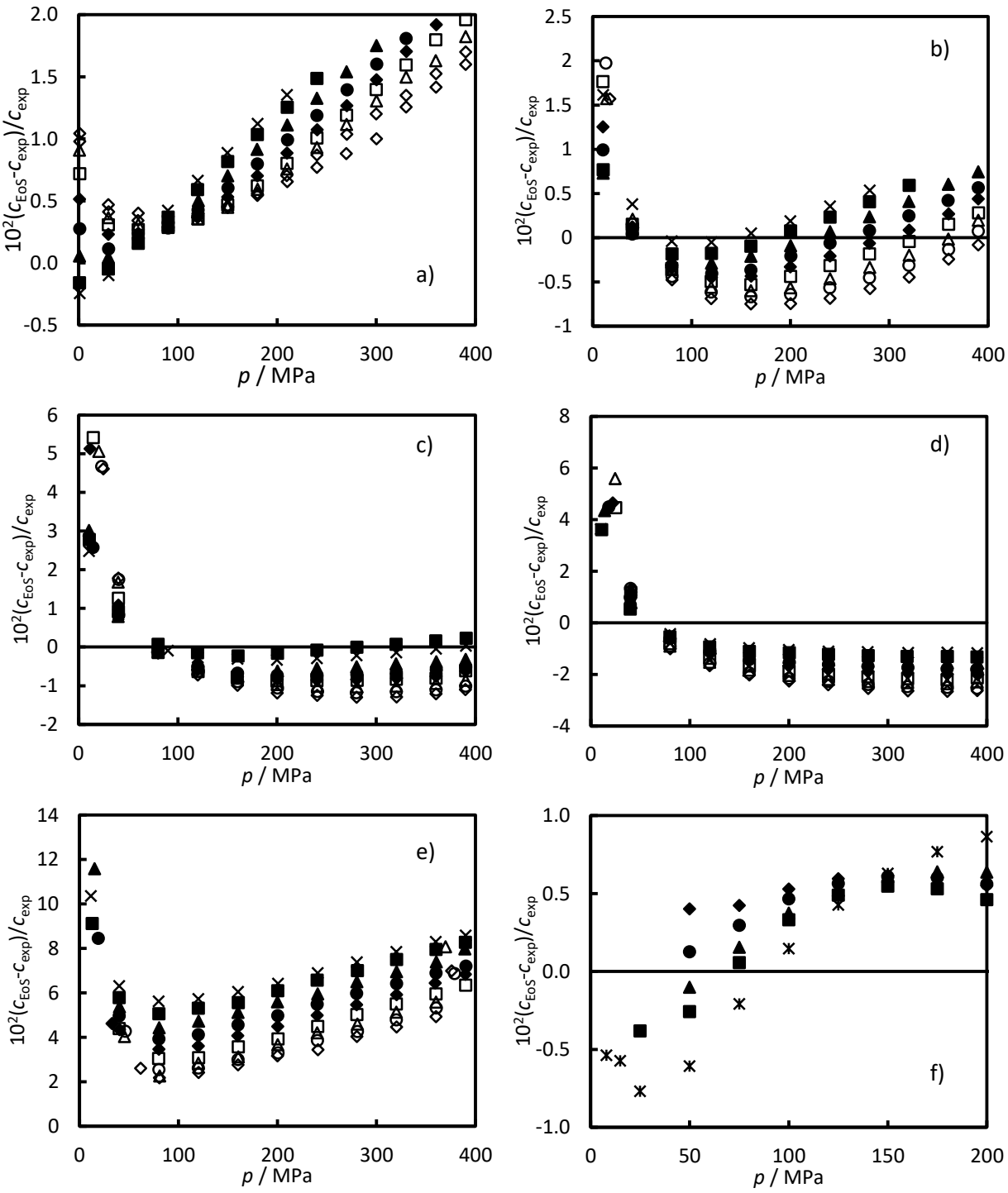



**Figure 6.35** Deviations between the experimental sound-speed $c_{exp}$ and the predictions from the multi-fluid Helmholtz energy approximation model $c_{EoS}$ of $CO_2$ + methylbenzene across nine isotherms as a function of pressure. Symbols represent experimental data: ×, 283.15 K; ■, 298.15 K; ▲, 323.15 K; ●, 348.15 K; ◆, 373.15 K; □, 398.15 K; △, 423.15 K; ○, 448.15 K; ◇, 473.15 K. a) $x = 0$; b) $x = 0.2$; c) $x = 0.4$; d) $x = 0.6$; e) $x = 0.8$; f) $x = 1$.

## 6.7 Summary

The compressed-liquid density of ($CO_2$ + *n*-heptane), ($CO_2$ + *n*-nonane) and ($CO_2$ + methylbenzene) has been measured precisely at temperatures between (283.15 and 473.15) K and pressures up to 68 MPa. The estimated standard uncertainty for density measurements was less than 1.0 $kg \cdot m^{-3}$ throughout the experimental conditions. Measurements carried out close to the critical region are found to have slightly higher uncertainty. A density crossover effect was discovered with the addition of $CO_2$ into hydrocarbons. At low temperatures, the overall densities increase with increasing mole fraction of $CO_2$, but a reverse trend was noticed at high temperatures. To allow interpolation/extrapolation of the experimental density data, a new empirical pressure explicit correlation was used to describe the compressed-liquid densities, and the $\Delta_{AARD}$ across four compositions is approximately 0.1 % for the three binary systems studied. The excess molar volume of the binary systems at four different compositions has been studied and the data were fitted with the Redlich-Kister equation isothermally along different isobars. In the composition range studied, the excess molar volume of the mixture is observed to be mostly negative. It becomes more negative with increasing temperature, but less negative with increasing pressure. For the cases of ($CO_2$ + *n*-heptane) and ($CO_2$ + methylbenzene), the compressed-liquid density data were combined with saturated-phase density to obtain bubble pressures at six temperatures. The obtained bubble pressures were compared with the direct VLE measurement made in our group, and they are in good agreement. The speed-of-sound measurements were carried out for ($CO_2$ + *n*-nonane) and ($CO_2$ + methylbenzene) at temperatures between (283.15 and 473.15) K and at pressures up to 390 MPa. The speeds-of-sound in both binary systems were measured for the first time in the literature. The standard uncertainty for the speed-of-sound measurements is calculated to be less than 0.6 $m \cdot s^{-1}$. The results show that the addition of $CO_2$ decreases the overall sound-speed in the binary mixtures. Similarly, the experimental speed-of-sound data have been correlated to an empirical correlation.

Furthermore, the predictive ability of three types of equations of states: the PPR78 and SAFT-γ Mie and Helmholtz energy explicit EoSs (GERG-2008 and the Multi-fluid approximation EoS) was tested against the experimental data collected in this work. No parameters were adjusted in all of the models during the comparison. The predictive capability of PPR78 and SAFT-γ Mie for compressed-liquid density predictions is quite similar with $\Delta_{AARD}$ of approximately 1.5 % between the predictions and experimental data for the three binary systems. The density predictions from the Helmholtz energy explicit EoSs have the worst agreement with the experimental data among the three equations of state with an $\Delta_{AARD}$ of approximately 5 %. An optimisation of the un-like parameters in the SAFT-γ Mie EoS was carried out. However, the optimised parameters did not significantly improve the predictions for compressed-liquid density, suggesting that there are limitations on the SAFT model to predict compressed-liquid density within the experimental uncertainty. Similarly, the experimental speed-of-

sound data have also been used to test the predictive capability of the models on second derivative properties. The predictions from SAFT-γ Mie and the Helmholtz energy explicit EoSs are quite similar, both with an $\Delta_{AARD}$ of approximately 3 %. It is generally expected to have high deviations with most equations of state when comparing with speed-of-sound experimental data. From the comparison of the results, it seems that there is scope for further improvement in the performance of the equations of state considered in this work. The results should make a valuable contribution to the future development of the current equations of state tested in this work.

# Chapter 7: Measurements of Calibration Fluids

## 7.1 Overview

In this chapter, the thermophysical properties and dynamic viscosity for two calibration fluids/hydrocarbon oils are reported at temperatures between (263.15 and 473.15) K and at pressures up to 300 MPa. To obtain the thermodynamic properties, the density of each fluid was measured with a vibrating-tube densimeter at low pressure and at temperatures between (283.15 and 473.15) K, with extrapolation down to 263.15 K; the heat capacity was measured with a flow calorimeter at near-ambient pressure and temperatures between (293.15 and 393.15) K, with extrapolation down to 263.15 K and up to 473.15 K. In addition, the speed-of-sound was measured with an ultrasonic cell at temperatures between (263.15 and 473.15) K at pressures up to 300 MPa. The thermodynamic properties of the fluid, including density and heat capacity, were then computed for temperatures between (263.15 and 473.15) K at pressures up to 300 MPa by thermodynamic integration. Finally, the viscosity was measured with a vibrating-wire viscometer at temperatures between (263.15 and 473.15) K at pressures up to 300 MPa. This chapter contains a summary of the apparatus, the experimental procedures, the experimental data obtained and the correlations developed.

# 7.2 Introduction

Calibration fluids which contain mixtures of heavy hydrocarbons are used during high-pressure and high-temperature calibrations for industrial processes. It is important to accurately determine the thermophysical properties of these fuels in order to characterise the process fully. The objectives of the study were to determine the thermophysical properties and dynamic viscosity of two types of hydrocarbon oils at temperatures between (263.15 and 473.15) K and at pressures up to 300 MPa. We also aim to test the operability of the flow calorimeter in this work. Hereby, we referred the two fluids as “Fluid A” and “Fluid B” in this chapter. The real compositions of the oils were unknown but they were specified to be mixtures of hydrocarbons by the supplier. The thermophysical properties of both fluids were evaluated, at the specified temperature and pressure range, by implementing the thermodynamic integration using the speed-of-sound data. In addition to speed-of-sound data, the thermodynamic integration requires density and isobaric heat capacity along an isobar (usually at 0.1 MPa) over the full temperature range as inputs.

In the present work, the speed-of-sound measurements were performed with the pulse-echo apparatus over the full temperature range of (263.15 and 473.15) K at pressures up to 300 MPa. Density was obtained by means of a vibrating-tube densimeter at temperatures between (283.15 and 473.15) K. The experimental density data were extrapolated down to 263.15 K accordingly. The heat capacity was measured with a flow calorimeter at temperatures between (263.15 and 423.15) K with extrapolation to 473.15 K. Knowing the density of the fluids over the full range from the results of the thermodynamic integration, the viscosity could then be determined using a vibrating-wire viscometer.

# 7.3 Experimental Apparatus and Procedures

## 7.3.1 Speed-of-Sound Apparatus

The speed-of-sound measurements were carried out with a state-of-the-art sound-speed apparatus. Both the apparatus and the experimental procedures were described in detail in Chapter 4.

## 7.3.2 Density Apparatus – Vibrating-Tube Densimeter

Density measurements were carried out with a vibrating-tube densimeter. The high-pressure density apparatus together with the experimental procedures have also been described in detail in Chapter 4.

## 7.3.3 Isobaric Heat Capacity Apparatus– Flow Calorimeter

The isobaric heat capacity measurements at near-ambient pressure were made with an isoperibol flow calorimeter illustrated schematically in Figure 7.1.

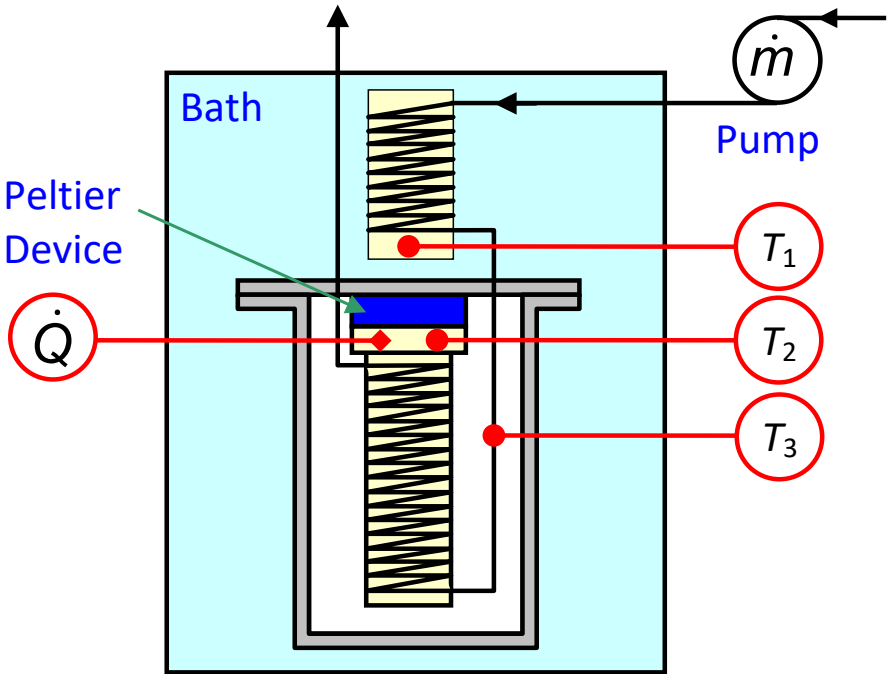



**Figure 7.1** Schematic of the calorimeter cell: $T_1$, $T_2$, $T_3$: platinum resistance thermometers (PRTs), Peltier device and isocratic HPLC pump.

The flow calorimeter was developed for the measurement of isobaric heat capacities over the temperature range (263 to 423) K at pressures ≤ 1 MPa. The principle is based on the heating and cooling of the calorimeter, under fluid circulated at a constant flow rate to maintain a fixed temperature difference between the inlet and the outlet [398]. The calorimeter consisted of a copper cylinder that was enclosed in a stainless-steel vessel. A dual-piston isocratic HPLC pump (Agilent 1200 G1310A) coupled with a degasser, delivered the liquid through the cell where a Peltier cooling device and a heater controlled the temperature. The inlet temperature was measured with a PRT and the outlet temperature was measured with a miniature thermistor periodically calibrated against a standard PRT. An additional thermistor is attached to the inlet tube inside the calorimeter enclosure to monitor the temperature $T_3$ at that location. Two thermostatic baths are available: one operating with a mixture of 50 % water and 50 % ethylene glycol for the temperature range (245 to 370) K (FLUKE 7040); and the other operating with silicon oil for the temperature range (320 to 450) K (FLUKE 6020). The stability of these baths varies from ±0.5 mK near 300 K to ±3 mK near 450 K. In use, the calorimeter was immersed in a thermostatic bath and was operated with a temperature difference, $\Delta T$ = 0.5 K, and a volumetric flow rates of between 0 and 5) ml·min$^{-1}$. The temperature of the calorimeter cell was regulated precisely 0.5 K below that of the bath by means of a constant cooling power developed by the Peltier device and a variable heat input developed by the heating resistance. The heat capacity of the liquid was obtained from the change in heating power required to maintain the constant cell temperature when liquid passed through the cell at a known flow rate, given in the following relation:

$$c_p = (\Delta P)/(\dot{m}\Delta T), \tag{7.1}$$

where $\Delta P = (P_{base} - P_{flow})$, the difference between the baseline control power without flow, $P_{base}$ and the control power $P_{flow}$ during operation at mass flow rate $\dot{m}$ and the temperature difference $\Delta T = 0.5$ K. The experimental parameters were collected through a multimeter (Agilent 34410A) and a data acquisition unit (Agilent 34970A). All aspects of experiment control and data acquisition were controlled using the software written in Agilent VEE. The results were corrected for viscous dissipation using an analytical method [398] and for heat loss by means of calibration measurements made on methylbenzene at temperatures between (293 and 423) K. The viscous dissipation effect can be estimated through the pressure drop in the calorimeter. Assuming fully-developed laminar flow, the pressure drop is given by

$$\Delta p = \eta(\dot{m}/\rho)(128L/\pi D^4), \tag{7.2}$$

where $\eta$ is the dynamic viscosity of the fluid, $L$ is the length and $D$ is the diameter of the capillary. It follows that the power passing from the fluid to the calorimeter cell is given by:

$$P_{Fl} = \dot{m}c_p\Delta T + \eta(1-\alpha_v T)(\dot{m}/\rho)^2(128L/\pi D^4), \tag{7.3}$$

where the second term on the right is expected to be very small in comparison with the first. This second term can be estimated in two ways: first, it can be measured experimentally in the blank run with $P_{cal} = 0$ and $\Delta T = 0$; alternatively, if all necessary terms are known then it can be calculated directly.

The estimated uncertainties in the measurement of the heat capacity were 1% near 313 K and within 2 % over the temperature range from (293 to 393) K. In the present work, it was found that the test liquids were too viscous to permit reliable measurements at temperatures below 293 K and, as discussed above, measurements at temperatures above 393 K were found to be unreliable. Heat capacity measurements were made at a near-ambient pressure at temperatures between (293.15 and 393.15) K in intervals of 10 K. At each temperature, the temperature difference, $\Delta T$ was set precisely to 0.5 K. The volumetric flow rates used during the experiments were (1, 3 and 5) ml·min$^{-1}$. The experimental data were corrected with the viscous dissipation correlation and the validated with the methylbenzene measurements.

## 7.3.4 Viscosity Apparatus – Vibrating-Wire Viscometer

The viscosity measurements were made using a compact vibrating-wire sensor designed to operate in the viscosity range (0.5 to 100) mPa·s [411]. As shown in Figure 7.2, the vibrating-wire sensor was comprised of a ceramic tube with metallic end pieces that were used to clamp the wire under an initial tension, imposed using a weight. A gold-plated tungsten wire of nominal diameter 0.15 mm was used, and this was tensioned to produce a resonance frequency in the air of approximately 1000 Hz. Two samarium-cobalt bar magnets measuring 40 mm × 10 mm × 4 mm, magnetised along the short axis,

were mounted on opposite internal faces of the gold-plated soft iron yoke (shown in Figure 7.2), and the sensor was inserted between the poles. This arrangement ensured a homogeneous perpendicular magnetic field along the length of the wire with a field strength of approximately 0.26 T at ambient temperature. The iron yoke was gold plated to inhibit corrosion. A pair of FKM o-rings located on ceramic tube served to anchor and centre the sensor inside the yoke without creating a short circuit.

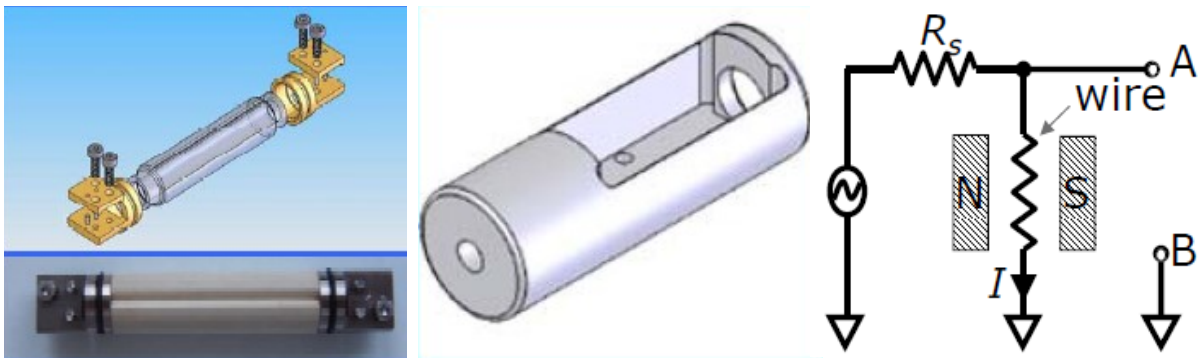



**Figure 7.2** Vibrating-wire sensor (*left*), soft-iron magnet yoke (*centre*), electrical circuit (*right*).

The viscometer capsule was used in the same pressure vessel and with the same fluid-handling system as described above in connection with the ultrasonic cell. All measurements with the vibrating-wire sensor were made in steady-state forced mode, utilising the fundamental transverse mode of oscillation. A lock-in amplifier with a built-in sinusoidal signal generator (Stanford Research Systems SRS830) was used to excite and detect the wire motion. The measurement circuit for the viscometer sensor is shown in Figure 7.2. It had one end of the vibrating-wire sensor grounded within the pressure vessel. A series resistance ($R_s$ in Figure 7.2) was incorporated in the circuit to ensure a constant alternating current through the vibrating wire. The driving voltage/current from the lock-in amplifier and the voltage developed across the vibrating-wire are both running on a single wire through the sensor to ground. The complex voltage $V$ measured across the wire (terminals A and B in Figure 7.2), which accounted for the impedance of the stationary wire and the movement of the wire, was assumed to conform to the following working equation [411, 412]:

$$V = \frac{\Lambda i f}{f_0^2 - f^2(1+\beta) + i f^2(\beta' + 2\Delta_0)} + a + bf + ci + dif\,. \tag{7.4}$$

Here, $\Lambda$ is the amplitude, $f$ is the drive frequency, and $f_0$ and $\Delta_0$ are the resonance frequency and logarithmic decrement of the wire in vacuum. The quantities $\beta$ and $\beta'$ account for the added mass and damping arising from the fluid around the wire and are given by

$$(\beta' + i\beta) = \frac{\rho}{\rho_w}\left[ i + \frac{4iK_1\left(\sqrt{i\Omega}\right)}{\sqrt{i\Omega}K_0\left(\sqrt{i\Omega}\right)} \right], \tag{7.5}$$

where

$$\Omega = 2\pi f \rho R^2 / \eta \,. \tag{7.6}$$

Here, $\rho$ and $\eta$ are the density and viscosity of the fluid, $\rho_w$ and $R$ are the density and radius of the wire, and $K_n$ is the modified Bessel functions of the second kind of order $n$. In the present work, the fluid density was an input parameter determined at each state point from the results of thermodynamic integration of the sound-speed data. The radius of the wire at $T$ = 298.15 K was determined by calibration in methylbenzene. Viscosity values of methylbenzene taken from the reference EoS over the entire temperature and pressure range were estimated to have an uncertainty of 0.5 % [40]. The viscosity of the liquid under study was then determined by means of a non-linear optimisation in which the values of $\Lambda$, $f_0$, $\eta$, $a$, $b$, $c$ and $d$ were adjusted to minimise the deviations between the experimental resonance data, $V$, and Equation (7.4). Considering also the reproducibility of the instrument and the uncertainties in temperature and pressure, we estimate a relative uncertainty of 3 % in the measured viscosity at 95% confidence. The viscosity measurements followed a similar pattern to that adopted for the sound-speed and extended across the full temperature range from (263.15 to 473.15) K. At the lower temperatures, the viscosity reached the upper limit of the sensor (about 100 mPa·s) at a pressure below 300 MPa, and hence the pressure range was limited at these temperatures.

## 7.4 Results and Discussions

The data reduction, analysis and validation for each measured property were described in this section. Since these fluids have not been the subject of published research and their compositions are not known, it is not possible to validate by comparison with previous work. However, a possibly-useful check on the general behaviour is to compare the properties with those of certain pure liquids. Since both test fluids are stated to be mixtures of paraffinic and aromatic hydrocarbons, we choose to compare with the properties of dodecane and methylbenzene, both of which are well-studied substances and the properties of which may be obtained from correlations incorporated in the NIST database REFPROP 9.1 [358].

### 7.4.1 Sound-speed Measurement

At temperatures above about 423.15 K, difficulties arose with material compatibility. The fluids caused rapid corrosion of the copper lead wires of the ultrasonic cell inside the pressure vessel and also dissolved the gold electrodes from the ultrasonic transducers. This therefore required frequent servicing and replacement of parts. After exposure to the highest temperatures, both fluids were discoloured and had a strong sulphurous odour which suggested that some decomposition had occurred resulting in the formation of volatile mercaptans or similar molecules. Despite this, the data

appeared to be repeatable within the claimed uncertainty, as judged by the check measurement made on each isotherm.



**Figure 7.3** (*left*) gold-plated piezo-transducer before and after the experiment, (*centre*) residue from lead wire corrosion, (*right*) seal extrusion on pressure vessel cap

The experimental sound-speeds in Fluid A and Fluid B across ten isotherms as a function of pressure were plotted in Figures 7.4 and 7.5. Figure 7.6 compares the experimental sound-speeds with the speeds-of-sound in dodecane and methylbenzene at two temperatures, (298.15 and 373.15) K. The graph illustrates two interesting behaviours. First, the speeds-of-sound in the two test liquids are very similar with relative differences being less than 1% over the entire surface. Second, the isotherms follow a general trend that is similar to that of pure hydrocarbons. The experimental sound-speeds were correlated by means of the implicit equation to facilitate the thermodynamic integration:

$$\left(p - p_0\right) = \sum_{i=1}^{3}\sum_{j=0}^{3} a_{ij}\left(c - c_0\right)^i \left(\frac{T_0}{T}\right)^j . \tag{7.7}$$

Here, $p_0$ = 0.1 MPa, $T_0$ = 273.15 K, and $c_0$ is the speed-of-sound at pressure $p_0$ which was correlated as a function of temperature as follows:

$$c_0 = \sum_{i=0}^{3} a_i \left(\frac{T}{T_0}\right)^i . \tag{7.8}$$

The parameters of Equations (7.7) and (7.8) were adjusted using the least square method for each fluid. The large ranges of temperature and pressure studied make it quite difficult to represent the data accurately with a simple equation but the implicit function, Equation (7.7), provides a generally excellent fit to the data with most of the points fitted to within their uncertainty of 0.1% shown in Figures 7.4 and 7.5.

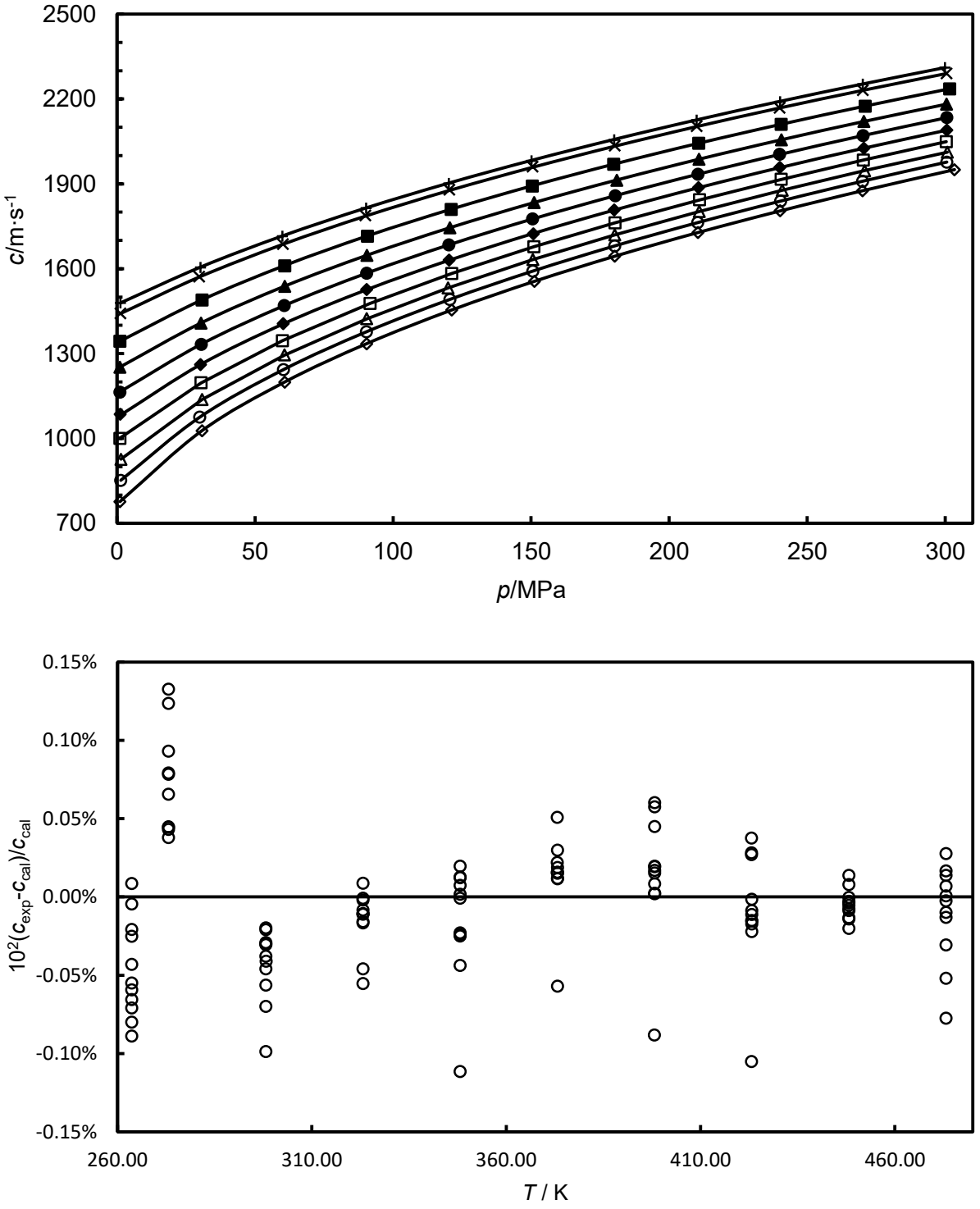



**Figure 7.4** (*top*) Experimental sound-speeds in Fluid A across ten isotherms at pressures up to 300 MPa. Symbols represent experimental data: ＋, 263.15 K;×, 273.15 K; ■, 298.15 K; ▲, 323.15 K; ●, 348.15 K; ◆, 373.15 K; □, 398.15 K; △, 423.15 K; ○, 448.15 K; ◇, 473.15 K. Solid lines: sound-speed calculated from correlation. (*bottom*) Deviations between the experimental sound-speeds and values calculated from the correlation.

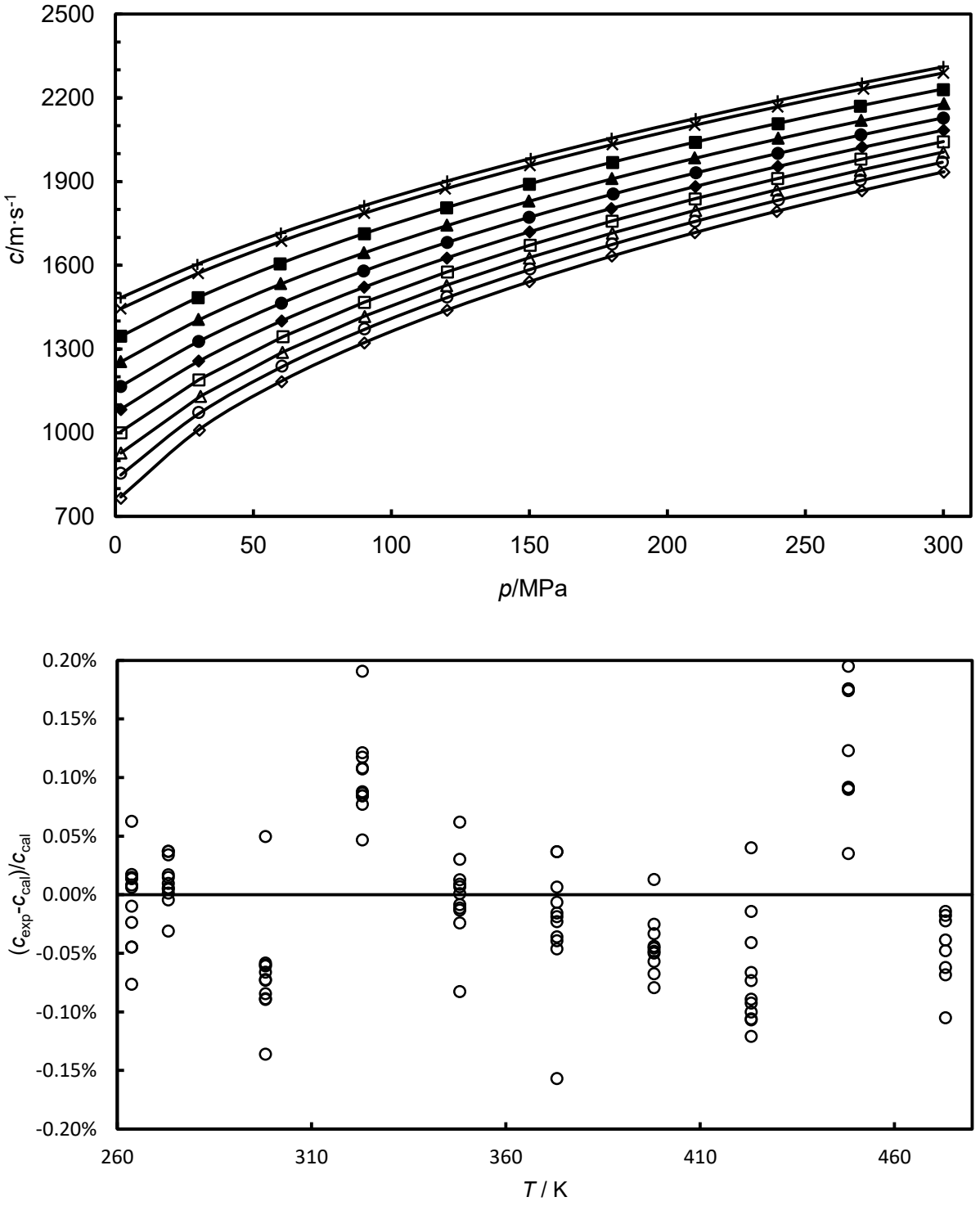



**Figure 7.5** (*top*) Experimental sound-speeds in Fluid B across ten isotherms at pressures up to 300 MPa. Symbols represent experimental data: +, 263.15 K;×, 273.15 K; ■, 298.15 K; ▲, 323.15 K; ●, 348.15 K; ◆, 373.15 K; □, 398.15 K; △, 423.15 K; ○, 448.15 K; ◇, 473.15 K. Solid lines: sound-speed calculated from correlation. (*bottom*) Deviations between the experimental sound-speeds and values calculated from the correlation.

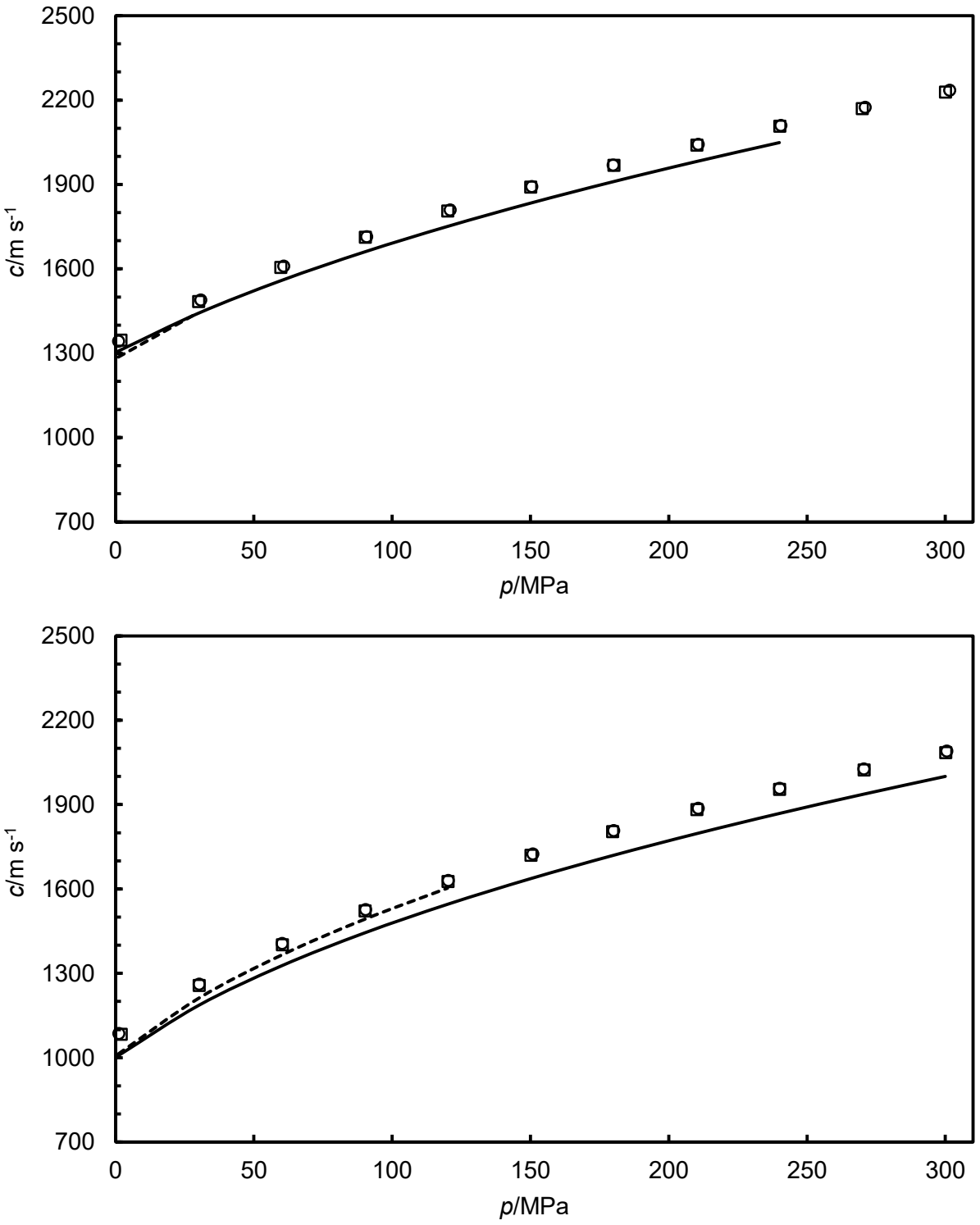



**Figure 7.6** Comparison between the sound-speeds measured for Fluid A and Fluid B and predictions from EoSs of methylbenzene and dodecane at (*top*) 298.15 K and (*bottom*) 373.15 K. Symbols represent experimental data: ○, Fluid A and □, Fluid B. Solid lines and dotted lines represent sound-speed values calculated from EoSs for methylbenzene and dodecane.

The $\Delta_{AARD}$ of the correlation for both fluids are 0.04 % and 0.08 %, respectively. The exceptions were mainly at low pressures and high temperatures where a few larger deviations of up to 0.5% were observed. The fitted surface is plotted along the experimental isotherms in Figures 7.4 and 7.5.

## 7.4.2 Density Measurement

The density measurements were made at nominal pressures of (0.2, 1.0 and 2.0) MPa, as shown in Figure 7.7. Over the pressure range investigated, the relative change in density was typically 0.2% and always less than 0.5%. The results at each temperature were found to be an almost perfectly linear function of pressure and hence the densities $\rho_0$ at the reference pressure $p_0$ = 0.1 MPa were obtained by simple linear extrapolation with negligible additional uncertainty. The results of these extrapolations are shown as a function of temperature in Figure 7.8 where we also plot the densities of pure dodecane and pure methylbenzene at the same pressure. The curve for methylbenzene is terminated at its boiling temperature at 0.1 MPa. It can be observed that the densities of the two fluids are almost identical and are intermediate between those of dodecane and methylbenzene.

The densities $\rho_0$ at the reference pressure were correlated as a function of temperature by means of the following polynomial:

$$\rho_0 /(\mathrm{kg}\cdot\mathrm{m}^{-3}) = \sum_{i=0}^{3} d_j (T/T_0)^i, \tag{7.9}$$

where $T_0$ = 273.15 K. The coefficients are adjusted to best fit the densities for each fluid.

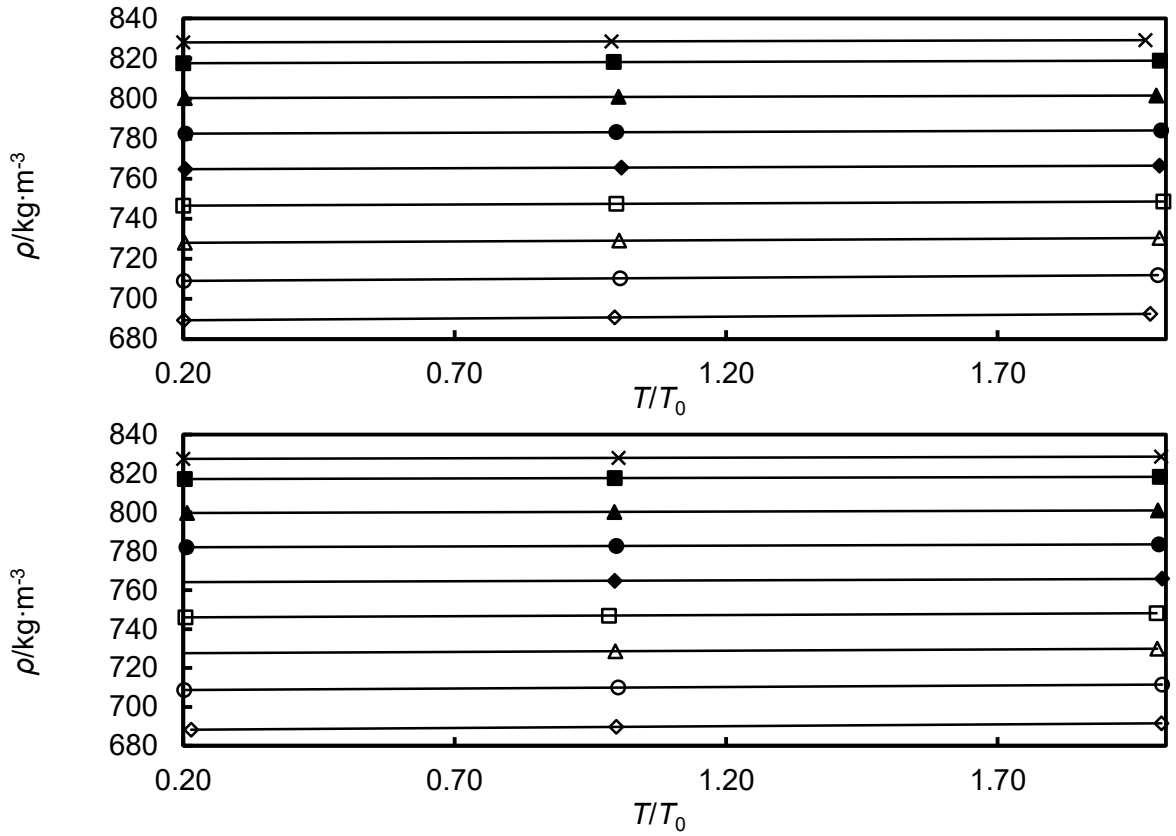



**Figure 7.7** Experimental density in (*top*) Fluid A and (*bottom*) Fluid B across ten isotherms at (0.2, 1 and 2) MPa. Symbols represent experimental data: +, 263.15 K;×, 273.15 K; ■, 298.15 K; ▲, 323.15 K; ●, 348.15 K; ◆, 373.15 K; □, 398.15 K; △, 423.15 K; ○, 448.15 K; ◇, 473.15 K. Lines are linear regression lines.

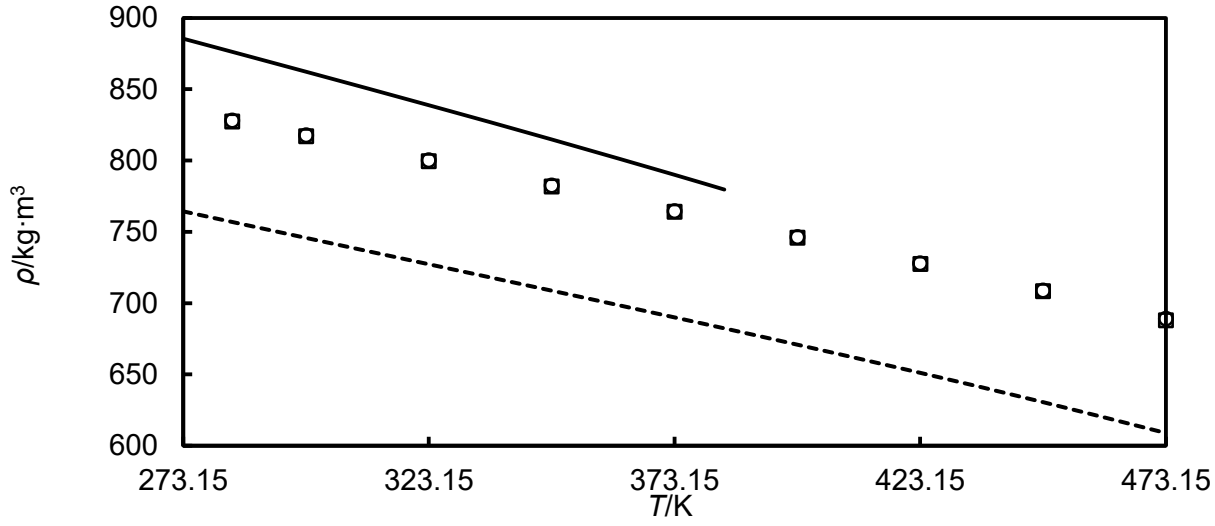



**Figure 7.8** Comparison between the densities extrapolated for Fluid A and Fluid B and predictions from EoSs of methylbenzene and dodecane at 0.1 MPa. Symbols represent experimental data: ○, Fluid A and □, Fluid B. Solid lines and dotted lines represent density values calculated from EoSs for methylbenzene and dodecane.

## 7.4.3 Isobaric Heat Capacity Measurement

At temperatures near 313.15 K, where the sample was chemically stable and viscosity and heat-loss effects were small, the results were highly repeatable with an estimated relative uncertainty of 1 %. In the extended temperature range of (293.15 to 393.15) K, the relative uncertainty was rather larger but not worse than 2 %. Unfortunately, attempts to make measurements at higher temperatures yielded unphysical results. Accordingly, as discussed further below, the missing data required as an input to the thermodynamic integration was obtained by an extrapolation that we validated by comparison with reference-quality data for pure substances. Satisfactory measurements of the isobaric heat capacity could be obtained only at temperatures between (293.15 and 393.15) K. At higher temperatures, erroneous results (apparently decreasing with temperature) were obtained and at lower temperatures, the fluids were viscous for the flow calorimeter to perform well. The experimental data are plotted as a function of temperature in Figure 7.9. The viscous corrections calculated with Equation (7.3) applied for $c_p$, range between (1 and 10) % for both fluids and with the largest correction occurred at the lowest temperature. The results were correlated as a function of temperature by the simple linear equation:

$$c_p = \sum_{i=0}^{1} e_i \left( \frac{T}{T_0} \right)^i , \tag{7.10}$$

where $T_0$ = 273.15 K. Equation (7.10) represented the experimental data to within its uncertainty and provided a reasonable basis for extrapolation. As shown in Figure 7.10, the linear correlations are approximately parallel with and intermediate between the reference data for dodecane and methylbenzene. An alternative extrapolation model was also considered based on the observation that the ratio $c_p$(fluid)/$c_p$(dodecane) was constant for $T \geq 323$ K and equal to 0.88 for both fluids. The curve corresponding to this is plotted in Figure 7.9 and is almost identical to the linear formula for Fluid A; for Fluid B, it differs by only 3 % at the highest temperature. Accordingly, the linear models were considered validated as inputs for the thermodynamic integration.

## 7.4.4 Thermodynamic Integration

As mentioned above, the viscosity measurement required density as input. To obtain density at high pressure, the thermodynamic integration was carried out. The method of the thermodynamic integration was described in Chapter 3. With the collected sound-speed data as functions of temperature and pressure, densities and isobaric heat capacities along one isobar, a full spectrum of thermophysical properties were derived up to 300 MPa using the following relations:

$$c^2 = \left[ \left( \frac{\partial \rho}{\partial p} \right)_T - \frac{T}{\rho^2 c_p} \left( \frac{\partial \rho}{\partial T} \right)_p^2 \right]^{-1} \tag{7.11}$$

$$\left(\frac{\partial c_p}{\partial p}\right) = -\frac{T}{\rho^3}\left[2\left(\frac{\partial \rho}{\partial T}\right)_p^2 - \rho\left(\frac{\partial^2 \rho}{\partial T^2}\right)_p\right] \tag{7.12}$$

The derived densities for Fluid A and Fluid B as a function of pressure at (373.15 and 473.15) K were shown in Figure 7.12. It can be noticed that the densities for both fluids were very similar with $\Delta_{AARD}$ of less than 0.1 % between the densities. The derived densities were compared with the densities of pure dodecane and pure methylbenzene at the same pressure.

## 7.4.5 Viscosity Measurement

As with the sound-speed work, serious problems of material compatibility arose. One manifestation was the complete stripping of gold plating from the soft iron yoke; another was corrosion of the copper lead wires. The samples were discoloured and had a strong sulphurous odour after use at high temperature and pressure. However, the measurements were repeatable, as judged by check measurements on each isotherm.



**Figure 7.9** Gold-plated iron yoke for viscometer (*left*) before and (*right*) after the experiment.

Viscosity measurements were made across ten isotherms from (263 to 473) K and up to either a pressure of 300 MPa or the pressure at which the viscosity reached the upper measurement limit of the apparatus (100 mPa·s). The results for the two fluids are plotted along isotherms in Figure 7.13. The viscosity measurement required density as an input, and the density values for the temperature and pressure range investigated were obtained from the thermodynamic integration mentioned above.

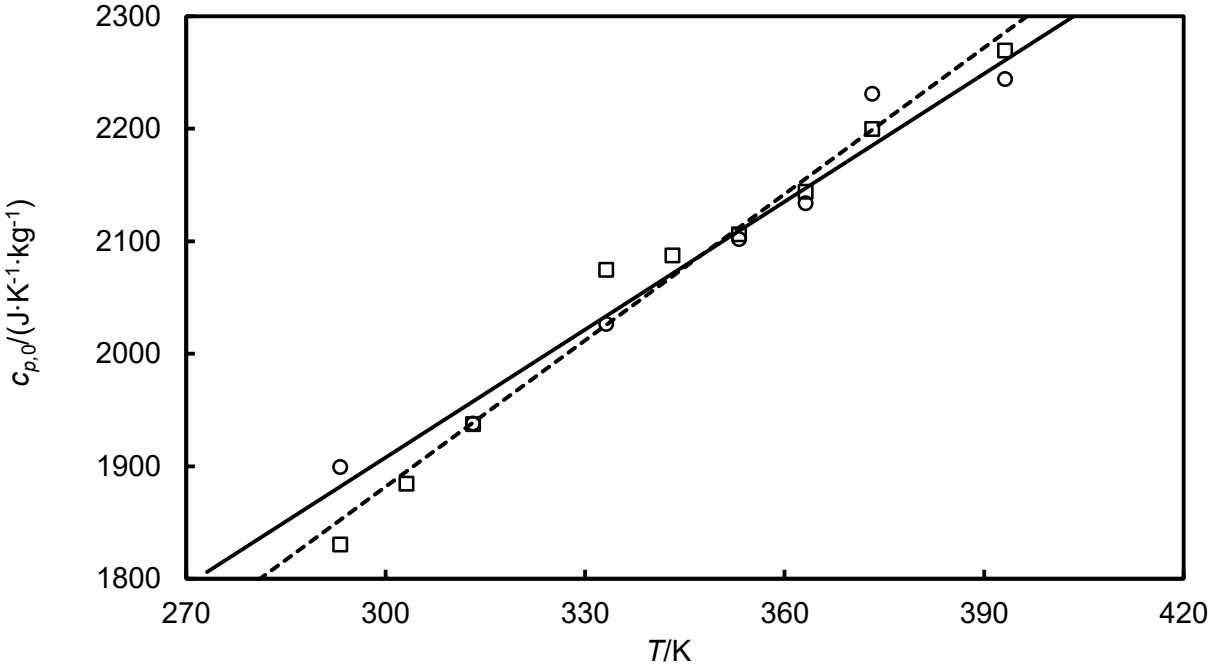



**Figure 7.10** Isobaric heat capacity measurements in Fluid A and Fluid B at temperatures up to 393.15 K at saturation pressure. Symbols represent experimental data: ○, Fluid A and □, Fluid B. Solid lines: viscosities calculated from correlation.

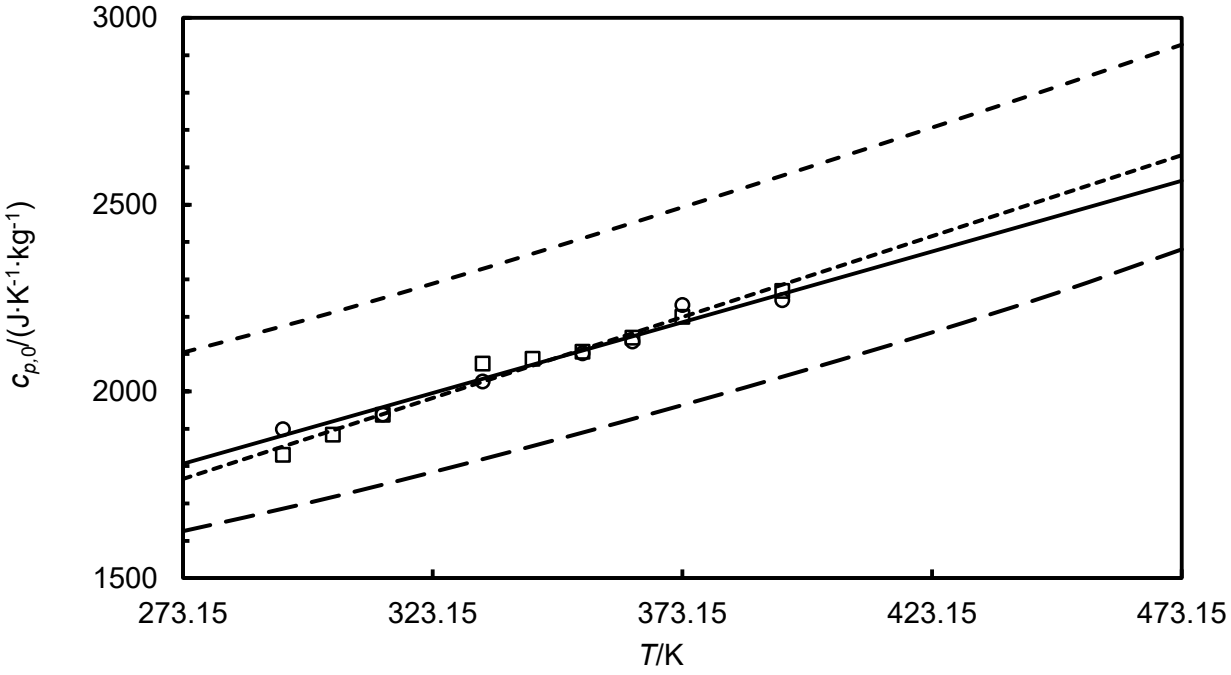



**Figure 7.11** Comparison of the isobaric heat capacities measured for Fluid A and Fluid B and predictions from EoSs of methylbenzene and dodecane. Symbols represent experimental data: ○, Fluid A and □, Fluid B. Solid lines: isobaric heat capacity values calculated from EoSs.

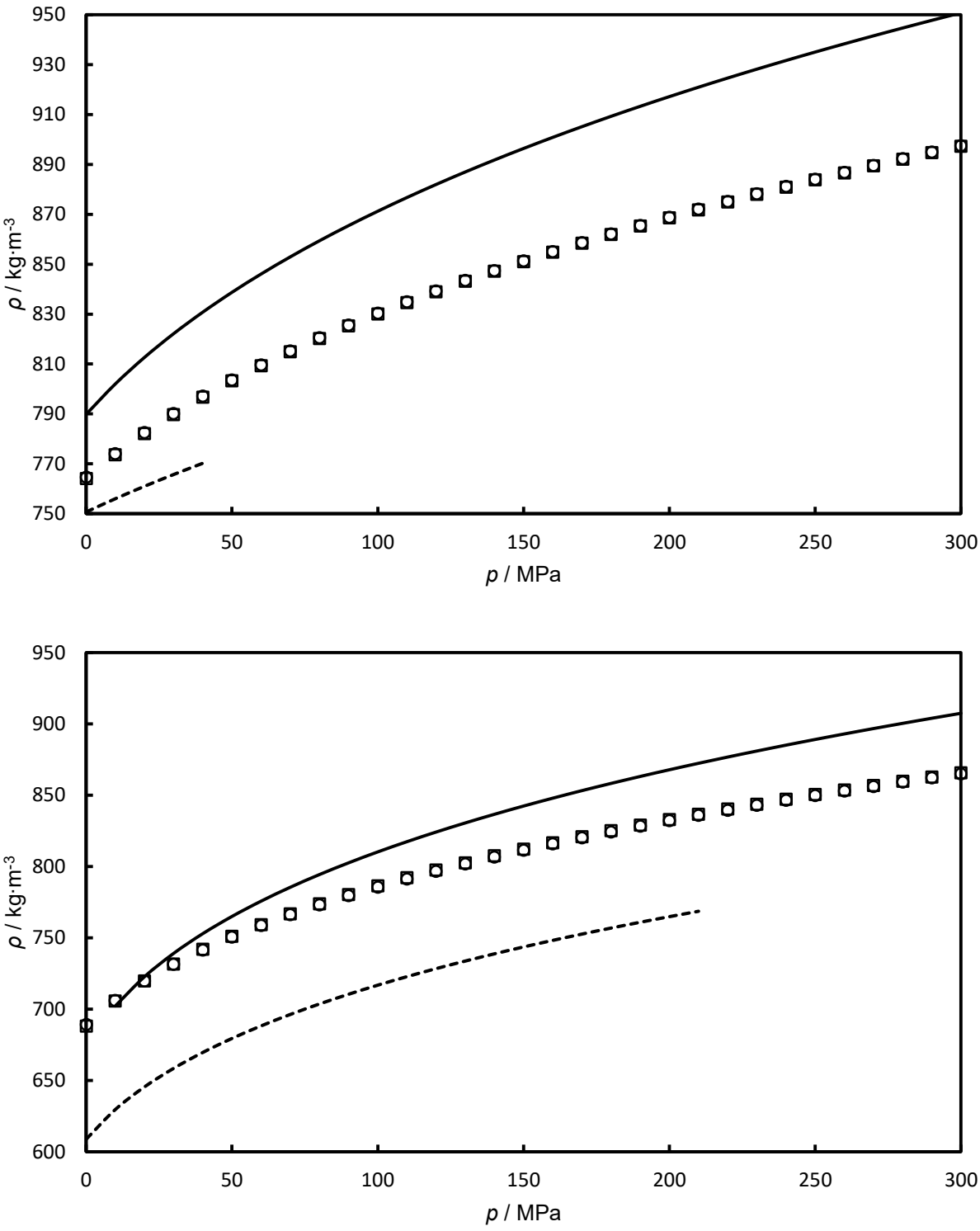



**Figure 7.12** Comparison between the densities derived from the sound-speed data up to 300 MPa for Fluid A and Fluid B and predictions from EoSs of methylbenzene and dodecane at (*top*) 373.15 K and (*bottom*) 473.15 K. Symbols represent experimental data: ○, Fluid A and □, Fluid B. Solid lines and dotted lines represent viscosity values calculated from EoSs for methylbenzene and dodecane.

Figure 7.14 compares the viscosity data with viscosity values calculated for dodecane and methylbenzene using their reference EoSs [413, 414]. The dynamic viscosities of the two test liquids are also very similar as shown in Figure 7.13. However, unlike the other properties considered, the viscosity of the test fluids is greater than either of the comparison fluids, suggesting that the mean molecular weight of the components in these liquids is considerably higher than that of dodecane and methylbenzene.

The accurate representation of viscosity over the very wide range of conditions studied is challenging, but satisfactory results have been obtained using a modified Vogel-Fulcher-Tammann (VFT) equation as follows:

$$\ln[\eta/(\mathrm{mPa\cdot s})] = a + b(p/p_1) + c(p/p_1)^2 + \frac{d + e(p/p_1) + f(p/p_1)^2}{(T/T_1 - 1)}. \tag{7.13}$$

In this equation, $p_1$ is a defined reducing constant, chosen to be 100 MPa, while $T_1$ and the coefficients $a$ to $f$ were adjustable parameters. The seven parameters in this model were fitted to the data for each fluid investigated, and isotherms calculated from the VFT model are plotted in Figure 7.13. Generally, the VFT model provided a satisfactory representation of the data with average absolute relative deviations of about 3% for both fluids. Nevertheless, the model fails to fully capture the behaviour of the experimental viscosity data to within the experimental uncertainty over the entire surface, as evidenced by the maximum absolute relative deviation of about 13% for each fluid.

The chemical composition of the fluids is unknown, but we suspect that their mean molecular weight is higher than dodecane and methylbenzene. An attempt was carried out to characterise both fluids using the viscosity data and the predictive smooth-hard-sphere model proposed by Dymond and Assael [415-419]. The model is based on a universal function with two parameters, the core volume and the roughness factor. In the model, the thermodynamic and transport properties are assumed athermal and can be expressed as functions of the reduced volume $V^* = V_m/V_0$, where $V_m$ is the molar volume, and $V_0$ is the molar core volume for close-packed hard spheres. The universal function is given in terms of the reduced viscosity $\eta^*$ is defined as follows:

$$\eta^* = \frac{16}{5}(2N_A)^{1/3}\left(\frac{\pi}{MRT}\right)^{1/2}\frac{\eta V_m^{2/3}}{R_\eta}, \tag{7.14}$$

where $N_A$ is Avogadro's constant, $M$ is the molar mass, $R_\eta$ is the roughness and $R$ the gas constant.

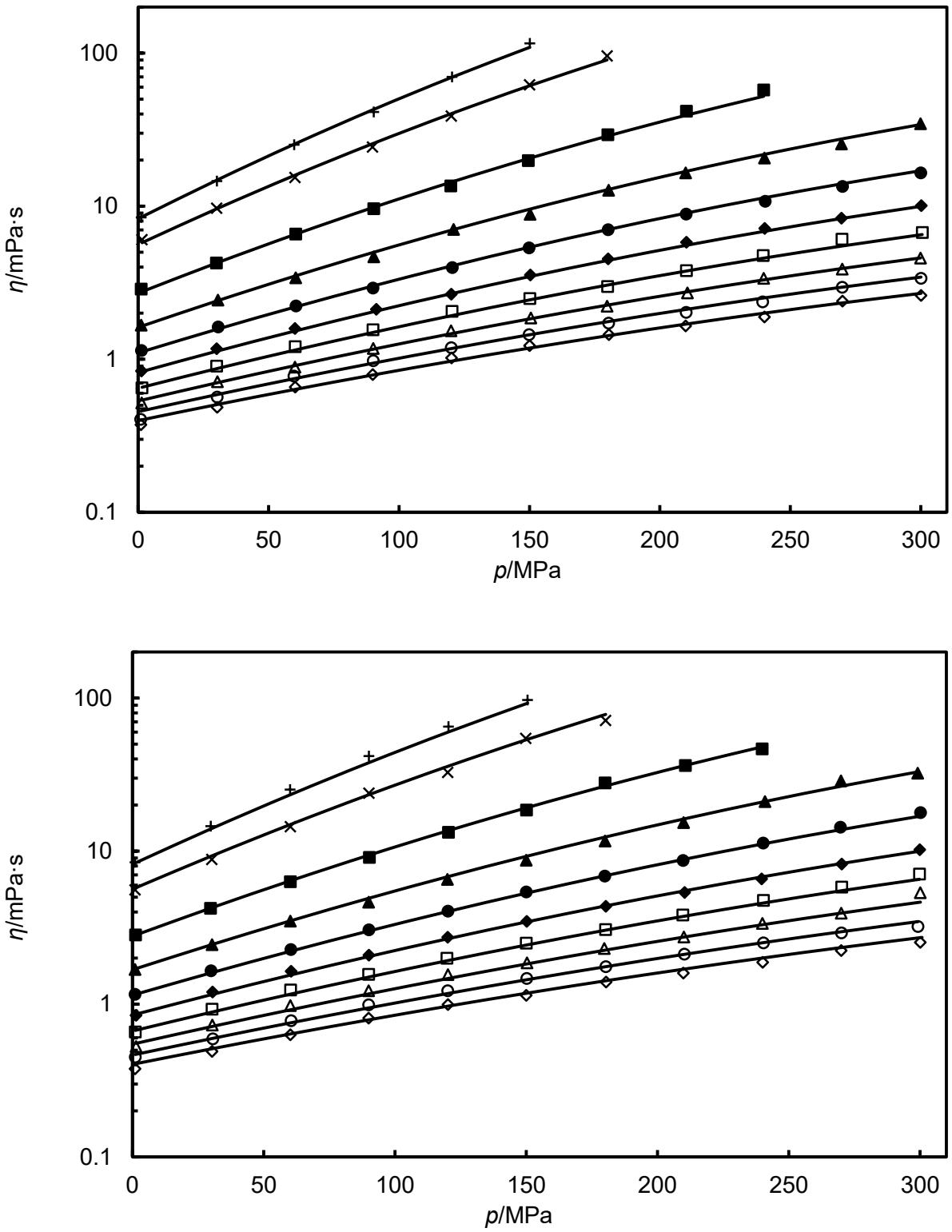



**Figure 7.13** Dynamic viscosity of (*top*) Fluid A and (*bottom*) Fluid B across ten isotherms at pressures up to 300 MPa. Symbols represent experimental data: ＋, 263.15 K;×, 273.15 K; ■, 298.15 K; ▲, 323.15 K; ●, 348.15 K; ◆, 373.15 K; □, 398.15 K; △, 423.15 K; ○, 448.15 K; ◇, 473.15 K. Solid lines: viscosities calculated from correlation.

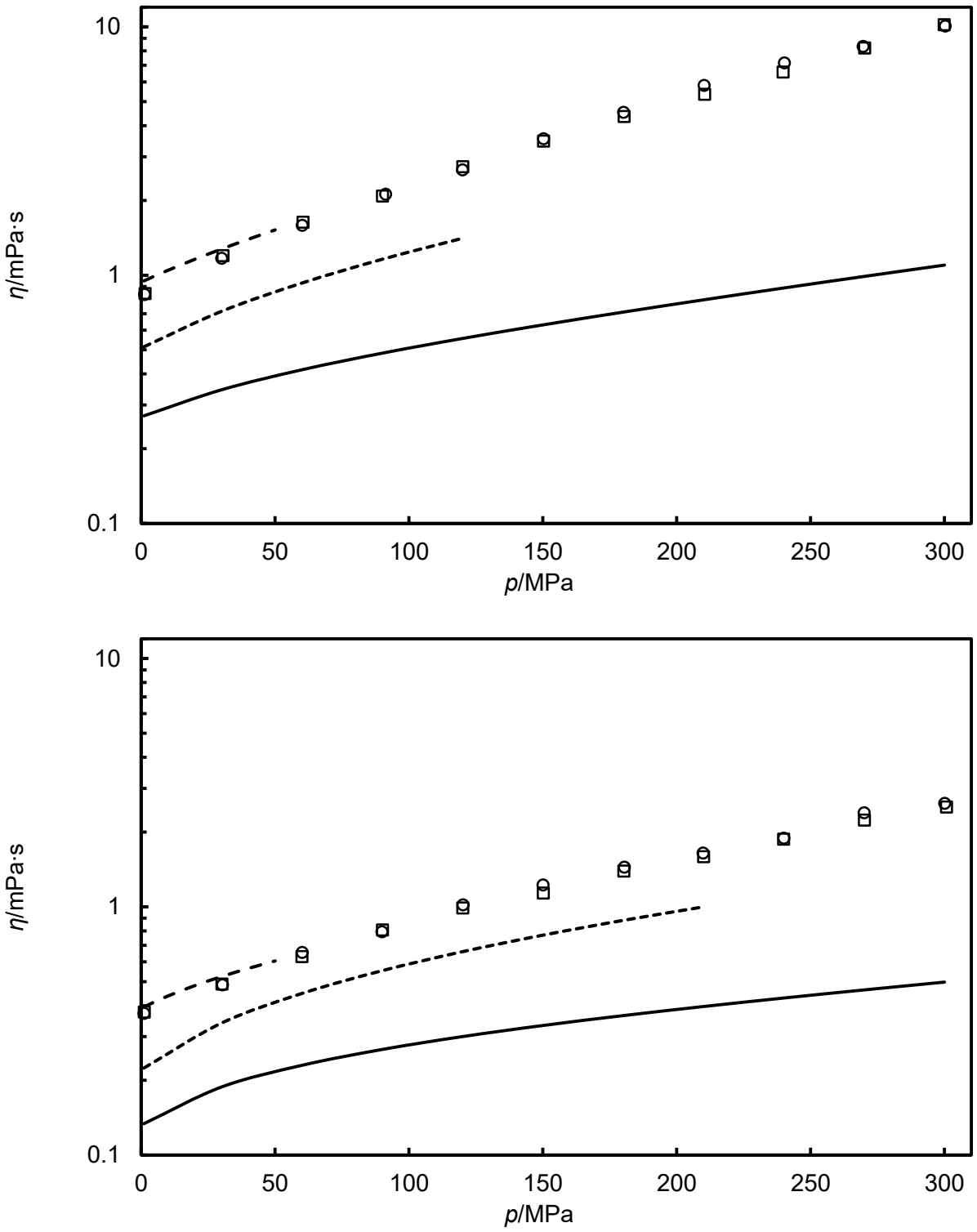



**Figure 7.14** Comparison between the viscosities measured for Fluid A and Fluid B and predictions from EoSs of methylbenzene, dodecane and hexadecane at (*top*) 373.15 K and (*bottom*) 473.15 K. Symbols represent experimental data: ○, Fluid A and □, Fluid B. Solid lines, dotted lines and dash lines represent viscosity values calculated from models for methylbenzene, dodecane and hexadecane, respectively.

For *n*-alkanes between *n*-hexane and *n*-hexadecane, the molar core volumes and the roughness factor can be calculated with the following empirical correlation regarding $T$ and carbon number $C_n$ given by Assael *et al.*[417]

$$V_0 = 117.874 + 0.15(-1)^n - 0.25275\theta + 0.000548\theta^2 - 4.246\times10^{-7}\theta^3 + (n-6)(1.27 - 0.0009\theta)(13.27 + 0.025C_n), \quad (7.15)$$

$$R_\eta = 0.995 - 0.0008944\ C_n + 0.005427\ C_n^{\,2}. \quad (7.16)$$

To make the expression for $V_0$ continuous, Equation (7.15) becomes:

$$V_0 = 117.874 + 0.15(\cos(n\pi)) - 0.25275\theta + 0.000548\theta^2 - 4.246\times10^{-7}\theta^3 + (n-6)(1.27 - 0.0009\theta)(13.27 + 0.025C_n). \quad (7.17)$$

It is believed that the model is capable of representing the experimental viscosity data within ±5 % with accurate density data [420]. With the trial and error method of changing the carbon number from ($C_6$ to $C_{16}$), we managed to obtain a good agreement between the experimental viscosity and the predictions when the carbon number is 16 as shown in Figure 7.14. The viscosities of both fluids are similar to hexadecane's, however, the densities do not match with hexadecane's and this implies that both fluids do not share the same chemical structure as *n*-alkanes.

## 7.5 Summary and Conclusions

The speed-of-sound, density, isobaric heat capacity and viscosity of Fluid A and Fluid B have been measured/derived at temperatures between (263.15 and 473.15) K and at pressures up to 300 MPa. Empirical correlations were developed to correlate the experimental data across the entire measurement range. The measured properties of both fluids were compared with the properties of methylbenzene and dodecane, and the results showed that both fluids exhibit heavy hydrocarbons behaviour. The viscosity results were compared with the predictions of the Dymond-Assael smooth-hard-sphere model. The exact compositions of both fluids are unknown, but from the comparisons, it can be seen that both Fluids A and B share a similar viscosity to hexadecane, but do not contain the same chemical structure as *n*-alkanes.

There are several challenges faced during the measurements. It was found that these fluids became chemically unstable and corrosive after exposing to high temperatures and pressures. Both fluids seem to contain a trace amount of sulphur compound in their compositions. Measurements became challenging due to the destructive nature of the fluids on the apparatus (as shown in Section 7.4) and frequent servicing of the apparatus was therefore required throughout the high-temperature measurements. It is worth noting that the gold-plated material may not be suitable for the mixtures of hydrocarbons measurements in the future and a different material should be considered. The

calorimeter used in this work has never been tested for high-temperature measurements, and the results reflected that the calorimeter became unreliable at high temperatures ($T \geq 393.15$ K). This might be due to a lack of accurate temperature control at high temperatures, and a vacuum isolation jacket can be considered to improve the performance of the calorimeter. Further investigation is hence recommended on the modification/design on the calorimeter.

Special thanks to Claudio Calabrese for assistance in setting up the vibrating-wire viscometer for this work.

# Chapter 8: Conclusions and Recommendations for Future Work

## 8.1 Summary and Conclusions

This research has been carried out intending to understand the behaviour of fluids involved in carbon sequestration and the oil and gas industry. In this work, extensive studies on the speed-of-sound and density of several pure hydrocarbons and binary mixtures of hydrocarbons and $CO_2$ have been carried out. These pure and binary systems are representatives of hydrocarbon mixtures that are likely to be encountered during the enhanced oil recovery of the CCS process. All of the measurements were carried out in a wide temperature range of $T$ = (263.15 to 473.15) K and pressures up to 390 MPa, some of which are conditions that are not previously explored in the literature. Although the present work extends to pressures much higher than the typical pressure limits of industrial processes or reservoir conditions, it is helpful in the development of equations of state to have data over the widest possible range of thermodynamic states. The density measurements in this research were carried out by means of a vibrating-tube densimeter, manufactured by Anton Parr which contained an estimated uncertainty of less than 1 $kg \cdot m^{-3}$ over the temperature and pressure range investigated. As for the speed-of-sound measurements, they were performed using the double-path pulse-echo technique, with a built-in-house equipment. The estimated expanded uncertainty of the speeds-of-sound is around 0.1 %. The collected experimental data were implemented to test the predictive capabilities of several thermodynamic models. The thermodynamic models tested in this work include PPR78, SAFT-γ Mie and Helmholtz energy explicit EoSs. These comparisons have allowed us to evaluate the predictive ability of the models that are widely used in both academic research and process design in the industry.

Density measurements were performed for (*n*-heptane, *n*-nonane, methylbenzene, $CO_2$, $CO_2$ + *n*-heptane, $CO_2$ + *n*-nonane and $CO_2$ + methylbenzene) at temperatures between (283.15 and 473.15) K at elevated pressures up to 68 MPa. Four compositions for each binary mixture have been measured, and the nominal mole fractions of $CO_2$ studied were $x_{CO2}$ = 0.2, 0.4, 0.6 and 0.8. The mixtures were prepared gravimetrically by means of a variable volume cell and an electronic balance. Details of the mixture preparation were described Chapter 4. Before measurements, different calibration methods for the vibrating-tube densimeter have been reviewed and it can be concluded the then parameters of the VTD can be fully determined with measurements of two calibration fluids. A robust calibration of the vibrating-tube densimeter with vacuum, helium and water was performed in the full temperature and pressure range of interest. In addition, comparison between two calibration models, the

polynomial model and the physical model, were carried out. The results suggested that the absolute density difference between the two models is very small and hence both calibration models are considered accurate for the VTD. The density measurements were always carried out in the homogeneous liquid-phase. The densities for all pure hydrocarbons show a classical density trend for liquids: the density increases with pressure but decreases with temperature. For densities of the binary mixtures, it has been noticed that the addition of $CO_2$ into the hydrocarbons causes a density crossover at high temperatures. The effect was likely to be due to the difference in compressibility between $CO_2$ and hydrocarbons. This phenomenon has been noticed for the three binary mixtures investigated in this work. The experimental density data were correlated with the modified Tait equation and a newly developed empirical correlation. Both correlations gave an $\Delta_{AARD}$ of approximately 0.1 % which is comparable to the estimated uncertainty of the measurements. The correlations allow the interpolation of data with respect to $T$ and $p$ which enables the comparison with the available experimental data in the literature reported at different conditions. The experimental data are mostly in good agreement with the available literature data. The excess molar volumes were also determined from the experimental densities, all three mixtures showed a non-ideal mixture behaviour. The excess molar volumes were fitted with the Redlich-Kister polynomial. The compressed-liquid densities of ($CO_2$ + *n*-heptane and $CO_2$ + methylbenzene) were combined with the saturated-phase densities to estimate the bubble pressures of the systems. The results are in good agreement with the bubble pressures measured directly with a VLE apparatus.

The existing literature data on the speed-of-sound for pure hydrocarbons/binary mixtures of hydrocarbons with $CO_2$ were limited, especially in the high-temperature, high-pressure conditions. In order to fill in the gaps in the literature, speed-of-sound measurements were carried out for (*n*-pentane, *n*-heptane, *n*-nonane, methylbenzene, $CO_2$ + *n*-nonane and $CO_2$ + methylbenzene) at temperatures between (263.15 and 473.15) K at pressures up to 390 MPa. The measurements were carried out in a single-liquid-phase in both sub-critical and supercritical regions. Most of these data exceed the previously available speed-of-sound data for the hydrocarbons. The speed-of-sound measurements were carried out using an unequal path-lengths ultrasonic cell which operated at 5 MHz. The path-lengths of the ultrasonic cell were calibrated using water at the full temperature range at 1 MPa before measurements. A correlation which accounts for the expansion/compression of the quartz tube was used to calculate the path-lengths at conditions other than the calibration. A new stainless-steel pressure vessel rated at 4 kbar was manufactured during the course of this research. For the measurements of the binary mixtures, the nominal mole fractions of $CO_2$ studied were 0.2, 0.4, 0.6 and 0.8. The binary mixtures were prepared externally using a variable volume cell prior to the measurements. A pressure-explicit empirical correlation was used to represent the speed-of-sound experimental data across wide temperature and pressure ranges. The pure components speeds-of-sound were compared with the available literature data, and most of our experimental data are in

agreement with the literature data to within 0.1 %; however, no literature data for the binary mixtures were available for comparison. The speeds-of-sound in binary mixtures indicated that the addition of $CO_2$ decreases the overall sound-speed in the mixtures at all temperatures and pressures studied.

As mentioned in Chapter 3, the speed-of-sound is related to several thermophysical properties, and with the knowledge of density and isobaric heat capacity, a full spectrum of thermophysical properties can be derived via thermodynamic integration. In this work, the speed-of-sound and density data for pure hydrocarbon components as a function of temperature and pressure, were combined with isobaric heat capacity data (along one isobar) from the literature; all observable thermophysical properties over the entire temperature and pressure surface for which speed-of-sound measurements were made, were derived via thermodynamic integration. The derived thermophysical properties include density, isobaric heat capacity, isobaric expansivity and isothermal compressibility. The derived data were compared with the predictions from the reference equation of state for each component. An estimation of the uncertainty of the derived properties was provided.

Detailed uncertainty analyses were performed for all measurements following the Guide to the Expression of Uncertainty in Measurements (GUM). In summary, the expanded uncertainties of the density measurements $U_c(\rho)$ range from (0.4 to 0.9) $kg \cdot m^{-3}$ for both pure components and binary mixtures across the temperatures and pressures investigated at 95 % confidence. The expanded standard uncertainties $U_c(c)$ vary between (0.4 and 0.8) $m \cdot s^{-1}$ over the temperature and pressure range investigated with a coverage factor of $k = 2$. Therefore, the expanded relative uncertainties of the speed-of-sound measurements were estimated to be between (0.04 and 0.14) % for all measurements. These uncertainty calculations considered uncertainties arose from pressure, temperature, calibration and repeatability of the equipment. The combined standard uncertainty in the mole fractions is approximately 0.00001 for all binary mixtures prepared in this work.

The binary experimental density data were compared with several predictive models. First, we implemented the predictive Peng-Robinson EoS (PPR78) to test against the compressed-liquid densities for the binary mixtures. The temperature-dependant binary interaction parameters, $k_{ij}$ were calculated using the group contribution method proposed by Jaubert and co-workers. The PPR78 EoS predicts the compressed-liquid densities with an $\Delta_{AARD}$ of approximately 2 % for the three binary mixture systems ($CO_2$ + *n*-heptane), ($CO_2$ + *n*-nonane) and ($CO_2$ + methylbenzene) across all temperatures, pressures and compositions. The volume translation method has also been tested with the PPR78 EoS; however, a clear conclusion cannot be drawn as the translation method did not improve the predictions accuracy for each mixture. Then predictive capability of SAFT-γ Mie was tested with the experimental densities. The density predictions were more accurate compared to PPR78, and the $\Delta_{AARD}$ were about 1.5 % for most of the experimental points measured. A series of

optimisation were carried out for the cross-interaction parameters of functional groups ($CO_2$-$CH_3$) and ($CO_2$-$CH_2$) in the SAFT-γ Mie EoS; however, the optimised parameters did not significantly improve the overall predictions. It seems that the SAFT-γ Mie model is unable to predict the compressed-densities accurately without compromising the accuracy on VLE and saturated-phase densities. Finally, the experimental density results were compared against the predicited values from two Helmholtz energy explicit EoSs: (1) GERG-2008 EoS by Kunz *et al.* and (2) a multi-fluid Helmholtz approximation model proposed by Bell and Lemmon. The experimental results of $CO_2$ + *n*-heptane and $CO_2$ + *n*-nonane were compared with the values calculated using the GERG-2008 EoS and the $\Delta_{AARD}$ between the experimental data and the predictions was about 5 %. This high-deviation is expected as GERG-2008 is designed to describe natural gas mixtures with a small amount of hydrocarbons. For the $CO_2$ + methylbenzene system, the experimental data were tested with the multi-fluid Helmholtz approximation, as methylbenzene was not included in GERG-2008. The $\Delta_{AARD}$ was calculated to be about 4 %. It seems that there is scope for further improvement in the performance of the equations of state in relation to the binary mixture considered in this work.

The binary speed-of-sound experimental data were compared with the predictions from SAFT-γ Mie and Helmholtz energy explicit EoSs. It was reported that cubic EoSs could not accurately model/predict second derivative properties; therefore PPR78 EoS was not chosen. The performance of predicting speed-of-sound in the $CO_2$ + *n*-nonane mixtures between GERG-2008 and SAFT-γ Mie are quite similar with an $\Delta_{AARD}$ of approximately 2 % for both models. The speed-of-sound in $CO_2$ + methylbenzene was predicted more accurately by the multi-fluid Helmholtz approximation model, with an $\Delta_{AARD}$ of 1 %. The prediction of derivative properties is a rigid test in any thermodynamic models, so high deviations are to be expected with most equations of state. Most equations of state have been rarely tested with second derivative properties such as speed-of-sound for binary mixtures of $CO_2$ + hydrocarbons, as measured data were scarce in the literature. The results should make a valuable contribution to the future development of the models tested in this work.

Finally, the speed-of-sound, density, isobaric heat capacity and viscosity of two calibration fluids have been measured/derived at temperatures between (263.15 and 473.15) K and at pressures up to 300 MPa. The speed-of-sound and viscosity measurements were challenging due to the destructive nature of the fluids on the apparatus and frequent servicing of the apparatus was required. It has also been noticed that the flow calorimeter becomes unreliable at high-temperature measurements ($T \geq$ 393.15 K) due to a lack of accurate temperature control. The measured properties of both fluids were compared with the properties of methylbenzene and dodecane, and the results showed that both fluids exhibit heavy hydrocarbons behaviour. The viscosity results were compared with the predictions of the Dymond-Assael smooth-hard-sphere model. From the comparison, both fluids share similar

viscosities with hexadecane but the densities are different. This implies that both fluids do not have the same chemical structure as *n*-alkanes.

## 8.2 Contribution of This Work

The research provides an extensive study of thermophysical properties of hydrocarbons and hydrocarbons with the addition of $CO_2$. A wide range of accurate experimental data were measured both in the sub-critical and supercritical region to fill in the existing gaps in the literature. These data provide a fundamental basis to understanding the behaviour of hydrocarbon mixtures that are relevant to the oil and gas industry and particularly the CCS process. These experimental data are providing information in the testing and development of thermodynamic models for pure hydrocarbons and hydrocarbon + $CO_2$ mixtures. The main contributions are summarised as below:

I. A comprehensive review of the speed-of-sound and density measurement techniques and the available data of $CO_2$ and hydrocarbon systems was provided. A detailed assessment of different calibration models for the vibrating-tube densimeter was described. A comparison between a commonly used calibration approach and a new calibration approach with physical parameters was carried out, detailed in Chapter 4.

II. The production of a large set of experimental thermophysical properties data for pure hydrocarbons (*n*-pentane, *n*-heptane, *n*-nonane and methylbenzene). Densities and speeds-of-sound have been determined precisely over a wide range of temperature and pressure, together with detailed uncertainty analyses. The experimental data were combined with isobaric heat capacity data from the literature and a full spectrum of thermophysical properties was derived. These properties include density, isobaric heat capacity, isobaric expansivity and isothermal compressibility and these data greatly extended the range in the current literature. The experimental results in this work can potentially be used as literature reference in comparison with other future studies.These will be of great importance in improving the current reference equations of state developed for each component.

III. The production of a large amount of new and experimentally challenging thermophysical properties data for mixtures of ($CO_2$ + *n*-heptane, $CO_2$ + *n*-nonane and $CO_2$ + methylbenzene) over a wide range of temperatures and pressures in the single-liquid-phase region. The measurements include compressed-liquid densities and speeds-of-sound which some of them have never been reported in the literature. These data not only provided a large contribution to literature, but also served as a basis for the understanding of the interaction between

hydrocarbons and $CO_2$ (the effect of the addition of $CO_2$ in hydrocarbons). These data will be of great importance in the context of data available in the open literature, regarding both filling the existing gap and in model development.

IV. The evaluation and assessment of the predictive capability of several thermodynamic models by means of the comparison with our experimental data. The thermodynamic models tested include PPR78 EoS with/without volume translation, SAFT-γ Mie EoS and Multi-parameter Helmholtz energy explicit EoSs. Limited number of studies has tested the models with the speed-of-sound data, as the measured data were scarce in the literature. A detailed comparison between the single-phase experimental density and speed-of-sound for binary $CO_2$ + hydrocarbon systems and the predictions of the models was presented.

# 8.3 Recommendation for Future Work

## 8.3.1 Further Experimental Investigation

In the present work, density and speed-of-sound of pure hydrocarbons and binary mixtures of hydrocarbons and $CO_2$ have been investigated under high-temperature, high-pressure conditions. These data have allowed rigorous testing, both qualitatively and quantitatively, of the predictive capabilities of several thermodynamic models. Most of the discussed models use group contribution approach in which the thermodynamic behaviour of a fluid was described by different functional groups. The parameters in these functional groups were determined using experimental data, and hence the new experimental data collected in this work can be utilized in the optimisation of parameters for the functional groups in the models.

Since one of the objectives of this research is to understand the behaviour of hydrocarbons during the EOR process, this research provides a fundamental basis for the understanding of the fluid behaviour by providing experimental data for both pure and binary mixtures. As we know the physical and chemical structures of real crude oils are very complex, their thermophysical properties are still very difficult to predict even with sophisticated predictive models. Therefore, it will be useful to perform further measurements on fluid mixtures that are more comparable to real crude oils that contain similar physical and chemical properties such as mixtures of (cycloalkanes + aromatics + heavier alkanes). The new density and speed-of-sound experimental data will provide more information for crude oil characterization. Further measurements could be carried out with either real crude oils or synthetic crude oils, and the addition of $CO_2$ in the mixtures would be highly beneficial to the understanding of the EOR process. In the past, Al Ghafri *et al.* and Forte *et al.* from our research group studied the phase behaviour of ternary systems of hydrocarbons + $CO_2$ + water. These ternary

mixtures are better representatives of the fluids during EOR since $H_2O$ and $CO_2$ are used at the same time to improve the sweep efficiency of the oil extraction process [421-424]. In their work, they measured the phase behaviour of (*n*-heptane + $CO_2$ + water), (*n*-decane + $CO_2$ + water), (*n*-propane + $CO_2$ + water) and (methane + $CO_2$ + water). They have also compared the experimental results with the predictive SAFT equation, and they concluded that the modelling work was more challenging with water present in the mixture since water contains hydrogen bonding association. However, the amount of $H_2O$ used in their work is very small due to solubility issues at the measuring conditions. With the measuring capability (high-temperature $T \leq 473.15$ K, high-pressure $p \leq 400$ MPa) of the density and sound-speed equipment, this would allow further investigation of mixtures with a higher concentration of water in the aqueous and non-aqueous phases. Another major fluid in the reservoir is brine; new experimental data measured under reservoir conditions for brines would provide new information about fluid behaviour. Density and viscosity experiments of brines have been carried out by our group previously. Speed-of-sound data would be valuable in the contribution of fluid characterisation. However, modifications to the existing equipment are required in order to measure mixtures with brines as they are highly corrosive. Hastelloy tubes which are more corrosion-resistant are preferred to stainless-steel tubes to handle brine mixtures. Lastly, to choose a suitable geological site for $CO_2$ storage, one of the technical requirements is the injectivity of the reservoir. Technical factors which control injectivity include reservoir pressure and the $CO_2$ stream composition. Impurities of other gases such as $O_2$, $N_2$ and $H_2$ may be present in the feed stream to $CO_2$ storage depending on the separation process and the purity of the $CO_2$ stream at the capture process. The present of these gases causes a change in the thermophysical properties of the reservoir fluid and hence the injectivity of the reservoir. Therefore, further measurements on ($CO_2$ + impurities + hydrocarbons) systems should be carried out to understand the effect of $CO_2$ impurities.

All of the above recommended experimental work will be carried out with fluids that are much more similar to real reservoir fluids and will provide invaluable data for accurate thermodynamic models to be developed.

## 8.3.2 Further Modelling Investigation

In previous chapters, the predictive ability of the GERG-2008 has been tested to predict density and speed-of-sound of binary mixtures of hydrocarbons and $CO_2$. Some of the predictions are satisfactory, but there's still room for improvement based on the comparisons. It was mentioned in work carried out by Kunz and Wagner that the development of the GERG-2008 model was hindered by a lack of accurate experimental data, and new experimental data would be advantageous for further development. This work provided new experimental data in a wide temperature and pressure range for relevant systems in the GERG-2008 such as ($CO_2$ + *n*-heptane and $CO_2$ + *n*-nonane). These accurate

experimental data could be used to optimise the adjustable parameters in the Helmholtz reducing function in order to describe the thermophysical properties at a higher accuracy.

For the equations of state that implement the group contribution approach, the predictive capability of the model depends heavily on the accuracy of the functional group parameters. It is, therefore, essential to ensure the parameters are determined by a large number of high-quality experimental data. In most cases for parameters in the SAFT-γ Mie model, it has been reported in the literature that the functional group parameters were only optimised with VLE, saturated-phase density and single-phase density due to the limitation of existing data. It has been proven in the past that sound-speed data provides useful information in the thermodynamic model development and especially ultrasonic measurement can be measured with a high accuracy at high pressure; speed-of-sound data should be included in the optimisation process. The wide pressure range measured in this work covers both the sub-critical and supercritical regions that could be beneficial to the development of equations of state. Once the parameters are optimised with high-pressure data, this should improve the high-pressure predictions given by the model.

# List of References

[1] IEA Energy Technology Perspectives 2015.
[2] Global CCS Institue The Global Status of CCS Summary Report; 2015.
[3] Olivier, J. G. J.; Janssens-Maenhout, G.; Muntean, M.; Peters, J. H. A. W. Trends in Global $CO_2$ Emissions: 2015 Report; 2015.
[4] United Nations Paris Climate Change Conference (COP21); 2015.
[5] IEA World Energy Outlook; 2014.
[6] IEA World Energy Outlook; 2015.
[7] IPCC Fifth Assessment Synthesis Report; 2014.
[8] IEA Technology Roadmap: Carbon Capture and Storage; 2013.
[9] IPCC Climate Change 2014: Synthesis Report Summary for Policymakers; 2014.
[10] SENAAT Emirates Steel Industries CCS Project. http://www.emiratessteel.com/index.php/en/corporate-responsibility/environmental/co2-capture-project
[11] Japan CCS Co. Ltd. Tomakomai CCS Demonstration Project. http://www.japanccs.com/en/business/demonstration/
[12] Global CCS Institue Abu Dhabi CCS Project. https://www.globalccsinstitute.com/projects/abu-dhabi-ccs-project-phase-1-being-emirates-steel-industries-esi-ccs-project
[13] Leung, D. Y. C.; Caramanna, G.; Maroto-Valer, M. M. An Overview of Current Status of Carbon Dioxide Capture and Storage Technologies. Renewable and Sustainable Energy Reviews 2014, 39, 426-443.
[14] Shell Quest Carbon Capture and Storage Project. http://www.shell.ca/en_ca/about-us/projects-and-sites/quest-carbon-capture-and-storage-project.html
[15] SaskPower Boundary Dam Carbon Capture Project. http://www.saskpower.com/our-power-future/carbon-capture-and-storage/boundary-dam-carbon-capture-project/
[16] Mazzoccoli, M.; De Guido, G.; Bosio, B.; Arato, E.; Pellegrin, L. A. $CO_2$-Mixture Properties for Pipeline Transportation in the CCS Process. Icheap-11: 11th International Conference on Chemical and Process Engineering, Pts 1-4 2013, 32, 1861-1866.
[17] Li, H. L.; Jakobsen, J. P.; Wilhelmsen, O.; Yan, J. Y. PVTxy Properties of $CO_2$ Mixtures Relevant for $CO_2$ Capture, Transport and Storage: Review of Available Experimental Data and Theoretical Models. Applied Energy 2011, 88, 3567-3579.
[18] Bentham, M.; Kirby, M. $CO_2$ Storage in Saline Aquifers. Oil & Gas Science and Technology - Rev. IFP 2005, 60, 559-567.
[19] Michael, K.; Golab, A.; Shulakova, V.; Ennis-King, J.; Allinson, G.; Sharma, S.; Aiken, T. Geological Storage of $CO_2$ in Saline Aquifers—a Review of the Experience from Existing Storage Operations. International Journal of Greenhouse Gas Control 2010, 4, 659-667.
[20] Bachu, S. $CO_2$ Storage in Geological Media: Role, Means, Status and Barriers to Deployment. Progress in Energy and Combustion Science 2008, 34, 254-273.
[21] Chadwick, R. A.; Marchant, B. P.; Williams, G. A. $CO_2$ Storage Monitoring: Leakage Detection and Measurement in Subsurface Volumes from 3D Seismic Data at Sleipner. Energy Procedia 2014, 63, 4224-4239.
[22] Comission, E. Implementation of Directive 2009/31/Ec on the Geological Storage of Carbon Dioxide; 2011.
[23] Global CCS Institue Sleipner $CO_2$ Storage Project. https://www.globalccsinstitute.com/projects/sleipner%C2%A0co2-storage-project
[24] Global CCS Institue IEA Greenhouse Gas Programme Weyburn-Midale $CO_2$ Monitoring and Storage Project. https://hub.globalccsinstitute.com/publications/what-happens-when-co2-stored-

underground-qa-ieaghg-weyburn-midale-co2-monitoring-and-storage-project/what-weyburn-midale-project-wmp
[25] Ringrose, P. S.; Mathieson, A. S.; Wright, I. W.; Selama, F.; Hansen, O.; Bissell, R.; Saoula, N.; Midgley, J. The in Salah $CO_2$ Storage Project: Lessons Learned and Knowledge Transfer. Energy Procedia 2013, 37, 6226-6236.
[26] Hartstein, A.; Kusskraa, V.; Godec, M. Recovering 'Stranded Oil' Can Substantially Add to Us Oil Supplies US Department of Energy Office of Fossil Energy: 2010.
[27] Orr, F. M.; Taber, J. J. Use of Carbon Dioxide in Enhanced Oil Recovery. Science 1984, 224, 563-569.
[28] Blunt, M.; Fayers, F. J.; Orr, F. M. Carbon-Dioxide in Enhanced Oil-Recovery. Energy Conversion and Management 1993, 34, 1197-1204.
[29] Saudi Aramco Uthmaniyah $CO_2$-EOR Demonstration Project.
http://www.saudiaramco.com/en/home/news-media/news/capturing-carbon.html
[30] Shell The Peterhead Carbon Capture and Storage Project.
[31] Global CCS Institue White Rose CCS Project.
https://www.globalccsinstitute.com/projects/white-rose-ccs-project
[32] Global CCS Institue The Global Status of CCS Summary Report; 2016.
[33] IPCC Special Report on Carbon Dioxide Capture and Storage; 2005.
[34] Jaubert, J. N.; Avaullee, L.; Souvay, J. F. A Crude Oil Data Bank Containing More Than 5000 Pvt and Gas Injection Data. Journal of Petroleum Science and Engineering 2002, 34, 65-107.
[35] Kiran, E.; Pöhler, H.; Xiong, Y. Volumetric Properties of Pentane+ Carbon Dioxide at High Pressures. Journal of Chemical & Engineering Data 1996, 41, 158-165.
[36] Cullick, A. S.; Mathis, M. L. Densities and Viscosities of Mixtures of Carbon Dioxide and n-Decane from 310 K to 403 K and 7 to 30 MPa. Journal of Chemical and Engineering Data 1984, 29, 393-396.
[37] Munkejord, S. T.; Hammer, M.; Lovseth, S. W. $CO_2$ Transport: Data and Models - a Review. Applied Energy 2016, 169, 499-523.
[38] Kunz, O.; Klimeck, R.; Wagner, W.; Jaeschke, M. The GERG-2004 Wide-Range Equation of State for Natural Gases and Other Mixtures. GERG TM15 2007 2007.
[39] Kunz, O.; Wagner, W. The GERG-2008 Wide-Range Equation of State for Natural Gases and Other Mixtures: An Expansion of GERG-2004. Journal of Chemical and Engineering Data 2012, 57, 3032-3091.
[40] Lemmon, E. W.; Span, R. Short Fundamental Equations of State for 20 Industrial Fluids. Journal of Chemical and Engineering Data 2006, 51, 785-850.
[41] Zimmerman, R. W.; King, M. S. In Propagation of Acoustic Waves through Cracked Rock, 20th Symposium on Rock Mechanics, Rapid City, SD, 1985; 1985.
[42] Ewing, M. B.; Mcglashan, M. L.; Trusler, J. P. M. The Speed of Sound in Gases .1. A Cylindrical Interferometer and the Speed of Sound in Argon and in Krypton. Journal of Chemical Thermodynamics 1985, 17, 549-559.
[43] Estrada-Alexanders, A. F.; Trusler, J. P. M. Virial Coefficients of Ethane and (Methane Plus Ethane) Determined from the Speed of Sound. 1994 IChemE Research Event, Vols 1 and 2 1994, 670-672.
[44] Natarajan, S.; Randolph, T. W. Ultrasonic Velocity Measurements in Supercritical Jet Fuel. The Journal of Supercritical Fluids 1997, 10, 65-70.
[45] Ke, J.; Han, B.; George, M. W.; Yan, H.; Poliakoff, M. Acoustic Measurements of Critical Points for Four-Component Mixtures in Hydroformylation Reactions in Carbon Dioxide. Fluid Phase Equilibria 2001, 185, 327-337.
[46] Ye, S. Y.; Lagourette, B.; Alliez, J.; Saintguirons, H.; Xans, P.; Montel, F. Comparison with Experimental-Data of Ultrasound Velocity in Pure Hydrocarbons Calculated from Equations of State. Fluid Phase Equilibria 1992, 74, 157-175.
[47] Davila, M. J.; Trusler, J. P. M. Thermodynamic Properties of Mixtures of n-Methyl-2-Pyrrolidinone and Methanol at Temperatures between 298.15 K and 343.15 K and Pressures up to 60 MPa. Journal of Chemical Thermodynamics 2009, 41, 35-45.
[48] Davis, L. A.; Gordon, R. B. Compression of Mercury at High Pressure. The Journal of Chemical Physics 1967, 46, 2650-2660.

[49] Estrada-Alexanders, A. F.; Trusler, J. P. M.; Zarari, M. P. Determination of Thermodynamic Properties from the Speed of Sound. International Journal of Thermophysics 1995, 16, 663-673.
[50] Lin, C. W.; Trusler, J. P. M. The Speed of Sound and Derived Thermodynamic Properties of Pure Water at Temperatures between (253 and 473) K and at Pressures up to 400 MPa. Journal of Chemical Physics 2012, 136.
[51] Sun, T. F.; Tenseldam, C. A.; Kortbeek, P. J.; Trappeniers, N. J.; Biswas, S. N. Acoustic and Thermodynamic Properties of Ethanol from 273.15 to 333.15 K and up to 280 MPa. Physics and Chemistry of Liquids 1988, 18, 107-116.
[52] Ball, S. J.; Trusler, J. P. M. Speed of Sound of n-Hexane and n-Hexadecane at Temperatures between 298 and 373 K and Pressures up to 100 MPa. International Journal of Thermophysics 2001, 22, 427-443.
[53] Trusler, J. P. M., Physical Acoustics and Metrology of Fluids - Adam Hilger Series on Measurement Science and Technology. Adam Hilger: 1991; Vol. 1.
[54] Mehl, J. B. Analysis of Resonance Standing-Wave Measurements. The Journal of the Acoustical Society of America 1978, 64, 1523-1525.
[55] Ewing, M. B.; Trusler, J. P. M. On the Analysis of Acoustic Resonance Measurement. The Journal of the Acoustical Society of America 1989, 85, 1780-1782.
[56] Ewing, M. B.; McGlashan, M. L.; Trusler, J. P. M. The Temperature-Jump Effect and the Theory of the Thermal Boundary Layer for a Spherical Resonator. Speeds of Sound in Argon at 273.16k. Metrologia 1986, 22, 93.
[57] Goodwin, A. R. H.; Martin Trusler, J. P., Chapter 9 Speed of Sound Measurements and Heat Capacities of Gases. In Heat Capacities: Liquids, Solutions and Vapours, The Royal Society of Chemistry: 2010; pp 185-217.
[58] Goodwin, A. R. H.; Moldover, M. R. Thermophysical Properties of Gaseous Refrigerants from Speed of Sound Measurements. I. Apparatus, Model, and Results for 1,1,1,2-Tetrafluoroethane R134a. The Journal of Chemical Physics 1990, 93, 2741-2753.
[59] Moldover, M. R.; Trusler, J. P. M.; Edwards, T. J.; Mehl, J. B.; Davis, R. S. Measurement of the Universal Gas-Constant R Using a Spherical Acoustic Resonator. Journal of Research of the National Bureau of Standards 1988, 93, 85-144.
[60] Ewing, M. B.; Goodwin, A. R. H. An Apparatus Based on a Spherical Resonator for Measuring the Speed of Sound in Gases at High Pressures. Results for Argon at Temperatures between 255 K and 300 K and at Pressures up to 7 MPa. The Journal of Chemical Thermodynamics 1992, 24, 531-547.
[61] Trusler, J. P. M.; Zarari, M. The Speed of Sound and Derived Thermodynamic Properties of Methane at Temperatures between 275 K and 375 K and Pressures up to 10 MPa. Journal of Chemical Thermodynamics 1992, 24, 973-991.
[62] Takagi, T.; Teranishi, H. Ultrasonic Speed in Compressed Liquid by a Sing-Around Method. Journal of Chemical Thermodynamics 1987, 19, 1299-1304.
[63] Takagi, T.; Teranishi, H. Ultrasonic Speeds and Thermodynamics for (Toluene + Ortho-Xylene) and (Toluene + Aniline) under High-Pressures. Journal of Chemical Thermodynamics 1985, 17, 1057-1062.
[64] Takagi, T.; Teranishi, H. Ultrasonic Speeds and Thermodynamics for Binary-Solutions of Normal-Alkanes under High-Pressures. Fluid Phase Equilibria 1985, 20, 315-320.
[65] Takagi, T.; Teranishi, H. Ultrasonic Speed in Liquid-Phase of Bromotrifluoromethane (R13b1) under High-Pressures. Journal of Chemical and Engineering Data 1986, 31, 291-293.
[66] Daridon, J. L.; Lagourette, B. Ultrasonic Velocity Measurements at High Pressure for the Thermophysical Characterization of a Ternary Mixture. Acustica 1996, 82, 32-38.
[67] Daridon, J. L.; Lagourette, B.; Gaubert, J. F.; Xans, P.; Montel, F. Ultrasonic Velocity in a Hyperbaric Reservoir Fluid. Ultrasonics 1996, 34, 447-449.
[68] Daridon, J. L.; Lagourette, B.; Grolier, J. P. E. Experimental Measurements of the Speed of Sound in n-Hexane from 293 to 373 K and up to 150 MPa. International Journal of Thermophysics 1998, 19, 145-+.
[69] Daridon, J. L.; Lagourette, B.; Lagrabette, A. Acoustic Determination of Thermodynamic Properties of Ternary Liquid Mixtures up to 150 MPa. Physics and Chemistry of Liquids 1999, 37, 137-160.

[70] Lainez, A.; Gopal, P.; Zollweg, J. A.; Streett, W. B. Speed-of-Sound Measurements for Liquid Trichlorofluoromethane under Pressure. Journal of Chemical Thermodynamics 1989, 21, 773-777.
[71] Lainez, A.; Miller, J. F.; Zollweg, J. A.; Streett, W. B. Volumetric and Speed-of-Sound Measurements for Liquid Tetrachloromethane under Pressure. Journal of Chemical Thermodynamics 1987, 19, 1251-1260.
[72] Lainez, A.; Zollweg, J. A.; Streett, W. B. Speed-of-Sound Measurements for Liquid n-Pentane and 2,2-Dimethylpropane under Pressure. Journal of Chemical Thermodynamics 1990, 22, 937-948.
[73] Kortbeek, P. J.; Muringer, M. J. P.; Trappeniers, N. J.; Biswas, S. N. Apparatus for Sound Velocity Measurements in Gases up to 10 kbar: Experimental Data for Argon. Review of Scientific Instruments 1985, 56, 1269-1273.
[74] Sun, T.; Bominaar, S.; Ten Seldam, C.; Biswas, S. Evaluation of the Thermophysical Properties of Toluene and n-Heptane from 180 to 320 K and up to 260 MPa from Speed-of-Sound Data. Berichte der Bunsengesellschaft für physikalische Chemie 1991, 95, 696-704.
[75] Takagi, T. Ultrasonic Speeds in Compressed Liquid and Vapor Pressures for 1,1,1,2-Tetrafluoroethane. Journal of Chemical and Engineering Data 1996, 41, 1061-1065.
[76] Sun, T.; Biswas, S. N.; Trappeniers, N. J.; Ten Seldam, C. A. Acoustic and Thermodynamic Properties of Methanol from 273 to 333 K and at Pressures to 280 MPa. Journal of Chemical & Engineering Data 1988, 33, 395-398.
[77] Sun, T. F.; Kortbeek, P. J.; Trappeniers, N. J.; Biswas, S. N. Acoustic and Thermodynamic Properties of Benzene and Cyclohexane as a Function of Pressure and Temperature. Physics and Chemistry of Liquids 1987, 16, 163-178.
[78] Papadakis, E. P. Ultrasonic Phase Velocity by the Pulse-Echo-Overlap Method Incorporating Diffraction Phase Corrections. The Journal of the Acoustical Society of America 1967, 42, 1045-1051.
[79] Jr., A. O. W. The Piston Source at High Frequencies. The Journal of the Acoustical Society of America 1951, 23, 1-6.
[80] Albo, P. A. G.; Lago, S.; Romeo, R.; Lorefice, S. High Pressure Density and Speed-of-Sound Measurements in n-Undecane and Evidence of the Effects of near-Field Diffraction. Journal of Chemical Thermodynamics 2013, 58, 95-100.
[81] Lin, C. W.; Trusler, J. P. M. Speed of Sound in (Carbon Dioxide + Propane) and Derived Sound Speed of Pure Carbon Dioxide at Temperatures between (248 and 373) K and at Pressures up to 200 MPa. Journal of Chemical and Engineering Data 2014, 59, 4099-4109.
[82] Rivas, C.; Gimeno, B.; Artal, M.; Blanco, S. T.; Fernandez, J.; Velasco, I. High-Pressure Speed of Sound in Pure $CO_2$ and in $CO_2$ with $So_2$ as an Impurity Using Methanol as a Doping Agent. International Journal of Greenhouse Gas Control 2016, 54, 737-751.
[83] Swanson, J. C. Pressure Coefficients of Acoustic Velocity for Nine Organic Liquids. The Journal of Chemical Physics 1934, 2, 689-693.
[84] Richardson, E. G.; Tait, R. I. Ratios of Specific Heat and High-Frequency Viscosities in Organic Liquids under Pressure, Derived from Ultrasonic Propagation. Philosophical Magazine 1957, 2, 441-454.
[85] Carnevale, E. H.; Litovitz, T. A. Pressure Dependence of Sound Propagation in the Primary Alcohols. The Journal of the Acoustical Society of America 1955, 27, 547-550.
[86] Boelhouwer, J. W. M. Sound Velocities and Adiabetic Compressibilities of Liquid Alkanes at Various Temperatures and Pressures. Physica 1967, 34, 484-492.
[87] Van Itterbeek, A.; Thoen, J.; Cops, A.; Van Dael, W. Sound Velocity Measurements in Liquid Methane as a Function of Pressure. Physica 1967, 35, 162-166.
[88] Oakley, B. A.; Barber, G.; Worden, T.; Hanna, D. Ultrasonic Parameters as a Function of Absolute Hydrostatic Pressure. I. A Review of the Data for Organic Liquids. Journal of Physical and Chemical Reference Data 2003, 32, 1501-1533.
[89] Oakley, B. A.; Hanna, D.; Shillor, M.; Barber, G. Ultrasonic Parameters as a Function of Absolute Hydrostatic Pressure. II. Mathematical Models of the Speed of Sound in Organic Liquids. Journal of Physical and Chemical Reference Data 2003, 32, 1535-1544.

[90] Bobik, M. Thermodynamic Quantities for Liquid Benzene 1. Sound Velocities between 283 and 463 K and up to 62 MPa. The Journal of Chemical Thermodynamics 1978, 10, 1137-1146.
[91] Bobik, M.; Niepmann, R.; Marius, W. Thermodynamic Quantities for Liquid Carbon Tetrachloride 1. Sound Velocities between 265 and 435 K and up to 62 MPa. The Journal of Chemical Thermodynamics 1979, 11, 351-357.
[92] Niepmann, R. Thermodynamic Properties of Propane and n-Butane 2. Speeds of Sound in the Liquid up to 60 MPa. The Journal of Chemical Thermodynamics 1984, 16, 851-860.
[93] Muringer, M. J. P.; Trappeniers, N. J.; Biswas, S. N. The Effect of Pressure on the Sound-Velocity and Density of Toluene and n-Heptane up to 2600 Bar. Physics and Chemistry of Liquids 1985, 14, 273-295.
[94] Estrada-Alexanders, A. F.; Trusler, J. P. M. The Speed of Sound and Derived Thermodynamic Properties of Ethane at Temperatures between 220 K and 450 K and Pressures up to 10.5 MPa. The Journal of Chemical Thermodynamics 1997, 29, 991-1015.
[95] Dutour, S.; Lagourette, B.; Daridon, J. L. High-Pressure Speed of Sound and Compressibilities in Heavy Normal Hydrocarbons: n-$C_{23}H_{48}$ and n-$C_{24}H_{50}$. Journal of Chemical Thermodynamics 2001, 33, 765-774.
[96] Lagourette, B.; Daridon, J. L. Speed of Sound, Density, and Compressibility of Petroleum Fractions from Ultrasonic Measurements under Pressure. Journal of Chemical Thermodynamics 1999, 31, 987-1000.
[97] Takagi, T. Ultrasonic Speed for Liquid Trichlorofluoromethane and 1,1-Dichloro-2,2,2-Trifluoroethane at Temperatures from 283 K to 373 K and Pressures up to 75 MPa. Journal of Chemical and Engineering Data 1991, 36, 394-398.
[98] Takagi, T. Ultrasonic Speeds in Compressed Liquid and Vapor Pressures for Pentafluoroethane. Journal of Chemical and Engineering Data 1996, 41, 1325-1328.
[99] Takagi, T.; Fukushima, M. Ultrasonic Speeds in Dense Liquid of 1,1,1,2,2-Pentafluoro-3,3-Dichloropropane and 1,1,2,2,3-Pentafluoro-1,3-Dichloropropane. Thermochimica Acta 1998, 317, 65-72.
[100] Takagi, T.; Hongo, M. Ultrasonic Speeds in Liquid 1,1-Dichloro-1-Fluoroethane at Temperatures from 283 to 373 K and Pressures up to 50 MPa. Journal of Chemical and Engineering Data 1993, 38, 60-62.
[101] Takagi, T.; Noguchi, M. Ultrasonic Speeds and Thermodynamic Properties for Pentafluoropropyl Alcohol, Tetrafluoropropyl Alcohol and Trifluoroethyl Alcohol under High-Pressures. Thermochimica Acta 1992, 195, 239-249.
[102] Takagi, T.; Teranishi, H. Ultrasonic Speeds in Liquid-Phase of Dichlorotetrafluoroethane (R114) under High-Pressures. Journal of Chemical and Engineering Data 1986, 31, 105-107.
[103] Takagi, T.; Teranishi, H. Ultrasonic Speeds in Liquid Monochlorodifluoromethane (R22) and Monochloropentafluoroethane (R115) under High-Pressures. Journal of Chemical and Engineering Data 1988, 33, 169-173.
[104] Richardson, E. G. The Rheology of Transitions. Rheologica Acta 1958, 1, 251-257.
[105] Kir'yakov, B.; Otpushchennikov, N. Dependence of Speed of Sound on Pressure in Liquids. Ul'trazvuk I Fiziko-himicheskie Svoisva Veshecva 1971, 104-112.
[106] Belinskii, B. A.; Ikramov, S. K. Comprehensive Investigation of Acoustical Parameters, Viscosity, and Density of n-Pentane over a Wide Pressure Interval. Soviet Physics Acoustics-Ussr 1973, 18, 300-303.
[107] Otpushchennikov, N. F.; Kir'yakov, B. S.; Panin, P. P. Velocity of Sound and Some Thermodynamic Properties of Liquid n-Pentane in a Wide Range of Temperatures and Pressures. Izv. Vyssh. Uchebn. Zaved., Neft Gaz 1974, 17, 73-7.
[108] Ismagilov, R. G.; Ermakov, G. V. Speed of Sound in Superheated Organic Liquids. Teplofizika Vysokikh Temperatur 1982, 20, 677-682.
[109] Zotov V V, M. Y. F., Mel'nikov G A, Neruchev Yu A Sound Velocity in Liquid Hydrocarbons. Skorost' Zvuka v Zhidkikh Uglevodorodakh 1995.
[110] Ding, Z. S.; Alliez, J.; Boned, C.; Xans, P. Automation of an Ultrasound Velocity Measurement System in High-Pressure Liquids. Measurement Science and Technology 1997, 8, 154-161.

[111] Tahani, H. Determination of the Velocity of Sound in Reservoir Fluids Using an Equation of State. Heriot-Watt University, 2011.
[112] Rolling, R. E.; Vogt, C. J. The Adiabatic Bulk Modulus of Normal Paraffin Hydrocarbons from Hexane to Hexadecane. Journal of Basic Engineering 1960, 82, 635-642.
[113] Eden, H.; Richardson, E. The Propagation of Ultrasonics in Organic Liquids under Pressure. Variation of Specific Heat Ratio and Viscosity with Pressure. Acta Acustica united with Acustica 1960, 10, 309-315.
[114] Allegra, J. R.; Hawley, S. A.; Holton, G. Attenuation of Sound in Suspensions and Emulsions. Journal of the Acoustical Society of America 1970, 48, 108-&.
[115] Hawley, S.; Allegra, J.; Holton, G. Ultrasonic-Absorption and Sound-Speed Data for 9 Liquids at High Pressures. Journal of the Acoustical Society of America 1970, 47, 137-&.
[116] Badalyan, A. L.; Otpushchennikov, N. F.; Shoitov, Y. S. Speed of Sound in n-Hexane, n-Heptane and n-Nonane:Dependence on Pressure and Temperature. Uch. Zap. Kursk. Gos. Pedagog. Inst. 1971, 135-143.
[117] Ermakov, G. V.; Ismagilov, R. G., Speed of Ultrasound, Adiabatic Compressibility, and Heat-Capacity of Superheated Liquid n-Hexane. In 1976; Vol. 14, pp 975-977.
[118] Kagramanyan, L.; Badalyan, A. Pulsed Experimental Arrangement for Measurements of Ultrasound Velocity in Liquids under Pressure up to 2 000 Atm. Izv. Akad. Nauk Arm. SSSR Fiz 1978, 13, 478.
[119] Bohidar, H. B. Brillouin-Scattering Study of Equation of State of Single Component Liquids. Journal of Applied Physics 1988, 64, 1810-1815.
[120] Khasanshin, T. S.; Shchemelev, A. P. Sound Velocity in Liquid n-Alkanes. High Temperature 2001, 39, 60-67.
[121] Khasanshin, T. S.; Samuilov, V. S.; Shchemelev, A. P. Speed of Sound in n-Hexane, n-Octane, n-Decane, and n-Hexadecane in the Liquid State. Journal of Engineering Physics and Thermophysics 2008, 81, 760-765.
[122] Golik, A. Z.; Adamenko, I. I.; Makhno, M. G. Equation of State, Elastic and Thermal-Properties of Molecular Liquids .1. Benzene, Toluene and Ethylbenzene. Ukrainskii Fizicheskii Zhurnal 1982, 27, 708-711.
[123] Nakamura, Y.; Fujishiro, I.; Tamura, T. Evaluation of Sound-Velocity and Density of Lubricants under High-Pressure by Brillouin-Scattering Using Diamond-Anvil Cell. Jsme International Journal Series C-Dynamics Control Robotics Design and Manufacturing 1995, 38, 122-127.
[124] Dzida, M.; Ernst, S. Speed of Sound in Propan-1-ol Plus Heptane Mixtures under Elevated Pressures. Journal of Chemical and Engineering Data 2003, 48, 1453-1457.
[125] Dzida, M.; Zak, A.; Ernst, S. Thermodynamic and Acoustic Properties of Binary Mixtures of Alcohols and Alkanes. I. Speed of Sound in (Ethanol Plus n-Heptane) under Elevated Pressures. Journal of Chemical Thermodynamics 2005, 37, 405-414.
[126] Dzida, M.; Cempa, M. Thermodynamic and Acoustic Properties of (Heptane Plus Dodecane) Mixtures under Elevated Pressures. Journal of Chemical Thermodynamics 2008, 40, 1531-1541.
[127] Dzida, M.; Waleczek, L. Speed of Sound, Density, and Heat Capacity for (2-Methyl-2-Butanol + Heptane) at Pressures up to 100 MPa and Temperatures from (293 to 318) K. Experimental Results and Theoretical Investigations. Journal of Chemical Thermodynamics 2010, 42, 312-322.
[128] Hasanov, V. H. The Speed of Sound of n-Heptane, n-Octane and Their Binary Mixtures at Temperatures T= 293.15 to 523.15 K and Pressures up to 60 MPa. High Temperature 2012, 50, 44-51.
[129] Badalyan, A. L.; Otpushchennikov, N. F.; Shoitov, Y. S. Experimental Study of Sound Velocity in Some Liquid Hydrocarbons of Ethylene Series over Wide Range of Temperatures and Pressures. Izvestiya Vysshikh Uchebnykh Zavedenii Fizika 1971.
[130] Lago, S.; Albo, P. A. G.; Ripa, D. M. Speed-of-Sound Measurements in n-Nonane at Temperatures between 293.15 and 393.15 K and at Pressures up to 100 MPa. International Journal of Thermophysics 2006, 27, 1083-1094.
[131] Ye, S.; Alliez, J.; Lagourette, B.; Saintguirons, H.; Arman, J.; Xans, P. Adapted Apparatus for Measurements of Ultrasonic Velocity and Attenuation in Liquids at High-Pressure. Revue De Physique Appliquee 1990, 25, 555-565.

[132] Nascimento, F. P.; Mehl, A.; Ribas, D. C.; Paredes, M. L. L.; Costa, A. L. H.; Pessoa, F. L. P. Experimental High Pressure Speed of Sound and Density of (Tetralin Plus n-Decane) and (Tetralin Plus n-Hexadecane) Systems and Thermodynamic Modeling. Journal of Chemical Thermodynamics 2015, 81, 77-88.
[133] Bessieres, D.; Plantier, F. Thermodynamic Consistency between Calorimetric Acoustic and Volumetric Measurements - Application to n-Undecane. Journal of Thermal Analysis and Calorimetry 2007, 89, 81-85.
[134] Daridon, J. L.; Lagourette, B. Ultrasonic Velocity of Liquid Tridecane and Tetradecane as a Function of Temperature and Pressure. High Temperatures-High Pressures 2000, 32, 83-87.
[135] Khasanshin, T. S.; Poddubskii, O. G.; Shchemelev, A. P. Experimental Study of the Velocity of Sound in Liquid n-Tetradecane at Temperatures from 303.15 to 433.15 K and Pressures to 100 MPa. Journal of Engineering Physics and Thermophysics 2004, 77, 185-188.
[136] Dovnar, D. V.; Lebedinskii, Y. A.; Khasanshin, T. S.; Shchemelev, A. P. The Thermodynamic Properties of n-Pentadecane in the Liquid State, Determined by the Results of Measurements of Sound Velocity. High Temperature 2001, 39, 835-839.
[137] Daridon, J. L.; Carrier, H.; Lagourette, B. Pressure Dependence of the Thermophysical Properties of n-Pentadecane and n-Heptadecane. International Journal of Thermophysics 2002, 23, 697-708.
[138] Richardson, E. G.; Tait, R. I. Ratios of Specific Heat and High-Frequency Viscosities in Organic Liquids under Pressure, Derived from Ultrasonic Propagation. Philosophical Magazine 1957, 2, 441-454.
[139] Takagi, T. Ultrasonic Speeds and Thermodynamic Properties of (Benzene + Cyclohexane) under High-Pressures. Journal of Chemical Thermodynamics 1980, 12, 1183-1190.
[140] Mustafaev, R. Thermophysical Properties of Hydrocarbons at High State Parameters. Energiya, Moscow 1980.
[141] Takagi, T.; Teranishi, H. Ultrasonic Speeds and Thermodynamic Properties of (Benzene + Nitrobenzene) under High-Pressures. Journal of Chemical Thermodynamics 1982, 14, 1167-1173.
[142] Takagi, T.; Sawada, K.; Urakawa, H.; Ueda, M.; Cibulka, I. Speed of Sound in Liquid Tetrachloromethane and Benzene at Temperatures from 283.15 K to 333.15 K and Pressures up to 30 MPa. Journal of Chemical Thermodynamics 2004, 36, 659-664.
[143] Wegge, R.; Richter, M.; Span, R. Speed of Sound Measurements in Ethanol and Benzene over the Temperature Range from (253.2 to 353.2) K at Pressures up to 30 MPa. Journal of Chemical and Engineering Data 2015, 60, 1345-1353.
[144] Kreutzenbeck, H. J.; Ledwig, R.; Wurflinger, A. Ultrasonic Measurements in Liquid and Plastic Phases. Berichte Der Bunsen-Gesellschaft-Physical Chemistry Chemical Physics 1983, 87, 893-898.
[145] Okhotin, V. S.; Razumeichenko, L. A.; Skorodumov, A. V. The Heat Capacity of Liquid Toluene at Saturation Line. TVT 1987, 25, 812–814.
[146] Okhotin, V. S.; Razumeichenko, L.; Kas' yanov, Y. I.; Skorodumov, A. V. Equation of State and Thermodynamic Properties of Liquid m-Xylene Obtained from Data on Sound Velocity. Teplofizika vysokikh temperatur 1998, 36, 903-907.
[147] Meier, K.; Kabelac, S. Measurements of the Speed of Sound in Liquid Toluene. Journal of Chemical and Engineering Data 2013, 58, 1398-1406.
[148] Herget, C. M. Ultrasonic Velocity in Carbon Dioxide and Ethylene in the Critical Region. The Journal of Chemical Physics 1940, 8, 537-542.
[149] Bass, R.; Lamb, J. Ultrasonic Relaxation of the Vibrational Specific Heat of Carbon Dioxide, Sulphur Hexafluoride, Nitrous Oxide, Cyclopropane and Methyl Chloride in the Liquid State. Proceedings of the Royal Society of London. Series A. Mathematical and Physical Sciences 1958, 247, 168-185.
[150] Gruzdev, V. A.; Slabnyak, V. I. Study of the Equilibrium Speed of Sound in Dissociating Nitrogen Tetroxide Vapors. Izv. Sib. Otd. Akad. Nauk SSSR, Ser. Tekh. Nauk. 1975, 3, 140-143.
[151] Vargaftik, N. B., Handbook of Physical Properties of Liquids and Gases: Pure Substances and Mixtures. Hemisphere Pub. Corp.: Washington, 1983; p xii, 758 p.
[152] Pitaevskaya, L. L.; Bilevich, A. V. Speed of Ultrasound in Carbonic-Acid Gas at Pressures to 4,5 Kilobars. Zhurnal Fizicheskoi Khimii 1973, 47, 227-229.

[153] Estrada-Alexanders, A. F.; Trusler, J. P. M. Speed of Sound in Carbon Dioxide at Temperatures between (220 and 450) K and Pressures up to 14 MPa. Journal of Chemical Thermodynamics 1998, 30, 1589-1601.
[154] Liu, Q.; Feng, X. J.; An, B. L.; Duan, Y. Y. Speed of Sound Measurements Using a Cylindrical Resonator for Gaseous Carbon Dioxide and Propene. Journal of Chemical and Engineering Data 2014, 59, 2788-2798.
[155] Al Ghafri, S.; Maitland, G. C.; Trusler, J. P. M. Densities of Aqueous $MgCl_2$(aq), $CaCl_2$(aq), KI(aq), NaCl(aq), KCl(aq), $AlCl_3$(aq), and (0.964 NaCl+00136 KCl)(aq) at Temperatures between (283 and 472) K, Pressures up to 68.5 MPa, and Molalities up to 6 $mol.kg^{-1}$. Journal of Chemical and Engineering Data 2012, 57, 1288-1304.
[156] Al Ghafri, S. Z.; Maitland, G. C.; Trusler, J. P. M. Densities of $SrCl_2$(aq), $Na_2SO_4$(aq), $NaHCO_3$(aq), and Two Synthetic Reservoir Brines at Temperatures between (298 and 473) K, Pressures up to 68.5 MPa, and Molalities up to 3 $mol.kg^{-1}$. Journal of Chemical and Engineering Data 2013, 58, 402-412.
[157] Wagner, W.; Kleinrahm, R.; Lösch, H. W.; Watson, J. T. R.; Majer, V.; Pádua, A. A. H.; Woolf, L. A.; Holste, J. C.; De Figueiredo Palavra, A. M.; Fujii, K.; Stansfeld, J. W., 5 - Density. In Experimental Thermodynamics, A.R.H. Goodwin, K. N. M.; Wakeham, W. A., Eds. Elsevier: 2003; Vol. Volume 6, pp 125-235.
[158] Beams, J. W. Magnetic Suspension Balance. Physical Review 1950, 78, 471-472.
[159] Kleinrahm, R.; Wagner, W. Measurement and Correlation of the Equilibrium Liquid and Vapour Densities and the Vapour Pressure Along the Coexistence Curve of Methane. The Journal of Chemical Thermodynamics 1986, 18, 739-760.
[160] Wagner, W.; Brachthauser, K.; Kleinrahm, R.; Losch, H. W. A New, Accurate Single-Sinker Densitometer for Temperatures from 233 to 523 K at Pressures up to 30 MPa. International Journal of Thermophysics 1995, 16, 399-411.
[161] Klimeck, J.; Kleinrahm, R.; Wagner, W. An Accurate Single-Sinker Densimeter and Measurements of the (p, ρ, T) Relation of Argon and Nitrogen in the Temperature Range from (235 to 520) K at Pressures up to 30 MPa. Journal of Chemical Thermodynamics 1998, 30, 1571-1588.
[162] Wagner, W.; Kleinrahm, R. Densimeters for Very Accurate Density Measurements of Fluids over Large Ranges of Temperature, Pressure, and Density. Metrologia 2004, 41, S24-S39.
[163] Assael, M. J.; Oliveira, C. P.; Papadaki, M.; Wakeham, W. A. Vibrating-Wire Viscometers for Liquids at High-Pressures. International Journal of Thermophysics 1992, 13, 593-615.
[164] Assael, M. J.; Papadaki, M.; Dix, M.; Richardson, S. M.; Wakeham, W. A. An Absolute Vibrating-Wire Viscometer for Liquids at High-Pressures. International Journal of Thermophysics 1991, 12, 231-244.
[165] Assael, M. J.; Wakeham, W. A. Vibrating-Wire Viscometry on Liquids at High-Pressure. Fluid Phase Equilibria 1992, 75, 269-285.
[166] Ciotta, F.; Trusler, J. P. M. Improved Understanding of Vibrating-Wire Viscometer-Densimeters. Journal of Chemical and Engineering Data 2010, 55, 2195-2201.
[167] Padua, A. A. H.; Fareleira, J. M. N. A.; Calado, J. C. G.; Wakeham, W. A. A Vibrating-Wire Densimeter for Liquids at High-Pressures - the Density of 2,2,4-Trimethylpentane from 298.15 to 348.15 K and up to 100 MPa. International Journal of Thermophysics 1994, 15, 229-243.
[168] Holcomb, C. D.; Outcalt, S. L. A Theoretically-Based Calibration and Evaluation Procedure for Vibrating-Tube Densimeters. Fluid Phase Equilibria 1998, 150, 815-827.
[169] Kratky, O.; Leopold, H.; Stabinger, H. Dichtemessungen an Fluessigkeiten Und Gasen Auf $10^{-6}$ $g/cm^3$ Bei 0, 6 $cm^3$ Praeparatvol-Umen. Z. Angew. Phys. 1969, 27, 273.
[170] Stabinger, H. Density Measurement Using Modern Oscillating Transducers. South Yorkshire Trading Unit 1994.
[171] Fandino, O.; Lugo, L.; Comunas, M. J. P.; Lopez, E. R.; Fernandez, J. Temperature and Pressure Dependences of Volumetric Properties of Two Poly(Propylene Glycol) Dimethyl Ether Lubricants. Journal of Chemical Thermodynamics 2010, 42, 84-89.
[172] Wagner, W.; Pruss, A. The IAPWS Formulation 1995 for the Thermodynamic Properties of Ordinary Water Substance for General and Scientific Use. Journal of Physical and Chemical Reference Data 2002, 31, 387-535.

[173] Span, R.; Lemmon, E. W.; Jacobsen, R. T.; Wagner, W.; Yokozeki, A. A Reference Equation of State for the Thermodynamic Properties of Nitrogen for Temperatures from 63.151 to 1000 K and Pressures to 2200 MPa. Journal of Physical and Chemical Reference Data 2000, 29, 1361-1433.
[174] Span, R.; Wagner, W. A New Equation of State for Carbon Dioxide Covering the Fluid Region from the Triple-Point Temperature to 1100 K at Pressures up to 800 MPa. Journal of Physical and Chemical Reference Data 1996, 25, 1509-1596.
[175] Ortiz-Vega, D. O. A New Wide-Range Equation of State for Helium-4. Texas A&M University, 2013.
[176] Dymond, J. H.; Malhotra, R. Densities of n-Alkanes and Their Mixtures at Elevated Pressures. International Journal of Thermophysics 1987, 8, 541-555.
[177] Dymond, J. H.; Malhotra, R. The Tait Equation - 100 Years On. International Journal of Thermophysics 1988, 9, 941-951.
[178] Assael, M. J.; Dymond, J. H.; Exadaktilou, D. An Improved Representation for n-Alkane Liquid Densities. International Journal of Thermophysics 1994, 15, 155-164.
[179] Cibulka, I.; Hnedkovsky, L. Liquid Densities at Elevated Pressures of n-Alkanes from C-5 to C-16: A Critical Evaluation of Experimental Data. Journal of Chemical and Engineering Data 1996, 41, 657-668.
[180] Liu, K.; Wu, Y.; McHugh, M. A.; Baled, H.; Enick, R. M.; Morreale, B. D. Equation of State Modeling of High-Pressure, High-Temperature Hydrocarbon Density Data. Journal of Supercritical Fluids 2010, 55, 701-711.
[181] NguyenHuynh, D.; Passarello, J. P.; Tobaly, P. In Situ Determination of Phase Equilibria of Methyl Benzoate + Alkane Mixtures Using an Infrared Absorption Method. Comparison with Polar Gc-SAFT Predictions. Journal of Chemical & Engineering Data 2009, 54, 1685-1691.
[182] Pecar, D.; Dolecek, V. Isothermal Compressibilities and Isobaric Expansibilities of Pentane, Hexane, Heptane and Their Binary and Ternary Mixtures from Density Measurements. Fluid Phase Equilibria 2003, 211, 109-127.
[183] Gozalpour, F.; Danesh, A.; Todd, A. C.; Tohidi, B. Viscosity and Density Data of Two North Sea Gas Condensate Samples at Temperatures to 423 K and Pressures to 140 MPa. Journal of Chemical and Engineering Data 2001, 46, 1305-1308.
[184] Tohidi, B.; Burgass, R. W.; Danesh, A.; Todd, A. C. Viscosity and Density of Methane Plus Methylcyclohexane from (323 to 423) K and Pressures to 140 MPa. Journal of Chemical and Engineering Data 2001, 46, 385-390.
[185] Byun, H.; DiNoia, T.; McHugh, M. High Pressure Density of Ethane, Pentane, Deuterated Pentane, 25.5 wt% Ethane in Deuterated Pentane, 2.4 wt% Deuterated Poly (Ethylene-Co-Butene)(Peb) in Ethane, 5.3 wt% Hydrogenated Peb in Pentane, 5.1 wt% Hydrogenated Peb in Deuterated Pentane, and 4.9 wt% Hydrogenated Peb in Deuterated Pentane+ 23.1 wt% Ethane. J. Chem. Eng. Data 2000, 45, 810.
[186] Pohler, H.; Kiran, E. Volumetric Properties of Sulfur Hexafluoride Plus Pentane and Sulfur Hexafluoride Plus Toluene at High Pressures. Journal of Chemical and Engineering Data 1997, 42, 389-394.
[187] Kiran, E.; Pohler, H.; Xiong, Y. Volumetric Properties of Pentane Plus Carbon Dioxide at High Pressures. Journal of Chemical and Engineering Data 1996, 41, 158-165.
[188] Ivanis, G. R.; Tasic, A. Z.; Radovic, I. R.; Djordjevic, B. D.; Serbanovic, S. P.; Kijevcanin, M. L. J. Modeling of Density and Calculations of Derived Volumetric Properties for n-Hexane, Toluene and Dichloromethane at Pressures 0.1-60 MPa and Temperatures 288.15-413.15 K. Journal of the Serbian Chemical Society 2015, 80, 1423-+.
[189] Lampreia, I. M. S.; de Castro, C. A. N. A New and Reliable Calibration Method for Vibrating Tube Densimeters over Wide Ranges of Temperature and Pressure. Journal of Chemical Thermodynamics 2011, 43, 537-545.
[190] Zhou, J. G.; Zhu, R. J.; Xu, H. F.; Tian, Y. L. Densities, Excess Molar Volumes, Isothermal Compressibilities, and Isobaric Expansivities of Dimethyl Carbonate Plus Cyclohexane Systems at Temperatures from (293.15 to 313.15) K and Pressures from (0.1 to 40) MPa. Journal of Chemical and Engineering Data 2010, 55, 5569-5575.
[191] Valencia, J. L.; Gonzalez-Salgado, D.; Troncoso, J.; Peleteiro, J.; Carballo, E.; Romani, L. Thermophysical Characterization of Liquids Using Precise Density and Isobaric Heat Capacity

Measurements as a Function of Pressure. Journal of Chemical and Engineering Data 2009, 54, 904-915.
[192] Sanmamed, Y. A.; Dopazo-Paz, A.; Gonzalez-Salgado, D.; Troncoso, J.; Romani, L. An Accurate Calibration Method for High Pressure Vibrating Tube Densimeters in the Density Interval (700 to 1600) kg . $m^{-3}$. Journal of Chemical Thermodynamics 2009, 41, 1060-1068.
[193] Lasarte, J. M.; Martin, L.; Langa, E.; Urieta, J. S.; Mainar, A. M. Setup and Validation of a P Rho T Measuring Device. Volumetric Behavior of the Mixture 1,8-Cineole + Ethanol. Journal of Chemical and Engineering Data 2008, 53, 1393-1400.
[194] Goldon, A.; Malka, I.; Hofman, T. Densities and Excess Volumes of the 1-Chlorobutane Plus n-Hexane System at Temperatures from (283.15 to 333.15) K and Pressures from (0.1 to 35) MPa. Journal of Chemical and Engineering Data 2008, 53, 1039-1045.
[195] Camacho-Camacho, L. E.; Galicia-Luna, L. A. Experimental Densities of Hexane Plus Benzothiophene Mixtures from (313 to 363) K and up to 20 MPa. Journal of Chemical and Engineering Data 2007, 52, 2455-2461.
[196] Kumagai, A.; Tomida, D.; Yokoyama, C. Measurements of the Liquid Viscosities of Mixtures of n-Butane, n-Hexane, and n-Octane with Squalane to 30 MPa. International Journal of Thermophysics 2006, 27, 376-393.
[197] Verdier, S.; Andersen, S. I. Internal Pressure and Solubility Parameter as a Function of Pressure. Fluid Phase Equilibria 2005, 231, 125-137.
[198] Troncoso, J.; Bessieres, D.; Cerdeirina, C. A.; Carballo, E.; Romani, L. Automated Measuring Device of (p, r, T) Data - Application to the 1-Hexanol Plus n-Hexane System. Fluid Phase Equilibria 2003, 208, 141-154.
[199] Pimentel-Rodas, A.; Galicia-Luna, L. A.; Castro-Arellano, J. J. Capillary Viscometer and Vibrating Tube Densimeter for Simultaneous Measurements up to 70 MPa and 423 K. Journal of Chemical & Engineering Data 2016, 61, 45-55.
[200] Haghbakhsh, R.; Zolghadr, A.; Raeissi, S.; Ayatollahi, S. Investigation of Volumetric Fluid Properties of (Heptane + Hexadecane) at Reservoir Conditions. Journal of Natural Gas Science and Engineering 2015, 22, 377-394.
[201] Iglesias-Silva, G. A.; Bravo-Sánchez, M.; Estrada-Baltazar, A.; Bouchot, C.; Hall, K. R. p–ρ–T Data for 1-Butanol and Isobutyl Alcohol from (283.15 to 363.15) K at Pressures up to 66 MPa. Journal of Chemical & Engineering Data 2015, 60, 1076-1090.
[202] Alaoui, F. E. M.; Montero, E. A.; Qiu, G. S.; Aguilar, F.; Wu, J. T. Liquid Density of Biofuel Mixtures: 1-Heptanol + Heptane System at Pressures up to 140 MPa and Temperatures from 298.15 K to 393.15 K. Journal of Chemical Thermodynamics 2013, 65, 174-183.
[203] Zolghadr, A.; Riazi, M.; Escrochi, M.; Ayatollahi, S. Investigating the Effects of Temperature, Pressure, and Paraffin Groups on the N2 Miscibility in Hydrocarbon Liquids Using the Interfacial Tension Measurement Method. Industrial & Engineering Chemistry Research 2013, 52, 9851-9857.
[204] Sagdeev, D. I.; Fomina, M. G.; Mukhamedzyanov, G. K.; Abdulagatov, I. M. Experimental Study of the Density and Viscosity of n-Heptane at Temperatures from 298 K to 470 K and Pressure Upto 245 MPa. International Journal of Thermophysics 2013, 34, 1-33.
[205] Schedemann, A.; Wallek, T.; Zeymer, M.; Maly, M.; Gmehling, J. Measurement and Correlation of Biodiesel Densities at Pressures up to 130 MPa. Fuel 2013, 107, 483-492.
[206] Quevedo-Nolasco, R.; Galicia-Luna, L. A.; Elizalde-Solis, O. Compressed Liquid Densities for the (n-Heptane Plus n-Decane) and (n-Octane Plus n-Decane) Systems from T = (313 to 363) K. Journal of Chemical Thermodynamics 2012, 44, 133-147.
[207] Abdulagatov, I. M.; Azizov, N. D. (p,ρ,T,x) and Viscosity Measurements of {x(1)n-Heptane + (1-x(1)) n-Octane} Mixtures at High Temperatures and High Pressures. Journal of Chemical Thermodynamics 2006, 38, 1402-1415.
[208] Watson, G.; Zeberg-Mikkelsen, C. K.; Baylaucq, A.; Boned, C. High-Pressure Density Measurements for the Binary System Ethanol Plus Heptane. Journal of Chemical and Engineering Data 2006, 51, 112-118.
[209] Schilling, G.; Kleinrahm, R.; Wagner, W. Measurement and Correlation of the (p, ρ, T) Relation of Liquid n-Heptane, n-Nonane, 2,4-Dichlorotoluene, and Bromobenzene in the Temperature

Range from (233.15 to 473.15) K at Pressures up to 30 MPa for Use as Density Reference Liquids. Journal of Chemical Thermodynamics 2008, 40, 1095-1105.
[210] Fandiño, O.; Pensado, A. S.; Lugo, L.; Comuñas, M. J. P.; Fernández, J. Compressed Liquid Densities of Squalane and Pentaerythritol Tetra(2-Ethylhexanoate). Journal of Chemical & Engineering Data 2005, 50, 939-946.
[211] Acevedo, I. L.; Lugo, L.; Comunas, M. J. P.; Arancibia, E. L.; Fernandez, J. Volumetric Properties of Binary Tetraethylene Glycol Dimethyl Ether Plus Heptane Mixtures between (278.15 and 353.15) K and up to 25 MPa. Journal of Chemical and Engineering Data 2003, 48, 1271-1278.
[212] Morávková, L.; Linek, J. Temperature Dependence of the Excess Molar Volume of (Heptane + 1-Chloroalkane). The Journal of Chemical Thermodynamics 2002, 34, 1387-1395.
[213] Comunas, M. J. P.; Lopez, E. R.; Pires, P.; Garcia, J.; Fernandez, J. p ρ T Measurements of Polyethylene Glycol Dimethylethers between 278.15 and 328.15 K at Pressures to 12 MPa. International Journal of Thermophysics 2000, 21, 831-851.
[214] Ihmels, E. Viscosity Measurements with a Ubbelohde-Viscosimeter and Density Measurements with a Resonance Frequency Transducer Prototype. Diplomarbeit 1998, 1-120.
[215] Ulbig, P.; Bubolz, M.; Kornek, C.; Schulz, S. Excess Volumes of Binary Mixtures Containing Diisopropyl Ether Plus 1-Butanol or Diisopropyl Ether Plus Diethyl Ketone and Ethanol Plus Heptane at High Pressures. Journal of Chemical and Engineering Data 1997, 42, 449-452.
[216] Baylaucq, A.; Boned, C.; Dauge, P.; Lagourette, B. Measurements of the Viscosity and Density of Three Hydrocarbons and the Three Associated Binary Mixtures Versus Pressure and Temperature. International Journal of Thermophysics 1997, 18, 3-23.
[217] Gayol, A.; Casas, L. M.; Martini, R. E.; Andreatta, A. E.; Legido, J. L. Volumetric Properties of (Dialkyl Carbonate Plus n-Alkane) Mixtures at High Pressures: Experimental Measurement and Nitta-Chao Model Prediction. Journal of Chemical Thermodynamics 2013, 58, 245-253.
[218] Sato, Y.; Yoshioka, H.; Aikawa, S.; Smith, R. L. A Digital Variable-Angle Rolling-Ball Viscometer for Measurement of Viscosity, Density, and Bubble-Point Pressure of $CO_2$ and Organic Liquid Mixtures. International Journal of Thermophysics 2010, 31, 1896-1903.
[219] Moravkova, L.; Wagner, Z.; Linek, J. (p, $V_m$, T) Measurements of (Octane Plus Benzene) at Temperatures from (298.15 to 328.15) K and at Pressures up to 40 MPa. Journal of Chemical Thermodynamics 2008, 40, 607-617.
[220] Goodwin, A. R. H.; Donzier, E. P.; Vancauwenberghe, O.; Fitt, A. D.; Ronaldson, K. A.; Wakeham, W. A.; de Lara, M. M.; Marty, F.; Mercier, B. A Vibrating Edge Supported Plate, Fabricated by the Methods of Micro Electro Mechanical System for the Simultaneous Measurement of Density and Viscosity: Results for Methylbenzene and Octane at Temperatures between (323 and 423) K and Pressures in the Range (0.1 to 68) MPa. Journal of Chemical and Engineering Data 2006, 51, 190-208.
[221] Moravkova, L.; Linek, J. Excess Molar Volumes of (Benzene Plus Isopropylbenzene, or 1,3,5-Trimethylbenzene, or 1,2,4-Trimethylbenzene) at Temperatures between 298.15 K and 328.15 K. Journal of Chemical Thermodynamics 2003, 35, 1139-1149.
[222] Goodwin, A. R. H.; Bradsell, C. H.; Toczylkin, L. S. (p,ρ,T) of Liquid n-Octane Obtained with a Spherical Pycnometer at Temperatures of 298.03 K and 313.15 K and Pressures in the Range 0.7 MPa to 32 MPa. Journal of Chemical Thermodynamics 1996, 28, 637-646.
[223] Moravkova, L.; Wagner, Z.; Linek, J. (p, $V_m$, T) Measurements of (Cyclohexane Plus Nonane) at Temperatures from 298.15 K to 328.15 K and at Pressures up to 40 MPa. Journal of Chemical Thermodynamics 2007, 39, 1637-1648.
[224] Kariznovi, M.; Nourozieh, H.; Abedi, J. Phase Composition and Saturated Liquid Properties in Binary and Ternary Systems Containing Carbon Dioxide, n-Decane, and n-Tetradecane. Journal of Chemical Thermodynamics 2013, 57, 189-196.
[225] Fandiño, O.; Lugo, L.; Segovia, J. J.; López, E. R.; Comuñas, M. J. P.; Fernández, J. High Pressure Densities of Carbon Dioxide + Dipentaerythritol Hexaheptanoate: New Experimental Setup and Volumetric Behavior. The Journal of Supercritical Fluids 2011, 58, 189-197.
[226] Caudwell, D. R.; Trusler, J. P. M.; Vesovic, V.; Wakeham, W. A. Viscosity and Density of Five Hydrocarbon Liquids at Pressures up to 200 MPa and Temperatures up to 473 K. Journal of Chemical and Engineering Data 2009, 54, 359-366.

[227] Segovia, J. J.; Fandino, O.; Lopez, E. R.; Lugo, L.; Martin, M. C.; Fernandez, J. Automated Densimetric System: Measurements and Uncertainties for Compressed Fluids. Journal of Chemical Thermodynamics 2009, 41, 632-638.
[228] Zuniga-Moreno, A.; Galicia-Luna, L. A.; Camacho-Camacho, L. E. Compressed Liquid Densities and Excess Volumes of $CO_2$ + Decane Mixtures from (313 to 363) K and Pressures up to 25 MPa. Journal of Chemical and Engineering Data 2005, 50, 1030-1037.
[229] Audonnet, F.; Padua, A. A. H. Viscosity and Density of Mixtures of Methane and n-Decane from 298 to 393 K and up to 75 MPa. Fluid Phase Equilibria 2004, 216, 235-244.
[230] Troncoso, J.; Bessieres, D.; Cerdeirina, C. A.; Carballo, E.; Romani, L. p ρ T x Data for the Dimethyl Carbonate Plus Decane System. Journal of Chemical and Engineering Data 2004, 49, 923-927.
[231] Bessieres, D.; Saint-Guirons, H.; Daridon, J. L. Volumetric Behavior of Decane Plus Carbon Dioxide at High Pressures. Measurement and Calculation. Journal of Chemical and Engineering Data 2001, 46, 1136-1139.
[232] Elizalde-Solis, O.; Garcia-Fuentes, D.; Alvarez-Badillo, S.; Zuniga-Moreno, A.; Camacho-Camacho, L. E.; Galicia-Luna, L. A. Densities of Cresols and Linear Alkane Mixtures at High Pressure. Journal of Chemical and Engineering Data 2013, 58, 2163-2175.
[233] Regueira, T.; Yan, W.; Stenby, E. H. Densities of the Binary Systems n-Hexane + n-Decane and n-Hexane + n-Hexadecane up to 60 MPa and 463 K. Journal of Chemical & Engineering Data 2015, 60, 3631-3645.
[234] Zhang, Y.; Liu, Z. Y.; Liu, W. G.; Zhao, J. F.; Yang, M. J.; Liu, Y.; Wang, D. Y.; Song, Y. C. Measurement and Modeling of the Densities for $CO_2$ + Dodecane System from 313.55 K to 353.55 K and Pressures up to 18 MPa. Journal of Chemical and Engineering Data 2014, 59, 3668-3676.
[235] Elizalde-Solis, O.; Galicia-Luna, L. A.; Camacho-Camacho, L. E. High-Pressure Vapor-Liquid Equilibria for $CO_2$ Plus Alkanol Systems and Densities of n-Dodecane and n-Tridecane. Fluid Phase Equilibria 2007, 259, 23-32.
[236] Caudwell, D. R.; Trusler, J. P. M.; Vesovic, V.; Wakeham, W. A. The Viscosity and Density of n-Dodecane and n-Octadecane at Pressures up to 200 MPa and Temperatures up to 473 K. International Journal of Thermophysics 2004, 25, 1339-1352.
[237] Dauge, P.; Canet, X.; Baylaucq, A.; Boned, C. Measurements of the Density and Viscosity of the Tridecane Plus 2,2,4,4,6,8,8-Heptamethylnonane Mixtures in the Temperature Range 293.15-353.15 K at Pressures up to 100 MPa. High Temperatures-High Pressures 2001, 33, 213-230.
[238] Nourozieh, H.; Kariznovi, M.; Abedi, J. Measurement and Correlation of Saturated Liquid Properties and Gas Solubility for Decane, Tetradecane and Their Binary Mixtures Saturated with Carbon Dioxide. Fluid Phase Equilibria 2013, 337, 246-254.
[239] Kariznovi, M.; Nourozieh, H.; Abedi, J. Measurement and Modeling of Liquid Saturated Properties (Solubility, Density, and Viscosity) of (Ethane Plus n-Tetradecane) Binary Systems. Journal of Chemical and Engineering Data 2011, 56, 3669-3672.
[240] Tarassov, I. N.; Wappmann, S.; Ludemann, H. D. p,T-Dependence of Self-Diffusion in the Fluid One Phase Region of the System Tetradecane/Methane. Polish Journal of Chemistry 1997, 71, 1763-1776.
[241] Baled, H. O.; Xing, D. Z.; Katz, H.; Tapriyal, D.; Gamwo, I. K.; Soong, Y.; Bamgbade, B. A.; Wu, Y.; Liu, K.; McHugh, M. A.; Enick, R. M. Viscosity of n-Hexadecane, n-Octadecane and n-Eicosane at Pressures up to 243 MPa and Temperatures up to 534 K. Journal of Chemical Thermodynamics 2014, 72, 108-116.
[242] Wu, Y.; Bamgbade, B.; Liu, K.; McHugh, M. A.; Baled, H.; Enick, R. M.; Burgess, W. A.; Tapriyal, D.; Morreale, B. D. Experimental Measurements and Equation of State Modeling of Liquid Densities for Long-Chain n-Alkanes at Pressures to 265 MPa and Temperatures to 523 K. Fluid Phase Equilibria 2011, 311, 17-24.
[243] Outcalt, S.; Laesecke, A.; Fortin, T. J. Density and Speed of Sound Measurements of Hexadecane. Journal of Chemical Thermodynamics 2010, 42, 700-706.
[244] Rajagopal, K.; Andrade, L. L. P. R.; Paredes, M. L. L. High-Pressure Viscosity Measurements for the Binary System Cyclohexane Plus n-Hexadecane in the Temperature Range of (318.15 to 413.15) K. Journal of Chemical and Engineering Data 2009, 54, 2967-2970.

[245] Amorim, J. A.; Chiavone-Filho, O.; Paredes, M. L. L.; Rajagopal, K. High-Pressure Density Measurements for the Binary System Cyclohexane Plus n-Hexadecane in the Temperature Range of (318.15 to 413.15) K. Journal of Chemical and Engineering Data 2007, 52, 613-618.
[246] Chang, J. S.; Lee, M. J.; Lin, H. M. Densities of Binary Mixtures of Hexadecane with m-Xylene and Tetralin from 333 K to 413 K and Pressures up to 30 MPa. Journal of Chemical and Engineering Data 1998, 43, 233-237.
[247] Moravkova, L.; Wagner, Z.; Linek, J. (p, V, T, x) Measurements of the System Benzene Plus 1,3,5-Trimethylbenzene at Temperatures from 298.15 to 328.15 K and at Pressures up to 40 MPa. Fluid Phase Equilibria 2003, 209, 81-94.
[248] Fornefeld-Schwarz, U. M.; Svejda, P. Refractive Indices and Relative Permittivities of Liquid Mixtures of γ-Butyrolactone, γ-Valerolactone, δ-Valerolactone, or ε-Caprolactone + Benzene, + Toluene, or + Ethylbenzene at 293.15 K and 313.15 K and Atmospheric Pressure. Journal of Chemical & Engineering Data 1999, 44, 597-604.
[249] Guan, J. G.; Kariznovi, M.; Nourozieh, H.; Abedi, J. Density and Viscosity for Mixtures of Athabasca Bitumen and Aromatic Solvents. Journal of Chemical and Engineering Data 2013, 58, 611-624.
[250] Sommer, D.; Kleinrahm, R.; Span, R.; Wagner, W. Measurement and Correlation of the (p, ρ, T) Relation of Liquid Cyclohexane, Toluene, and Ethanol in the Temperature Range from 233.15 K to 473.15 K at Pressures up to 30 MPa for Use as Density Reference Liquids. Journal of Chemical Thermodynamics 2011, 43, 117-132.
[251] Chorazewski, M.; Grolier, J. P. E.; Randzio, S. L. Isobaric Thermal Expansivities of Toluene Measured by Scanning Transitiometry at Temperatures from (243 to 423) K and Pressures up to 200 MPa. Journal of Chemical and Engineering Data 2010, 55, 5489-5496.
[252] Glen, N. F.; Johns, A. I. Determination of the Density of Toluene in the Range from (293 to 373) K and from (0.1 to 30) MPa. Journal of Chemical and Engineering Data 2009, 54, 2538-2545.
[253] McLinden, M. O.; Splett, J. D. A Liquid Density Standard over Wide Ranges of Temperature and Pressure Based on Toluene. Journal of Research of the National Institute of Standards and Technology 2008, 113, 29-67.
[254] Kiselev, V. D.; Bolotov, A. V.; Satonin, A.; Shakirova, I.; Kashaeva, H. A.; Konovalov, A. I. Compressibility of Liquids. Rule of Noncrossing V-P Curvatures. Journal of Physical Chemistry B 2008, 112, 6674-6682.
[255] Watson, G.; Lafitte, T.; Zeberg-Mikkelsen, C. K.; Baylaucq, A.; Bessieres, D.; Boned, C. Volumetric and Derivative Properties under Pressure for the System 1-Propanol Plus Toluene: A Discussion of Pc-SAFT and SAFT-VR. Fluid Phase Equilibria 2006, 247, 121-134.
[256] Zeberg-Mikkelsen, C. K.; Lugo, L.; Garcia, J.; Fernandez, J. Volumetric Properties under Pressure for the Binary System Ethanol Plus Toluene. Fluid Phase Equilibria 2005, 235, 139-151.
[257] Avelino, H. M. T.; Fareleira, J. M. N. A.; Wakeham, W. A. Simultaneous Measurement of the Density and Viscosity of Compressed Liquid Toluene. International Journal of Thermophysics 2003, 24, 323-336.
[258] Gu, Z. Y.; Brennecke, J. F. Volume Expansivities and Isothermal Compressibilities of Imidazolium and Pyridinium-Based Ionic Liquids. Journal of Chemical and Engineering Data 2002, 47, 339-345.
[259] Masui, R. Development of a Magnetic Suspension Densimeter and Measurement of the Density of Toluene. International Journal of Thermophysics 2002, 23, 921-935.
[260] Ihmels, E. C.; Gmehling, J. Densities of Toluene, Carbon Dioxide, Carbonyl Sulfide, and Hydrogen Sulfide over a Wide Temperature and Pressure Range in the Sub- and Supercritical State. Industrial & Engineering Chemistry Research 2001, 40, 4470-4477.
[261] Belonenko, V. N.; Troitsky, V. M.; Belyaev, Y. E.; Dymond, J. H.; Glen, N. F. Application of a Micro-(p, V, T) Apparatus for Measurement of Liquid Densities at Pressures up to 500 MPa. Journal of Chemical Thermodynamics 2000, 32, 1203-1219.
[262] Franck, E. U.; Kerschbaum, S.; Wiegand, G. The Density of Toluene at High Pressures to 673 K and 300 MPa. Berichte Der Bunsen-Gesellschaft-Physical Chemistry Chemical Physics 1998, 102, 1794-1797.
[263] Magee, J. W.; Bruno, T. J. Isochoric (p,ρ,T) Measurements for Liquid Toluene from 180 K to 400 K at Pressures to 35 MPa. Journal of Chemical and Engineering Data 1996, 41, 900-905.

[264] Pohler, H.; Kiran, E. Volumetric Properties of Carbon Dioxide Plus Toluene at High Pressures. Journal of Chemical and Engineering Data 1996, 41, 482-486.
[265] Padua, A.; Wakeham, W. A.; Wilhelm, J. The Viscosity of Liquid Carbon-Dioxide. International Journal of Thermophysics 1994, 15, 767-777.
[266] Duarte-Garza, H. A.; Magee, J. W. Isochoric p-r-T Measurements on {(x)$CO_2$+(1-x)$C_2H_6$, x Approximate to 0.25, 0.49, 0.74} from (220 to 400) K at Pressures to 35 MPa. Journal of Chemical and Engineering Data 2001, 46, 1095-1100.
[267] Harris, J. G.; Yung, K. H. Carbon Dioxides Liquid-Vapor Coexistence Curve and Critical Properties as Predicted by a Simple Molecular-Model. Journal of Physical Chemistry 1995, 99, 12021-12024.
[268] Gokmenoglu, Z.; Xiong, Y.; Kiran, E. Volumetric Properties of Carbon Dioxide Plus Sulfur Hexafluoride at High Pressures. Journal of Chemical and Engineering Data 1996, 41, 354-360.
[269] Teng, H.; Yamasaki, A.; Chun, M. K.; Lee, H. Solubility of Liquid $CO_2$ in Water at Temperatures from 278 K to 293 K and Pressures from 6.44 MPa to 29.49 MPa and Densities of the Corresponding Aqueous Solutions. Journal of Chemical Thermodynamics 1997, 29, 1301-1310.
[270] Lau, W. W. R.; Hwang, C. A.; Holste, J. C.; Hall, K. R.; Gammon, B. E.; Marsh, K. N. Densities of Carbon Dioxide Plus Ethane Mixtures from 240 K to 450 K at Pressures up to 35 MPa. Journal of Chemical and Engineering Data 1997, 42, 900-902.
[271] van der Gulik, P. S. Viscosity of Carbon Dioxide in the Liquid Phase. Physica A: Statistical Mechanics and its Applications 1997, 238, 81-112.
[272] Klimeck, J.; Kleinrahm, R.; Wagner, W. Measurements of the (p, ρ, T) Relation of Methane and Carbon Dioxide in the Temperature Range 240 K to 520 K at Pressures up to 30 MPa Using a New Accurate Single-Sinker Densimeter. Journal of Chemical Thermodynamics 2001, 33, 251-267.
[273] Saleh, B.; Wendland, M. Measurement of Vapor Pressures and Saturated Liquid Densities of Pure Fluids with a New Apparatus. Journal of Chemical and Engineering Data 2005, 50, 429-437.
[274] Liu, Z. T.; Wu, J.; Liu, L.; Sun, C. A.; Song, L. P.; Gao, Z. W.; Dong, W. S.; Lu, J. Solubilities of Aot Analogues Surfactants in Supercritical $CO_2$ and HFC-134a Fluids. Journal of Chemical and Engineering Data 2006, 51, 1761-1768.
[275] Pensado, A. S.; Padua, A. A. H.; Comunas, M. J. P.; Fernandez, J. High-Pressure Viscosity and Density of Carbon Dioxide Plus Pentaerythritol Ester Mixtures: Measurements and Modeling. Aiche Journal 2008, 54, 1625-1636.
[276] Tallon, S.; Fenton, K. The Solubility of Water in Mixtures of Dimethyl Ether and Carbon Dioxide. Fluid Phase Equilibria 2010, 298, 60-66.
[277] Gil, L.; Martinez-Lopez, J. F.; Artal, M.; Blanco, S. T.; Embid, J. M.; Fernandez, J.; Otin, S.; Velasco, I. Volumetric Behavior of the {$CO_2$ (1) + $C_2H_6$ (2)} System in the Subcritical (T=293.15 K), Critical, and Supercritical (T=308.15 K) Regions. Journal of Physical Chemistry B 2010, 114, 5447-5469.
[278] Mazzoccoli, M.; Bosio, B.; Arato, E. Analysis and Comparison of Equations-of-State with p-ρ-T Experimental Data for $CO_2$ and $CO_2$-Mixture Pipeline Transport. 6th Trondheim Conference on $CO_2$ Capture, Transport and Storage 2012, 23, 274-283.
[279] Hrncic, M. K.; Skerget, M.; Knez, Z. Density and Viscosity of the Binary Polyethylene Glycol/CO2 Systems. Journal of Supercritical Fluids 2014, 95, 641-668.
[280] Chen, J. W.; Wu, W. Z.; Han, B. X.; Gao, L.; Mu, T. C.; Liu, Z. M.; Jiang, T.; Du, J. M. Phase Behavior, Densities, and Isothermal Compressibility of $CO_2$ Plus Pentane and $CO_2$ Plus Acetone Systems in Various Phase Regions. Journal of Chemical and Engineering Data 2003, 48, 1544-1548.
[281] Tolley, W. K.; Izatt, R. M.; Oscarson, J. L. Simultaneous Measurement of Excess-Enthalpies and Solution Densities in a Flow Calorimeter. Thermochimica Acta 1991, 181, 127-141.
[282] Zhu, R.; Yu, J.; Xu, W.; Liu, Z.; Tian, Y. High Pressure Vapor-Liquid Equilibrium of Carbon Dioxide + Hexane System. CIESC Journal 2006, 57, 2270-2277.
[283] Rabe, D. Experimental Determination of Dynamic Viscosity and Density of Binary Liquid Mixtures of n-Heptane with $CO_2$, $CH_4$, $C_2H_6$, $C_3H_8$ and of Toluene with $CH_4$ and $C_3H_8$. 1981.
[284] Khristoforov, A. V.; Dautov, R. A. Solvation of Gaseous Carbon-Dioxide in Liquid Normal-Heptane as the Phase-Transformation of the 1st Type. Zhurnal Fizicheskoi Khimii 1987, 61, 2656-2659.

[285] Fenghour, A.; Trusler, J. P. M.; Wakeham, W. A. Densities and Bubble Points of Binary Mixtures of Carbon Dioxide and n-Heptane and Ternary Mixtures of n-Butane, n-Heptane and n-Hexadecane. Fluid Phase Equilibria 2001, 185, 349-358.
[286] Medina-Bermudez, M.; Saavedra-Molina, L. A.; Escamilla-Tiburcio, W.; Galicia-Luna, L. A.; Elizalde-Solis, O. (p, ρ, T) Behavior for the Binary Mixtures Carbon Dioxide Plus Heptane and Carbon Dioxide Plus Tridecane. Journal of Chemical and Engineering Data 2013, 58, 1255-1264.
[287] Yu, J. L.; Wang, S. J.; Tian, Y. L. Experimental Determination and Calculation of Thermodynamic Properties of $CO_2$ Plus Octane to High Temperatures and High Pressures. Fluid Phase Equilibria 2006, 246, 6-14.
[288] Nagarajan, N.; Robinson, R. L. Equilibrium Phase Compositions, Phase Densities, and Interfacial-Tensions for $CO_2$ + Hydrocarbon Systems. 2. $CO_2$ + Normal-Decane. Journal of Chemical and Engineering Data 1986, 31, 168-171.
[289] Barrufet, M. A.; Salem, S. K. E.; Tantawy, M.; IglesiasSilva, G. A. Liquid Viscosities of Carbon Dioxide Plus Hydrocarbons from 310 K to 403 K. Journal of Chemical and Engineering Data 1996, 41, 436-439.
[290] Bessieres, D.; Saint-Guirons, H.; Daridon, J. L. Thermodynamic Properties of Liquid n-Pentadecane. Physics and Chemistry of Liquids 2001, 39, 301-313.
[291] Shaver, R. D.; Robinson, R. L.; Gasem, K. A. M. An Automated Apparatus for Equilibrium Phase Compositions, Densities, and Interfacial Tensions: Data for Carbon Dioxide Plus Decane. Fluid Phase Equilibria 2001, 179, 43-66.
[292] Tsuji, T.; Tanaka, S.; Hiaki, T.; Saito, R. Measurements of Bubble Point Pressure $CO_2$ Plus Decane and $CO_2$ Plus Lubricating Oil. Fluid Phase Equilibria 2004, 219, 87-92.
[293] Nourozieh, H.; Bayestehparvin, B.; Kariznovi, M.; Abedi, J. Equilibrium Properties of (Carbon Dioxide Plus n-Decane Plus n-Octadecane) Systems: Experiments and Thermodynamic Modeling. Journal of Chemical and Engineering Data 2013, 58, 1236-1243.
[294] Mejia, A.; Cartes, M.; Segura, H.; Muller, E. A. Use of Equations of State and Coarse Grained Simulations to Complement Experiments: Describing the Interfacial Properties of Carbon Dioxide Plus Decane and Carbon Dioxide Plus Eicosane Mixtures. Journal of Chemical and Engineering Data 2014, 59, 2928-2941.
[295] Enick, R.; Holder, G. D.; Morsi, B. I. Critical and 3 Phase-Behavior in the Carbon-Dioxide Tridecane System. Fluid Phase Equilibria 1985, 22, 209-224.
[296] Gasem, K. A. M.; Dickson, K. B.; Dulcamara, P. B.; Nagarajan, N.; Robinson, R. L. Equilibrium Phase Compositions, Phase Densities, and Interfacial-Tensions for $CO_2$ + Hydrocarbon Systems .5. $CO_2$ + n-Tetradecane. Journal of Chemical and Engineering Data 1989, 34, 191-195.
[297] Tanaka, H.; Yamaki, Y.; Kato, M. Solubility of Carbon-Dioxide in Pentadecane, Hexadecane, and Pentadecane Plus Hexadecane. Journal of Chemical and Engineering Data 1993, 38, 386-388.
[298] King, M. B.; Kassim, K.; Bott, T. R.; Sheldon, J. R.; Mahmud, R. S. Prediction of Mutual Solubilities of Heavy Components with Super-Critical and Slightly Sub-Critical Solvents - the Role of Equations of State and Some Applications of a Simple Expanded Lattice Model at Subcritical Temperatures. Berichte Der Bunsen-Gesellschaft-Physical Chemistry Chemical Physics 1984, 88, 812-820.
[299] Nagarajan, N.; Robinson, R. L. Equilibrium Phase Compositions, Phase Densities, and Interfacial-Tensions for $CO_2$ + Hydrocarbon Systems .3. $CO_2$ + Cyclohexane. 4. $CO_2$ + Benzene. Journal of Chemical and Engineering Data 1987, 32, 369-371.
[300] Chang, C. J.; Chen, C. Y.; Lin, H. C. Solubilities of Carbon Dioxide and Nitrous Oxide in Cyclohexanone, Toluene, and N,N-Dimethylformamide at Elevated Pressures. Journal of Chemical & Engineering Data 1995, 40, 850-855.
[301] Park, S. D.; Kim, C. H.; Choi, C. S. Phase Equilibria and Mixture Densities Measurements of Carbon Dioxide-Toluene System under High Pressure. Korean Chemical Engineering Research 1990, 28, 438.
[302] van der Waals, J. D. The Equation of State for Gases and Liquids (Reprinted from Nobel Lecture, December, 1910). Journal of Supercritical Fluids 2010, 55, 403-414.
[303] H., v. d. W. J. Over De Continuıteit Van Den Gas- En Vloeistoftoestand (on the Continuity of the Gaseous and Liquid State). Leiden University, 1873.

[304] Assael, M. J.; Trusler, J. P. M.; Tsolakis, T. F., Thermophysical Properties of Fluids: An Introduction to Their Prediction. Imperial College Press: 1996.
[305] Soave, G. Equilibrium Constants from a Modified Redlich-Kwong Equation of State. Chemical Engineering Science 1972, 27, 1197-&.
[306] Peng, D.; Robinson, D. B. A New Two-Constant Equation of State. Industrial & Engineering Chemistry Fundamentals 1976, 15, 59-64.
[307] Redlich, O.; Kwong, J. N. S. On the Thermodynamics of Solutions. V. An Equation of State. Fugacities of Gaseous Solutions. Chemical Reviews 1949, 44, 233-244.
[308] Poling, B. E.; Prausnitz, J. M.; O' Connell, J. P., The Properties of Gases and Liquids. 5th ed.; McGraw-Hill: New York, 2000.
[309] Patel, N. C.; Teja, A. S. A New Cubic Equation of State for Fluids and Fluid Mixtures. Chemical Engineering Science 1982, 37, 463-473.
[310] Neau, E.; Hernandez-Garduza, O.; Escandell, J.; Nicolas, C.; Raspo, I. The Soave, Twu and Boston-Mathias Alpha Functions in Cubic Equations of State Part I. Theoretical Analysis of Their Variations According to Temperature. Fluid Phase Equilibria 2009, 276, 87-93.
[311] Neau, E.; Raspo, I.; Escandell, J.; Nicolas, C.; Hernandez-Garduza, O. The Soave, Twu and Boston-Mathias Alpha Functions in Cubic Equations of State. Part II. Modeling of Thermodynamic Properties of Pure Compounds. Fluid Phase Equilibria 2009, 276, 156-164.
[312] Mathias, P. M.; Copeman, T. W. Extension of the Peng-Robinson Equation of State to Complex-Mixtures - Evaluation of the Various Forms of the Local Composition Concept. Fluid Phase Equilibria 1983, 13, 91-108.
[313] Nasrifar, K.; Moshfeghian, M. A Saturated Liquid Density Equation in Conjunction with the Predictive-Soave-Redlich-Kwong Equation of State for Pure Refrigerants and Lng Multicomponent Systems. Fluid Phase Equilibria 1998, 153, 231-242.
[314] Peneloux, A.; Rauzy, E.; Freze, R. A Consistent Correction for Redlich-Kwong-Soave Volumes. Fluid Phase Equilibria 1982, 8, 7-23.
[315] Magoulas, K.; Tassios, D. Thermophysical Properties of Normal-Alkanes from C1 to C20 and Their Prediction for Higher Ones. Fluid Phase Equilibria 1990, 56, 119-140.
[316] Jaubert, J. N.; Mutelet, F. VLE Predictions with the Peng-Robinson Equation of State and Temperature Dependent $k_{ij}$ Calculated through a Group Contribution Method. Fluid Phase Equilibria 2004, 224, 285-304.
[317] Jaubert, J. N.; Vitu, S.; Mutelet, F.; Corriou, J. P. Extension of the PPR78 Model (Predictive 1978, Peng-Robinson EOS with Temperature Dependent $k_{ij}$ Calculated through a Group Contribution Method) to Systems Containing Aromatic Compounds. Fluid Phase Equilibria 2005, 237, 193-211.
[318] Vitu, S.; Jaubert, J. N.; Mutelet, F. Extension of the PPR78 Model (Predictive 1978, Peng-Robinson EOS with Temperature Dependent $k_{ij}$ Calculated through a Group Contribution Method) to Systems Containing Naphtenic Compounds. Fluid Phase Equilibria 2006, 243, 9-28.
[319] Vitu, S.; Privat, R.; Jaubert, J. N.; Mutelet, F. Predicting the Phase Equilibria of $CO_2$ + Hydrocarbon Systems with the PPR78 Model (PR EOS and $k_{ij}$ Calculated through a Group Contribution Method). The Journal of Supercritical Fluids 2008, 45, 1-26.
[320] Jaubert, J. N.; Privat, R. Relationship between the Binary Interaction Parameters ($k_{ij}$) of the Peng-Robinson and Those of the Soave-Redlich-Kwong Equations of State: Application to the Definition of the $PR_2SRK$ Model. Fluid Phase Equilibria 2010, 295, 26-37.
[321] Wertheim, M. S. Fluids with Highly Directional Attractive Forces. 2. Thermodynamic Perturbation-Theory and Integral-Equations. Journal of Statistical Physics 1984, 35, 35-47.
[322] Wertheim, M. S. Fluids with Highly Directional Attractive Forces. 1. Statistical Thermodynamics. Journal of Statistical Physics 1984, 35, 19-34.
[323] Wertheim, M. S. Fluids with Highly Directional Attractive Forces. 4. Equilibrium Polymerization. Journal of Statistical Physics 1986, 42, 477-492.
[324] Wertheim, M. S. Fluids with Highly Directional Attractive Forces. 3. Multiple Attraction Sites. Journal of Statistical Physics 1986, 42, 459-476.
[325] Wertheim, M. S. Fluids of Dimerizing Hard-Spheres, and Fluid Mixtures of Hard-Spheres and Dispheres. Journal of Chemical Physics 1986, 85, 2929-2936.
[326] Chapman, W. G.; Gubbins, K. E.; Jackson, G.; Radosz, M. SAFT - Equation-of-State Solution Model for Associating Fluids. Fluid Phase Equilibria 1989, 52, 31-38.

[327] Chapman, W. G.; Gubbins, K. E.; Jackson, G.; Radosz, M. New Reference Equation of State for Associating Liquids. Industrial & Engineering Chemistry Research 1990, 29, 1709-1721.
[328] McCabe, C.; Galindo, A., Chapter 8 SAFT Associating Fluids and Fluid Mixtures. In Applied Thermodynamics of Fluids, The Royal Society of Chemistry: 2010; pp 215-279.
[329] Chapman, W. G.; Jackson, G.; Gubbins, K. E. Phase-Equilibria of Associating Fluids Chain Molecules with Multiple Bonding Sites. Molecular Physics 1988, 65, 1057-1079.
[330] Jackson, G.; Chapman, W. G.; Gubbins, K. E. Phase-Equilibria of Associating Fluids - Spherical Molecules with Multiple Bonding Sites. Molecular Physics 1988, 65, 1-31.
[331] Johnson, J. K.; Muller, E. A.; Gubbins, K. E. Equation of State for Lennard-Jones Chains. Journal of Physical Chemistry 1994, 98, 6413-6419.
[332] Blas, F. J.; Vega, L. F. Thermodynamic Behaviour of Homonuclear and Heteronuclear Lennard-Jones Chains with Association Sites from Simulation and Theory. Molecular Physics 1997, 92, 135-150.
[333] Blas, F. J.; Vega, L. F. Prediction of Binary and Ternary Diagrams Using the Statistical Associating Fluid Theory (SAFT) Equation of State. Industrial & Engineering Chemistry Research 1998, 37, 660-674.
[334] Goodwin, A.; Marsh, K.; Wakeham, W., Measurement of the Thermodynamic Properties of Single Phases. Elsevier: 2003.
[335] Johnson, J. K.; Zollweg, J. A.; Gubbins, K. E. The Lennard-Jones Equation of State Revisited. Molecular Physics 1993, 78, 591-618.
[336] GilVillegas, A.; Galindo, A.; Whitehead, P. J.; Mills, S. J.; Jackson, G.; Burgess, A. N. Statistical Associating Fluid Theory for Chain Molecules with Attractive Potentials of Variable Range. Journal of Chemical Physics 1997, 106, 4168-4186.
[337] Galindo, A.; Davies, L. A.; Gil-Villegas, A.; Jackson, G. The Thermodynamics of Mixtures and the Corresponding Mixing Rules in the SAFT-VR Approach for Potentials of Variable Range. Molecular Physics 1998, 93, 241-252.
[338] Gross, J.; Sadowski, G. Perturbed-Chain SAFT: An Equation of State Based on a Perturbation Theory for Chain Molecules. Industrial & Engineering Chemistry Research 2001, 40, 1244-1260.
[339] Gross, J.; Sadowski, G. Modeling Polymer Systems Using the Perturbed-Chain Statistical Associating Fluid Theory Equation of State. Industrial & Engineering Chemistry Research 2002, 41, 1084-1093.
[340] Gross, J.; Sadowski, G. Application of the Perturbed-Chain SAFT Equation of State to Associating Systems. Industrial & Engineering Chemistry Research 2002, 41, 5510-5515.
[341] Lafitte, T.; Bessieres, D.; Pineiro, M. M.; Daridon, J. L. Simultaneous Estimation of Phase Behavior and Second-Derivative Properties Using the Statistical Associating Fluid Theory with Variable Range Approach. Journal of Chemical Physics 2006, 124.
[342] Lafitte, T.; Pineiro, M. M.; Daridon, J. L.; Bessieres, D. A Comprehensive Description of Chemical Association Effects on Second Derivative Properties of Alcohols through a SAFT-VR Approach. Journal of Physical Chemistry B 2007, 111, 3447-3461.
[343] Lymperiadis, A.; Adjiman, C. S.; Galindo, A.; Jackson, G. A Group Contribution Method for Associating Chain Molecules Based on the Statistical Associating Fluid Theory (SAFT-Gamma). Journal of Chemical Physics 2007, 127.
[344] Lymperiadis, A.; Adjiman, C. S.; Galindo, A.; Jackson, G. A Heteronuclear Group Contribution Method for Associating Chain Molecules (SAFT-Gamma). 18th European Symposium on Computer Aided Process Engineering 2008, 25, 871-876.
[345] Lymperiadis, A.; Adjiman, C. S.; Jackson, G.; Galindo, A. A Generalisation of the SAFT-Gamma Group Contribution Method for Groups Comprising Multiple Spherical Segments. Fluid Phase Equilibria 2008, 274, 85-104.
[346] Muller, E. A.; Gubbins, K. E. Molecular-Based Equations of State for Associating Fluids: A Review of SAFT and Related Approaches. Industrial & Engineering Chemistry Research 2001, 40, 2193-2211.
[347] Economou, I. G. Statistical Associating Fluid Theory: A Successful Model for the Calculation of Thermodynamic and Phase Equilibrium Properties of Complex Fluid Mixtures. Industrial & Engineering Chemistry Research 2002, 41, 953-962.

[348] Avendano, C.; Lafitte, T.; Galindo, A.; Adjiman, C. S.; Jackson, G.; Muller, E. A. SAFT-Gamma Force Field for the Simulation of Molecular Fluids. 1. A Single-Site Coarse Grained Model of Carbon Dioxide. Journal of Physical Chemistry B 2011, 115, 11154-11169.
[349] Mie, G. Zur Kinetischen Theorie Der Einatomigen Körper. Annalen der Physik 1903, 316, 657-697.
[350] Papaioannou, V.; Lafitte, T.; Avendano, C.; Adjiman, C. S.; Jackson, G.; Muller, E. A.; Galindo, A. Group Contribution Methodology Based on the Statistical Associating Fluid Theory for Heteronuclear Molecules Formed from Mie Segments. Journal of Chemical Physics 2014, 140.
[351] Papaioannou, V.; Calado, F.; Lafitte, T.; Dufal, S.; Sadeqzadeh, M.; Jackson, G.; Adjiman, C. S.; Galindo, A. Application of the SAFT-g Mie Group Contribution Equation of State to Fluids of Relevance to the Oil and Gas Industry. Fluid Phase Equilibria 2016, 416, 104-119.
[352] Lafitte, T.; Apostolakou, A.; Avendano, C.; Galindo, A.; Adjiman, C. S.; Muller, E. A.; Jackson, G. Accurate Statistical Associating Fluid Theory for Chain Molecules Formed from Mie Segments. Journal of Chemical Physics 2013, 139.
[353] Span, R., Multiparameter Equations of State: An Accurate Source of Thermodynamic Property Data Springer-Verlag Berlin Heidelberg: 2000.
[354] Span, R.; Wagner, W. On the Extrapolation Behavior of Empirical Equations of State. International Journal of Thermophysics 1997, 18, 1415-1443.
[355] Lemmon, E. W.; Jacobsen, R. T. A Generalized Model for the Thermodynamic Properties of Mixtures. International Journal of Thermophysics 1999, 20, 825-835.
[356] Lemmon, E. W.; Tillner-Roth, R. A Helmholtz Energy Equation of State for Calculating the Thermodynamic Properties of Fluid Mixtures. Fluid Phase Equilibria 1999, 165, 1-21.
[357] Bell, I. H.; Lemmon, E. W. Automatic Fitting of Binary Interaction Parameters for Multi-Fluid Helmholtz-Energy-Explicit Mixture Models. Journal of Chemical & Engineering Data 2016.
[358] Lemmon, E. W.; Huber, M. L.; McLinden, M. O. NIST Standard Reference Database 23: Reference Fluid Thermodynamic and Transport Properties-REFPROP, 9.1; National Institute of Standards and Technology, National Institute of Standards and Technology, Gaithersburg, 2013.
[359] Span, R.; Eckermann, T.; Herrig, S.; Hielscher, S.; Jager, A.; Thol, M., Trend: Thermodynamic Reference and Engineering Data 2.0. In 2015.
[360] Redlich, O.; Kister, A. T. Algebraic Representation of Thermodynamic Properties and the Classification of Solutions. Industrial & Engineering Chemistry 1948, 40, 345-348.
[361] Ye, S. Y.; Lagourette, B.; Alliez, J.; Saintguirons, H.; Xans, P.; Montel, F. Speed of Sound in Binary-Mixtures as a Function of Temperature and Pressure. Fluid Phase Equilibria 1992, 74, 177-202.
[362] Faradonbeh, M. R.; Abedi, J.; Harding, T. G. Comparative Study of Eight Cubic Equations of State for Predicting Thermodynamic Properties of Alkanes. The Canadian Journal of Chemical Engineering 2013, 91, 101-110.
[363] Lin, C. W.; Ramjugernath, D.; Reddy, P.; Trusler, J. P. M. Speeds of Sound in Liquid and Supercritical Hexafluoropropylene (HFP) and Hexafluoropropylene Oxide (HFPO) at Pressures up to 400 MPa. Journal of Chemical and Engineering Data 2012, 57, 2568-2575.
[364] Peleties, F.; Segovia, J. J.; Trusler, J. P. M.; Vega-Maza, D. Thermodynamic Properties and Equation of State of Liquid Di-Isodecyl Phthalate at Temperature between (273 and 423) K and at Pressures up to 140 MPa. Journal of Chemical Thermodynamics 2010, 42, 631-639.
[365] Okaji, M.; Birch, K. P. Intercomparison of Interferometric Dilatometers at NRLM and NPL. Metrologia 1991, 28, 27-32.
[366] Okaji, M.; Yamada, N.; Nara, K.; Kato, H. Laser Interferometric Dilatometer at Low-Temperatures - Application to Fused-Silica SRM-739. Cryogenics 1995, 35, 887-891.
[367] Berthold, J. W.; Jacobs, S. F.; Norton, M. A. Dimensional Stability of Fused Silica, Invar, and Several Ultralow Thermal-Expansion Materials. Metrologia 1977, 13, 9-16.
[368] McSkimin, H. J. Measurement of Elastic Constants at Low Temperatures by Means of Ultrasonic Waves–Data for Silicon and Germanium Single Crystals, and for Fused Silica. Journal of Applied Physics 1953, 24, 988-997.
[369] Evaluation of Measurement Data – Guide to the Expression of Uncertainty in Measurement. JCGM 100 2008.

[370] Lagourette, B.; Boned, C.; Saintguirons, H.; Xans, P.; Zhou, H. Densimeter Calibration Method Versus Temperature and Pressure. Measurement Science and Technology 1992, 3, 699-703.
[371] Sousa, A. T.; Fialho, P. S.; Decastro, C. A. N.; Tufeu, R.; Leneindre, B. Density of HCFC 142b and of Its Mixture with HCFC 22. Fluid Phase Equilibria 1992, 80, 213-225.
[372] Bouchot, C.; Richon, D. An Enhanced Method to Calibrate Vibrating Tube Densimeters. Fluid Phase Equilibria 2001, 191, 189-208.
[373] Bouchot, C.; Richon, D. Direct Pressure-Volume-Temperature and Vapor-Liquid Equilibrium Measurements with a Single Equipment Using a Vibrating Tube Densimeter up to 393 K and 40 MPa: Description of the Original Apparatus and New Data. Industrial & Engineering Chemistry Research 1998, 37, 3295-3304.
[374] May, E. F.; Tay, W. J.; Nania, M.; Aleji, A.; Al-Ghafri, S.; Trusler, J. P. M. Physical Apparatus Parameters and Model for Vibrating Tube Densimeters at Pressures to 140 MPa and Temperatures to 473 K. Review of Scientific Instruments 2014, 85.
[375] Span, R.; Wagner, W. Equations of State for Technical Applications. III. Results for Polar Fluids. International Journal of Thermophysics 2003, 24, 111-162.
[376] Span, R.; Wagner, W. Equations of State for Technical Applications. II. Results for Nonpolar Fluids. International Journal of Thermophysics 2003, 24, 41-109.
[377] Span, R.; Wagner, W. Equations of State for Technical Applications. I. Simultaneously Optimized Functional Forms for Nonpolar and Polar Fluids. International Journal of Thermophysics 2003, 24, 1-39.
[378] Neruchev, Y. A.; Zotov, V. V.; Otpushchennikov, N. F. Velocity of Sound in the Homologous Series of n-Alkanes. Russ. J. Phys. Chem. 1969, 43, 1597-1599.
[379] Ginnings, D. C.; Furukawa, G. T. Heat Capacity Standards for the Range 14 to 1200°K. Journal of the American Chemical Society 1953, 75, 522-527.
[380] Cerdeirina, C. A.; Tovar, C. A.; Gonzalez-Salgado, D.; Carballo, E.; Romani, L. Isobaric Thermal Expansivity and Thermophysical Characterization of Liquids and Liquid Mixtures. Physical Chemistry Chemical Physics 2001, 3, 5230-5236.
[381] Zhao, X. M.; Liu, Z. G.; Chen, Z. Q. Heat Capacities of Five Mixtures and Emulsion of Buna-S. Journal of Chemical and Engineering Data 2006, 51, 867-870.
[382] Vega-Maza, D.; Segovia, J. J.; Martin, M. C.; Villamanan, R. M.; Villamanan, M. A. Thermodynamic Properties of Biofuels: Heat Capacities of Binary Mixtures Containing Ethanol and Hydrocarbons up to 20 MPa and the Pure Compounds Using a New Flow Calorimeter. Journal of Chemical Thermodynamics 2011, 43, 1893-1896.
[383] Doolittle, A. K. Specific Volumes of n-Alkanes. Journal of Chemical and Engineering Data 1964, 9.
[384] Brostow, W.; Grindley, T.; Macip, M. A. Volumetric Properties of Organic Liquids as a Function of Temperature and Pressure - Experimental-Data and Prediction of Compressibility. Materials Chemistry and Physics 1985, 12, 37-97.
[385] Grindley, T.; Lind, J. E. Residual Energy and Entropy of Hydrocarbon Liquids and Their Relation to Liquid Structure. Journal of Chemical Physics 1978, 68, 5046-5052.
[386] Banipal, T. S.; Garg, S. K.; Ahluwalia, J. C. Heat Capacities and Densities of Liquid n-Octane, n-Nonane, n-Decane, and n-Hexadecane at Temperatures from 318.15-K to 373.15-K and at Pressures up to 10 MPa. Journal of Chemical Thermodynamics 1991, 23, 923-931.
[387] Aminabhavi, T. M.; Gopalkrishna, B. Densities, Viscosities, Refractive-Indexes, and Speeds of Sound of the Binary-Mixtures of Bis(2-Methoxyethyl) Ether with Nonane, Decane, Dodecane, Tetradecane, and Hexadecane at 298.15-K, 308.15-K, and 318.15-K. Journal of Chemical and Engineering Data 1994, 39, 529-534.
[388] Casas, L. M.; Orge, B.; Tojo, J. Liquid-Liquid Equilibria of Methyl Acetate Plus Methanol Plus Octane or Nonane. Journal of Chemical and Engineering Data 2004, 49, 664-667.
[389] Pereira, S. M.; Rivas, M. A.; Real, J. N.; Legido, J. L.; Iglesias, T. P. Densities, Speeds of Sound, and Refractive Indices of the Mixture Nonane Plus Triethylene Glycol Dimethyl Ether at 288.15 K, 293.15 K, 298.15 K, and 308.15 K. Journal of Chemical and Engineering Data 2002, 47, 919-922.
[390] Osborne, N. S.; Ginnings, D. C. Measurements of Heat of Vaporization and Heat Capacity of a Number of Hydrocarbons. Journal of Research of the National Bureau of Standards 1947, 39.

[391] Kuznetsov, M. A.; Kharin, V. E.; Gerasimov, A. A.; Grigor'ev, M. D. Isobaric Heat Capacity of n-Alkanes C7 to C10 at Temperatures 293 to 630 K and Pressures up to 60 MPa. Neft i Gaz 1988, 31.
[392] Finke, H. L.; Gross, M. E.; Waddington, G.; Huffman, H. M. Low-Temperature Thermal Data for the Nine Normal Paraffin Hydrocarbons from Octane to Hexadecane. Journal of the American Chemical Society 1954, 76, 333-341.
[393] Okhotin, V. S.; Razumeichenko, L. A.; Kas'yanov, Y. I.; Skorodumov, A. V. Equation of State and Thermodynamic Properties of Liquid m-Xylene Obtained from Data on Sound Velocity. High Temperature 1998, 36, 880-884.
[394] Dufal, S.; Papaioannou, V.; Sadeqzadeh, M.; Pogiatzis, T.; Chremos, A.; Adjiman, C. S.; Jackson, G.; Galindo, A. Prediction of Thermodynamic Properties and Phase Behavior of Fluids and Mixtures with the SAFT-g Mie Group-Contribution Equation of State. Journal of Chemical and Engineering Data 2014, 59, 3272-3288.
[395] Chirico, R. D.; Steele, W. V. Reconciliation of Calorimetrically and Spectroscopically Derived Thermodynamic Properties at Pressures Greater-Than 0.1 MPa for Benzene and Methylbenzene - the Importance of the 3rd Virial-Coefficient. Industrial & Engineering Chemistry Research 1994, 33, 157-167.
[396] Becker, L.; Aufderhaar, O.; Gmehling, J. Measurement of Heat Capacities for Nine Organic Substances by Tian-Calvet Calorimetry. Journal of Chemical and Engineering Data 2000, 45, 661-664.
[397] Cerdeirina, C. A.; Tovar, C. A.; Carballo, E.; Romani, L.; Delgado, M. D.; Torres, L. A.; Costas, M. Temperature Dependence of the Excess Molar Heat Capacities for Alcohol-Alkane Mixtures. Experimental Testing of the Predictions from a Two-State Model. Journal of Physical Chemistry B 2002, 106, 185-191.
[398] Segovia, J. J.; Vega-Maza, D.; Chamorro, C. R.; Martin, M. C. High-Pressure Isobaric Heat Capacities Using a New Flow Calorimeter. Journal of Supercritical Fluids 2008, 46, 258-264.
[399] Sanchez-Vicente, Y.; Tay, W. J.; Al Ghafri, S. Z.; Trusler, J. P. M. Thermodynamics of the ($CO_2$ + n-Heptane) System. (to be submitted) 2017.
[400] Tay, W. J.; Sanchez-Vicente, Y.; Al Ghafri, S. Z.; Trusler, J. P. M. Thermodynamics of the ($CO_2$ + Methylbenzene) System. (to be submitted) 2017.
[401] Camacho-Camacho, L. E.; Galicia-Luna, L. A.; Elizalde-Solis, O.; Martinez-Ramirez, Z. New Isothermal Vapor-Liquid Equilibria for the $CO_2$ + n-Nonane, and $CO_2$ Plus n-Undecane Systems. Fluid Phase Equilibria 2007, 259, 45-50.
[402] Choi, E. J.; Yeo, S. D. Critical Properties for Carbon Dioxide + n-Alkane Mixtures Using a Variable-Volume View Cell. Journal of Chemical and Engineering Data 1998, 43, 714-716.
[403] Jennings, D. W.; Schucker, R. C. Comparison of High-Pressure Vapor-Liquid Equilibria of Mixtures of $CO_2$ or Propane with Nonane and C-9 Alkylbenzenes. Journal of Chemical and Engineering Data 1996, 41, 831-838.
[404] Ashcroft, S. J.; Isa, M. B. Effect of Dissolved Gases on the Densities of Hydrocarbons. Journal of Chemical & Engineering Data 1997, 42, 1244-1248.
[405] Tay, W. J.; Trusler, J. P. M. Density, Sound Speed and Derived Thermophysical Properties of n-Nonane at Temperatures between (283.15 and 473.15) K and at Pressures up to 390 MPa. Journal of Chemical & Engineering Data 2017, (to be submitted).
[406] Lay, E. N. Measurement and Correlation of Bubble Point Pressure in ($CO_2$ + $C_6H_6$), ($CO_2$ + $CH_3C_6H_5$), ($CO_2$ + $C_6H_{14}$), and ($CO_2$ + $C_7H_{16}$) at Temperatures from (293.15 to 313.15) K. Journal of Chemical and Engineering Data 2010, 55, 223-227.
[407] Chang, C. M. J. The Solubility of Carbon Dioxide in Organic Solvents at Elevated Pressures. Fluid Phase Equilibria 1992, 74, 235-242.
[408] Wu, W. Z.; Ke, J.; Poliakoff, M. Phase Boundaries of $CO_2$ + Toluene, $CO_2$ + Acetone, and $CO_2$ + Ethanol at High Temperatures and High Pressures. Journal of Chemical and Engineering Data 2006, 51, 1398-1403.
[409] Al Ghafri, S.; Maitland, G. C.; Trusler, J. P. M. Phase Behaviour of the System (Carbon Dioxide + n-Heptane + Methylbenzene): A Comparison between Experimental Data and SAFT-γ Mie Predictions. Fluid Phase Equilibria 2017, (to be submitted).

[410] Tay, W. J.; Trusler, J. P. M. Density, Sound Speed and Derived Thermophysical Properties of Methylbenzene at Temperatures between (283.15 and 473.15) K and at Pressures up to 390 MPa. Journal of Chemical & Engineering Data 2017, (to be submitted).
[411] Peleties, F.; Trusler, J. P. M. Viscosity of Liquid Di-Isodecyl Phthalate at Temperatures between (274 and 373) K and at Pressures up to 140 MPa. Journal of Chemical and Engineering Data 2011, 56, 2236-2241.
[412] Retsina, T.; Richardson, S. M.; Wakeham, W. A. The Theory of a Vibrating-Rod Viscometer. Applied Scientific Research 1987, 43, 325-346.
[413] Santos, F. J. V.; de Castro, C. A. N.; Dymond, J. H.; Dalaouti, N. K.; Assael, M. J.; Nagashima, A. Standard Reference Data for the Viscosity of Toluene. Journal of Physical and Chemical Reference Data 2006, 35, 1-8.
[414] Huber, M. L.; Laesecke, A.; Perkins, R. Transport Properties of n-Dodecane. Energy & Fuels 2004, 18, 968-975.
[415] Assael, M. J.; Dymond, J. H.; Papadaki, M.; Patterson, P. M. Correlation and Prediction of Dense Fluid Transport-Coefficients. 2. Simple Molecular Fluids. Fluid Phase Equilibria 1992, 75, 245-255.
[416] Assael, M. J.; Dymond, J. H.; Papadaki, M.; Patterson, P. M. Correlation and Prediction of Dense Fluid Transport-Coefficients. 3. Normal-Alkane Mixtures. International Journal of Thermophysics 1992, 13, 659-669.
[417] Assael, M. J.; Dymond, J. H.; Papadaki, M.; Patterson, P. M. Correlation and Prediction of Dense Fluid Transport-Coefficients. 1. Normal-Alkanes. International Journal of Thermophysics 1992, 13, 269-281.
[418] Assael, M. J.; Dymond, J. H.; Patterson, P. M. Correlation and Prediction of Dense Fluid Transport-Coefficients. 5. Aromatic-Hydrocarbons. International Journal of Thermophysics 1992, 13, 895-905.
[419] Assael, M. J.; Dymond, J. H.; Patterson, P. M. Correlation and Prediction of Dense Fluid Transport-Coefficients. 4. A Note on Diffusion. International Journal of Thermophysics 1992, 13, 729-733.
[420] Riesco, N.; Vesovic, V. Extended Hard-Sphere Model for Predicting the Viscosity of Long-Chain n-Alkanes. Fluid Phase Equilibria 2016, 425, 385-392.
[421] Al Ghafri, S. Z. S.; Forte, E.; Galindo, A.; Maitland, G. C.; Trusler, J. P. M. Experimental and Modeling Study of the Phase Behavior of (Heptane + Carbon Dioxide + Water) Mixtures. Journal of Chemical and Engineering Data 2015, 60, 3670-3681.
[422] Al Ghafri, S. Z. S.; Forte, E.; Maitland, G. C.; Rodriguez-Henriquez, J. J.; Trusler, J. P. M. Experimental and Modeling Study of the Phase Behavior of (Methane + $CO_2$ + Water) Mixtures. Journal of Physical Chemistry B 2014, 118, 14461-14478.
[423] Forte, E.; Galindo, A.; Trusler, J. P. M. Experimental and Molecular Modeling Study of the Three-Phase Behavior of (n-Decane Plus Carbon Dioxide Plus Water) at Reservoir Conditions. Journal of Physical Chemistry B 2011, 115, 14591-14609.
[424] Forte, E.; Galindo, A.; Trusler, J. P. M. Experimental and Molecular Modelling Study of the Three-Phase Behaviour of (Propane Plus Carbon Dioxide Plus Water) at Reservoir Conditions. Journal of Supercritical Fluids 2013, 75, 30-42.

# Appendix A:

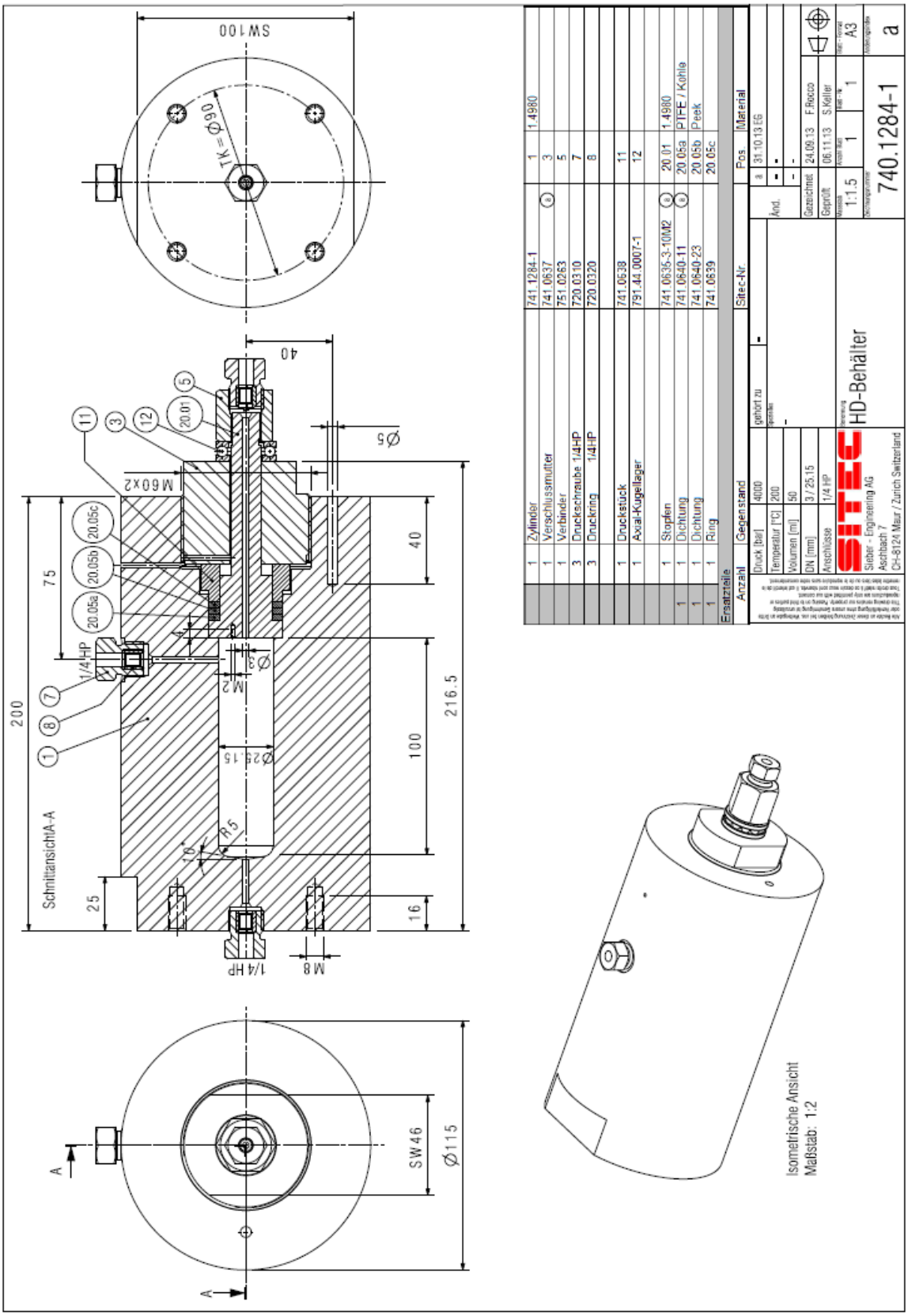
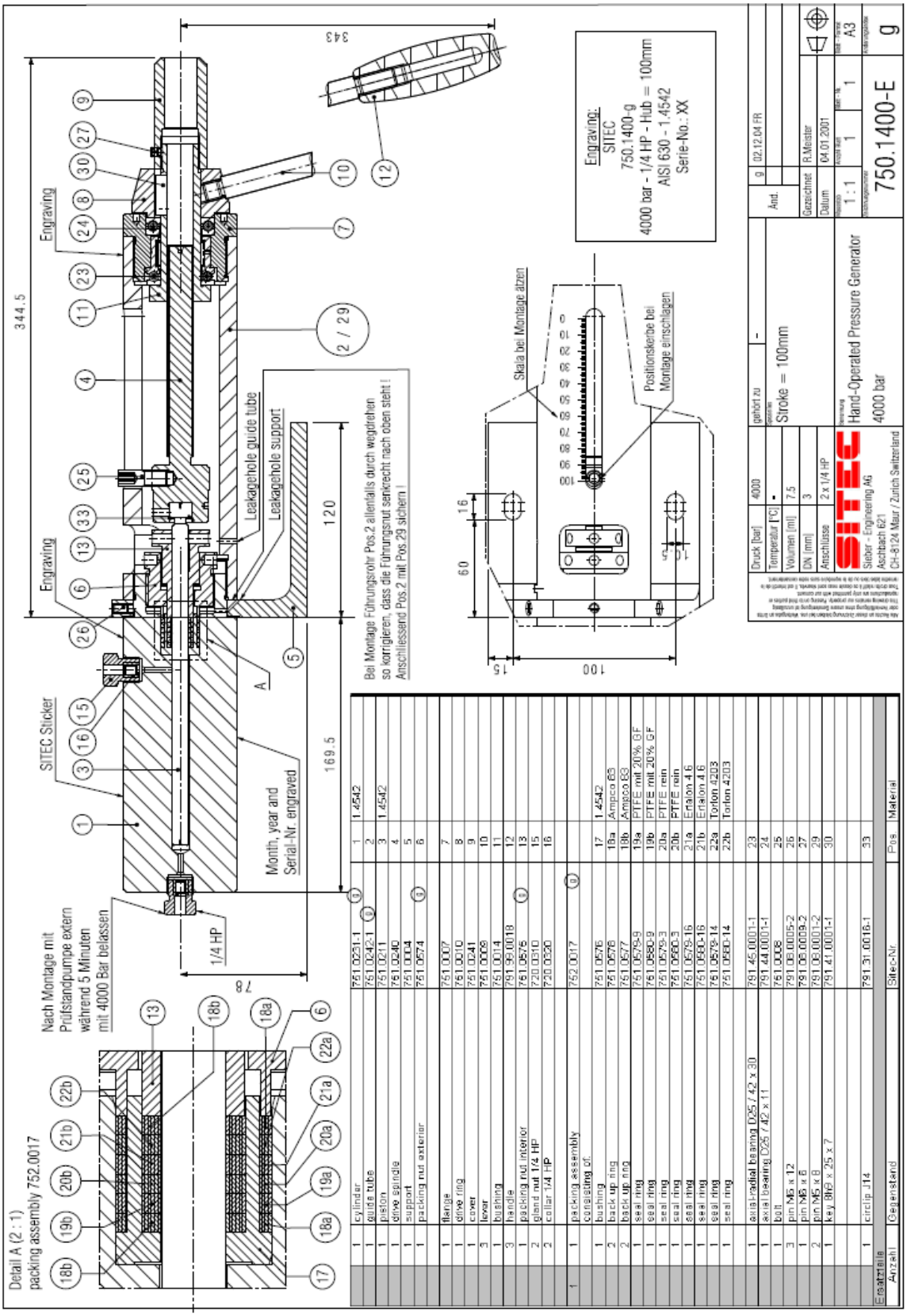



**Figure A.1** Detailed drawings of the 4 kbar pressure vessel and a list of serviceable parts from SITEC.




| Anzahl | Gegenstand | Sitec-Nr. | Pos. | Material |
|---|---|---|---|---|
| 1 | cylinder | 751.0231-1 ③ | 1 | 1.4542 |
| 1 | guide tube | 751.0242-1 ④ | 2 | |
| 1 | piston | 751.0211 | 3 | 1.4542 |
| 1 | drive spindle | 751.0040 | 4 | |
| 1 | support | 751.0004 | 5 | |
| 1 | packing nut exterior | 751.0674 ① | 6 | |
| 1 | flange | 751.0007 | 7 | |
| 1 | drive ring | 751.0010 | 8 | |
| 1 | cover | 751.0041 | 9 | |
| 3 | lever | 751.0009 | 10 | |
| 1 | bushing | 751.0014 | 11 | |
| 3 | handle | 791.99.0018 | 12 | |
| 1 | packing nut interior | 751.0676 ① | 13 | |
| 2 | gland nut 1/4 HP | 720.0310 | 15 | |
| 2 | collar 1/4 HP | 720.0320 | 16 | |
| 1 | packing assembly | 752.0017 ① | | |
| | consisting of: | | | |
| 1 | bushing | 751.0676 | 17 | 1.4542 |
| 2 | back up ring | 751.0676 | 18a | Ampco 63 |
| 2 | back up ring | 751.0677 | 18b | Ampco 63 |
| 1 | seal ring | 751.0579-9 | 19a | PTFE mit 20% GF |
| 1 | seal ring | 751.0580-9 | 19b | PTFE mit 20% GF |
| 1 | seal ring | 751.0579-3 | 20a | PTFE rein |
| 1 | seal ring | 751.0580-3 | 20b | PTFE rein |
| 1 | seal ring | 751.0579-16 | 21a | Etalon 4.6 |
| 1 | seal ring | 751.0580-16 | 21b | Etalon 4.6 |
| 1 | seal ring | 751.0579-14 | 22a | Torlon 4203 |
| 1 | seal ring | 751.0580-14 | 22b | Torlon 4203 |
| 1 | axial-radial bearing D25 / 42 x 30 | 791.45.0001-1 | 23 | |
| 1 | axial-bearing D25 / 42 x 11 | 791.44.0001-1 | 24 | |
| 1 | bolt | 751.0008 | 25 | |
| 3 | pin M5 x 12 | 791.06.0005-2 | 26 | |
| 1 | pin M5 x 6 | 791.06.0009-2 | 27 | |
| 2 | pin M5 x 8 | 791.06.0001-2 | 29 | |
| 1 | key 8H9 x 25 x 7 | 791.41.0001-1 | 30 | |
| 1 | circlip J14 | 791.31.0016-1 | 33 | |
| Ersatzteile | | | | |

**Figure A.2** Detailed drawings of the high-pressure syringe pump and a list of serviceable parts from SITEC.

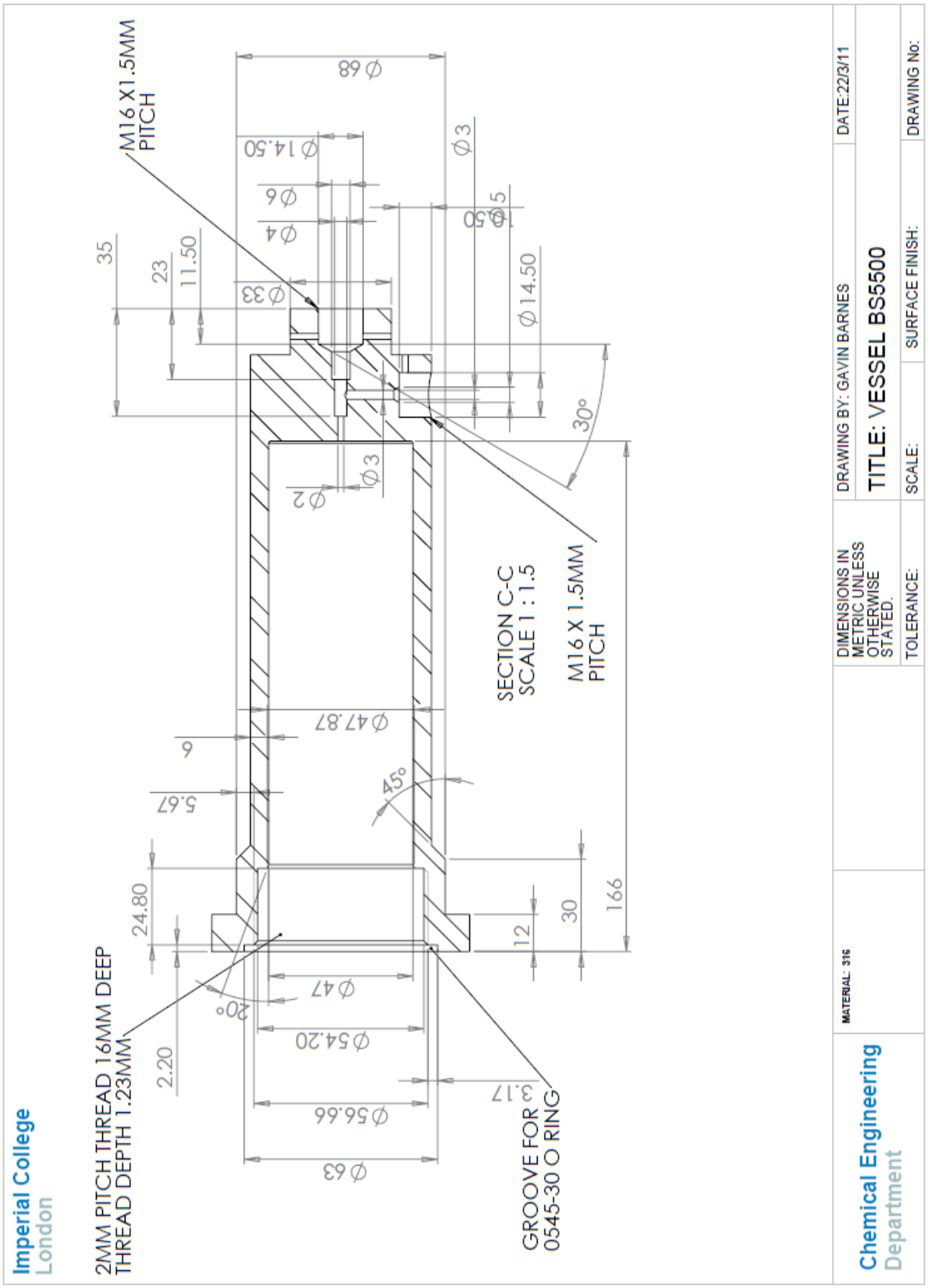



**Figure A.3a** Detailed drawings with the dimensions of the variable volume cell.

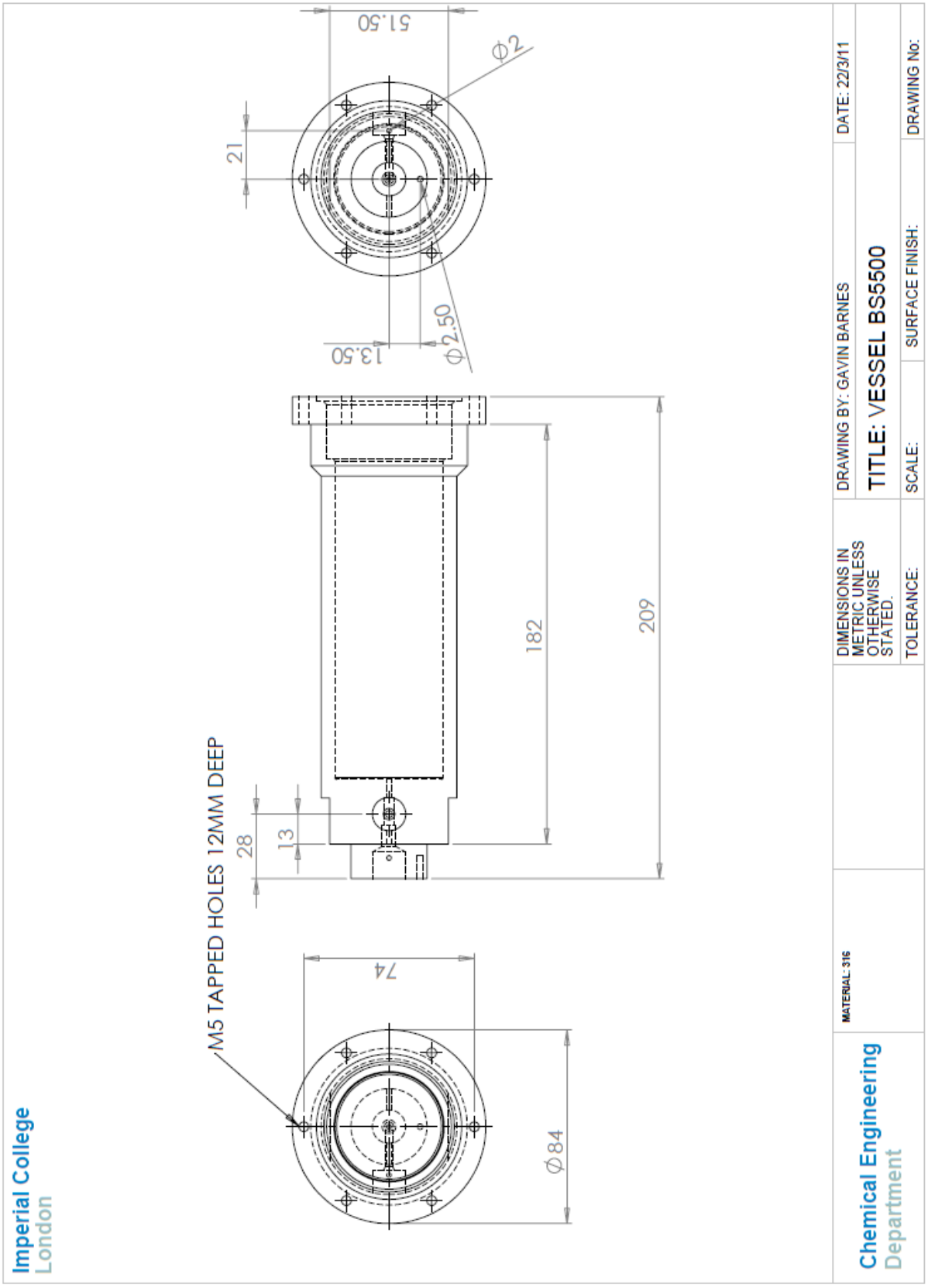



**Figure A.3b** Detailed drawings with the dimensions of the variable volume cell.

**Table A.4** Calibration density $\rho$ for the vibrating-tube densimeter (DMA-HP) measured with water, helium and vacuum at temperature $T$, pressure $p$ and period of oscillation $\tau$. The reference density calculated from reference equations of state $\rho_{ref}$ and the density difference ($\rho$-$\rho_{ref}$).

| Component | $\rho_{ref}$ / kg·m$^{-3}$ | $T$ / K | $p$ / MPa | $\tau$ / μs | $\rho$ / kg·m$^{-3}$ | ($\rho$-$\rho_{ref}$)/ kg·m$^{-3}$ |
|---|---|---|---|---|---|---|
| Water 1 | 1000.10 | 283.15 | 1.01 | 2645.78 | 1000.11 | 0.01 |
| Water 2 | 1002.10 | 283.16 | 5.07 | 2646.27 | 1002.04 | -0.06 |
| Water 3 | 1004.40 | 283.16 | 10.02 | 2646.87 | 1004.40 | 0.00 |
| Water 4 | 1006.70 | 283.16 | 15.05 | 2647.47 | 1006.76 | 0.06 |
| Water 5 | 1009.00 | 283.16 | 20.02 | 2648.05 | 1009.01 | 0.01 |
| Water 6 | 1011.30 | 283.16 | 25.08 | 2648.64 | 1011.31 | 0.01 |
| Water 7 | 1013.50 | 283.16 | 30.02 | 2649.22 | 1013.57 | 0.07 |
| Water 8 | 1015.80 | 283.16 | 35.06 | 2649.79 | 1015.76 | -0.04 |
| Water 9 | 1018.00 | 283.16 | 40.08 | 2650.37 | 1018.00 | 0.00 |
| Water 10 | 1020.20 | 283.16 | 45.04 | 2650.93 | 1020.15 | -0.05 |
| Water 11 | 1022.40 | 283.16 | 50.07 | 2651.50 | 1022.35 | -0.05 |
| Water 12 | 1024.50 | 283.16 | 55.07 | 2652.06 | 1024.49 | -0.01 |
| Water 13 | 1026.60 | 283.16 | 60.04 | 2652.62 | 1026.63 | 0.03 |
| Water 14 | 1028.70 | 283.16 | 65.04 | 2653.17 | 1028.72 | 0.02 |
| Vacuum | 0.01 | 283.16 | 0.00 | 2441.80 | -0.03 | -0.04 |
| Helium 1 | 1.71 | 283.15 | 1.01 | 2442.20 | 1.77 | 0.06 |
| Helium 2 | 8.32 | 283.15 | 5.02 | 2443.67 | 8.39 | 0.06 |
| Helium 3 | 16.22 | 283.15 | 10.01 | 2445.42 | 16.24 | 0.03 |
| Helium 4 | 23.76 | 283.15 | 15.00 | 2447.10 | 23.77 | 0.02 |
| Helium 5 | 30.98 | 283.15 | 20.01 | 2448.71 | 30.97 | -0.01 |
| Helium 6 | 37.88 | 283.15 | 25.01 | 2450.25 | 37.84 | -0.04 |
| Helium 7 | 44.50 | 283.15 | 30.01 | 2451.74 | 44.47 | -0.03 |
| Helium 8 | 50.85 | 283.15 | 35.00 | 2453.16 | 50.77 | -0.07 |
| Helium 9 | 56.96 | 283.15 | 40.00 | 2454.54 | 56.89 | -0.07 |
| Helium 10 | 62.84 | 283.15 | 45.00 | 2455.88 | 62.81 | -0.03 |
| Helium 11 | 68.51 | 283.15 | 50.01 | 2457.17 | 68.49 | -0.02 |
| Helium 12 | 73.98 | 283.15 | 55.00 | 2458.42 | 73.99 | 0.02 |
| Helium 13 | 79.26 | 283.15 | 60.00 | 2459.63 | 79.30 | 0.04 |
| Helium 14 | 84.37 | 283.15 | 65.01 | 2460.81 | 84.46 | 0.09 |
| Water 1 | 997.46 | 298.15 | 1.01 | 2650.48 | 997.64 | 0.18 |
| Water 2 | 999.26 | 298.15 | 5.04 | 2650.90 | 999.21 | -0.05 |
| Water 3 | 1001.50 | 298.15 | 10.04 | 2651.48 | 1001.46 | -0.04 |
| Water 4 | 1003.70 | 298.15 | 15.08 | 2652.05 | 1003.65 | -0.05 |
| Water 5 | 1005.90 | 298.15 | 20.03 | 2652.62 | 1005.86 | -0.04 |
| Water 6 | 1008.00 | 298.15 | 25.06 | 2653.17 | 1007.94 | -0.06 |
| Water 7 | 1010.10 | 298.15 | 30.05 | 2653.74 | 1010.14 | 0.04 |
| Water 8 | 1012.20 | 298.15 | 35.03 | 2654.28 | 1012.18 | -0.02 |
| Water 9 | 1014.30 | 298.15 | 39.99 | 2654.84 | 1014.32 | 0.02 |
| Water 10 | 1016.40 | 298.15 | 45.05 | 2655.38 | 1016.35 | -0.05 |
| Water 11 | 1018.50 | 298.15 | 50.04 | 2655.94 | 1018.49 | -0.01 |
| Water 12 | 1020.50 | 298.15 | 55.09 | 2656.47 | 1020.47 | -0.03 |
| Water 13 | 1022.50 | 298.15 | 60.10 | 2657.02 | 1022.55 | 0.05 |

| Component | $\rho_{ref}$ / kg·m$^{-3}$ | $T$ / K | $p$ / MPa | $\tau$ / µs | $\rho$ / kg·m$^{-3}$ | ($\rho$-$\rho_{ref}$)/ kg·m$^{-3}$ |
|---|---|---|---|---|---|---|
| Water 14 | 1024.50 | 298.15 | 65.03 | 2657.55 | 1024.54 | 0.04 |
| Vacuum | 0.01 | 298.15 | 0.00 | 2446.52 | -0.02 | -0.03 |
| Helium 1 | 1.63 | 298.15 | 1.01 | 2446.90 | 1.69 | 0.06 |
| Helium 2 | 7.90 | 298.15 | 5.01 | 2448.30 | 7.95 | 0.05 |
| Helium 3 | 15.44 | 298.15 | 10.01 | 2449.98 | 15.46 | 0.02 |
| Helium 4 | 22.65 | 298.15 | 15.00 | 2451.60 | 22.68 | 0.04 |
| Helium 5 | 29.57 | 298.15 | 20.01 | 2453.14 | 29.53 | -0.04 |
| Helium 6 | 36.19 | 298.15 | 25.00 | 2454.63 | 36.14 | -0.04 |
| Helium 7 | 42.55 | 298.15 | 30.00 | 2456.07 | 42.52 | -0.03 |
| Helium 8 | 48.68 | 298.15 | 35.00 | 2457.45 | 48.62 | -0.06 |
| Helium 9 | 54.58 | 298.15 | 40.01 | 2458.79 | 54.52 | -0.06 |
| Helium 10 | 60.26 | 298.15 | 45.00 | 2460.09 | 60.24 | -0.02 |
| Helium 11 | 65.76 | 298.15 | 50.01 | 2461.34 | 65.72 | -0.04 |
| Helium 12 | 71.06 | 298.15 | 55.01 | 2462.56 | 71.06 | -0.01 |
| Helium 13 | 76.19 | 298.15 | 60.01 | 2463.75 | 76.25 | 0.06 |
| Helium 14 | 81.16 | 298.15 | 65.01 | 2464.90 | 81.26 | 0.10 |
| Water 1 | 988.44 | 323.15 | 1.02 | 2657.52 | 988.45 | 0.01 |
| Water 2 | 990.18 | 323.15 | 5.05 | 2657.98 | 990.20 | 0.02 |
| Water 3 | 992.31 | 323.15 | 10.02 | 2658.54 | 992.33 | 0.02 |
| Water 4 | 994.45 | 323.15 | 15.05 | 2659.10 | 994.45 | 0.00 |
| Water 5 | 996.56 | 323.15 | 20.07 | 2659.66 | 996.57 | 0.01 |
| Water 6 | 998.62 | 323.15 | 25.03 | 2660.20 | 998.60 | -0.02 |
| Water 7 | 1000.70 | 323.15 | 30.04 | 2660.75 | 1000.67 | -0.03 |
| Water 8 | 1002.70 | 323.15 | 35.03 | 2661.29 | 1002.68 | -0.02 |
| Water 9 | 1004.70 | 323.15 | 40.06 | 2661.84 | 1004.75 | 0.05 |
| Water 10 | 1006.70 | 323.15 | 45.01 | 2662.36 | 1006.67 | -0.03 |
| Water 11 | 1008.70 | 323.15 | 50.02 | 2662.90 | 1008.68 | -0.02 |
| Water 12 | 1010.70 | 323.15 | 55.06 | 2663.43 | 1010.64 | -0.06 |
| Water 13 | 1012.60 | 323.15 | 60.01 | 2663.96 | 1012.61 | 0.01 |
| Water 14 | 1014.50 | 323.15 | 65.04 | 2664.49 | 1014.57 | 0.07 |
| Vacuum | 0.01 | 323.15 | 0.00 | 2454.52 | 0.03 | 0.02 |
| Helium 1 | 1.48 | 323.15 | 1.00 | 2454.87 | 1.59 | 0.10 |
| Helium 2 | 7.31 | 323.15 | 5.01 | 2456.18 | 7.39 | 0.08 |
| Helium 3 | 14.29 | 323.15 | 10.00 | 2457.75 | 14.33 | 0.04 |
| Helium 4 | 21.01 | 323.15 | 15.00 | 2459.26 | 20.99 | -0.02 |
| Helium 5 | 27.48 | 323.15 | 20.01 | 2460.73 | 27.46 | -0.02 |
| Helium 6 | 33.68 | 323.15 | 25.01 | 2462.13 | 33.61 | -0.08 |
| Helium 7 | 39.67 | 323.15 | 30.01 | 2463.49 | 39.56 | -0.11 |
| Helium 8 | 45.44 | 323.15 | 35.00 | 2464.81 | 45.33 | -0.11 |
| Helium 9 | 51.02 | 323.15 | 40.00 | 2466.09 | 50.92 | -0.10 |
| Helium 10 | 56.41 | 323.15 | 45.00 | 2467.33 | 56.31 | -0.10 |
| Helium 11 | 61.63 | 323.15 | 50.01 | 2468.55 | 61.61 | -0.03 |
| Helium 12 | 66.67 | 323.15 | 55.00 | 2469.73 | 66.72 | 0.05 |
| Helium 13 | 71.57 | 323.15 | 60.00 | 2470.88 | 71.68 | 0.12 |
| Helium 14 | 76.32 | 323.15 | 65.00 | 2471.99 | 76.47 | 0.15 |

| Component | $\rho_{ref}$ / kg·m$^{-3}$ | $T$ / K | $p$ / MPa | $\tau$ / µs | $\rho$ / kg·m$^{-3}$ | ($\rho$-$\rho_{ref}$)/ kg·m$^{-3}$ |
|---|---|---|---|---|---|---|
| Water 1 | 975.25 | 348.15 | 1.02 | 2663.92 | 975.23 | -0.02 |
| Water 2 | 977.02 | 348.15 | 5.03 | 2664.40 | 977.07 | 0.05 |
| Water 3 | 979.21 | 348.15 | 10.05 | 2664.97 | 979.23 | 0.02 |
| Water 4 | 981.37 | 348.15 | 15.06 | 2665.54 | 981.38 | 0.01 |
| Water 5 | 983.49 | 348.15 | 20.04 | 2666.11 | 983.54 | 0.05 |
| Water 6 | 985.62 | 348.15 | 25.08 | 2666.66 | 985.58 | -0.04 |
| Water 7 | 987.68 | 348.15 | 30.04 | 2667.22 | 987.69 | 0.01 |
| Water 8 | 989.76 | 348.15 | 35.07 | 2667.76 | 989.69 | -0.07 |
| Water 9 | 991.79 | 348.15 | 40.06 | 2668.32 | 991.79 | 0.00 |
| Water 10 | 993.81 | 348.15 | 45.09 | 2668.86 | 993.78 | -0.03 |
| Water 11 | 995.79 | 348.15 | 50.05 | 2669.40 | 995.78 | -0.01 |
| Water 12 | 997.77 | 348.15 | 55.07 | 2669.93 | 997.72 | -0.05 |
| Water 13 | 999.70 | 348.15 | 60.02 | 2670.47 | 999.73 | 0.03 |
| Water 14 | 1001.60 | 348.15 | 65.07 | 2671.00 | 1001.66 | 0.06 |
| Vacuum | 0.01 | 348.15 | 0.00 | 2462.71 | 0.14 | 0.13 |
| Helium 1 | 1.39 | 348.15 | 1.01 | 2463.02 | 1.50 | 0.11 |
| Helium 2 | 6.80 | 348.15 | 5.01 | 2464.24 | 6.85 | 0.06 |
| Helium 3 | 13.31 | 348.15 | 10.00 | 2465.70 | 13.24 | -0.07 |
| Helium 4 | 19.60 | 348.15 | 15.01 | 2467.13 | 19.48 | -0.11 |
| Helium 5 | 25.66 | 348.15 | 20.01 | 2468.52 | 25.54 | -0.11 |
| Helium 6 | 31.51 | 348.15 | 25.01 | 2469.87 | 31.41 | -0.09 |
| Helium 7 | 37.15 | 348.15 | 30.00 | 2471.17 | 37.05 | -0.10 |
| Helium 8 | 42.62 | 348.15 | 35.01 | 2472.45 | 42.59 | -0.02 |
| Helium 9 | 47.91 | 348.15 | 40.02 | 2473.69 | 47.95 | 0.04 |
| Helium 10 | 53.02 | 348.15 | 45.00 | 2474.88 | 53.07 | 0.06 |
| Helium 11 | 57.99 | 348.15 | 50.01 | 2476.03 | 58.01 | 0.02 |
| Helium 12 | 62.80 | 348.15 | 55.00 | 2477.16 | 62.85 | 0.05 |
| Helium 13 | 67.48 | 348.15 | 60.01 | 2478.25 | 67.50 | 0.02 |
| Helium 14 | 72.03 | 348.15 | 65.00 | 2479.32 | 72.06 | 0.03 |
| Water 1 | 958.78 | 373.15 | 1.02 | 2669.80 | 958.71 | -0.07 |
| Water 2 | 960.66 | 373.15 | 5.06 | 2670.31 | 960.69 | 0.03 |
| Water 3 | 962.95 | 373.16 | 10.04 | 2670.91 | 962.99 | 0.04 |
| Water 4 | 965.23 | 373.16 | 15.07 | 2671.51 | 965.27 | 0.04 |
| Water 5 | 967.45 | 373.15 | 20.03 | 2672.09 | 967.47 | 0.02 |
| Water 6 | 969.67 | 373.16 | 25.06 | 2672.67 | 969.65 | -0.02 |
| Water 7 | 971.83 | 373.16 | 30.02 | 2673.25 | 971.84 | 0.01 |
| Water 8 | 973.99 | 373.16 | 35.05 | 2673.82 | 973.97 | -0.02 |
| Water 9 | 976.11 | 373.15 | 40.02 | 2674.39 | 976.11 | 0.00 |
| Water 10 | 978.23 | 373.16 | 45.08 | 2674.95 | 978.18 | -0.05 |
| Water 11 | 980.29 | 373.15 | 50.06 | 2675.51 | 980.26 | -0.03 |
| Water 12 | 982.34 | 373.16 | 55.06 | 2676.07 | 982.35 | 0.01 |
| Water 13 | 984.36 | 373.15 | 60.05 | 2676.62 | 984.38 | 0.02 |
| Water 14 | 986.37 | 373.15 | 65.06 | 2677.17 | 986.40 | 0.03 |
| Vacuum | 0.01 | 373.15 | 0.00 | 2471.01 | 0.06 | 0.06 |
| Helium 1 | 1.30 | 373.15 | 1.01 | 2471.29 | 1.28 | -0.02 |

| Component | $\rho_{ref}$ / kg·m$^{-3}$ | $T$ / K | $p$ / MPa | $\tau$ / µs | $\rho$ / kg·m$^{-3}$ | ($\rho$-$\rho_{ref}$)/ kg·m$^{-3}$ |
|---|---|---|---|---|---|---|
| Helium 2 | 6.34 | 373.15 | 5.00 | 2472.45 | 6.32 | -0.01 |
| Helium 3 | 12.45 | 373.15 | 10.00 | 2473.85 | 12.40 | -0.05 |
| Helium 4 | 18.38 | 373.15 | 15.02 | 2475.21 | 18.29 | -0.09 |
| Helium 5 | 24.08 | 373.15 | 20.02 | 2476.55 | 24.08 | 0.00 |
| Helium 6 | 29.59 | 373.15 | 25.00 | 2477.83 | 29.60 | 0.01 |
| Helium 7 | 34.93 | 373.15 | 30.00 | 2479.08 | 34.98 | 0.05 |
| Helium 8 | 40.11 | 373.15 | 35.01 | 2480.30 | 40.21 | 0.10 |
| Helium 9 | 45.13 | 373.16 | 40.00 | 2481.46 | 45.17 | 0.03 |
| Helium 10 | 50.01 | 373.15 | 45.00 | 2482.60 | 50.03 | 0.02 |
| Helium 11 | 54.76 | 373.15 | 50.02 | 2483.71 | 54.75 | -0.01 |
| Helium 12 | 59.36 | 373.16 | 55.01 | 2484.79 | 59.34 | -0.02 |
| Helium 13 | 63.83 | 373.15 | 60.00 | 2485.84 | 63.78 | -0.05 |
| Helium 14 | 68.19 | 373.15 | 65.00 | 2486.88 | 68.17 | -0.02 |
| Water 1 | 939.43 | 398.15 | 1.02 | 2675.25 | 939.44 | 0.01 |
| Water 2 | 941.46 | 398.15 | 5.03 | 2675.77 | 941.46 | 0.00 |
| Water 3 | 943.94 | 398.15 | 10.03 | 2676.41 | 943.93 | -0.01 |
| Water 4 | 946.38 | 398.15 | 15.02 | 2677.05 | 946.40 | 0.02 |
| Water 5 | 948.82 | 398.15 | 20.07 | 2677.69 | 948.86 | 0.04 |
| Water 6 | 951.19 | 398.15 | 25.05 | 2678.30 | 951.18 | -0.01 |
| Water 7 | 953.51 | 398.15 | 30.02 | 2678.91 | 953.50 | -0.01 |
| Water 8 | 955.83 | 398.15 | 35.07 | 2679.52 | 955.81 | -0.02 |
| Water 9 | 958.09 | 398.15 | 40.04 | 2680.12 | 958.07 | -0.02 |
| Water 10 | 960.35 | 398.15 | 45.09 | 2680.72 | 960.33 | -0.02 |
| Water 11 | 962.53 | 398.15 | 50.04 | 2681.31 | 962.55 | 0.02 |
| Water 12 | 964.72 | 398.15 | 55.04 | 2681.89 | 964.71 | -0.01 |
| Water 13 | 966.88 | 398.15 | 60.06 | 2682.47 | 966.86 | -0.02 |
| Water 14 | 968.98 | 398.15 | 65.03 | 2683.05 | 969.03 | 0.05 |
| Vacuum | 0.01 | 398.15 | 0.00 | 2479.45 | -0.09 | -0.10 |
| Helium 1 | 1.22 | 398.16 | 1.01 | 2479.75 | 1.21 | 0.00 |
| Helium 2 | 5.96 | 398.15 | 5.01 | 2480.84 | 5.92 | -0.04 |
| Helium 3 | 11.70 | 398.16 | 10.01 | 2482.19 | 11.75 | 0.04 |
| Helium 4 | 17.28 | 398.16 | 15.02 | 2483.49 | 17.34 | 0.06 |
| Helium 5 | 22.68 | 398.15 | 20.02 | 2484.75 | 22.75 | 0.07 |
| Helium 6 | 27.89 | 398.16 | 25.01 | 2485.96 | 27.92 | 0.03 |
| Helium 7 | 32.96 | 398.16 | 30.00 | 2487.14 | 32.96 | 0.00 |
| Helium 8 | 37.89 | 398.16 | 35.00 | 2488.30 | 37.90 | 0.01 |
| Helium 9 | 42.67 | 398.16 | 40.01 | 2489.42 | 42.66 | -0.02 |
| Helium 10 | 47.33 | 398.16 | 45.00 | 2490.52 | 47.32 | -0.01 |
| Helium 11 | 51.86 | 398.16 | 50.02 | 2491.59 | 51.84 | -0.02 |
| Helium 12 | 56.26 | 398.15 | 55.01 | 2492.63 | 56.23 | -0.04 |
| Helium 13 | 60.57 | 398.16 | 60.02 | 2493.66 | 60.56 | -0.01 |
| Helium 14 | 64.75 | 398.16 | 65.01 | 2494.66 | 64.76 | 0.01 |
| Water 1 | 917.31 | 423.16 | 1.02 | 2680.26 | 917.36 | 0.05 |
| Water 2 | 919.58 | 423.15 | 5.04 | 2680.83 | 919.61 | 0.03 |
| Water 3 | 922.33 | 423.15 | 10.01 | 2681.52 | 922.31 | -0.02 |

| Component | $\rho_{ref}$ / kg·m$^{-3}$ | $T$ / K | $p$ / MPa | $\tau$ / µs | $\rho$ / kg·m$^{-3}$ | ($\rho$-$\rho_{ref}$)/ kg·m$^{-3}$ |
|---|---|---|---|---|---|---|
| Water 4 | 925.07 | 423.15 | 15.06 | 2682.22 | 925.06 | -0.01 |
| Water 5 | 927.71 | 423.15 | 20.04 | 2682.90 | 927.71 | 0.00 |
| Water 6 | 930.33 | 423.15 | 25.06 | 2683.57 | 930.31 | -0.02 |
| Water 7 | 932.89 | 423.15 | 30.05 | 2684.23 | 932.86 | -0.03 |
| Water 8 | 935.43 | 423.15 | 35.08 | 2684.89 | 935.40 | -0.03 |
| Water 9 | 937.87 | 423.15 | 40.02 | 2685.54 | 937.90 | 0.03 |
| Water 10 | 940.32 | 423.15 | 45.05 | 2686.17 | 940.30 | -0.02 |
| Water 11 | 942.73 | 423.14 | 50.05 | 2686.80 | 942.69 | -0.04 |
| Water 12 | 945.09 | 423.15 | 55.06 | 2687.43 | 945.08 | -0.01 |
| Water 13 | 947.40 | 423.15 | 60.04 | 2688.05 | 947.43 | 0.03 |
| Water 14 | 949.67 | 423.15 | 65.00 | 2688.66 | 949.72 | 0.05 |
| Vacuum | 0.01 | 423.15 | 0.00 | 2488.07 | -0.01 | -0.01 |
| Helium 1 | 1.15 | 423.15 | 1.01 | 2488.32 | 1.06 | -0.09 |
| Helium 2 | 5.61 | 423.15 | 5.01 | 2489.40 | 5.70 | 0.09 |
| Helium 3 | 11.05 | 423.15 | 10.02 | 2490.66 | 11.09 | 0.04 |
| Helium 4 | 16.31 | 423.15 | 15.02 | 2491.89 | 16.33 | 0.02 |
| Helium 5 | 21.41 | 423.15 | 20.01 | 2493.08 | 21.40 | -0.02 |
| Helium 6 | 26.38 | 423.15 | 25.01 | 2494.25 | 26.37 | -0.01 |
| Helium 7 | 31.21 | 423.15 | 30.01 | 2495.39 | 31.19 | -0.01 |
| Helium 8 | 35.90 | 423.15 | 35.00 | 2496.50 | 35.89 | -0.01 |
| Helium 9 | 40.46 | 423.15 | 40.00 | 2497.58 | 40.44 | -0.03 |
| Helium 10 | 44.93 | 423.15 | 45.02 | 2498.65 | 44.94 | 0.01 |
| Helium 11 | 49.25 | 423.15 | 50.00 | 2499.68 | 49.26 | 0.01 |
| Helium 12 | 53.48 | 423.15 | 55.01 | 2500.69 | 53.48 | 0.00 |
| Helium 13 | 57.60 | 423.15 | 60.00 | 2501.67 | 57.57 | -0.03 |
| Helium 14 | 61.63 | 423.15 | 65.01 | 2502.65 | 61.66 | 0.03 |
| Water 1 | 892.36 | 448.16 | 1.02 | 2684.75 | 892.31 | -0.05 |
| Water 2 | 894.97 | 448.15 | 5.07 | 2685.41 | 894.97 | 0.00 |
| Water 3 | 898.08 | 448.15 | 10.02 | 2686.19 | 898.10 | 0.02 |
| Water 4 | 901.16 | 448.15 | 15.03 | 2686.97 | 901.21 | 0.05 |
| Water 5 | 904.17 | 448.15 | 20.07 | 2687.72 | 904.17 | 0.00 |
| Water 6 | 907.11 | 448.15 | 25.07 | 2688.47 | 907.14 | 0.03 |
| Water 7 | 909.95 | 448.15 | 30.03 | 2689.19 | 909.96 | 0.01 |
| Water 8 | 912.79 | 448.15 | 35.07 | 2689.91 | 912.77 | -0.02 |
| Water 9 | 915.53 | 448.15 | 40.05 | 2690.62 | 915.54 | 0.01 |
| Water 10 | 918.22 | 448.15 | 45.03 | 2691.31 | 918.20 | -0.02 |
| Water 11 | 920.89 | 448.15 | 50.06 | 2692.00 | 920.86 | -0.03 |
| Water 12 | 923.49 | 448.15 | 55.06 | 2692.68 | 923.47 | -0.02 |
| Water 13 | 926.03 | 448.15 | 60.02 | 2693.35 | 926.04 | 0.01 |
| Water 14 | 928.54 | 448.15 | 65.04 | 2694.01 | 928.55 | 0.01 |
| Vacuum | 0.01 | 448.15 | 0.00 | 2496.82 | 0.02 | 0.01 |
| Helium 1 | 1.09 | 448.15 | 1.02 | 2497.08 | 1.12 | 0.04 |
| Helium 2 | 5.29 | 448.15 | 5.00 | 2498.08 | 5.38 | 0.09 |
| Helium 3 | 10.44 | 448.15 | 10.01 | 2499.27 | 10.42 | -0.02 |
| Helium 4 | 15.44 | 448.15 | 15.01 | 2500.45 | 15.42 | -0.02 |

| Component | $\rho_{ref}$ / kg·m$^{-3}$ | $T$ / K | $p$ / MPa | $\tau$ / µs | $\rho$ / kg·m$^{-3}$ | ($\rho$-$\rho_{ref}$)/ kg·m$^{-3}$ |
|---|---|---|---|---|---|---|
| Helium 5 | 20.29 | 448.15 | 20.01 | 2501.60 | 20.27 | -0.02 |
| Helium 6 | 25.02 | 448.15 | 25.01 | 2502.72 | 24.99 | -0.03 |
| Helium 7 | 29.63 | 448.15 | 30.01 | 2503.81 | 29.57 | -0.05 |
| Helium 8 | 34.10 | 448.15 | 35.00 | 2504.88 | 34.06 | -0.05 |
| Helium 9 | 38.47 | 448.15 | 40.00 | 2505.93 | 38.45 | -0.02 |
| Helium 10 | 42.73 | 448.15 | 45.00 | 2506.95 | 42.71 | -0.03 |
| Helium 11 | 46.89 | 448.15 | 50.00 | 2507.95 | 46.87 | -0.02 |
| Helium 12 | 50.95 | 448.15 | 55.00 | 2508.94 | 50.98 | 0.03 |
| Helium 13 | 54.92 | 448.15 | 60.00 | 2509.90 | 54.96 | 0.04 |
| Helium 14 | 58.79 | 448.15 | 65.00 | 2510.84 | 58.84 | 0.05 |
| Water 1 | 867.28 | 473.15 | 5.02 | 2689.48 | 867.28 | 0.00 |
| Water 2 | 870.95 | 473.15 | 10.02 | 2690.38 | 870.96 | 0.01 |
| Water 3 | 874.56 | 473.15 | 15.08 | 2691.27 | 874.58 | 0.02 |
| Water 4 | 877.99 | 473.15 | 20.05 | 2692.12 | 878.01 | 0.02 |
| Water 5 | 881.39 | 473.15 | 25.08 | 2692.96 | 881.39 | 0.00 |
| Water 6 | 884.62 | 473.15 | 30.01 | 2693.76 | 884.58 | -0.04 |
| Water 7 | 887.84 | 473.15 | 35.04 | 2694.58 | 887.86 | 0.02 |
| Water 8 | 890.96 | 473.15 | 40.04 | 2695.36 | 890.94 | -0.02 |
| Water 9 | 894.03 | 473.15 | 45.07 | 2696.14 | 894.02 | -0.01 |
| Water 10 | 896.97 | 473.15 | 50.01 | 2696.89 | 896.96 | -0.01 |
| Water 11 | 899.91 | 473.15 | 55.04 | 2697.65 | 899.94 | 0.03 |
| Water 12 | 902.78 | 473.15 | 60.07 | 2698.38 | 902.76 | -0.02 |
| Water 13 | 905.58 | 473.15 | 65.07 | 2699.11 | 905.59 | 0.01 |
| Vacuum | 0.01 | 473.15 | 0.00 | 2505.70 | 0.03 | 0.02 |
| Helium 1 | 1.02 | 473.15 | 1.01 | 2505.94 | 1.04 | 0.02 |
| Helium 2 | 5.03 | 473.15 | 5.01 | 2506.89 | 5.04 | 0.02 |
| Helium 3 | 9.91 | 473.15 | 10.01 | 2508.05 | 9.92 | 0.01 |
| Helium 4 | 14.65 | 473.15 | 15.00 | 2509.19 | 14.70 | 0.05 |
| Helium 5 | 19.29 | 473.15 | 20.01 | 2510.29 | 19.30 | 0.01 |
| Helium 6 | 23.80 | 473.15 | 25.01 | 2511.36 | 23.76 | -0.04 |
| Helium 7 | 28.20 | 473.15 | 30.01 | 2512.41 | 28.13 | -0.07 |
| Helium 8 | 32.48 | 473.15 | 35.01 | 2513.44 | 32.41 | -0.08 |
| Helium 9 | 36.67 | 473.15 | 40.01 | 2514.46 | 36.64 | -0.04 |
| Helium 10 | 40.76 | 473.15 | 45.01 | 2515.45 | 40.73 | -0.03 |
| Helium 11 | 44.76 | 473.15 | 50.02 | 2516.42 | 44.72 | -0.04 |
| Helium 12 | 48.66 | 473.15 | 55.01 | 2517.38 | 48.67 | 0.01 |
| Helium 13 | 52.48 | 473.15 | 60.01 | 2518.32 | 52.53 | 0.06 |
| Helium 14 | 56.21 | 473.15 | 65.01 | 2519.24 | 56.30 | 0.08 |

# Appendix B:

**Table B.1** Experimental speed-of-sound $c$ in *n*-pentane as a function of temperature and pressure, $T$: (263.21 to 473.15) K and $p$: (1 to 390) MPa.

| $p$ (MPa) | $c$ (m·s$^{-1}$) | $p$ (MPa) | $c$ (m·s$^{-1}$) | $p$ (MPa) | $c$ (m·s$^{-1}$) |
|---|---|---|---|---|---|
| | | $T$ = 263.21 K | | | |
| 1.1 | 1186.05 | 120.1 | 1741.73 | 240.5 | 2071.96 |
| 30.1 | 1367.73 | 150.1 | 1835.39 | 270.3 | 2139.03 |
| 60.0 | 1514.29 | 180.1 | 1920.36 | 299.9 | 2202.06 |
| 90.0 | 1636.15 | 210.2 | 1998.74 | | |
| | | $T$ = 273.15 K | | | |
| 1.1 | 1134.50 | 120.0 | 1713.62 | 240.1 | 2046.89 |
| 30.04 | 1327.10 | 150.3 | 1808.96 | 280.0 | 2136.91 |
| 60.17 | 1479.83 | 180.2 | 1894.73 | 300.1 | 2179.97 |
| 90.11 | 1605.12 | 210.1 | 1973.55 | | |
| | | $T$ = 283.14 K | | | |
| 1.1 | 1085.74 | 150.0 | 1780.49 | 300.2 | 2158.00 |
| 30.1 | 1287.40 | 180.1 | 1868.57 | 330.4 | 2219.96 |
| 60.1 | 1445.05 | 210.0 | 1948.60 | 360.0 | 2277.18 |
| 90.1 | 1573.49 | 240.1 | 2023.34 | 390.0 | 2332.68 |
| 120.1 | 1683.75 | 270.3 | 2092.98 | | |
| | | $T$ = 298.15 K | | | |
| 1.0 | 1013.67 | 150.1 | 1741.65 | 300.0 | 2124.02 |
| 30.0 | 1231.62 | 180.1 | 1831.61 | 330.0 | 2186.38 |
| 60.0 | 1396.08 | 210.5 | 1912.63 | 360.0 | 2245.63 |
| 90.0 | 1528.38 | 240.2 | 1987.96 | 390.6 | 2302.96 |
| 120.2 | 1642.53 | 269.9 | 2057.68 | | |
| | | $T$ = 323.14 K | | | |
| 1.1 | 894.89 | 150.1 | 1680.55 | 300.0 | 2074.70 |
| 30.3 | 1145.00 | 180.1 | 1772.98 | 329.8 | 2137.86 |
| 59.9 | 1318.19 | 209.9 | 1857.19 | 360.1 | 2198.76 |
| 90.1 | 1459.06 | 240.1 | 1935.15 | 390.3 | 2255.91 |
| 120.2 | 1577.88 | 270.2 | 2007.51 | | |
| | | $T$ = 348.15 K | | | |
| 1.1 | 775.00 | 150.0 | 1624.20 | 300.5 | 2028.67 |
| 30.1 | 1058.40 | 180.0 | 1719.27 | 330.1 | 2092.46 |
| 60.1 | 1247.59 | 210.2 | 1806.94 | 360.0 | 2153.90 |
| 90.1 | 1394.80 | 240.3 | 1885.80 | 390.1 | 2212.09 |
| 120.1 | 1517.00 | 270.0 | 1958.68 | | |
| | | $T$ = 373.15 K | | | |
| 1.0 | 652.69 | 150.1 | 1570.00 | 300.0 | 1981.05 |
| 29.9 | 977.08 | 180.3 | 1668.16 | 330.0 | 2046.74 |

| $p$ (MPa) | $c$ (m·s$^{-1}$) | $p$ (MPa) | $c$ (m·s$^{-1}$) | $p$ (MPa) | $c$ (m·s$^{-1}$) |
|---|---|---|---|---|---|
| 60.5 | 1181.80 | 210.1 | 1755.57 | 359.9 | 2108.41 |
| 90.0 | 1332.51 | 240.2 | 1836.88 | 390.0 | 2167.75 |
| 120.3 | 1461.07 | 270.1 | 1911.54 | | |
| | | $T$ = 398.15 K | | | |
| 1.6 | 536.79 | 150.0 | 1521.83 | 300.0 | 1940.39 |
| 30.0 | 906.85 | 180.1 | 1622.31 | 330.2 | 2007.36 |
| 60.1 | 1119.78 | 210.4 | 1712.21 | 360.0 | 2069.80 |
| 90.0 | 1278.57 | 240.1 | 1793.46 | 390.2 | 2129.71 |
| 120.0 | 1408.71 | 270.2 | 1869.89 | | |
| | | $T$ = 423.15 K | | | |
| 30.5 | 844.50 | 180.3 | 1580.23 | 329.9 | 1969.88 |
| 60.8 | 1069.13 | 210.0 | 1670.49 | 360.1 | 2033.35 |
| 90.2 | 1229.41 | 240.1 | 1753.79 | 390.1 | 2093.30 |
| 120.1 | 1362.91 | 270.1 | 1830.95 | | |
| 150.3 | 1478.69 | 300.1 | 1902.73 | | |
| | | $T$ = 448.15 K | | | |
| 30.0 | 778.97 | 180.1 | 1539.04 | 330.2 | 1934.74 |
| 60.2 | 1013.48 | 210.2 | 1631.94 | 360.2 | 1998.64 |
| 90.1 | 1180.58 | 240.2 | 1716.10 | 389.2 | 2055.99 |
| 120.1 | 1318.05 | 270.1 | 1793.75 | | |
| 150.1 | 1434.77 | 300.0 | 1866.12 | | |
| | | $T$ = 473.15 K | | | |
| 30.2 | 725.89 | 180.3 | 1500.95 | 329.7 | 1898.49 |
| 60.2 | 967.23 | 210.0 | 1593.64 | 360.1 | 1962.78 |
| 90.2 | 1139.35 | 240.2 | 1679.25 | 380.0 | 2002.53 |
| 120.2 | 1278.23 | 270.0 | 1757.04 | | |
| 150.3 | 1396.58 | 300.1 | 1830.58 | | |

Standard uncertainties at 95 % confidence are $u(T)$ = 0.05 K and $u(p)$ = 50 kPa, and $u_c(c) \sim 0.0003c$.

**Table B.2** Experimental compressed-liquid density $\rho$ for *n*-heptane as a function of temperature and pressure, $T$: (283.15 to 473.15) K and $p$: (1 to 68) MPa.

| $p$ (MPa) | $\rho$ (kg·m$^{-3}$) | $p$ (MPa) | $\rho$ (kg·m$^{-3}$) | $p$ (MPa) | $\rho$ (kg·m$^{-3}$) |
|---|---|---|---|---|---|
| | | $T$ = 283.15 K | | | |
| 1.01 | 693.19 | 30.02 | 715.03 | 60.00 | 732.72 |
| 5.00 | 696.64 | 35.01 | 718.25 | 65.01 | 735.39 |
| 10.01 | 700.72 | 40.00 | 721.33 | 68.01 | 736.91 |
| 15.01 | 704.55 | 45.01 | 724.35 | 5.02 | 696.64 |
| 20.01 | 708.23 | 50.01 | 727.23 | | |
| 25.01 | 711.70 | 55.01 | 730.00 | | |
| | | $T$ = 298.15 K | | | |

| $p$ (MPa) | $\rho$ (kg·m$^{-3}$) | $p$ (MPa) | $\rho$ (kg·m$^{-3}$) | $p$ (MPa) | $\rho$ (kg·m$^{-3}$) |
|---|---|---|---|---|---|
| 1.01 | 680.29 | 30.01 | 704.10 | 60.00 | 722.88 |
| 5.01 | 684.08 | 35.00 | 707.51 | 65.03 | 725.69 |
| 10.01 | 688.54 | 40.00 | 710.83 | 68.02 | 727.30 |
| 15.02 | 692.71 | 45.01 | 713.99 | 5.01 | 684.08 |
| 20.01 | 696.67 | 50.00 | 717.05 | | |
| 25.02 | 700.48 | 55.01 | 720.02 | | |
| | | $T$ = 323.15 K | | | |
| 1.01 | 658.94 | 30.00 | 686.61 | 60.01 | 707.55 |
| 5.00 | 663.50 | 35.02 | 690.49 | 65.00 | 710.58 |
| 10.03 | 668.76 | 40.00 | 694.17 | 68.01 | 712.38 |
| 15.00 | 673.63 | 45.01 | 697.70 | 5.02 | 663.49 |
| 20.01 | 678.21 | 50.01 | 701.13 | | |
| 25.01 | 682.53 | 55.00 | 704.42 | | |
| | | $T$ = 348.15 K | | | |
| 1.02 | 636.71 | 30.00 | 669.09 | 60.01 | 692.47 |
| 5.02 | 642.21 | 35.01 | 673.53 | 65.02 | 695.77 |
| 10.01 | 648.47 | 40.01 | 677.67 | 68.00 | 697.70 |
| 15.02 | 654.24 | 45.00 | 681.57 | 5.00 | 642.21 |
| 20.01 | 659.52 | 50.00 | 685.37 | | |
| 25.01 | 664.45 | 55.00 | 688.97 | | |
| | | $T$ = 373.15 K | | | |
| 1.00 | 613.15 | 30.01 | 651.67 | 60.01 | 677.64 |
| 5.01 | 620.08 | 35.01 | 656.62 | 65.01 | 681.31 |
| 10.00 | 627.62 | 40.02 | 661.28 | 68.01 | 683.43 |
| 15.00 | 634.48 | 45.01 | 665.69 | 5.01 | 620.12 |
| 20.01 | 640.70 | 50.02 | 669.85 | | |
| 25.00 | 646.38 | 55.02 | 673.82 | | |
| | | $T$ = 398.15 K | | | |
| 5.01 | 596.93 | 35.03 | 639.86 | 65.02 | 667.13 |
| 10.00 | 606.22 | 40.01 | 645.08 | 68.01 | 669.43 |
| 15.01 | 614.40 | 45.01 | 649.95 | 5.00 | 596.98 |
| 20.00 | 621.60 | 50.01 | 654.57 | | |
| 25.02 | 628.23 | 55.01 | 658.95 | | |
| 30.00 | 634.22 | 60.01 | 663.14 | | |
| | | $T$ = 423.15 K | | | |
| 5.01 | 572.32 | 35.02 | 623.11 | 65.01 | 653.17 |
| 10.00 | 583.92 | 40.01 | 628.92 | 68.02 | 655.74 |
| 15.01 | 593.74 | 45.01 | 634.35 | 5.01 | 572.37 |
| 20.01 | 602.20 | 50.01 | 639.48 | | |
| 25.01 | 609.90 | 55.00 | 644.27 | | |
| 30.01 | 616.72 | 60.00 | 648.86 | | |
| | | $T$ = 448.15 K | | | |
| 5.02 | 545.93 | 35.00 | 606.42 | 65.00 | 639.52 |

| $p$ (MPa) | $\rho$ (kg·m$^{-3}$) | $p$ (MPa) | $\rho$ (kg·m$^{-3}$) | $p$ (MPa) | $\rho$ (kg·m$^{-3}$) |
|---|---|---|---|---|---|
| 10.01 | 560.67 | 40.00 | 612.95 | 68.01 | 642.27 |
| 15.01 | 572.63 | 45.01 | 619.01 | 5.00 | 545.94 |
| 20.00 | 582.62 | 50.01 | 624.58 | | |
| 25.02 | 591.51 | 55.01 | 629.87 | | |
| 30.00 | 599.30 | 60.01 | 634.82 | | |
| | | $T$ = 473.15 K | | | |
| 5.01 | 516.85 | 35.00 | 589.84 | 65.01 | 626.11 |
| 10.00 | 536.05 | 40.01 | 597.10 | 68.01 | 629.03 |
| 15.01 | 550.84 | 45.01 | 603.74 | 5.00 | 516.85 |
| 20.01 | 562.72 | 50.01 | 609.89 | | |
| 25.02 | 572.94 | 55.01 | 615.62 | | |
| 30.00 | 581.82 | 60.00 | 621.01 | | |

Standard uncertainties at 95 % confidence are $u(T)$ = 0.03 K and $u(p)$ = 20 kPa, and $u_c(\rho) \sim 0.0005\rho$.

**Table B.3** Experimental speed-of-sound $c$ in $n$-heptane as a function of temperature and pressure, $T$: (283.14 to 473.15) K and $p$: (1 to 180) MPa.

| $p$ (MPa) | $c$ (m·s$^{-1}$) | $p$ (MPa) | $c$ (m·s$^{-1}$) | $p$ (MPa) | $c$ (m·s$^{-1}$) |
|---|---|---|---|---|---|
| | | $T$ = 283.14 K | | | |
| 1.04 | 1201.10 | 90.33 | 1634.32 | 180.11 | 1911.00 |
| 30.15 | 1374.99 | 120.35 | 1736.78 | 1.05 | 1201.36 |
| 60.15 | 1515.97 | 150.29 | 1828.17 | | |
| | | $T$ = 298.15 K | | | |
| 1.04 | 1136.20 | 90.16 | 1590.72 | 180.26 | 1875.31 |
| 30.14 | 1321.41 | 120.17 | 1696.09 | 1.04 | 1136.20 |
| 60.14 | 1468.57 | 150.47 | 1790.98 | | |
| | | $T$ = 323.15 K | | | |
| 1.03 | 1029.17 | 90.39 | 1522.17 | 180.15 | 1816.69 |
| 30.33 | 1236.32 | 120.51 | 1632.61 | 1.01 | 1028.65 |
| 60.13 | 1392.28 | 150.14 | 1728.78 | | |
| | | $T$ = 348.15 K | | | |
| 1.04 | 925.60 | 90.14 | 1457.55 | 180.19 | 1763.32 |
| 30.06 | 1154.45 | 120.02 | 1571.82 | 0.98 | 925.30 |
| 60.10 | 1322.49 | 150.32 | 1673.40 | | |
| | | $T$ = 373.15 K | | | |
| 1.02 | 824.56 | 90.07 | 1398.57 | 180.50 | 1715.18 |
| 30.03 | 1079.67 | 120.14 | 1517.70 | 1.05 | 824.70 |
| 60.29 | 1259.14 | 150.06 | 1621.13 | | |
| | | $T$ = 398.15 K | | | |
| 1.01 | 725.53 | 90.44 | 1346.67 | 180.11 | 1668.87 |
| 30.08 | 1011.13 | 120.36 | 1468.53 | 1.01 | 725.53 |

| $p$ (MPa) | $c$ (m·s$^{-1}$) | $p$ (MPa) | $c$ (m·s$^{-1}$) | $p$ (MPa) | $c$ (m·s$^{-1}$) |
|---|---|---|---|---|---|
| 60.00 | 1198.55 | 150.21 | 1574.45 | | |
| | | $T$ = 423.15 K | | | |
| 1.00 | 625.46 | 90.28 | 1296.44 | 179.98 | 1626.56 |
| 30.25 | 947.86 | 120.09 | 1421.13 | 1.00 | 625.46 |
| 60.21 | 1145.11 | 150.20 | 1530.56 | | |
| | | $T$ = 448.15 K | | | |
| 2.13 | 546.94 | 90.05 | 1249.77 | 180.16 | 1588.11 |
| 30.89 | 893.35 | 120.29 | 1379.13 | | |
| 60.31 | 1095.42 | 150.20 | 1489.75 | | |
| | | $T$ = 473.15 K | | | |
| 10.12 | 604.77 | 90.26 | 1208.54 | 180.00 | 1551.93 |
| 30.67 | 836.53 | 120.16 | 1339.28 | | |
| 60.12 | 1047.91 | 150.01 | 1451.74 | | |

Standard uncertainties at 95 % confidence are $u(T)$ = 0.05 K and $u(p)$ = 50 kPa, and $u_c(c) \sim 0.0003c$.

**Table B.4** Derived thermophysical properties for *n*-heptane at $T$: (298.15 to 473.15) K and pressures up to 180 MPa: density $\rho$, isobaric heat capacity $c_p$, isothermal compressibility $\beta$ and isobaric expansivity $\alpha$.

| | | | | $\rho$/(kg·m$^{-3}$) | | | | |
|---|---|---|---|---|---|---|---|---|
| $p$/MPa | 298.15 K | 323.15 K | 348.15 K | 373.15 K | 398.15 K | 423.15 K | 448.15 K | 473.15 K |
| 0.1 | 679.32 | 657.51 | 635.34 | 611.98 | 586.58 | 558.30 | 526.30 | 489.75 |
| 30 | 703.83 | 686.36 | 669.38 | 652.35 | 634.93 | 617.17 | 599.62 | 583.61 |
| 60 | 722.29 | 707.20 | 692.78 | 678.45 | 663.87 | 649.09 | 634.73 | 622.14 |
| 90 | 737.34 | 723.87 | 711.10 | 698.41 | 685.45 | 672.27 | 659.52 | 648.58 |
| 120 | 750.17 | 737.92 | 726.36 | 714.83 | 702.97 | 690.84 | 679.11 | 669.18 |
| 150 | 761.43 | 750.14 | 739.53 | 728.90 | 717.87 | 706.51 | 695.51 | 686.26 |
| 180 | 771.49 | 761.00 | 751.18 | 741.28 | 730.92 | 720.17 | 709.73 | 700.97 |
| | | | | $c_p$/(J·kg$^{-1}$·K$^{-1}$) | | | | |
| $p$/MPa | 298.15 K | 323.15 K | 348.15 K | 373.15 K | 398.15 K | 423.15 K | 448.15 K | 473.15 K |
| 0.1 | 2243.2 | 2341.6 | 2447.3 | 2561.3 | 2684.8 | 2818.7 | 2964.1 | 3122.2 |
| 30 | 2196.1 | 2284.3 | 2377.7 | 2476.6 | 2580.8 | 2689.5 | 2800.8 | 2911.8 |
| 60 | 2165.4 | 2253.1 | 2347.0 | 2447.7 | 2555.3 | 2669.4 | 2788.7 | 2910.8 |
| 90 | 2141.6 | 2230.3 | 2326.4 | 2430.7 | 2543.5 | 2664.8 | 2793.8 | 2928.2 |
| 120 | 2120.5 | 2210.6 | 2309.4 | 2417.6 | 2536.0 | 2664.7 | 2803.1 | 2949.4 |
| 150 | 2100.5 | 2192.3 | 2293.8 | 2406.0 | 2529.7 | 2665.4 | 2812.8 | 2970.0 |
| 180 | 2081.5 | 2174.9 | 2278.9 | 2394.8 | 2523.5 | 2665.7 | 2821.2 | 2988.3 |
| | | | | $10^4\alpha$/K$^{-1}$ | | | | |
| $p$/MPa | 298.15 K | 323.15 K | 348.15 K | 373.15 K | 398.15 K | 423.15 K | 448.15 K | 473.15 K |
| 0.1 | 12.90 | 13.29 | 14.24 | 15.85 | 18.21 | 21.49 | 25.94 | 31.95 |
| 30 | 9.46 | 9.95 | 10.37 | 10.72 | 11.00 | 11.20 | 11.31 | 11.30 |
| 60 | 7.92 | 8.26 | 8.51 | 8.68 | 8.76 | 8.74 | 8.61 | 8.35 |
| 90 | 6.86 | 7.16 | 7.38 | 7.50 | 7.54 | 7.48 | 7.30 | 7.00 |

| | | | | | | | | |
|---|---|---|---|---|---|---|---|---|
| 120 | 6.06 | 6.36 | 6.58 | 6.70 | 6.73 | 6.67 | 6.50 | 6.20 |
| 150 | 5.44 | 5.75 | 5.97 | 6.10 | 6.14 | 6.09 | 5.94 | 5.67 |
| 180 | 4.94 | 5.25 | 5.47 | 5.62 | 5.68 | 5.65 | 5.53 | 5.30 |
| | | | | $10^4\beta$/MPa$^{-1}$ | | | | |
| $p$/MPa | 298.15 K | 323.15 K | 348.15 K | 373.15 K | 398.15 K | 423.15 K | 448.15 K | 473.15 K |
| 0.1 | 14.811 | 18.331 | 23.242 | 30.414 | 41.577 | 60.525 | 97.042 | 184.412 |
| 30 | 9.862 | 11.582 | 13.545 | 15.782 | 18.340 | 21.277 | 24.632 | 28.385 |
| 60 | 7.609 | 8.669 | 9.804 | 11.002 | 12.262 | 13.593 | 15.007 | 16.496 |
| 90 | 6.241 | 6.993 | 7.770 | 8.555 | 9.347 | 10.153 | 10.976 | 11.804 |
| 120 | 5.315 | 5.890 | 6.470 | 7.044 | 7.610 | 8.170 | 8.726 | 9.260 |
| 150 | 4.644 | 5.102 | 5.561 | 6.010 | 6.445 | 6.869 | 7.279 | 7.654 |
| 180 | 4.133 | 4.510 | 4.886 | 5.252 | 5.605 | 5.945 | 6.265 | 6.546 |

**Table B.5** Experimental compressed-liquid density $\rho$ for *n*-nonane as a function of temperature and pressure, $T$: (283.15 to 473.15) K and $p$: (1 to 65) MPa.

| $p$ (MPa) | $\rho$ (kg·m$^{-3}$) | $p$ (MPa) | $\rho$ (kg·m$^{-3}$) | $p$ (MPa) | $\rho$ (kg·m$^{-3}$) |
|---|---|---|---|---|---|
| | | | $T$ = 283.15 K | | |
| 1.01 | 726.34 | 25.02 | 742.67 | 50.01 | 756.76 |
| 5.04 | 729.29 | 30.04 | 745.65 | 55.02 | 759.33 |
| 10.02 | 732.88 | 35.05 | 748.58 | 60.03 | 761.80 |
| 15.02 | 736.26 | 40.01 | 751.36 | 65.01 | 764.23 |
| 20.04 | 739.54 | 45.05 | 754.13 | 5.02 | 729.34 |
| | | | 298.15 K | | |
| 1.02 | 714.88 | 25.04 | 732.60 | 50.01 | 747.63 |
| 5.01 | 718.12 | 30.01 | 735.82 | 55.04 | 750.39 |
| 10.03 | 721.99 | 35.05 | 738.93 | 60.02 | 753.01 |
| 15.06 | 725.76 | 40.01 | 741.95 | 65.01 | 755.57 |
| 20.04 | 729.23 | 45.06 | 744.86 | 5.04 | 718.17 |
| | | | 323.15 K | | |
| 1.03 | 695.36 | 25.02 | 715.72 | 50.03 | 732.45 |
| 5.03 | 699.12 | 30.02 | 719.30 | 55.05 | 735.44 |
| 10.05 | 703.66 | 35.08 | 722.83 | 60.01 | 738.28 |
| 15.02 | 707.89 | 40.05 | 726.17 | 65.01 | 741.12 |
| 20.05 | 711.93 | 45.06 | 729.36 | 5.06 | 699.17 |
| | | | 348.15 K | | |
| 1.01 | 675.29 | 25.05 | 698.89 | 50.04 | 717.46 |
| 5.04 | 679.86 | 30.03 | 702.94 | 55.05 | 720.77 |
| 10.03 | 685.10 | 35.05 | 706.84 | 60.00 | 723.88 |
| 15.02 | 689.95 | 40.02 | 710.50 | 65.04 | 726.94 |
| 20.04 | 694.54 | 45.07 | 714.10 | 5.03 | 679.86 |
| | | | 373.15 K | | |
| 1.01 | 654.64 | 25.06 | 682.04 | 50.07 | 702.73 |
| 5.05 | 660.10 | 30.04 | 686.60 | 55.06 | 706.31 |
| 10.03 | 666.24 | 35.06 | 690.91 | 60.04 | 709.74 |

| $p$ (MPa) | $\rho$ (kg·m$^{-3}$) | $p$ (MPa) | $\rho$ (kg·m$^{-3}$) | $p$ (MPa) | $\rho$ (kg·m$^{-3}$) |
|---|---|---|---|---|---|
| 15.07 | 671.88 | 40.02 | 695.04 | 65.03 | 713.02 |
| 20.03 | 677.13 | 45.07 | 698.95 | 5.05 | 660.10 |
| | | 398.15 K | | | |
| 1.02 | 633.17 | 25.03 | 665.13 | 50.02 | 688.12 |
| 5.02 | 639.63 | 30.05 | 670.29 | 55.04 | 692.06 |
| 10.05 | 646.99 | 35.05 | 675.16 | 60.03 | 695.75 |
| 15.07 | 653.62 | 40.02 | 679.70 | 65.04 | 699.40 |
| 20.02 | 659.57 | 45.07 | 684.02 | 5.03 | 639.68 |
| | | 423.15 K | | | |
| 1.02 | 610.57 | 25.04 | 648.18 | 50.04 | 673.72 |
| 5.03 | 618.54 | 30.02 | 653.99 | 55.02 | 677.97 |
| 10.03 | 627.26 | 35.05 | 659.40 | 60.03 | 682.02 |
| 15.03 | 634.96 | 40.02 | 664.44 | 65.04 | 685.93 |
| 20.04 | 641.88 | 45.02 | 669.18 | 5.03 | 618.59 |
| | | 448.15 K | | | |
| 1.00 | 586.46 | 25.04 | 631.30 | 50.02 | 659.54 |
| 5.02 | 596.49 | 30.03 | 637.79 | 55.04 | 664.18 |
| 10.04 | 607.11 | 35.03 | 643.79 | 60.03 | 668.54 |
| 15.01 | 616.11 | 40.01 | 649.36 | 65.02 | 672.76 |
| 20.01 | 624.04 | 45.05 | 654.64 | 5.02 | 596.53 |
| | | 473.15 K | | | |
| 5.01 | 573.20 | 30.02 | 621.58 | 55.02 | 650.51 |
| 10.04 | 586.19 | 35.03 | 628.26 | 60.01 | 655.26 |
| 15.04 | 596.89 | 40.05 | 634.46 | 65.01 | 659.78 |
| 20.02 | 606.07 | 45.05 | 640.17 | 5.01 | 573.21 |
| 25.05 | 614.28 | 50.04 | 645.51 | | |

Standard uncertainties at 95 % confidence are $u(T) = 0.03$ K and $u(p) = 20$ kPa, and $u_c(\rho) \sim 0.0005\rho$.

**Table B.6** Experimental speed-of-sound $c$ in *n*-nonane as a function of temperature and pressure, $T$: (283.15 to 473.15) K and $p$: (1 to 390) MPa.

| $p$ (MPa) | $c$ (m·s$^{-1}$) | $p$ (MPa) | $c$ (m·s$^{-1}$) | $p$ (MPa) | $c$ (m·s$^{-1}$) |
|---|---|---|---|---|---|
| | | $T$ = 283.15 K | | | |
| 1.09 | 1273.87 | 149.99 | 1862.27 | 300.01 | 2212.69 |
| 30.10 | 1432.39 | 180.13 | 1943.28 | 330.30 | 2271.25 |
| 59.97 | 1563.77 | 210.07 | 2017.44 | 360.22 | 2326.25 |
| 90.37 | 1676.88 | 240.00 | 2086.39 | 389.88 | 2378.37 |
| 120.25 | 1774.69 | 270.32 | 2152.00 | 1.09 | 1273.87 |
| | | $T$ = 298.15 K | | | |
| 1.04 | 1212.52 | 150.12 | 1824.93 | 300.10 | 2181.51 |
| 30.04 | 1380.09 | 180.37 | 1907.92 | 330.26 | 2240.67 |
| 60.13 | 1517.96 | 210.41 | 1983.73 | 360.03 | 2296.15 |

| $p$ (MPa) | $c$ ($m \cdot s^{-1}$) | $p$ (MPa) | $c$ ($m \cdot s^{-1}$) | $p$ (MPa) | $c$ ($m \cdot s^{-1}$) |
|---|---|---|---|---|---|
| 90.11 | 1633.46 | 240.02 | 2053.19 | 390.03 | 2349.42 |
| 120.20 | 1734.73 | 270.23 | 2119.71 | 1.04 | 1212.52 |
| | | $T$ = 323.15 K | | | |
| 1.02 | 1112.26 | 150.13 | 1765.53 | 300.07 | 2131.61 |
| 30.05 | 1297.66 | 179.98 | 1850.06 | 330.05 | 2191.41 |
| 60.21 | 1445.11 | 210.41 | 1929.20 | 360.04 | 2247.98 |
| 90.15 | 1566.72 | 239.98 | 2000.40 | 390.06 | 2301.88 |
| 120.24 | 1672.30 | 270.33 | 2068.76 | 1.02 | 1112.26 |
| | | $T$ = 348.15 K | | | |
| 1.06 | 1017.96 | 150.18 | 1710.37 | 300.42 | 2084.39 |
| 30.15 | 1220.77 | 180.31 | 1798.04 | 330.17 | 2144.53 |
| 59.87 | 1375.15 | 210.23 | 1877.74 | 360.17 | 2202.28 |
| 90.06 | 1503.74 | 240.36 | 1951.76 | 390.07 | 2256.63 |
| 120.21 | 1613.80 | 269.99 | 2019.22 | 1.04 | 1017.14 |
| | | $T$ = 373.15 K | | | |
| 1.02 | 924.85 | 150.20 | 1659.01 | 300.13 | 2040.39 |
| 30.12 | 1147.86 | 180.54 | 1749.03 | 330.24 | 2102.31 |
| 60.04 | 1312.29 | 210.01 | 1829.24 | 360.09 | 2160.13 |
| 90.42 | 1446.93 | 240.37 | 1905.46 | 389.86 | 2212.99 |
| 120.19 | 1559.47 | 270.13 | 1974.70 | 1.02 | 924.85 |
| | | $T$ = 398.15 K | | | |
| 1.10 | 835.35 | 150.15 | 1610.27 | 299.86 | 1999.68 |
| 30.14 | 1079.71 | 180.17 | 1701.67 | 330.01 | 2063.72 |
| 60.24 | 1253.99 | 210.02 | 1784.31 | 360.01 | 2124.07 |
| 90.22 | 1391.83 | 240.15 | 1861.34 | 389.95 | 2182.25 |
| 120.20 | 1508.49 | 270.21 | 1933.10 | 1.10 | 835.37 |
| | | $T$ = 423.15 K | | | |
| 1.11 | 747.61 | 150.11 | 1565.43 | 299.98 | 1964.50 |
| 29.69 | 1013.55 | 180.16 | 1658.83 | 330.04 | 2029.51 |
| 60.21 | 1199.06 | 210.18 | 1744.07 | 360.02 | 2089.84 |
| 90.05 | 1340.95 | 239.99 | 1822.35 | 389.72 | 2146.18 |
| 120.57 | 1462.66 | 270.12 | 1895.74 | 1.12 | 747.66 |
| | | $T$ = 448.15 K | | | |
| 1.04 | 660.86 | 150.28 | 1525.09 | 299.83 | 1929.88 |
| 30.44 | 960.25 | 180.15 | 1619.48 | 330.05 | 1996.06 |
| 60.49 | 1150.47 | 209.90 | 1704.98 | 359.98 | 2059.33 |
| 90.22 | 1295.96 | 239.92 | 1784.42 | 390.31 | 2115.24 |
| 120.32 | 1418.81 | 270.08 | 1858.46 | 1.04 | 660.85 |
| | | $T$ = 473.15 K | | | |
| 1.01 | 574.55 | 150.23 | 1490.76 | 300.08 | 1902.11 |
| 30.43 | 906.07 | 180.26 | 1587.82 | 330.03 | 1965.04 |
| 60.39 | 1104.68 | 210.23 | 1675.99 | 360.07 | 2026.61 |
| 90.20 | 1255.45 | 240.07 | 1755.65 | 390.06 | 2084.29 |

| $p$ (MPa) | $c$ (m·s$^{-1}$) | $p$ (MPa) | $c$ (m·s$^{-1}$) | $p$ (MPa) | $c$ (m·s$^{-1}$) |
|---|---|---|---|---|---|
| 120.10 | 1381.11 | 270.13 | 1831.01 | 1.02 | 574.55 |

Standard uncertainties at 95 % confidence are $u(T)$ = 0.05 K and $u(p)$ = 50 kPa, and $u_c(c) \sim 0.0003c$.

**Table B.7** Derived thermophysical properties for *n*-nonane at $T$: (298.15 to 473.15) K and pressures up to 390 MPa: density $\rho$, isobaric heat capacity $c_p$, isothermal compressibility $\beta$ and isobaric expansivity $\alpha$.

| | | | | $\rho$/(kg·m$^{-3}$) | | | | |
|---|---|---|---|---|---|---|---|---|
| $p$/MPa | 298.15 K | 323.15 K | 348.15 K | 373.15 K | 398.15 K | 423.15 K | 448.15 K | 473.15 K |
| 0.1 | 714.05 | 694.43 | 674.36 | 653.59 | 631.83 | 608.82 | 584.29 | 557.95 |
| 30 | 735.74 | 719.40 | 703.20 | 687.02 | 670.80 | 654.56 | 638.43 | 622.76 |
| 60 | 752.77 | 738.36 | 724.21 | 710.24 | 696.40 | 682.73 | 669.37 | 656.62 |
| 90 | 767.00 | 753.89 | 741.09 | 728.51 | 716.12 | 703.94 | 692.09 | 680.83 |
| 120 | 779.34 | 767.19 | 755.36 | 743.79 | 732.42 | 721.25 | 710.39 | 700.08 |
| 150 | 790.30 | 778.90 | 767.84 | 757.03 | 746.42 | 736.01 | 725.87 | 716.24 |
| 180 | 800.22 | 789.41 | 778.97 | 768.78 | 758.78 | 748.95 | 739.38 | 730.28 |
| 210 | 809.29 | 798.99 | 789.06 | 779.38 | 769.88 | 760.53 | 751.41 | 742.74 |
| 240 | 817.68 | 807.82 | 798.32 | 789.07 | 779.99 | 771.04 | 762.31 | 754.00 |
| 270 | 825.49 | 816.01 | 806.89 | 798.01 | 789.29 | 780.69 | 772.28 | 764.28 |
| 300 | 832.82 | 823.67 | 814.88 | 806.33 | 797.92 | 789.62 | 781.49 | 773.77 |
| 330 | 839.73 | 830.88 | 822.39 | 814.13 | 805.99 | 797.95 | 790.07 | 782.60 |
| 360 | 846.27 | 837.70 | 829.47 | 821.47 | 813.58 | 805.76 | 798.10 | 790.86 |
| 390 | 852.49 | 844.16 | 836.19 | 828.41 | 820.74 | 813.13 | 805.67 | 798.62 |
| | | | | $c_p$/(J·kg$^{-1}$·K$^{-1}$) | | | | |
| $p$/MPa | 298.15 K | 323.15 K | 348.15 K | 373.15 K | 398.15 K | 423.15 K | 448.15 K | 473.15 K |
| 0.1 | 2214.8 | 2301.8 | 2392.7 | 2487.5 | 2586.0 | 2688.0 | 2793.4 | 2902.0 |
| 30 | 2186.1 | 2266.7 | 2349.9 | 2435.3 | 2522.3 | 2610.0 | 2697.6 | 2783.6 |
| 60 | 2169.2 | 2248.9 | 2331.5 | 2416.6 | 2503.7 | 2592.2 | 2681.1 | 2769.4 |
| 90 | 2158.9 | 2238.7 | 2321.7 | 2407.7 | 2496.2 | 2586.7 | 2678.3 | 2769.9 |
| 120 | 2152.4 | 2232.4 | 2316.1 | 2403.1 | 2492.9 | 2585.1 | 2678.9 | 2773.3 |
| 150 | 2148.3 | 2228.7 | 2312.9 | 2400.6 | 2491.5 | 2585.0 | 2680.4 | 2776.8 |
| 180 | 2145.8 | 2226.5 | 2311.1 | 2399.4 | 2491.0 | 2585.4 | 2681.9 | 2779.7 |
| 210 | 2144.4 | 2225.3 | 2310.2 | 2398.9 | 2491.0 | 2586.0 | 2683.3 | 2781.8 |
| 240 | 2143.8 | 2224.9 | 2310.0 | 2398.9 | 2491.3 | 2586.7 | 2684.3 | 2783.4 |
| 270 | 2143.7 | 2224.9 | 2310.1 | 2399.2 | 2491.8 | 2587.3 | 2685.2 | 2784.5 |
| 300 | 2143.9 | 2225.2 | 2310.5 | 2399.7 | 2492.3 | 2588.0 | 2686.0 | 2785.4 |
| 330 | 2144.3 | 2225.6 | 2311.0 | 2400.2 | 2493.0 | 2588.7 | 2686.7 | 2786.2 |
| 360 | 2144.7 | 2226.1 | 2311.5 | 2400.8 | 2493.6 | 2589.4 | 2687.5 | 2787.0 |
| 390 | 2145.0 | 2226.5 | 2312.0 | 2401.4 | 2494.3 | 2590.2 | 2688.4 | 2788.0 |
| | | | | $10^4\alpha$/K$^{-1}$ | | | | |
| $p$/MPa | 298.15 K | 323.15 K | 348.15 K | 373.15 K | 398.15 K | 423.15 K | 448.15 K | 473.15 K |
| 0.1 | 10.92 | 11.41 | 12.08 | 12.99 | 14.14 | 15.59 | 17.38 | 19.59 |
| 30 | 8.78 | 9.03 | 9.26 | 9.47 | 9.66 | 9.84 | 9.99 | 10.11 |
| 60 | 7.61 | 7.72 | 7.81 | 7.86 | 7.89 | 7.88 | 7.83 | 7.74 |

| | | | | | | | | |
|---|---|---|---|---|---|---|---|---|
| 90 | 6.81 | 6.86 | 6.88 | 6.88 | 6.85 | 6.79 | 6.70 | 6.58 |
| 120 | 6.23 | 6.24 | 6.23 | 6.19 | 6.14 | 6.07 | 5.98 | 5.86 |
| 150 | 5.77 | 5.76 | 5.72 | 5.68 | 5.62 | 5.55 | 5.46 | 5.36 |
| 180 | 5.40 | 5.37 | 5.33 | 5.27 | 5.21 | 5.14 | 5.07 | 4.98 |
| 210 | 5.10 | 5.05 | 5.00 | 4.94 | 4.88 | 4.82 | 4.75 | 4.67 |
| 240 | 4.83 | 4.78 | 4.72 | 4.67 | 4.61 | 4.55 | 4.49 | 4.42 |
| 270 | 4.60 | 4.54 | 4.49 | 4.43 | 4.38 | 4.32 | 4.26 | 4.20 |
| 300 | 4.39 | 4.34 | 4.28 | 4.23 | 4.17 | 4.12 | 4.07 | 4.02 |
| 330 | 4.21 | 4.16 | 4.10 | 4.05 | 4.00 | 3.95 | 3.90 | 3.85 |
| 360 | 4.04 | 3.99 | 3.94 | 3.89 | 3.85 | 3.8 | 3.75 | 3.7 |
| 390 | 3.89 | 3.84 | 3.8 | 3.75 | 3.71 | 3.66 | 3.62 | 3.57 |
| | | | | $10^4\beta$/MPa$^{-1}$ | | | | |
| $p$/MPa | 298.15 K | 323.15 K | 348.15 K | 373.15 K | 398.15 K | 423.15 K | 448.15 K | 473.15 K |
| 0.1 | 11.863 | 14.372 | 17.670 | 22.094 | 28.164 | 36.722 | 49.195 | 68.146 |
| 30 | 8.574 | 9.888 | 11.369 | 13.053 | 14.979 | 17.191 | 19.726 | 22.603 |
| 60 | 6.831 | 7.662 | 8.553 | 9.517 | 10.560 | 11.682 | 12.875 | 14.114 |
| 90 | 5.726 | 6.312 | 6.929 | 7.579 | 8.262 | 8.973 | 9.700 | 10.424 |
| 120 | 4.956 | 5.398 | 5.859 | 6.338 | 6.833 | 7.336 | 7.840 | 8.332 |
| 150 | 4.385 | 4.734 | 5.097 | 5.470 | 5.850 | 6.232 | 6.609 | 6.973 |
| 180 | 3.942 | 4.228 | 4.523 | 4.825 | 5.129 | 5.432 | 5.728 | 6.016 |
| 210 | 3.587 | 3.828 | 4.075 | 4.325 | 4.576 | 4.823 | 5.066 | 5.301 |
| 240 | 3.296 | 3.503 | 3.714 | 3.926 | 4.137 | 4.344 | 4.548 | 4.746 |
| 270 | 3.053 | 3.233 | 3.416 | 3.599 | 3.780 | 3.957 | 4.130 | 4.302 |
| 300 | 2.845 | 3.005 | 3.166 | 3.326 | 3.483 | 3.636 | 3.787 | 3.937 |
| 330 | 2.666 | 2.809 | 2.953 | 3.094 | 3.232 | 3.366 | 3.499 | 3.632 |
| 360 | 2.510 | 2.640 | 2.769 | 2.895 | 3.017 | 3.136 | 3.254 | 3.373 |
| 390 | 2.372 | 2.491 | 2.608 | 2.721 | 2.830 | 2.937 | 3.042 | 3.150 |

**Table B.8** Experimental compressed-liquid density $\rho$ for methylbenzene as a function of temperature and pressure, $T$: (283.15 to 473.15) K and $p$: (1 to 65) MPa.

| $p$ (MPa) | $\rho$ (kg·m$^{-3}$) | $p$ (MPa) | $\rho$ (kg·m$^{-3}$) | $p$ (MPa) | $\rho$ (kg·m$^{-3}$) |
|---|---|---|---|---|---|
| | | $T$ = 283.15 K | | | |
| 1.02 | 876.54 | 25.06 | 892.35 | 50.01 | 906.43 |
| 5.01 | 879.35 | 30.04 | 895.27 | 55.06 | 909.08 |
| 10.03 | 882.78 | 35.08 | 898.23 | 60.03 | 911.65 |
| 15.05 | 886.10 | 40.06 | 901.05 | 65.05 | 914.15 |
| 20.08 | 889.22 | 45.05 | 903.76 | | |
| | | $T$ = 298.15 K | | | |
| 1.04 | 862.84 | 25.05 | 879.91 | 50.04 | 895.05 |
| 5.04 | 865.89 | 30.06 | 883.12 | 55.04 | 897.86 |
| 10.03 | 869.56 | 35.02 | 886.24 | 60.03 | 900.56 |
| 15.05 | 873.18 | 40.04 | 889.24 | 65.02 | 903.21 |
| 20.04 | 876.59 | 45.07 | 892.20 | | |
| | | $T$ = 323.15 K | | | |

| $p$ (MPa) | $\rho$ (kg·m$^{-3}$) | $p$ (MPa) | $\rho$ (kg·m$^{-3}$) | $p$ (MPa) | $\rho$ (kg·m$^{-3}$) |
|---|---|---|---|---|---|
| 1.05 | 839.47 | 25.06 | 859.05 | 50.01 | 875.92 |
| 5.05 | 843.04 | 30.08 | 862.68 | 55.01 | 879.00 |
| 10.03 | 847.29 | 35.02 | 866.13 | 60.05 | 882.03 |
| 15.01 | 851.38 | 40.01 | 869.51 | 65.03 | 884.91 |
| 20.01 | 855.27 | 45.06 | 872.84 | | |
| | | $T$ = 348.15 K | | | |
| 1.06 | 815.56 | 25.02 | 838.19 | 50.02 | 857.08 |
| 5.07 | 819.76 | 30.08 | 842.29 | 55.06 | 860.47 |
| 10.01 | 824.67 | 35.05 | 846.20 | 60.04 | 863.78 |
| 15.03 | 829.43 | 40.05 | 849.96 | 65.07 | 866.98 |
| 20.03 | 833.88 | 45.06 | 853.61 | | |
| | | $T$ = 373.15 K | | | |
| 1.05 | 790.86 | 25.08 | 817.35 | 50.04 | 838.49 |
| 5.02 | 795.88 | 30.07 | 821.93 | 55.04 | 842.22 |
| 10.04 | 801.74 | 35.04 | 826.36 | 60.01 | 845.80 |
| 15.04 | 807.26 | 40.04 | 830.58 | 65.04 | 849.32 |
| 20.03 | 812.38 | 45.03 | 834.56 | | |
| | | $T$ = 398.15 K | | | |
| 1.07 | 765.25 | 25.05 | 796.25 | 50.02 | 819.95 |
| 5.03 | 771.27 | 30.04 | 801.48 | 55.04 | 824.14 |
| 10.04 | 778.23 | 35.04 | 806.47 | 60.02 | 828.09 |
| 15.08 | 784.74 | 40.02 | 811.17 | 65.08 | 831.98 |
| 20.01 | 790.62 | 45.04 | 815.70 | | |
| | | $T$ = 423.15 K | | | |
| 1.05 | 738.06 | 25.02 | 774.88 | 50.04 | 801.62 |
| 5.03 | 745.46 | 30.02 | 780.87 | 55.06 | 806.23 |
| 10.06 | 753.93 | 35.06 | 786.56 | 60.04 | 810.54 |
| 15.03 | 761.54 | 40.02 | 791.81 | 65.05 | 814.76 |
| 20.00 | 768.41 | 45.04 | 796.86 | | |
| | | $T$ = 448.15 K | | | |
| 1.04 | 708.97 | 25.05 | 753.39 | 50.03 | 783.38 |
| 5.07 | 718.49 | 30.04 | 760.21 | 55.06 | 788.43 |
| 10.04 | 728.71 | 35.04 | 766.59 | 60.01 | 793.16 |
| 15.07 | 737.86 | 40.02 | 772.48 | 65.06 | 797.81 |
| 20.05 | 745.94 | 45.03 | 778.12 | | |
| | | $T$ = 473.15 K | | | |
| 1.03 | 676.81 | 25.04 | 731.38 | 50.05 | 765.17 |
| 5.05 | 689.34 | 30.01 | 739.17 | 55.02 | 770.68 |
| 10.05 | 702.19 | 35.04 | 746.42 | 60.03 | 775.94 |
| 15.06 | 713.21 | 40.05 | 753.09 | 65.02 | 780.91 |
| 20.02 | 722.73 | 45.06 | 759.37 | | |

Standard uncertainties at 95 % confidence are $u(T)$ = 0.03 K and $u(p)$ = 20 kPa, and $u_c(\rho) \sim 0.0005\rho$.

**Table B.9** Experimental speed-of-sound $c$ in methylbenzene as a function of temperature and pressure, $T$: (283.15 to 473.15) K and $p$: (1 to 390) MPa.

| $p$ (MPa) | $c$ ($m \cdot s^{-1}$) | $p$ (MPa) | $c$ ($m \cdot s^{-1}$) | $p$ (MPa) | $c$ ($m \cdot s^{-1}$) |
|---|---|---|---|---|---|
| | | $T$ = 283.15 K | | | |
| 1.05 | 1375.85 | 149.99 | 1863.04 | 300.05 | 2169.82 |
| 30.19 | 1502.39 | 180.43 | 1934.00 | 330.05 | 2221.18 |
| 60.14 | 1609.63 | 210.03 | 1997.94 | 360.25 | 2270.54 |
| 90.04 | 1703.20 | 240.31 | 2059.12 | 389.98 | 2317.01 |
| 120.24 | 1787.54 | 269.98 | 2115.45 | 1.07 | 1376.31 |
| | | $T$ = 298.15 K | | | |
| 0.99 | 1309.58 | 150.23 | 1819.34 | 300.15 | 2132.53 |
| 30.08 | 1443.49 | 180.19 | 1891.02 | 329.91 | 2184.37 |
| 60.20 | 1557.01 | 210.16 | 1957.36 | 360.02 | 2234.29 |
| 90.13 | 1654.39 | 240.26 | 2019.46 | 390.01 | 2282.09 |
| 119.97 | 1740.39 | 270.46 | 2078.03 | 1.05 | 1310.03 |
| | | $T$ = 323.15 K | | | |
| 1.00 | 1203.13 | 150.27 | 1750.52 | 300.07 | 2074.27 |
| 30.00 | 1350.79 | 179.98 | 1824.20 | 330.00 | 2127.69 |
| 60.17 | 1473.56 | 210.22 | 1893.85 | 360.29 | 2179.26 |
| 90.20 | 1577.76 | 240.02 | 1957.41 | 389.93 | 2227.48 |
| 120.66 | 1670.01 | 270.09 | 2017.64 | 1.04 | 1203.62 |
| | | $T$ = 348.15 K | | | |
| 1.06 | 1101.47 | 150.46 | 1687.69 | 300.32 | 2021.20 |
| 30.15 | 1265.36 | 180.23 | 1764.23 | 330.13 | 2075.74 |
| 60.13 | 1395.96 | 210.54 | 1836.00 | 360.14 | 2127.73 |
| 90.31 | 1506.73 | 240.10 | 1900.99 | 390.00 | 2176.92 |
| 120.32 | 1602.26 | 270.60 | 1963.70 | 1.07 | 1101.62 |
| | | $T$ = 373.15 K | | | |
| 1.01 | 1002.14 | 150.34 | 1628.84 | 300.19 | 1971.49 |
| 30.07 | 1183.47 | 180.20 | 1708.20 | 330.35 | 2027.37 |
| 60.00 | 1323.42 | 210.11 | 1781.11 | 360.55 | 2080.74 |
| 90.34 | 1440.60 | 240.27 | 1849.24 | 390.03 | 2130.48 |
| 120.24 | 1540.23 | 270.18 | 1912.25 | 1.01 | 1002.34 |
| | | $T$ = 398.15 K | | | |
| 1.08 | 906.54 | 150.32 | 1574.92 | 300.00 | 1925.01 |
| 30.07 | 1107.29 | 180.22 | 1656.81 | 330.09 | 1982.29 |
| 60.01 | 1256.71 | 210.00 | 1731.10 | 360.01 | 2036.20 |
| 90.31 | 1379.44 | 240.20 | 1800.46 | 390.00 | 2088.55 |
| 120.39 | 1483.63 | 270.09 | 1864.90 | 1.08 | 906.73 |
| | | $T$ = 423.15 K | | | |
| 1.02 | 810.90 | 150.23 | 1524.26 | 300.10 | 1883.03 |
| 30.08 | 1035.61 | 180.33 | 1608.84 | 329.96 | 1940.82 |
| 60.12 | 1194.96 | 210.09 | 1684.92 | 360.00 | 1997.13 |
| 90.12 | 1322.02 | 240.21 | 1755.96 | 390.00 | 2049.64 |

| $p$ (MPa) | $c$ (m·s$^{-1}$) | $p$ (MPa) | $c$ (m·s$^{-1}$) | $p$ (MPa) | $c$ (m·s$^{-1}$) |
|---|---|---|---|---|---|
| 120.03 | 1429.30 | 270.10 | 1821.45 | 1.02 | 811.06 |
| | | $T$ = 448.15 K | | | |
| 1.04 | 716.02 | 150.22 | 1477.59 | 300.00 | 1844.24 |
| 30.30 | 969.48 | 180.07 | 1563.71 | 330.05 | 1904.07 |
| 59.95 | 1136.31 | 209.85 | 1641.64 | 360.26 | 1960.61 |
| 90.25 | 1269.95 | 240.09 | 1714.35 | 389.97 | 2013.46 |
| 119.95 | 1379.82 | 270.23 | 1781.81 | 1.08 | 716.71 |
| | | $T$ = 473.15 K | | | |
| 1.03 | 619.52 | 150.13 | 1434.05 | 300.11 | 1810.67 |
| 30.06 | 903.93 | 180.09 | 1522.51 | 330.02 | 1869.02 |
| 60.11 | 1082.96 | 210.21 | 1603.20 | 360.02 | 1926.03 |
| 90.33 | 1221.13 | 240.00 | 1676.68 | 390.03 | 1979.82 |
| 120.36 | 1335.44 | 269.85 | 1745.42 | 1.02 | 619.30 |

Standard uncertainties at 95 % confidence are $u(T)$ = 0.05 K and $u(p)$ = 50 kPa, and $u_c(c) \sim 0.0003c$.

**Table B.10** Derived thermophysical properties for methylbenzene at $T$: (298.15 to 473.15) K and pressures up to 390 MPa: density $\rho$, isobaric heat capacity $c_p$, isothermal compressibility $\beta$ and isobaric expansivity $\alpha$.

| | | | | $\rho$/(kg·m$^{-3}$) | | | | |
|---|---|---|---|---|---|---|---|---|
| $p$/MPa | 298.15 K | 323.15 K | 348.15 K | 373.15 K | 398.15 K | 423.15 K | 448.15 K | 473.15 K |
| 0.1 | 861.91 | 838.41 | 814.53 | 789.84 | 763.89 | 736.28 | 706.55 | 674.28 |
| 30 | 882.91 | 862.53 | 842.36 | 822.17 | 801.77 | 781.09 | 760.22 | 739.54 |
| 60 | 900.19 | 881.82 | 863.88 | 846.13 | 828.43 | 810.75 | 793.24 | 776.31 |
| 90 | 915.02 | 898.11 | 881.69 | 865.55 | 849.55 | 833.67 | 818.07 | 803.18 |
| 120 | 928.12 | 912.32 | 897.05 | 882.08 | 867.29 | 852.65 | 838.33 | 824.77 |
| 150 | 939.89 | 925.00 | 910.64 | 896.58 | 882.71 | 868.99 | 855.61 | 843.01 |
| 180 | 950.63 | 936.49 | 922.88 | 909.57 | 896.43 | 883.44 | 870.79 | 858.92 |
| 210 | 960.52 | 947.03 | 934.05 | 921.36 | 908.83 | 896.44 | 884.37 | 873.08 |
| 240 | 969.71 | 956.78 | 944.36 | 932.21 | 920.19 | 908.30 | 896.72 | 885.90 |
| 270 | 978.30 | 965.88 | 953.94 | 942.26 | 930.69 | 919.23 | 908.06 | 897.65 |
| 300 | 986.39 | 974.42 | 962.91 | 951.64 | 940.47 | 929.38 | 918.57 | 908.50 |
| 330 | 994.03 | 982.47 | 971.35 | 960.45 | 949.63 | 938.88 | 928.38 | 918.61 |
| 360 | 1001.28 | 990.09 | 979.33 | 968.77 | 958.27 | 947.82 | 937.60 | 928.09 |
| 390 | 1008.18 | 997.34 | 986.91 | 976.66 | 966.45 | 956.26 | 946.30 | 937.03 |
| | | | | $c_p$/(J·kg$^{-1}$·K$^{-1}$) | | | | |
| $p$/MPa | 298.15 K | 323.15 K | 348.15 K | 373.15 K | 398.15 K | 423.15 K | 448.15 K | 473.15 K |
| 0.1 | 1703.8 | 1783.2 | 1869.4 | 1961.5 | 2058.6 | 2160.1 | 2264.9 | 2372.4 |
| 30 | 1682.3 | 1754.6 | 1831.8 | 1912.6 | 1995.3 | 2078.2 | 2159.0 | 2234.9 |
| 60 | 1668.6 | 1738.8 | 1813.6 | 1891.6 | 1971.3 | 2050.7 | 2127.6 | 2199.1 |
| 90 | 1659.7 | 1729.1 | 1803.1 | 1880.4 | 1959.5 | 2038.3 | 2114.7 | 2185.9 |
| 120 | 1653.4 | 1722.5 | 1796.5 | 1873.8 | 1953.0 | 2032.3 | 2109.3 | 2181.3 |
| 150 | 1648.6 | 1717.8 | 1791.9 | 1869.7 | 1949.4 | 2029.5 | 2107.5 | 2180.9 |
| 180 | 1644.8 | 1714.1 | 1788.6 | 1866.9 | 1947.4 | 2028.4 | 2107.6 | 2182.5 |

| | | | | | | | | |
|---|---|---|---|---|---|---|---|---|
| 210 | 1641.5 | 1711.2 | 1786.1 | 1864.9 | 1946.3 | 2028.3 | 2108.8 | 2185.3 |
| 240 | 1638.6 | 1708.6 | 1784.0 | 1863.5 | 1945.7 | 2028.8 | 2110.6 | 2188.6 |
| 270 | 1636.0 | 1706.3 | 1782.1 | 1862.3 | 1945.3 | 2029.5 | 2112.6 | 2192.1 |
| 300 | 1633.5 | 1704.1 | 1780.4 | 1861.3 | 1945.1 | 2030.3 | 2114.7 | 2195.7 |
| 330 | 1631.1 | 1702.0 | 1778.8 | 1860.3 | 1945.0 | 2031.1 | 2116.7 | 2199.1 |
| 360 | 1628.7 | 1699.9 | 1777.2 | 1859.3 | 1944.8 | 2031.9 | 2118.6 | 2202.4 |
| 390 | 1626.3 | 1697.9 | 1775.6 | 1858.3 | 1944.5 | 2032.5 | 2120.4 | 2205.4 |
| | | | | $10^4\alpha$/K$^{-1}$ | | | | |
| $p$/MPa | 298.15 K | 323.15 K | 348.15 K | 373.15 K | 398.15 K | 423.15 K | 448.15 K | 473.15 K |
| 0.1 | 10.88 | 11.27 | 11.89 | 12.79 | 13.98 | 15.54 | 17.51 | 19.98 |
| 30 | 9.14 | 9.37 | 9.63 | 9.91 | 10.22 | 10.57 | 10.96 | 11.38 |
| 60 | 8.10 | 8.21 | 8.31 | 8.42 | 8.52 | 8.61 | 8.71 | 8.80 |
| 90 | 7.35 | 7.40 | 7.44 | 7.46 | 7.48 | 7.49 | 7.48 | 7.46 |
| 120 | 6.77 | 6.79 | 6.79 | 6.79 | 6.76 | 6.73 | 6.68 | 6.60 |
| 150 | 6.29 | 6.30 | 6.29 | 6.27 | 6.23 | 6.17 | 6.10 | 6.01 |
| 180 | 5.90 | 5.90 | 5.89 | 5.85 | 5.81 | 5.74 | 5.66 | 5.56 |
| 210 | 5.57 | 5.57 | 5.55 | 5.51 | 5.46 | 5.39 | 5.31 | 5.20 |
| 240 | 5.28 | 5.27 | 5.26 | 5.22 | 5.17 | 5.11 | 5.02 | 4.92 |
| 270 | 5.02 | 5.02 | 5.01 | 4.97 | 4.93 | 4.86 | 4.78 | 4.68 |
| 300 | 4.79 | 4.80 | 4.78 | 4.75 | 4.71 | 4.65 | 4.57 | 4.47 |
| 330 | 4.58 | 4.59 | 4.58 | 4.56 | 4.52 | 4.47 | 4.39 | 4.30 |
| 360 | 4.40 | 4.41 | 4.41 | 4.39 | 4.35 | 4.30 | 4.23 | 4.15 |
| 390 | 4.23 | 4.24 | 4.24 | 4.23 | 4.20 | 4.15 | 4.09 | 4.01 |
| | | | | $10^4\beta$/MPa$^{-1}$ | | | | |
| $p$/MPa | 298.15 K | 323.15 K | 348.15 K | 373.15 K | 398.15 K | 423.15 K | 448.15 K | 473.15 K |
| 0.1 | 9.22 | 11.05 | 13.47 | 16.71 | 21.19 | 27.59 | 37.10 | 52.05 |
| 30 | 7.12 | 8.23 | 9.52 | 11.02 | 12.78 | 14.87 | 17.36 | 20.32 |
| 60 | 5.89 | 6.65 | 7.48 | 8.39 | 9.41 | 10.53 | 11.77 | 13.15 |
| 90 | 5.06 | 5.62 | 6.22 | 6.85 | 7.53 | 8.26 | 9.04 | 9.87 |
| 120 | 4.45 | 4.89 | 5.35 | 5.82 | 6.32 | 6.84 | 7.39 | 7.96 |
| 150 | 3.98 | 4.34 | 4.71 | 5.08 | 5.47 | 5.87 | 6.28 | 6.70 |
| 180 | 3.61 | 3.91 | 4.22 | 4.52 | 4.84 | 5.16 | 5.48 | 5.80 |
| 210 | 3.30 | 3.56 | 3.82 | 4.08 | 4.34 | 4.61 | 4.87 | 5.13 |
| 240 | 3.05 | 3.28 | 3.50 | 3.73 | 3.95 | 4.17 | 4.39 | 4.61 |
| 270 | 2.84 | 3.04 | 3.24 | 3.43 | 3.62 | 3.81 | 4.00 | 4.19 |
| 300 | 2.65 | 2.83 | 3.01 | 3.18 | 3.35 | 3.52 | 3.68 | 3.84 |
| 330 | 2.49 | 2.66 | 2.81 | 2.97 | 3.12 | 3.27 | 3.41 | 3.55 |
| 360 | 2.35 | 2.50 | 2.65 | 2.79 | 2.92 | 3.05 | 3.18 | 3.30 |
| 390 | 2.23 | 2.36 | 2.50 | 2.62 | 2.75 | 2.87 | 2.98 | 3.09 |

**Table B.11** Experimental compressed-liquid density $\rho$ for carbon dioxide as a function of temperature and pressure, $T$: (283.15 to 473.15) K and $p$: (10 to 65) MPa.

| $p$ (MPa) | $\rho$ (kg·m$^{-3}$) | $p$ (MPa) | $\rho$ (kg·m$^{-3}$) | $p$ (MPa) | $\rho$ (kg·m$^{-3}$) |
|---|---|---|---|---|---|

| $p$ (MPa) | $\rho$ (kg·m$^{-3}$) | $p$ (MPa) | $\rho$ (kg·m$^{-3}$) | $p$ (MPa) | $\rho$ (kg·m$^{-3}$) |
|---|---|---|---|---|---|
| | | $T$ = 283.15 K | | | |
| 10.01 | 920.13 | 30.02 | 1019.31 | 50.00 | 1075.40 |
| 15.01 | 954.10 | 35.02 | 1035.90 | 55.00 | 1086.55 |
| 20.00 | 979.44 | 40.01 | 1049.44 | 60.00 | 1096.83 |
| 25.01 | 1001.30 | 45.01 | 1063.28 | 65.01 | 1106.39 |
| | | $T$ = 298.15 K | | | |
| 10.03 | 818.47 | 30.01 | 965.99 | 50.00 | 1033.41 |
| 15.01 | 876.55 | 35.01 | 986.09 | 55.01 | 1046.44 |
| 20.00 | 913.82 | 40.00 | 1003.46 | 60.01 | 1058.51 |
| 25.03 | 943.12 | 45.03 | 1019.32 | 65.01 | 1068.95 |
| | | $T$ = 323.15 K | | | |
| 10.02 | 388.56 | 30.00 | 869.92 | 50.00 | 961.51 |
| 15.00 | 701.06 | 35.01 | 898.94 | 55.02 | 977.96 |
| 20.00 | 784.40 | 40.01 | 922.57 | 60.00 | 992.80 |
| 25.00 | 834.25 | 45.01 | 943.67 | 65.00 | 1006.28 |
| | | $T$ = 348.15 K | | | |
| 10.02 | 235.50 | 30.02 | 766.65 | 50.01 | 889.42 |
| 15.03 | 466.20 | 35.01 | 807.15 | 55.00 | 909.77 |
| 20.01 | 626.94 | 40.01 | 839.39 | 60.00 | 927.93 |
| 25.02 | 712.10 | 45.03 | 866.41 | 65.00 | 944.15 |
| | | $T$ = 373.15 K | | | |
| 10.01 | 189.61 | 30.02 | 661.93 | 50.01 | 818.07 |
| 15.00 | 333.02 | 35.01 | 714.85 | 55.01 | 842.73 |
| 20.00 | 481.64 | 40.01 | 756.29 | 60.00 | 864.24 |
| 25.02 | 589.15 | 45.02 | 789.89 | 65.01 | 883.60 |
| | | $T$ = 398.15 K | | | |
| 10.03 | 164.19 | 30.00 | 567.81 | 50.01 | 749.77 |
| 15.01 | 271.55 | 35.02 | 629.20 | 55.01 | 778.27 |
| 20.02 | 386.59 | 40.00 | 677.26 | 60.00 | 803.03 |
| 25.01 | 487.98 | 45.00 | 716.53 | 65.00 | 824.37 |
| | | $T$ = 423.15 K | | | |
| 10.02 | 146.37 | 30.01 | 492.12 | 50.00 | 686.47 |
| 15.02 | 234.66 | 35.01 | 555.19 | 55.00 | 718.06 |
| 20.02 | 327.81 | 40.01 | 606.76 | 60.00 | 745.62 |
| 25.01 | 415.82 | 45.02 | 650.15 | 65.01 | 769.86 |
| | | $T$ = 448.15 K | | | |
| 10.00 | 132.91 | 30.01 | 434.08 | 50.02 | 629.98 |
| 15.01 | 209.12 | 35.01 | 494.67 | 55.01 | 663.32 |
| 20.00 | 287.68 | 40.00 | 546.83 | 60.02 | 692.95 |
| 25.02 | 364.36 | 45.02 | 591.58 | 65.01 | 718.86 |
| | | $T$ = 473.15 K | | | |
| 10.01 | 122.67 | 30.01 | 389.60 | 50.02 | 580.33 |
| 15.01 | 190.08 | 35.00 | 446.35 | 55.00 | 614.62 |

| $p$ (MPa) | $\rho$ (kg·m$^{-3}$) | $p$ (MPa) | $\rho$ (kg·m$^{-3}$) | $p$ (MPa) | $\rho$ (kg·m$^{-3}$) |
|---|---|---|---|---|---|
| 20.00 | 258.90 | 40.01 | 496.97 | 60.01 | 645.35 |
| 25.01 | 326.62 | 45.01 | 541.26 | 65.01 | 672.58 |

Standard uncertainties at 95 % confidence are $u(T) = 0.03$ K and $u(p) = 20$ kPa, and $u_c(\rho) \sim 0.0005\rho$.

Experimental compressed-liquid densities were fitted to the following empirical equation:

$$p = A\rho + B\rho^2 + C\frac{(\rho - \rho_r)^\delta}{\delta} \tag{5.10}$$

The correlation describes the pressure as a function of density at each temperature and composition. The delta was 4.82. The parameters $A$, $B$ and $\rho_r$, are adjustable parameters, reported in Table B.12.

**Table B.12** Parameters $A$, $B$ and $\rho_r$ in Equation (6.1) for compressed-liquid densities and the values of the average absolute deviation, $\Delta_{AAD,}$ and average absolute relative deviation, $\Delta_{AARD}$ for $CO_2$.

| Parameter | | Parameter | | Parameter | |
|---|---|---|---|---|---|
| 283.15 K | | 348.15 K | | 423.15 K | |
| $A$ | $7.863\times10^{-4}$ | $A$ | $4.136\times10^{-2}$ | $A$ | $7.473\times10^{-2}$ |
| $B$ | $-2.722\times10^{-6}$ | $B$ | $-2.022\times10^{-5}$ | $B$ | $-4.999\times10^{-5}$ |
| $C$ | $1.238\times10^{-11}$ | $C$ | $4.806\times10^{-12}$ | $C$ | $1.462\times10^{-12}$ |
| $\rho_r$ | $4.982\times10^{2}$ | $\rho_r$ | $2.671\times10^{2}$ | $\rho_r$ | $-6.673\times10^{1}$ |
| $\Delta_{AAD}$ / MPa | 0.07 | $\Delta_{AAD}$ / MPa | 0.03 | $\Delta_{AAD}$ / MPa | 0.06 |
| $\Delta_{AARD}$ | 0.22% | $\Delta_{AARD}$ | 0.11% | $\Delta_{AARD}$ | 0.24% |
| 298.15 K | | 373.15 K | | 448.15 K | |
| $A$ | $1.137\times10^{-2}$ | $A$ | $6.039\times10^{-2}$ | $A$ | $8.059\times10^{-2}$ |
| $B$ | $-6.087\times10^{-6}$ | $B$ | $-4.594\times10^{-5}$ | $B$ | $-4.962\times10^{-5}$ |
| $C$ | $1.041\times10^{-11}$ | $C$ | $2.255\times10^{-12}$ | $C$ | $1.305\times10^{-12}$ |
| $\rho_r$ | $4.543\times10^{2}$ | $\rho_r$ | $7.880\times10^{1}$ | $\rho_r$ | $-1.157\times10^{2}$ |
| $\Delta_{AAD}$ / MPa | 0.05 | $\Delta_{AAD}$ / MPa | 0.11 | $\Delta_{AAD}$ / MPa | 0.04 |
| $\Delta_{AARD}$ | 0.15% | $\Delta_{AARD}$ | 0.51% | $\Delta_{AARD}$ | 0.16% |
| 323.15 K | | 398.15 K | | 473.15 K | |
| $A$ | $3.696\times10^{-2}$ | $A$ | $6.764\times10^{-2}$ | $A$ | $8.595\times10^{-2}$ |
| $B$ | $-2.887\times10^{-5}$ | $B$ | $-4.649\times10^{-5}$ | $B$ | $-5.043\times10^{-5}$ |
| $C$ | $5.795\times10^{-12}$ | $C$ | $1.875\times10^{-12}$ | $C$ | $1.140\times10^{-12}$ |
| $\rho_r$ | $3.188\times10^{2}$ | $\rho_r$ | $1.424\times10^{1}$ | $\rho_r$ | $-1.705\times10^{2}$ |
| $\Delta_{AAD}$ / MPa | 0.05 | $\Delta_{AAD}$ / MPa | 0.10 | $\Delta_{AAD}$ / MPa | 0.03 |
| $\Delta_{AARD}$ | 0.17% | $\Delta_{AARD}$ | 0.38% | $\Delta_{AARD}$ | 0.09% |

# Appendix C:

**Table C.1** Experimental compressed-liquid density $\rho$ for $CO_2$ + *n*-heptane at four compositions as a function of temperature, *T*: (283.15 to 473.15) K and *p*: (10 to 68) MPa.

| *p* (MPa) | $\rho$ (kg·m$^{-3}$) | *p* (MPa) | $\rho$ (kg·m$^{-3}$) | *p* (MPa) | $\rho$ (kg·m$^{-3}$) |
|---|---|---|---|---|---|
| | | **$x_{CO2}$ = 0.2053** | | | |
| | | *T* = 283.15 K | | | |
| 10.01 | 717.20 | 35.00 | 737.65 | 60.01 | 754.16 |
| 15.01 | 721.73 | 40.01 | 741.22 | 65.02 | 757.13 |
| 20.00 | 726.01 | 45.00 | 744.65 | 68.01 | 759.01 |
| 25.00 | 730.09 | 50.01 | 747.92 | 10.00 | 717.20 |
| 30.00 | 733.97 | 55.01 | 751.09 | | |
| | | *T* = 298.15 K | | | |
| 10.01 | 703.68 | 35.00 | 726.19 | 60.01 | 743.90 |
| 15.00 | 708.79 | 40.02 | 730.05 | 65.01 | 747.06 |
| 20.00 | 713.50 | 45.01 | 733.72 | 68.00 | 748.97 |
| 25.00 | 717.97 | 50.00 | 737.23 | 10.02 | 703.73 |
| 30.00 | 722.18 | 55.01 | 740.59 | | |
| | | *T* = 323.15 K | | | |
| 10.01 | 680.60 | 35.01 | 706.85 | 60.01 | 726.69 |
| 15.02 | 686.66 | 40.01 | 711.18 | 65.00 | 730.17 |
| 20.01 | 692.18 | 45.00 | 715.36 | 68.01 | 732.32 |
| 25.01 | 697.40 | 50.02 | 719.28 | 10.00 | 680.60 |
| 30.01 | 702.28 | 55.00 | 723.07 | | |
| | | *T* = 348.15 K | | | |
| 10.00 | 656.67 | 35.00 | 687.50 | 60.00 | 709.70 |
| 15.01 | 664.02 | 40.01 | 692.43 | 65.02 | 713.59 |
| 20.01 | 670.58 | 45.01 | 697.07 | 68.00 | 715.92 |
| 25.02 | 676.69 | 50.00 | 701.51 | 10.01 | 656.72 |
| 30.00 | 682.27 | 55.01 | 705.70 | | |
| | | *T* = 373.15 K | | | |
| 10.00 | 631.77 | 35.01 | 668.16 | 60.00 | 692.99 |
| 15.02 | 640.72 | 40.00 | 673.74 | 65.01 | 697.25 |
| 20.01 | 648.56 | 45.00 | 678.94 | 68.01 | 699.75 |
| 25.01 | 655.66 | 50.00 | 683.93 | 10.01 | 631.82 |
| 30.01 | 662.18 | 55.01 | 688.58 | | |
| | | *T* = 398.15 K | | | |
| 10.00 | 605.54 | 35.01 | 648.79 | 60.00 | 676.62 |
| 15.01 | 616.62 | 40.01 | 655.11 | 65.01 | 681.24 |
| 20.01 | 626.01 | 45.01 | 661.00 | 68.01 | 684.02 |
| 25.00 | 634.43 | 50.01 | 666.50 | 10.01 | 605.53 |
| 30.01 | 641.92 | 55.01 | 671.66 | | |
| | | *T* = 423.15 K | | | |

| $p$ (MPa) | $\rho$ (kg·m$^{-3}$) | $p$ (MPa) | $\rho$ (kg·m$^{-3}$) | $p$ (MPa) | $\rho$ (kg·m$^{-3}$) |
|---|---|---|---|---|---|
| 10.00 | 577.56 | 35.00 | 629.41 | 60.00 | 660.34 |
| 15.01 | 591.51 | 40.00 | 636.56 | 65.00 | 665.41 |
| 20.00 | 602.91 | 45.01 | 643.13 | 68.02 | 668.41 |
| 25.00 | 612.82 | 50.00 | 649.22 | 10.01 | 577.65 |
| 30.01 | 621.57 | 55.01 | 654.97 | | |
| | | $T$ = 448.15 K | | | |
| 10.02 | 547.50 | 35.01 | 610.02 | 60.01 | 644.28 |
| 15.01 | 565.29 | 40.01 | 618.04 | 65.01 | 649.84 |
| 20.00 | 579.20 | 45.01 | 625.38 | 68.00 | 653.01 |
| 25.00 | 590.96 | 50.01 | 632.15 | 10.01 | 547.50 |
| 30.01 | 601.00 | 55.00 | 638.43 | | |
| | | $T$ = 473.15 K | | | |
| 10.01 | 514.54 | 35.00 | 590.53 | 60.00 | 628.51 |
| 15.01 | 537.86 | 40.00 | 599.59 | 65.01 | 634.50 |
| 20.00 | 554.82 | 45.01 | 607.79 | 68.01 | 638.08 |
| 25.00 | 568.74 | 50.01 | 615.22 | 10.00 | 514.54 |
| 30.01 | 580.37 | 55.01 | 622.13 | | |
| | | **$x_{CO2}$ = 0.3989** | | | |
| | | $T$ = 283.15 K | | | |
| 10.00 | 738.68 | 35.01 | 763.73 | 60.00 | 783.20 |
| 15.01 | 744.36 | 40.01 | 767.90 | 65.01 | 786.67 |
| 20.01 | 749.59 | 45.01 | 771.98 | 68.01 | 788.74 |
| 25.01 | 754.57 | 50.01 | 775.85 | 10.01 | 738.67 |
| 30.01 | 759.25 | 55.00 | 779.58 | | |
| | | $T$ = 298.15 K | | | |
| 10.00 | 722.79 | 35.01 | 750.74 | 60.01 | 771.79 |
| 15.01 | 729.25 | 40.01 | 755.31 | 65.00 | 775.50 |
| 20.01 | 735.11 | 45.01 | 759.72 | 68.01 | 777.66 |
| 25.01 | 740.67 | 50.01 | 763.92 | 10.00 | 722.79 |
| 30.00 | 745.83 | 55.02 | 767.93 | | |
| | | $T$ = 323.15 K | | | |
| 10.00 | 694.35 | 35.00 | 727.85 | 60.00 | 751.81 |
| 15.00 | 702.35 | 40.01 | 733.17 | 65.01 | 755.93 |
| 20.00 | 709.45 | 45.01 | 738.19 | 68.01 | 758.33 |
| 25.00 | 716.06 | 50.01 | 742.96 | 10.01 | 694.35 |
| 30.00 | 722.13 | 55.01 | 747.48 | | |
| | | $T$ = 348.15 K | | | |
| 10.00 | 664.24 | 35.01 | 704.88 | 60.01 | 732.01 |
| 15.01 | 674.44 | 40.00 | 711.00 | 65.00 | 736.65 |
| 20.01 | 683.12 | 45.01 | 716.77 | 68.01 | 739.32 |
| 25.01 | 691.11 | 50.02 | 722.15 | 10.01 | 664.29 |
| 30.01 | 698.22 | 55.01 | 727.23 | | |
| | | $T$ = 373.15 K | | | |

| $p$ (MPa) | $\rho$ (kg·m$^{-3}$) | $p$ (MPa) | $\rho$ (kg·m$^{-3}$) | $p$ (MPa) | $\rho$ (kg·m$^{-3}$) |
|---|---|---|---|---|---|
| 10.00 | 631.96 | 35.00 | 681.76 | 60.01 | 712.53 |
| 15.01 | 645.07 | 40.01 | 688.82 | 65.00 | 717.63 |
| 20.01 | 655.90 | 45.01 | 695.38 | 68.01 | 720.62 |
| 25.00 | 665.54 | 50.01 | 701.46 | 10.00 | 632.06 |
| 30.01 | 674.02 | 55.00 | 707.15 | | |
| | | $T$ = 398.15 K | | | |
| 10.00 | 596.61 | 35.01 | 659.00 | 60.00 | 693.27 |
| 15.00 | 614.05 | 40.01 | 666.64 | 65.01 | 698.96 |
| 20.01 | 627.71 | 45.02 | 674.09 | 68.01 | 702.18 |
| 25.00 | 639.44 | 50.00 | 680.91 | 10.01 | 596.75 |
| 30.01 | 649.51 | 55.01 | 687.33 | | |
| | | $T$ = 423.15 K | | | |
| 10.00 | 556.99 | 35.00 | 635.11 | 60.00 | 674.23 |
| 15.01 | 581.00 | 40.01 | 644.39 | 65.00 | 680.41 |
| 20.01 | 598.43 | 45.02 | 652.86 | 68.00 | 684.00 |
| 25.01 | 612.68 | 50.00 | 660.55 | 10.00 | 557.04 |
| 30.01 | 624.62 | 55.01 | 667.65 | | |
| | | $T$ = 448.15 K | | | |
| 10.00 | 511.21 | 35.01 | 611.70 | 60.01 | 655.54 |
| 15.00 | 545.61 | 40.00 | 622.27 | 65.01 | 662.31 |
| 20.01 | 567.98 | 45.01 | 631.83 | 68.00 | 666.20 |
| 25.01 | 585.49 | 50.01 | 640.37 | 10.00 | 511.41 |
| 30.01 | 599.56 | 55.00 | 648.25 | | |
| | | $T$ = 473.15 K | | | |
| 10.01 | 458.14 | 35.01 | 588.38 | 60.00 | 637.12 |
| 15.00 | 508.00 | 40.01 | 600.35 | 65.00 | 644.50 |
| 20.00 | 536.53 | 45.00 | 610.94 | 68.01 | 648.79 |
| 25.00 | 557.82 | 50.02 | 620.48 | 10.00 | 458.10 |
| 30.00 | 574.36 | 55.01 | 629.16 | | |
| | | **$x_{CO2}$ = 0.6037** | | | |
| | | $T$ = 283.15 K | | | |
| 10.02 | 771.71 | 35.01 | 805.91 | 60.01 | 830.80 |
| 15.01 | 779.70 | 40.00 | 811.29 | 65.00 | 835.18 |
| 20.01 | 786.84 | 45.01 | 816.72 | 68.01 | 837.90 |
| 25.01 | 793.83 | 50.01 | 821.50 | 10.00 | 771.71 |
| 30.00 | 799.82 | 55.01 | 826.43 | | |
| | | $T$ = 298.15 K | | | |
| 10.00 | 749.37 | 35.00 | 788.74 | 60.01 | 816.14 |
| 15.01 | 758.88 | 40.01 | 794.80 | 65.01 | 820.85 |
| 20.01 | 767.29 | 45.01 | 800.66 | 68.01 | 823.57 |
| 25.01 | 775.16 | 50.00 | 806.02 | 10.01 | 749.47 |
| 30.00 | 782.12 | 55.00 | 811.24 | | |
| | | $T$ = 323.15 K | | | |

| $p$ (MPa) | $\rho$ (kg·m$^{-3}$) | $p$ (MPa) | $\rho$ (kg·m$^{-3}$) | $p$ (MPa) | $\rho$ (kg·m$^{-3}$) |
|---|---|---|---|---|---|
| 10.00 | 709.06 | 35.00 | 759.00 | 60.01 | 790.89 |
| 15.01 | 722.07 | 40.01 | 766.22 | 65.02 | 796.21 |
| 20.00 | 732.65 | 45.02 | 773.08 | 68.01 | 799.30 |
| 25.01 | 742.54 | 50.01 | 779.30 | 10.00 | 709.16 |
| 30.00 | 751.00 | 55.01 | 785.32 | | |
| | | $T$ = 348.15 K | | | |
| 10.00 | 663.70 | 35.01 | 728.84 | 60.00 | 765.83 |
| 15.00 | 681.92 | 40.00 | 737.38 | 65.01 | 771.85 |
| 20.00 | 696.22 | 45.00 | 745.39 | 68.01 | 775.32 |
| 25.01 | 708.65 | 50.01 | 752.59 | 10.01 | 663.75 |
| 30.00 | 719.21 | 55.01 | 759.46 | | |
| | | $T$ = 373.15 K | | | |
| 10.01 | 610.44 | 35.01 | 698.27 | 60.01 | 741.09 |
| 15.02 | 638.28 | 40.01 | 708.38 | 65.01 | 747.86 |
| 20.01 | 657.56 | 45.00 | 717.70 | 68.00 | 751.74 |
| 25.01 | 673.57 | 50.01 | 726.08 | 10.01 | 610.39 |
| 30.01 | 686.70 | 55.02 | 733.88 | | |
| | | $T$ = 398.15 K | | | |
| 15.00 | 591.88 | 40.01 | 679.36 | 65.00 | 724.72 |
| 20.01 | 617.66 | 45.01 | 690.17 | 68.01 | 729.16 |
| 25.01 | 637.30 | 50.01 | 699.97 | 15.03 | 590.91 |
| 30.00 | 653.40 | 55.01 | 708.93 | | |
| 35.01 | 667.33 | 60.00 | 717.12 | | |
| | | $T$ = 423.15 K | | | |
| 15.00 | 535.53 | 40.01 | 650.30 | 65.02 | 701.36 |
| 20.01 | 573.98 | 45.02 | 662.83 | 68.01 | 706.16 |
| 25.01 | 600.03 | 50.00 | 673.62 | 15.01 | 536.49 |
| 30.01 | 619.93 | 55.00 | 683.84 | | |
| 35.01 | 636.42 | 60.01 | 692.84 | | |
| | | $T$ = 448.15 K | | | |
| 15.01 | 477.35 | 40.01 | 621.84 | 65.01 | 678.78 |
| 20.01 | 529.65 | 45.01 | 635.91 | 68.01 | 684.17 |
| 25.01 | 562.29 | 50.00 | 648.17 | 15.00 | 477.69 |
| 30.01 | 586.36 | 55.02 | 659.42 | | |
| 35.01 | 605.75 | 60.01 | 669.46 | | |
| | | $T$ = 473.15 K | | | |
| 15.01 | 421.66 | 40.00 | 593.62 | 65.01 | 656.80 |
| 20.01 | 486.09 | 45.02 | 609.36 | 68.01 | 662.44 |
| 25.01 | 524.79 | 50.00 | 623.06 | 15.00 | 421.61 |
| 30.01 | 553.34 | 55.01 | 635.47 | | |
| 35.01 | 575.31 | 60.01 | 646.54 | | |
| | | **$x_{CO2}$ = 0.8001** | | | |
| | | $T$ = 283.15 K | | | |

| $p$ (MPa) | $\rho$ (kg·m$^{-3}$) | $p$ (MPa) | $\rho$ (kg·m$^{-3}$) | $p$ (MPa) | $\rho$ (kg·m$^{-3}$) |
|---|---|---|---|---|---|
| 10.02 | 823.37 | 35.01 | 875.59 | 60.01 | 910.17 |
| 15.00 | 836.52 | 40.01 | 883.25 | 65.00 | 916.06 |
| 20.00 | 847.31 | 45.01 | 890.86 | 68.01 | 919.40 |
| 25.01 | 857.89 | 50.01 | 897.57 | 10.00 | 823.43 |
| 30.00 | 866.87 | 55.01 | 904.27 | | |
| | | $T$ = 298.15 K | | | |
| 10.01 | 787.40 | 35.01 | 852.33 | 60.00 | 891.36 |
| 15.01 | 805.05 | 40.00 | 860.97 | 65.01 | 897.94 |
| 20.01 | 818.49 | 45.01 | 869.76 | 68.01 | 901.66 |
| 25.00 | 831.29 | 50.01 | 877.25 | 10.01 | 787.50 |
| 30.00 | 841.99 | 55.01 | 884.73 | | |
| | | $T$ = 323.15 K | | | |
| 10.01 | 714.71 | 35.00 | 808.42 | 60.01 | 855.85 |
| 15.01 | 743.80 | 40.00 | 819.39 | 65.00 | 863.33 |
| 20.01 | 763.84 | 45.01 | 829.96 | 68.01 | 867.68 |
| 25.01 | 781.32 | 50.00 | 839.04 | 10.00 | 714.96 |
| 30.00 | 795.12 | 55.01 | 847.82 | | |
| | | $T$ = 348.15 K | | | |
| 15.01 | 671.20 | 40.01 | 776.79 | 65.01 | 829.23 |
| 20.00 | 703.32 | 45.01 | 789.62 | 68.00 | 834.35 |
| 25.00 | 728.14 | 50.01 | 800.66 | 15.01 | 671.20 |
| 30.01 | 746.27 | 55.01 | 811.26 | | |
| 35.01 | 763.24 | 60.01 | 820.42 | | |
| | | $T$ = 373.15 K | | | |
| 15.01 | 584.27 | 40.01 | 734.45 | 65.01 | 795.86 |
| 20.01 | 638.35 | 45.01 | 749.78 | 68.01 | 801.53 |
| 25.01 | 671.56 | 50.01 | 762.71 | 15.01 | 584.27 |
| 30.00 | 695.82 | 55.00 | 775.01 | | |
| 35.02 | 717.21 | 60.01 | 785.73 | | |
| | | $T$ = 398.15 K | | | |
| 15.00 | 485.04 | 40.00 | 691.40 | 65.01 | 763.20 |
| 20.00 | 565.87 | 45.01 | 709.88 | 68.00 | 769.86 |
| 25.01 | 612.72 | 50.01 | 725.11 | 15.00 | 485.04 |
| 30.01 | 644.79 | 55.00 | 739.42 | | |
| 35.01 | 671.03 | 60.01 | 751.68 | | |
| | | $T$ = 423.15 K | | | |
| 15.01 | 405.23 | 40.00 | 650.30 | 65.00 | 732.11 |
| 20.01 | 500.26 | 45.01 | 671.89 | 68.02 | 739.30 |
| 25.01 | 556.15 | 50.00 | 689.19 | 15.00 | 405.18 |
| 30.00 | 595.07 | 55.01 | 705.53 | | |
| 35.01 | 626.55 | 60.00 | 719.20 | | |
| | | $T$ = 448.15 K | | | |
| 15.01 | 345.50 | 40.01 | 610.78 | 65.00 | 701.56 |

| $p$ (MPa) | $\rho$ (kg·m$^{-3}$) | $p$ (MPa) | $\rho$ (kg·m$^{-3}$) | $p$ (MPa) | $\rho$ (kg·m$^{-3}$) |
|---|---|---|---|---|---|
| 20.01 | 442.28 | 45.01 | 634.57 | 68.02 | 709.71 |
| 25.00 | 503.19 | 50.01 | 654.29 | 15.01 | 345.74 |
| 30.00 | 548.42 | 55.00 | 672.19 | | |
| 35.01 | 583.15 | 60.01 | 687.55 | | |
| | | | $T$ = 473.15 K | | |
| 15.01 | 301.93 | 40.01 | 573.06 | 65.00 | 672.05 |
| 20.01 | 393.82 | 45.00 | 599.00 | 68.01 | 680.33 |
| 25.01 | 456.39 | 50.01 | 620.62 | 15.02 | 300.99 |
| 30.01 | 505.33 | 55.01 | 640.02 | | |
| 35.02 | 542.77 | 60.01 | 656.80 | | |

Standard uncertainties at 95 % confidence are $u(T)$ = 0.03 K, $u(p)$ = 20 kPa, $u(x) = 10^{-5}$ and $u_c(\rho) \sim 0.0005\rho$.

Experimental compressed-liquid densities were fitted to the following empirical equation:

$$p = A\rho + B\frac{(\rho - \rho_r)^{\delta}}{\delta} \tag{6.1}$$

The correlation describes the pressure as a function of density at each temperature and composition. The delta was 4.82. The parameters $A$, $B$ and $\rho_r$, are adjustable parameters, reported in Table C.2.

**Table C.2** Parameters $A$, $B$ and $\rho_r$ in Equation (6.1) for compressed-liquid densities and the values of the average absolute deviation, $\Delta_{AAD,}$ and average absolute relative deviation, $\Delta_{AARD}$ for ($CO_2$ + $n$-heptane) system.

| Parameters | Mole fraction of $CO_2$ | | | |
|---|---|---|---|---|
| | 0.2053 | 0.3989 | 0.6037 | 0.8001 |
| | | 283.15 K | | |
| $A$ | $-1.021\times10^{-1}$ | $-7.717\times10^{-2}$ | $-4.934\times10^{-2}$ | $-2.410\times10^{-2}$ |
| $B$ | $2.543\times10^{-10}$ | $1.919\times10^{-10}$ | $1.176\times10^{-10}$ | $5.817\times10^{-11}$ |
| $\rho_r$ | $3.779\times10^{2}$ | $3.947\times10^{2}$ | $4.163\times10^{2}$ | $4.508\times10^{2}$ |
| $\Delta_{AAD}$ / MPa | 0.040 | 0.030 | 0.081 | 0.065 |
| $\Delta_{AARD}$ ($p$) | 0.12% | 0.11% | 0.24% | 0.23% |
| | | 298.15 K | | |
| $A$ | $-8.605\times10^{-2}$ | $-6.284\times10^{-2}$ | $-3.621\times10^{-2}$ | $-1.292\times10^{-2}$ |
| $B$ | $2.709\times10^{-10}$ | $2.012\times10^{-10}$ | $1.245\times10^{-10}$ | $5.615\times10^{-11}$ |
| $\rho_r$ | $3.800\times10^{2}$ | $3.954\times10^{2}$ | $4.165\times10^{2}$ | $4.415\times10^{2}$ |
| $\Delta_{AAD}$ / MPa | 0.036 | 0.024 | 0.026 | 0.080 |
| $\Delta_{AARD}$ ($p$) | 0.14% | 0.10% | 0.10% | 0.31% |
| | | 323.15 K | | |
| $A$ | $-6.837\times10^{-2}$ | $-4.606\times10^{-2}$ | $-2.131\times10^{-2}$ | $6.521\times10^{-4}$ |
| $B$ | $2.565\times10^{-10}$ | $1.905\times10^{-10}$ | $1.138\times10^{-10}$ | $4.911\times10^{-11}$ |
| $\rho_r$ | $3.680\times10^{2}$ | $3.817\times10^{2}$ | $3.965\times10^{2}$ | $4.106\times10^{2}$ |
| $\Delta_{AAD}$ / MPa | 0.035 | 0.014 | 0.039 | 0.21 |
| $\Delta_{AARD}$ ($p$) | 0.12% | 0.07% | 0.18% | 1.72% |
| | | 348.15 K | | |

| | | | | |
|---|---|---|---|---|
| $A$ | $-5.236\times10^{-2}$ | $-3.117\times10^{-2}$ | $-7.880\times10^{-3}$ | $1.189\times10^{-2}$ |
| $B$ | $2.446\times10^{-10}$ | $1.805\times10^{-10}$ | $1.051\times10^{-10}$ | $4.011\times10^{-11}$ |
| $\rho_r$ | $3.564\times10^{2}$ | $3.680\times10^{2}$ | $3.772\times10^{2}$ | $3.721\times10^{2}$ |
| $\Delta_{AAD}$ / MPa | 0.042 | 0.028 | 0.033 | 0.081 |
| $\Delta_{AARD}$ ($p$) | 0.15% | 0.12% | 0.15% | 0.31% |
| | | 373.15 K | | |
| $A$ | $-3.805\times10^{-2}$ | $-1.863\times10^{-2}$ | $3.420\times10^{-3}$ | $2.103\times10^{-2}$ |
| $B$ | $2.328\times10^{-10}$ | $1.650\times10^{-10}$ | $9.379\times10^{-11}$ | $3.096\times10^{-11}$ |
| $\rho_r$ | $3.447\times10^{2}$ | $3.510\times10^{2}$ | $3.545\times10^{2}$ | $3.267\times10^{2}$ |
| $\Delta_{AAD}$ / MPa | 0.029 | 0.024 | 0.043 | 0.056 |
| $\Delta_{AARD}$ ($p$) | 0.11% | 0.10% | 0.20% | 0.20% |
| | | 398.15 K | | |
| $A$ | $-2.637\times10^{-2}$ | $-7.100\times10^{-3}$ | $1.004\times10^{-2}$ | $2.949\times10^{-2}$ |
| $B$ | $2.092\times10^{-10}$ | $1.542\times10^{-10}$ | $6.458\times10^{-11}$ | $2.381\times10^{-11}$ |
| $\rho_r$ | $3.281\times10^{2}$ | $3.357\times10^{2}$ | $3.067\times10^{2}$ | $2.808\times10^{2}$ |
| $\Delta_{AAD}$ / MPa | 0.040 | 0.054 | 0.032 | 0.056 |
| $\Delta_{AARD}$ ($p$) | 0.16% | 0.16% | 0.15% | 0.16% |
| | | 423.15 K | | |
| $A$ | $-1.520\times10^{-2}$ | $2.090\times10^{-3}$ | $1.986\times10^{-2}$ | $3.642\times10^{-2}$ |
| $B$ | $1.952\times10^{-10}$ | $1.337\times10^{-10}$ | $6.074\times10^{-11}$ | $1.802\times10^{-11}$ |
| $\rho_r$ | $3.144\times10^{2}$ | $3.137\times10^{2}$ | $2.885\times10^{2}$ | $2.317\times10^{2}$ |
| $\Delta_{AAD}$ / MPa | 0.030 | 0.026 | 0.038 | 0.063 |
| $\Delta_{AARD}$ ($p$) | 0.12% | 0.12% | 0.13% | 0.18% |
| | | 448.15 K | | |
| $A$ | $-5.600\times10^{-3}$ | $1.034\times10^{-2}$ | $2.713\times10^{-2}$ | $4.293\times10^{-2}$ |
| $B$ | $1.779\times10^{-10}$ | $1.158\times10^{-10}$ | $5.027\times10^{-11}$ | $1.\cdot10^{-11}$ |
| $\rho_r$ | $2.986\times10^{2}$ | $2.914\times10^{2}$ | $2.576\times10^{2}$ | $1.847\times10^{2}$ |
| $\Delta_{AAD}$ / MPa | 0.025 | 0.025 | 0.023 | 0.059 |
| $\Delta_{AARD}$ ($p$) | 0.10% | 0.11% | 0.07% | 0.21% |
| | | 473.15 K | | |
| $A$ | $2.440\times10^{-3}$ | $1.734\times10^{-2}$ | $3.314\times10^{-2}$ | $4.924\times10^{-2}$ |
| $B$ | $1.550\times10^{-10}$ | $9.714\times10^{-11}$ | $3.974\times10^{-11}$ | $1.174\times10^{-11}$ |
| $\rho_r$ | $2.790\times10^{2}$ | $2.660\times10^{2}$ | $2.213\times10^{2}$ | $1.455\times10^{2}$ |
| $\Delta_{AAD}$ / MPa | 0.031 | 0.022 | 0.015 | 0.069 |
| $\Delta_{AARD}$ ($p$) | 0.12% | 0.08% | 0.05% | 0.26% |

Redlich – Kister equation is given in the following form:

$$V_m^E = x_1(1-x_1)\sum_{i=1}^{3} A_i(2x_1-1)^{i-1} \tag{6.3}$$

where $V_m^E$ and $x_1$ represent excess molar volume and mole fraction of $CO_2$, respectively. $A_i$ are the correlation parameters shown in Table A6.2.

**Table C.3** Parameters of the Redlich-Kister correlation for the excess molar volume of $CO_2$ + *n*-heptane and the average absolute deviation $\Delta_{AAD}$.

| $T$ / K | $p$ / MPa | $A_1$ | $A_2$ | $A_3$ | $\Delta_{AAD}$ /cm$^3$·mol$^{-1}$ |
|---|---|---|---|---|---|
| 283.15 | 10 | 1.308 | 0.511 | 0.002 | 0.009 |
| 283.15 | 15 | 2.896 | 1.852 | 1.124 | 0.001 |
| 283.15 | 20 | 3.822 | 2.692 | 2.006 | 0.008 |
| 283.15 | 25 | 4.295 | 2.864 | 2.161 | 0.015 |
| 283.15 | 30 | 4.679 | 3.185 | 2.296 | 0.012 |
| 283.15 | 35 | 4.842 | 3.141 | 2.457 | 0.016 |
| 283.15 | 40 | 5.020 | 3.280 | 2.460 | 0.019 |
| 283.15 | 45 | 5.071 | 3.166 | 2.469 | 0.022 |
| 283.15 | 50 | 5.153 | 3.246 | 2.505 | 0.019 |
| 283.15 | 55 | 5.127 | 3.141 | 2.492 | 0.024 |
| 283.15 | 60 | 5.156 | 3.230 | 2.612 | 0.022 |
| 283.15 | 65 | 5.151 | 3.164 | 2.641 | 0.022 |
| 283.15 | 68 | 5.074 | 3.222 | 2.620 | 0.030 |
| 298.15 | 10 | -6.207 | -5.441 | -4.222 | 0.071 |
| 298.15 | 15 | -1.259 | -1.082 | -1.416 | 0.054 |
| 298.15 | 20 | 0.998 | 0.943 | -0.113 | 0.026 |
| 298.15 | 25 | 2.189 | 1.658 | 0.392 | 0.022 |
| 298.15 | 30 | 2.968 | 2.244 | 0.893 | 0.018 |
| 298.15 | 35 | 3.434 | 2.398 | 0.803 | 0.020 |
| 298.15 | 40 | 3.787 | 2.699 | 1.086 | 0.013 |
| 298.15 | 45 | 3.983 | 2.647 | 0.920 | 0.014 |
| 298.15 | 50 | 4.143 | 2.807 | 1.159 | 0.013 |
| 298.15 | 55 | 4.243 | 2.746 | 1.124 | 0.013 |
| 298.15 | 60 | 4.299 | 2.843 | 1.226 | 0.009 |
| 298.15 | 65 | 4.349 | 2.792 | 1.194 | 0.009 |
| 298.15 | 68 | 4.366 | 2.842 | 1.088 | 0.007 |
| 323.15 | 10 | -120.016 | -139.015 | -105.302 | 2.025 |
| 323.15 | 15 | -24.916 | -12.523 | 2.311 | 1.083 |
| 323.15 | 20 | -15.479 | 1.041 | 17.962 | 1.138 |
| 323.15 | 25 | -12.195 | 5.736 | 23.820 | 1.224 |
| 323.15 | 30 | -10.626 | 8.618 | 27.845 | 1.305 |
| 323.15 | 35 | -8.590 | 8.844 | 26.308 | 1.221 |
| 323.15 | 40 | -6.613 | 8.675 | 23.970 | 1.080 |
| 323.15 | 45 | -0.770 | 4.459 | 9.153 | 0.412 |
| 323.15 | 50 | 4.402 | 0.750 | -3.758 | 0.186 |
| 323.15 | 55 | 9.759 | -3.488 | -17.947 | 0.829 |
| 323.15 | 60 | 15.577 | -8.145 | -33.670 | 1.537 |
| 323.15 | 65 | 22.110 | -13.525 | -51.553 | 2.346 |
| 323.15 | 68 | 25.992 | -16.709 | -62.433 | 2.830 |
| 348.15 | 15 | -72.515 | -73.086 | -49.176 | 0.972 |
| 348.15 | 20 | -25.969 | -25.459 | -22.870 | 0.206 |
| 348.15 | 25 | -12.781 | -11.111 | -10.026 | 0.106 |
| 348.15 | 30 | -6.804 | -4.885 | -4.139 | 0.053 |
| 348.15 | 35 | -3.508 | -2.397 | -2.454 | 0.047 |
| 348.15 | 40 | -1.468 | -0.578 | -0.911 | 0.032 |

| $T$ / K | $p$ / MPa | $A_1$ | $A_2$ | $A_3$ | $\Delta_{AAD}$ /cm$^3$·mol$^{-1}$ |
|---|---|---|---|---|---|
| 348.15 | 45 | -0.171 | 0.278 | -0.437 | 0.030 |
| 348.15 | 50 | 0.807 | 1.004 | 0.038 | 0.026 |
| 348.15 | 55 | 1.480 | 1.292 | 0.070 | 0.026 |
| 348.15 | 60 | 2.001 | 1.638 | 0.492 | 0.019 |
| 348.15 | 65 | 2.354 | 1.895 | 0.520 | 0.018 |
| 348.15 | 68 | 2.536 | 2.021 | 0.324 | 0.017 |
| 373.15 | 15 | -134.720 | -127.663 | -77.117 | 1.482 |
| 373.15 | 20 | -56.994 | -58.088 | -52.288 | 0.440 |
| 373.15 | 25 | -28.902 | -26.290 | -22.332 | 0.199 |
| 373.15 | 30 | -16.450 | -13.068 | -10.311 | 0.098 |
| 373.15 | 35 | -9.907 | -7.448 | -6.250 | 0.076 |
| 373.15 | 40 | -6.002 | -4.094 | -3.762 | 0.060 |
| 373.15 | 45 | -3.545 | -2.315 | -2.420 | 0.052 |
| 373.15 | 50 | -1.856 | -0.848 | -1.347 | 0.038 |
| 373.15 | 55 | -0.648 | -0.153 | -1.054 | 0.035 |
| 373.15 | 60 | 0.233 | 0.472 | -0.434 | 0.031 |
| 373.15 | 65 | 0.911 | 0.858 | -0.275 | 0.028 |
| 373.15 | 68 | 1.206 | 1.108 | -0.177 | 0.027 |
| 398.15 | 15 | -177.287 | -154.953 | -93.632 | 0.213 |
| 398.15 | 20 | -88.901 | -81.617 | -61.646 | 0.388 |
| 398.15 | 25 | -48.370 | -42.457 | -33.325 | 0.262 |
| 398.15 | 30 | -28.634 | -23.125 | -17.725 | 0.158 |
| 398.15 | 35 | -18.241 | -13.813 | -10.496 | 0.143 |
| 398.15 | 40 | -11.817 | -8.370 | -6.393 | 0.078 |
| 398.15 | 45 | -7.862 | -5.464 | -4.704 | 0.067 |
| 398.15 | 50 | -5.217 | -3.324 | -2.812 | 0.042 |
| 398.15 | 55 | -3.370 | -2.192 | -2.151 | 0.039 |
| 398.15 | 60 | -1.991 | -1.131 | -1.418 | 0.024 |
| 398.15 | 65 | -0.989 | -0.521 | -0.961 | 0.024 |
| 398.15 | 68 | -0.516 | -0.260 | -1.092 | 0.017 |
| 423.15 | 15 | -205.338 | -136.027 | -39.008 | 0.315 |
| 423.15 | 20 | -112.926 | -91.209 | -59.557 | 0.349 |
| 423.15 | 25 | -66.373 | -54.244 | -38.916 | 0.286 |
| 423.15 | 30 | -41.275 | -32.438 | -23.817 | 0.191 |
| 423.15 | 35 | -26.890 | -21.096 | -16.707 | 0.162 |
| 423.15 | 40 | -18.210 | -13.446 | -10.722 | 0.115 |
| 423.15 | 45 | -12.689 | -9.564 | -8.453 | 0.102 |
| 423.15 | 50 | -8.853 | -6.395 | -5.890 | 0.085 |
| 423.15 | 55 | -6.256 | -4.765 | -5.042 | 0.071 |
| 423.15 | 60 | -4.267 | -3.235 | -3.741 | 0.059 |
| 423.15 | 65 | -2.856 | -2.333 | -3.136 | 0.049 |
| 423.15 | 68 | -2.150 | -1.873 | -2.905 | 0.046 |
| 448.15 | 15 | -218.671 | -102.419 | 10.563 | 0.442 |
| 448.15 | 20 | -129.150 | -88.156 | -45.700 | 0.251 |
| 448.15 | 25 | -80.553 | -58.524 | -36.224 | 0.256 |
| 448.15 | 30 | -52.355 | -39.116 | -27.038 | 0.222 |
| 448.15 | 35 | -35.426 | -26.488 | -19.604 | 0.177 |

| $T$ / K | $p$ / MPa | $A_1$ | $A_2$ | $A_3$ | $\Delta_{AAD}$ /cm$^3$·mol$^{-1}$ |
|---|---|---|---|---|---|
| 448.15 | 40 | -24.674 | -18.290 | -14.034 | 0.140 |
| 448.15 | 45 | -17.655 | -13.328 | -10.965 | 0.126 |
| 448.15 | 50 | -12.801 | -9.585 | -8.377 | 0.103 |
| 448.15 | 55 | -9.389 | -7.379 | -6.988 | 0.090 |
| 448.15 | 60 | -6.885 | -5.492 | -5.454 | 0.078 |
| 448.15 | 65 | -5.003 | -4.177 | -4.523 | 0.064 |
| 448.15 | 68 | -4.128 | -3.773 | -4.227 | 0.060 |
| 473.15 | 15 | -217.946 | -64.691 | 34.999 | 0.002 |
| 473.15 | 20 | -137.906 | -77.491 | -30.062 | 0.210 |
| 473.15 | 25 | -90.191 | -57.095 | -30.043 | 0.234 |
| 473.15 | 30 | -61.059 | -42.091 | -26.857 | 0.223 |
| 473.15 | 35 | -42.565 | -30.105 | -20.862 | 0.207 |
| 473.15 | 40 | -30.463 | -21.788 | -15.935 | 0.168 |
| 473.15 | 45 | -22.272 | -16.404 | -13.170 | 0.147 |
| 473.15 | 50 | -16.559 | -12.304 | -10.204 | 0.125 |
| 473.15 | 55 | -12.498 | -9.655 | -8.575 | 0.106 |
| 473.15 | 60 | -9.459 | -7.504 | -6.857 | 0.090 |
| 473.15 | 65 | -7.197 | -6.018 | -5.612 | 0.073 |
| 473.15 | 68 | -6.104 | -4.986 | -5.103 | 0.067 |

**Table C.4** Experimental compressed-liquid density $\rho$ for $CO_2$ + *n*-nonane at four compositions as a function of temperature, $T$: (283.15 to 473.15) K and $p$: (10 to 68) MPa.

| $p$ (MPa) | $\rho$ (kg·m$^{-3}$) | $p$ (MPa) | $\rho$ (kg·m$^{-3}$) | $p$ (MPa) | $\rho$ (kg·m$^{-3}$) |
|---|---|---|---|---|---|
| | | **$x_{CO2}$ = 0.2391** | | | |
| | | $T$ = 283.15 K | | | |
| 10.02 | 748.47 | 35.03 | 766.7752 | 60.00 | 781.80 |
| 15.02 | 752.46 | 40.00 | 770.0045 | 65.00 | 784.52 |
| 20.03 | 756.29 | 45.02 | 773.0771 | 68.01 | 786.09 |
| 25.02 | 759.92 | 50.02 | 776.1003 | 10.03 | 748.47 |
| 30.02 | 763.45 | 55.03 | 778.972 | | |
| | | $T$ = 298.15 K | | | |
| 10.01 | 735.95 | 35.04 | 756.03 | 60.00 | 772.19 |
| 15.03 | 740.41 | 40.03 | 759.49 | 65.01 | 775.15 |
| 20.02 | 744.58 | 45.04 | 762.85 | 68.01 | 776.86 |
| 25.02 | 748.60 | 50.02 | 766.07 | 10.01 | 735.95 |
| 30.00 | 752.37 | 55.03 | 769.18 | | |
| | | $T$ = 323.15 K | | | |
| 10.04 | 714.70 | 35.04 | 737.71 | 60.03 | 755.72 |
| 15.02 | 719.89 | 40.02 | 741.64 | 65.04 | 758.95 |
| 20.00 | 724.67 | 45.01 | 745.38 | 68.01 | 760.86 |
| 25.04 | 729.29 | 50.04 | 748.96 | 10.04 | 714.70 |
| 30.00 | 733.58 | 55.03 | 752.39 | | |
| | | $T$ = 348.15 K | | | |

| $p$ (MPa) | $\rho$ (kg·m$^{-3}$) | $p$ (MPa) | $\rho$ (kg·m$^{-3}$) | $p$ (MPa) | $\rho$ (kg·m$^{-3}$) |
|---|---|---|---|---|---|
| 10.03 | 692.89 | 35.01 | 719.47 | 60.02 | 739.51 |
| 15.04 | 698.96 | 40.01 | 723.86 | 65.04 | 743.06 |
| 20.04 | 704.64 | 45.04 | 728.06 | 68.02 | 745.14 |
| 25.04 | 709.88 | 50.01 | 732.01 | 10.03 | 692.84 |
| 30.01 | 714.82 | 55.02 | 735.86 | | |
| | | $T$ = 373.15 K | | | |
| 10.01 | 670.36 | 35.02 | 701.26 | 60.03 | 723.56 |
| 15.02 | 677.67 | 40.02 | 706.22 | 65.02 | 727.43 |
| 20.02 | 684.29 | 45.01 | 710.88 | 68.01 | 729.70 |
| 25.03 | 690.37 | 50.02 | 715.33 | 10.00 | 670.36 |
| 30.01 | 696.02 | 55.02 | 719.55 | | |
| | | $T$ = 398.15 K | | | |
| 10.04 | 647.14 | 35.01 | 683.11 | 60.02 | 707.85 |
| 15.03 | 655.91 | 40.00 | 688.67 | 65.03 | 712.03 |
| 20.03 | 663.66 | 45.02 | 693.88 | 68.01 | 714.52 |
| 25.02 | 670.73 | 50.01 | 698.75 | 10.02 | 647.09 |
| 30.01 | 677.12 | 55.02 | 703.42 | | |
| | | $T$ = 423.15 K | | | |
| 10.05 | 622.90 | 35.03 | 664.98 | 60.02 | 692.30 |
| 15.02 | 633.51 | 40.03 | 671.22 | 65.00 | 696.85 |
| 20.03 | 642.70 | 45.04 | 676.98 | 68.01 | 699.56 |
| 25.01 | 650.84 | 50.02 | 682.35 | 10.03 | 622.85 |
| 30.02 | 658.25 | 55.03 | 687.47 | | |
| | | $T$ = 448.15 K | | | |
| 10.04 | 597.44 | 35.01 | 646.88 | 60.01 | 677.03 |
| 15.03 | 610.48 | 40.02 | 653.85 | 65.01 | 682.01 |
| 20.00 | 621.30 | 45.01 | 660.23 | 68.01 | 684.95 |
| 25.02 | 630.87 | 50.00 | 666.19 | 10.03 | 597.40 |
| 30.02 | 639.28 | 55.03 | 671.80 | | |
| | | $T$ = 473.15 K | | | |
| 10.04 | 570.38 | 35.04 | 628.83 | 60.02 | 661.97 |
| 15.04 | 586.61 | 40.02 | 636.52 | 65.01 | 667.30 |
| 20.03 | 599.56 | 45.01 | 643.63 | 68.01 | 670.45 |
| 25.03 | 610.64 | 50.02 | 650.16 | 10.05 | 570.42 |
| 30.03 | 620.24 | 55.03 | 656.26 | | |
| | | **$x_{CO2}$ = 0.4238** | | | |
| | | $T$ = 283.15 K | | | |
| 10.04 | 759.88 | 35.03 | 780.44 | 60.03 | 797.11 |
| 15.04 | 764.47 | 40.02 | 784.02 | 65.00 | 800.08 |
| 20.00 | 768.70 | 45.03 | 787.49 | 68.02 | 801.90 |
| 25.01 | 772.83 | 50.03 | 790.76 | 10.04 | 759.88 |
| 30.01 | 776.71 | 55.02 | 793.99 | | |
| | | $T$ = 298.15 K | | | |

| $p$ (MPa) | $\rho$ (kg·m$^{-3}$) | $p$ (MPa) | $\rho$ (kg·m$^{-3}$) | $p$ (MPa) | $\rho$ (kg·m$^{-3}$) |
|---|---|---|---|---|---|
| 10.02 | 746.02 | 35.03 | 768.70 | 60.04 | 786.60 |
| 15.04 | 751.14 | 40.04 | 772.56 | 65.05 | 789.86 |
| 20.07 | 755.90 | 45.06 | 776.32 | 68.01 | 791.68 |
| 25.02 | 760.37 | 50.08 | 779.88 | | |
| 30.04 | 764.63 | 55.02 | 783.30 | | |
| | | $T$ = 323.15 K | | | |
| 10.04 | 722.09 | 35.03 | 748.57 | 60.04 | 768.72 |
| 15.05 | 728.21 | 40.03 | 752.95 | 65.04 | 772.25 |
| 20.04 | 733.79 | 45.05 | 757.18 | 68.01 | 774.30 |
| 25.06 | 739.06 | 50.01 | 761.17 | 10.04 | 722.09 |
| 30.04 | 743.94 | 55.06 | 765.04 | | |
| | | $T$ = 348.15 K | | | |
| 10.04 | 697.32 | 35.03 | 728.49 | 60.02 | 751.06 |
| 15.02 | 704.68 | 40.04 | 733.48 | 65.05 | 755.00 |
| 20.00 | 711.30 | 45.03 | 738.22 | 68.02 | 757.28 |
| 25.03 | 717.48 | 50.05 | 742.71 | 10.04 | 697.32 |
| 30.02 | 723.16 | 55.04 | 747.01 | | |
| | | $T$ = 373.15 K | | | |
| 10.05 | 671.48 | 35.02 | 708.08 | 60.03 | 733.23 |
| 15.03 | 680.41 | 40.00 | 713.63 | 65.01 | 737.54 |
| 20.03 | 688.26 | 45.04 | 719.02 | 68.01 | 740.05 |
| 25.03 | 695.47 | 50.02 | 723.97 | 10.05 | 671.48 |
| 30.01 | 701.95 | 55.01 | 728.73 | | |
| | | $T$ = 398.15 K | | | |
| 10.06 | 644.75 | 35.03 | 687.84 | 60.04 | 715.89 |
| 15.00 | 655.43 | 40.05 | 694.08 | 65.03 | 720.61 |
| 20.00 | 664.88 | 45.01 | 700.12 | 68.02 | 723.40 |
| 25.03 | 673.36 | 50.03 | 705.62 | 10.06 | 644.75 |
| 30.01 | 680.77 | 55.04 | 710.98 | | |
| | | $T$ = 423.15 K | | | |
| 10.02 | 615.36 | 35.04 | 667.74 | 60.02 | 698.46 |
| 15.05 | 629.44 | 40.00 | 674.62 | 65.04 | 703.58 |
| 20.02 | 641.20 | 45.02 | 681.44 | 68.02 | 706.50 |
| 25.01 | 651.04 | 50.02 | 687.34 | 10.03 | 615.26 |
| 30.01 | 659.70 | 55.03 | 693.19 | | |
| | | $T$ = 448.15 K | | | |
| 10.04 | 584.23 | 35.03 | 647.65 | 60.02 | 682.38 |
| 15.04 | 602.20 | 40.04 | 655.82 | 65.02 | 687.95 |
| 20.05 | 616.48 | 45.02 | 663.22 | 68.01 | 691.17 |
| 25.04 | 628.36 | 50.04 | 670.09 | 10.02 | 583.85 |
| 30.00 | 638.51 | 55.03 | 676.43 | | |
| | | $T$ = 473.15 K | | | |
| 10.05 | 549.91 | 35.02 | 627.45 | 60.01 | 666.00 |

| $p$ (MPa) | $\rho$ (kg·m$^{-3}$) | $p$ (MPa) | $\rho$ (kg·m$^{-3}$) | $p$ (MPa) | $\rho$ (kg·m$^{-3}$) |
|---|---|---|---|---|---|
| 15.03 | 573.57 | 40.02 | 636.61 | 65.02 | 672.10 |
| 20.01 | 591.05 | 45.05 | 644.97 | 68.01 | 675.58 |
| 25.02 | 605.19 | 50.04 | 652.50 | 10.03 | 549.58 |
| 30.03 | 617.13 | 55.03 | 659.52 | | |
| | | **$x_{CO2}$ = 0.6033** | | | |
| | | $T$ = 283.15 K | | | |
| 10.02 | 786.65 | 35.00 | 813.39 | 60.00 | 833.97 |
| 15.02 | 792.64 | 40.00 | 817.92 | 65.01 | 837.59 |
| 20.01 | 798.43 | 45.02 | 822.19 | 68.00 | 839.71 |
| 25.02 | 803.67 | 50.01 | 826.27 | 10.01 | 786.55 |
| 30.00 | 808.70 | 55.00 | 830.15 | | |
| | | $T$ = 298.15 K | | | |
| 10.00 | 770.25 | 35.04 | 801.64 | 60.01 | 824.85 |
| 15.04 | 777.61 | 40.01 | 806.76 | 65.01 | 828.91 |
| 20.03 | 784.28 | 45.02 | 811.62 | 68.02 | 831.38 |
| 25.01 | 790.46 | 50.01 | 816.23 | 10.02 | 770.29 |
| 30.00 | 796.17 | 55.04 | 820.64 | | |
| | | $T$ = 323.15 K | | | |
| 10.04 | 737.38 | 35.03 | 775.70 | 60.04 | 802.33 |
| 15.03 | 746.73 | 40.03 | 781.68 | 65.01 | 806.91 |
| 20.01 | 754.90 | 45.00 | 787.25 | 68.01 | 809.65 |
| 25.02 | 762.46 | 50.02 | 792.53 | 10.04 | 737.38 |
| 30.00 | 769.28 | 55.03 | 797.55 | | |
| | | $T$ = 348.15 K | | | |
| 10.02 | 702.06 | 35.04 | 749.68 | 60.01 | 780.07 |
| 15.04 | 714.30 | 40.02 | 756.55 | 65.03 | 785.21 |
| 20.02 | 724.63 | 45.01 | 762.98 | 68.01 | 788.13 |
| 25.01 | 733.82 | 50.00 | 769.01 | 10.03 | 702.06 |
| 30.01 | 742.07 | 55.03 | 774.74 | | |
| | | $T$ = 373.15 K | | | |
| 10.03 | 664.18 | 35.01 | 723.01 | 60.01 | 757.81 |
| 15.01 | 679.82 | 40.01 | 731.06 | 65.00 | 763.55 |
| 20.03 | 693.06 | 45.03 | 738.52 | 68.01 | 766.99 |
| 25.01 | 704.30 | 50.01 | 745.34 | 10.02 | 662.23 |
| 30.02 | 714.12 | 55.03 | 751.82 | | |
| | | $T$ = 398.15 K | | | |
| 15.02 | 643.11 | 40.00 | 705.84 | 65.01 | 742.36 |
| 20.03 | 660.30 | 45.01 | 714.38 | 68.01 | 746.02 |
| 25.04 | 674.34 | 50.00 | 722.08 | 15.00 | 643.06 |
| 30.04 | 686.18 | 55.03 | 729.39 | | |
| 35.04 | 696.62 | 60.03 | 736.07 | | |
| | | $T$ = 423.15 K | | | |
| 15.02 | 602.85 | 40.00 | 680.73 | 65.00 | 721.56 |

| $p$ (MPa) | $\rho$ (kg·m$^{-3}$) | $p$ (MPa) | $\rho$ (kg·m$^{-3}$) | $p$ (MPa) | $\rho$ (kg·m$^{-3}$) |
|---|---|---|---|---|---|
| 20.03 | 625.86 | 45.03 | 690.46 | 68.02 | 725.58 |
| 25.01 | 643.29 | 50.02 | 699.19 | 15.02 | 602.85 |
| 30.03 | 657.76 | 55.01 | 707.18 | | |
| 35.02 | 669.97 | 60.02 | 714.68 | | |
| | | $T$ = 448.15 K | | | |
| 15.02 | 559.20 | 40.01 | 655.82 | 65.02 | 701.17 |
| 20.02 | 590.14 | 45.02 | 666.69 | 68.00 | 705.51 |
| 25.01 | 611.96 | 50.02 | 676.51 | 15.00 | 559.68 |
| 30.02 | 629.12 | 55.02 | 685.41 | | |
| 35.02 | 643.46 | 60.01 | 693.58 | | |
| | | $T$ = 473.15 K | | | |
| 15.04 | 513.50 | 40.01 | 631.20 | 65.00 | 681.26 |
| 20.01 | 553.73 | 45.02 | 643.39 | 68.01 | 686.19 |
| 25.01 | 580.29 | 50.01 | 654.24 | 15.01 | 514.12 |
| 30.01 | 600.63 | 55.01 | 664.03 | | |
| 35.03 | 617.15 | 60.02 | 673.05 | | |
| | | **$x_{CO2}$ = 0.7992** | | | |
| | | $T$ = 283.15 K | | | |
| 10.02 | 835.91 | 35.01 | 880.73 | 60.01 | 911.78 |
| 15.02 | 846.59 | 40.00 | 887.84 | 65.01 | 916.92 |
| 20.01 | 856.63 | 45.03 | 894.19 | 10.01 | 835.56 |
| 25.02 | 865.20 | 50.00 | 900.45 | | |
| 30.02 | 873.47 | 55.02 | 906.09 | | |
| | | $T$ = 298.15 K | | | |
| 15.02 | 817.28 | 40.01 | 865.50 | 65.01 | 897.79 |
| 20.00 | 829.53 | 45.01 | 872.78 | 20.01 | 829.63 |
| 25.03 | 839.82 | 50.00 | 879.61 | | |
| 30.01 | 849.07 | 55.02 | 886.04 | | |
| 35.01 | 857.61 | 60.01 | 892.11 | | |
| | | $T$ = 323.15 K | | | |
| 15.02 | 765.62 | 40.01 | 827.98 | 65.01 | 866.23 |
| 20.02 | 782.01 | 45.00 | 836.76 | 15.02 | 765.28 |
| 25.02 | 795.71 | 50.01 | 844.94 | | |
| 30.01 | 807.68 | 55.02 | 852.57 | | |
| 35.02 | 818.40 | 60.00 | 859.60 | | |
| | | $T$ = 348.15 K | | | |
| 15.02 | 705.82 | 40.00 | 789.88 | 65.01 | 834.80 |
| 20.00 | 730.41 | 45.01 | 800.47 | 20.02 | 730.36 |
| 25.02 | 749.14 | 50.01 | 810.13 | | |
| 30.00 | 764.68 | 55.01 | 818.95 | | |
| 35.01 | 778.14 | 60.01 | 827.22 | | |
| | | $T$ = 373.15 K | | | |
| 20.02 | 670.08 | 45.02 | 766.12 | 20.01 | 669.69 |

| $p$ (MPa) | $\rho$ (kg·m$^{-3}$) | $p$ (MPa) | $\rho$ (kg·m$^{-3}$) | $p$ (MPa) | $\rho$ (kg·m$^{-3}$) |
|---|---|---|---|---|---|
| 25.02 | 698.22 | 50.03 | 777.78 | | |
| 30.01 | 720.01 | 55.02 | 788.56 | | |
| 35.02 | 737.80 | 60.02 | 798.30 | | |
| 40.02 | 752.74 | 65.01 | 807.21 | | |
| | | $T$ = 398.15 K | | | |
| 20.00 | 603.93 | 45.01 | 728.70 | 20.01 | 604.12 |
| 25.02 | 644.00 | 50.01 | 742.38 | | |
| 30.01 | 672.54 | 55.02 | 754.83 | | |
| 35.02 | 694.52 | 60.00 | 765.93 | | |
| 40.00 | 712.78 | 65.01 | 776.09 | | |
| | | $T$ = 423.15 K | | | |
| 20.02 | 537.28 | 45.00 | 691.58 | 20.02 | 537.81 |
| 25.02 | 589.32 | 50.00 | 707.54 | | |
| 30.01 | 624.57 | 55.01 | 721.81 | | |
| 35.02 | 651.46 | 60.01 | 734.47 | | |
| 40.02 | 673.26 | 65.02 | 746.07 | | |
| | | $T$ = 448.15 K | | | |
| 20.01 | 476.11 | 45.02 | 655.94 | 20.02 | 476.77 |
| 25.02 | 537.27 | 50.01 | 673.81 | | |
| 30.01 | 579.60 | 55.02 | 689.61 | | |
| 35.03 | 610.31 | 60.01 | 703.63 | | |
| 40.01 | 635.26 | 65.01 | 716.35 | | |
| | | $T$ = 473.15 K | | | |
| 20.01 | 425.33 | 45.01 | 621.65 | 20.01 | 425.33 |
| 25.00 | 489.48 | 50.00 | 641.34 | | |
| 30.02 | 537.25 | 55.02 | 658.65 | | |
| 35.02 | 570.87 | 60.01 | 674.01 | | |
| 40.01 | 598.82 | 65.01 | 687.93 | | |

Standard uncertainties at 95 % confidence are $u(T)$ = 0.03 K and $u(p)$ = 20 kPa, $u(x) = 10^{-5}$ and $u_c(\rho) \sim 0.0005\rho$.

**Table C.5** Parameters $A$, $B$ and $\rho_r$ in Equation (6.1) for compressed-liquid densities and the values of the average absolute deviation, $\Delta_{AAD,}$ and average absolute relative deviation, $\Delta_{AARD}$ for ($CO_2$ + $n$-nonane) system.

| Parameters | Mole fraction of $CO_2$ | | | |
|---|---|---|---|---|
| | 0.2391 | 0.4238 | 0.6033 | 0.7992 |
| | | 283.15 K | | |
| $A$ | $7.863\times10^{-4}$ | -9.482E-02 | -6.236E-02 | -2.817E-02 |
| $B$ | $-2.722\times10^{-6}$ | 2.515E-10 | 1.963E-10 | 8.400E-11 |
| $\rho_r$ | $1.238\times10^{-11}$ | 4.207E+02 | 4.531E+02 | 4.820E+02 |
| $\Delta_{AAD}$ / MPa | 0.02 | 0.03 | 0.03 | 0.07 |
| $\Delta_{AARD}$ ($p$) | 0.11% | 0.18% | 0.13% | 0.29% |
| | | 298.15 K | | |
| $A$ | $1.137\times10^{-2}$ | $-8.359\times10^{-3}$ | $-5.239\times10^{-2}$ | $-1.835\times10^{-2}$ |

| | | | | |
|---|---|---|---|---|
| $B$ | $-6.087\times10^{-6}$ | $2.394\times10^{-10}$ | $1.527\times10^{-10}$ | $8.059\times10^{-11}$ |
| $\rho_r$ | $1.041\times10^{-11}$ | $4.122\times10^{2}$ | $4.304\times10^{2}$ | $4.689\times10^{2}$ |
| $\Delta_{AAD}$ / MPa | 0.03 | 0.02 | 0.03 | 0.04 |
| $\Delta_{AARD}$ ($p$) | 0.11% | 0.08% | 0.12% | 0.17% |
| | | 323.15 K | | |
| $A$ | $-8.000\times10^{-2}$ | $-6.457\times10^{-2}$ | $-3.631\times10^{-2}$ | $-6.350\times10^{-3}$ |
| $B$ | $2.770\times10^{-10}$ | $2.390\times10^{-10}$ | $1.445\times10^{-10}$ | $6.493\times10^{-11}$ |
| $\rho_r$ | $3.957\times10^{2}$ | $4.047\times10^{2}$ | $4.153\times10^{2}$ | $4.310\times10^{2}$ |
| $\Delta_{AAD}$ / MPa | 0.03 | 0.02 | 0.04 | 0.02 |
| $\Delta_{AARD}$ ($p$) | 0.15% | 0.14% | 0.17% | 0.05% |
| | | 348.15 K | | |
| $A$ | $-6.371\times10^{-2}$ | $-4.564\times10^{-2}$ | $-2.159\times10^{-2}$ | $5.900\times10^{-3}$ |
| $B$ | $2.673\times10^{-10}$ | $2.551\times10^{-10}$ | $1.412\times10^{-10}$ | $5.852\times10^{-11}$ |
| $\rho_r$ | $3.856\times10^{2}$ | $4.030\times10^{2}$ | $4.029\times10^{2}$ | $4.045\times10^{2}$ |
| $\Delta_{AAD}$ / MPa | 0.03 | 0.08 | 0.03 | 0.03 |
| $\Delta_{AARD}$ ($p$) | 0.16% | 0.29% | 0.15% | 0.11% |
| | | 373.15 K | | |
| $A$ | $-5.047\times10^{-2}$ | $-3.758\times10^{-2}$ | $-1.050\times10^{-2}$ | $1.753\times10^{-2}$ |
| $B$ | $2.468\times10^{-10}$ | $2.048\times10^{-10}$ | $1.242\times10^{-10}$ | $4.575\times10^{-11}$ |
| $\rho_r$ | $3.714\times10^{2}$ | $3.745\times10^{2}$ | $3.803\times10^{2}$ | $3.698\times10^{2}$ |
| $\Delta_{AAD}$ / MPa | 0.02 | 0.03 | 0.10 | 0.02 |
| $\Delta_{AARD}$ ($p$) | 0.06% | 0.13% | 0.33% | 0.07% |
| | | 398.15 K | | |
| $A$ | $-3.768\times10^{-2}$ | $-2.734\times10^{-2}$ | $-1.070\times10^{-3}$ | $2.604\times10^{-2}$ |
| $B$ | $2.350\times10^{-10}$ | $1.798\times10^{-10}$ | $1.087\times10^{-10}$ | $3.668\times10^{-11}$ |
| $\rho_r$ | $3.599\times10^{2}$ | $3.546\times10^{2}$ | $3.568\times10^{2}$ | $3.301\times10^{2}$ |
| $\Delta_{AAD}$ / MPa | 0.02 | 0.04 | 0.03 | 0.02 |
| $\Delta_{AARD}$ ($p$) | 0.09% | 0.13% | 0.10% | 0.05% |
| | | 423.15 K | | |
| $A$ | $-2.681\times10^{-2}$ | $-1.245\times10^{-2}$ | $8.550\times10^{-3}$ | $3.289\times10^{-2}$ |
| $B$ | $2.183\times10^{-10}$ | $2.123\times10^{-10}$ | $1.004\times10^{-10}$ | $2.658\times10^{-11}$ |
| $\rho_r$ | $3.461\times10^{2}$ | $3.599\times10^{2}$ | $3.386\times10^{2}$ | $2.792\times10^{2}$ |
| $\Delta_{AAD}$ / MPa | 0.02 | 0.05 | 0.03 | 0.01 |
| $\Delta_{AARD}$ ($p$) | 0.09% | 0.19% | 0.09% | 0.03% |
| | | 448.15 K | | |
| $A$ | $-1.735\times10^{-2}$ | $-4.660\times10^{-3}$ | $1.620\times10^{-2}$ | $3.933\times10^{-2}$ |
| $B$ | $1.985\times10^{-10}$ | $1.719\times10^{-10}$ | $8.773\times10^{-11}$ | $2.156\times10^{-11}$ |
| $\rho_r$ | $3.306\times10^{2}$ | $3.347\times10^{2}$ | $3.148\times10^{2}$ | $2.382\times10^{2}$ |
| $\Delta_{AAD}$ / MPa | 0.03 | 0.02 | 0.02 | 0.02 |
| $\Delta_{AARD}$ ($p$) | 0.10% | 0.10% | 0.09% | 0.06% |
| | | 473.15 K | | |
| $A$ | $-8.710\times10^{-3}$ | $2.920\times10^{-3}$ | $2.237\times10^{-2}$ | $4.499\times10^{-2}$ |
| $B$ | $1.816\times10^{-10}$ | $1.486\times10^{-10}$ | $7.211\times10^{-11}$ | $1.683\times10^{-11}$ |
| $\rho_r$ | $3.154\times10^{2}$ | $3.139\times10^{2}$ | $2.852\times10^{2}$ | $1.927\times10^{2}$ |
| $\Delta_{AAD}$ / MPa | 0.02 | 0.02 | 0.03 | 0.03 |
| $\Delta_{AARD}$ ($p$) | 0.08% | 0.09% | 0.10% | 0.10% |

**Table C.6** Parameters of the Redlich-Kister correlation for the excess molar volume of $CO_2$ + *n*-nonane and the average absolute deviation $\Delta_{AAD}$.

| $T$ / K | $p$ / MPa | $A_1$ | $A_2$ | $A_3$ | $\Delta_{AAD}$ /cm$^3$·mol$^{-1}$ |
|---|---|---|---|---|---|
| 283.15 | 10 | 2.244 | -1.641 | -12.886 | 0.118 |
| 283.15 | 15 | 4.312 | 0.283 | -11.641 | 0.124 |
| 283.15 | 20 | 5.600 | 1.090 | -11.633 | 0.133 |
| 283.15 | 25 | 6.460 | 1.749 | -11.425 | 0.133 |
| 283.15 | 30 | 7.057 | 2.072 | -11.829 | 0.136 |
| 283.15 | 35 | 7.529 | 2.342 | -11.828 | 0.136 |
| 283.15 | 40 | 7.856 | 2.455 | -12.156 | 0.137 |
| 283.15 | 45 | 8.130 | 2.555 | -12.086 | 0.136 |
| 283.15 | 50 | 8.358 | 2.608 | -12.471 | 0.137 |
| 283.15 | 55 | 8.527 | 2.683 | -12.464 | 0.135 |
| 283.15 | 60 | 8.639 | 2.678 | -12.721 | 0.134 |
| 283.15 | 65 | 8.753 | 2.718 | -12.794 | 0.135 |
| 298.15 | 15 | -1.011 | -4.120 | -10.952 | 0.193 |
| 298.15 | 20 | 1.631 | -1.837 | -9.669 | 0.208 |
| 298.15 | 25 | 3.233 | -0.495 | -8.996 | 0.224 |
| 298.15 | 30 | 4.302 | 0.295 | -8.646 | 0.232 |
| 298.15 | 35 | 5.038 | 0.779 | -8.592 | 0.242 |
| 298.15 | 40 | 5.601 | 1.046 | -8.610 | 0.249 |
| 298.15 | 45 | 5.998 | 1.271 | -8.626 | 0.253 |
| 298.15 | 50 | 6.309 | 1.429 | -8.721 | 0.258 |
| 298.15 | 55 | 6.584 | 1.500 | -8.797 | 0.263 |
| 298.15 | 60 | 6.770 | 1.575 | -8.939 | 0.267 |
| 298.15 | 65 | 6.899 | 1.688 | -8.970 | 0.271 |
| 323.15 | 15 | -20.149 | -21.528 | -17.478 | 0.328 |
| 323.15 | 20 | -8.414 | -9.510 | -9.600 | 0.241 |
| 323.15 | 25 | -3.097 | -5.453 | -11.552 | 0.171 |
| 323.15 | 30 | -0.314 | -2.932 | -9.833 | 0.192 |
| 323.15 | 35 | 1.502 | -1.527 | -9.060 | 0.208 |
| 323.15 | 40 | 2.753 | -0.583 | -8.660 | 0.222 |
| 323.15 | 45 | 3.642 | 0.062 | -8.437 | 0.229 |
| 323.15 | 50 | 4.334 | 0.462 | -8.428 | 0.236 |
| 323.15 | 55 | 4.844 | 0.736 | -8.403 | 0.240 |
| 323.15 | 60 | 5.232 | 1.007 | -8.432 | 0.247 |
| 323.15 | 65 | 5.577 | 1.167 | -8.471 | 0.254 |
| 348.15 | 15 | -77.229 | -82.861 | -59.247 | 1.038 |
| 348.15 | 20 | -28.745 | -32.605 | -35.846 | 0.043 |
| 348.15 | 25 | -14.566 | -16.145 | -19.327 | 0.082 |
| 348.15 | 30 | -7.872 | -9.170 | -13.384 | 0.136 |
| 348.15 | 35 | -4.007 | -5.620 | -10.662 | 0.166 |
| 348.15 | 40 | -1.489 | -3.402 | -9.359 | 0.185 |
| 348.15 | 45 | 0.286 | -2.046 | -8.638 | 0.197 |
| 348.15 | 50 | 1.538 | -1.124 | -8.236 | 0.207 |
| 348.15 | 55 | 2.492 | -0.455 | -7.966 | 0.219 |
| 348.15 | 60 | 3.243 | 0.025 | -8.021 | 0.226 |

| $T$ / K | $p$ / MPa | $A_1$ | $A_2$ | $A_3$ | $\Delta_{AAD}$ /cm$^3$·mol$^{-1}$ |
|---|---|---|---|---|---|
| 348.15 | 65 | 3.808 | 0.426 | -7.892 | 0.234 |
| 373.15 | 20 | -64.311 | -60.382 | -35.983 | 0.664 |
| 373.15 | 25 | -32.761 | -33.177 | -31.633 | 0.018 |
| 373.15 | 30 | -19.008 | -19.122 | -20.602 | 0.062 |
| 373.15 | 35 | -11.573 | -12.175 | -15.746 | 0.097 |
| 373.15 | 40 | -6.916 | -8.225 | -13.545 | 0.129 |
| 373.15 | 45 | -3.886 | -5.903 | -12.500 | 0.139 |
| 373.15 | 50 | -1.666 | -4.275 | -12.036 | 0.154 |
| 373.15 | 55 | -0.092 | -3.263 | -11.872 | 0.164 |
| 373.15 | 60 | 1.130 | -2.486 | -11.834 | 0.171 |
| 373.15 | 65 | 2.038 | -1.870 | -11.752 | 0.181 |
| 398.15 | 20 | -98.313 | -95.533 | -73.759 | 0.228 |
| 398.15 | 25 | -55.248 | -51.767 | -40.687 | 0.072 |
| 398.15 | 30 | -33.499 | -30.711 | -25.589 | 0.023 |
| 398.15 | 35 | -21.568 | -19.531 | -17.950 | 0.070 |
| 398.15 | 40 | -14.162 | -13.190 | -14.704 | 0.106 |
| 398.15 | 45 | -9.400 | -9.430 | -12.977 | 0.121 |
| 398.15 | 50 | -6.011 | -6.893 | -12.042 | 0.138 |
| 398.15 | 55 | -3.647 | -5.242 | -11.548 | 0.148 |
| 398.15 | 60 | -1.820 | -3.962 | -11.469 | 0.160 |
| 398.15 | 65 | -0.391 | -3.123 | -11.292 | 0.167 |
| 423.15 | 20 | -128.890 | -107.710 | -56.129 | 0.020 |
| 423.15 | 25 | -77.220 | -65.401 | -39.873 | 0.067 |
| 423.15 | 30 | -49.107 | -40.862 | -26.473 | 0.003 |
| 423.15 | 35 | -32.766 | -26.796 | -18.747 | 0.036 |
| 423.15 | 40 | -22.430 | -18.498 | -15.339 | 0.089 |
| 423.15 | 45 | -15.827 | -13.242 | -12.712 | 0.106 |
| 423.15 | 50 | -10.976 | -9.948 | -11.958 | 0.136 |
| 423.15 | 55 | -7.598 | -7.581 | -11.657 | 0.141 |
| 423.15 | 60 | -5.013 | -5.954 | -11.665 | 0.165 |
| 423.15 | 65 | -3.021 | -4.808 | -11.749 | 0.169 |
| 448.15 | 20 | -153.518 | -106.073 | -17.919 | 0.355 |
| 448.15 | 25 | -96.429 | -72.041 | -27.940 | 0.031 |
| 448.15 | 30 | -63.701 | -48.826 | -24.297 | 0.018 |
| 448.15 | 35 | -43.924 | -33.249 | -17.768 | 0.010 |
| 448.15 | 40 | -31.207 | -23.479 | -14.161 | 0.037 |
| 448.15 | 45 | -22.592 | -17.094 | -11.817 | 0.061 |
| 448.15 | 50 | -16.610 | -12.767 | -10.539 | 0.080 |
| 448.15 | 55 | -12.206 | -9.762 | -10.178 | 0.095 |
| 448.15 | 60 | -8.942 | -7.576 | -9.908 | 0.106 |
| 448.15 | 65 | -6.384 | -5.998 | -9.991 | 0.119 |
| 473.15 | 20 | -172.304 | -97.007 | 23.974 | 0.665 |
| 473.15 | 25 | -112.215 | -71.940 | -7.325 | 0.182 |
| 473.15 | 30 | -76.495 | -53.052 | -16.730 | 0.001 |
| 473.15 | 35 | -54.200 | -37.438 | -13.246 | 0.018 |
| 473.15 | 40 | -39.396 | -27.581 | -11.605 | 0.025 |
| 473.15 | 45 | -29.285 | -20.371 | -9.822 | 0.042 |

| $T$ / K | $p$ / MPa | $A_1$ | $A_2$ | $A_3$ | $\Delta_{AAD}$ /cm$^3$·mol$^{-1}$ |
|---|---|---|---|---|---|
| 473.15 | 50 | -22.054 | -15.457 | -8.996 | 0.059 |
| 473.15 | 55 | -16.776 | -11.931 | -8.703 | 0.070 |
| 473.15 | 60 | -12.789 | -9.388 | -8.559 | 0.086 |
| 473.15 | 65 | -9.681 | -7.542 | -8.681 | 0.089 |

**Table C.7** Experimental speed-of-sound $c$ in $CO_2$ + $n$-nonane at four compositions as a function of temperature and pressure, $T$: (283.15 to 473.15) K and $p$: (10 to 390) MPa.

| $p$ (MPa) | $c$ (m·s$^{-1}$) | $p$ (MPa) | $c$ (m·s$^{-1}$) | $p$ (MPa) | $c$ (m·s$^{-1}$) |
|---|---|---|---|---|---|
| | | **$x_{CO2}$ = 0.2032** | | | |
| | | $T$ = 283.15 K | | | |
| 10.58 | 1239.75 | 160.25 | 1817.87 | 320.18 | 2179.23 |
| 40.26 | 1399.58 | 200.06 | 1921.21 | 360.04 | 2252.95 |
| 80.59 | 1566.9 | 239.92 | 2014.08 | 390.14 | 2305.60 |
| 120.23 | 1700.77 | 280.11 | 2099.83 | | |
| | | $T$ = 298.15 K | | | |
| 10.87 | 1190.78 | 160.21 | 1783.65 | 320.00 | 2150.66 |
| 40.06 | 1351.71 | 200.29 | 1889.33 | 359.97 | 2225.29 |
| 80.07 | 1524.33 | 240.11 | 1983.87 | 389.99 | 2278.33 |
| 120.15 | 1664.87 | 280.3 | 2071.07 | | |
| | | $T$ = 323.15 K | | | |
| 10.29 | 1091.37 | 160.09 | 1724.01 | 320.02 | 2100.45 |
| 40.08 | 1271.26 | 200.02 | 1832.56 | 359.98 | 2176.62 |
| 80.08 | 1453.62 | 240.15 | 1930.55 | 390.06 | 2230.92 |
| 120.26 | 1600.65 | 280.06 | 2019.01 | | |
| | | $T$ = 348.15 K | | | |
| 10.43 | 999.02 | 160.05 | 1668.64 | 320.00 | 2054.79 |
| 40.31 | 1197.22 | 200.54 | 1781.50 | 360.04 | 2132.52 |
| 80.25 | 1389.60 | 240.19 | 1880.62 | 389.92 | 2186.86 |
| 120.08 | 1541.11 | 279.99 | 1971.46 | | |
| | | $T$ = 373.15 K | | | |
| 10.32 | 911.61 | 160.11 | 1618.73 | 320.09 | 2012.81 |
| 40.59 | 1129.21 | 200.12 | 1733.60 | 359.61 | 2090.79 |
| 79.97 | 1328.40 | 240.23 | 1836.24 | 390.05 | 2146.74 |
| 120.19 | 1487.37 | 280.19 | 1928.60 | | |
| | | $T$ = 398.15 K | | | |
| 10.45 | 831.50 | 160.02 | 1573.65 | 320.07 | 1974.57 |
| 40.08 | 1063.49 | 200.36 | 1690.96 | 360.08 | 2054.08 |
| 80.51 | 1277.95 | 240.21 | 1794.71 | 390.14 | 2110.54 |
| 120.12 | 1438.5 | 279.67 | 1887.72 | | |
| | | $T$ = 423.15 K | | | |
| 11.85 | 769.98 | 160.03 | 1530.09 | 319.96 | 1937.45 |
| 40.61 | 1006.46 | 200.02 | 1649.51 | 360.09 | 2017.93 |

| $p$ (MPa) | $c$ (m·s$^{-1}$) | $p$ (MPa) | $c$ (m·s$^{-1}$) | $p$ (MPa) | $c$ (m·s$^{-1}$) |
|---|---|---|---|---|---|
| 80.02 | 1224.04 | 240.01 | 1754.32 | 390.14 | 2074.39 |
| 120.05 | 1391.26 | 280.14 | 1850.71 | | |
| | | $T$ = 448.15 K | | | |
| 11.46 | 688.48 | 159.97 | 1489.40 | 319.96 | 1902.97 |
| 40.16 | 948.03 | 200.08 | 1611.05 | 360.05 | 1984.33 |
| 80.19 | 1177.94 | 240.05 | 1718.4 | 389.64 | 2041.02 |
| 120.06 | 1348.95 | 280.06 | 1814.69 | | |
| | | $T$ = 473.15 K | | | |
| 10.68 | 605.29 | 160.05 | 1455.03 | 320.00 | 1875.07 |
| 40.31 | 898.29 | 200.11 | 1578.96 | 360.1 | 1958.88 |
| 80.24 | 1135.88 | 240.02 | 1687.58 | 390.11 | 2015.03 |
| 120.19 | 1311.73 | 280.06 | 1785.65 | | |
| | | **$x_{CO2}$ = 0.4034** | | | |
| | | $T$ = 283.15 K | | | |
| 10.29 | 1129.08 | 160.05 | 1730.50 | 320.27 | 2091.53 |
| 40.02 | 1301.38 | 200.04 | 1834.15 | 359.94 | 2164.38 |
| 80.08 | 1474.43 | 240.29 | 1928.03 | 390.00 | 2216.41 |
| 120.08 | 1613.14 | 280.22 | 2012.85 | | |
| | | $T$ = 298.15 K | | | |
| 10.65 | 1071.92 | 160.29 | 1695.00 | 319.89 | 2061.09 |
| 40.14 | 1250.85 | 200.36 | 1800.60 | 360.40 | 2136.40 |
| 80.06 | 1429.91 | 240.17 | 1895.06 | 390.28 | 2188.89 |
| 120.05 | 1572.77 | 280.2 | 1981.91 | | |
| | | $T$ = 323.15 K | | | |
| 10.42 | 972.40 | 159.99 | 1641.71 | 320.15 | 2020.06 |
| 40.34 | 1173.68 | 200.17 | 1751.38 | 359.92 | 2095.35 |
| 79.97 | 1364.38 | 239.84 | 1848.65 | 390.46 | 2150.10 |
| 120.23 | 1516.6 | 280.29 | 1938.72 | | |
| | | $T$ = 348.15 K | | | |
| 10.88 | 877.78 | 160.19 | 1587.27 | 320.02 | 1975.25 |
| 40.19 | 1096.92 | 200.42 | 1700.89 | 360.14 | 2052.96 |
| 80.14 | 1301.03 | 240.37 | 1801.37 | 390.30 | 2108.06 |
| 119.97 | 1457.32 | 280.39 | 1892.53 | | |
| | | $T$ = 373.15 K | | | |
| 10.75 | 784.29 | 160.07 | 1538.91 | 320.16 | 1935.85 |
| 40.51 | 1028.38 | 200.26 | 1655.31 | 360.05 | 2014.29 |
| 79.93 | 1240.31 | 240.34 | 1758.21 | 390.01 | 2068.81 |
| 120.07 | 1404.01 | 280.67 | 1851.77 | | |
| | | $T$ = 398.15 K | | | |
| 10.56 | 687.75 | 159.99 | 1491.92 | 320.13 | 1896.98 |
| 40.02 | 959.00 | 200.53 | 1611.95 | 360.02 | 1976.06 |
| 80.31 | 1186.70 | 240.24 | 1715.87 | 389.54 | 2030.80 |
| 120.01 | 1353.69 | 279.96 | 1809.75 | | |

| $p$ (MPa) | $c$ (m·s$^{-1}$) | $p$ (MPa) | $c$ (m·s$^{-1}$) | $p$ (MPa) | $c$ (m·s$^{-1}$) |
|---|---|---|---|---|---|
| | | $T$ = 423.15 K | | | |
| 10.94 | 605.95 | 160.16 | 1447.99 | 320.17 | 1858.80 |
| 40.78 | 904.38 | 200.12 | 1568.53 | 359.75 | 1938.50 |
| 80.38 | 1136.79 | 240.05 | 1674.67 | 389.93 | 1995.79 |
| 120.01 | 1306.84 | 280.17 | 1770.81 | | |
| | | $T$ = 448.15 K | | | |
| 15.08 | 585.43 | 160.03 | 1408.26 | 319.86 | 1824.91 |
| 39.89 | 840.28 | 200.29 | 1531.81 | 359.90 | 1906.28 |
| 80.16 | 1087.94 | 240.01 | 1639.29 | 382.29 | 1949.67 |
| 120.26 | 1265.43 | 280.1 | 1736.63 | | |
| | | $T$ = 473.15 K | | | |
| 20.78 | 599.12 | 160.09 | 1372.92 | 320.05 | 1793.74 |
| 40.29 | 793.59 | 200.15 | 1497.67 | 359.39 | 1875.08 |
| 80.44 | 1047.66 | 240.01 | 1606.85 | 388.19 | 1930.01 |
| 120.48 | 1228.28 | 280.06 | 1704.52 | | |
| | | **$x_{CO2}$ = 0.6009** | | | |
| | | $T$ = 283.15 K | | | |
| 10.22 | 1015.29 | 160.07 | 1644.68 | 320.12 | 2005.06 |
| 39.96 | 1199.70 | 200.1 | 1749.07 | 360.04 | 2077.35 |
| 79.90 | 1382.50 | 240.25 | 1842.41 | 389.83 | 2133.61 |
| 120.03 | 1525.52 | 279.92 | 1926.52 | | |
| | | $T$ = 298.15 K | | | |
| 12.00 | 968.71 | 160.16 | 1608.81 | 320.28 | 1976.82 |
| 40.26 | 1153.07 | 200.46 | 1718.69 | 359.94 | 2050.11 |
| 80.02 | 1339.64 | 240.09 | 1810.61 | 390 | 2102.42 |
| 120.06 | 1485.79 | 279.97 | 1896.66 | | |
| | | $T$ = 323.15 K | | | |
| 14.25 | 879.48 | 160.02 | 1554.9 | 320.49 | 1934.86 |
| 40.22 | 1070.71 | 200.25 | 1666.17 | 359.81 | 2008.85 |
| 80.00 | 1272.38 | 240.34 | 1764.49 | 389.81 | 2062.01 |
| 120.11 | 1427.50 | 280.05 | 1852.61 | | |
| | | $T$ = 348.15 K | | | |
| 14.70 | 784.90 | 160.1 | 1501.5 | 320.08 | 1888.66 |
| 40.25 | 993.82 | 200.22 | 1616.35 | 360.02 | 1965.07 |
| 80.04 | 1208.71 | 240.22 | 1715.22 | 390.08 | 2019.3 |
| 120.01 | 1368.82 | 280.38 | 1806.19 | | |
| | | $T$ = 373.15 K | | | |
| 15.43 | 698.56 | 160.44 | 1450.23 | 320.19 | 1844.22 |
| 40.32 | 921.13 | 200.31 | 1565.77 | 360.18 | 1921.72 |
| 79.97 | 1146.91 | 240.06 | 1667.49 | 389.38 | 1974.06 |
| 120.06 | 1313.64 | 279.95 | 1759.35 | | |
| | | $T$ = 398.15 K | | | |
| 20.36 | 666.52 | 160.02 | 1401.26 | 319.96 | 1804.61 |

| $p$ (MPa) | $c$ (m·s$^{-1}$) | $p$ (MPa) | $c$ (m·s$^{-1}$) | $p$ (MPa) | $c$ (m·s$^{-1}$) |
|---|---|---|---|---|---|
| 40.38 | 853.53 | 200.13 | 1521.48 | 360.08 | 1883.96 |
| 79.92 | 1089.89 | 240.41 | 1626.16 | 389.97 | 1938.12 |
| 120.02 | 1262.13 | 280.07 | 1719.15 | | |
| | | $T$ = 423.15 K | | | |
| 21.88 | 611.85 | 160.04 | 1357.97 | 319.92 | 1763.98 |
| 40.11 | 790.72 | 200.09 | 1478.43 | 360 | 1842.38 |
| 79.97 | 1039.94 | 240.11 | 1584.24 | 390.05 | 1895.4 |
| 119.59 | 1214.74 | 280.15 | 1678.71 | | |
| | | $T$ = 448.15 K | | | |
| 27.28 | 606.09 | 160.18 | 1316.71 | 320.25 | 1731.94 |
| 40.26 | 733.7 | 200.07 | 1440.54 | 360.12 | 1811.81 |
| 80.5 | 993.34 | 240.19 | 1547.86 | 390.20 | 1867.50 |
| 120.17 | 1172.21 | 280.20 | 1644.04 | | |
| | | $T$ = 473.15 K | | | |
| 30.48 | 590.29 | 160.02 | 1278.45 | 320.26 | 1693.23 |
| 40.65 | 688.63 | 200.16 | 1401.95 | 359.62 | 1771.64 |
| 80.01 | 950.02 | 239.93 | 1508.42 | 389.95 | 1828.31 |
| 120.05 | 1132.61 | 280.25 | 1605.39 | | |
| | | **$x_{CO2}$ = 0.8008** | | | |
| | | $T$ = 283.15 K | | | |
| 10.19 | 784.09 | 159.84 | 1467.43 | | |
| 40.09 | 1010.38 | 200.00 | 1571.03 | | |
| 80.35 | 1205.86 | 239.98 | 1662.32 | | |
| 120.09 | 1348.69 | | | | |
| | | $T$ = 298.15 K | | | |
| 11.85 | 721.95 | 159.97 | 1438.14 | 320.35 | 1794.27 |
| 39.89 | 961.70 | 200.07 | 1542.92 | 359.91 | 1863.91 |
| 80.06 | 1167.39 | 240.07 | 1634.86 | | |
| 120 | 1316.11 | 280.05 | 1717.95 | | |
| | | $T$ = 323.15 K | | | |
| 12.29 | 621.52 | 160.18 | 1395.80 | 319.85 | 1765.96 |
| 39.91 | 888.82 | 200.01 | 1504.71 | 361.70 | 1842.31 |
| 80.3 | 1110.50 | 239.81 | 1600.57 | | |
| 119.9 | 1266.53 | 280.00 | 1687.27 | | |
| | | $T$ = 348.15 K | | | |
| 20.29 | 614.20 | 160.22 | 1337.84 | 320.05 | 1718.60 |
| 40.2 | 806.13 | 200.29 | 1452.78 | 360.28 | 1793.30 |
| 80.31 | 1041.08 | 240.18 | 1550.04 | 390.18 | 1844.31 |
| 120.01 | 1205.31 | 280.24 | 1638.53 | | |
| | | $T$ = 373.15 K | | | |
| 23.85 | 562.27 | 159.94 | 1282.28 | 319.97 | 1667.02 |
| 40.59 | 733.09 | 200.22 | 1396.70 | 359.68 | 1741.63 |
| 80.03 | 976.94 | 240.04 | 1496.35 | 390.13 | 1794.70 |

| $p$ (MPa) | $c$ (m·s$^{-1}$) | $p$ (MPa) | $c$ (m·s$^{-1}$) | $p$ (MPa) | $c$ (m·s$^{-1}$) |
|---|---|---|---|---|---|
| 120.37 | 1148.68 | 279.95 | 1586.14 | | |
| | | $T$ = 398.15 K | | | |
| 30.29 | 558.42 | 160.11 | 1233.66 | 320.07 | 1628.08 |
| 40.15 | 657.70 | 200.10 | 1351.06 | 360.15 | 1704.16 |
| 80.1 | 918.33 | 240.21 | 1453.59 | 390.12 | 1757.12 |
| 120.46 | 1096.15 | 279.91 | 1544.81 | | |
| | | $T$ = 423.15 K | | | |
| 40.26 | 602.52 | 200.06 | 1306.55 | 360.09 | 1662.34 |
| 80.02 | 869.30 | 240.14 | 1409.72 | 390.02 | 1716.26 |
| 120.57 | 1049.77 | 280.15 | 1501.95 | | |
| 159.86 | 1188.27 | 320.32 | 1586.45 | | |
| | | $T$ = 448.15 K | | | |
| 45.26 | 595.93 | 200.14 | 1271.05 | 360.33 | 1631.77 |
| 79.96 | 823.26 | 240.09 | 1375.12 | 389.89 | 1683.97 |
| 120.13 | 1006.84 | 280.05 | 1468.54 | | |
| 160.14 | 1150.28 | 320.15 | 1553.72 | | |
| | | $T$ = 473.15 K | | | |
| 44.55 | 554.24 | 200.23 | 1235.31 | 360.51 | 1599.39 |
| 80.24 | 788.47 | 240.26 | 1341.42 | 390.23 | 1651.79 |
| 120.28 | 970.93 | 280.12 | 1435.34 | | |
| 160.07 | 1113.53 | 320.31 | 1521.11 | | |

Standard uncertainties at 95 % confidence are $u(T)$ = 0.05 K and $u(p)$ = 50 kPa, $u(x) = 10^{-5}$ and $u_c(c) \sim 0.0004c$.

**Table C.8** Fitting parameters for the speed-of-sound correlation, Equation (6.7) and (6.8) for $CO_2$ + *n*-nonane at four compositions. The average absolute deviations $\Delta_{AARD}$ are also provided.

| | | | | | | | | | |
|---|---|---|---|---|---|---|---|---|---|
| $x_{CO2}$ = 0.2 | $a_{10}$ | -1.199 | $a_{20}$ | $1.123\times10^{-3}$ | $a_{30}$ | $-7.436\times10^{-7}$ | $b_0$ | $3.197\times10^{3}$ | $\Delta_{AARD}$ = 0.07 % |
| | $a_{11}$ | 4.450 | $a_{21}$ | $-4.536\times10^{-3}$ | $a_{31}$ | $3.127\times10^{-6}$ | $b_1$ | $-3.126\times10^{3}$ | |
| | $a_{12}$ | -5.251 | $a_{22}$ | $6.366\times10^{-3}$ | $a_{32}$ | $-4.132\times10^{-6}$ | $b_2$ | $1.519\times10^{3}$ | |
| | $a_{13}$ | 2.162 | $a_{23}$ | $-2.826\times10^{-3}$ | $a_{33}$ | $1.791\times10^{-6}$ | $b_3$ | $-3.709\times10^{2}$ | |
| $x_{CO2}$ = 0.4 | $a_{10}$ | $4.799\times10^{-1}$ | $a_{20}$ | $-1.054\times10^{-3}$ | $a_{30}$ | $4.439\times10^{-7}$ | $b_0$ | $1.421\times10^{3}$ | $\Delta_{AARD}$ = 0.06 % |
| | $a_{11}$ | -2.394 | $a_{21}$ | $4.309\times10^{-3}$ | $a_{31}$ | $-1.726\times10^{-6}$ | $b_1$ | $7.982\times10^{2}$ | |
| | $a_{12}$ | 3.798 | $a_{22}$ | $-5.439\times10^{-3}$ | $a_{32}$ | $2.372\times10^{-6}$ | $b_2$ | $-1.441\times10^{3}$ | |
| | $a_{13}$ | -1.754 | $a_{23}$ | $2.354\times10^{-3}$ | $a_{33}$ | $-1.066\times10^{-6}$ | $b_3$ | $3.498\times10^{2}$ | |
| $x_{CO2}$ = 0.6 | $a_{10}$ | $-4.006\times10^{-1}$ | $a_{20}$ | $-3.038\times10^{-5}$ | $a_{30}$ | $1.106\times10^{-8}$ | $b_0$ | $2.923\times10^{3}$ | $\Delta_{AARD}$ = 0.10 % |
| | $a_{11}$ | 1.414 | $a_{21}$ | $1.074\times10^{-4}$ | $a_{31}$ | $7.974\times10^{-8}$ | $b_1$ | $-2.611\times10^{3}$ | |
| | $a_{12}$ | -1.539 | $a_{22}$ | $1.627\times10^{-4}$ | $a_{32}$ | $-4.737\times10^{-8}$ | $b_2$ | $9.348\times10^{2}$ | |
| | $a_{13}$ | $6.658\times10^{-1}$ | $a_{23}$ | $-7.769\times10^{-5}$ | $a_{33}$ | $-1.418\times10^{-8}$ | $b_3$ | $-1.845\times10^{2}$ | |
| $x_{CO2}$ = 0.8 | $a_{10}$ | 2.033 | $a_{20}$ | $-2.493\times10^{-3}$ | $a_{30}$ | $2.107\times10^{-6}$ | $b_0$ | $3.165\times10^{2}$ | $\Delta_{AARD}$ = 0.34 % |
| | $a_{11}$ | -7.814 | $a_{21}$ | $1.064\times10^{-2}$ | $a_{31}$ | $-8.633\times10^{-6}$ | $b_1$ | $3.467\times10^{3}$ | |
| | $a_{12}$ | $1.002\times10$ | $a_{22}$ | $-1.452\times10^{-2}$ | $a_{32}$ | $1.188\times10^{-5}$ | $b_2$ | $-4.031\times10^{3}$ | |

| | | | | | | | |
|---|---|---|---|---|---|---|---|
| $a_{13}$ | -4.123 | $a_{23}$ | $6.624\times10^{-3}$ | $a_{33}$ | $-5.368\times10^{-6}$ | $b_3$ | $1.167\times10^{3}$ |

**Table C.9** Experimental compressed-liquid density $\rho$ for $CO_2$ + methylbenzene at four compositions as a function of temperature and pressure, $T$: (283.15 to 473.15) K and $p$: (10 to 65) MPa.

| $p$ (MPa) | $\rho$ (kg·m$^{-3}$) | $p$ (MPa) | $\rho$ (kg·m$^{-3}$) | $p$ (MPa) | $\rho$ (kg·m$^{-3}$) |
|---|---|---|---|---|---|
| | | **$x_{CO2}$ = 0.2030** | | | |
| | | $T$ = 283.15 K | | | |
| 10.01 | 893.34 | 35.00 | 911.81 | 60.02 | 927.50 |
| 15.01 | 897.33 | 40.00 | 915.13 | 65.01 | 930.42 |
| 20.01 | 901.12 | 45.01 | 918.35 | 10.00 | 893.34 |
| 25.02 | 904.80 | 50.01 | 921.47 | | |
| 30.00 | 908.33 | 55.01 | 924.54 | | |
| | | $T$ = 298.15 K | | | |
| 10.02 | 877.46 | 35.01 | 897.67 | 60.01 | 914.58 |
| 15.02 | 881.89 | 40.01 | 901.24 | 65.01 | 917.63 |
| 20.02 | 886.07 | 45.02 | 904.75 | 10.02 | 877.46 |
| 25.00 | 890.04 | 50.02 | 908.11 | | |
| 30.01 | 893.96 | 55.02 | 911.42 | | |
| | | $T$ = 323.15 K | | | |
| 10.02 | 851.19 | 35.01 | 874.61 | 60.01 | 893.54 |
| 15.02 | 856.39 | 40.00 | 878.65 | 65.01 | 897.02 |
| 20.02 | 861.28 | 45.02 | 882.63 | 10.03 | 851.19 |
| 25.00 | 865.93 | 50.01 | 886.37 | | |
| 30.02 | 870.37 | 55.03 | 890.05 | | |
| | | $T$ = 348.15 K | | | |
| 10.02 | 824.19 | 35.00 | 851.52 | 60.01 | 872.79 |
| 15.02 | 830.39 | 40.00 | 856.12 | 65.02 | 876.64 |
| 20.01 | 836.10 | 45.01 | 860.58 | 10.02 | 824.19 |
| 25.02 | 841.55 | 50.01 | 864.78 | | |
| 30.03 | 846.66 | 55.02 | 868.89 | | |
| | | $T$ = 373.15 K | | | |
| 10.01 | 796.27 | 35.00 | 828.36 | 60.00 | 852.30 |
| 15.02 | 803.72 | 40.01 | 833.62 | 65.02 | 856.47 |
| 20.00 | 810.47 | 45.02 | 838.64 | 10.01 | 796.27 |
| 25.01 | 816.88 | 50.00 | 843.36 | | |
| 30.01 | 822.79 | 55.01 | 847.93 | | |
| | | $T$ = 398.15 K | | | |
| 10.03 | 767.08 | 35.01 | 805.09 | 60.01 | 832.00 |
| 15.01 | 776.15 | 40.00 | 811.06 | 65.01 | 836.63 |
| 20.01 | 784.28 | 45.01 | 816.72 | 10.01 | 767.08 |
| 25.01 | 791.78 | 50.00 | 822.00 | | |
| 30.02 | 798.63 | 55.01 | 827.12 | | |
| | | $T$ = 423.15 K | | | |

| $p$ (MPa) | $\rho$ (kg·m$^{-3}$) | $p$ (MPa) | $\rho$ (kg·m$^{-3}$) | $p$ (MPa) | $\rho$ (kg·m$^{-3}$) |
|---|---|---|---|---|---|
| 10.02 | 736.67 | 35.01 | 781.98 | 60.01 | 812.13 |
| 15.01 | 747.97 | 40.01 | 788.74 | 65.01 | 817.26 |
| 20.01 | 757.76 | 45.02 | 795.15 | 10.02 | 736.82 |
| 25.02 | 766.61 | 50.00 | 801.07 | | |
| 30.02 | 774.59 | 55.02 | 806.79 | | |
| | | $T$ = 448.15 K | | | |
| 10.01 | 703.60 | 35.02 | 758.28 | 60.00 | 792.17 |
| 15.02 | 717.92 | 40.00 | 766.05 | 65.01 | 797.79 |
| 20.02 | 729.86 | 45.00 | 773.24 | 10.00 | 703.60 |
| 25.02 | 740.45 | 50.01 | 779.94 | | |
| 30.01 | 749.73 | 55.01 | 786.25 | | |
| | | $T$ = 473.15 K | | | |
| 15.01 | 685.76 | 40.01 | 743.09 | 65.01 | 778.49 |
| 20.03 | 700.74 | 45.00 | 751.23 | 15.01 | 685.80 |
| 25.01 | 713.38 | 50.01 | 758.75 | | |
| 30.02 | 724.42 | 55.02 | 765.73 | | |
| 35.02 | 734.26 | 60.01 | 772.29 | | |
| | | **$x_{CO2}$ = 0.4030** | | | |
| | | $T$ = 283.15 K | | | |
| 10.02 | 907.26 | 35.01 | 930.08 | 60.01 | 948.91 |
| 15.02 | 912.16 | 40.00 | 934.06 | 65.01 | 952.38 |
| 20.00 | 916.91 | 45.02 | 937.99 | 10.02 | 907.21 |
| 25.02 | 921.55 | 50.00 | 941.72 | | |
| 30.01 | 925.84 | 55.02 | 945.44 | | |
| | | $T$ = 298.15 K | | | |
| 10.01 | 888.05 | 35.02 | 913.36 | 60.02 | 933.69 |
| 15.02 | 893.69 | 40.01 | 917.73 | 65.03 | 937.35 |
| 20.02 | 898.98 | 45.02 | 921.95 | 10.03 | 888.05 |
| 25.02 | 904.01 | 50.01 | 925.97 | | |
| 30.02 | 908.79 | 55.03 | 929.93 | | |
| | | $T$ = 323.15 K | | | |
| 10.01 | 855.90 | 35.02 | 886.14 | 60.03 | 909.33 |
| 15.02 | 862.80 | 40.02 | 891.18 | 65.01 | 913.42 |
| 20.02 | 869.15 | 45.01 | 896.02 | 10.01 | 855.90 |
| 25.02 | 875.15 | 50.02 | 900.61 | | |
| 30.01 | 880.74 | 55.03 | 905.10 | | |
| | | $T$ = 348.15 K | | | |
| 10.02 | 822.15 | 35.02 | 858.64 | 60.03 | 885.20 |
| 15.03 | 830.79 | 40.01 | 864.50 | 65.01 | 889.81 |
| 20.00 | 838.49 | 45.01 | 870.05 | 10.03 | 822.20 |
| 25.01 | 845.74 | 50.02 | 875.35 | | |
| 30.02 | 852.39 | 55.01 | 880.36 | | |
| | | $T$ = 373.15 K | | | |

| $p$ (MPa) | $\rho$ (kg·m$^{-3}$) | $p$ (MPa) | $\rho$ (kg·m$^{-3}$) | $p$ (MPa) | $\rho$ (kg·m$^{-3}$) |
|---|---|---|---|---|---|
| 10.01 | 786.18 | 35.02 | 830.88 | 60.01 | 861.22 |
| 15.01 | 797.19 | 40.00 | 837.63 | 65.01 | 866.38 |
| 20.01 | 806.81 | 45.02 | 844.09 | 10.01 | 786.19 |
| 25.01 | 815.54 | 50.03 | 850.09 | | |
| 30.02 | 823.48 | 55.02 | 855.80 | | |
| | | $T$ = 398.15 K | | | |
| 15.02 | 760.97 | 40.01 | 810.61 | 65.01 | 843.43 |
| 20.01 | 773.32 | 45.01 | 818.05 | 15.01 | 760.97 |
| 25.03 | 784.25 | 50.00 | 824.95 | | |
| 30.02 | 793.85 | 55.02 | 831.51 | | |
| 35.03 | 802.63 | 60.01 | 837.62 | | |
| | | $T$ = 423.15 K | | | |
| 15.03 | 722.20 | 40.00 | 783.07 | 65.02 | 820.29 |
| 20.01 | 738.22 | 45.01 | 791.68 | 20.02 | 738.27 |
| 25.02 | 751.76 | 50.02 | 799.55 | | |
| 30.02 | 763.40 | 55.00 | 806.89 | | |
| 35.03 | 773.82 | 60.01 | 813.79 | | |
| | | $T$ = 448.15 K | | | |
| 20.02 | 701.30 | 45.02 | 765.31 | 20.02 | 701.30 |
| 25.01 | 718.13 | 50.02 | 774.20 | | |
| 30.00 | 732.20 | 55.01 | 782.50 | | |
| 35.02 | 744.58 | 60.01 | 790.17 | | |
| 40.01 | 755.36 | 65.02 | 797.35 | | |
| | | $T$ = 473.15 K | | | |
| 20.02 | 661.61 | 45.01 | 738.72 | 20.02 | 661.65 |
| 25.02 | 683.02 | 50.00 | 748.85 | | |
| 30.02 | 700.16 | 55.03 | 758.19 | | |
| 35.02 | 714.81 | 60.03 | 766.72 | | |
| 40.00 | 727.35 | 65.00 | 774.63 | | |
| | | **$x_{CO2}$ = 0.5999** | | | |
| | | $T$ = 283.15 K | | | |
| 10.01 | 921.75 | 35.01 | 953.40 | 60.01 | 977.82 |
| 15.02 | 928.98 | 40.01 | 958.55 | 65.01 | 982.20 |
| 20.00 | 935.40 | 45.02 | 963.80 | 10.02 | 921.75 |
| 25.01 | 941.82 | 50.00 | 968.59 | | |
| 30.00 | 947.59 | 55.04 | 973.38 | | |
| | | $T$ = 298.15 K | | | |
| 10.01 | 896.78 | 35.01 | 933.01 | 60.00 | 959.82 |
| 15.02 | 905.30 | 40.02 | 938.85 | 65.01 | 964.54 |
| 20.00 | 912.86 | 45.02 | 944.59 | 10.01 | 896.83 |
| 25.01 | 920.12 | 50.02 | 949.82 | | |
| 30.00 | 926.66 | 55.00 | 954.95 | | |
| | | $T$ = 323.15 K | | | |

| $p$ (MPa) | $\rho$ (kg·m$^{-3}$) | $p$ (MPa) | $\rho$ (kg·m$^{-3}$) | $p$ (MPa) | $\rho$ (kg·m$^{-3}$) |
|---|---|---|---|---|---|
| 10.01 | 852.14 | 35.01 | 898.03 | 60.02 | 929.57 |
| 15.00 | 863.25 | 40.02 | 905.03 | 65.00 | 934.92 |
| 20.02 | 873.21 | 45.03 | 911.73 | 10.02 | 852.24 |
| 25.00 | 882.22 | 50.01 | 917.93 | | |
| 30.00 | 890.33 | 55.02 | 923.93 | | |
| | | $T$ = 348.15 K | | | |
| 15.02 | 818.15 | 40.01 | 870.73 | 65.01 | 905.48 |
| 20.01 | 831.27 | 45.01 | 878.63 | 15.00 | 818.15 |
| 25.02 | 842.80 | 50.01 | 885.93 | | |
| 30.02 | 852.99 | 55.00 | 892.88 | | |
| 35.00 | 862.28 | 60.01 | 899.33 | | |
| | | $T$ = 373.15 K | | | |
| 15.02 | 768.29 | 40.00 | 835.80 | 65.02 | 876.25 |
| 20.02 | 786.34 | 45.01 | 845.23 | 15.02 | 768.29 |
| 25.02 | 801.44 | 50.02 | 853.81 | | |
| 30.00 | 814.18 | 55.01 | 861.76 | | |
| 35.02 | 825.73 | 60.02 | 869.25 | | |
| | | $T$ = 398.15 K | | | |
| 20.01 | 737.64 | 45.02 | 811.55 | 20.00 | 737.65 |
| 25.02 | 757.78 | 50.00 | 821.51 | | |
| 30.02 | 774.05 | 55.01 | 830.82 | | |
| 35.01 | 788.17 | 60.02 | 839.34 | | |
| 40.00 | 800.38 | 65.01 | 847.27 | | |
| | | $T$ = 423.15 K | | | |
| 20.01 | 684.96 | 45.02 | 777.74 | 20.00 | 685.01 |
| 25.03 | 712.03 | 50.01 | 789.23 | | |
| 30.00 | 732.56 | 55.01 | 799.90 | | |
| 35.01 | 749.94 | 60.01 | 809.58 | | |
| 40.00 | 764.55 | 65.01 | 818.53 | | |
| | | $T$ = 448.15 K | | | |
| 20.01 | 627.08 | 45.02 | 744.00 | 20.01 | 627.65 |
| 25.03 | 663.99 | 50.00 | 757.20 | | |
| 30.01 | 690.06 | 55.01 | 769.33 | | |
| 35.01 | 711.22 | 60.01 | 780.20 | | |
| 40.00 | 728.67 | 65.00 | 790.30 | | |
| | | $T$ = 473.15 K | | | |
| 20.01 | 567.27 | 45.02 | 710.65 | 20.01 | 567.74 |
| 25.00 | 614.81 | 50.01 | 725.78 | | |
| 30.01 | 647.56 | 55.00 | 739.22 | | |
| 35.03 | 672.69 | 60.00 | 751.41 | | |
| 40.00 | 693.18 | 65.00 | 762.50 | | |
| | | **$x_{CO2}$ = 0.7999** | | | |
| | | $T$ = 283.15 K | | | |

| $p$ (MPa) | $\rho$ (kg·m$^{-3}$) | $p$ (MPa) | $\rho$ (kg·m$^{-3}$) | $p$ (MPa) | $\rho$ (kg·m$^{-3}$) |
|---|---|---|---|---|---|
| 10.02 | 933.16 | 35.02 | 984.99 | 60.01 | 1020.53 |
| 15.03 | 945.67 | 40.01 | 992.64 | 65.01 | 1026.64 |
| 20.00 | 956.31 | 45.01 | 1000.49 | 10.01 | 933.16 |
| 25.02 | 966.90 | 50.00 | 1007.27 | | |
| 30.01 | 975.87 | 55.00 | 1014.41 | | |
| | | $T$ = 298.15 K | | | |
| 10.00 | 892.44 | 35.01 | 955.83 | 60.01 | 995.93 |
| 15.02 | 909.14 | 40.02 | 964.86 | 65.01 | 1002.63 |
| 20.01 | 922.26 | 45.01 | 973.59 | 10.01 | 892.49 |
| 25.01 | 935.03 | 50.00 | 981.31 | | |
| 30.01 | 945.63 | 55.02 | 989.07 | | |
| | | $T$ = 323.15 K | | | |
| 10.02 | 812.93 | 35.02 | 905.31 | 60.00 | 954.58 |
| 15.02 | 840.16 | 40.00 | 916.79 | 65.02 | 962.39 |
| 20.01 | 860.48 | 45.02 | 927.47 | 10.01 | 812.93 |
| 25.01 | 878.01 | 50.00 | 937.09 | | |
| 30.01 | 892.24 | 55.01 | 946.21 | | |
| | | $T$ = 348.15 K | | | |
| 15.02 | 757.70 | 40.01 | 867.24 | 65.02 | 922.17 |
| 20.01 | 790.76 | 45.01 | 880.63 | 15.02 | 757.70 |
| 25.00 | 815.98 | 50.01 | 892.12 | | |
| 30.01 | 835.46 | 55.01 | 903.27 | | |
| 35.02 | 852.91 | 60.01 | 913.07 | | |
| | | $T$ = 373.15 K | | | |
| 20.01 | 711.62 | 45.00 | 833.09 | 20.01 | 711.72 |
| 25.01 | 749.14 | 50.00 | 847.22 | | |
| 30.01 | 775.99 | 55.00 | 860.22 | | |
| 35.02 | 798.53 | 60.00 | 871.88 | | |
| 40.02 | 816.84 | 65.01 | 882.51 | | |
| | | $T$ = 398.15 K | | | |
| 20.01 | 622.95 | 45.01 | 785.40 | 20.00 | 623.34 |
| 25.02 | 678.00 | 50.00 | 802.37 | | |
| 30.00 | 714.76 | 55.00 | 817.48 | | |
| 35.01 | 742.98 | 60.02 | 831.02 | | |
| 40.01 | 765.99 | 65.01 | 843.18 | | |
| | | $T$ = 423.15 K | | | |
| 20.02 | 535.60 | 45.00 | 738.22 | 20.01 | 535.41 |
| 25.01 | 605.97 | 50.01 | 758.07 | | |
| 30.01 | 653.84 | 55.01 | 775.36 | | |
| 35.00 | 687.44 | 60.00 | 790.95 | | |
| 40.00 | 715.51 | 65.01 | 804.78 | | |
| | | $T$ = 448.15 K | | | |
| 20.00 | 460.89 | 45.01 | 692.33 | 20.01 | 460.84 |

| $p$ (MPa) | $\rho$ (kg·m$^{-3}$) | $p$ (MPa) | $\rho$ (kg·m$^{-3}$) | $p$ (MPa) | $\rho$ (kg·m$^{-3}$) |
|---|---|---|---|---|---|
| 25.01 | 538.61 | 50.02 | 714.78 | | |
| 30.01 | 594.76 | 55.01 | 734.40 | | |
| 35.02 | 633.92 | 60.01 | 751.85 | | |
| 40.01 | 666.05 | 65.02 | 771.98 | | |
| | | $T$ = 473.15 K | | | |
| 20.02 | 402.90 | 45.01 | 648.90 | 20.01 | 402.76 |
| 25.01 | 479.05 | 50.00 | 674.00 | | |
| 30.01 | 541.39 | 55.00 | 695.39 | | |
| 35.02 | 583.65 | 60.00 | 714.72 | | |
| 40.00 | 619.91 | 65.01 | 731.33 | | |

Standard uncertainties at 95 % confidence are $u(T)$ = 0.03 K and $u(p)$ = 20 kPa, $u(x) = 10^{-5}$ and $u_c(\rho) \sim 0.0005\rho$.

**Table C.10** Parameters $A$, $B$ and $\rho_r$ in Equation (6.1) for compressed-liquid densities and the values of the average absolute deviation, $\Delta_{AAD,}$ and average absolute relative deviation, $\Delta_{AARD}$ for $CO_2$ + methylbenzene system.

| Parameters | Mole fraction of $CO_2$ | | | |
|---|---|---|---|---|
| | 0.2030 | 0.4030 | 0.5999 | 0.7999 |
| | | 283.15 K | | |
| $A$ | $-1.229\times10^{-1}$ | $-9.477\times10^{-2}$ | $-5.999\times10^{-2}$ | $-2.817\times10^{-2}$ |
| $B$ | $1.247\times10^{-10}$ | 9.339E-11 | $6.742\times10^{-11}$ | $3.574\times10^{-11}$ |
| $\rho_r$ | $4.690\times10^{2}$ | $4.769\times10^{2}$ | $4.967\times10^{2}$ | $5.038\times10^{2}$ |
| $\Delta_{AAD}$ / MPa | 0.019 | 0.033 | 0.054 | 0.095 |
| $\Delta_{AARD}$ ($p$) | 0.06% | 0.13% | 0.19% | 0.29% |
| | | 298.15 K | | |
| $A$ | $-1.063\times10^{-1}$ | $-7.727\times10^{-2}$ | $-4.478\times10^{-2}$ | $-1.591\times10^{-2}$ |
| $B$ | $1.312\times10^{-10}$ | $1.074\times10^{-10}$ | $7.708\times10^{-11}$ | $3.947\times10^{-11}$ |
| $\rho_r$ | $4.703\times10^{2}$ | $4.870\times10^{2}$ | $5.054\times10^{2}$ | $5.060\times10^{2}$ |
| $\Delta_{AAD}$ / MPa | 0.023 | 0.014 | 0.034 | 0.069 |
| $\Delta_{AARD}$ ($p$) | 0.09% | 0.05% | 0.13% | 0.27% |
| | | 323.15 K | | |
| $A$ | $-8.562\times10^{-2}$ | $-5.899\times10^{-2}$ | $-2.909\times10^{-2}$ | $-1.790\times10^{-3}$ |
| $B$ | $1.321\times10^{-10}$ | $1.043\times10^{-10}$ | $7.096\times10^{-11}$ | $3.560\times10^{-11}$ |
| $\rho_r$ | $4.627\times10^{2}$ | $4.738\times10^{2}$ | $4.831\times10^{2}$ | $4.749\times10^{2}$ |
| $\Delta_{AAD}$ / MPa | 0.023 | 0.014 | 0.024 | 0.043 |
| $\Delta_{AARD}$ ($p$) | 0.07% | 0.05% | 0.09% | 0.17% |
| | | 348.15 K | | |
| $A$ | $-6.781\times10^{-2}$ | $-4.323\times10^{-2}$ | $-1.538\times10^{-2}$ | $9.430\times10^{-3}$ |
| $B$ | $1.302\times10^{-10}$ | $9.903\times10^{-11}$ | $6.504\times10^{-11}$ | $2.905\times10^{-11}$ |
| $\rho_r$ | $4.527\times10^{2}$ | $4.580\times10^{2}$ | $4.600\times10^{2}$ | $4.313\times10^{2}$ |
| $\Delta_{AAD}$ / MPa | 0.023 | 0.022 | 0.018 | 0.052 |
| $\Delta_{AARD}$ ($p$) | 0.08% | 0.09% | 0.05% | 0.14% |
| | | 373.15 K | | |
| $A$ | $-5.185\times10^{-2}$ | $-2.910\times10^{-2}$ | $-3.280\times10^{-3}$ | $1.919\times10^{-2}$ |

| | | | | |
|---|---|---|---|---|
| $B$ | $1.287\times10^{-10}$ | $9.422\times10^{-11}$ | $5.899\times10^{-11}$ | $2.312\times10^{-11}$ |
| $\rho_r$ | $4.427\times10^{2}$ | $4.423\times10^{2}$ | $4.357\times10^{2}$ | $3.845\times10^{2}$ |
| $\Delta_{AAD}$ / MPa | 0.013 | 0.022 | 0.023 | 0.033 |
| $\Delta_{AARD}$ ($p$) | 0.05% | 0.09% | 0.07% | 0.09% |
| | | 398.15 K | | |
| $A$ | $-3.896\times10^{-2}$ | $-1.675\times10^{-2}$ | $6.490\times10^{-3}$ | $2.787\times10^{-2}$ |
| $B$ | $1.195\times10^{-10}$ | $8.473\times10^{-11}$ | $4.955\times10^{-11}$ | $1.863\times10^{-11}$ |
| $\rho_r$ | $4.263\times10^{2}$ | $4.215\times10^{2}$ | $4.028\times10^{2}$ | $3.380\times10^{2}$ |
| $\Delta_{AAD}$ / MPa | 0.024 | 0.014 | 0.018 | 0.019 |
| $\Delta_{AARD}$ ($p$) | 0.08% | 0.04% | 0.05% | 0.05% |
| | | 423.15 K | | |
| $A$ | $-2.748\times10^{-2}$ | $-6.040\times10^{-3}$ | $1.519\times10^{-2}$ | $3.534\times10^{-2}$ |
| $B$ | $1.115\times10^{-10}$ | $7.752\times10^{-11}$ | $4.176\times10^{-11}$ | $1.433\times10^{-11}$ |
| $\rho_r$ | $4.103\times10^{2}$ | $4.013\times10^{2}$ | $3.697\times10^{2}$ | $2.852\times10^{2}$ |
| $\Delta_{AAD}$ / MPa | 0.028 | 0.022 | 0.021 | 0.030 |
| $\Delta_{AARD}$ ($p$) | 0.12% | 0.07% | 0.06% | 0.08% |
| | | 448.15 K | | |
| $A$ | $-1.685\times10^{-2}$ | $2.750\times10^{-3}$ | $2.316\times10^{-2}$ | $4.144\times10^{-2}$ |
| $B$ | $1.034\times10^{-10}$ | $6.734\times10^{-11}$ | $3.528\times10^{-11}$ | $8.256\times10^{-12}$ |
| $\rho_r$ | $3.937\times10^{2}$ | $3.756\times10^{2}$ | $3.367\times10^{2}$ | $1.993\times10^{2}$ |
| $\Delta_{AAD}$ / MPa | 0.018 | 0.014 | 0.020 | 0.24 |
| $\Delta_{AARD}$ ($p$) | 0.08% | 0.04% | 0.06% | 0.53% |
| | | 473.15 K | | |
| $A$ | $-7.870\times10^{-3}$ | $1.116\times10^{-2}$ | $3.002\times10^{-2}$ | $4.891\times10^{-2}$ |
| $B$ | $9.170\times10^{-11}$ | $5.913\times10^{-11}$ | $2.938\times10^{-11}$ | $9.088\times10^{-12}$ |
| $\rho_r$ | $3.725\times10^{2}$ | $3.510\times10^{2}$ | $3.014\times10^{2}$ | $1.863\times10^{2}$ |
| $\Delta_{AAD}$ / MPa | 0.016 | 0.010 | 0.006 | 0.066 |
| $\Delta_{AARD}$ ($p$) | 0.05% | 0.03% | 0.02% | 0.19% |

**Table C .11** Parameters of the Redlich-Kister correlation for the excess molar volume of $CO_2$ + methylbenzene.

| $T$ / K | $p$ / MPa | $A_1$ | $A_2$ | $A_3$ | AAD /cm$^3$·mol$^{-1}$ |
|---|---|---|---|---|---|
| 283.15 | 10 | -6.584 | -4.900 | -1.906 | 0.021 |
| 283.15 | 15 | -4.181 | -1.169 | -4.042 | 0.053 |
| 283.15 | 20 | -2.619 | 1.630 | -6.389 | 0.108 |
| 283.15 | 25 | -1.546 | 3.520 | -9.046 | 0.153 |
| 283.15 | 30 | -0.719 | 5.228 | -11.356 | 0.195 |
| 283.15 | 35 | -0.102 | 6.428 | -13.712 | 0.230 |
| 283.15 | 40 | 0.334 | 6.571 | -13.069 | 0.224 |
| 283.15 | 45 | 0.315 | 2.970 | -4.552 | 0.095 |
| 283.15 | 50 | 0.262 | -0.632 | 4.395 | 0.036 |
| 283.15 | 55 | 0.122 | -4.591 | 13.436 | 0.177 |
| 283.15 | 60 | -0.038 | -8.603 | 23.121 | 0.319 |
| 283.15 | 65 | -0.280 | -12.905 | 33.216 | 0.471 |
| 298.15 | 10 | -14.563 | -13.451 | -8.478 | 0.063 |
| 298.15 | 15 | -8.470 | -10.634 | -11.210 | 0.144 |
| 298.15 | 20 | -5.358 | -10.149 | -14.594 | 0.213 |
| 298.15 | 25 | -3.451 | -10.207 | -17.151 | 0.259 |

| $T$ / K | $p$ / MPa | $A_1$ | $A_2$ | $A_3$ | AAD /cm$^3$·mol$^{-1}$ |
|---|---|---|---|---|---|
| 298.15 | 30 | -2.094 | -10.326 | -19.370 | 0.296 |
| 298.15 | 35 | -1.130 | -10.578 | -21.101 | 0.323 |
| 298.15 | 40 | -0.512 | -9.404 | -19.252 | 0.297 |
| 298.15 | 45 | -0.481 | -4.016 | -7.161 | 0.111 |
| 298.15 | 50 | -0.543 | 1.688 | 5.677 | 0.083 |
| 298.15 | 55 | -0.770 | 7.875 | 19.815 | 0.297 |
| 298.15 | 60 | -1.131 | 14.802 | 35.827 | 0.541 |
| 298.15 | 65 | -1.685 | 23.188 | 55.415 | 0.838 |
| 323.15 | 10 | -130.740 | -148.843 | -108.058 | 0.964 |
| 323.15 | 15 | -26.430 | -32.866 | -34.523 | 0.379 |
| 323.15 | 20 | -14.548 | -21.970 | -28.410 | 0.376 |
| 323.15 | 25 | -9.313 | -18.489 | -28.139 | 0.404 |
| 323.15 | 30 | -6.222 | -16.923 | -28.958 | 0.431 |
| 323.15 | 35 | -4.246 | -16.122 | -29.794 | 0.451 |
| 323.15 | 40 | -2.961 | -13.876 | -26.390 | 0.405 |
| 323.15 | 45 | -2.566 | -6.433 | -10.200 | 0.159 |
| 323.15 | 50 | -2.465 | 1.349 | 7.072 | 0.102 |
| 323.15 | 55 | -2.632 | 9.892 | 26.447 | 0.395 |
| 323.15 | 60 | -3.038 | 19.885 | 49.537 | 0.745 |
| 323.15 | 65 | 22.110 | -13.525 | -51.553 | 1.225 |
| 348.15 | 15 | -84.030 | -82.833 | -50.611 | 0.448 |
| 348.15 | 20 | -36.013 | -33.819 | -23.673 | 0.173 |
| 348.15 | 25 | -21.547 | -17.608 | -9.442 | 0.068 |
| 348.15 | 30 | -14.645 | -10.593 | -3.721 | 0.024 |
| 348.15 | 35 | -10.603 | -7.169 | -1.661 | 0.013 |
| 348.15 | 40 | -7.961 | -4.902 | -0.117 | 0.000 |
| 348.15 | 45 | -6.096 | -3.591 | 0.400 | 0.003 |
| 348.15 | 50 | -4.749 | -2.522 | 1.072 | 0.008 |
| 348.15 | 55 | -3.700 | -1.926 | 1.110 | 0.010 |
| 348.15 | 60 | -2.884 | -1.364 | 1.418 | 0.011 |
| 348.15 | 65 | -2.226 | -0.900 | 1.556 | 0.015 |
| 373.15 | 20 | -70.140 | -59.214 | -28.060 | 0.252 |
| 373.15 | 25 | -39.217 | -33.587 | -20.495 | 0.142 |
| 373.15 | 30 | -25.442 | -19.336 | -9.063 | 0.063 |
| 373.15 | 35 | -17.935 | -12.585 | -4.381 | 0.034 |
| 373.15 | 40 | -13.231 | -8.543 | -1.808 | 0.016 |
| 373.15 | 45 | -10.156 | -6.116 | -0.483 | 0.007 |
| 373.15 | 50 | -7.930 | -4.485 | 0.486 | 0.000 |
| 373.15 | 55 | -6.283 | -3.373 | 0.842 | 0.001 |
| 373.15 | 60 | -5.041 | -2.527 | 1.185 | 0.006 |
| 373.15 | 65 | -4.048 | -1.885 | 1.521 | 0.009 |
| 398.15 | 20 | -103.3 | -89.871 | -54.311 | 0.247 |
| 398.15 | 25 | -60.386 | -49.778 | -28.605 | 0.166 |
| 398.15 | 30 | -38.894 | -29.528 | -14.509 | 0.095 |
| 398.15 | 35 | -27.063 | -18.956 | -7.4379 | 0.054 |
| 398.15 | 40 | -19.815 | -12.905 | -3.7552 | 0.036 |
| 398.15 | 45 | -15.096 | -9.163 | -1.431 | 0.019 |

| $T$ / K | $p$ / MPa | $A_1$ | $A_2$ | $A_3$ | AAD /cm$^3$·mol$^{-1}$ |
|---|---|---|---|---|---|
| 398.15 | 50 | -11.791 | -6.7084 | -0.1341 | 0.015 |
| 398.15 | 55 | -9.4095 | -5.0429 | 0.71338 | 0.009 |
| 398.15 | 60 | -7.6074 | -3.8001 | 1.19481 | 0.005 |
| 398.15 | 65 | -6.2017 | -2.8632 | 1.70734 | 0.001 |
| 423.15 | 20 | -130.89 | -92.083 | -30.719 | 0.150 |
| 423.15 | 25 | -80.351 | -58.427 | -25.84 | 0.053 |
| 423.15 | 30 | -52.722 | -37.62 | -17.607 | 0.087 |
| 423.15 | 35 | -36.887 | -24.457 | -9.2854 | 0.042 |
| 423.15 | 40 | -26.957 | -17.029 | -5.694 | 0.035 |
| 423.15 | 45 | -20.532 | -12.077 | -2.6504 | 0.013 |
| 423.15 | 50 | -15.994 | -8.8897 | -1.1369 | 0.012 |
| 423.15 | 55 | -12.748 | -6.6387 | -0.0179 | 0.002 |
| 423.15 | 60 | -10.333 | -5.068 | 0.62591 | 0.001 |
| 423.15 | 65 | -8.471 | -3.8164 | 1.2245 | 0.003 |
| 448.15 | 20 | -149.960 | -78.125 | 7.455 | 0.502 |
| 448.15 | 25 | -96.280 | -57.721 | -11.467 | 0.117 |
| 448.15 | 30 | -64.961 | -41.215 | -13.957 | 0.037 |
| 448.15 | 35 | -46.201 | -28.112 | -8.093 | 0.019 |
| 448.15 | 40 | -34.066 | -20.028 | -5.199 | 0.016 |
| 448.15 | 45 | -26.053 | -14.573 | -2.466 | 0.007 |
| 448.15 | 50 | -20.345 | -10.804 | -1.050 | 0.005 |
| 448.15 | 55 | -16.276 | -8.207 | 0.113 | 0.002 |
| 448.15 | 60 | -13.213 | -6.299 | 0.726 | 0.003 |
| 448.15 | 65 | -10.694 | -6.622 | -2.698 | 0.054 |
| 473.15 | 20 | -159.869 | -56.557 | 39.109 | 0.583 |
| 473.15 | 25 | -107.263 | -48.687 | 9.791 | 0.299 |
| 473.15 | 30 | -74.536 | -40.712 | -7.220 | 0.032 |
| 473.15 | 35 | -54.122 | -28.966 | -3.726 | 0.039 |
| 473.15 | 40 | -40.421 | -21.984 | -3.614 | 0.011 |
| 473.15 | 45 | -31.143 | -16.372 | -1.583 | 0.011 |
| 473.15 | 50 | -24.505 | -12.538 | -0.752 | 0.007 |
| 473.15 | 55 | -19.690 | -9.549 | 0.430 | 0.007 |
| 473.15 | 60 | -16.031 | -7.559 | 0.843 | 0.006 |
| 473.15 | 65 | -13.235 | -5.722 | 1.711 | 0.016 |

**Table C.12** Experimental speed-of-sound $c$ in $CO_2$ +methylbenzene at four compositions as a function of temperature and pressure, $T$: (283.15 to 473.15) K and $p$: (10 to 390) MPa.

| $p$ (MPa) | $c$ (m·s$^{-1}$) | $p$ (MPa) | $c$ (m·s$^{-1}$) | $p$ (MPa) | $c$ (m·s$^{-1}$) |
|---|---|---|---|---|---|
| | | **$x_{CO2}$ = 0.2014** | | | |
| | | $T$ = 283.15 K | | | |
| 10.69 | 1300.31 | 160.24 | 1804.71 | 320.03 | 2126.84 |
| 40.06 | 1437.73 | 199.93 | 1895.86 | 359.85 | 2193.11 |
| 80.03 | 1582.45 | 240.04 | 1979.28 | 390.00 | 2240.52 |
| 120.23 | 1701.81 | 280.20 | 2056.00 | | |

| $p$ (MPa) | $c$ (m·s$^{-1}$) | $p$ (MPa) | $c$ (m·s$^{-1}$) | $p$ (MPa) | $c$ (m·s$^{-1}$) |
|---|---|---|---|---|---|
| | | $T$ = 298.15 K | | | |
| 10.63 | 1243.44 | 160.08 | 1761.30 | 320.12 | 2090.72 |
| 40.21 | 1382.94 | 200.18 | 1855.16 | 360.00 | 2158.02 |
| 80.19 | 1532.43 | 240.24 | 1940.59 | 390.00 | 2206.02 |
| 120.11 | 1655.04 | 280.06 | 2018.28 | | |
| | | $T$ = 323.15 K | | | |
| 10.66 | 1138.19 | 160.20 | 1692.95 | 320.00 | 2033.50 |
| 39.96 | 1290.17 | 200.33 | 1791.34 | 359.92 | 2102.44 |
| 80.10 | 1451.37 | 240.06 | 1878.71 | 390.06 | 2151.67 |
| 120.09 | 1581.64 | 280.18 | 1959.50 | | |
| | | $T$ = 348.15 K | | | |
| 10.55 | 1035.13 | 160.19 | 1630.88 | 320.02 | 1980.79 |
| 40.12 | 1206.00 | 200.40 | 1731.79 | 359.65 | 2051.08 |
| 80.02 | 1377.30 | 240.19 | 1822.03 | 390.01 | 2101.65 |
| 120.49 | 1515.83 | 280.13 | 1904.79 | | |
| | | $T$ = 373.15 K | | | |
| 10.54 | 937.70 | 160.26 | 1572.76 | 320.23 | 1932.83 |
| 40.21 | 1126.53 | 199.91 | 1676.03 | 360.17 | 2004.70 |
| 80.07 | 1308.95 | 240.25 | 1770.18 | 390.04 | 2054.80 |
| 120.27 | 1452.76 | 280.13 | 1854.61 | | |
| | | $T$ = 398.15 K | | | |
| 10.41 | 840.87 | 160.1 | 1519.18 | 320.14 | 1887.69 |
| 40.15 | 1052.31 | 200.27 | 1626.65 | 360.21 | 1960.75 |
| 80.11 | 1245.73 | 240.19 | 1721.73 | 390.24 | 2012.78 |
| 119.97 | 1394.30 | 280.16 | 1808.24 | | |
| | | $T$ = 423.15 K | | | |
| 14.07 | 786.77 | 160.15 | 1470.21 | 320.21 | 1847.06 |
| 40.45 | 984.76 | 200.05 | 1580.24 | 359.82 | 1920.51 |
| 80.01 | 1186.97 | 240.16 | 1678.03 | 390.12 | 1972.05 |
| 120.01 | 1341.92 | 280.41 | 1766.62 | | |
| | | $T$ = 448.15 K | | | |
| 13.42 | 695.65 | 160.12 | 1424.93 | 320.06 | 1808.45 |
| 40.04 | 918.73 | 200.22 | 1537.77 | 360.10 | 1883.80 |
| 80.21 | 1134.66 | 240 | 1636.76 | 390.04 | 1935.48 |
| 119.95 | 1293.35 | 279.99 | 1726.41 | | |
| | | $T$ = 473.15 K | | | |
| 17.28 | 661.06 | 160.10 | 1383.46 | 320.26 | 1774.03 |
| 40.69 | 863.86 | 200.29 | 1498.90 | 360.17 | 1849.53 |
| 80.27 | 1085.67 | 240.10 | 1599.70 | 390.21 | 1902.76 |
| 120.06 | 1249.42 | 280.52 | 1691.55 | | |
| | | **$x_{CO2}$ = 0.3963** | | | |
| | | $T$ = 283.15 K | | | |
| 10.42 | 1168.40 | 160.06 | 1703.22 | 320.19 | 2031.26 |

| $p$ (MPa) | $c$ ($m \cdot s^{-1}$) | $p$ (MPa) | $c$ ($m \cdot s^{-1}$) | $p$ (MPa) | $c$ ($m \cdot s^{-1}$) |
|---|---|---|---|---|---|
| 40.05 | 1317.39 | 199.97 | 1797.42 | 360.09 | 2097.45 |
| 90.08 | 1505.75 | 240.27 | 1882.72 | 390.16 | 2144.68 |
| 120.15 | 1597.51 | 280.10 | 1959.56 | | |
| | | $T$ = 298.15 K | | | |
| 10.67 | 1097.06 | 160.55 | 1658.05 | 320.01 | 1988.34 |
| 40.16 | 1256.85 | 200.42 | 1752.64 | 359.97 | 2055.57 |
| 80.18 | 1419.09 | 240.06 | 1837.29 | 390.53 | 2104.28 |
| 119.93 | 1546.75 | 280.35 | 1916.41 | | |
| | | $T$ = 323.15 K | | | |
| 10.46 | 984.21 | 160.42 | 1596.00 | 319.94 | 1937.70 |
| 39.81 | 1163.31 | 200.48 | 1693.85 | 360.33 | 2008.30 |
| 80.17 | 1339.90 | 240.08 | 1781.69 | 390.06 | 2057.06 |
| 120.08 | 1477.02 | 280.10 | 1863.28 | | |
| | | $T$ = 348.15 K | | | |
| 14.60 | 912.63 | 160.26 | 1529.66 | 320.18 | 1886.41 |
| 40.27 | 1078.65 | 200.09 | 1633.07 | 360.44 | 1958.02 |
| 79.96 | 1264.01 | 240.19 | 1725.73 | 390.06 | 2007.43 |
| 120.04 | 1408.83 | 280.29 | 1809.66 | | |
| | | $T$ = 373.15 K | | | |
| 11.52 | 772.42 | 160.09 | 1471.38 | 320.29 | 1837.87 |
| 40.03 | 994.60 | 200.26 | 1578.61 | 360.19 | 1910.40 |
| 80.05 | 1195.88 | 240.04 | 1672.94 | 390.03 | 1959.68 |
| 119.97 | 1346.6 | 280.05 | 1758.70 | | |
| | | $T$ = 398.15 K | | | |
| 14.72 | 705.12 | 159.77 | 1416.15 | 320.22 | 1790.82 |
| 40.23 | 919.71 | 199.99 | 1526.66 | 360.09 | 1864.85 |
| 80.02 | 1132.21 | 240.09 | 1623.18 | 390.11 | 1914.08 |
| 120.51 | 1291.27 | 280.63 | 1711.69 | | |
| | | $T$ = 423.15 K | | | |
| 20.45 | 675.13 | 160.19 | 1368.02 | 320.12 | 1750.21 |
| 39.97 | 845.85 | 200.12 | 1480.73 | 360.03 | 1824.44 |
| 80.11 | 1073.29 | 240.57 | 1580.7 | 389.97 | 1876.43 |
| 120.07 | 1235.88 | 280.66 | 1669.98 | | |
| | | $T$ = 448.15 K | | | |
| 23.42 | 630.98 | 160.01 | 1323.16 | 320.17 | 1712.71 |
| 40.47 | 785.68 | 200.29 | 1438.89 | 360.05 | 1788.18 |
| 80.05 | 1020.24 | 240.58 | 1540.70 | 390.11 | 1840.69 |
| 120.67 | 1190.56 | 279.98 | 1629.92 | | |
| | | $T$ = 473.15 K | | | |
| 24.92 | 579.93 | 160.12 | 1283.14 | 320.36 | 1678.42 |
| 40.05 | 725.19 | 200.12 | 1400.32 | 360.09 | 1753.92 |
| 79.58 | 970.68 | 240.28 | 1502.76 | 389.76 | 1805.98 |
| 120.2 | 1145.9 | 280.07 | 1594.26 | | |

| $p$ (MPa) | $c$ (m·s$^{-1}$) | $p$ (MPa) | $c$ (m·s$^{-1}$) | $p$ (MPa) | $c$ (m·s$^{-1}$) |
|---|---|---|---|---|---|
| | | **$x_{CO2}$ = 0.6022** | | | |
| | | $T$ = 283.15 K | | | |
| 10.35 | 1002.42 | 160.05 | 1589.46 | 320.50 | 1921.91 |
| 39.89 | 1179.24 | 200.01 | 1685.32 | 360.14 | 1987.55 |
| 80.18 | 1348.35 | 240.23 | 1771.81 | 390.39 | 2035.23 |
| 120.56 | 1480.97 | 279.61 | 1848.34 | | |
| | | $T$ = 298.15 K | | | |
| 10.96 | 933.82 | 160.19 | 1547.12 | 319.61 | 1884.62 |
| 40.06 | 1119.93 | 200.49 | 1645.72 | 360.04 | 1953.09 |
| 80.00 | 1296.31 | 240.01 | 1732.36 | 390.14 | 2001.23 |
| 120.20 | 1433.66 | 280.16 | 1812.56 | | |
| | | $T$ = 323.15 K | | | |
| 14.06 | 833.83 | 160.18 | 1478.55 | 320.17 | 1829.54 |
| 40.74 | 1025.22 | 200.34 | 1581.67 | 360.06 | 1898.67 |
| 79.41 | 1211.37 | 240.31 | 1672.51 | 390.93 | 1949.40 |
| 120.43 | 1360.25 | 279.98 | 1753.93 | | |
| | | $T$ = 348.15 K | | | |
| 18.27 | 758.63 | 160.12 | 1416.95 | 320.27 | 1777.51 |
| 40.00 | 930.75 | 200.53 | 1523.36 | 359.91 | 1848.40 |
| 80.04 | 1139.49 | 240.02 | 1615.56 | 389.90 | 1898.58 |
| 120.27 | 1292.43 | 280.01 | 1699.89 | | |
| | | $T$ = 373.15 K | | | |
| 22.4 | 695.48 | 159.88 | 1358.01 | 320.03 | 1729.19 |
| 40.82 | 852.40 | 200.00 | 1467.95 | 360.24 | 1802.44 |
| 80.12 | 1070.85 | 239.98 | 1564.24 | 390.93 | 1854.60 |
| 120.56 | 1231.84 | 280.05 | 1650.65 | | |
| | | $T$ = 398.15 K | | | |
| 25.22 | 635.69 | 160.20 | 1307.66 | 320.06 | 1685.95 |
| 40.52 | 776.09 | 200.32 | 1420.03 | 359.93 | 1759.46 |
| 80.09 | 1010.15 | 240.07 | 1517.56 | 390.20 | 1810.02 |
| 120.04 | 1175.08 | 280.06 | 1605.82 | | |
| | | $T$ = 423.15 K | | | |
| 24.66 | 547.86 | 159.69 | 1259.32 | 320.11 | 1645.31 |
| 40.40 | 707.35 | 200.49 | 1376.03 | 359.98 | 1719.83 |
| 79.95 | 953.60 | 240.16 | 1475.32 | 390.13 | 1770.87 |
| 120.12 | 1125.21 | 280.39 | 1565.14 | | |
| | | $T$ = 448.15 K | | | |
| 40.12 | 645.31 | 200.27 | 1334.15 | 360.16 | 1683.65 |
| 80.07 | 903.43 | 240.12 | 1434.81 | 390.14 | 1736.87 |
| 120.31 | 1079.55 | 280.13 | 1525.79 | | |
| 160.01 | 1217.14 | 319.82 | 1607.69 | | |
| | | $T$ = 473.15 K | | | |
| 40.80 | 599.29 | 200.32 | 1296.75 | 360.20 | 1650.56 |

| $p$ (MPa) | $c$ (m·s$^{-1}$) | $p$ (MPa) | $c$ (m·s$^{-1}$) | $p$ (MPa) | $c$ (m·s$^{-1}$) |
|---|---|---|---|---|---|
| 80.22 | 859.77 | 239.98 | 1398.44 | 390.22 | 1703.33 |
| 119.99 | 1037.21 | 280.10 | 1490.96 | | |
| 160.31 | 1178.73 | 320.36 | 1574.97 | | |
| | | **$x_{CO2}$ = 0.7989** | | | |
| | | $T$ = 283.15 K | | | |
| 11.46 | 808.52 | 160.16 | 1452.92 | 320.02 | 1783.86 |
| 39.94 | 1019.52 | 200.34 | 1550.82 | 359.88 | 1849.04 |
| 79.92 | 1202.33 | 240.46 | 1636.43 | 390.03 | 1895.98 |
| 120.03 | 1339.76 | 280.02 | 1713.36 | | |
| | | $T$ = 298.15 K | | | |
| 12.72 | 745.70 | 160.28 | 1411.90 | 320.14 | 1748.87 |
| 40.12 | 958.74 | 200.05 | 1510.09 | 359.99 | 1815.42 |
| 80.15 | 1152.4 | 240.12 | 1597.68 | 389.86 | 1862.37 |
| 119.94 | 1293.73 | 280.53 | 1677.39 | | |
| | | $T$ = 323.15 K | | | |
| 15.04 | 625.88 | 160.08 | 1342.77 | 320.12 | 1693.89 |
| 40.30 | 858.07 | 199.86 | 1445.99 | 360.24 | 1762.50 |
| 80.46 | 1071.21 | 240.55 | 1538.83 | 389.11 | 1805.72 |
| 120.22 | 1221.00 | 280.01 | 1619.33 | | |
| | | $T$ = 348.15 K | | | |
| 18.82 | 546.46 | 160.00 | 1281.96 | 320.16 | 1643.46 |
| 40.08 | 765.66 | 200.28 | 1389.79 | 359.92 | 1713.05 |
| 80.06 | 996.47 | 240.09 | 1483.08 | 390.15 | 1762.70 |
| 120.05 | 1155.65 | 279.87 | 1566.64 | | |
| | | $T$ = 373.15 K | | | |
| 32.79 | 617.16 | 159.87 | 1226.57 | 320.14 | 1596.92 |
| 40.29 | 684.96 | 200.04 | 1337.24 | 359.35 | 1667.20 |
| 80.02 | 929.79 | 240.01 | 1433.15 | 389.67 | 1716.35 |
| 120.02 | 1096.26 | 279.92 | 1518.98 | | |
| | | $T$ = 398.15 K | | | |
| 39.98 | 611.74 | 200.40 | 1291.58 | 360.12 | 1626.45 |
| 79.97 | 871.27 | 240.47 | 1388.45 | 390.08 | 1676.21 |
| 120.32 | 1044.08 | 280.12 | 1474.91 | | |
| 160.3 | 1177.52 | 320.00 | 1553.88 | | |
| | | $T$ = 423.15 K | | | |
| 45.22 | 595.54 | 200.06 | 1247.10 | 360.15 | 1587.80 |
| 80.79 | 824.25 | 239.96 | 1345.58 | 369.78 | 1604.67 |
| 120.06 | 995.84 | 280.57 | 1435.25 | | |
| 160.36 | 1133.78 | 320.04 | 1514.34 | | |
| | | $T$ = 448.15 K | | | |
| 46.07 | 556.85 | 200.51 | 1209.18 | 360.21 | 1551.24 |
| 80.13 | 776.48 | 240.23 | 1308.42 | 378.65 | 1585.11 |
| 120.06 | 953.93 | 280.54 | 1398.56 | | |

| $p$ (MPa) | $c$ (m·s$^{-1}$) | $p$ (MPa) | $c$ (m·s$^{-1}$) | $p$ (MPa) | $c$ (m·s$^{-1}$) |
|---|---|---|---|---|---|
| 160.04 | 1092.00 | 320.07 | 1478.56 | | |
| | | $T$ = 473.15 K | | | |
| 61.57 | 632.64 | 200.01 | 1173.07 | 360.17 | 1520.31 |
| 80.65 | 741.58 | 240.78 | 1276.30 | 375.73 | 1546.51 |
| 120.22 | 917.74 | 280.13 | 1364.47 | | |
| 160.05 | 1056.57 | 320.11 | 1446.15 | | |

Standard uncertainties at 95 % confidence are $u(T)$ = 0.05 K and $u(p)$ = 50 kPa, $u(x) = 10^{-5}$ and $u_c(c) \sim 0.0004c$.

**Table C.13** Fitting parameters for the speed-of-sound correlation, Equations (6.7) and (6.8) for $CO_2$ + methylbenzene at four compositions. The average absolute relative deviations $\Delta_{AARD}$ are also provided.

| | | | | | | | | | |
|---|---|---|---|---|---|---|---|---|---|
| $x_{CO2}$ = 0.2 | $a_{10}$ | -4.106×10$^{-1}$ | $a_{20}$ | -2.778×10$^{-4}$ | $a_{30}$ | -8.834×10$^{-8}$ | $b_0$ | 2.784×10$^{3}$ | $\Delta_{AARD}$ = 0.04 % |
| | $a_{11}$ | 1.070 | $a_{21}$ | 1.062×10$^{-3}$ | $a_{31}$ | 4.662×10$^{-7}$ | $b_1$ | -1.927×10$^{3}$ | |
| | $a_{12}$ | -5.296×10$^{-1}$ | $a_{22}$ | -9.877×10$^{-4}$ | $a_{32}$ | -5.179×10$^{-7}$ | $b_2$ | 5.886×10$^{2}$ | |
| | $a_{13}$ | 4.376×10$^{-2}$ | $a_{23}$ | 4.043×10$^{-4}$ | $a_{33}$ | 1.718×10$^{-7}$ | $b_3$ | -1.568×10$^{2}$ | |
| $x_{CO2}$ = 0.4 | $a_{10}$ | -3.418×10$^{-1}$ | $a_{20}$ | -5.899×10$^{-4}$ | $a_{30}$ | -3.886×10$^{-7}$ | $b_0$ | 3.603×10$^{3}$ | $\Delta_{AARD}$ = 0.10 % |
| | $a_{11}$ | 7.568×10$^{-1}$ | $a_{21}$ | 1.809×10$^{-3}$ | $a_{31}$ | 1.831×10$^{-6}$ | $b_1$ | -4.094×10$^{3}$ | |
| | $a_{12}$ | -2.569×10$^{-1}$ | $a_{22}$ | -1.370×10$^{-3}$ | $a_{32}$ | -2.544×10$^{-6}$ | $b_2$ | 2.309×10$^{3}$ | |
| | $a_{13}$ | 1.003×10$^{-2}$ | $a_{23}$ | 3.259×10$^{-4}$ | $a_{33}$ | 1.158×10$^{-6}$ | $b_3$ | -6.339×10$^{2}$ | |
| $x_{CO2}$ = 0.6 | $a_{10}$ | 3.606 | $a_{20}$ | -4.109×10$^{-3}$ | $a_{30}$ | 2.916×10$^{-6}$ | $b_0$ | -2.885×10$^{3}$ | $\Delta_{AARD}$ = 0.25 % |
| | $a_{11}$ | -1.503×10 | $a_{21}$ | 1.697×10$^{-2}$ | $a_{31}$ | -1.204×10$^{-5}$ | $b_1$ | 1.113×10$^{4}$ | |
| | $a_{12}$ | 2.043×10 | $a_{22}$ | -2.281×10$^{-2}$ | $a_{32}$ | 1.656×10$^{-5}$ | $b_2$ | -9.665×10$^{3}$ | |
| | $a_{13}$ | -8.917 | $a_{23}$ | 1.023×10$^{-2}$ | $a_{33}$ | -7.458×10$^{-6}$ | $b_3$ | 2.446×10$^{3}$ | |
| $x_{CO2}$ = 0.8 | $a_{10}$ | 5.685 | $a_{20}$ | -6.978×10$^{-3}$ | $a_{30}$ | 5.574×10$^{-6}$ | $b_0$ | -2.394×10$^{3}$ | $\Delta_{AARD}$ = 0.57 % |
| | $a_{11}$ | -2.276×10 | $a_{21}$ | 2.946×10$^{-2}$ | $a_{31}$ | -2.306×10$^{-5}$ | $b_1$ | 1.015×10$^{4}$ | |
| | $a_{12}$ | 3.006×10 | $a_{22}$ | -4.046×10$^{-2}$ | $a_{32}$ | 3.160×10$^{-5}$ | $b_2$ | -9.382×10$^{3}$ | |
| | $a_{13}$ | -1.292×10 | $a_{23}$ | 1.833×10$^{-2}$ | $a_{33}$ | -1.418×10$^{-5}$ | $b_3$ | 2.547×10$^{3}$ | |